Springer Proceedings in Physics 151

Eric Beaurepaire
Hervé Bulou
Loic Joly
Fabrice Scheurer *Editors*

Magnetism and Synchrotron Radiation: Towards the Fourth Generation Light Sources

Proceedings of the 6th International School "Synchrotron Radiation and Magnetism", Mittelwihr (France), 2012

Springer

Springer Proceedings in Physics

Volume 151

For further volumes:
http://www.springer.com/series/361

Eric Beaurepaire · Hervé Bulou
Loic Joly · Fabrice Scheurer
Editors

Magnetism and Synchrotron Radiation: Towards the Fourth Generation Light Sources

Proceedings of the 6th International School "Synchrotron Radiation and Magnetism", Mittelwihr (France), 2012

Springer

Editors
Eric Beaurepaire
Hervé Bulou
Fabrice Scheurer
IPCMS
Université Strasbourg CNRS
Strasbourg
France

Loic Joly
IPCMS Department of Magnetic Objects
on the NanoScale
Université Strasbourg CNRS
Strasbourg Cedex 2
France

ISSN 0930-8989 ISSN 1867-4941 (electronic)
ISBN 978-3-319-03031-9 ISBN 978-3-319-03032-6 (eBook)
DOI 10.1007/978-3-319-03032-6
Springer Cham Heidelberg New York Dordrecht London

Library of Congress Control Number: 2013953223

Printed on acid-free paper

Springer is part of Springer Science+Business Media (www.springer.com)

Foreword

When the Editors asked me to write a foreword for these Lecture Notes, modesty suggested I should decline at the sight of the impressive list of internationally recognized expert contributors: the notes cover the 6th International School "Synchrotron Radiation and Magnetism", held in Mittelwihr (France) in the Autumn 2012. But my thoughts went back to the 1990's when it all started with the annual "Grand-Est" workshops of the "Institut de Physique et de Chimie des Matériaux de Strasbourg" (IPCMS) that boosted my involvement in spectroscopic studies of magnetism using synchrotron light and my participation, first as a novice, later as a lecturer, in the quadriennal series of these schools organized by the IPCMS. At the 4th school (2004), I, like the rest of the audience, was particularly impressed by François GAUTIER's lecture providing a fascinating, clear, and insightful picture of magnetism. Unfortunately his extensive responsibilities left him no room to write down a manuscript and we, the students, did not take the initiative of recording this highly pedagogical moment. His lecture contributed strongly to our enthusiasm for studying magnetism and convinced us that publishing lecture notes was an essential consolidation of the various view points brought to this field. That past frustration convinced me that this foreword was an opportunity to stress how important and timely this pedagogical book seems to me. It is a snapshot of both our present understanding of magnetism acquired via synchrotron radiation based techniques and a glimpse into the future as tools develop at more advanced light sources.

Magnetism is one of the most important physical effects in life as we know it. The Earth's magnetic field has probably been crucial to the appearance of Life on the Blue Planet: it avoids the erosion of our atmosphere by the solar

wind, and thus protects our biosphere. Magnetism has played a prominent role in the determination of the geography of our world thanks to the use of the "magnetic" compass as a navigational instrument at the beginning of the XIth century. Today we can hardly imagine living without electricity produced by the conversion of mechanical energy using magnets. Magnetic effects are at the forefront of modern electronics involving research into the size and speed limits inherent in the manipulation of magnetization and the development of spintronics, i.e., the use of both the charge and the spin information carried by the electron. This is where spectroscopic tools using synchrotron radiation come into play.

Synchrotron radiation is the light emitted by relativistic charged particles moving along a curved trajectory. Considered by nuclear physicists as a nuisance because responsible of particle energy loss, it was recognized in the 1960's as a light source of tremendous interest for spectroscopy. Under the impulse of Yvette CAUCHOIS, head at this time of the "Laboratoire de Chimie Physique de la Faculté des Sciences de Paris", the first spectroscopic experiments in Europe using the orbit radiation of the Frascati synchrotron were done, in collaboration with the "Istituto Superiore di Sanità" (Rome). The new physics that can be explored using the unique properties of synchrotron radiation, namely continuous spectral range from the infrared to the x-rays, high intensity, angular collimation, polarization, and pulsed structure, attracted an ever-growing scientific community and led in the 1970's to the building of storage rings dedicated to the sole production of "synchrotron" light (called second generation synchrotron radiation sources). The next step has been, as in the current (third-generation) synchrotron radiation sources, to increase their brightness and obtain full control of the polarisation of the light. Now efforts are made to develop fourth-generation light sources: x-ray free-electron lasers.

The first experimental evidence that light and electromagnetism were linked was given by FARADAY (1845) and KERR (1875) who observed a rotation of the plane of polarization of visible light either transmitted or reflected by a magnetic system. Synchrotron light being naturally polarized, it was tempting to extend magneto-optics to the x-ray range. Strong magneto-optical effects were indeed theoretically predicted (1975) and experimentally observed (1987). This discovery of magnetic dichroism in x-ray absorption has made a great impact on the understanding of magnetic interactions in matter because it opens the way to element- and orbital-specific investigations. The technique soon became a standard probe of magnetic properties as, via the "sum rules" (1992-3), it allows the determination of elemental orbital

and spin magnetic moments. It turns out that x-ray magnetic dichroism is a facet of related x-ray magneto-optical effects such as x-ray resonant magnetic scattering, magnetodichroic x-ray/electron (micro-)spectroscopies and x-ray holography, to cite a few, that are now classical characterization tools of magnetic (nano-)objects.

Thus 2012 was the Silver Wedding Anniversary between synchrotron radiation and magnetism. There is no doubt that in the coming years this partnership will give birth to interesting "new offspring" in the exploration of magnetism at large light source facilities, in particular at lower length scales (< 10 nm) and shorter time scales (< 100 fs).

This book is a fitful celebration of this anniversary because it is an illustration of the progress made in the physics of magnetic materials by closely coupling synchrotron radiation and magnetism and forms an excellent textbook on magnetism and spectroscopy with synchrotron radiation, including the presentation of new hot topics and perspectives in x-ray radiography of magnetism.

I would like to underline that the contributors, all leaders in the field, have made a remarkable pedagogical effort.

Paris, Trieste, March 2013 *Jean-Michel Mariot*

Preface

This volume contains the lecture notes of the fifth school on Magnetism and Synchrotron Radiation held in *Mittelwihr*, France, from 14 to 19 October 2012.

Twenty three years ago, in March 1989, was held the first edition of this school, which ended by a one-day international Workshop. The elder ones of us vividly remember the talk given in this workshop by G. Schütz, who presented the first x-ray magnetic circular dichroism results obtained two years earlier. This discovery was important enough to open new perspectives in the study of magnetism, which kept on feeding the school with new topics for the following 25 years.

We would like to thank all the teachers for the interesting and very much appreciated lectures they gave and for animating the practicals of this school, as well as the members of the scientific committee for their help in establishing the school program (see lists next pages). We are very grateful to J.-M. Mariot, a long-date supporter who kindly accepted to write the foreword of this book.

The success of this school is also due to the hard work of our colleagues from the local organization committee, J.-L. Bubendorff (LPSE, Mulhouse), F. Gautier, V. Wernher and S. Cherifi (IPCMS). Particular thanks go to J.-P. Kappler, one of the main and early initiators of this exciting adventure, and faithfull organizer since 1989. Thank you for pushing us to make this school live further.

Last but not least, it is a great pleasure to acknowledge the kind hospitality of the *Centre de Mittelwihr* and the *Communauté des Communes de Ribeauvillé* which have been welcoming us since 1989.

This school would not have been possible without financial support by following institutions and companies, which we gratefully acknowledge:

- Formation Permanente du CNRS
- Université de Haute Alsace
- Région Alsace
- Conseil Général du Haut-Rhin
- Institut de Physique et Chimie des Matériaux de Strasbourg
- Synchrotron SOLEIL, St Aubin
- ALTEC Equipment
- SPECS
- VAT

Strasbourg, May 2013

E. Beaurepaire
H. Bulou
L. Joly
F. Scheurer

Teachers

M. ALTARELLI	(European XFEL, Hambourg, Germany)
U. BOVENSIEPEN	(Universität Duisburg-Essen, Germany)
S.G. CHIUZBĂIAN	(LCPMR, Paris, France)
M.-E COUPRIE	(Synchrotron SOLEIL, Gif-sur-Yvette, France)
P. FISCHER	(LBNL, Berkeley, United States)
A. FOGNINI	(ETH Zürich, Switzerland)
R. HERTEL	(IPCMS, Strasbourg, France)
P. HOFMANN	(Aarhus University, Aahrus, Denmark)
P. OHRESSER	(Synchrotron SOLEIL, Gif-sur-Yvette, France)
B. PFAU	(Helmholtz Zentrum Berlin-Bessy, Germany)
N. JAOUEN	(Synchrotron SOLEIL, Gif-sur-Yvette, France)
A. JUHIN	(IMPMC, Paris, France)
P. KRÜGER	(Université de Bourgogne, Dijon, France)
A. ROGALEV	(ESRF, Grenoble, France)
P. SAINCTAVIT	(CNRS, IMPMC, Paris, France)
R.L. STAMPS	(University of Glasgow, United Kingdom)
G. VAN DER LAAN	(Diamond Light Source, Didcot, United Kingdom)
C. VETTIER	(ESRF, Grenoble, France)

Scientific Committee

M. ALTARELLI	(European XFEL, Hambourg, France)
M. BOWEN	(IPCMS, Strasbourg, France)
D. CHANDESRIS	(LPS, Orsay, France)
P. CRESPO	(UCM, Madrid, Spain)
K. DUMESNIL	(IJL, Nancy, France)
V. DUPUIS	(ILM, Lyon, France)
P. GAMBARDELLA	(ALBA, Barcelona, Spain)
G. VAN DER LAAN	(Diamond Light Source, Didcot, UK)
J.-M. MARIOT	(LCPMR, Paris, France)
F. PETROFF	(CNRS-THALES, Palaiseau, France)
A. ROGALEV	(ESRF, Grenoble, France)
M. SACCHI	(Synchrotron SOLEIL, Gif sur Yvette, France)
A. SCHUHL	(Institut Néel, Grenoble, France)
C. STAMM	(Helmholtz Zentrum Berlin-Bessy, Germany)
U. STAUB	(SLS, Villigen, Switzerland)
M. ZACCHIGNA	(ELETTRA, Trieste, Italy)

Contents

Chapter 1
Magnetism

Robert L. Stamps

Abstract A summary of concepts and ideas useful for an understanding of measurable phenomena in thin film and nanostructured magnetic materials is presented. Beginning with the base definitions of magnetic moment and its relation to angular momentum, mechanisms are discussed for long range ordering based on electronic orbital overlap in insulators, and electronic band structure in metals. The nature of excitations about this ground state are also discussed, and how these can be understood by analogy to the quanta of harmonic oscillations associated with vibrations in crystals. A phenomenological model of magnetic ordering and excitations is also described, and key parameters defined in terms of symmetries allowed by the local atomic environment. Lastly, a thermodynamic view of magnetic states and configurations is summarised, and here the focus is on mechanisms for magnetic reversal and coercivity and the concepts of magnetic domain walls and domain wall mobilities are discussed.

1.1 Introduction

In this chapter we will examine magnetic phenomena arising in materials. This is a remakably rich field not only at present, but also in the past. Indeed,

Robert L. Stamps
SUPA School of Physics and Astronomy, University of Glasgow, e-mail: robert.stamps@glasgow.ac.uk

E. Beaurepaire et al. (eds.), *Magnetism and Synchrotron Radiation: Towards the Fourth Generation Light Sources*, Springer Proceedings in Physics 151,
DOI: 10.1007/978-3-319-03032-6_1,

William Gilbert produced one of the first great works in modern science– perhaps the first– with his book *De Magnete*. Gilbert based *De Magnete* on work he began in 1581 that some historians suggest marked the invention of the modern scientific process of experiment and hypothesis. Moreover, Gilbert recognised and noted numerous possibilities for application of magnetic materials in navigation (and also mining and military technologies). This recognition of the practical benefits that can follow from scientific research is something that permeates the field of magnetism, and continues on today.

Modern applications are fascinating because of their diversity, important because of the key technological advances they underpin, and interesting because of close linkages to fundamental problems in condensed matter research. Examples include:

- Permanent magnets: used in motors and activators, an important current materials problem is to produce low cost "super-magnets" for alternative energy production schemes;
- High density data storage and digital logic circuits: magnetic grains are used to store information, and collections of patterned, interacting magnetic particles have been proposed as basic elements in low power consumption logic circuits that can in principle approach the Landauer efficiency limit;
- Magnetic based spintronics: The Nobel Prize in 2007 was awarded in recognition of the discovery and application of ultra-sensitive magnetoresistive devices that utilise the spin dependent scattering that can exist at metallic magnetic interfaces (and which have enabled modern high density hard disk drive technologies;
- Microwave device applications: electromagnetic properties of some magnetic materials have been used for signal processing since the early days of radar, and new discoveries of how voltages and charge currents interact with magnetic moments enable entirely new types of microwave devices.

The field of magnetism is characterized by scientific research and technical applications progressing jointly. Many of recent developments will be mentioned in what follows, but the main purpose of this chapter is to provide an introduction to the essential concepts and principles underlying our understanding and descriptions of the wide variety of phenomena studied in magnetic materials. To begin, the fundamental origins of magnetic moments are discussed, along with the physical processes resulting in their possible long range orderings. Fundamental excitations and different types of dynamics exhibited by magnetic spin systems are then discussed.

Lastly, a comment on referencing is in order. This is a brief introductory summary of a large body of knowledge. A full listing of all the fine works existing would be well outside the scope of this article, and instead only a small handful of references have been included. These either reference directly research results reproduced here, or point the reader for further information to examples of relevant texts and monographs.

1.2 Magnetization and Long Range Ordering

We will be concerned exclusively with magnetic properties asociated with electrons in a material. For the most part in fact, we are concerned specifically with how a material responds magnetically to an applied magnetic field.

1.2.1 Magnetic Moment

Before talking about atoms and materials, let us first consider the behaviour of a free electron in a magnetic field $\mathbf{H} = \mathbf{B}/\mu_o$ (where $\mathbf{B}$ is the magnetic induction and μ_o is the permeability of vacuum). An electron will rotate through a circular orbit centered on $\mathbf{H}$, with frequency $\omega_c = eH/m$ where e is the charge and m is the mass of the electron. A rotating electron defines a loop of current I that encloses a circular area A. The associated magnetic moment is $\mu = IA$. Writing the current in terms of ω_c and using $A = \pi r^2$, where r is the radius of the loop, the magnetic moment is

$$\mu = -\frac{\mu_o e^2 H}{2m} r^2 \,. \tag{1.1}$$

Note that we have neglected the intrinsic spin of the electron, and will discuss this later. From this circulation of charge, we can make an important connection between magnetic moment and angular momentum. The angular momentum $\mathbf{L}$ of the circulating electron has magnitude $L = mrv$ where v is the tangential speed defined in terms of frequency as $\omega_c = v/2\pi r$. Using this with (1.1), we arrive at

$$\mu = -\frac{e}{2m}\mathbf{L} \,, \tag{1.2}$$

thereby illustrating that the magnitude of the magnetic moment is proportional to the angular momentum, and oriented oppositely.

With this in mind, we now consider the magnetic moment of electrons in atomic orbitals. Suppose that there is no field and the orbital is that of a simple Bohr model with $L = m_l\hbar$, where m_l is the Bohr angular momentum quantum number. Neglecting spin, we now expect that for $m_l = 1$,

$$\mu = \mu_B = -\frac{e\hbar}{2m} , \tag{1.3}$$

which is called the Bohr magneton.

What now is the effect of an applied magnetic field H? In the frame of reference of the electron, it turns out that H has no effect at least to first order in perturbation theory. Therefore if H is not too large, the energy is simply shifted by the amount $\hbar\omega_L$, where ω_L is the rotation frequency of the electron.

It is interesting to note that $\omega_L \neq \omega_c$. This can be seen by examining the dynamics of the atomic moment when in the presence of a field H. In order to do this, we first recall the energy and equations of motion for a moment in a magnetic field. The energy is defined as

$$E = -\mu_o \mu \cdot \mathbf{H} , \tag{1.4}$$

and the precession of angular momentum is described by the torque Γ experienced by the magnetic moment

$$\Gamma = \frac{\mathrm{d}\mathbf{L}}{\mathrm{d}t} = \mu_o \mu \times \mathbf{H} = \mu \times \mathbf{B} . \tag{1.5}$$

Placing $\mathbf{H}$ along the z direction, and assuming $\mathbf{L} = a(\hat{x} + \mathrm{i}\hat{y})\exp(-\mathrm{i}\omega_L t) + \hat{z}$, one finds the Larmor frequency

$$\omega_L = \frac{\mu_B}{\hbar} . \tag{1.6}$$

The Larmor frequency characterizes the precession of μ locally around a field $\mathbf{H}$.

The above considerations apply for multi-electron atoms, however we should at this point take electron spin $\mathbf{S}$ into account. In this case we consider the total angular momentum $\mathbf{J} = \mathbf{L} + \mathbf{S}$, so that there are two contributions to the angular momentum and correspondingly two contributions to the magnetic moment. Denoting these μ_S and μ_L, the total moment is now $\mu = \mu_L + \mu_S$, with magnitude

$$\mu = g\mu_B \sqrt{j(j+1)}\,, \tag{1.7}$$

where j is the angular momentum quantum number. The g-factor is defined by the total, orbital, and spin quantum numbers j, l, and s as

$$g = 1 + \frac{j(j+1)+s(s+1)-l(l+1)}{2j(j+1)}\,. \tag{1.8}$$

The gyromagnetic ratio $\gamma = -g\mu_B/\hbar$ determines the ratio of magnetic moment to angular momentum via $\mu = \hbar\gamma J$. Note that the total moment μ is generally not in the direction of $\mathbf{J}$.

1.2.2 Mechanisms for Exchange

In some materials, strong correlations between magnetic moments exist that give rise to long range ordering and thermodynamic phases. The energy associated with these correlations can arise from different mechanisms. The largest of these energies are associated with the Coulomb interaction, and are often referred to as "exchange energies". Before discussing mechanisms for exchange, it is useful to review the relevant energy scales in matter. Following Anderson and Mattis, [1] we summarize some key energy scales in Table 1.1.

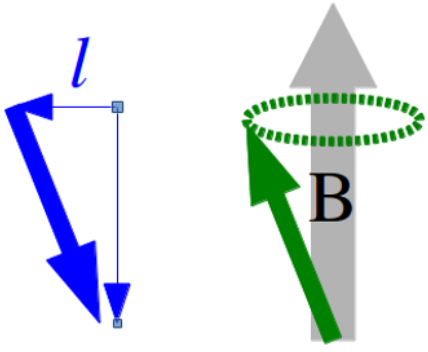

Fig. 1.1 Illustration of precession of an orbital magnetic moment. The angular momentum is oriented opposite to the moment, and the transverse component rotates about axis defined by the local field

Table 1.1 Relevant energy scales for materials, as tabulated by P. W. Anderson

Energy Range (eV)	Mechanisms
$1-10$	Atomic Coulomb integrals; Electronic band widths; Energy/state at ε_F
$0.1-1.0$	Crystal field splitting
$10^{-2}-10^{-1}$	Spin-orbit coupling; $k_B T_C$ or $k_B T_N$
10^{-4}	Magnetic spin-spin coupling; Interaction of a spin with a 1 T field
$10^{-6}-10^{-5}$	Hyperfine electron-nuclear coupling

The Coulombic interaction is the most important for correlating individual magnetic moments, however quantum mechanical effects must be taken into account. In particular, the correlation energy for insulators is determined by overlap of atomic orbitals and these are strongly dependent on the spin state of electrons occupying the orbitals. As we will see, this provides an important insight into the nature of magnetic ordering via exchange.

We can appreciate the strength of the interaction by the following qualitative argument. Pauli exclusion acts to separate electrons in the same spin state. Suppose two electrons are in orbitals on neighbouring atoms. Further suppose that their average separation with antiparallel spins is 0.3 nm, whereas with parallel spins the average separation changes to 0.31 nm. The corresponding change in Coulombic energy is $\Delta E = 0.05$ eV. In units of temperature, this is 580 K. The equivalent field is $\Delta E/\mu_B = 870$ T.

A great insight into how to think about exchange can be obtained by calculating more precisely the exchange energy of overlapping orbitals on neighbouring atoms. A simple model is represented by the following hamiltonian for two nuclear cores (located at positions $\mathbf{R}_a$ and $\mathbf{R}_b$) and two electrons (located at positions $\mathbf{r}_1$ and $\mathbf{r}_2$ defined relative to an atomic core)

Fig. 1.2 Sketch of two orbitals and the average distance for two different spin orderings

$$H = \frac{p_1^2}{2m} + \frac{p_1^2}{2m} + \frac{e^2}{|\mathbf{R}_a - \mathbf{R}_b|} - \frac{e^2}{|\mathbf{r}_1|} - \frac{e^2}{|\mathbf{r}_2|} + \frac{e^2}{|\mathbf{r}_1 - \mathbf{r}_2|} \,. \tag{1.9}$$

The first two terms represent the electron kinetic energies, the third term is the repulsion between cores, the fourth and fifth term is the interaction between the electrons and their respective cores, and the last term is the electron-electron repulsion. The two electron problem can be solved in terms of product orbitals, defined as the two possible orbital occupations of the electrons

$$\Psi_I = \psi_a(\mathbf{r}_1)\psi_b(\mathbf{r}_2) \tag{1.10}$$
$$\Psi_{II} = \psi_a(\mathbf{r}_2)\psi_b(\mathbf{r}_1) \,. \tag{1.11}$$

The two electron wavefunction is a linear combination of these two orbitals

$$\Psi = c_I \Psi_I + c_{II} \Psi_{II} \,. \tag{1.12}$$

Substitution into the hamiltonian of (1.9) allows us to solve for energies and coefficients. Two cases result: a symmetric ($c_I = c_{II}$) and an antisymmetric ($c_I = -c_{II}$) one. The energy of the symmetric case is

$$E_+ = 2E + \frac{V+U}{1+l^2} \,, \tag{1.13}$$

and the antisymmetric case is

$$E_- = 2E + \frac{V-U}{1-l^2} \,. \tag{1.14}$$

The overlap integrals appearing in these energies are

$$V = \int\int \Psi_{I,II}^2 e^2 \left(\frac{e^2}{|\mathbf{R}_a - \mathbf{R}_b|} - \frac{e^2}{|\mathbf{r}_1|} - \frac{e^2}{|\mathbf{r}_2|} + \frac{e^2}{|\mathbf{r}_1 - \mathbf{r}_2|} \right) \mathrm{d}\mathbf{r}_1 \mathrm{d}\mathbf{r}_2 \tag{1.15}$$
$$U = \int\int \Psi_I^* \Psi_{II} e^2 \left(\frac{e^2}{|\mathbf{R}_a - \mathbf{R}_b|} - \frac{e^2}{|\mathbf{r}_1|} - \frac{e^2}{|\mathbf{r}_2|} + \frac{e^2}{|\mathbf{r}_1 - \mathbf{r}_2|} \right) \mathrm{d}\mathbf{r}_1 \mathrm{d}\mathbf{r}_2 \tag{1.16}$$
$$l = \int \psi_a(\mathbf{r})^* \psi_b(\mathbf{r}) \mathrm{d}\mathbf{r} \tag{1.17}$$

The exchange energy J_{ex} corresponds to the difference

$$J_{ex} = E_- - E_+ \sim U l^2 - V \,. \tag{1.18}$$

This is called "exchange" because the symmetric and antisymmetric cases are tied to the requirement of antisymmetric symmetry imposed by Pauli exclusion. The total wavefunction for the two electrons must be antisymmetric. This is accomplished by a product of a symmetric spatial wavefunction with an antisymmetric spin function, or the product of an antisymmetric spatial wavefunction with a symmetric spin function. Note that the antisymmetric spin function has spin zero, whereas the symmetric spin function can have spin $-1, 0$ or 1.

The magnitude of the energy J_{ex} is determined by the Coulomb interaction, and can be indexed to the possible spin states of the two electrons. This feature was noticed independently by Dirac and Heisenberg, who then established that a basis of spin functions could be used to produce the same energy eigenvalues. This allows one to rewrite the hamiltonian in terms of Pauli spin operators: i.e., $H = -J_{ex}\sigma_1 \cdot \sigma_2$. A number of authors, including van Vleck, extended this idea to multi-electron orbitals, producing what is now often called, the exchange hamiltonian

$$H_{ex} = -\sum_{i,j} J_{ex}(\mathbf{r}_i - \mathbf{r}_j)\mathbf{S}(\mathbf{r}_i) \cdot \mathbf{S}(\mathbf{r}_j) \, . \tag{1.19}$$

There are many issues involved with creating a theory for the exchange integral $J_{ex}(\mathbf{r}_i - \mathbf{r}_j)$ for a many atom system. Methods based on perturbation theory have been successful in estimating J_{ex} for many insulating magnets. More details and links to original literature can be found in many standard texts, including [1], [2], and [3]. The problem of constructing an analogous picture for conducting magnets will be discussed later.

We conclude this session by commenting on the sign and range of J_{ex}. The sign can be either positive or negative, depending upon details of the specific overlap integrals. The convention is usually that positive exchange leads to parallel ordering of magnetic moments (ferromagnetism) and negative exchange leads to antiparallel ordering (antiferromagnetism). In many compounds, magnetic ions sit in inequivalent sites with different valences, and can have differently sized magnetic moments. When these order antiferromagnetically, there can still be a residual magnetic moment. These orderings are called ferrimagnetic . Examples are sketched in Fig. 1.3.

In such materials, exchange is mediated by hopping of electrons through orbitals on neighbouring, non-magnetic atoms such as oxygen or fluoride. In these cases additional considerations enter concerning the occupancy and

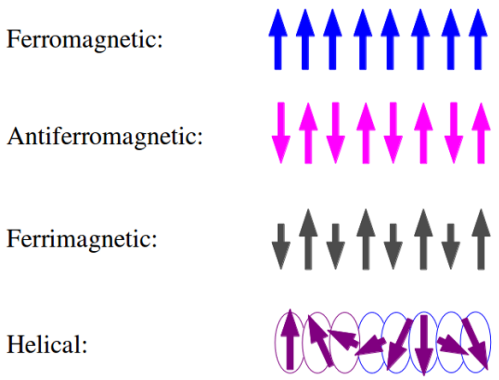

Fig. 1.3 Sketches of four different types of magnetic orderings: parallel (ferromagnetic), antiparallel (antiferromagnetic and ferrimagnetic), and non-colinear (helical in this case)

geometry of multielectron orbitals. The results describe mechanisms for exchange that include what are called "super" and "double" exchange.

Interactions between magnetic atoms beyond nearest neighbour can be signficant. Depending on the geometry, it is possible to have competing ferro- and antiferromagnetic interactions. This can lead to non-colinear orderings, such as the helical ordering depicted in Fig. 1.3. In some cases of particularly low symmetry, it is possible to have interactions that are described by exchange energies of the form $\mathbf{D} \cdot \mathbf{S}_1 \times \mathbf{S}_2$, where $\mathbf{D}$ is a vector that may describe, for example, distortions of the crystal lattice associated with strain fields. This form often appears in descriptions of magnetoelectric effects.

1.3 Response to Applied Magnetic Fields

Experimental studies of magnetic phenomena are quite often made through measurement of response to magnetic fields. There are a number of aspects to this, and we will begin by defining the magnetic susceptibility and how it varies with temperature.

1.3.1 Magnetic Susceptibility

Measurement of macroscopic samples usually involves some sort of averaging over atomic moments. Because of this, it is useful to define a magnetic moment per volume V, called the "magnetization" M

$$\mathbf{M} = \frac{1}{V}\sum_i \mu_i \,. \tag{1.20}$$

The linear response to a magnetic field H is characterized by a susceptibility χ

$$\mathbf{M} = \chi \mathbf{H} \,. \tag{1.21}$$

In general χ is a tensor, but we consider here only the simpler case of an isotropic magnetic system such that the magnetization responds in a direction defined by the orientation of the applied field. This can be along the field direction, or opposite. We consider first the case of non-interacting moments. If the response is in the direction of the magnetic field, it is called "paramagnetic". Example materials include rare earth ions and alkali metals, and typical values range from 10^{-2} to 10^{-4} per mole. If the response is opposite to that of the applied field, the response is called "diamagnetic". Electrons in nearly all materials have some sort of diamagnetic response, and typical values are on the order of -1.0×10^{-6} per mole.

1.3.1.1 Langevin Diamagnetism

The Langevin picture of diamagnetism follows directly from our Bohr orbital model discussed earlier in relation to the Larmor frequency. Using the Larmor frequency $\omega_L = \mu_o He/(2m)$, we can write (following Kittel [4])

$$\mu = I\pi r^2 = \left(-\frac{e\omega_L}{2\pi}\right)\pi r^2 = -\frac{e^2\mu_o H}{4m}r^2 \,. \tag{1.22}$$

We can generalise this to a multi-electron Bohr atom by noting that orbits can occur in any plane, so that the projection of an orbit onto a plane perpendicular to the field $\mathbf{H}$ is on average $2/3$ of the Bohr radius $\sqrt{x^2+y^2+z^2}$. Additionally, the moment scales with the number of contributing electrons Z. The diamagnetic moment then becomes

$$\mu = -\frac{Ze^2\mu_o}{6m}H\langle r^2\rangle \tag{1.23}$$

so that the susceptibility is $\chi_{dia} = -Ze^2\mu_o\langle r^2\rangle/(6m)$. This is negative so that application of an external field induces a moment opposite the field direction.

1.3.1.2 Paramagnetic Suceptibility

Paramagnetism can occur in atoms and molecules with an odd number of electrons so that the total electronic spin is not zero. Defects in crystals can also support such states. Likewise, free atoms and ions with partly filled inner shells can support uncompensated spin. Examples include Mn^{2+} and Gd^{3+} . In some cases solids constructed from such ions will be paramagnetic. We will also see that paramagnetism can appear over restricted temperature ranges in some materials. Finally, we will later mention superparamagnetism where nanoscopic dimensions lead to paramagnetic behaviour.

One obvious example of this is hydrogen. Hydrogen atoms have spin $1/2$ and no orbital moment in the ground state. In this case $J = S$ and $E = -\mu_o\mu H = -\mu_o\mu_B H$ since $g \approx 2$ and $S = 1/2$. Writing $B = \mu_B|H|$, the energy is $E = \mp\mu_B B$, where the minus sign applies when the moment is parallel to H, and the plus sign applies when the moment is antiparallel to H.

We next consider what happens at finite temperatures. When $B = 0$, the number of up spins and down spins should be equal since "up" and "down" are arbitrary. This should also be true at high temperatures even with non-zero field if $k_B T \gg |E|$. However at low temperatures with finite field, one expects more spin up than spin down since the up state is energetically favored. As a function of field, we expect that at low temperatures the populations of up spins will saturate as the field strength is increased, and the population of down spins will tend to zero.

We can make these considerations precise by calculating the fractions of up and down spins according to Boltzman statistics. The fraction $N_\uparrow$ of N spins should be proportional to the thermal probability to be in the $E < 0$ state

$$\frac{N_\uparrow}{N} = \frac{1}{Z}\mathrm{e}^{+\frac{\mu_B}{k_B T}} , \tag{1.24}$$

where Z is a constant for normalization. The fraction of down spins, $N_\downarrow$, should go as

$$\frac{N_\downarrow}{N} = \frac{1}{Z} e^{-\frac{\mu_B}{k_B T}} . \tag{1.25}$$

Normalization gives Z as

$$Z = e^{\frac{\mu_B}{k_B T}} + e^{-\frac{\mu_B}{k_B T}} . \tag{1.26}$$

The difference in populations is the average magnetic moment

$$\langle \mu \rangle = \mu_B N \tanh\left(\frac{\mu_B B}{k_B T}\right) . \tag{1.27}$$

For $B = 0$, this gives zero moment at any temperature, as expected. For large T, the lowest order term is linear in B and one has

$$\langle \mu \rangle = \mu_B N \frac{\mu_B B}{k_B T} \tag{1.28}$$

so that the susceptibility is

$$\chi_{para} = \frac{\langle \mu \rangle}{B} = \frac{\mu_B^2 N}{k_B T} . \tag{1.29}$$

The inverse dependence on temperature is the Curie Law: $\chi_{para} = C/T$ where C is the Curie constant. This is a useful experimental parameter to measure, and the inverse is usually plotted as a function of temperature, allowing the Curie constant to be determined from the slope.

The above equations for χ_{para} are valid for spin $1/2$. Generalisation to arbitrary angular momentum J is straightforward. A higher value of J corresponds to more possible angular momentum states, and the thermal average needs to account for these different possible values. The average moment is then defined as

$$\langle \mu \rangle = \frac{1}{Z_J} \left(\sum_j e^{\mu_B j B} - \sum_j e^{-\mu_B j B} \right) . \tag{1.30}$$

The sum and normalization factor can be worked out, and the result is

$$\langle \mu \rangle = N g J \mu_B B_J \left(\frac{g J \mu_B}{k_B T}\right) , \tag{1.31}$$

where $B_J(x)$ is the Brillouin function, and defined by

$$B_J(x) = \frac{2J+1}{2J}\coth\left(\frac{2J+1}{2J}x\right) - \frac{1}{2J}\coth\left(\frac{x}{2J}\right) . \tag{1.32}$$

The first term in an expansion of 1.32 for small x is linear in $1/T$, consistent with the Curie Law. It is useful to note that values of C will depend very much upon the relative contributions of the spin and orbital components of the magnetic moment. In materials this will involve details of how the spin and orbital angular momenta couple. An extended tutorial discussion can be found in [5].

1.3.1.3 Paramagnetism of Metals

Experimentally, metals show a weak paramagnetic response. This is not what one expects from classical arguments such as those discussed in the previous section. Instead for metals one finds that the paramagnetic susceptibility is roughly independent of temperature. This turns out to be another consequence of Pauli excusion and spin, and can be understood as follows.

The important electron states in a metal are those near the Fermi energy ε_F . In terms of the number, or density, of states at energy ε one can expect a density of states $D(\varepsilon)$ to be roughly of the form shown in Fig. 1.4. The left panel shows the spin up and down density of states without an applied field, and the panel on the right shows the state densities with an applied field. A non-zero applied field favours magnetic moments that are parallel to the field direction, and so lowers the electronic energies of the spin down electrons. Likewise, the electronic energies of up spin electrons is increased.

The shift in energy per spin is $\pm\mu_B B$, leading to an imbalance of numbers between spin up and spin down states that lie beneath the Fermi energy. This corresponds to an overall magnetic moment that is approximately given by

$$\langle\mu\rangle = \frac{1}{2}g\mu_B\left(D(\varepsilon_F)\mu_B B\right) , \tag{1.33}$$

where the factor $1/2$ appears since $D = D_\uparrow + D_\downarrow$. Using results for free electron gases, $D(\varepsilon_F) = 3N/(2k_B T_F)$, where $k_B T_F = \varepsilon_F$. One then arrives at

$$\chi_P = \frac{2N\mu_B^2}{2k_B T_F} , \tag{1.34}$$

independent of temperature. Note that at room temperatures, $\chi_{para}/\chi_P \ll 1$ so that contributions to metallic paramagnetism are due almost exclusively to field induced shifts of the electronic energies. We note that the diamagnetic contribution is significant: Landau showed that it is given by $\chi_{dia} = -\chi_P/3$.

1.3.1.4 Magnetic Ordering in Correlated Spin Systems

We now consider the case when interactions between spins represented by exchange energies lead to long range ordering. Following on from our discussion of paramagnetic response in the previous sections, one can imagine that at finite temperatures the thermal reduction of magnetization arises due to local misalignments of magnetic moments with a local field.

Consider a ferromagnet in which the ground state is one with parallel spins. In the sketch shown in Fig. 1.5, a "snapshot" of spins randomly deviated away from parallel alignment is shown. If one considers a single spin, as indicated by the circle, on average the local exchange field will be proportional to the thermally averaged spin of the system. This is as if the local exchange field were being produced by static, aligned, neighbouring spins with reduced magnitudes. This interaction is depicted on the right hand side by purple coloured arrows surrounding a fluctuating spin.

This approximation to the local field is an example of mean field theory, and is represented by writing

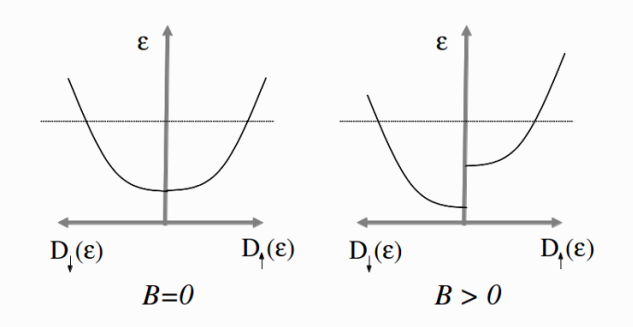

Fig. 1.4 Sketch of density of states for a nonmagnetic metal as a function of energy. In zero applied field the state distributions are independent of spin. An applied field breaks the symmetry of the up and down states

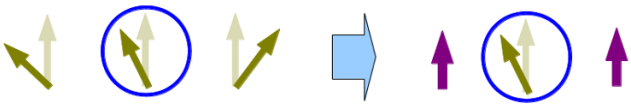

Fig. 1.5 The mean field approximation amounts to replacing the local field of a moment (indicted here by a circle) with a field proportional to the average magnetization of the entire system (represented by purple arrows)

$$\mathbf{B}_{ex} = \lambda \mathbf{M} = \left(\frac{2Z_{nn}J_{ex}}{N\mu_B} \right) \mathbf{M} \,, \tag{1.35}$$

where $\mathbf{M}$ is the magnetization and λ is a constant representing the exchange integral and the number of nearest neighbours Z_{nn} . The field B_{ex} is sometimes called a Weiss molecular field. At zero temperatures this is entirely equivalent to the classical form of the Heisenberg hamiltonian.

At finite temperatures, this approach provides a good first approximation to thermal reduction of magnetic order. In this picture, B_{ex} adds to the external applied field, and one can define a susceptibility based on that for χ_{para}

$$\chi = \frac{C}{T - \lambda M} \,. \tag{1.36}$$

Solving for M/B , one arrives at

$$\chi_F = \frac{C}{T - T_C} \,, \tag{1.37}$$

where $T_C = \lambda C$. This susceptibility shows that a ferromagnetically ordered system can behave as a paramagnet above some critical temperature T_C . Below this temperature, ordering due to exchange will dominate, and (1.37) will not apply. Above T_C, $1/\chi_F$ is linear in temperature, but intersects the temperature axis at T_C, a clear experimental signature of the possibility of an onset of magnetic ordering.

Below T_C, we need to revist the calculation of thermal averages. In zero applied field, there is still a non-zero probability of finding an average magnetization at finite temperatures. Consider a simplified model in wich magnetic moments μ only point up or down with respect to one another (corresponding to the spin half case above). Denoting the numbers pointing up with N_+ and those down with N_- , the fractions are

$$\frac{N_{\pm}}{N} = \frac{e^{\pm\frac{\mu\lambda M}{k_B T}}}{e^{\frac{\mu\lambda M}{k_B T}} + e^{-\frac{\mu\lambda M}{k_B T}}} . \tag{1.38}$$

The difference between up and down fractions again gives the magnetization. This is

$$M = \mu_B N \tanh\left(\frac{\mu\lambda M}{k_B T}\right) . \tag{1.39}$$

This is an implicit equation for M , and can be solved graphically when put in the form $x = \tanh(x)$. A solution for $M = 0$ always exists, but an additional solution for $M > 0$ exists for temperatures between $T = 0$ and $T = T_{mf}$, where T_{mf} is the critical temperature corresponding to T_C in the Curie theory.

The theory can be generalised to larger J values as before, with the result that self consistent equation now has the form

$$M = Ng\mu_B J B_J\left(\frac{g\mu_B\lambda M}{k_B T}\right) . \tag{1.40}$$

Solutions for M for different values of J are shown in Fig. 1.6. Note that the critical temperature is determined by J_{ex}, not the angular momentum number J.

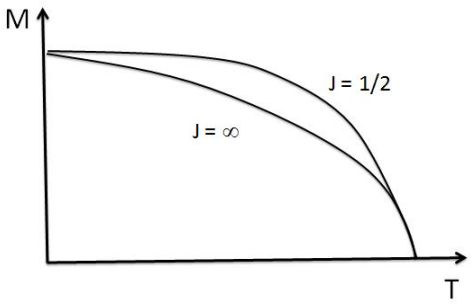

Fig. 1.6 Solution of (1.40) for different values of angular momentum quantum number J

We note that this mean field description of temperature dependence is a strong approximation, and breaks down in a number of ways. The problem is

that it neglects correlations which are important at low temperatures and also near T_C. Moreover, it is also not able to capture effects associated with dimensionality. These aspects will be discussed later when we introduce models for fluctuations.

We complete this section with a few words about antiferromagnetic ordering. The simplest example of antiferromagnetic ordering is to reverse the direction of neighbouring moments, as depicted earlier in Fig. 1.3. This can be modelled simply by changing the sign of J_{ex}, or equivalently, the sign of λ . One can again show that a paramagnetic response exists above a critical temperature T_N, but the susceptibility is now

$$\chi_{AF} = \frac{C}{T + T_N} \,. \tag{1.41}$$

In this case the inverse susceptibility is still linear in T, but it now intercepts the temperature axis at a negative value. The three susceptibilities discussed above are plotted in Fig. 1.7 for comparison.

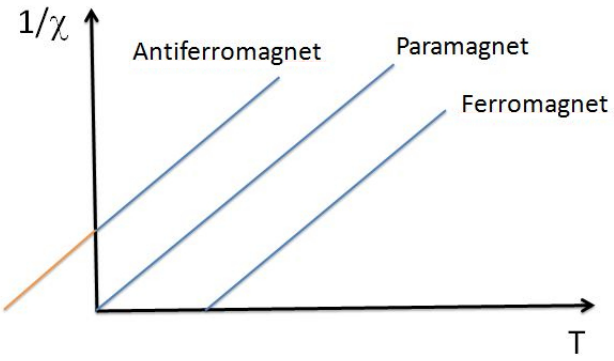

Fig. 1.7 Examples of paramagnetic susceptibilities. A simple paramagnet is compared with a ferromagnet (with $T > T_C$) and an antiferromagnet (with $T > T_N$)

1.3.2 Magnetic Ordering and Magnetoelectric Coupling

As noted earlier, non-collinear ordering of spins can arise from competing exchange interactions in some classes of materials. The Dzyaloshinski-Moriya interaction is often used to provide a phenomenological description of interactions that lead to a so-called "weak" ferromagnetism arising from canted moments in an otherwise antiferromagnetic ordering.

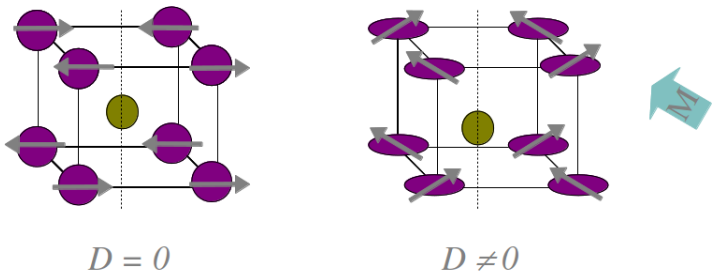

Fig. 1.8 The spin structure in a material such as $BiFeO_3$ would be antiferroelectric for a crystal with inversion symmetry, such as that depicted on the left. A Dzyaloshinski-Moriya interaction can arise for distortions that remove inversion symmetry, leading also to a canting of spins as shown on the right

An example is shown in Fig. 1.8, where spins in a cubic lattice align antiparallel if D is zero in a hamiltonian of the form $H = \sum_{i,j}[J\mathbf{S}_i \cdot \mathbf{S}_j - D\mathbf{S}_i \times \mathbf{S}_j]$.

In some multiferroic materials, a coupling between dielectric and magnetic order parameters exists. One model for this is through a Dzyaloshinski-Moriya interaction with a coupling constant that depends on the dielectric polarization P . A geometry for this is shown in Fig. 1.9. A phenomenological free energy for such a system can be written as

$$F = \frac{1}{2}\beta_1 P^2 + \frac{1}{4}\beta_2 P^4 - PE - \lambda \mathbf{m}_a \cdot \mathbf{m}_b - K(m_a^2 z + m_b^2 z) - MH + F_{ME} \ . \quad (1.42)$$

The first three terms in (1.42) are a continuous transition Landau-Ginzburg energy density for the ferroelectric component, with landau parameters β_1 and β_2. The third term is the energy of a static electric field applied along the

direction of P. The next three terms are the exchange, anisotropy (assumed to be uniaxial along the z direction) and the Zeeman field aligned along the canting direction. The final term is the magneto-electric coupling, which is often taken as a Dzyaloshinski-Moriya form. An example appropriate for $BaMnF_4$ and $FeTiO_3$ is [6]

$$F_{ME} = -\alpha P(\mathbf{m}_a + \mathbf{m}_b)_x(\mathbf{m}_a - \mathbf{m}_b)_z = -\alpha P M_x L_z \,. \tag{1.43}$$

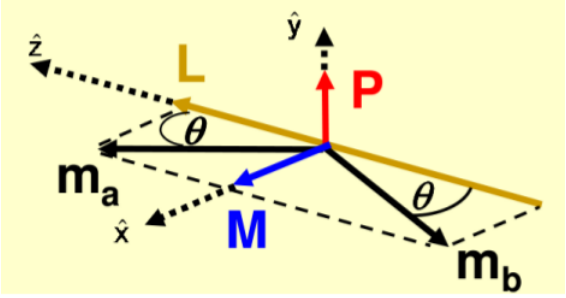

Fig. 1.9 Weak magnetization for a canted antiferromagnet in a multiferroic. Here there are two sublattices with magnetizations $\mathbf{m}_a$ and $\mathbf{m}_b$. **L** and **M** are the sum and differences between the sublattice magnetization vectors. A dielectric polarization **P** is oriented perpendicular to the plane of canting. **L** and **M** are the sum and differences between the sublattice magnetization vectors

The temperature dependence of the magnetization can be calculated in a mean field approximation as described earlier. The temperature dependence of the ferroelectric is obtained from the Landau-Ginzburg parameter $\beta_1 \sim (T - T_f)$ where T_f is the critical temperature of the ferroelectric. The canting angle determining M is found by minimizing the total free energy with respect to the orientations of the magnetic sublattices and the magnitude of P . An example is shown in Fig. 1.10 where parameters are chosen to represent $BaMnF_4$. Results for different strengths of magnetoelectric coupling are shown.

For this material, the ordering temperature T_f for the ferroelectric is larger than that for the magnetic ordering. The magneto-electric coupling serves to enhance the dielectric polarization at low temperatures when M is non-zero, but the enhancement disappears when M goes to zero. Also, the magnetoelectric energy favours orientation of M and P such that M will reverse if P is

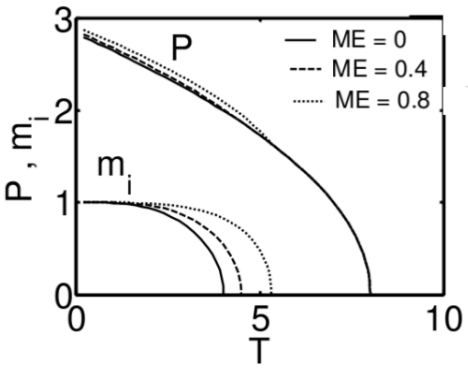

Fig. 1.10 Temperature dependence of a the ferroelectric and magnetic components calculated for a model multiferroic. After [6] (Used with permission)

reversed, or P will reverse if M is reversed. Thus one can control the orientation of P with a magnetic field, and the orientation of M with an electric field.

1.3.3 Magnetic Impurities in Metals

We mention briefly another type of magnetic ordering interaction that is mediated by conduction electrons. Consider a local magnetic moment immersed in a nonmagnetic metal. Spin dependent scattering of conduction electrons from the impurity will result in oscillations of the spin density in proximity to the impurity, in analogy to Friedel oscillations. The period of oscillations depends upon the Fermi wavevector of the conduction spins.

A second magnetic impurity placed some distance r away from the first will likewise interact with the conduction spins. The electronic states responsible for the magnetic moment of the impurity will hybridize to some extent with the conduction band of the host metal. As a result, the relative orientation of the impurity moments will have an energy associated with the oscillations in the conduction spin densities. The energy will depend on the separation r of the impurities, and favour parallel alignment of the moments for some dis-

tances, and antiparallel alignment for other distances. The lowest order terms for this energy are

$$F(r) = \frac{\sin(2k_F r) - 2k_F r \cos(2k_F r)}{(2k_F r)^4} , \tag{1.44}$$

where k_F is the magnitude of the fermi wavevector. This interaction is responsible for the oscillatory magnetic coupling between ferromagnets across thin transition metal films and known as the Ruderman-Kittel-Kasuya-Yosida interaction [7]. In an alloy such as CoMn or AuMn, where local moments are distributed randomly, this interaction can give rise to frustration due to competition between parallel and antiparallel ordering energies.

1.3.4 Magnetic Metals

It is possible to find some metals with spins that order spontaneously without the application of an external magnetic field. Consider transition metals which have a both *s* and *d* like states at the Fermi energy. The energy states for a non-magnetic metal are degenerate with respect to the spin state of the electrons.

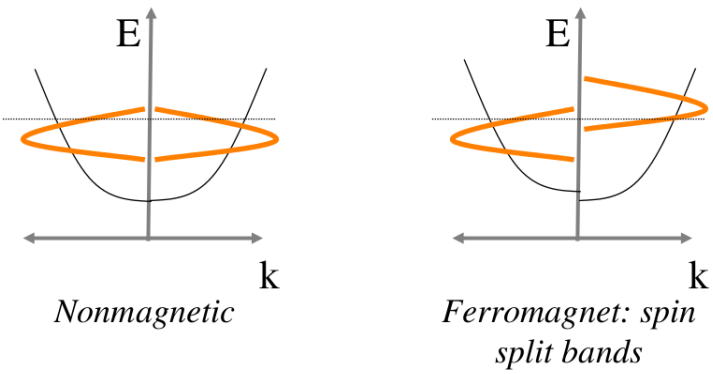

Fig. 1.11 Left: Sketch of energies for *s* and *d* bands of a non-magnetic transition metal. Right: Some metals have spontaneous splitting of spin up and down levels, creating a net magnetization

A sketch of this is shown in Fig. 1.11. The d band is narrow compared to the s band, and is found in some metals to have spin dependence for sufficiently low temperatures. In these cases, there is a majority of spins of one orientation, and the material has a ferromagnetic magnetization.

A simple way to conceptualise this is with the single band Stoner model. The central idea is that Pauli exclusion creates correlations between spins, which was also the principle underlying the theory for the exchange integral for insulators. In the case of conductors, we can think of a Hubbard hamiltonian with a correlation energy U of the form

$$Un_{\downarrow\uparrow} = \frac{1}{4}U[n^2 - (n_\uparrow - n_\downarrow)^2] \,, \tag{1.45}$$

where $n_\uparrow$ and $n_\downarrow$ are the number of up and down spins in the band, and $n = n_\uparrow + n_\downarrow$. The magnetization is then defined as $M = n_\uparrow - n_\downarrow$. The Stoner model then proposes a spin dependent potential for single electron energies where the spin up/down energies are given by

$$\varepsilon_{\uparrow\downarrow}(k) = \varepsilon_o(k) - \frac{I}{n}n_{\uparrow\downarrow} \,. \tag{1.46}$$

Here $\varepsilon_o(k)$ is the non-magnetic energy level, and I is the so-called Stoner parameter, which relates to the correlation energy.

One can now calculate a susceptibility to an applied magnetic field. This can be approached by calculating $\langle M(k)\rangle$ using a free energy hamiltonian, and then requiring $\partial\langle M(k)\rangle/\partial t = 0$. This can be used to derive a relation between M and the applied field B, from which the susceptibility is identified. One finds an enhanced Pauli susceptibility (χ_P)

$$\chi = \frac{\chi_P}{1 - ID(\varepsilon_F)} \,. \tag{1.47}$$

The key result is that the unpolarized ground state becomes unstable when $D(\varepsilon_F)I = 1$. A magnetically ordered ground state can appear then for a sufficiently large density of states at the Fermi level. It is useful to note that there exist metals which have an enhancement factor that is not large enough to provide spontaneous order, but can result in the appearance of local moments induced by magnetic impurities immersed in a paramagnetic host. This has been observed for impurities in Pd and interfaces of Pt with ferromagnetic metals.

1.4 Magnons and Thermal Fluctuations

It was noted at the end of the last section that mean field theory breaks down when correlations between spins become important. We can see how mean field theory neglects fluctuations by looking at how the mean field approximation is applied to the Heisenberg hamiltonian. Assume a hamiltonian for classical spins of the form

$$H = -\frac{1}{2}\sum_{<i,j>} J_{ex}\mathbf{S}_i \cdot \mathbf{S}_j \,, \tag{1.48}$$

where the notation $< i, j >$ is used to indicate that the sum is over only near neighbours. The factor of $1/2$ appears because spin pairs are counted twice. The minus sign ensures that a positive exchange integral J_{ij} leads to ferromagnetic ordering. Now consider fluctuations $\mathbf{s}_i$ at site i defined relative to the mean $\langle S \rangle$. These are written as

$$\mathbf{S}_i = \mathbf{s}_i + \langle S \rangle \,. \tag{1.49}$$

Substitution into the hamiltonian of (1.48) produces the expression

$$H = -\sum_{i,\delta} J_{ex}\mathbf{s}_i \cdot \mathbf{s}_\delta + Z_{nn}N\,|\langle \mathbf{S} \rangle|^2 - 2\sum_i Z_{nn}J_{ex}\mathbf{S}_i \cdot \langle \mathbf{S} \rangle \,. \tag{1.50}$$

The first term represents contributions from interactions between fluctuations, and the last term is the interaction of the fluctuations with the mean magnetization. The mean field approximation amounts to neglecting the first term.

Interactions between fluctuations create correlations that can become important in determining the thermal behaviour of the spin system. At high temperatures near the critical point, correlations can occur over any lengthscale. Mean field theory predicts that at these temperatures $\langle \mathbf{S} \rangle \sim (T - T_C)^{1/2}$. When correlations are taken into account, $\langle \mathbf{S} \rangle \sim (T - T_C)^{\beta}$, where $\beta \approx 0.34$ for ferromagnets. Moreover, dimensionality is very important: It is expected in two dimensions for any finite temperature that there is no long range ordering if the interactions are only through short range exchange.

1.4.1 Magnons in Insulators

At low temperatures, $\langle \mathbf{S} \rangle$ is not much changed from its zero temperature value in a mean field model, and deviations from the mean field behaviour are directly attributable to the correlations described by the first term in (1.50). The nature of these low temperature excitations can be understood through an insight provided by Holstein and Primakoff. They noticed that the angular momentum ladder operators $L_{\pm}$, defined to act on an angular momentum function $\psi_{m,l}$ according to

$$L_{\pm}\psi_{m,l} = \hbar\sqrt{(l \mp m)(l \pm m + 1)}\,\psi_{m\pm 1,l} \,, \tag{1.51}$$

can be put in the form of harmonic oscillator raising and lowering operators. The idea is to define a spin deviation number n_s from the angular momentum quantization numbers l and m according to $n_s = l - m$. n_s can be thought of as the number of quanta associated with a reduction of L_z from its minimal value.

The correspondence to harmonic oscillators is made in the limit of small n_s. In this case, the raising and lowering operators become

$$L_{+}\psi_{n_s} \approx \hbar\sqrt{2l}\sqrt{n_s}\,\psi_{n_s-1} \tag{1.52}$$

$$L_{-}\psi_{n_s} \approx \hbar\sqrt{2l}\sqrt{n_s+1}\,\psi_{n_s+1} \,. \tag{1.53}$$

These have exactly the same form as harmonic oscillator raising and lowering operators. Note that the increase in n_s corresponds to the angular momentum lowering operator. It is therefore convenient to define spin ladder operators in analogy to the harmonic oscillator operators ($a^{+} = x + \mathrm{i}p_x$, for example) as

$$S^{-}\psi_{n_s} = \sqrt{2S}\sqrt{2S}a^{+}\psi_{n_s} = \sqrt{2S}\sqrt{n_s}\,\psi_{n_s-1} \tag{1.54}$$

$$S^{+}\psi_{n_s} = \sqrt{2S}\sqrt{2S}a\psi_{n_s} = \sqrt{2S}\sqrt{n_s+1}\,\psi_{n_s+1} \tag{1.55}$$

$$S^{z}\psi_{n_s} = (-S + a^{+}a)\psi_{n_s} = (-S + n_s)\,\psi_{n_s} \,. \tag{1.56}$$

The number operator then appears in the definition for S^z, and counts the number of spin excitations. The spin hamiltonian can be expanded in terms of a Fourier expansion of the spin operators, where the operators b_k^{+} and b_k now describe raising and lowering operators for momentum states k

$$S_j^- = \frac{1}{\sqrt{N}} \sum_k \mathrm{e}^{-\mathrm{i}\mathbf{k}\cdot\mathbf{x}_j} b_k \tag{1.57}$$

$$S_j^+ = \frac{1}{\sqrt{N}} \sum_k \mathrm{e}^{\mathrm{i}\mathbf{k}\cdot\mathbf{x}_j} b_k^+ \,. \tag{1.58}$$

The hamiltonian expressed in terms of these operators is now diagonal in low orders of b

$$H = -J_{ex} N z S^2 + \sum_k \left[2 J_{ex} z S \left(1 - \frac{1}{z} \sum_\delta \mathrm{e}^{\mathrm{i}\mathbf{k}\cdot\delta} \right) \right] b_k^+ b_k + \mathscr{O}(b^4) \,. \tag{1.59}$$

The z refers to the number of nearest neighbours. The second term in (1.59) is the magnon contribution to the energy, and the b are magnon operators. For a cubic lattice of constant a, the energy in the long wavelength limit for a ferromagnet is

$$\hbar\omega_k = (J_{ex} S a^2) k^2 \,. \tag{1.60}$$

One can use this approximation to estimate the total reduction of magnetization due to thermal fluctuations. The excitations are bosons, so that the thermodynamic average over fluctuations is estimated using a Bose-Einstein statistics

$$\sum_k \langle b_k^+ b_k \rangle = \frac{1}{(2\pi)^2} \int \left[\mathrm{e}^{\frac{\omega_k}{k_B T}} - 1 \right]^{-1} d^3\mathbf{k} \sim T^{3/2} \,. \tag{1.61}$$

This is the Bloch law describing the reduction of magnetization as a function of temperature. It applies for low temperatures only, and Dyson showed how taking higher order magnon interactions into account, one can expect corrections that go as higher powers of $T^{1/2}$, i.e. $M(0) - M(T) \sim c_1 T^{3/2} + c_2 T^{5/2} + c_3 T^{7/2} + \ldots$ [8].

There are different experimental probes of spinwave excitations, including inelastic neutron scattering, inelastic light scattering, and various microwave absorption techniques. Inelastic neutron scattering is able to sample a wide range of energies across the magnon band structure whereas other techniques typically sample long wavelength excitations near the magnon Brillouin zone center. More will be said in the next sections about long wavelength excitations.

1.4.2 Magnons in Metals

As discussed earlier, one must take electronic band structure into account for a description of metallic magnetism. One can cast this theory in a form reminiscent of the above theory for magnons in insulators by writing the electronic hamiltonian in terms of the fermion analogy to raising and lowering operators. In this picture, we define state and site occupation operators c and c^+whose mathematical effect is to lower or raise the occupation of an electronic state. The hamiltonian in this picture has the form

$$H = \sum_{lm\sigma} H_o c^+_{m\sigma} c_{l\sigma} + \sum_{lm\sigma} \sum_{l'm'\sigma'} H_i c^+_{m\sigma} c^+_{l\sigma} c_{m'\sigma'} c_{l'\sigma'} \ , \tag{1.62}$$

where the energies are the kinetic and positive core interactions (H_o) and the Coulombic repulsion (H_i). The sums are over sites and spin states. These are given by integrals involving the single particle wavefunctions $\psi_j(r)$ associated with site j

$$H_o = \int \psi^*_l(\mathbf{r}) \left[\frac{p^2}{2m} + \sum_{\mathbf{R}} V(\mathbf{r}-\mathbf{R}) \right] \psi_m(\mathbf{r}) \mathrm{d}^3\mathbf{r} \tag{1.63}$$

$$H_i = \int \psi^*_l(\mathbf{r}) \psi^*_{l'}(\mathbf{r}') \frac{e^2}{|\mathbf{r}-\mathbf{r}'|} \psi_{m'}(\mathbf{r}') \psi_m(\mathbf{r}) \mathrm{d}^3\mathbf{r} \ . \tag{1.64}$$

We next define spin raising and lowering operators at site m as

$$S^z_m = \frac{1}{2} \left(c^+_{m\uparrow} c_{m\uparrow} - c^+_{m\downarrow} c_{m\downarrow} \right) \tag{1.65}$$

$$S^+_m = c^+_{m\uparrow} c_{m\downarrow} \tag{1.66}$$

$$S^+_m = c^+_{m\downarrow} c_{m\uparrow} \ . \tag{1.67}$$

This theoretical formulation can be used to identify low energy excitations of the electron gas in a perturbative approach. In the context of a Stoner model wherein the Coulomb interaction is replaced by a local energy $I\delta(\mathbf{r}_i - \mathbf{r}_j)$, the excitation energies are found to obey $\omega_k \ Dk^2$, similar in form to the dispersion for magnons in an insulator. The exchange constant for metals however depends upon details of the band structure and spin densities. Moreover, the magnons run into a band of spin flip excitations (Stoner excitations) for large

wavevectors, that are not found in the Heisenberg model discussed for insulators.

1.5 Macroscopic Models of Magnetic Ordering and Excitations

So far in our treatment we have concentrated on exploring how magnetism arises from underlying electronic states. A more phenomenological description is possible, and preferrable in some cases for understanding and modelling details of many types of experiments. These models start from a continuum formulation of the energies and equations of motion. Comprehensive accounts of original spin wave theories can be found in [9], [2], and [10]. More recent summaries are contained in [12], [11], and [13].

A magnetic density field can be defined in terms of local electronic spins formally as

$$\hat{\mathbf{M}}(\mathbf{r}) = g\mu_B \sum_j \delta(\mathbf{r} - \mathbf{r}_j)\hat{\sigma}_j \; . \tag{1.68}$$

It is most convenient to work with a macroscopic magnetization, $\mathbf{m}(\mathbf{r}) = \mathrm{Tr}(\rho\hat{\mathbf{M}}(\mathbf{r}))$, where ρ is the density matrix. This defines a classical quantity M for the magnetic moment density at a location $\mathbf{r}$ in a material.

1.5.1 Exchange and Anisotropy Effective Fields

An exchange energy can now be postulated that is compatible with the symmetry of the crystal

$$E_{ex} = \sum_{\alpha kl} C_{kl} \frac{\partial m_\alpha(\mathbf{r})}{\partial r_k} \frac{\partial m_\alpha(\mathbf{r})}{\partial r_l} \; , \tag{1.69}$$

where α indexes the components of the magnetization, and k indexes the components of the position vector. In an isotropic medium this becomes, for example,

$$E_{ex} = C\left[(\nabla m_x)^2 + (\nabla m_y)^2 + (\nabla m_z)^2\right] \; . \tag{1.70}$$

There are additional effects associated with the local atomic environment that can also be constructed using symmetry arguments. Small perturbations due to spin orbit coupling can introduce an orientational dependence to the magnetization. Symmetry allowed terms to an expansion of the energy associated with these perturbations can take the form

$$E_{anis} = -K_u m_z^2 + K_4 \left(m_x^2 m_y^2 + m_x^2 m_z^2 + m_y^2 m_z^2 \right) + \ldots , \tag{1.71}$$

where the coefficients K_u and K_4 denote uniaxial and four-fold anisotropies, respectively. As an example, consider hexagonal Co. This crystal has a two fold axis of rotation, and allows uniaxial anisotropies. The two largest terms can be written in terms of an angle θ measured from the axis of rotation

$$E_{ani} = K_u^{(1)} \sin^2 \theta + K_u^{(2)} sin^4 \theta \, . \tag{1.72}$$

A typical value for $K^{(1)}$ is 5×10^5 J/m^3 .

1.5.2 Magnetostatic Fields

Exchange and anisotropy are "local" in the sense that the range of interactions are mostly limited to the immediate atomic environment. Magnetic moments themselves act as sources of magnetic fields through interactions mediated by the electromagnetic field. An individual point moment generates a dipolar magnetic field, and the site local field in an ensemble of point dipoles can be represented by a sum over other dipoles in the system

$$\mathbf{h}_{dip} = \frac{1}{2} g^2 \mu_B^2 \sum_{ij} \left[\frac{\mathbf{S}_i \cdot \mathbf{S}_j}{r_{ij}^3} - 3 \frac{(\mathbf{r}_{ij} \cdot \mathbf{S}_i)(\mathbf{r}_{ij} \cdot \mathbf{S}_j)}{r_{ij}^5} \right] , \tag{1.73}$$

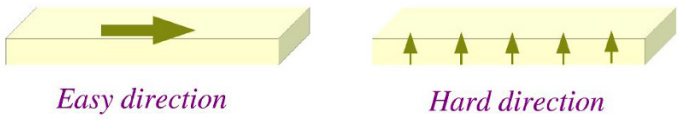

Fig. 1.12 Easy and hard directions sketched for a single domain rectangular magnetic element

where $\mathbf{r}_{ij}$ is the position vector defined by the sites i and j . This interaction is long ranged, and can drive complex magnetic configurations because of dipolar fields created by sources over large lengthscales. The shape of a magnetic element is important in this regards. A uniformly magnetized element will generate demagnetizing fields through the magnetostatic fields that can appear as a "shape anisotropy".

Dipoles with a component normal to a surface generate uncompensated poles. The magnitude of the field produced by surfaces is proportional to the magnetic field flux generated by these poles. In a rectangular planar element, such as that depicted in Fig. 1.12, alignment of the magnetization along the long axis will produce the smallest magnetic field flux, thus defining an "easy" direction for the orientation of the magnetization. Alignment of the magnetization normal to the largest area will generate a correspondingly large flux, and defines a "hard" axis orientation for the magnetization.

It is possible to calculate exactly the demagnetizing fields and energies only for a few simple geometries. A uniformly magnetized ellipsoid will have a shape anisotropy energy density arising from demagnetizing fields, that can be described in terms of shape factors N_x , N_y , and N_z :

$$E_{shape} = \frac{M_S^2}{2\mu_o}(N_x \sin^2\theta\cos^2\phi + N_y \sin^2\theta\sin^2\phi + N_z\cos^2\theta)\,. \qquad (1.74)$$

Calculation of magnetostatic fields for specific element shapes and different magnetic configurations is far from trivial. Although there are some specific geometries which can be treated analytically, in general numerical methods are used. These approaches are called "micromagnetic", and involve various approaches to taking the long range magnetostatic fields into account in addition to local exchange, anisotropy, and other energies.

1.5.3 Spinwaves in Continuum Models

The macroscopic model outlined above can be used to also describe magnonic excitations in the long wavelength limit. We refer to this description as "spinwaves", with the understanding that it is the classical analogue of the quantum physics picture presented earlier.

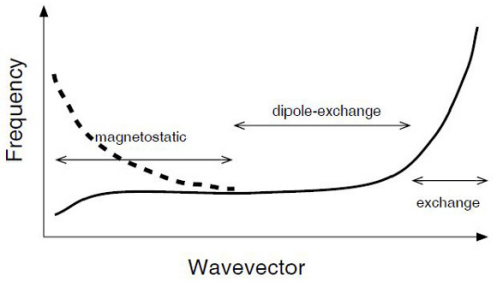

Fig. 1.13 Illustration of different wavenumber regimes for magnetostatic, dipole-exchange, and exchange spin-waves. Propagation directions along the magnetization axis can have negative group velocities at long wavelengths

We begin with a total energy constructed from the exchange, anisotropy, magnetostatic, and any additional contributions that might arise (such as interlayer magnetic coupling, Dzyaloshinski-Moriya interactions, etc). An effective field $\mathbf{H}_{eff}$ can be constructed as a gradient of the energy E_{tot}

$$\mathbf{H}_{eff} = -\nabla_{\mathbf{M}} E_{tot} \ . \tag{1.75}$$

An effective field constructed from an applied field H_a, exchange with strength A, anisotropy with strength K, and a dipolar field $\mathbf{h}_{dip}$ will have the form

$$\mathbf{H}_{eff} = \mathbf{H}_a + A\nabla^2\mathbf{M}(\mathbf{r}) + \mathbf{M}(\mathbf{r}) \cdot K\mathbf{M}(\mathbf{r}) - \mathbf{h}_{dip} \ . \tag{1.76}$$

The dipolar field can be calculated from Maxwell's equations, and is usually done in the magnetostatic limit where $\nabla \times \mathbf{h}_{dip} = 0$. This is valid for the long wavelength limit in non-conductive materials. In the case of ohmic conductors, this condition needs to be augmented with the associated currents generated by the time varying magnetic field.

The equations of motion in this formulation are of the form of torque equations

$$\frac{\partial}{\partial t}\mathbf{M}(\mathbf{r}) = \gamma\mathbf{M}(\mathbf{r}) \times \mathbf{H}_{eff} - \Gamma_{diss} \ , \tag{1.77}$$

where Γ_{diss} is a torque introduced to describe redistribution and loss of energy from the magnetic system. The redistribution occurs because of interactions between spinwaves and interactions with other degrees of freedom in the system (including elastic, electronic, and electromagnetic). In the original form proposed by Landau and Lifshitz, [14] a damping was chosen such that the

magnitude of the magnetization was conserved. This requirement is served by the construction

$$\Gamma_{diss} = \alpha \mathbf{M}(\mathbf{r}) \times (\mathbf{M}(\mathbf{r}) \times \mathbf{H}_{eff}) \, . \tag{1.78}$$

From the point of view of non-conservative dynamics, the dissipation should be of the form $|\mathrm{d}\mathbf{M}/\mathrm{d}t|^2$. A commonly used form is consistent with this (Rayleigh) dissipation is called "Gilbert damping" [15]. In its more common representation, the equations of motion and damping are written explicitly as

$$(1+\gamma^2\alpha^2 M_S^2)\frac{\partial}{\partial t}\mathbf{M}(\mathbf{r}) = \gamma \mathbf{M}(\mathbf{r}) \times \mathbf{H}_{eff} - \gamma\alpha \mathbf{M}(\mathbf{r}) \times \frac{\partial}{\partial t}\mathbf{M}(\mathbf{r}) \, . \tag{1.79}$$

Illuminating discussions of non-linearities, spinwave interactions, and damping processes observed in microwave resonance experiments can be found in [13], [16], [17], and [18].

The zero wavevector excitations are especially important for a variety of resonance experiments. As an example, consider a ferromagnet illuminated uniformly by a microwave frequency alternating field. Suppose further that the ferromagnet has a uniaxial anisotropy along the y direction, and there is a static applied field along the z direction. The effective field acting on the magnetization is

$$\mathbf{H}_{eff} = \hat{z}H_a + \hat{y}\frac{2K}{M_S^2}M \, . \tag{1.80}$$

Ignore dissipation for simplicity. Substitution into the torque equations gives

$$\frac{\mathrm{d}M_x}{\mathrm{d}t} = -\gamma[H_a M_y - (2K/M_S^2)M_z M_y] \tag{1.81}$$

$$\frac{\mathrm{d}M_y}{\mathrm{d}t} = -\gamma[H_a M_x] \tag{1.82}$$

$$\frac{\mathrm{d}M_z}{\mathrm{d}t} = -\gamma[(2K/M_S^2)M_x M_y] \, . \tag{1.83}$$

These equations are non-linear. However if one considers only small amplitude precessions, then $M_x M_y \approx 0$ and the third equation reduces to a statement that M_z is constant. The small amplitude resonance then corresponds to precession of the magnetization around the z direction, with time varying com-

ponents in the transverse plane. The transverse components oscillated with resonance frequency $\omega = \gamma\sqrt{H_a(H_a - 2K/M_S)}$. The precession is elliptical, and exists only for an applied field large enough to align the magnetization in the hard direction $(H_a > (2K/M_S))$.

Non-zero wavevector excitations are spinwaves. If one considers only the exchange interaction, then the additional contribution to the effective field is $A\nabla^2\mathbf{M}(\mathbf{r})$, and the dispersion of plane waves with wavenumber k is

$$\frac{\omega^2}{\gamma^2} = (H_a + Ak^2)(H_a - 2K/M_S + Ak^2) \, . \tag{1.84}$$

Dipolar interactions can also contribute to the dispersion. In the longest wavelength regime, dipolar contributions dominate and can even lead to waves with negative group velocities (backward travelling waves). For some propagation directions, surface magnetostatic waves can exist as excitations localized to interfaces. At short wavelengths, the exchange contribution dominates, and $\omega \sim k^2$. The waves in the intermediate wavelength range are called "dipole-exchange" modes since the exchange and dipolar contibutions are comparable. These ranges are illustrated in Fig. 1.13.

1.6 Reversal of Magnetization

Fig. 1.14 Analogy between reversal of a single domain particle and a double well potential. Thermal activated reversal can be likened to a chemical rate problem

We have discussed linear dynamics in two contexts: first in terms of linear response to quasi-static applied fields, and next in the context of small amplitude precession and spinwaves. The dynamics of magnetization reversal are now examined, and this goes well beyond linear response in either of the pre-

vious senses. Indeed, magnetic systems have often been used as experimental and theoretical models for different aspects of non-linear dynamics and behaviours far from equilibrium. Some of these will be surveyed here, within the context of magnetization reversal mechanisms.

1.6.1 Reversal of Single Domain Particles

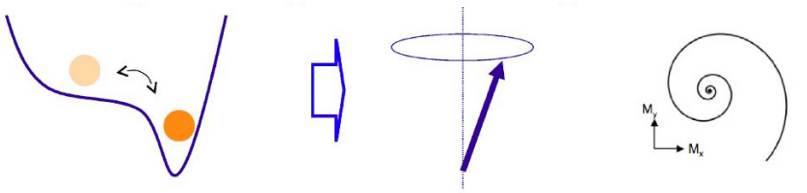

Fig. 1.15 Illustration of the precession driven reversal process. A magnetic field can make an orientation unstable, and reversal then occurs through damped precession

It was noted that the phenomenological equations of motion describing precession are inherently non-linear. A useful conceptual analogy is the double well potential that is perhaps best known from chemical rate theory wherein a barrier separates two minimizing energy states. The barrier must be overcome in order to make the transition from one state to the other.

This analogy is illustrated in Fig. 1.14 where the orientation of a single domain particle is identified with positions in a double well potential. It is assumed that the particle has a large uniaxial anisotropy so that only two alignments parallel with the anisotropy axis are energetically favorable. In magnetic systems, an external magnetic field will break the degeneracy of the two otherwise equivalent configurations, as indicated by the lowering of one well minimum relative to the other.

A sufficiently strong field can make one configuration unstable. The critical field at which this occurs is the one for which the energy well curvature for that configuration becomes zero. This situation is sketched in Fig. 1.15. In this case, any fluctuation will cause the moment to begin a precession trajectory and dissipation will bring the moment to rest in the lower energy, stable orientation.

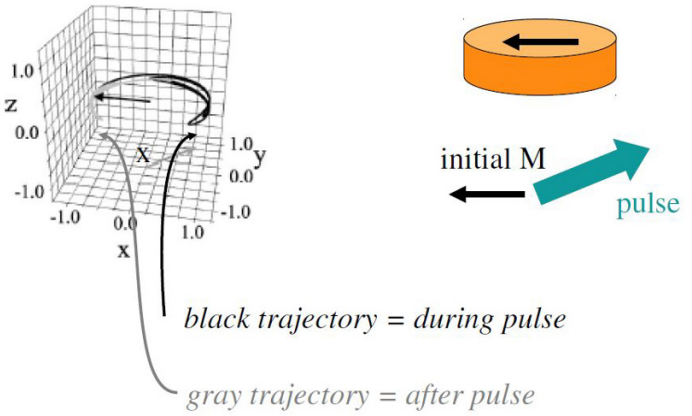

Fig. 1.16 Trajectory of a single domain elliptically shaped particle. After [19] (Used with permission.) Shape anisotropies align the magnetization in plane along the major axis. A static field is applied opposite to the initial magnetization. A pulsed field is applied at an oblique angle to the moment, causing a precessional reversal

1.6.1.1 Field driven precessional reversal

The approximation of a single domain particle is quite severe, but does serve to illustrate general features observed in experiment. Most importantly, it allows for a simple analysis using torque equations wherein the magnetization is replaced by a single block vector representing the instantaneous orientation of the particle's magnetization. An example is shown in Fig. 1.16.

An elliptical dot of soft material is modelled by a single block spin. The geometry in used to define an easy direction in the plane: Shape anisotropies align the magnetization in plane along the major axis, and are represented by uniaxial anisotropies in the effective fields. A static field is applied opposite to the initial magnetization. A pulsed field is applied at an oblique angle to the moment, causing a precessional reversal. The length of the pulse is greater than the relaxation time. Dynamics is modelled by numerically integrating the Landau-Lifshitz equations with Landau damping. The tip of the magnetization vector is traced over the course of the precession. The highly elliptical precession is due to the strong in-plane shape anisotropy.

The success of creating reversal depends sensitively on pulse field duration, magnitude and orientation. Results are shown in Fig. 1.17 for a pulse field that is much shorter than the characteristic relaxation time [19]. A phase diagram is shown where the axes give the orientation and magnitude of the pulse field in a polar plot. The grey shaded regions are ones which lead to reversal, whereas the unshaded areas leave the moment in its initial direction.

1.6.1.2 Thermally driven reversal

Thermal fluctuations can also serve to drive reversal. In Néel's fluctuation model, one imagines that a moment experiences instantaneous effective magnetic fields that are random in orientation and magnitude, with a distribution that depends upon temperature. This is described by a random vector field $\mathbf{h}_f$ included in the torque equations of motion.

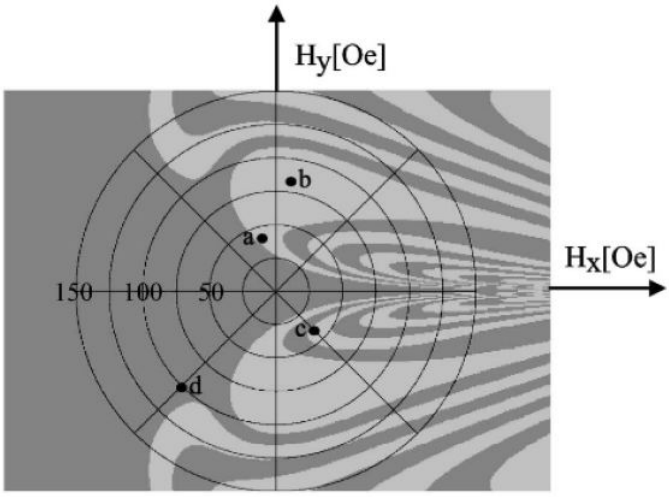

Fig. 1.17 The success of creating reversal using a pulse much shorter than the characteristic relaxation time depends sensitively on field magnitude and orientation. A phase diagram is shown where the axes give the orientation and magnitude of the pulse field in a polar plot. The grey shaded regions are ones which lead to reversal, whereas the unshaded areas leave the moment in its initial direction. After [19] (Used with permission)

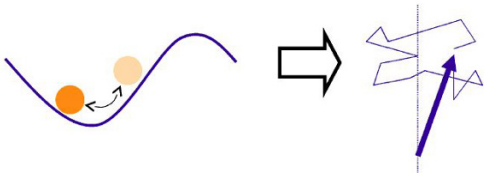

Fig. 1.18 Schematic of thermally driven reversal in a two state model. Some fluctuations are able to drive the magnetization over the barrier

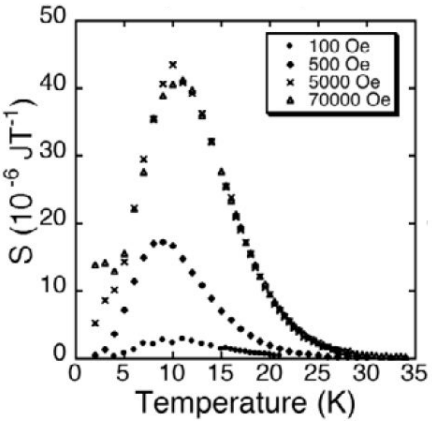

Fig. 1.19 Energy barrier determination for an ensemble of FePt nanoparticles. The distribution is proportional to the magnetic viscosity divided by temperature. After [20] (Used with permission)

Fluctuations can occur on very short timescales in this model, leading to discontinuous changes in the trajectory during otherwise precessional dynamics. A sketch is given in Fig. 1.18. In terms of the two state potential well model, there is a probability that some thermal fluctations will lead to precession that takes the magnetization across the barrier with a final orientation in the opposite direction.

On average, it is possible to construct an estimate of the reversal rate based on the statistics of the fluctuations. Details of a full calculation are complex, but the resulting form is relatively simple

$$\frac{1}{\tau} = f_o \mathrm{e}^{-\frac{\varepsilon}{k_B T}} \ , \tag{1.85}$$

where ε is the barrier "activation" energy, $k_B T$ is the thermal energy at temperature T , and f_o is an "attempt" frequency. The attempt frequency can be

thought of as a measure of the number of ways the magnetic system can fluctuate in such a way as to lead to reversal.

In the Stoner model, the activation energy is estimated for a simple single domain particle from an energy of the form

$$E = V\left(-H_a M_S \cos\theta + K\sin^2\theta\right) , \tag{1.86}$$

where V is the volume and θ is an angle taken relative to a unixaxial anisotropy axis. The activation energy in this model is the energy of the energy maximum at $\theta = \pi/2$. Then $\varepsilon = VK + [H_a M_S/(2K)]^2$.

Reversal in an ensemble of particles is sometimes considered as a chemical rate problem where concentrations of up and down oriented particles are denoted by $n_\uparrow$ and $n_\downarrow$. The rate equations are

$$\frac{\mathrm{d}n_\uparrow}{\mathrm{d}t} = W_{\downarrow\uparrow} n_\downarrow - W_{\uparrow\downarrow} n_\uparrow \tag{1.87}$$

$$\frac{\mathrm{d}n_\downarrow}{\mathrm{d}t} = W_{\uparrow\downarrow} n_\uparrow - W_{\downarrow\uparrow} n_\downarrow . \tag{1.88}$$

Here, transition probabilities $W_{\sigma\sigma'}$ are defined for processes that convert a spin of orientation σ to a spin of orientation σ'. Conservation of particles means that $n_\uparrow + n_\downarrow = 1$ and the magnetization is related to the difference $m(t)$ between concentrations. One finds

$$m(t) = n_\uparrow - n_\downarrow = m(0)\mathrm{e}^{-\Gamma t} , \tag{1.89}$$

where $m(0)$ is a constant determined by the initial conditions, and the relaxation time is defined as $\Gamma = 1/\tau$.

A distribution of relaxation times, $P(\Gamma)$ is taken into account by writing

$$m(t) = m(0)\int P(\Gamma)\mathrm{e}^{-\Gamma t}\mathrm{d}\Gamma . \tag{1.90}$$

In a single process approximation, $\exp(-\Gamma t) \approx 1 - \Theta(t - 1/\Gamma)$. The integral in (1.90) simplifies in this case. Using $P(\Gamma) = P(\varepsilon)\,|d\varepsilon/d\Gamma|$ to convert to an energy barrier distribution, one obtains

$$\frac{\mathrm{d}m}{\mathrm{d}t} \sim -\frac{k_B T}{t} P\left(\varepsilon = k_B T \ln(t/\tau_o)\right) , \tag{1.91}$$

where the time $\tau_o = 1/f_o$ is the inverse activation frequency.

The result represented by (1.91) allows the experimental measure of energy barrier distributions by varying temperature and time. The barrier distribution can be accessed by defining a "viscosity" parameter S defined as

$$P(\varepsilon = k_B T \ln(t/\tau_o)) \approx \frac{1}{m(0)k_B T}\left(-t\frac{\mathrm{d}m}{\mathrm{d}t}\right) = \frac{S}{m(0)k_B T}\,. \tag{1.92}$$

One then plots $S/k_B T$ as a function of temperature to obtain a plot of the barrier distribution. An example of results from this procedure is shown in Fig. 1.19 where S was obtained from an ensemble of FePt particles measured using SQUID magnetometry [20]. Note that the accuracy of this method depends on measurements of the magnetization over very large time scales due to the lograthmic dependence of P on time.

1.6.2 Domain Walls and Magnetization Processes

The reversal process described for a single domain particle in reference to Figs. 1.14 and 1.15 pretained specifically to a magnetic system with two degrees of freedom, corresponding to the two angles used to specify the instantaneous orientation of the magnetic moment. This picture can be generalized to macroscopic magnetic systems with many degrees of freedom corresponding to the orientation of the spatial and time varying magnetization.

Instead of a simple two state system, one then needs to consider an energy landscape with many wells and barriers. Reversal then corresponds to a path through the energy landscape that navigates across saddle points between minima in a landscape controlled by the many degrees of freedom associated with non-uniform magnetic order.

1.6.2.1 Characteristic Lengths

In consequence, magnetization processes in large systems can be complex with new phenomena appearing. How large does a system need to be? A characteristic length is

$$L_{ex} = \sqrt{\mu_o A/M_S^2}\,, \tag{1.93}$$

which is a measure of the distance over which magnetic order can vary. In exchange coupled magnets, deformation of otherwise uniform magnetic order incurs additional exchange energy, and if compared to magnetostatic energy as in (1.93), one can define an "exchange" length below which one would expect uniformly ordered magnetic moments.

Magnetocrystalline anisotropy creates preferred directions for magnetic moments. Different and incompatible orientations can be degenerate in energy, and a large enough system can support multiple orientations. Regions of different orientation will be separated by boundary walls, in much the way that different thermodynamic phases in other many body systems can be separated by phase boundary wall. A comprehensive discussion of domain and wall structure is given by [21].

A characteristic length for this type of magnetic phase separation is called a domain wall length

$$\lambda = \sqrt{A/K}\,. \tag{1.94}$$

This ratio of exchange to anisotropy defines a length over which magnetization can deform across a hard direction. Only ferromagnetic systems are considered for the remainder of this section, although many of the ideas and concepts carry over into multisublattice magnets.

1.6.2.2 Nucleation and Growth of Domains

Consider a ferromagnetic film much thinner than either of the lengths L_{ex} or λ . Magnetic nonuniformities will then occur across the film plane, but not the film thicknesses, at least for temperatures away from the critical point. For definiteness, consider also a strong out of plane oriented uniaxial anisotropy so that the magnetization orients spontaneously perpendicular to the film

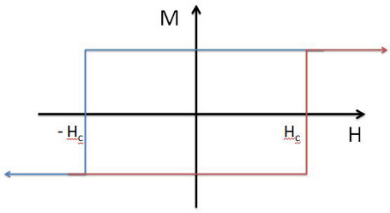

Fig. 1.20 Sketch of average magnetization during an adiabatic field driven reversal

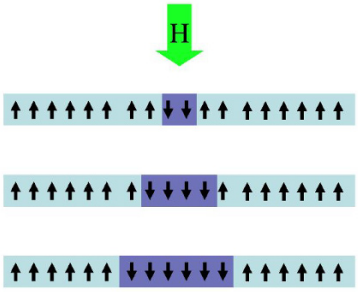

Fig. 1.21 Illustration of domain nucleation. Initially the magnetization is saturated in an easy direction. A magnetic field is applied in the opposite direction, and a small domain can nucleate and grow in size

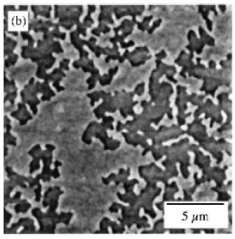

Fig. 1.22 Example of domain structure nucleated in TbFeCo by a sequence of short pulsed fields. The image was taken using a magneto-optical microscope [22]

plane. Note: If the anisotropy is large enough, λ approaches the length of a lattice spacing which is the minimum width of a domain wall. The system then approximates an Ising magnet which is the theoretical construct for a two state magnetic system.

The magnetic film is assumed to be able to exchange heat energy freely with a reservoir (such as a substrate). Now suppose that the magnetization is aligned by a large magnetic field applied along the film normal. Suppose now that the field is now reduced in magnitude slowly, so that the magnetization can respond adiabatically. In a system free from defects or large thermal fluctuations, the magnetization will remain pefectly aligned as the field is reduced to zero and reversed.

It is only until some coercive field $-h_c$ is reached that magnetization can reverse. In a single domain particle at zero temperature, this field corresponds to the field at which the original state becomes unstable and the activation barrier is removed. At finite temperatures, thermal fluctuations can overcome the activation energy barrier (within a time scale set by the experiment) at a field less than the zero temperature coercive field. Once reversal is accomplished, the magnetization aligns along the applied field direction. The aver-

age magnetization for this process is sketched in Fig. 1.20 by the path from positive to negative fields. If now the field is again reduced in magnitude and reversed, the magnetization follows the lower path from negative to positive fields, changing sign to align with the field at $+h_c$.

In an extended film, the change in magnetization orientation at the coercive fields typically begins with the nucleation of domains of reversed magnetization. The process is sketched in Fig. 1.21. Nucleation occurs with a competition between two energies: there is an energy gained by aligning some volume V with the applied field: $E_{Zeeman} = -\mu_o M_S V H_a$. There is an energy cost per area σ_{DW} of forming a domain wall boundary around this volume. If the bounded area is $\mathscr{A}$, then the domain can form when the energies $E_{Zeeman} + \sigma_{DW}\mathscr{A}$ is minimized. This defines a critical size for the domain, given by the ratio $\sigma_{DW}/(\mu_o M_S H_a)$.

An example of a domain structure nucleated in a FeTbCo thin film is shown in Fig. 1.22 [22]. This image was made using a magneto-optical microscope, and the domain pattern is the result of first saturating the magnetization out of plane, and then applying a sequence of small field pulses to nucleate reversal. Several domains nucleate, and then grow in size. The image is taken after several domains have coalesced, thus resulting in a complex pattern of connected regions.

Domains typically nucleate at magnetic or structural defects in a material. Domains grow through motion of domain walls, and the walls themselves can be pinned at defects. This competition between domain wall nucleation and motion results in coercivity and hysteresis, and is strongly dependent on time, temperature, and structural details of the material.

1.6.2.3 Domain Wall Motion in the Creep and Viscous Regimes

As noted earlier, magnetic domain walls are examples of thermodynamic phase boundary walls. They are configurational (topological) excitations of the uniform magnetized ground state, and can be modelled using micromagnetics. Quite often a useful qualitative description can be constructed by approximating the walls as elastic lines with a characteristic width and energy per area.

Some analytical models can be constructed simply in one dimension. These provide insight into the behaviour and properties of domain walls in general, and we review some of the essentials here. A simple model begins with exchange and anisotropy energy and a wall in one dimension

$$E = \int \left[A \left(\frac{\partial u(x)}{\partial x} \right)^2 - K u(x)^2 \right] \mathrm{d}x \,, \tag{1.95}$$

where $u(x) = M_z/M_S$, a normalised component of the magnetization profile. Note that there are two ways to obtain this projection $u(x)$. The magnetization can rotate around the x axis in a Bloch wall configuration, or the magnetization can rotate through the $x-z$ plane in a planar Néel type wall configuration. In the case of the latter, uncompensated magnetic poles exist in the wall, and additional contributions from dipolar energies modify the wall profile and energy. Description of these contributions can be obtained using more advanced approaches or numerical micromagnetics.

The energy of (1.95) can be minimized for a domain wall excitation by first constructing a Euler-Lagrange equation for the integrand. Writing $u(x) = \cos(\theta(x))$, this is of the form

$$A \frac{\partial^2 \theta(x)}{\partial y^2} + K \sin^2(\theta(x)) = 0 \,. \tag{1.96}$$

One solution describes a soliton centered at $x = 0$ with profile parametrized by $\theta(x)$

$$\cos(\theta(x)) = \tanh \left[\frac{x}{\sqrt{A/K}} \right] \,. \tag{1.97}$$

The width λ can be defined from $\lambda = \sqrt{A/K}$ and represents a competition between the exchange, which tends to align moments relative to one another, and anisotropy, which tends to align magnetization relative to a direction in the material. Substitution of this solution into the energy of (1.95) results in the energy per length

$$\sigma_{DW} = \sqrt{4AK} \,. \tag{1.98}$$

In materials with small anisotropy, wall like structures will be strongly modified by dipolar energies, and the above model is less applicable. High anisotropy materials produce narrow domain walls which more closely resemble the above model. In these materials, walls can move freely if no pinning sites or other defects exist.

Motion of a domain wall is still governed by torque equations, and involves precession. A wall will move under the influence of magnetic field, for example, to a first approximation without changing its profile. Dissipation

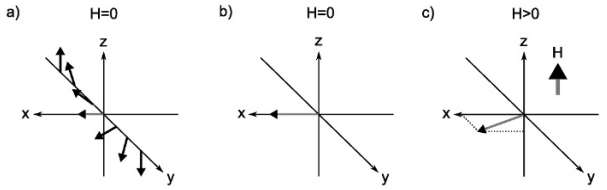

Fig. 1.23 Moments inside a Bloch wall at rest will rotate in a plane normal to the wall axis. In motion, the plane of rotation is tilted so that a component of the moments lies along the wall axis [23]

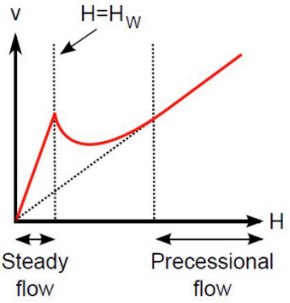

Fig. 1.24 Walker breakdown occurs when magnetostatic charges built up within a propagating wall drive internal dynamics. The onset occurs at a critical driving field, and drastically modify the wall velocity [25]

Fig. 1.25 Motion of a domain wall in the creep regime is governed by avalanche dynamics. Depinning from one site can lead to a cascade of other depinnings that reverse an area of magnetization

will determine the speed, and the wall will move at a constant rate determined by the field magnitude. The rate, or speed v_{DW} , will be determined by the dissipated power averaged over time (the overbar stands for time-averaging)

$$v_{DW} \propto \alpha \int \overline{|\mathbf{M} \times H_{eff}|^2} \mathrm{d}x \,. \tag{1.99}$$

This is a terminal velocity. The wall speed will be linear in the applied field magnitude and proportional to the damping constant.

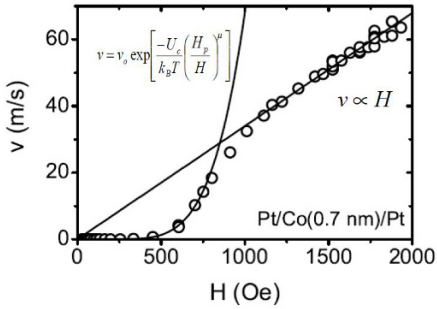

Fig. 1.26 Measured velocities for domain wall creep in a 0.5 nm thick Co film. The lines are fits to the data in the creep and viscous regimes [25]

We note here also an effect that can occur for large speeds and driving fields. Taking into account some modifications of the profile, one finds that the moments in a Bloch wall will tilt slightly out of the plane of the wall. This is shown schematically in Fig. 1.23. This means that a component of the magnetization will appear along the wall axis, leading to uncompensated magnetic charge. As a result there will be a magnetostatic contribution to the wall energy. In a nanowire, the magnitude of the tilt will also depend on the shape of the wire through demagnetizing factors. At high fields, this angle will increase and can lead to an instability known as Walker breakdown. In this type of motion, internal oscillations appear that result in a change the wall velocity. The corresponding effects on the field dependence of the wall velocity are illustrated in Fig. 1.24. Internal oscillations set in at a critical field H_W, and at higher fields the velocity is strongly reduced and wall motion involves precession within the wall itself. Shape anisotropies in nanostructures can affect the onset of criticality, through shape anisotropies [24].

Motion at low fields in the presence of pinning can lead to a phenomena known as “creep”. Suppose that a narrow wall exists in a planar ferromagnet with a distribution of point defects that can pin a wall. Such a site might be associated with a local variation in anisotropy or exchange, for example, which lowers the magnetic energy if intersected by a wall. The wall energy depends upon its length, and there will be a competition between wall and pinning energies that determine the wall configuration.

Application of a magnetic field will exert a pressure on the wall and can cause an adjustment of the configuration as the wall again seeks to minimize its length against the constraint of intersecting pinning sites. Each pinning site itself represents a potential energy well for a wall to sit in, and so ther-

mal fluctuations can cause portions of the wall to depin and move to a new pinning site. However depinning from one site may increase the probability of depinning from a nearby site, thereby leading to an avalanche dynamics, as depicted in Fig. 1.25.

In this way, motion of the wall occurs in a series of discrete jumps associated with depinning avalanches. This is also known as Barkhausen noise in that each jump corresponds to the reversal of an area of magnetization and change in the net magnetization.

A description of creep as avalanche dynamics provides a useful means of determining the average velocity of a wall. An applied field of sufficient strength will overcome all barriers and the wall will move linearly with field as in the viscous regime discussed above. At zero temperature, thermal fluctuations will not play a role, and there will be a critical value H_{depin} for the applied field that defines a depinning transition. At this field, any magnitude of avalanche becomes possible, and this insight allows one to define scaling relations for the size of the avalanches. Scaling arguments can then be used to define a depinning energy as the difference between elastic and applied field Zeeman energies

$$E_{elastic} - E_{Zeeman} = E_{depin} \approx U_C \left(\frac{H_{depin}}{H_a} \right)^{\frac{2\zeta - 2 + D}{2 - \zeta}} . \tag{1.100}$$

The exponent ζ in (1.100) and other critical exponents can be derived from renormalization group methods, and D is the dimensionality. The constant U_C is a measure of the pinning potential distribution. The energy E_{depin} represents a barrier to motion of the domain wall in analogy to the activation energy presented earlier in the context of single particle reversal. One can then define an average displacement for a wall overcoming this energy, and assign a characteristic time τ_o to the process. This then allows definition of a speed in the creep regime

$$v_{creep} \approx \frac{\xi}{\tau_o} \exp \left[- \frac{U_C}{k_B T} \left(\frac{H_{depin}}{H_a} \right)^{\mu} \right] , \tag{1.101}$$

where the exponent μ is calculated to be $1/4$ for films thin enough to be considered two dimensional.

An example of measured creep motion for a specially constructed thin 0.5 nm thick Co film is shown in Fig. 1.26 [25]. The measurements were made using magneto-optical microscopy, with motion of the wall created by a pulsed magnetic field. The sample was held at room temperature. Velocities were de-

termined by measuring the distance travelled for a known duration pulse. The straight line is a fit to the wall motion in the viscous regime. The low field data is fit with the creep law (1.101) using $\mu = 0.25$. The transition region between creep and viscous motion lies between 500 and 1200 Oe. A recent summary of creep dynamic experiments can be found in [23].

1.6.2.4 Summary

A summary of concepts and ideas useful for an understanding of measurable phenomena in thin film and nanostructured magnetic materials has been provided. Materials magnetism begins with electronic spin and chemical bonds. Beginning with the base definitions of magnetic moment and its relation to angular momentum, mechanisms were discussed for long range ordering based on electronic orbital overlap in insulators, and electronic band structure in metals.

Equally important to the existence of a magnetically ordered ground state, is the nature of excitations about this ground state. Correlations between spin fluctuations define the lowest energy excitations in ordered magnetic systems, and it was shown how these can be understood by analogy to the quanta of harmonic oscillations associated with vibrations in crystals. A phenomenological model of magnetic ordering and excitations is also described, and key parameters defined in terms of symmetries allowed by the local atomic environment.

The thermodynamic view of magnetic states and configurations is particularly useful for understanding a variety of phenomena, and also for many applications. Here the focus has been on mechanisms for magnetic reversal and coercivity and the concepts of magnetic domain walls and domain wall mobilities are discussed.

The scope of the discussion has been limited to introductory ideas, neglecting a number of very interesting and technologically important developments of recent years. In particular, there is a wealth of new knowledge accumulated regarding electron transport and spin torque transfer that has not been presented. These topics themselves fill several reviews and fall well outside the scope of this brief introduction.

Before closing, there is one other area that is currently developing very quickly. As modern lithographic techniques advance, so to is the ability to define magnetic elements with nanoscale precision in two and three dimensional arrays. The dimensions and geometry of the arrays can be defined such that

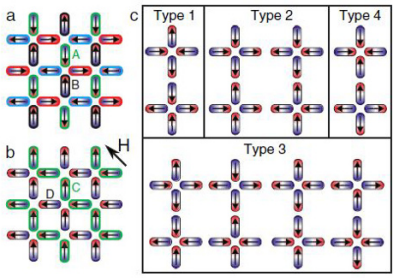

Fig. 1.27 Geometry for a square artificial spin ice array. Configurations can be characterized by arrangements of magnetic poles at vertices. Sixteen different vertex configurations are possible. After [26] (Used with permission)

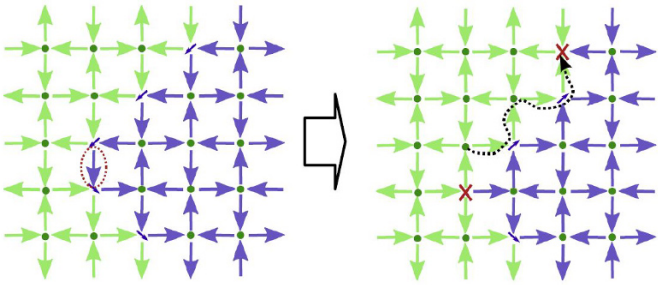

Fig. 1.28 Sketch of a square artificial magnetic ice array. The arrows indicated the domain magnetization of individual elements. Two array ground states are shown with a boundary indicated by the small arrows at vertices. Domain growth occurs through an avalanche along the boundary triggered by a single element reversal at an array domain corner. After [27] (Used with permission)

the individual element interact strongly through, for example, stray dipolar magnetic fields.

These arrays are intriguing as they represent new classes of "artificial" magnetic materials. The materials are artificial in that the interaction strengths can be controlled to a large extent, and response to thermal fluctuations engineered. These systems, in various geometries, have been realized experimentally and typically the element sizes have been chosen to around 200 nm in length, and usually of a soft material such as FeNi. The larger sizes approximate single domain particles and are stable against thermal fluctuations.

A particularly interesting class of arrays use geometry to create frustration in what are called "artificial spin ices". It is useful in these systems to

think of the magnetic orientations at vertices. There are sixteen possible vertex configurations in a square spin ice, and they can be ranked in terms of their corresponding energies due to interactions. There are four distinct energies, allowing for a defintion of four vertex classes. The square ice geometry and corresponding vertex classes are shown in Fig. 1.27 [26].

Reversal of elements accomplished through applied fields, and generally involve a cascade of elemental reversals due to strong inter-element interactions. An example of a spin configuration is sketched in Fig. 1.28 for a square lattice [27]. The lattice is designed to encourage the magnetic elements to align such that the net magnetization is zero, as in a multisublattice antiferromagnet. The large arrows indicate the orientation of element magnetizations, and in this geometry two incompatible ground states are possible for the array. Each ground state is characterized by two arrows in and two arrows out, in analogy to the polar bonds in water ice that obey a similar "ice" rule for the lowest energy configuration.

The arrangement shown in Fig. 1.28 shows the boundary between two neighbouring array ground states. The boundary carries a net magnetic moment, as indicated by the small arrows. Growth of a domain occurs by motion of the boundary. Motion of the boundary occurs via reversals of element magnetizations. The first element to reverse is at a corner of the array domain, and leads to a cascade of other element reversals in a one dimensional avalanche. This avalanche may be triggered by an external field or, if the elements are small enough, by thermal fluctuations.

This example illustrates that the concepts and models developed for continuous films and materials have extensions and applicability to a new class of magnetic systems. The potentials to define key characteristic lengths and energies through nanoscale design allow one to create and engineer new properties and functionalities. The phase space of possibilities is extraordinarily large, and to date only a few examples have been examined. The history of magnetism is one punctuated by the discovery of new and useful phenomena with each advance in materials technology, suggestive of a very interesting future ahead indeed.

References

1. D. C. Mattis, *The Theory of Magnetism* (Harper & Row, 1965)
2. R. M. White, *Quantum Theory of Magnetism* (Springer-Verlag, 1983)

3. J. M. D. Coey, *Magnetism and Magnetic Materials* (Cambridge University Press, 2010)
4. C. Kittel, *Introduction to Solid State Physics*, 8th edn. (John Wiley & Sons, 2004)
5. A.H. Morrish, *Physical Principles of Magnetism* (Wiley-IEEE Press, 2001)
6. V. Gunawan and R.L. Stamps, J. Phys.: Cond. Matter, **23**, 105901 (2011)
7. M.A. Ruderman and C. Kittel, Phys. Rev. **96**, 99 (1954)
8. F.J. Dyson, Phys. Rev., **102**, 1217 (1956)
9. A. I. Akhiezer , V. G. Baryakhtar, S. V. Peletminskii, *Spin Waves* (North-Holland, 1968)
10. Z. S. Borovik-Romanov and S. K. Sinha, *Spin waves and Magnetic Excitations* (Elsevier, 1988)
11. S. O. Demokritov, *Magnonics: From Fundamentals to Applications* (Springer, 2012)
12. D. D. Stancil and A. Prabhakar, *Spin Waves: Theory and Applications* (Springer, 2009)
13. A. Gurevich, G. A. Melkov, Magnetization Oscillations and Waves (CRC Press, 1996)
14. L. Landau and L. Lifshitz, Physik Z. Sowjet. **8**, 153 (1935)
15. T. L. Gilbert, Phys. Rev. **100**, 1243 (1955)
16. M. Sparks, *Ferromagnetic-relaxation theory* (McGraw-Hill, 1964)
17. V. S. L'Vov, *Wave Turbulence Under Parametric Excitation: Applications to Magnets* (Springer, 1994)
18. G. Bertotti, I. D. Mayergoyz, C. Serpico, *Nonlinear Magnetization Dynamics in Nanosystems* (Elsevier, 2009)
19. M. Bauer, J. Fassbender, B. Hillebrands, R.L. Stamps, Phys. Rev. B **61**, 3410 (2000)
20. R. O. Fuller, G.A. Koutsantonis, R.L. Stamps, J. Phys.: Cond. Matter. **21**, 124203 (2009)
21. A. Hubert and R. Schäfer, *Magnetic Domains: The analysis of Magnetic Microstructures* (Springer-Verlag, 1998)
22. R.C. Woodward, K.L. Livesey, R.L. Stamps, J. Magn. Magn. Mater. **272-276**, E531(2004)
23. P.J. Metaxas, Solid State Physics **62**, 75 (2011)
24. A. Mougin, M. Cormier, J.P. Adam, P.J. Metaxas and J. Ferré, Europhys. Lett. **78**, 57007 (2007)
25. P. Metaxas, J.-P. Jamet, A. Mougin, M. Cormier, J. Ferré, V. Baltz, B. Rodmacq, B. Dieny, and R. L. Stamps, Phys. Rev. Lett. **99**, 217208 (2007)
26. Z. Budrikis, J. P. Morgan, J. Akerman, A. Stein, Paolo Politi, S. Langridge, C. H. Marrows, and R. L. Stamps, Phys. Rev. Lett. **109**, 037203 (2012)
27. Z. Budrikis, P. Politi, R. L. Stamps, New J. Phys. **14**, 045008 (2012)

Chapter 2
Synchrotron radiation, polarization, devices and new sources

Marie-Emmanuelle Couprie and Mathieu Valléau

Abstract Synchrotron radiation is emitted by accelerated relativistic charged particles. In accelerators, it is produced when the particle trajectory is subjected to a magnetic field, either in bending magnets or in specific insertion devices (undulators or wigglers) made of an alternated succession of magnets, allowing the number of curvatures to be increased and the radiation to be reinforced. Synchrotron radiation, tunable from infra-red to x-rays, has a low divergence and small size source, and it can provide different types of polarization. It produces radiation pulses, whose duration results from that of the electron bunch from which they are generated. The repetition rate also depends on the accelerator type: high (typically MHz for storage rings, kHz for superconducting linear accelerators) and 10 to 100 Hz (for normal conducting linear accelerators). Longitudinally coherent radiation can also be generated for long bunches with respect to the emitted wavelength or thanks to the Free Electron Laser process.

Marie-Emmanuelle Couprie
Synchrotron-SOLEIL, Accelerator Division, L'Orme des Merisiers, Saint-Aubin, BP48, F-91192 Gif-sur-Yvette, France, e-mail: couprie@synchrotron-soleil.fr

Mathieu Valléau
Synchrotron-SOLEIL, Accelerator Division, L'Orme des Merisiers, Saint-Aubin, BP48, F-91192 Gif-sur-Yvette, France, e-mail: valleau@synchrotron-soleil.fr

E. Beaurepaire et al. (eds.), *Magnetism and Synchrotron Radiation: Towards the Fourth Generation Light Sources*, Springer Proceedings in Physics 151,
DOI: 10.1007/978-3-319-03032-6_2,

2.1 Introduction

Synchrotron radiation, the electromagnetic radiation emitted by accelerated charged particles, is generally produced artificially in particle accelerators, but it can be also observed in astrophysics [1, 8], such as in the sun where hydrogen submitted to loops of magnetic fields emits in the center in the visible and on the edges in the x-ray domain for example.

Theoretical foundations were established at the end of the nineteenth century by Larmor [9] and Liénard [10]. The angular and spectral distribution and polarization properties were then described by Schott [2, 11]. In 1944, Ivanenko and Pomeranchuk estimated a calculated limit on the energy obtainable in a betatron (of the order of 0.5 GeV) due to energy losses due to radiating electrons [12]. Particles slow down and lose synchronism. Because of the spread in revolution frequency with energy, the frequency cannot simply be reduced to maintain synchronism [13] but the particle bunch should be injected in the RF at a proper phase (phase stability), as proposed by McMillan [14] and Veksler [15] in a "synchrotron"-type accelerator, which was then built [16]. After the construction of first accelerators, J.-P. Blewett could measure the particle energy loss on the 100 MeV betatron and he found it in good agreement with the theoretical expectation, but failed to observe synchrotron radiation in the micro-waves [17, 18]. J. Schwinger described the peaked spectrum and predicted that higher photon energies should be observed [19, 20]. The first synchrotron radiation was then observed in the visible tangent to the electron orbit one year later on the 70 MeV General Electric synchrotron, of 29.3 m radius and 0.8 T peak magnetic field [21]. The rapid increase of the intensity with the electron beam energy was measured (fourth power of the energy). The emitted light was found polarized with an electron vector parallel to the plane of the electron orbit. Besides, H. Motz calculated the field created by a relativistic particle in the magnetic sinusoidal field (i.e. such as produced by undulators) [22], and he examined the influence of the bunching of the electrons on the coherence of the radiation. He then observed the polarized visible radiation from an undulator installed on the 100 MeV Stanford accelerator [23]. A buncher set-up after a 3.5 MeV accelerator enabled to achieve 1 W peak power at 1.9 mm thanks the the bunching of the electrons. In parallel, the emission of the radiation spectrum produced from an undulator installed on a 2.3 MeV accelerator was investigated by R. Combe and T. Frelot [24].

In accelerators, synchrotron is produced when the particle trajectory is subjected to a magnetic field, which is for example generated in bending magnets in circular accelerators. The coordinate system given in Fig. 2.1 with s the longitudinal coordinate, x (resp. z) the horizontal (resp. vertical) position is adopted.

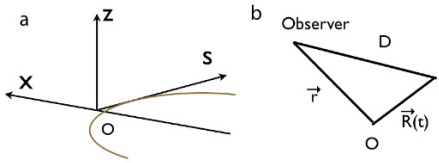

Fig. 2.1 **a** Adopted coordinate system: s the longitudinal coordinate of the electron, transverse coordinates x in horizontal and z in vertical, **b** position of the observer with respect to the emitting particle

When a relativistic particle of normalized energy γ given by $\gamma = \frac{E}{m_o c^2}$ (with E its energy, m_o the particle mass, e the particle charge and c the speed of light) is submitted to the magnetic field B_d of a dipole, its movement is given by the Lorentz equation, as $\gamma m_o \frac{\mathrm{d}\mathbf{v}}{\mathrm{d}\tau} = e\mathbf{v} \times \mathbf{B_d}$, with the particle time τ , its velocity $\mathbf{v}(\tau) = \beta(\tau)c$, and its position $\mathbf{R}(\tau)$. In case of an uniform magnetic field, the particle follows an arc of circle, whose radius ρ is given by

$$\rho = \frac{m_o \gamma \beta c}{eB_d} \tag{2.1}$$

The observer receives the emitted radiation in a cone of solid angle $\frac{1}{\gamma}$ because of the relativistic transformation of the angles from the particle frame to the laboratory frame (see Fig. 2.2). Synchrotron radiation is very collimated, and the higher the electron beam energy, the smaller the collimation angle.

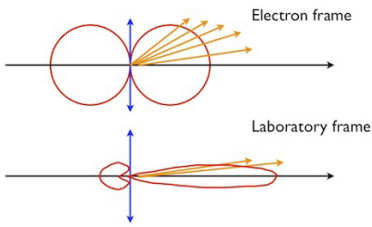

Fig. 2.2 Relativistic projection of the radiation angles, dipole emission in the laboratory frame of the particle and projected emission in the observation frame, within a cone of $\frac{1}{\gamma}$

The dipoles (bending magnets) bend the trajectory of the electron in short arcs, and the observer placed on axis receives the radiation for a very short time: this narrow electric field in the time domain corresponds to a broadband radiation in the frequency domain. In consequence, synchrotron radiation covers a wide spectral range. More intense radiation can be then obtained by alternating a series of N_w dipoles (so-called "wigglers") resulting in an intensity enhancement by N_w . The angle of emission results from the different poles, and it is then wider.

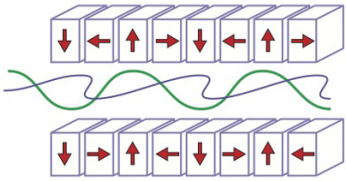

Fig. 2.3 Undulator sketch with a periodic magnetic field created by alternated poles. Case of a periodic field created with permanent magnets according to the Halbach configuration [57].

A periodic magnetic field (period λ_u), as expressed in Tab 2.1 can also be generated in the so-called "insertion devices" (undulator or wigglers) [4] made of an alternated succession of magnets, enabling the radiation to be more intense due to the higher number of emitters (as shown in Fig. 2.3). Insertion devices can be built either using permanent magnets and high permeability steel poles (such as Vanadium Permendur) or with coils (normal or superconducting ones). The movement of electrons in a sinusoidal periodic field B_u (B_{ux} , B_{uz}) is ruled by the first Lorentz equation, i.e. $\gamma m_o \frac{\mathrm{d}\beta}{\mathrm{d}\tau} = e\beta \times \mathbf{B_u}$. A first integration leads to the normalized velocity β, given in Table 2.1, considering that $\frac{1}{\gamma} = \sqrt{1-\beta_x^2-\beta_z^2-\beta_s^2}$ with the deflection parameter K_u , K_{ux} , K_{uz} given by $K_u = \frac{eB_u\lambda_u}{2\pi m_o c}$ ($K_{ux} = \frac{eB_{ux}\lambda_u}{2\pi m_o c}$, $K_{uz} = \frac{eB_{uz}\lambda_u}{2\pi m_o c}$). In the wiggler regime, the angle of the velocity $\frac{K_u}{\gamma}$ is large with respect to $\frac{1}{\gamma}$. For $K_{ux} = K_{uz} = K_u$ and the dephasing between the horizontal and vertical field components $\varphi = \frac{\pi}{2}$, one has $\beta_s = 1 - \frac{1}{\gamma^2} - \frac{K_u^2}{2\gamma^2}$. A second integration gives the trajectory. In the planar case, the electrons execute smooth sinusoïdal oscillations in the horizontal plane, so that the radiation is kept in the same emitted cone. In addition, the beam oscillates at twice the pulsation in the longitudinal direction. The interference takes place for the wavelengths λ_n for which $n\lambda_n = c(1-\beta_s)t$, with n an integer, β_s the longitudinal reduced velocity of the electrons. The fundamental resonant wavelength is obtained for $n = 1$, i.e. for $\lambda_1 = \lambda_u(1-\beta_s)$.

Table 2.1 Velocity and trajectory of a single electron in the magnetic fields for the planar or ellipsoidal undulator cases

Planar Undulator	**Elliptical Polarized Undulator**
Field	**Field**
$\begin{cases} B_{uz} = B_{uz}\cos\left(\frac{2\pi}{\lambda_u}s\right) \\ B_{ux} = 0 \\ B_{us} = 0 \end{cases}$	$\begin{cases} B_{uz} = -B_{uz}sin\left(\frac{2\pi}{\lambda_u}s\right) \\ B_{ux} = B_{ux}sin\left(\frac{2\pi}{\lambda_u}s+\varphi\right) \\ \mathbf{B_{us}} = 0 \end{cases}$
Velocity	**Velocity**
$\begin{cases} \beta_z = 0 \\ \beta_x = \frac{K_u}{\gamma}\sin\left(\frac{2\pi}{\lambda_u}s\right) \\ \beta_s = \sqrt{1-\frac{1}{\gamma^2}-\frac{K_u^2}{\gamma^2}\sin^2\left(\frac{2\pi}{\lambda_u}s\right)} \end{cases}$	$\begin{cases} \beta_z = -\frac{K_{ux}}{\gamma}\cos\left(\frac{2\pi}{\lambda_u}s+\varphi\right) \\ \beta_x = \frac{K_{uz}}{\gamma}\cos\left(\frac{2\pi}{\lambda_u}s\right) \\ \beta_s = 1-\frac{1}{\gamma^2}-\frac{K_{ux}^2}{4\gamma^2}-\frac{K_{uz}^2}{4\gamma^2} \\ \quad +\frac{K_{ux}^2}{4\gamma^2}\cos\left(\frac{4\pi}{\lambda_u}s\right) \\ \quad +\frac{K_{uz}^2}{4\gamma^2}\cos\left(\frac{4\pi}{\lambda_u}s+2\varphi\right) \end{cases}$
Trajectory	**Trajectory**
$\begin{cases} z = 0 \\ x = \frac{K_u\lambda_u}{2\pi\gamma}\cos\left(\frac{2\pi}{\lambda_u}\tau\right) \\ s = \left(1-\frac{1}{2\gamma^2}-\frac{K_u^2}{\gamma^2}\right)c\tau+\frac{cK_u^2\lambda_u}{16\pi\gamma^2}\sin\left(\frac{4\pi}{\lambda_u c}\tau\right) \end{cases}$	$\begin{cases} z = -\frac{K_{ux}\lambda_u}{2\pi\gamma}\sin\left(\frac{2\pi}{\lambda_u}s+\varphi\right) \\ x = \frac{K_{uz}\lambda_u}{2\pi\gamma}\sin\left(\frac{2\pi}{\lambda_u}s\right) \\ s = \left(1-\frac{1}{2\gamma^2}-\frac{K_{uz}^2}{\gamma^2}-\frac{K_{ux}^2}{\gamma^2}\right)c\tau \\ \quad +\frac{cK_{uz}^2\lambda_u}{16\pi\gamma^2}\sin\left(\frac{4\pi}{\lambda_u c}\tau+2\varphi\right) \\ \quad +\frac{cK_{ux}^2\lambda_u}{16\pi\gamma^2}\sin\left(\frac{4\pi}{\lambda_u c}\tau\right) \end{cases}$

Using the expression of β_s , it comes for the resonant wavelength and its harmonics in the planar case

$$n\lambda_n = \frac{\lambda_u}{2\gamma^2}\left(1+\frac{K_u^2}{2}\right) \tag{2.2}$$

The wavelength λ_n of the emitted radiation can be varied by a modification of the undulator magnetic field (by changing the gap for permanent magnet insertion devices or the power supply current for electromagnetic insertion devices). In the time domain, the observer receives a train of N_u magnetic periods which can be considered as quasi-continuous emission of radiation with respect to the bending magnet radiation. The radiation spectrum, square of the

Fourier transform of this train, is then composed of a series of square sinus cardinal, centered on odd harmonics. The "homogeneous" relative linewidth of the harmonics is thus given by

$$\frac{\Delta\lambda}{\lambda_n} = \frac{1}{nN_u} \tag{2.3}$$

The so-called "homogeneous linewidth" refers to the case of a single electron. The emission is then a narrow-band in the frequency domain. In other words, the emitted field interferes between different points of the trajectory, leading to sharp spectral peak emission. The "inhomogeneous" broadening of the undulator line results from the electron beam energy spread, size and divergence.

2.2 Electron beam characteristics

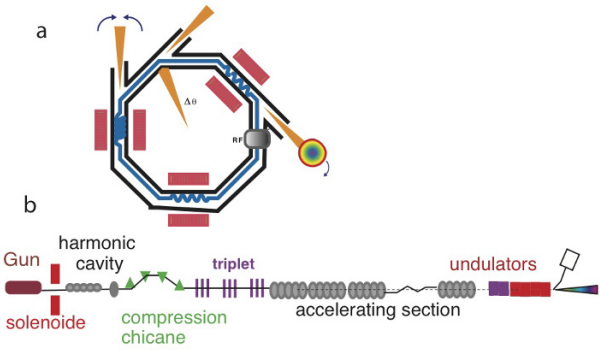

Fig. 2.4 Accelerator schemes: **a** storage ring, **b** linear accelerator

Storage rings [26] (see Fig. 2.4) are composed of a succession of magnetic elements for keeping the particle in a close trajectory. Bending magnets ensure the curvature of the trajectory, quadrupoles the focusing, sextupoles and possibly octupoles the compensation of the non linear terms. The transverse dynamics is ruled by the so-called betatron motion defined by the electron

beam lattice with evolution of the betatron function β_i (i being either x or z) and the dispersion functionη_i . Electron beam size and divergence are given by

$$\sigma_i = \sqrt{\varepsilon_i \beta_i + \eta_i^2 \sigma_\gamma^2} \qquad \sigma_i' = \sqrt{\varepsilon_i (1 + \beta_i'^2/4)/\beta_i + \eta_i'^2 \sigma_\gamma^2} \tag{2.4}$$

with σ_γ the energy spread. The emittance ε (horizontal ε_x and vertical ε_z), the product of the beam size by its divergence, is a figure of merit. ε_x strongly depends on the electron energy, the number of bending magnets as well as the magnetic focalization strengths (optical lattice). For a given ring size, the beam emittance rises quadratically with the electron energy. Different lattices are studied now to reach very low emittances in the so-called ultimate storage rings [30]. The energy loss due to synchrotron radiation is restored by the electric field of the radio frequency (RF) cavity which re-accelerates the particles. The electrons are packed in a large number of bunches. The longitudinal dynamics involving the longitudinal particle position and its deviation with respect to the synchronous particle is called the synchrotron motion. The energy loss and acceleration lead to so-called "synchrotron" energy and position oscillations with respect to the reference particle (the synchronous one at nominal energy in phase with the RF field), these oscillations are damped with the synchrotron damping time. The beam is then kept circulating during several hours. The electron longitudinal oscillation imposed by the RF system induces a pulse minimum duration of few tens of picoseconds, to which is added a systematic bunch lengthening following the interaction with the emitted microwave field [29]. Radiation is emitted via a quantic process, leading to discrete changes in the energy of the particles. The equilibrium between the quantum excitation and the synchrotron damping regime (Fokker-Planck equation) enables to derive the energy spread. Short bunches produced with a specific magnetic field configuration where the value of the momentum compaction factor α relating the orbit distortion to the energy of the particles is decreased. Considering independent electrons, i.e. without collective effects [27, 28], the bunch length scales as α [12], so that the so-called low-α configuration [32, 33] leads to a bunch length of a few ps against tens of ps with traditional storage ring configuration, but at very low current. Further reduction down to hundred of fs is achieved in the slicing scheme [54, 55] where a fs intense laser interacts with the electron beam in an undulator.

In a linear accelerator, the electron beam comes in long μs (even ms for superconducting linacs) macro-pulses containing a large number of micro-

pulses with duration of few tens of ps. Electrons generated at the gun are accelerated with sections of RF cavities and shortened by the longitudinal compression with magnetic chicanes or by velocity bunching. The beam emittance decreases with energy ($\sim 1/\gamma$). Linear accelerators have dramatically progressed thanks to the requirements of the colliders in term of electron beam density, energy spread and stability. State-of-the-art relativistic electron beams are presently delivered by RF linear accelerators with accelerating section gradients of few tens of MV/m, with for example at 1 GeV, 1 nC charge, 1 π .mm.mrad emittance, $\sigma_\gamma \sim 0.01\%$.

In Laser WakeField Accelerators (LWFAs) [34], high-intensity laser pulses are focused in an under dense plasma from a gas target. Due to the intense laser field, the plasma electrons are pushed out of the laser path, and separated from the ions, creating a strong traveling longitudinal electric field, on a length given by the plasma wavelength, providing field gradients up to ~ 100 GV/m. In the bubble regime [35, 36, 37, 38], using a single laser pulse, electron beams in the 100 MeV range can be produced over mm distances ($\sigma_\gamma \sim 5-10\%$, ~ 100 pC charge), or in the 1 GeV range with lower charge with the laser pulse guided over a few cm in a capillary plasma discharge. Scaling laws predict that multi-GeV electron beams with nC charges might be attainable [39, 40] with $\sigma_\gamma \sim 5-10\%$. Two-stage laser plasma accelerators have recently delivered GeV electron bunches with $\sigma_\gamma \sim 1\%$ [41]. Charge and energy spread can be controlled in the colliding laser pulses scheme, leading to $1-10\%$ energy spread, $10-100$ pC charge, 4 fs duration, $5-10\%$ stability [42, 43, 44].

2.3 General characteristics of synchrotron radiation

2.3.1 Retarded Liénard-Wiechert potentials

Let us consider an electron traveling on a curved trajectory and emitting radiation at time τ (the electron time or retarded time) at the position $\mathbf{R}(\tau)$ with a velocity $\mathbf{v}(\tau) = \beta(\tau)c$. The stationary observer receives the emission at time t at the fixed position $\mathbf{r}(\mathbf{t})$. With D the distance between the electron when it emits light and the observer receiving it, one has $t = \tau + \frac{D(\tau)}{c}$ and $D(\tau) = |\mathbf{r}(\mathbf{t}) - \mathbf{R}(\tau)|$. After derivation, it comes $\frac{\mathrm{d}t}{\mathrm{d}\tau} = 1 - \mathbf{n}\cdot\beta c$. Thanks to the Maxwell equations in the Lorentz gauge, the electric $\mathbf{E}(\mathbf{r},t)$ and mag-

netic $\mathbf{B}(\mathbf{r},t)$ fields can be expressed with $\mathbf{B}(\mathbf{r},t) = \left[\frac{\mathbf{n}(\tau)}{c} \times \mathbf{E}(r,t)\right]_{ret}$ and the retarded Liénard-Wiechert potential, as [3]

$$\begin{cases} \mathbf{E}(\mathbf{r},t) = \dfrac{e}{4\pi\varepsilon_0}\left(\left[\dfrac{\mathbf{n}-\beta}{\gamma^2(1-\beta\mathbf{n})^3D^2}\right]_{ret} + \left[\dfrac{\mathbf{n}\times\left[(\mathbf{n}-\beta)\times\frac{\mathrm{d}\beta}{\mathrm{d}\tau}\right]}{(1-\beta\mathbf{n})^3D}\right]_{ret}\right) \\ \mathbf{B}(\mathbf{r},t) = \dfrac{e}{4\pi\varepsilon_0 c}\left(\left[\dfrac{\beta\times\mathbf{n}}{\gamma^2(1-\beta\mathbf{n})^3D^2}\right]_{ret} + \left[\dfrac{\mathbf{n}\left[\mathbf{n}\times[\mathbf{n}-\beta]\times\frac{\mathrm{d}\beta}{\mathrm{d}\tau}\right]}{c(1-\mathbf{n}\beta)^3D}\right]_{ret}\right) \end{cases} \tag{2.5}$$

with ε_o the dielectric vacuum permittivity. For a rest particle, one gets the Coulomb law. The electric field comports two terms, the so-called "velocity field" in $1/D^2$, vanishing at long distances, and so-called "acceleration field" in $1/D$, which is predominant at long distances (far-field case).

2.3.2 Energy loss per turn and power

The radiated power is given by the flux of the Poynting $\mathbf{E}\times\mathbf{B}/\mu_o$ vector through a closed surface S with μ_o the magnetic vacuum permittivity. In case of the far field approximation, the Coulomb term in $1/D$ is neglected, the electric field, the magnetic field and the observation direction are orthogonal to each other. After calculations, the radiated power P by a particle is given by $P = \frac{2r_o}{3m_oc}\left[p_{/\!/}^2 + \gamma^2 p_\perp^2\right]$, with r_o the classical radius of the electron given by $r_o = \frac{e^2}{4\pi\varepsilon_o m_o c^2}$ and $p_{/\!/}$ (resp. $p_\perp$) the parallel (resp. perpendicular) momentum. The radiated power is γ^2 times larger for a perpendicular force than for a longitudinal one. Radiation losses are then very small in linear accelerators. This term is neglected from now. From $\beta \approx 1$ it comes: $P = \frac{2r_o m_o c^3 \gamma^4}{\rho^2}$. The energy loss U_o per turn is given by

$$U_o = \frac{4r_o m_o c^2 \gamma^4}{\rho}. \tag{2.6}$$

In practical units it comes: $U_o[\mathrm{keV}] = 88.5\frac{E^4[\mathrm{GeV}]}{\rho[\mathrm{m}]} = 26.6E^3[\mathrm{GeV}]B_{d\perp}[\mathrm{T}]$. For example, in the case of SOLEIL at 2.75 GeV for a current I of 500 mA, the energy loss per turn due to the bending magnets (field of 1.7 T) is 0.94 MeV,

to which adds the contribution of the insertion devices (0.205 MeV) and of the parasitic modes power (22 keV).

2.3.3 Frequency domain

In the frame of the Lorentz gauge, the field potential can be expressed in the frequency domain [3, 50]. The total power $\frac{\mathrm{d}P}{\mathrm{d}s}$ radiated by a filament mono-energetic beam of current I per unit surface orthogonal to the unit vectors becomes

$$\frac{\mathrm{d}P}{\mathrm{d}S} = \int_0^\infty \frac{\mathrm{d}P}{\mathrm{d}S\mathrm{d}\omega}\,\mathrm{d}\omega = 4\pi\varepsilon_o c^2 \frac{I}{e}\int_0^\infty \mathrm{Re}\left(\mathbf{E}(\mathbf{r},\omega)\times\mathbf{B}^*(\mathbf{r},\omega)\right)\mathbf{s}\,\mathrm{d}\omega \tag{2.7}$$

The spectral flux $\frac{\mathrm{d}\Phi}{\mathrm{d}s}$ per unit surface (i.e. the number of photons per unit surface, per second, per relative frequency bandwidth) is then

$$\frac{\mathrm{d}\Phi}{\mathrm{d}s} = \frac{2\pi\omega}{h\omega}\frac{\mathrm{d}P}{\mathrm{d}S\mathrm{d}\omega} = \frac{8\pi\varepsilon_o c^2}{h}\frac{I}{e}\mathrm{Re}\left(\mathbf{E}(\mathbf{r},\omega)\times\mathbf{B}^*(\mathbf{r},\omega)\right)\mathbf{s} \tag{2.8}$$

with h the Planck constant. In the far-field approximation case, the fields can then be expressed as

$$\begin{cases}\mathbf{E}(\mathbf{r},\omega) = \frac{-ie\omega}{4\pi c\varepsilon_o D}\exp\frac{i\omega\mathbf{n}\cdot\mathbf{r}}{c}\mathbf{H}(\mathbf{n},\omega)\\ \mathbf{B}(\mathbf{r},\omega) = -\frac{1}{c}\mathbf{E}(\mathbf{r},\omega)\times\mathbf{n}\end{cases} \tag{2.9}$$

with the dimensionless field vector $\mathbf{H}$ given by

$$\mathbf{H}(\mathbf{n},\omega) = \frac{\omega}{2\pi}\int_{-\infty}^{\infty}(\mathbf{n}-\beta)\exp\left(i\omega\left(\tau-\mathbf{n}\cdot\mathbf{R}/c\right)\right)\mathrm{d}\tau \tag{2.10}$$

$$\mathbf{H}(\mathbf{n},\omega) = \frac{\omega}{2\pi}\int_{-\infty}^{\infty}\mathbf{n}\times(\mathbf{n}\times\beta)\exp\left(i\omega\left(\tau-\mathbf{n}\cdot\mathbf{R}/c\right)\right)\mathrm{d}\tau \tag{2.11}$$

It enables to express the different physical quantities [25]. It can also be seen that $\mathbf{E}(\mathbf{r},\omega)$ is the Fourier transform of $\frac{e}{2c\varepsilon_o D}\frac{d}{dt}\left(\mathbf{n}\times(\mathbf{n}\times\beta)\right)$, representing the electric field seen by the observer in the time domain [7].

$$\mathbf{E}(\mathbf{r},t) = \frac{e}{4\pi\varepsilon_0}\left(\left[\frac{\mathbf{n}-\beta}{\gamma^2\left(1-\beta\cdot\mathbf{n}\right)^3 D^2}\right]_{ret} + \left[\frac{\mathbf{n}\times\left[(\mathbf{n}-\beta)\times\frac{\mathrm{d}\beta}{\mathrm{d}\tau}\right]}{\left(1-\beta\cdot\mathbf{n}\right)^3 D}\right]_{ret}\right) \tag{2.12}$$

The general treatment (without the far-field approximation) should be applied for the infrared edge radiation and in some cases of off-axis undulator emission. The approximation of ultra-relativistic beams ($\frac{1}{\gamma} << 1$) can also be considered; it comes

$$\beta = \left(\beta_x, \beta_z, \sqrt{1-\frac{1}{\gamma^2}-(\beta_x^2+\beta_z^2)}\right) \approx \left(\beta_x, \beta_z, 1-\frac{1}{2\gamma^2}-\frac{\beta_x^2+\beta_z^2}{2}\right). \tag{2.13}$$

In the small angle (or paraxial) approximation with small values of the angle of observation θ, the direction of observation $\mathbf{n}$ is then given by

$$\mathbf{n} = \left(\theta_x, \theta_z, \sqrt{1-\theta_x^2-\theta_z^2}\right) \approx \left(\theta_x, \theta_z, 1-\frac{\theta_x^2+\theta_z^2}{2}\right). \tag{2.14}$$

2.3.4 Brilliance and mutual coherence

The common approach is to define the brilliance as the number of photons per second and per unit of phase space (or the density distribution in phase space), which corresponds to the geometrical optics frame. It enables to describe somehow the propagation properties of the rays through optical elements. The general expression of the brilliance $\mathscr{B}$ (or spectral brightness in a narrow bandwidth) is given by means of the Wigner distribution [45, 46] as defined in quantum mechanics as a quasi-probability density of a quantum system in phase space. The Wigner distribution [47], first developed in the statistical quantum mechanics, has also been adopted for the treatment of optical waves [48].

$$\mathscr{B}(\chi,\chi',s,\omega,\widehat{u}) = \frac{\varepsilon_0\omega^2 I}{2\pi^2 hce}\int_{-\infty}^{+\infty}\int_{-\infty}^{+\infty}\mathbf{E}\left(\chi'+\tfrac{\xi}{2},s,\omega\right)\widehat{u^*}.\mathbf{E}^*\left(\chi'-\tfrac{\xi}{2},s,\omega\right)\widehat{u} \times\exp\left(-\mathrm{i}\tfrac{\omega}{c}\chi.\xi\right)\mathrm{d}^2\xi\,. \tag{2.15}$$

with $\widehat{u}$ the polarization state, $\mathbf{E}$ the electric field in its angular representation, $*$ for its complex conjugate, χ and χ' representing transverse position (x,z)

and angles (θ_x, θ_z) . This concept inherently incorporates the complete information on the electric field, from different position. It thus properly provides information on the transverse coherence (ability to interfere [49]). Indeed, the one of mutual intensity, defined as

$$\mathscr{M}(\chi,\chi',s,\omega,\widehat{u}) = \left(\mathbf{E}\left(\chi+\frac{\xi}{2},s,\omega\right)\widehat{u}^*\right)\left(\mathbf{E}^*\left(\chi'-\frac{\xi}{2},s,\omega\right)\widehat{u}\right) \tag{2.16}$$

simply relates to the generalized brilliance definition, as

$$\mathscr{M}(\chi,\chi',s,\omega,\widehat{u}) = \frac{h}{2\pi\varepsilon_0 c}\frac{e}{I}\int_{-\infty}^{+\infty}\int_{-\infty}^{+\infty}\mathscr{B}(\chi,\chi',s,\omega,\widehat{u})\exp\left(-\mathrm{i}\frac{\omega}{c}\chi'.\xi\right)\mathrm{d}^2\chi'. \tag{2.17}$$

The generalized Wigner brilliance enables to recover the usual quantities. The density of photons per unit surface and solid angle results from the integration of the brilliance over spatial coordinates. This general spectral brightness, by relating directly to the electric field, contains the information on the phase and enables a proper treatment of the wavefront propagation within Fresnel diffraction, and transformation through optical elements. Such a brightness is real, but not necessarily positive. This could appear as a paradox for a quantity describing a photon density, but it could result from the quantum nature of photon for which position and momentum cannot be measured at the same time, forbidding strictly speaking to define a photon density [45]. More precisely, its projections are positive [46]. A part from the specific case of bunching (such as in free electron laser), the classical approximation to sum over the electrons from a statistical point of view can be applied, provided that the electron bunch duration is long with respect to the coherence time and long with respect to $2\pi c N_u/\lambda_u$. Concerning the thick beam analysis, the convolution between the electron/ photon beam sizes, divergences can be applied provided the trajectory inside the undulator or wiggler induces small deviation in position and angle and that the undulator does not introduce important modifications of the electron beam (such as focusing modifying the electron beam size) or strong cosh type dependance (term neglected here in Table 2.1, required in principle to verify Maxwell equation).

In the approximation of Gaussian distributions, the brilliance becomes

$$\mathscr{B} = \left(\frac{w}{\pi c}\right)^2 \Phi(\omega,\mathbf{u})\exp\left(-\frac{\theta_x^2}{2\sigma_{x'ph}}-\frac{\theta_z^2}{2\sigma_{z'ph}}-\frac{x^2}{2\sigma_{xph}}-\frac{z^2}{2\sigma_{zph}}\right) \tag{2.18}$$

with the horizontal $\sigma_{x'ph}$ (resp. σ_{xph}) and vertical (resp. σ_{zph}) divergence (resp. size) of the photon beam resulting from the single electron emission and from

the contribution of the electron beam emittance and energy spread. In this case, one recovers the usual definition of brilliance. Besides the fact that propagation is treated in the geometrical optics frame, it is unlikely that undulator radiation can be assimilated to a Gaussian beam, as it will be discussed in the next sections. In consequence, the use of such a definition should be handled with great care in considering ultimate storage ring issues or partial coherence of synchrotron radiation. A proper treatment has been derived in the frame of the Wigner distribution [45, 46].

2.3.5 Generations of accelerator based light source

The so-called first generation took advantage of the parasitic synchrotron radiation emitted in the storage rings initially built for high energy physics. The second generation was developed on dedicated storage ring accelerators. The third generation light sources arose on storage rings with reduced emittances [31] and high number of installed undulators or wigglers. They provide a high average brilliance and a partial transverse coherence [56] thanks to the low beam emittance in the storage ring and to the high number of insertion devices generating spontaneous emission. Light pulses are limited in terms of pulse duration to a few ps, unless particular optics [32] or slicing scheme [54, 55] are applied, but to the detriment of the total flux. Fourth Generation Light Sources generally use linear accelerators for short pulse duration. In addition, they enable longitudinal coherence by setting in phase the emitting electrons thanks to the free electron laser (FEL) process. A light wave of wavelength λ (spontaneous emission progressing along the undulator or stored in an optical cavity, or external seed) interacts with the electron bunch in the undulator, inducing an energy modulation of the electrons which is gradually transformed into density modulation at the wavelength and leads to a coherent radiation emission. After the theoretical proposal of the FEL [51], the first FEL experience was carried out in 1977 on MARK-III at Stanford, USA using an oscillator configuration in the infrared [53]. Whereas great hope was put in re-circulating accelerators such as storage rings in the early FEL times, the dramatic progress of linear accelerator has enormously contributed to the success of x-ray FELs. However decrease in wavelength requires an increase in energy of the accelerated electrons (typically hundreds of MeV to several GeV for VUV/soft and hard x-rays). Light sources using energy recovery linear accelerators are also somehow considered as fourth generation

light source, since sub-ps bunches are produced. The fifth generation is not yet clearly defined; among possible understandings, the conventional linear accelerator is replaced by a laser wakefield one, for a more compact source.

2.4 Radiation from a bending magnet and from wigglers

2.4.1 Radiation from a bending magnet

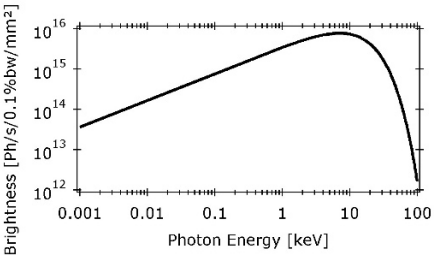

Fig. 2.5 Brightness from a SOLEIL dipole magnet generating 1.7 T with a curvature radius of 11.25 m observed at 20 m through a 1 mm squared window. Beam parameters: $E = 2.75$ GeV, $I = 400$ mA, $\sigma_\gamma = 0.1\%$, $\varepsilon_x = 4$ nm.rad, $\varepsilon_z = 40$ pm.rad.

In a bending magnet, the electron emits radiation during $\Delta t' = \rho/\gamma c$ towards the observer, who receives it during $\Delta t = (1 - \mathbf{n}\cdot\beta)$, i.e. during $\Delta t \sim \frac{2\rho}{3\gamma^3 c}$. The so-called "critical pulsation" ω_c becomes by Fourier analysis $\omega_c \sim \frac{3\gamma^3 c}{2\rho}$. The "critical wavelength" is $\lambda_c \sim \frac{4\pi\rho}{3\gamma^3}$. It is less than 1 keV for storage rings below 1 GeV, in the $1-10$ keV range for several GeV rings. For a direction of observation in the (xOz) plane, with ψ the angle between the observation direction and the axis x, the emitted angular flux is given by

$$\frac{\mathrm{d}\Phi}{\mathrm{d}\Omega} = \frac{3e\gamma^2}{16\pi^3\varepsilon_o c}\frac{\omega^2}{\omega_c^2}\left(1+(\gamma\psi)^2\right)^2 K_{2/3}^2(\xi) + \frac{(\gamma\psi)^2}{1+(\gamma\psi)^2}K_{1/3}^2(\xi) \qquad (2.19)$$

with the angle $\xi = \left(1+(\gamma\psi)^2\right)^{3/2}\omega/\omega_c$, $K_{1/3}$ and $K_{2/3}$ the modified Bessel functions. In practical units, in the orbit plane, it comes

$$\frac{\mathrm{d}\Phi}{\mathrm{d}\Omega}(\psi=0)\left(ph/s/mrad^2/0.1\%BW\right)= 1.327\times10^{13}E^2(GeV)\,I(A)\,\frac{\omega^2}{\omega_c^2}K_{2/3}^2\left(\frac{\omega}{\omega_c}\right). \tag{2.20}$$

It can be integrated over the ψ angle. The horizontal angle of emission is spanned by the particle movement, and it is rather wide. Several beamlines can use jointly the bending magnet radiation. The bending magnet radiation is polarized linearly in its plane. Out of it, the elliptical polarization can be decomposed in a vertical $I_\perp$ and horizontal $I_{/\!/}$ components as

$$\frac{I_{/\!/}}{d\Omega}+\frac{I_\perp}{d\Omega}=\frac{7e^2}{4\pi\varepsilon_o}\frac{1}{16\rho}\left(\frac{\gamma^2}{1+(\gamma\psi)^2}\right)^{5/3}\left(1+\frac{5}{7}\frac{(\gamma\psi)^2}{1+(\gamma\psi)^2)^2}\right). \tag{2.21}$$

$I_{/\!/}$ is centered at $\Psi=0$ within $\Delta\psi=1.13/\gamma$. $I_\perp$ is maximum for $\psi=\pm0.63/\gamma$. The cone of the whole emission is $1.3/\gamma$. Out of the orbit plane, the rate of linearly polarization decreases whereas the rate of circular polarization is larger.

2.4.2 Radiation from a wiggler

In the wiggler case (N_w periods), the deflection parameter K_w being large, the radiation from the different periods does not interfere but simply adds. The wiggler radiation can then be treated as the sum of the radiation from the equivalent different $2N_w$ dipoles trajectory curvatures, considering the magnetic field where the electron trajectory is tangential to the observation direction. The critical pulsation thus also depends on the observation direction, according to $\omega_c(\theta)=\sqrt{1-(\theta K_w/\gamma)^2}$. The total emission angle is of $2K_w/\gamma$ with two transverse source points given by $x_{source}=\pm\frac{Kw}{\gamma}\frac{\lambda_w}{2\pi}$ whereas the depth of field along s should be considered. In the case of planar vertical field wigglers, polarization is linear in the orbit plane. Out of this plane, it becomes circular right (resp. left) for positive (resp. negative) half-period magnetic fields. Adding for the $2N_w$ dipoles of the wiggler, the incoherent superposition of left and right circular components cancels out in non polarized radiation besides the remaining linear components. Radiation is extended towards the higher photon energies with a several pole wiggler [115].

2.5 Undulator radiation

2.5.1 Emitted field

In the case of periodic fields (period λ_{ux} and λ_{uz}) with a N_u number of periods, the field vector $\mathbf{H}(\theta_x, \theta_z, \omega)$ can be expressed as

$$\mathbf{H}(\theta_x, \theta_z, \omega) = N_u \mathbf{h_n}(\theta_x, \theta_z, \omega) \operatorname{sinc} \frac{\pi N_u (\omega - \omega_1)}{\omega_n} \tag{2.22}$$

with $\operatorname{sinc}(x) = \frac{\sin x}{x}$. The general expression of the resonant wavelength is

$$\lambda_n = \frac{\lambda_u}{2\gamma^2 n}(1 + \frac{K_{ux}^2}{2} + \frac{K_{uz}^2}{2} + \gamma^2\theta_x^2 + \gamma^2\theta_z^2) \tag{2.23}$$

with the general deflection parameters K_x and K_z given by $K_x = \sqrt{\frac{2\gamma^2}{\lambda_u}\int_0^{\lambda_u} \beta_x^2 \mathrm{d}s}$ and $K_z = \sqrt{\frac{2\gamma^2}{\lambda_u}\int_0^{\lambda_u} \beta_z^2 \mathrm{d}s}$. Considering a planar undulator, in the temporal domain (Fig. 2.6), the field is nearly sinusoidal for small values of the deflection parameter, resulting in an emission mainly on the fundamental wavelength. When the deflection parameter increases, the distance between the peaks in time gets larger and the radiation is red-shifted. The temporal pulses are getting narrower, deviating from a sinusoid, and inducing emission on different harmonics. For even larger deflection parameters, the radiation tends to be equivalent to that of twice the number of period dipoles of equivalent peak field, getting into the wiggler regime.

The far-field electric field for small angles presents a periodicity resulting from that of the magnetic field, leading to a harmonic spectrum. A typical on-axis spectrum for a typical planar in-vacuum undulator of SOLEIL is shown in Fig. 2.7a in the case of a filament mono-energetic electron beam. On-axis radiation is mainly emitted on the odd harmonics, whereas the even harmonics start to appear with increasing harmonic order, because of the finite observation window. The influence of the electron beam contribution is illustrated in Fig. 2.7b–e on zooming on one odd and one even harmonic. The emittance contribution enlarges the lines on the red side of the spectrum, because the electron beam dispersion of position and divergence can be assimilated to an off-axis emission at wavelengths larger than the harmonic resonant one, via the $\gamma^2\theta^2$ of the resonant condition. Indeed, it results in a significant growth of

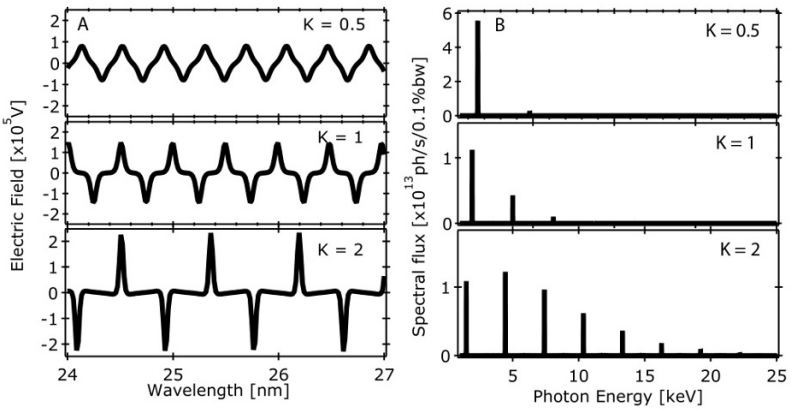

Fig. 2.6 **A** Electric field. **B** associated spectra for different values of the deflection parameter: $K = 0.5$, $K = 1$ and $K = 2$ calculated with SRW [93] at 20 m from the source through a 250 μm squared aperture. Case of a planar undulator: $\lambda_u = 2$ cm, $N_u = 100$, $K_u = 1.81$ (corresponding to Sm_2Co_{17} magnets with vanadium/permendur poles). Beam parameters: $E = 2.75$ GeV, $I = 400$ mA, $\sigma_\gamma = 0.1\%$, $\varepsilon_x = 4$ nm.rad, $\varepsilon_z = 40$ pm.rad

the even harmonic whereas a side-band appears on the odd one. The energy spread contribution to the inhomogeneous broadening can be easily expressed from the resonant condition, as $\Delta\lambda/\lambda = 2\sigma_\gamma$. For example, for 0.1% energy spread, it equals the homogeneous linewidth for $N_u n = 500$, i.e. for a 100 periods undulator, for the fifth harmonic. It results in Fig. 2.7d to a reduction of the undulator odd line peak intensity (by more than a factor of 10) and to a line widening (by 65 eV). The even harmonic grows as well significantly. Adding both the thick beam contributions due to the emittance and the energy spread makes the eleventh harmonic to be reduced in intensity (by a factor of 15) and to be widened (from 16 eV to 87 eV). The higher the harmonic order, the larger is the effect, since the homogeneous relative linewidth inversely decreases with the harmonic number.

The influence of the aperture observation size is shown in Fig. 2.8. When the observation size gets larger, off-axis radiation is seen with wavelength different from the resonant one. In addition, even harmonics, which are not emitted for a filament electron beam on-axis, are getting more intense with respect to the even harmonics. In the frequency domain, the normalized on-axis field vector can be expressed as

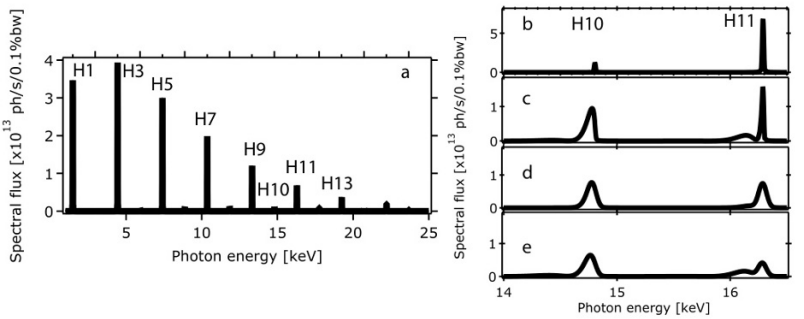

Fig. 2.7 On-axis spectrum calculated with SRW at 20 m from the source through a 250 μm squared aperture. Case of a planar undulator: $\lambda_u = 2$ cm, $N_u = 100$, $K_u = 1.81$ (corresponding to Sm_2Co_{17} magnets with vanadium/permendur poles). Beam parameters: $E = 2.75$ GeV, $I = 400$ mA. **a** $\sigma_\gamma = 0$, $\varepsilon_x = \varepsilon_z = 0$ pm.rad. Zooms on the tenth and the eleventh harmonics (b-e): **b** $\sigma_\gamma = 0$, $\varepsilon_x = \varepsilon_z = 0$ pm.rad. **c** $\sigma_\gamma = 0$, $\varepsilon_x = 4$ nm.rad, $\varepsilon_z = 40$ pm.rad. **d** $\sigma_\gamma = 0.1\%$, $\varepsilon_x = \varepsilon_z = 0$ pm.rad. **e** $\sigma_\gamma = 0.1\%$, $\varepsilon_x = 4$ nm.rad, $\varepsilon_z = 40$ pm.rad

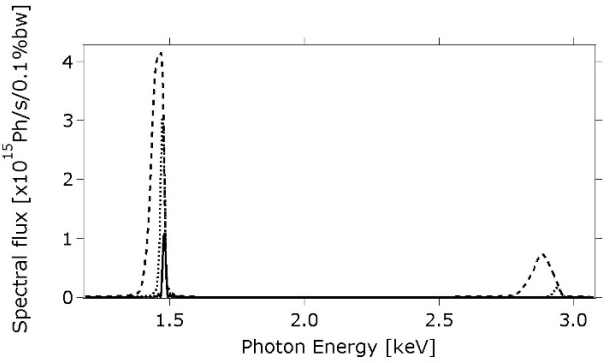

Fig. 2.8 Undulator spectra calculated with SRW through a 50 μm (-) squared aperture ($\times 100$) , 1 mm ($\cdots$) or a 2 mm ($--$) one. Case of a planar undulator: $\lambda_u = 2$ cm, $N_u = 100$, $K_u = 1.81$. Beam parameters: $E = 2.75$ GeV, $I = 400$ mA, $\sigma_\gamma = 0.1\%$, $\varepsilon_x = 4$ nm.rad, $\varepsilon_z = 40$ pm.rad

$$\begin{cases} \text{For odd harmonics, } \mathbf{h_n}(0,0) = \gamma \frac{nK_u}{1+K_u^2/2} \left[J_{\frac{n+1}{2}} \left(\frac{nK_u^2/2}{4+2K_u^2/2} \right) - J_{\frac{n-1}{2}} \left(\frac{nK_u^2/2}{4+2K_u^2/2} \right) \right] \mathbf{u} \\ \text{For even harmonics, } \mathbf{h_n}(0,0) = 0 \end{cases} \tag{2.24}$$

The Bessel functions can also be seen as resulting from the oscillation at twice the pulsation in the expression of the position s . Off-axis radiation leads to more complex expressions.

2.5.2 Angular and angle integrated spectral flux

The angular spectral flux $\frac{\mathrm{d}\phi}{\mathrm{d}\Omega}(\theta_x, \theta_z, \omega, \mathbf{u})$ at the pulsation ω close the one of the undulator harmonics can be expressed for a filament mono-energetic beam in the direction (θ_x , θ_z) as

$$\frac{\mathrm{d}\phi}{\mathrm{d}\Omega}(\theta_x, \theta_z, \omega, \mathbf{u}) = \frac{\alpha I N_u^2}{e} |\mathbf{h_n}(\theta_x, \theta_z, \mathbf{u})|^2 \,\mathrm{sinc}^2\left(\frac{\pi N_u(\omega - \omega_1)}{\omega_n}\right) \qquad (2.25)$$

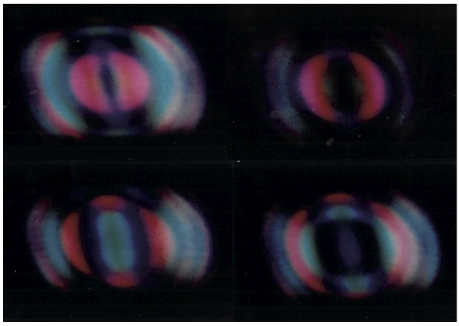

Fig. 2.9 Transverse images of the free electron laser two undulators ($N_u = 2x7$, $\lambda_u = 78$ mm) installed on the ACO storage ring for different gaps at 170 MeV. The large size of the vacuum chamber enables to observe the different rings of the radiation due to the off-axis and harmonic emission

The angular spectral flux comports two terms, the "interference term" term and the "lobe function" one. The "interference term", varying as sinus cardinal, gives the homogeneous linewidth of the radiation: the higher the number of period, the sharper the line. It depends also on the observation angle through the resonant frequency. The "lobe function" term ($\mathbf{h_n}(\theta_x, \theta_z, \mathbf{u})$) depends on the magnetic field characteristics. Radiation is emitted in a narrow cone, which gets larger for higher harmonics. Off-axis radiation for a resonant wavelength is emitted at higher wavelength, as seen in the images shown in Fig. 2.9. The resonant wavelength is emitted in the center, with larger ring for longer wavelengths (such as the red ring). Further blue rings correspond to the

off-axis emission of the successive harmonics. The black holes in the ring are related to the form factor. When the gap is opened, the deflection parameter is lowered, the resonant wavelength is reduced and the red off-axis emission shifts to a larger ring size. The angle integrated spectral $\Phi(\omega,\mathbf{u})$ flux over angles leads on resonant harmonics to

$$\Phi(\omega_n,\mathbf{u}) = \frac{\alpha\pi N}{2en\gamma^2}\left(1+\frac{K_{ux}^2}{2}+\frac{K_{uz}^2}{2}\right)|\mathbf{h_n}(0,0)\mathbf{u}|^2 \tag{2.26}$$

and close to the resonant harmonic to

$$\Phi(\omega_n',\mathbf{u}) = \frac{\alpha\pi N}{en\gamma^2}\left(1+\frac{K_{ux}^2}{2}+\frac{K_{uz}^2}{2}\right)|\mathbf{h_n}(0,0)\mathbf{u}|^2 \tag{2.27}$$

corresponding to a flux twice larger than for the resonant frequency. The flux does not depend on the electron beam energy, even though, for a given spectral range, the value of the energy determines that of the K value.

2.5.3 Divergence and beam size

The divergence can be evaluated considering the angular spectral flux. In the approximation of small angles and large number of periods, it comes $\mathbf{H_n}(0,0,\omega) = N_u\sum_{n=1}^{\infty}(-1)^{n(N_u-1)}\mathbf{h_n}(0,0)\,\mathrm{sinc}(\Gamma)$ with $\Gamma = \frac{\pi n(\theta_x^2+\theta_z^2)L_u}{\lambda_1} + \pi N_u(\lambda_1/\lambda - n)$ and L_u the length of the undulator. For a given harmonic, the photon spatial distribution depends on the energy as illustrated in Fig. 2.10. In the case of the first harmonic Fig. 2.10(a-c), for a photon wavelength smaller than the resonant one (blue side of the spectrum), the cone presents a smooth distribution with the smallest divergence, but with less flux. At resonant wavelength, the distribution is larger and presents a flat-top, with a larger intensity. For wavelength larger than the resonant wavelength (red side of the spectrum), the radiation is emitted in a ring, corresponding to the particular cone of emission. It is not Gaussian. Divergence is then larger. Cuts of the images Fig. 2.10(a-c) are given in Fig. 2.10g, illustrating clearly that the distribution is far from being Gaussian. The ring thickness comes from the electron beam contribution, the higher the harmonic, the thicker the ring as shown in Fig. 2.10(d-f). The separated contributions of the energy spread and of the emittance are shown in Fig. 2.11. Both are smearing out the structure,

indeed because the considered radiation is in the hard x-ray. Structures can be better kept with the thick beam contribution for undulators emitting in the VUV.

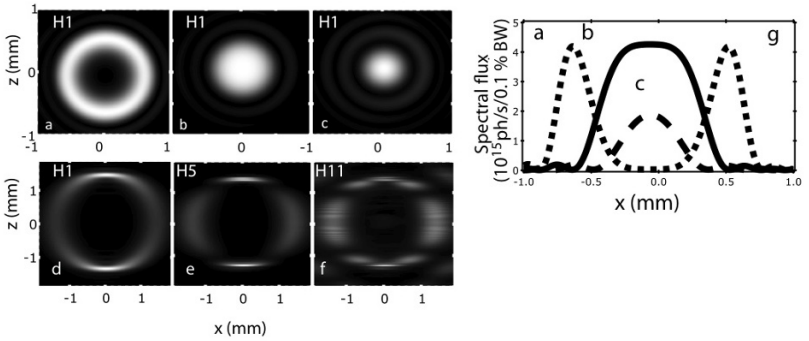

Fig. 2.10 Angular flux calculated with SRW at 20 m from the source through a 250 μm squared aperture in the case of planar undulator: $\lambda_u = 2$ cm, $N_u = 100$, $K_u = 1.81$ (corresponding to Sm_2Co_{17} magnets with vanadium/permendur poles). Beam parameters: $E = 2.75$ GeV, $I = 400$ mA $\sigma_\gamma = 0.1\%$, $\varepsilon_x = 4$ nm.rad, $\varepsilon_z = 40$ pm.rad. (a-d) First , (e) fifth, and (f) eleventh harmonics. **a** H1 low energy side 1.465 keV, **b** H1 resonant energy 1.47 keV, **c**H1 high energy side 1.472 keV in a 0.5 eV resolution. **d** H1 1.465 keV, **e** H5 7.38 keV, **f** H11 16.35 keV, **g** horizontal cuts of images (a-c)

The divergence can be properly calculated with the *rms* value of the distribution. For practical reasons, the divergence of the resonant radiation Σ'_{ph} can be fitted and provides an estimation of the undulator divergence as

$$\Sigma'_{ph} = 0.69\sqrt{\frac{\lambda_n}{2L}} = \frac{0.69}{2\gamma}\sqrt{\frac{\left(1+\frac{K_{ux}^2}{2}+\frac{K_{uz}^2}{2}\right)}{nN}} \tag{2.28}$$

The higher the number of periods, the smaller the divergence. The expression does not contain all the proper information for an exact evaluation of the transport in the beamline. One can however perform the fit for an energy where the flux is twice larger, what modifies the numerical coefficient of the expression.

The photon undulator beam size can be conceived as the source point which can be imaged by a lens with an observation plane which is a conjugate to the undulator center. The expression can be derived as

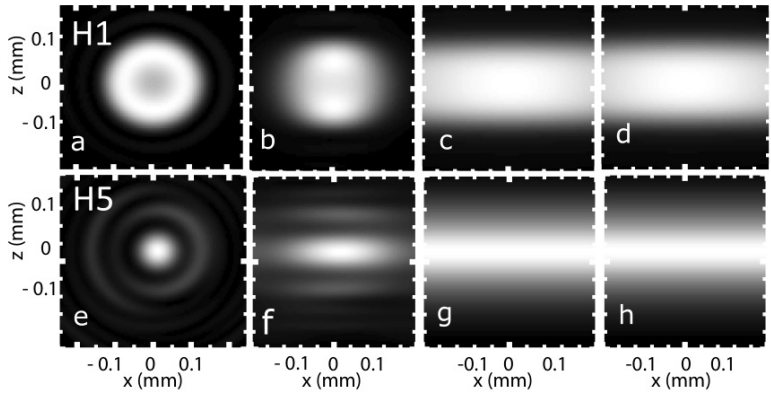

Fig. 2.11 Spectral flux calculated with SRW on H1 (a-d) at 1.47 keV in 10 eV and on H5 (e-h) at 7.4 keV in 10 eV at 20 m from the source through a 250 μm squared aperture for a planar undulator ($\lambda_u = 2$ cm, $N_u = 100$, $K_u = 1.81$) at $E = 2.75$ GeV, $I = 400$ mA for various beam parameters: (a,e) $\sigma_\gamma = 0$, $\varepsilon_x = \varepsilon_z = 0$ pm.rad; (b,f) $\sigma_\gamma = 0$, $\varepsilon_x = 4$ nm.rad, $\varepsilon_z = 40$ pm.rad; (c,g) $\sigma_\gamma = 0.1\%$, $\varepsilon_x = \varepsilon_z = 0$ pm.rad; (d, h) $\sigma_\gamma = 0.1\%$, $\varepsilon_x = 4$ nm.rad, $\varepsilon_z = 40$ pm.rad

$$\frac{\mathrm{d}\Phi_n}{\mathrm{d}l}(r,\omega,\mathbf{u}) = \alpha_o \frac{I}{e} N_u^2 \left(\frac{\omega}{2\pi c}\right)^2 |\mathbf{h_n}(0,0)|^2 \left| \int_{-\infty}^{+\infty} \mathrm{sinc}\left[\pi N_u \left(\frac{\omega}{\omega_1(\theta)} - n\right)\right] \times J_0\left(\frac{\omega\theta_r}{c}\right)\theta \mathrm{d}\theta \right|^2 . \quad (2.29)$$

Instead of properly calculating the *rms* value of the distribution, a fit for the resonant wavelength distribution with a Gaussian provides an estimation of the sources size

$$\Sigma_{ph} = 2.74\sqrt{\lambda_n L}/4\pi = \frac{1.89\lambda_u}{4\pi\gamma}\sqrt{\frac{N}{2}\frac{\left(1+\frac{K_{ux}^2}{2}+\frac{K_{uz}^2}{2}\right)}{nN}} . \quad (2.30)$$

2.6 Undulator technology

The requirements for the insertion devices depend on the accelerator type. Multi-turn recirculating vacuum chambers should be rather wide, especially in the horizontal dimensions for accelerators such as storage rings for synchrotron radiation because of the beam excursion during injection, leading to a flat vacuum chamber. In contrast, single or few pass accelerator such as Linac, Energy Recovery Linac or LWFA enable small aperture cylindrical vacuum chamber, enabling to add magnetic material on the sides. Again, because of recirculation, multipolar terms can be critical for storage rings for lifetime and beam injection efficiency. A small value of the phase error enables operation on the undulator harmonics, especially on third generation storage rings of intermediate energy. It is then less critical for a FEL application where operation takes place mainly on the fundamental wavelength and its first harmonics. Impedance restrictions result from extremely short bunches, vacuum chambers type (size, roughness, discontinuity) and number of turns. Using permanent magnets for undulator fabrication [95, 57] enables to provide a steady-state magnetic field, with extremely low operating cost. Poles are added to enhance the peak magnetic field for a given period.

To reach a higher magnetic field, the physical limitation of the magnetic gap due to the vacuum chamber is eliminated by the mounting beams supporting the magnet arrays inside the vacuum chamber for in-vacuum undulators. To avoid demagnetization, proper grades of magnets should be selected, compromising between the value of the remanent field B_r and the coercitivty H_{cj}: either Sm_2Co_{17} ($B_r \leqslant 1.05\,\mathrm{T}$, $\mu H_{cj} = 2.8\,\mathrm{T}$) or $Nd_2Fe_{14}B$ ($B_r \leqslant 1.25\,\mathrm{T}$, $H_{cj} = 2.4\,\mathrm{T}$) whereas for out-of-vacuum devices, grades with larger fields can be used ($B_r = 1.4\,\mathrm{T}$, $\mu H_{cj} = 1.5\,\mathrm{T}$). In addition, machine protection to avoid beam losses on the magnets requires a proper setting of the scraper values. After a first prototype built at BESSY [58], in-vacuum undulators were actively developed in Japan. A first undulator with 90 periods of 40 mm, using $Nd_2Fe_{14}B$ magnets ($B_r = 1.2\,\mathrm{T}$, $iH_c = 21\,\mathrm{kOe}$) has been installed on TRISTAN [59] and operated with a minimum gap 10 mm, leading to a field of 0.82-0.36 T . Equipped with NEG and sputter ion pumps, a magnet stabilization at 125° C enabled vacuum commissioning at 115° C. In-vacuum undulators were then actively built at SPring-8, where a 30 m long in-vacuum undulator made of different segments (with 780 periods of 32 mm, a 12 mm gap, a peak field of 0.59 T) has been installed [60, 61]. The very fine adjustments of the gap segments enabled to reduce the phase error (qualifying the period

interfering merit) from 11° to 3.6°. A revolver in-vacuum undulator comporting four rotating undulators (133 periods of 6 mm, 100 periods of 10 mm, 66 periods of 15 mm, 50 periods of 20 mm providing respectively a field of 0.74, 1.07, 1.32, 1.44 T for a gap of 3.2 mm) [62] has been built by the SPring-8 group and installed on Pohang Light Source [63]. Placing directly the magnet arrays inside the vacuum introduces some impedance issues, for keeping it as smooth as possible. The RF transition can comport different fingers in a grid-type arrangement, with cooling water in a spring-type pipe enabling flexibility for the gap change, flexible Cu plates with crenels or flexible plates. Besides, power deposition resulting from the electron beam image current, the heat load due to the wakefields [64], and up-stream synchrotron radiation implies to install a liner, i.e. a conductive foil, on the magnet arrays to prevent from degradation of the magnets. Some liner degradation has been observed, such as for the first in-vacuum installed at ESRF [65] with a stainless steel foil led to a local heating and ablation, and a 0.5% magnet demagnetization. Practically, outgassing and beam loss on the stored beam appear, liner degradation can be diagnosed with bumps.

Cooling down rare earth based permanent magnets $Pr_2Fe_{14}B$ enables to increase the remanent field by 10% and the coercivity by a factor of 3 [67]. Whereas $Nd_2Fe_{14}B$ cannot be operated below 130 K because of the appearance of the spin reorientation transition (SRT) [68] requiring the cryogenic undulator to be cooled down to the liquid nitrogen temperature and heated back to the working temperature to 140 K, $Pr_2Fe_{14}B$ based undulators can be directly cooled and operated at 77 K because of the absence of the SRT, without thermal resistances. Cryogenic Permanent Magnet Undulator have been proposed and tested at SPring-8 [69] with a prototype built with $Nd_2Fe_{14}B$ permanent magnet at cryogenic temperature. Full scale installed $Nd_2Fe_{14}B$ cryogenic undulators have been built at ESRF [70], at SLS [71] and DIAMOND [72]. $Pr_2Fe_{14}B$ cryogenic prototypes have been built at NSLS-II [73], SOLEIL [67], BESSY [74]. A full scale $Pr_2Fe_{14}B$ cryogenic undulator has been built and installed at SOLEIL [75]. The gap opening due to the contraction of the supporting rods at low temperature, the period reduction due to the girder contraction and the phase error should be compensated. Compared to an in-vacuum undulator of equivalent spectral range (i.e. same deflection parameter), the flux is enhanced thanks to the field increase and to additional periods for a given total length (a smaller period leads to the same deflection parameter).

Electromagnetic undulators consisting of alternated poles are also widely used. In particular, room temperature electromagnetic undulators enable flex-

ible control of the different field components and of the polarization as described in the following section. Superconducting undulators are also rapidly developing. After first systems such as the one installed on ACO [76], research and development rapidly progressed [77], with achieved 0.69 T (7 mm gap, 15 mm period) [78], 0.81 T (14 mm period, 4 mm gap) on a small scale device, and 1.15 T (11.5 mm period, 5.85 mm gap) on a 1.74 m device [79]. Use of high temperature superconductors is also under way [80]. Besides, combined permanent magnet undulator with high temperature superconducting coils, as proposed and tested in SPring-8 [81] enables the field for a U15 undulator at 5.5 mm to grow by 7% with coils at 77 K and 22% with coils at 40 K. The proposed adaptive gap undulator concept [82], satisfying the stay-clear and impedance constraints with segments of different periods, leads to a flux enhancement of typically 10%.

Usually, magnetic measurements are performed with conventional bench based on the displacement of magnetic sensor (Hall probes, rotating coils) by an actuation stage of high precision, requiring to remove the magnet arrays for the installation of the vacuum chamber. Stretched and pulse wire techniques are also currently used. More recently, direct in-vacuum measurements with calibration of the Hall probe at low temperature and feedback on the position have been developed, such as SAFALI for the SACLA Free Electron Laser undulator segments of 5 m each [66].

2.7 Polarization from insertion devices

Polarization can be decomposed on unit vectors: $\mathbf{u_x}$ ($\mathbf{u_z}$) for the horizontal (vertical) linear one, $\mathbf{u_{u_{x45}}}$ ($\mathbf{u_{u_{x135}}}$) linear one at 45° (135°), circular right as $\mathbf{u_r} = (\mathbf{u_x} + \mathrm{i}\mathbf{u_z})/\sqrt{2}$ and left as $\mathbf{u_l} = (\mathbf{u_x} - \mathrm{i}\mathbf{u_z})/\sqrt{2}$. In complex notation, an i multiplication correspond to a $\pi/2$ dephasing. On an orthogonal basis decomposition, Stokes parameters are defined as $s_0 = \Phi(\mathbf{u_x}) + \Phi(\mathbf{u_z})$, $s_1 = \Phi(\mathbf{u_x}) - \Phi(\mathbf{u_z})$, $s_2 = \Phi(\mathbf{u_{x45}}) + \Phi(\mathbf{u_{x135}})$, $s_3 = \Phi(\mathbf{u_r}) - \Phi(\mathbf{u_l})$. Polarization rates are defined as the Stokes components normalized with respect to the total intensity as

$$I_1 = \frac{s_1}{s_0} \qquad I_2 = \frac{s_2}{s_0} \qquad I_3 = \frac{s_3}{s_0} \tag{2.31}$$

For a mono-energetic filament electron beam with on-axis observation, one gets: $I_1 = \frac{ra^2-1}{ra^2+1}$, $I_2 = \frac{2ra\times\cos\varphi}{ra^2+1}$, $I_3 = \frac{2ra\times\sin\varphi}{ra^2+1}$ with $ra = \frac{B_{ux}}{B_{uz}}$.

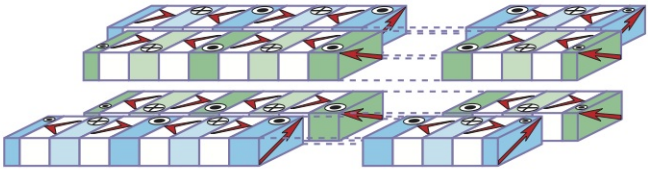

Fig. 2.12 Sketch of an APPLE-I undulator

In case of planar undulators (for example, with a vertical field), the particles execute an oscillating trajectory in the horizontal plane, leading to a horizontal polarization of the radiation. Using two crossed planar undulators [83, 84, 85, 86] generating perpendicular magnetic fields is the simplest way for producing elliptically polarized radiation with insertion devices. The phase between vertical and horizontal field components, hence the polarization, is modified by sliding longitudinally an undulator with respect to the other. For permanent magnet based systems, further magnetic designs embedded in one single undulator carriage have been proposed and tested. One of the most popular is the APPLE-II undulator (Advanced Planar Polarized Light Emitter-II) [87, 88, 89, 90, 91, 92], for which each jaw comports two rows of permanent magnets arrays above and below the electron beam in Halbach configuration. Each row is composed of a succession of pure permanent magnet blocks magnetized along vertical or longitudinal axis. APPLE-I undulator, first proposed [99] (see Fig. 2.12), differs from APPLE-II one as vertically magnetized blocks magnetization axis is tilted from 45°. The APPLE-III undulator [100], with vertically magnetized blocks magnetization tilted from 45° as for the APPLE-I, comports a special magnet shape capable of accepting a round bore vacuum chamber at a lower magnetic gap (down to 5.5 mm), ideal for single pass machines. Besides, elliptically polarized undulators (EPU) with various magnet arrangements have been proposed and built, such as Helios [96, 97], or a "fixed circular polarization device" [98], a 6-arrays device [101, 102]. Using D_{up}, D_{down} for the phase shift of one given magnet array, the APPLE magnetic fields can be expressed as

$$\begin{cases} B_{ux} = B_{ux1}\left[2\sin\left(\frac{2\pi}{\lambda_u}s\right) + \sin\left(\frac{2\pi}{\lambda_u}s + \pi + D_{up}\right) + \sin\left(\frac{2\pi}{\lambda_u}s + \pi + D_{down}\right)\right] \\ B_{uz} = B_{uz1}\left[2\sin\left(\frac{2\pi}{\lambda_u}s\right) + \sin\left(\frac{2\pi}{\lambda_u}s + D_{up}\right) + \sin\left(\frac{2\pi}{\lambda_u}s + D_{down}\right)\right] \end{cases} \tag{2.32}$$

with, B_{ux1} (resp. B_{uz1}), the vertical (resp. horizontal) peak field value generated by a single row. For circular polarization $D_{up} = D_{down} = D_0$ (The phase φ in Table 2.1 being $\frac{2\pi D_0}{\lambda_u}$), magnetic components become

$$\begin{cases} B_{ux} = 4B_{ux1}\cos\left(\frac{\pi+D_0}{2}\right)\sin\left(\frac{2\pi}{\lambda_u}s+\frac{\pi+D_0}{2}\right) \\ B_{uz} = 4B_{uz1}\cos\left(\frac{D_0}{2}\right)\sin\left(\frac{2\pi}{\lambda_u}s+\frac{D_0}{2}\right) \end{cases} \tag{2.33}$$

For linear polarization, either horizontal or vertical $D_{up} = -D_{down} = D_0$, magnetic components are then reduced to

$$\begin{cases} B_{ux} = 2B_{ux1}\sin\left(\frac{\pi+D_0}{2}\right)(1-\cos(D_0)) \\ B_{uz} = 2B_{uz1}\sin\left(\frac{\pi+D_0}{2}\right)(1+\cos(D_0)) \end{cases} \tag{2.34}$$

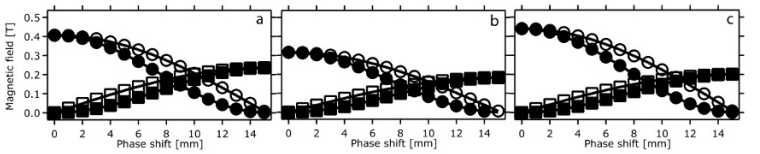

Fig. 2.13 APPLE peak magnetic field computed with RADIA [94] for 30 mm square $Nd_2Fe_{14}B$ magnets with a remnant magnetization of 1.26 T for a 15.5 mm gap, in linear (• vertical, ■ horizontal fields) and circular (○ vertical, □ horizontal fields) polarizations. **a** APPLE II case: $B_z = 0.4$ T, $B_x = 0.23$ T. **b** APPLE III case: $B_z = 0.315$ T, $B_x = 0.185$ T. **c** APPLE I case: $B_z = 0.43$ T, $B_x = 0.2$ T. For the same gap of 15.5 mm and magnet parameters, HELIOS fields [96] are $B_z = 0.17$ T, $B_x = 0.12$ T and "fixed device" [98] $B_z = 0.13$ T, $B_x = 0.21$ T.

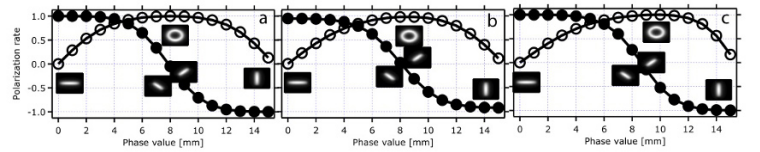

Fig. 2.14 APPLE linear (•) and circular (○) polarization rate computed with SRW for the case of Fig. 2.12: **a** APPLE II, **b** APPLE III, **c** APPLE I for a photon energy of 1.5 keV.

The magnetic field amplitude can be adjusted by changing the gap between upper and lower jaws (constituted of two rows) whatever the polarization produced. Diagonally opposed rows can be moved longitudinally in order to produce vertical field at 0 mm shift and horizontal one at $\pm\frac{\lambda}{2}$ mm (see Fig. 2.13). Helical polarization results from moving diagonally opposed rows of the same quantity in parallel. Tilting the direction of the linear polarization from linear horizontal to vertical comes in shifting two diagonally opposed arrays by the same value but with opposite signs. Compared to an APPLE-II device, APPLE-I provides a slightly higher vertical magnetic field ($+7.5\%$) but the horizontal component is decreased (-13%). With same block sizes, APPLE-III fields at the same gap value are decreased due to a chamfer close to the magnetic axis on magnet blocks. They can however reach higher fields at lower gaps.

The polarization rates derived from Stokes parameters calculated with SRW [93] for the different APPLE undulators as a function of the shift for each mode are compared in Fig. 2.14. The circular polarization is only a particular case of the helical configuration where field components in both plane have the same amplitude and shifted by $\frac{\lambda}{4}$ mm. The linear one is equal to 1 (resp. -1) for an horizontal polarization (resp. vertical) and 0 when the circular one is maximal. Compared to the APPLE-II, the APPLE-I circular polarization rate curve becomes asymmetric and the linear one is equal to zero for a higher shift value. The maximal linear rate of APPLE-III differs from 1, due to the non-zero residual field of the minor magnetic component. Photon density transverse distributions are illustrated in the APPLE-II case for the various polarizations in Fig. 2.15.

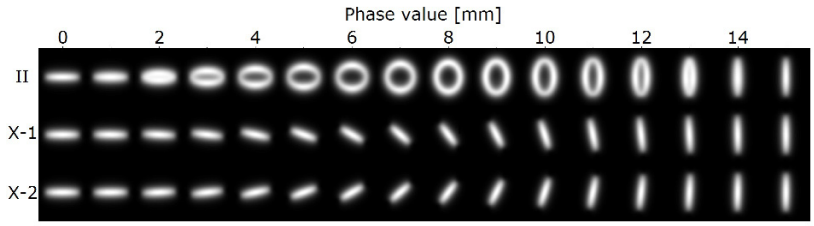

Fig. 2.15 Transverse density generated in circular polarization (II , $D_{up} = \phi$, $D_{down} = \phi$), linear tilted 45° polarization (X-1 , $D_{up} = -\phi$, $D_{down} = \phi$), and linear tilted 135° polarization (X-2 , $D_{up} = \phi$, $D_{down} = -\phi$) for a photon energy of 1.5 keV. Case of Fig. 2.13

Recently, a new kind of device [103], called DELTA, inspired from the first elliptical undulator has successfully been built. Instead of using a rectangular magnet shape, it uses a triangular one, enabling to lower the magnetic gap (down to 5.5 mm, Fig. 2.16). The major advantage, its compactness, permits to encapsulate the whole undulator in a small vacuum chamber. Nevertheless, its exploitation on a storage ring is difficult due the low gap and the absence of motorization for gap movements. However, it is very useful on FEL machines or energy recovery linacs.

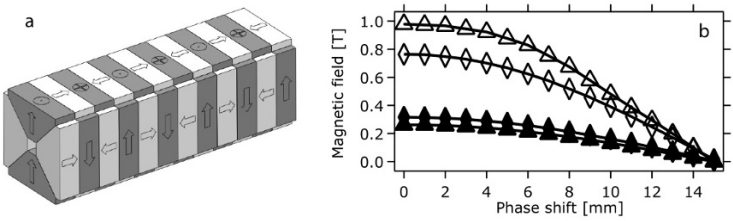

Fig. 2.16 **a** Sketch of DELTA undulator using triangular shape. **b** Peak value of the magnetic fields versus phase. APPLE III (♦ for 15.5 mm gap, ◊ for 5.5 mm gap) and DELTA ($Nd_2Fe_{14}B$ magnets with a remnant magnetization of 1.26 T, ▲ for 15.5 mm gap, △ for 5.5 mm gap).

Quasi-periodic EPU can be applied to APPLE-II [104] or to the so-called Figure-8 [106, 105], for out-of-vacuum and in-vacuum versions.

Electromagnetic technology with [107] or without poles [108] suits well for the fabrication of rather long period EPU, providing the possibility of any type of polarization or aperiodicity. Analogue feedforward ensures the synchronization of the main and corrector power supplies, enabling for the transient orbit deviations to be canceled.

Combining electromagnets and permanent magnets provides a fast switching of the polarization from circular right to circular left and vice versa as installed at NSLS [109] and at ESRF [110]. Real-time synchronization is necessary to ensure a proper compensation of the Eddy currents. For short periods, conventional coils have been replaced by copper sheets alternated with cooled copper ones [111, 112, 113]. The ElectroMagnetic Permanent magnet Helical Undulator (EMPHU) developed in such a way at SOLEIL [114] employs three series of coils for independent compensations of the field integral, the exit position and the photon emission direction: after static corrections, dynamical corrections without and with the vacuum chamber are measured

thanks to the analysis of the pulse response, so that tables prepared in the magnetic measurement laboratory are directly applied for the undulator commissioning, leading to typical less than $10\,\mu$m residual close orbit distortion.

Specific wiggler design also enable to produce various polarizations. For example, with peak positive and negative fields of the different amplitudes [116], polarization can be selected by modification of the position of the analyzing slit. Crossed wigglers with a $\pi/2$ dephasing generate different polarization according to the vertical observation angle [117].

2.8 Temporally coherent synchrotron radiation

Longitudinal coherence for which electrons emit in phase can occur either if the electron bunch length is small with respect to the considered wavelength of emission, or if a modulation is imprinted on the electron bunch, such as in the free electron laser process.

Coherent synchrotron radiation (CSR) [118] results from in-phase emission of electrons, with a bandwidth related to the longitudinal shape of the bunch. For CSR in the THz range, correlation between electron radiations is achieved either by imprinting a modulation on the electron bunch profile with an external laser [120, 121], or by modifying the electron-bunch length so that its length becomes shorter than the THz wavelength [119, 122, 123, 124]. Bunches with structures induced by short or modulated laser pulses enable to reach higher THz frequencies, but with a rather low repetition rate (kHz).

With a FEL, the generated radiation is not only based on the spontaneous synchrotron radiation emitted in the undulator: a wavelength λ light wave interacts with the electron bunch in the undulator, inducing an energy modulation of the electrons which is gradually transformed into density modulation at λ and leads to a coherent radiation emission at λ and λ/n , n being an integer (fundamental and harmonics) [52]. The laser tunability, one of the major advantages of FEL sources, is obtained by merely modifying the magnetic field of the undulator in a given spectral range set by the electron beam energy. The polarization depends on the undulator configuration. The small signal gain is proportional to the electronic density and varies as $1/\gamma^3$, depending on the undulator length. Operation at short wavelengths requires high beam energies for reaching the resonant wavelength, and thus long undulators (0.1–1 km for 0.1 nm) and high electron beam density (small emittance and short bunches) for ensuring a sufficient gain. On single pass FEL, transverse coherence re-

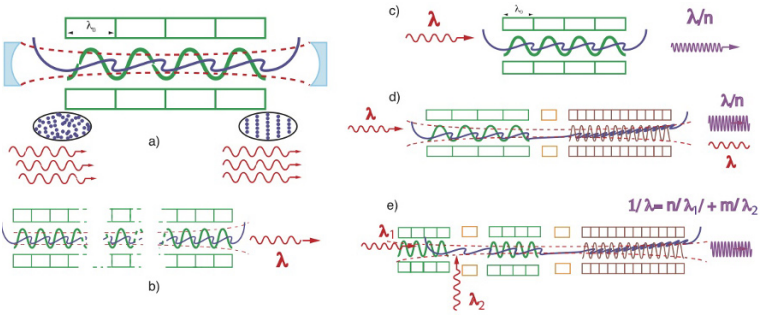

Fig. 2.17 FEL configurations: **a** oscillator case with an optical cavity enabling to store the spontaneous emission (insert with the energy exchange between the electron and the radiation leading to density modulation), **b** Self amplified spontaneous emission (SASE) where the spontaneous emission emitted in the beginning of the undulator is amplified in one single pass, **c** seeding, where a coherent source tuned on the resonant wavelength of the undulator enables to perform efficiently the energy echange leading further to the density modulation, **d** high gain harmonic generation, **e** echo enable harmonic generation (EEHG).

sults from the electron beam emittance (which should be of the order of the emitted wavelength) and from possible gain guiding. FELs can be declined in different configurations. In the oscillator mode [126, 127], the laser field, starting from synchrotron radiation, is stored in an optical cavity (see Fig. 2.17a), enabling interaction with the optical wave on many passes. FEL oscillators cover a spectral range from the THz to the VUV, where mirrors are available. After the theoretical prediction of the FEL concept in 1971, the first IR FEL was achieved in 1977 on the MARK-III linac (Stanford, USA) in the oscillator configuration. ACO (Orsay, France) [128] provided the second worldwide FEL (first visible radiation) in 1983 and first FEL based harmonic generation [129] in the UV and VUV [130], followed by results on the SuperACO FEL (Orsay, France) [131]. First FEL applications started in the infrared and in the UV-FELs in biology [132, 133] and surface science [134] in 1993. Various FEL oscillators were then built down to 190 nm [135].

Because of the limited performance of mirrors, short wavelength FEL are usually operated in the so-called self amplified spontaneous emission (SASE) (see Fig. 2.17b) setup [136, 138, 137], where the spontaneous emission at the input of the FEL amplifier is amplified, typically up to saturation in a single pass after a regime of exponential growth. Once the saturation is reached, the amplification process is replaced by a cyclic energy exchange between the

electrons and the radiated field. The uncorrelated trains of radiation, which result from the interaction of electrons progressing jointly with the previously emitted spontaneous radiation, lead to spiky longitudinal and temporal distributions, apart from single spike operation for low charge short bunch regime [139, 140]. The emission usually presents poor longitudinal coherence properties. Thanks to recent accelerator advances (high peak current, small energy spread, low emittance) and long undulator linac based single pass SASE FEL are blooming worldwide. They now provide tuneable coherent sub-ps pulses in the UV/x-ray region, with record peak powers (*MW* to *GW*) and a substantial gain in peak and average brilliance. After LEULT (Argonne, USA) in the VUV [141], FLASH (Germany) [142] (30–4.5 nm), SCSS Test Accelerator (Japan, 40–60 nm) [143] operate for users. In the angström region, the first tuneable fs x-ray FELs at 0.15 nm achieved at the Linear Coherent Light Source (LCLS, Stanford, USA, 2 mJ, 14 GeV) in 2009 [144, 145] and down to 0.12 nm since June 2011 in SACLA (Japan, 8 GeV) [146] constitute the brightest x-ray beams ever produced on earth and has been already used by scientists. European XFEL [147], the Korean XFEL and the SwissFEL are expected soon. Presently, no conventional laser can compete with the performance of LCLS or SACLA. These x-ray FELs, of a typical km length, use more than 100 m of undulators. Fifty years after the laser discovery [148], the emergence of several mJ x-ray lasers for users in the angström range constitutes a major breakthrough. The recent advent of tunable coherent x-ray FELs (XFELs) [149] opened a new era for the investigation of matter. They enable to decrypt the structure of biomolecules and cells [150, 151, 152], to provide novel insight in the electronic structure of atoms and molecules [153, 154, 155, 156], to observe non-equilibrium nuclear motion, disordered media and distorted crystal lattices, thanks to recent progress of fs spectroscopy [157] and pump-probe techniques [158]. Detailed structural dynamics can be inferred from spectroscopic signatures [161]. XFELs can also reveal chemical reactions movies. With new imaging techniques [159, 160], they are exceptional tools for the investigation of ultrafast evolution of the electronic structure and provide a deeper insight in the extreme states of matter [162]. Higher availability of x-ray pulses with stable energy, synchronized to an external pump laser, enabling jitter-free optical pump/resonant x-ray probe experiments will enable to step further.

For suppressing the spikes, improving the longitudinal coherence, reducing the intensity fluctuations and the jitter, a typical strategy consists in seeding the FEL amplifier using an external seed that possesses the required coherence properties [163] [164] (see Fig. 2.17c). Saturation is also more rapidly

reached than in the SASE case, which makes the system more compact. The seed can be an external laser wave or a short wavelength coherent light source, such as High order Harmonics generated in Gas (HHG) [165, 166], injected in order to interact with the electron beam in the undulator. HHG seeding has been first performed on SCSS Test Accelerator at 160 nm [167] and at 60 nm [168], at SPARC [172] with cascading demonstration and at 30 nm at s-FLASH [173]. In the high gain harmonic generation scheme (HGHG) [169] (see Fig. 2.17d), an injected laser source induces the modulation in density of the electron bunch in the first undulator. The radiation is produced in the second undulator tuned on the fundamental or harmonic (cascade scheme) [170] of the injected wavelength. Tunability can be achieved on the injection source coupled to a gap change [174] or by applying a chirp (frequency drift) both on the seed and on the electron bunch [174]. Coherent nonlinear harmonics of the fundamental wavelength are also generated. FEL pulse temporal and spectral distributions result from the seed itself and the FEL intrinsic dynamics. In particular cases, super-radiant modes exhibit further pulse duration narrowing and intensity increase [171]. Self-seeding [176] suits better the hard x-ray domain: a monochromator installed after the first undulator spectrally cleans the radiation before the last amplification in the final undulator. Recently, self-seeding with the spectral cleaning of the SASE radiation in a crystal monochromator [177] appears to be very promising with the first results [178, 179]. At shorter wavelengths (89 nm), seeded FELs found first applications in molecular physics [180]. FERMI@ELETTRA (Italy) is the only seeded FEL user facility, using a conventional laser as a seed [181]. In the Echo Enabled Harmonic Generation [182] (EEHG) scheme (see Fig. 2.17e), without equivalent in classical optics, two successive laser-electron interactions are performed, using two undulators, in order to imprint a sheet-like structure in phase space. As a result, higher order harmonics can be obtained in an extraordinary efficient way. EEHG opens the way to shorter wavelengths when operating on a high order harmonic of the seed wavelength. Experimentally demonstrated so far in the UV experiment on the Next Linear Collider Test Accelerator (ECHO7) at SLAC [183] and on the Shanghai FEL Test Facility [184], it constitutes a breakthrough in up-frequency conversion from a conceptual point of view, and in terms of compactness and pulse properties (e.g., duration and wavelengths). Schemes derived from EEHG such as the Triple Mode Chicane open perspectives for very short wavelength (nm) and short duration at moderate cost [185].

One path towards the fifth generation (5G) is to replace the conventional linac by a LWFA, which provides GV/m of acceleration with very short

bunches [190] with GeV electron beams. Using electron beams with the presently achieved performance in terms of energy spread and divergence however does not lead to direct FEL amplification whereas spontaneous emission from undulators has been observed [191, 192]. Experiments are under way in various places [187, 188, 189]. LWFA beams provide in longitudinal, short bunch duration and large relative energy spread and in transverse, large divergence and micrometer size. The large divergence can be handled by strong quadrupoles located very close to the electron source [193]. Electron beam manipulation by chicane decompression [194] or by the use of transverse gradient undulator [196] suggest that significant amplification with the present LWFA performance has become possible.

Acknowledgements M.E. Couprie would like to acknowledge P. Elleaume, who guided her in this field, the members of her group at SOLEIL : H. Abualrob, T. El Ajjouri, C. Benaderrahmane, P. Berteaud, F. Briquez, L. Chapuis, O. Marcouillé, F. Marteau, J. Vétéran and former collaborators O. Chubar and C. Kitégi.

References

1. Y. Petroff, *Les rayons X, de l'astrophysique à la nanophysique*, Collection Domino vol.161(Flammarion 1998)
2. G.A. Schott , *Electromagnetic Radiation*, (Cambridge University Press, 1912)
3. P. Elleaume, H. Onuki, *Undulators, wigglers and their applications*, (Taylor and Francis, London 2003)
4. F. Ciocci, G. Dattoli, A. Torre, A. Renieri, *Insertion devices for Synchrotron Radiation and Free Electron Laser*, Series on Synchrotron Radiation Techniques and Applications, vol.6, ed. by D. H. Bilderback, K. O. Hodgson, M. P. Kiskinova, R. Rossi (World Scientific, Singapore, 2000)
5. A. Bordovitsyn, *Synchrotron Radiation Theory and Its Development: In Memory of I.M. Ternov*, Series on Synchrotron Radiation Techniques and Applications, vol.5, ed. by V. A. Bordovitsyn (World Scientific, Singapore, 1999)
6. M.M. Nikitin, V. Ya Epp, *Undulator radiation (Undulatornoe Izlutchenie)*, Energoatomizdat, (Singapore 1988) (in Russian)
7. J.D. Jackson, *Classical electrodynamics*, (John Wiley and Sons Ltd., 1962)
8. U.E. Kruse, L. Marshall, J.R. Platt, Astrophys. J. **124**, 601 (1956)
9. J. Larmor, Phil. Mag. 5^{th} Series **44**, 503 (1897)
10. A. Liénard, L'éclairage électrique, **16**, 5 (1898)
11. G.A. Schott, Ann. Phys.**24**, 635 (1907)
12. D. Ivanenko, I. Pomeranchuk, Phys. Rev. **65**, 343 (1944)
13. M.O Oliphant in *The acceleration of particles to very high energies*, Classified memo submitted to DSIR, United Kingdom, now in University of Birmingham archive (1944)

14. E.M. McMillan, Phys. Rev. Lett. **68**, 1434 (1945)
15. V. Veksler, J. Phys, USSR. **9**, 153 (1946)
16. F.K. Goward, D.E. Barnes, Nature **158**, 413 (1946)
17. J.P. Blewett, Phys. Rev. **69**, 87 (1946)
18. J.P. Blewett, J. Synch. Rad. **5**, 135 (1998)
19. J. Schwinger, Phys. Rev. **70**, 798 (1946)
20. J. Schwinger, Phys. Rev. **75**, 1912 (1946)
21. F.R. Elder, A.M. Gurewitsch, R.V. Langmuir, H.C. Pollock, Phys. Rev. **71**, 829 (1947)
22. H. Motz, Journ. Appl. Phys. **22**, 527 (1951)
23. H. Motz, W. Thon, R.N. Whitehurst, J. Appl. Phys. **24**, 826 (1953)
24. R. Combes, T. Frelot, C.R. Acad. Sci. Paris, **241**, 1559 (1955)
25. I.M. Ternov, V.R. Khalilov, V.G. Bagrov, M.M. Nikitin, Sov. Phys. J. **23**, 79 (1980)
26. M. Sands, SLAC report **121** (1970)
27. A.W. Chao, *Physics of Collective Beam Instabilities in High Energy Accelerators*, (John Wiley and Sons, inc, 1993)
28. A.W. Chao, M. Tigner, *Handbook of Accelerator Physics and Engineering*, (World Scientific 2006)
29. J. Haissinski, Nuovo Cimento B **18**, 72 (1973)
30. M. Borland, in *Proceedings of IPAC 2012*, New Orleans, Louisiana, USA 2012, p.1035
31. W. Guo. and F.J. Willeke, in *Proceedings of 2011 Particle Accelerator Conference*, New York, USA, 2011, p.2363
32. D.A.G. Deacon and J.M.J Madey, Phys. Rev. Lett. **44**, 449 (1980)
33. D. Robin, E. Fores, C. Pellegrini, and A. Amiry, Phys. Rev. E. **48**, 2149 (1993)
34. T. Tajima and J.M. Dawson, Phys. Rev. Lett. **43**, 267 (1979)
35. V. Malka, J. Faure, Y. Glinec, A. Pukhov and J.-P. Rousseau, Phys. Plasmas **12**, 056702 (2005)
36. C.G. Geddes, C.S. Toth, J. van Tilborg, E. Esarey, C.B. Schroeder, D. Bruhwiler, C. Nieter, J. Cary Geddes, and W.P. Leemans, Nature **431**, 538 (2004)
37. W. P. Leemans, B. Nagler, A.J. Gonsalves, C.S. Toth, K. Nakamura, C.G.R. Geddes, E. Esarey, C.B. Schroeder, and S.M. Hooker, Nature Phys. **2**, 696 (2006)
38. J. Faure, C. Rechatin , A. Norlin, A. Lifschitz, Y. Glinec, and V. Malka, Nature **444**, 737 (2006)
39. W. Lu, M. Tzoufras, C. Joshi, F.S. Tsung, W.B. Mori, J. Vieira, R.A. Fonseca, and L.O. Silva, Phys. Rev. ST Accel. Beams **10**, 061301 (2007)
40. S. Cipiccia, M.R. Islam, B. Ersfeld, R.P. Shanks, E. Brunetti, G. Vieux, X. Yang, R.C. Issac, S. M. Wiggins, G.H. Welsh, M.P. Anania, D. Maneuski, R. Montgomery, G. Smith, M. Hoek, D.J. Hamilton, N.R.C. Lemos, D. Symes, P.P. Rajeev, V.O. Shea, J.M. Dias, D.A. Jaroszynski, Nature Phys. **7**, 867 (2011)
41. V. Malka, A. Lifschitz, J. Faure, and Y. Glinec, Phys. Rev. ST Accel. Beams **9**, 091301 (2005)
42. E. Esarey, R.F. Hubard, W.P. Leemans, A. Ting, and P. Sprangle, Phys. Rev. Lett. **79**, 2682 (1997)
43. O. Lundh, J. Lim, C. Rechatin, L. Ammoura, A. Ben-Ismail, X. Davoine, G. Gallo, J.-P. Goddet , E. Lefebvre, V. Malka, and J. Faure, Nature Phys. **7**, 219 (2011)
44. C. Rechatin, J. Faure, A. Ben-Ismail, J. Lim, R. Fitour, A. Specka, H. Videau, A. Tafzi, F. Burgy, and V. Malka, Phys. Rev. Lett. **102**, 164801 (2009)
45. K.J. Kim, Nucl. Instr. Meth. A **246**, 71 (1986)

46. I.V. Bazanov, Phys. Rev. ST Accel. Beams **15**, 050703 (2012)
47. E. Wigner, Phys. Rev. **40**, 749 (1932)
48. A. Walther, J. Opt. Soc. Am. **58**, 1256 (1968)
49. G.L. Geloni, E. Saldin, E. Schneidmiller, M. Yurkov, Nucl. Instr. Meth. A. **588**, 463 (2008)
50. O. Chubar, Rev. Sci. Instr. **66**, 1872 (1995)
51. J.M.J. Madey, J. Appl. Phys. **42**, 1906 (1971)
52. W. B. Colson, IEEE J. Quantum Electron. **17**, 1417 (1981)
53. D.A.G. Deacon, L.R. Elias, G.J. Ramian, H.A. Schwettman, T.I. Smith, Phys. Rev. Lett. **38**, 892 (1977)
54. A.A. Zholents, and M.S. Zolotorev, Phys. Rev. Lett. **76**, 912 (1996)
55. R. W. Schoenlein, S. Chattopadhyay, H.H.W. Chong, T.E. Glover, P.A. Heimann, C.V. Shank, A.A. Zholents, and M.S. Zolotorev, Science **287**, 2237 (2000)
56. M.-E. Couprie, J.-M. Filhol, C. R. Physique **9**, 487 (2008)
57. K. Halbach, J. Phys. Coll. **44**, 211 (1983)
58. W. Gudat, J. Pflüger, J. Chatzipetros, and W. Peatman, Nucl. Instr. Meth. A. **246**, 50 (1986)
59. S. Yamamoto, T. Shioya, M. Hara, H. Kitamura, W. Wei Zhang, T. Mochizuki, H. Sugiyama, and M. Ando, Rev. Sci. Instr. **63**, 400 (1992)
60. H. Kitamura, T. Bizen, T. Hara, X.-M. Maréchal, T. Seike, and T. Tanaka, Nucl. Instr. Meth. A **467**, 110 (2001)
61. T. Tanaka, T. Seike, X.-M. Maréchal, T. Bizen, T. Hara, and H. Kitamura, Nucl. Instr. Meth. A **467**, 149 (2001)
62. T. Bizen, T. Hara, X.-M Maréchal, T. Seike, T. Tanaka, and H. Kitamura, AIP Conf. Proc. **705**, 175 (2004)
63. T.H.S. Kang, T.Y. Lee, M.G. Kim, C.D. Park, T.Y. Koo, J. Choi, in *Proceedings of EPAC 2006 Conference, Edinburgh*, p.2771
64. O. Henry, O. Napoly, Part. Accel. **35**, 235 (1991)
65. T. Hara, T. Tanaka, T. Tanabe, X.-M. Maréchal, H. Kitamura, P. Elleaume, B. Morrison, J. Chavanne, P. van Vaerenbergh, and D. Schmidt, J. Synch. Rad. **5**, 406 (1998)
66. T. Tanaka, R. Tsusu, T. Nakajima, T. Seike, and H. Kitamura, in *Proceedings of FEL 2007, Novosibirsk* p.468
67. C. Benabderrahmane, P. Berteaud, M. Valléau, C. Kitegi, K. Tavakol, N. Béchu, A. Mary, J.-M. Filhol, and M.-E. Couprie, Nuc. Instr. Meth. Phys. Res. **669**, 1 (2012)
68. D. Givord, S.H. Li, R. Perrier de la Bathie, Solid State Commun. **51**, 857 (1984)
69. T. Hara, T. Tanaka, H. Kitamura, T. Bizen, X.-M. Maréchal, T. Seike, T. Kohda, and Y. Matsuura, Phys. Rev. ST Accel. Beams **7**, 050702 (2004)
70. J. Chavanne, M. Hahn, R. Kersevan, C. Kitegi, C. Penel, and F. Revol, in *Proceedings of EPAC 2008 Conference, Genoa*, p.2243
71. T. Tanaka, H. Kitamura, A. Anghel, M. Bruegger, W. Bulgheroni, B. Jakob, T. Schmidt, A. Kagamihata, and T. Seike, in *Proceedings of IPAC 2010 Conference, Kyoto*, p.3147
72. J. Schouten, and E.C.M. Rial, in *Proceedings of IPAC 2011 Conference, San Sebástian*, p.3323
73. T. Tanabe, O. Chubar, D.A. Harder, M. Lehecka, J. Rank, G. Rakowsky, and C. Spatar, AIP Conf. Proc. **1234**, 29 (2010)

74. J. Bahrdt, H.-J. Baecker, M. Dirsat, W. Frentrup, A. Gaupp, D. Pflückhahn, M. Scheer, B. Schulz, F.J. Grüner, R. Weingartner, D. Jus, F.H. O'Shea, in *Proceedings of IPAC 2010 Conference, San Sebástian*, p.3111
75. C. Benabderrahmane, P. Berteaud, N. Béchu, L. Chapuis, M.-E. Couprie, J.-P. Daguerre, J.-M. Filhol, C. Herbeaux, A. Lestrade, M. Louve, J.-L. Marlats, K. Tavakoli, M. Valléau, and D. Zerbib , in *Proceedings of IPAC 2010 Conference, San Sebástian*, p.3233
76. C. Bazin, M. Billardon, D. Deacon, Y. Farge, J.M. Ortega, J. Pérot, Y. Petroff, M. Velghe J. Phys. Lett. **41**, 547 (1980)
77. Y. Ivanyushenkov, K.D. Boerste, T.W. Buffington, C.L. Doose, Q.B. Hasse, M.S. Jaski, M. Kasa, S.H. Kim, R. Kustom, E.R. Moog, D.L. Peters, E. Trakhtenberg, I. Vasserman, A.V. Makarov, Proc. of PAC09, Vancouver, BC, Canada, 313 (2009)
78. S. Casalbuoni, T. Baumbach, S. Gerstl, A.W. Grau, M. Hagelstein, T. Holubek, D. Saez de Jauregui, C. Boffo, and W. Walter, in *Proceedings of IPAC 2012 Conference, New-Orleans*, p.711
79. D.J. Scott, J.A. Clarke, D.E. Baynham, V. Bayliss, T. Bradshaw, G. Burton, A. Brummitt, S. Carr, A. Lintern, J. Rochford, O. Taylor, and Y. Ivanyushenko, Phys. Rev. Lett. **107**, 174803 (2011)
80. S. Prestemon, D. Arbelaez, S. Davies, D.R. Dietderich, D. Lee, F. Minervini, R.D. Schlueter, IEEE Trans. Appl. Supercond. **21**, 1880 (2011)
81. T. Tanaka, T. Hara, H. Kitamura, R. Tsuru, T. Bizen, X.-M. Maréchal, and T. Seike, Phys. Rev. ST Accel. Beams **7**, 090704 (2004)
82. O. Chubar, Communication at SRI Conference, Lyon, 2012
83. H. Onuki, Nucl. Instr. Meth. A **246**, 94 (1986)
84. H. Onuki, N. Saito, and T. Saito, Appl. Phys. Lett. **52**, 173 (1988)
85. K.J. Kim, Nucl. Instr. Meth. A **219**, 425 (1986)
86. M. Moissev, M. Nikitin, N. Fedorov, Sov. Phys. J. **21**, 332 (1978)
87. S. Sasaki, K. Miyata, and T. Takada, Jpn. J. Appl. Phys. **31**, 1794 (1992)
88. S. Sasaki, K. Kakuno, T. Takada, T. Shimada, K. Yanagida, and Y. Miyahara, Nucl. Instr. Meth. A **331**, 763 (1993)
89. R. Carr, B. Kincaid, and W. Hassenzahl, Rev. Sci. Instr. **63**, 3564 (1992)
90. R. Carr, Nucl. Instr. Meth. A **306**, 391 (1991)
91. S. Sasaki, Nucl. Instr. Meth. A **347**, 83 (1994)
92. S. Sasaki, T. Shimada, K. Ichi Yanagida, H. Kobayashi, and Y. Miyahara, Nucl. Instr. Meth. A **347**, 87 (1994)
93. O. Chubar, P. Elleaume, A. Snigirev, S. Kuznetzov, Optical Engineering, **4769** 145 (2002)
94. O. Chubar, P. Elleaume, and J. Chavanne, J. Synch. Rad. **5**, 481 (1998)
95. K. Halbach, Nucl. Instr. Meth. A **169**,1 (1980)
96. P. Elleaume, Nucl. Instrum. Meth. A **291**, 371 (1990)
97. P. Elleaume, J. Synch. Rad. **1**, 19 (1994)
98. B. Diviacco and R.P. Walker, Nucl. Instr. Meth. A **292**, 517 (1990)
99. S. Sasaki, K. Miyata, and T. Takada, Jpn. J. Appl. Phys.**31**, L1794 (1992)
100. J. Bahrdt, W. Frentrup, A. Gaupp, B. Kuske, A. Meseck, M. Scheer, in *Proceedings of FEL 2004 Conference*, p.610
101. S.I. Kimura, M. Kamada, H. Hama, X.-M. Maréchal, T. Tanaka, H. Kitamura, J. Electron Spectrosc. Relat. Phenom. **80**, 437 (1996)

102. A. Hiraya, K. Yoshida, S. Yagi, M. Taniguchi, S. Kimura, H. Hama, T. Takayama, and D. Amano, J. Synch. Rad. **5**, 445 (1998)
103. A.B. Temnykh, Phys. Rev. ST Accel. Beams **11**, 120702 (2008)
104. S. Sasaki, H. Kobayash, M. Takao, Y. Miyahara, and S. Hashimoto, Rev. Sci. Instr. **66**, 1953 (1995)
105. T. Hara, T. Tanaka, T. Seike, T. Bizen, X.-M. Maréchal, T. Kohda, K. Inoue, T. Oka, T. Suzuki, N. Yag. and H. Kitamura, Nucl. Instr. Meth. A **467-468**, 165 (2001)
106. T. Tanaka, X.-M. Maréchal, T. Hara, T. Tanabe, H. Kitamura, J. Synch. Rad. **5**, 412 (1998)
107. A. Batrakov, F. Briquez, O. Chuba, I. Churkin, A. Dael, I. Ilyin, Y. Kolokolnikov, O. Marcouillé, F. Marteau, G. Roux, E. Rouvinski, E. Semenov, A. Steshov, M. Valléau, P. Vobly, AIP Conf. Proc. **879**, 412 (2007)
108. O. Marcouillé , L. Chapuis, P. Brunelle, P. Berteaud, M.-E. Couprie, J.-M. Filhol, C. Herbeaux J.-L. Marlats, M. Massal, A. Mary, K. Tavakoli, M. Valléau M, J. Vétéran, AIP Conf. Proc. **879**, 396 (2007)
109. O. Singh, S. Krinsky, Nucl. Instr. Meth. A **418**, 269 (1998)
110. J. Chavanne, P. Elleaume, P. VanVaerenbergh, in *Proceedings of EPAC 1998 Conference*, p. 317
111. G.H. Biallas, S.V. Benson, T. Hiatt, G. Neil, and M. Snyder, in *Proceedings of FEL 2004 Conference*, p.554
112. G.H. Biallas, S.V. Benson, T. Hiatt, G. Neil, and M. Snyder, in *Proceedings of PAC 2005, Knoxville*, p.4093
113. R. Stoner, S.C. Chen, and G. Bekefi, IEEE Trans. on Plasma Science, **18**, 387 (1990)
114. F. Marteau, P. Berteaud, F. Bouvet, L. Chapuis, M.-E. Couprie, J.-P. Daguerre, T. El Ajjouri, J.-M. Filhol, P. Lebasque, J.L. Marlats, A. Mary, K. Tavakoli, IEEE Trans. Appl. Supercond. **22**, 4102004 (2012)
115. C. Bazin, J.-M. Dubuisson, J.-P. Jacquemin, J. Perot, and D. Raoux, Nucl. Instr. Meth. A **266**, 132 (1988)
116. J. Goulon, P. Elleaume, D. Raoux, Nucl. Instr. Meth. A **254**, 192 (1987)
117. S. Yamamoto, T. Shioya, S. Sasak, H. Kitamura, Rev. Sci Instr. **60**, 1834 (1989)
118. G.P. Williams, Rep. Prog. Phys. **69**, 301 (2006)
119. G.L. Carr, M.C. Martin, W.R. McKinney, K. Jordan, G.R. Neil, and G.P. Williams, Nature **420**, 15 (2002)
120. S. Bielawski, C. Evain, T. Hara, M. Hosaka, M. Katoh, S. Kimura, A. Mochihashi, C. Szwaj, T. Takahashi, and Y. Takashima, Nature Phys. **4**, 39 (2008)
121. J. M. Byrd, Z. Hao, M.C. Martin, D.S. Robin, F. Sannibale, R.W. Schoenlein, A.A. Zholents, and M.S. Zolotorev, Phys. Rev. Lett. **96**, 16480 (2006)
122. J.S. Nodvick, and S.D. Saxon, Phys. Rev. **96**, 180 (1954)
123. M. Abo-Bakr, J. Feikes, K. Holldack, and G. Wüstefeld, Phys. Rev. Lett. **88**, 254801 (2002)
124. F. Sannibale, J. M. Byrd, A. Loftsdóttir, M. Venturini, M. Abo-Bakr, J. Feikes, K. Holldack, P. Kuske, G. Wüstefeld, H.-W. Hübers, R. Warnock, Phys. Rev. Lett. **93**, 094801 (2004)
125. C. Evain, J. Barros, A. LoulergueA., M.-A. Tordeux, R. Nagaoka, M. Labat, L. Cassinari, G. Creff, L. Manceron, J.-B. Brubach, P. Roy, M.-E. Couprie, Europhys. Lett. **98**, 4006 (2012)
126. R.R. Freeman, and B.M. Kincaid, AIP. Conf. Proc. **119**, 227 (1984)

127. R. Coisson, F. De Martini, Phys. Quant. Electron. **9**, 939 (1982)
128. M. Billardon, P. Elleaume, J.-M. Ortega, C. Bazin, M. Bergher, M. Velghe, Y. Petroff, D.A.G. Deacon, K.E. Robinson, and J.M.J. Mady, Phys. Rev. Lett. **51**, 1652 (1983)
129. B. Girard , Y. Lapierre, J.-M. Ortega, C. Bazin, M. Billardon, P. Elleaume, M. Bergher, M. Velghe, Y. Petroff, Phys. Rev. Lett. **53**, 2405 (1984)
130. R. Prazeres, J.-M. Ortega, M. Billardon, C. Bazin, M. Bergher, M.-E. Couprie, H. Fang, M. Velghe Y. Petroff, Nucl. Inst. Meth. A **272**, 68 (1988)
131. R. Prazeres, P. Guyot-Sionnnest, D. Jaroszynski, J.M. Ortega, M. Billardon, M.-E. Couprie, M. Velghe, Nucl. Inst. Meth. A **304**, 72 (1991)
132. M.-E. Couprie, P. Tauc, F. Merola, A. Delboulbé, D. Garzella, T. Hara, M. Billardon, Rev. Sci. Instr. **65**, 1485 (1994)
133. G. S. Edwards, R.H. Austin, F.E. Caroll, M.L. Copeland, M.-E. Couprie, W.E. Gabella, R.F. Haglund, B.A. Hooper, M.S. Huston, E.D. Jansen, K.M. Joss, D.P. Klehart, L. Lindau, J. Miao, H.S. Pratisto, J.H. Shen, Y. Tokukate, A.F. van der Meer, and A. Xie, Rev. Sci. Instr. **74**, 158478 (2003)
134. M. Marsi, M.-E. Couprie, L. Nahon, D. Garzella, A. Delboulbé, T. Hara, R. Bakker, G. Indlekofer, M. Billardon, A. Taleb-Ibrahimi, Phys. Lett. **70**, 895 (1997)
135. M. Marsi, M. Trovo, R. P. Walker, L. Giannessi, G. Dattoli, A. Gatto, N. Kaiser, S. Gunster, D. Ristau, M.-E. Couprie, D. Garzella, J. A. Clarke, M.W. Poole, Appl. Phys. Lett. **80**, 2851 (2002)
136. R. Bonifacio, C. Pellegrini, and L.M. Narducci, Optics Comm. **50**, 373 (1984)
137. K.J. Kim, Phys. Rev. Lett. **15**, 1871 (1986)
138. A.M. Kondratenko, E.L. Saldin, Part. Accel. **10**, 207 (1986)
139. Y. Din, A. Brachmann, F.-J. Decker, D. Dowell, P. Emma, J. Frisch, S. Gilevich, G. Hays, Ph. Hering, Z. Huang, R. Iverson, H. Loos, A. Miahnahri, H.-D. Nuhn, D. Ratner, J. Turner, J. Welch, W. White, and J. Wu, Phys. Rev. Lett. **102**, 254801 (2009)
140. E.L. Saldin, E.A. Schneidmiller, and M.V. Yurkov, Opt. Comm. **148**, 383 (1998)
141. V. Milton, E. Gluskin, N.D. Arnold, C. Benson, W. Berg, S.G. Biedron, M. Borland, Y.-C. Chae, R.J. Dejus, Den P.K. den Hartog, B. Deriy, M. Erdmann, Y.I. Eidelman, M.W. Hahne, Z. Huang, K.-J. Kim, J.W. Lewellen, Y. Li, A.H. Lumpkin, O. Makarov, E.R. Moog, A. Massiri, V. Sajaev, R. Soliday, B.J. Tieman, E.M. Trakhtenberg, G. Travish, I.B. Vasserman, N.A. Vinokurov, X.J. Wang, G. Wiemerslage, and B.X. Yang, Science **292**, 2037 (2001)
142. W. Ackermann, G. Asova, V. Ayvazyan, A. Azima, N. Baboi, J. Bähr, V. Balandin, B. Beutner, A. Brandt, A. Bolzmann, R. Brinkmann, O.I. Brovko, M. Castellano, P. Castro, L. Catani, E. Chiadroni, S. Choroba, A. Cianchi, J.T. Costello, D. Cubaynes, J. Dardis, W. Decking, H. Delsim-Hashemi, A. Delserieys, G. Di Pirro, M. Dohlus, S.Düsterer, A. Eckhardt, H. T. Edwards, B. Faatz, J. Feldhaus, K. Fl"ottmann, J. Frisch, L. Fr"ohlich, T. Garvey, U. Gensch, Ch. Gerth, M. G"orler, N. Golubeva, H.-J. Grabosch, M. Grecki, O. Grimm, K. Hacker, U. Hahn, J.H. Han, K. Honkavaara, T. Hott, M. Hüning, Y. Ivanisenko, E. Jaeschke, W. Jalmuzna, T. Jezynski, R. Kammering, V. Katalev, K. Kavanagh, E. T. Kennedy, S. Khodyachykh, K. Klose, V. Kocharyan, M. Körfer, M. Kollewe, W. Koprek, S. Korepanov, D. Kostin, M. Krassilnikov, G. Kube, M. Kuhlmann, C.L. Lewis, L. Lilje, T. Limberg, D. Lipka, F. Löhl, H. Luna, M. Luong, M. Martins, M. Meyer, P. Michelato, V. Miltchev, W.D. Möller, L. Monaco, W.F. Müller, O. Napieralski, O. Napoly, P. Nicolosi, D. Nölle, T. Nuñez,

A. Oppelt, C. Pagani, R. Paparella, N. Pchalek, J. Pedregosa-Gutierrez, B. Petersen, B. Petrosyan, G. Petrosyan, L. Petrosyan, J. Pflüger, E. Plönjes, L. Poletto, K. Pozniak, E. Prat, D. Proch, P. Pucyk, P. Radcliffe, H. Redlin, K. Rehlich, M. Richter, M. Roehrs, J. Roensch, R. Romaniuk, M. Ross, J. Rossbach, V. Rybnikov, M. Sachwitz, E.L. Saldin, W. Sandner, H. Schlarb, B. Schmidt, M. Schmitz, P. Schmüser, J.R. Schneider, E.A. Schneidmiller, S. Schnepp, S. Schreiber, M. Seidel, D. Sertore, A.V. Shabunov, C. Simon, S. Simrock, E. Sombrowski, A.A. Sorokin, P. Spanknebel, R. Spesyvtsev, L. Staykov, B. Steffen, F. Stephan, F. Stulle, H. Thom, K. Tiedtke, M. Tischer, S. Toleikis, R. Treusch, D. Trines, I. Tsakov, E. Vogel, T. Weiland, H. Weise, M. Wellhöfer, M. Wendt, I. Will, A. Winter, K. Wittenburg, W. Wurth, P. Yeates, M. V. Yurkov, I. Zagorodnov, and K. Zapfe, Nature Photon. **1**, 336 (2007)

143. T. Shintake, H. Tanaka, T. Hara, T. Tanaka, K. Togawa, M. Yabashi, Y. Otake, Y. Asano, T. Bizen, T. Fukui, S. Goto, A. Higashiya, T. Hirono, N. Hosoda, T. Inagaki, S. Inoue, M. Ishii, Y. Kim, H. Kimura, M. Kitamura, T. Kobayashi, H. Maesaka, T. Masuda, S. Matsui, T. Matsushita, X.-M. Maréchal, M. Nagasono, H. Ohashi, T. Ohata, T. Ohshima, K. Onoe, K. Shirasawa, T. Takagi, S. Takahashi, M. Takeuchi, K. Tamasaku, R. Tanaka, Y. Tanaka, T. Tanikawa, T. Togashi, S. Wu, A. Yamashita, K. Yanagida, C. Zhang, H. Kitamura, and T.Ishikawa, Nature Photon. **2**, 555 (2008)
144. P. Emma, R. Akre, J. Arthur, R. Bionta, C. Bostedt, J. Bozek, A. Brachmann, P. Bucksbaum, R. Coffee, F.-J. Decker, Y. Ding, D. Dowell, S. Edstrom, A. Fisher, J. Frisch, S. Gilevich, J. Hastings, G. Hays, Ph. Hering, Z. Huang, R. Iverson, H. Loos, M. Messerschmidt, A. Miahnahri, S. Moeller, H.-D. Nuhn, G. Pile, D. Ratner, J. Rzepiela, D. Schultz, T. Smith, P. Stefan, H. Tompkins, J. Turner, J. Welch, W. White, J. Wu, G. Yocky, and J. Galayda, Nature Photon. **4**, 641 (2010)
145. Z. Huang, A. Brachmann, F.-J. Decker, Y. Ding, D. Dowell, P. Emma, J. Frisch, S. Gilevich, G. Hays, Ph. Hering, R. Iverson, H. Loos, A. Miahnahri, H.-D. Nuhn, D. Ratner, G. Stupakov, J. Turner, J. Welch, W. White, J. Wu, and D. Xiang, Phys. Rev. ST Accel. Beams **13**, 020703 (2010)
146. T. Ishikawa, H. Aoyagi, T. Asaka, Y. Asano, N. Azumi, T. Bizen, H. Ego, K. Fukami, T. Fukui, Y. Furukawa, S. Goto, H. Hanaki, T. Hara, T. Hasegawa, T. Hatsui, A. Higashiya, T. Hirono, N. Hosoda, M. Ishii, T. Inagaki, Y. Inubushi, T. Itoga, Y. Joti, M. Kago, T. Kameshima, H. Kimura, Y. Kirihara, A. Kiyomichi, T. Kobayashi, C. Kondo, T. Kudo, H. Maesaka, X.-M. Maréchal, T. Masuda, S. Matsubara, T. Matsumoto, T. Matsushita, S. Matsui, M. Nagasono, N. Nariyama, H. Ohashi, T. Ohata, T. Ohshima, S. Ono, Y. Otake, C. Saji, T. Sakurai, T. Sato, K. Sawada, T. Seike, K. Shirasawa, T. Sugimoto, S. Suzuki, S. Takahashi, H. Takebe, K. Takeshita, K. Tamasaku, H. Tanaka, R. Tanaka, T. Tanaka, T. Togashi, K. Togawa, A. Tokuhisa, H. Tomizawa, K. Tono, S. Wu, M. Yabashi, M. Yamaga, A. Yamashita, K. Yanagida, C. Zhang, T. Shintake, H. Kitamura, and N. Kumagai, Nature Photon. **6**, 540 (2012)
147. The European X-Ray Laser Project XFEL, TDR July 2006, www.xfel.eu/
148. C. Townes, in *A Century of Nature, 21 Discoveries that Changes Science in the World*, ed. by L. Garwin, T. Lincoln, (Univ. Chicago Press, 2003), p.107
149. B. McNeil, Nature Photon. **3**, 375 (2009)
150. H.N. Chapman, P. Fromme, A. Barty, T.A. White, R.A. Kirian, A. Aquila, M.S. Hunter, J. Schulz, D.P. DePonte, U. Weierstall, R.B. Doak, F.R.N.C. Maia, A.V. Martin, I. Schlichting, L. Lomb, N. Coppola, R.L. Shoeman, S.W. Epp, R. Hartmann, D. Rolles, A. Rudenko, L. Foucar, N. Kimmel, G. Weidenspointner, P. Holl,

M. Liang, M. Barthelmess, C. Caleman, S. Boutet, M.J. Bogan, J. Krzywinski, C. Bostedt, S. Bajt, L. Gumprecht, B. Rudek, B. Erk, C. Schmidt, A. Hömke, C. Reich, D. Pietschner, L. Strüder, G. Hauser, H. Gorke, J. Ullrich, S. Herrmann, G. Schaller, F. Schopper, H. Soltau, K.-U. K"uhnel, M. Messerschmidt, J.-D. Bozek, S.P. Hau-Riege, M. Frank, C.Y. Hampton, R.G. Sierra, D. Starodub, G.J. Williams, J. Hajdu, N. Timneanu, M.M. Seibert, J. Andreasson, A. Rocker, O. Jönsson, M. Svenda, S. Stern, K. Nass, R. Andritschke, C.D. Schröter, F. Krasniqi, M. Bott, K.E. Schmidt, X. Wang, I. Grotjohann, J.M. Holton, T.R.M. Barends, R. Neutze, S. Marchesini, R. Fromme, S. Schorb, D. Rupp, M. Adolph, T. Gorkhover, I. Andersson, H. Hirsemann, G. Potdevin, H. Graafsma, B. Nilsson, and J.C.H. Spence, Nature **470**, 73 (2010)

151. M.M. Seibert, T. Ekeberg, F.R.N.C. Maia, M. Svenda, J. Andreasson, O. Jönsson, D. Odić, B. Iwan, A. Rocker, D. Westphal, M. Hantke, D.P. DePonte, A. Barty, J. Schulz, L. Gumprecht, N. Coppola, A. Aquila, M. Liang, T.A. White, A. Martin, C. Caleman, S. Stern, C. Abergel, V. Seltzer, J.-M. Claverie, C. Bostedt, J.D. Bozek, S. Boutet, A.A. Miahnahri, M. Messerschmidt, J. Krzywinski, G. Williams, K.O. Hodgson, M.J. Bogan, C.Y. Hampton, R.G. Sierra, D. Starodub, I. Andersson, S. Bajt, M. Barthelmess, J.C.H. Spence, P. Fromme, U. Weierstall, R. Kirian, M. Hunter, R.B. Doak, S. Marchesini, S.P. Hau-Riege, M. Frank, R.L. Shoeman, L. Lomb, S.W. Epp, R. Hartmann, D. Rolles, A. Rudenko, C. Schmidt, L. Foucar, N. Kimmel, P. Holl, B. Rudek, B. Erk, A. Hömke, C. Reich, D. Pietschner, G. Weidenspointner, L. Strüder, G. Hauser, H. Gorke, J. Ullrich, I. Schlichting, S. Herrmann, G. Schaller, F. Schopper, H. Soltau, K.U. Kühnel, R. Andritschke, C.-D. Schröter, F. Krasniqi, M. Bott, S. Schorb, D. Rupp, M. Adolph, T. Gorkhover, H. Hirsemann, G. Potdevin, H. Graafsma, B. Nilsson, H.N. Chapman, and J. Hajdu, Nature **470**, 78 (2011)
152. R.A. Kirian, T.A. White, J.M. Holton, H.N. Chapman, P. Fromme, A. Barty, L. Lomb, A. Aquila, F.R.N.C Maia, A.V. Martin, R. Fromme, X. Wang, M.S. Hunter, K.E. Schmidt, and J.C.H. Spence, Acta Crystallog. A **67**, 131 (2011)
153. L. Young, E. P. Kanter, B. Krässig, Y. Li, A.M. March, S.T. Pratt, R. Santra, S.H. Southworth, N. Rohringer, L.F. Di Mauro, G. Doumy, C.A. Roedig, N. Berrah, L. Fang, M. Hoener, P.H. Bucksbaum, J.P. Cryan, S. Ghimire, J.M. Glownia, D.A. Reis, J.D. Bozek, C. Bostedt, M. Messerschmidt, Nature **466**, 56 (2010)
154. N. Berrah, J. Bozek, J.T. Costello, S. Düsterer, L. Fang, J. Feldhaus, H. Fukuzawa, M. Hoener, Y.H. Jiang, P. Johnsson, E.T. Kennedy, M. Meyer, R. Moshammer, P. Radcliffe, M. Richter, A. Rouzée, A. Rudenko, A.A. Sorokin, K. Tiedtke, K. Ueda, J. Ullrich, and M.J.J. Vrakking, J. Mod. Optics **57**, 1015 (2010)
155. G. Doumy, C. Roedig, S.-K. Son, C.I. Blaga, A.D. DiChiara, R. Santra, N. Berrah, C. Bostedt, J.D. Bozek, P.H. Bucksbaum, J.P. Cryan, L. Fang, S. Ghimire, J.M. Glownia, M. Hoener, E.P. Kanter, B. Krässig, M. Kuebel, M. Messerschmidt, G.G. Paulus, D.A. Reis, N. Rohringer, L. Young, P. Agostini, and L.F. DiMauro, Phys. Rev. Lett. **106**, 083002 (2011)
156. M. Richter, S.V. Bobashev, A.A. Sorokin, and K. Tiedtke, J. Phys. B **43**, 194005 (2010)
157. A.H. Zewail, J. Phys. Chem. **104**, 5660 (2000)
158. M. Meyer, J.T. Costello, S. Düsterer, W.B. Li, and P. Radcliffe, J. Phys. B **43**, 194006 (2010)

159. J.M. Glownia, J. Cryan, J. Andreasson, A. Belkacem, N. Berrah, C. I. Blaga, C. Bostedt, J. Bozek, L.F. DiMauro, L. Fang, J. Frisch, O. Gessner, M. Gühr, J. Hajdu, M.P. Hertlein, M. Hoener, G. Huang, O. Kornilov, J.P. Marangos, A. M. March, B.K. McFarland, H. Merdji, V.S. Petrovic, C. Raman, D. Ray, D.A. Reis, M. Trigo, J.L. White, W. White, R. Wilcox, L. Young, R.N. Coffee, and P.H. Bucksbaum, Optics Express **18**, 017620 (2010)
160. S. Roy, D. Parks, K.A. Seu, R. Su, J.J. Turner, W. Chao, E.H. Anderson, S. Cabrini, and S.D. Kevan, Nature Photon. **5**, 243 (2011)
161. C.M. Günther, B. Pfau, R. Mitzner, B. Siemer, S. Roling, H. Zacharias, O. Kutz, I. Rudolph, D. Schondelmaier, R. Treusch, and S. Eisebitt, Nature Photon. **5**, 99 (2011)
162. E. Galtier, F.B. Rosmej, T. Dzelzainis, D. Riley, F.Y. Khattak, P. Heimann, R.W. Lee, A.J. Nelson, S.M. Vinko, T. Whitcher, J.S. Wark, T. Tschentscher, S. Toleikis, R. R. Fäustlin, R. Sobierajski, M. Jurek, L. Juha, J. Chalupsky, V. Hajkova, M Kozlova, J. Krzywinski, and B. Nagler, Phys. Rev. Lett. **106**, 164801 (2011)
163. L.-H. Yu and I. Ben Zvi, Nucl. Instr. Meth. A **393**, 96 (1997)
164. L.-H. Yu, M. Babzien, I. Ben-Zvi, L.F. DiMauro, A. Doyuran, W. Graves, E. Johnson, S. Krinsky, R. Malone, I. Pogorelsky, J. Skaritka, G. Rakowsky, L. Solomon, X.J. Wang, M. Woodle, V. Yakimenko, S.G. Biedron, J.N. Galayda, E. Gluskin, J. Jagger, V. Sajaev, and I. Vasserman, Science **289**, 932 (2000)
165. M. Ferray, A. L'Huillier, X.F. Li, L.A. Lompre, G. Mainfray, and C. Manus, J. Phys. B **21**, L31 (1988)
166. A. McPherson, G. Gibson, H. Jara, U. Johann, T.S. Luk, I.A. McIntyre, K. Boyer, and C.K. Rhodes, J. Opt. Soc. Am. **4**, 595 (1987)
167. G. Lambert, T. Hara, D. Garzella, T. Tanikawa, M. Labat, B. Carre, H. Kitamura, T. Shintake, M. Bougeard, S. Inoue, Y. Tanaka, P. Salieres, H. Merdji, O. Chubar, O. Gobert, K. Tahara, and M.-E. Couprie, Nature Phys. **4**, 296 (2008)
168. T. Togashi, E. Takahashi, K. Midorikawa, M. Aoyama, K. Yamakawa, T. Sato, A. Iwasaki, S. Owada, T. Okino, K. Yamanouchi, F. Kannari, A. Yagishita, H. Nakano, M.E. Couprie, K. Fukami, T. Hatsui, T. Hara, T. Kameshima, H. Kitamura, N. Kumagai, S. Matsubara, M. Nagasono, H. Ohashi, T. Ohshima, Y. Otake, T. Shintake, K. Tamasaku, H. Tanaka, T. Tanaka, K. Togawa, H. Tomizawa, T. Watanabe, M. Yabashi, and T. Ishikawa, Optics Express **19**, 317 (2011)
169. L.-H. Yu, M. Babzien, I. Ben-Zvi, L.F. DiMauro, A. Doyuran, W. Graves, E. Johnson, S. Krinsky, R. Malone, I. Pogorelsky, J. Skaritka, G. Rakowsky, L. Solomon, X.J. Wang, M. Woodle, V. Yakimenko, S.G. Biedron, J.N. Galayda, E. Gluskin, J. Jagger, V. Sajaev, and I. Vasserman I, Science **289**, 932 (2000)
170. L. Giannessi, P. Musumeci, New J. Phys. **8**, 294 (2006)
171. L. Giannessi, P. Musumeci, and S. Spampinati, J. Appl. Phys. **98**, 043110 (2005)
172. M. Labat, M. Bellaveglia, M. Bougeard, B. Carré, F. Ciocci, E. Chiadroni, A. Cianchi, M. E. Couprie, L. Cultrera, M. Del Franco, G. Di Pirro, A. Drago, M. Ferrario, D. Filippetto, F. Frassetto, A. Gallo, D. Garzella, G. Gatti, L. Giannessi, G. Lambert, A. Mostacci, A. Petralia, V. Petrillo, L. Poletto, M. Quattromini, J.V. Rau, C. Ronsivalle, E. Sabia, M. Serluca, I. Spassovsky, V. Surrenti, C. Vaccarezza, and C. Vicario, Phys. Rev. Lett. **107**, 224801 (2011)
173. C. Lechner, Ackermann, A. Boedewadt Azima, M. Drescher, E. Hass, U. Hipp, T. Mitchev Matzezopoulos, M. Mittenzwey, M. Redhers, J. Roensch, J. Rossbach,

R. Tarkeshian, M. Wieland, S. Khan, S. Bajt, S. Düsterer, K. Honkavaara, T. Laarmann, H. Schlarb, S. Schrieber, M. Curbis Tischer, R. Ischebeck, Proc. of FEL 2012, Nara, Japan, (2012) (to be published)
174. E. Allaria, A. Battistoni, F. Bencivenga, R. Borghes, C. Callegari, F. Capotondi, D. Castronovo, P. Cinquegrana, D. Cocco, M. Coreno, P. Craievich, R. Cucini, F. D'Amico, M.B. Danailov, A. Demidovich, G. De Ninno, A. Di Cicco, S. Di Fonzo, M. Di Fraia, S. Di Mitri, B. Diviacco, W.M. Fawley, E. Ferrari, A. Filipponi, L. Froehlich, A. Gessini, E. Giangrisostomi, L. Giannessi, D. Giuressi, C. Grazioli, R. Gunnella, R. Ivanov, B. Mahieu, N. Mahne, C. Masciovecchio, I.P. Nikolov, G. Passos, E. Pedersoli, G. Penco, E. Principi, L. Raimondi, R. Sergo, P. Sigalotti, C. Spezzani, C. Svetina, M. Trovó, and M. Zangrando, New J. Phys. **14**, 113009 (2012)
175. T. Shaftan, and L.-H. Yu, Phys. Rev. E **71**, 046501 (2005)
176. J. Feldhaus, E.L. Saldin , J.R. Schneider, E.A. Schneidmiller, and M.V. Yurkov, Optics Comm. **140**, 341 (1997)
177. G.L. Geloni, V. Kocharyan,and E. Saldin, J. Mod. Optics **58**, 1391 (2011)
178. J. Amann, W. Berg, V. Blank, F.-J. Decker, Y. Ding, P. Emma, Y. Feng, J. Frisch, D. Fritz, J. Hastings, Z. Huang, J. Krzywinski, R. Lindberg, H. Loos, A. Lutman, H.-D. Nuhn, D. Ratner, J. Rzepiela, D. Shu, Yu. Shvyd'ko, S. Spampinati, S. Stoupin, S. Terentyev, E. Trakhtenberg, D. Walz, J. Welch, J. Wu, A. Zholents, and D. Zhu, Nature Photon. **6**, 693 (2012)
179. M. Yabashi, and T. Tanaka, Nature Photon. **6**, 648 (2012)
180. W. Li, R.R. Lucchese, A. Doyuran, Z. Wu, H. Loos, G.E. Hall, and A.G. Suits, Phys. Rev. Lett. **92**, 083002 (2004)
181. E. Allaria, R. Appio, L. Badano, W.A. Barletta, S. Bassanese, S.G. Biedron, A. Borga, E. Busetto, D. Castronovo, P. Cinquegrana, S. Cleva, D. Cocco, M. Cornacchia, P. Craievich, I. Cudin, G. D'Auria, M. Dal Forno, M.B. Danailov, R. De Monte, G. De Ninno, P. Delgiusto, A. Demidovich, S. Di Mitri, B. Diviacco, A. Fabris, R. Fabris, W. Fawley, M. Ferianis, E. Ferrari, S. Ferry, L. Froehlich, P. Furlan, G. Gaio, F. Gelmetti, L. Giannessi, M. Giannini, R. Gobessi, R. Ivanov, E. Karantzoulis, M. Lonza, A. Lutman, B. Mahieu, M. Milloch, S.V. Milton, M. Musardo, I. Nikolov, S. Noe, F. Parmigiani, G. Penco, M. Petronio, L. Pivetta, M. Predonzani, F. Rossi, L. Rumiz, A. Salom, C. Scafuri, C. Serpico, P. Sigalotti, S. Spampinati, C. Spezzani, M. Svandrlik, C. Svetina, S. Tazzari, M. Trovo, R. Umer, A. Vascotto, M. Veronese, R. Visintini, M. Zaccaria, D. Zangrando, and M. Zangrando, Nature Photon. **6**, 699 (2012)
182. S. Stupakov, Phys. Rev. Lett. **102**, 074801 (2009)
183. D. Xiang, E. Colby, M. Dunning, S. Gilevich, C. Hast, K. Jobe, D. McCormick, J. Nelson, T. O. Raubenheimer, K. Soong, G. Stupakov, Z. Szalata, D. Walz, S. Weathersby, and M. Woodley, Phys. Rev. Lett. **105**, 114801 (2010)
184. Z.T. Zhao, D. Wang, J.H. Chen, Z.H. Chen, H.X. Deng, J.G. Ding, C. Feng, Q. Gu, M.M. Huang, T.H. Lan, Y.B. Leng, D.G. Li, G.Q. Lin, B. Liu, E. Prat, X.T. Wang, Z.S. Wang, K.R. Ye, L.Y. Yu, H.O. Zhang, J.Q. Zhang, Me. Zhang, Mi. Zhang, T. Zhang, S.P. Zhong, and Q.G. Zhou, Nature Photon. **6**, 360 (2012)
185. D. Xiang, and G. Stupakov, New J. Phys. **13**, 093028 (2011)
186. W. Leemans, E. Esarey, Physics Today **62**, 44 (2009)
187. M.P. Anania, E. Brunetti, S. Cipiccia, D. Clark, R.C. Issac, D.A. Jaroszynski, G.G. Manahan, T. McCanny, A. J. Reitsma, R.P. Shanks, G.H. Wiggins Welsh, J.A. Clarke, M.W. Poole, B.J.A. Shepherd, M.J. de Loos, S.B. van der Geer, Proc. IPAC10, Kyoto, Japan, 2263 (2010)

188. http://www.mpq.mpg.de/APS/gruener.php
189. G. Lambert, S. Corde, K. Ta Phuoc, V. Malka, A. Ben Ismail, E. Specka, A. Benveniste, M. Labat, A. Loulergue, R. Bachelard, M.-E Couprie, Proc. FEL conf., Nara, Japan (2012) (to be published)
190. K. Nakajima, Nature Phys. **4**, 92 (2008)
191. H.-P. Schlenvoigt, K. Haupt, A. Debus, F. Budde, O. Jäckel, S. Pfotenhauer, H. Schwoerer, E. Rohwer, J.G. Gallacher, E. Brunetti, R.P. Shanks, S. M. Wiggins, and D.A. Jaroszynski, Nature Phys. **4**, 130 (2008)
192. M. Fuchs, R. Weingartner, A. Popp , Z. Major, S. Becker, J. Osterhoff, I. Cortrie, B. Zeitler, R. Hörlein, G.D. Tsakiris, U. Schramm, T.P. Rowlands-Rees, S.M. Hooker, D. Habs, F. Krausz, S. Karsch, and F. Grüner, Nature Phys. **5**, 826 (2009)
193. M. P. Anania, D. Clark, S.B. van der Geer, M.J. de Loos, R. Isaac, A.J.W. Reitsma, G.H. Welsh, S.M. Wiggins, and D.A. Jaroszynski, Proc. of SPIE Conf. **7359**, 735916 (2009)
194. A. R. Maier, A. Meseck, S. Reiche, C.B. Schroeder, T. Seggebrock, and F. Grüner, Phys. Rev. X **2**, 031019 (2012)
195. C.B. Schroeder, C. Benedetti, E. Esarey, W. Leemans, J. van Tilborg, Y. Ding, Z. Huang, Proc. of FEL Conf. 2012, Nara, Japan (2012) (to be published)
196. Z. Huang, Y. Ding, and C.B. Schroeder, Phys. Rev. Lett. **109**, 204801 (2012)

Chapter 3
Theoretical Basis of Photon Spectroscopies

Massimo Altarelli

Abstract The theoretical basis of x-ray spectroscopies most commonly used in the investigation of magnetic systems is reviewed. A systematic derivation of the cross sections of the different processes (elastic and inelastic, resonant and non-resonant scattering, absorption spectroscopies and dichroism) is attempted, emphasizing the conceptual common aspects of these techniques and, at the same time, the variety of information that they deliver.

3.1 Introduction

The purpose of this article is to review the basic aspects of photon spectroscopies, with special emphasis on the techniques that find widespread application to magnetic systems. Our aim is to give a pedagogical presentation, by providing a step-by-step guide through the sometimes elaborate calculations of the relevant scattering amplitudes and cross sections.

Crystallographers have used x-ray diffraction for almost one hundred years, as a tool for the determination of crystal structures. A particularly important development of more recent years was the realization that the scattering of polarized x-rays can deliver information not only on the electron

Massimo Altarelli
European XFEL, Albert-Einstein-Ring 19, 22761 Hamburg, Germany, e-mail: massimo.altarelli@xfel.eu

E. Beaurepaire et al. (eds.), *Magnetism and Synchrotron Radiation: Towards the Fourth Generation Light Sources*, Springer Proceedings in Physics 151,
DOI: 10.1007/978-3-319-03032-6_3,

density distribution, but also on the distribution of magnetic moments. Although the application of magnetic x-ray scattering has only recently become popular, thanks to the development of modern synchrotron light sources, the coupling between photons and magnetic moments is predicted by quantum electrodynamics, and in fact it was described as early as 1954 by Low [1] and Gell-Mann and Goldberger [2] in their derivations of the low-energy limit of the Compton cross section. Later, Platzman and Tzoar [3] pointed out the possibility to use this effect to investigate magnetic structures.

Due to the very small cross section, it was not until 1981, however, that the first magnetic scattering experiment was carried out by de Bergevin and Brunel [4] on NiO, demonstrating the basic features of non-resonant scattering. The truly heroic apects of this first experiment performed with an x-ray tube were later alleviated by the advent of synchrotron sources, and experiments were performed to take advantage of the attractive features of x-ray magnetic scattering, as compared to neutron scattering, i.e. the very high momentum resolution and the possibility of a separate determination of the spin and of the orbital contributions to the magnetic moment by the different polarization dependence.

A further important step forward was the discovery that in the anomalous or resonant region (when the x-ray photon energy is close to an absorption edge of one of the atomic species of the sample), the scattering amplitude often displays a strong dependence on the polarization of the incoming and scattered beams. This is formally translated in the description of the atomic scattering amplitude as a *tensor* (rather than as a *scalar*) quantity, with important consequences for the selection rules for the diffracted beams [5, 6].

The particular significance of the resonant scattering for magnetism studies was realized in 1988, with the discovery by Gibbs et al. [7] of resonant magnetic scattering (also called resonant exchange scattering), i.e. of an enhancement of several orders of magnitude of the magnetic scattering intensity when the photon energy is close to an absorption edge of the material. A very large number of studies in rare earth, actinide and transition metal systems followed. Although the price to pay for the resonant enhancement is the loss of a direct interpretation of the scattering intensity in terms of spin and orbital magnetic structure factors, many experiments followed, and contributed to clarify many issues on the electronic structure of magnetic materials: as we shall see, the selection rules for optical transitions make the resonant process sensitive to electronic states with specific orbital character, and enhance their contribution to the magnetic properties.

This last remark leads naturally to another recent development, the exploitation of the sensitivity of resonant scattering not only to charge and magnetic order, but also to orbital order, because the atomic scattering amplitude can vary substantially depending on the occupation of selected spin or orbital states and therefore on their availability to serve as intermediate states in the second order scattering process.

Modern x-ray sources, providing high brilliance and controlled polarization, allowed two more techniques to acquire paramount importance: on the one hand the use of the polarization dependence of absorption cross sections (circular or linear dichroism); on the other, the resonant enhancement of the scattering amplitude for inelastic scattering, which has a cross section much smaller than the corresponding elastic process. The study of electronic, including magnetic, excitations by resonant inelastic x-ray scattering (RIXS) is becoming an increasingly popular technique, and great progress in energy resolution, on the one hand, and in the interpretation of the resulting spectra, on the other, is taking place.

The structure of the article is the following: in Section 3.2 we recall the formalism necessary to set up the Hamiltonian for the interaction between radiation and matter, and to develop a perturbation description of scattering processes (in the range of radiation intensities where the perturbation approach is justifiable). In Section 3.3 the cross section for the non-resonant case is obtained and discussed, while the resonant elastic case is treated in Section 3.4. Section 3.5 is devoted to absorption spectroscopy, showing how the relevant quantities are related to those for resonant scattering by the "optical theorem" of scattering theory, and how their dependence on polarization in anisotropic and magnetic systems can be derived. Finally, Section 3.6 is devoted to a discussion of resonant inelastic scattering and of some recent applications to the study of electronic and magnetic excitations and properties.

3.2 Interaction of Radiation with Electronic Matter

A microscopic discussion of the electronic properties of matter must necessarily be formulated in the language of quantum mechanics. We also need to consider relativistic effects, if we want to consider magnetic x-ray scattering, because quantities such as the magnetic moment associated to the electron spin appear only in a relativistic theory, and relativistic effects such as the

spin-orbit interaction play an essential role in determining the coupling between radiation and magnetic moments, as we shall see.

We therefore expect the reader to be familiar with basic quantum mechanics and its general formalism, including some aspects of advanced topics such as relativistic quantum mechanics and the second quantization formalism.

In discussing the scattering of electromagnetic waves on a material system composed of electrons and nuclei, we shall follow the usual approach and consider the Hamiltonian for the material system, plus the Hamiltonian for the free electromagnetic field, plus an interaction term between the two systems. As it will be clear soon, the scattering from electrons is much more intense than the scattering from nuclei, and we shall therefore consider matter as a system of electrons, interacting with one another and with a set of nuclei in fixed positions, through a potential energy which can be written

$$V(\mathbf{r}_1,...,\mathbf{r}_N) = \sum_{i=1}^{N} V_{nuc}(\mathbf{r}_i) + \sum_{i>j} V_C\left(\left|\mathbf{r}_i - \mathbf{r}_j\right|\right) \tag{3.1}$$

where the first term represents the interaction with the nuclei, and in the second the Coulomb interaction is $V_C(r) = e^2/r$. The system of electrons and nuclei is a many-body system and, in general, not much progress is possible without suitable approximations. Although it is not indispensable for our derivations, a *self-consistent field* approximation, in which the dependence of (3.1) on the positions of all electrons is replaced by a one-electron average

$$V(\mathbf{r}_1,...,\mathbf{r}_N) \simeq \sum_{i=1}^{N} V(\mathbf{r}_i) \tag{3.2}$$

is convenient to simplify the notations and the developments. The potential energy is the key ingredient that allows to write the Hamiltonian for the i-th electron, which, in relativistic quantum mechanics, is the Dirac Hamiltonian [8, 9]

$$H_{el} = \sum_{i=1}^{N} (c\alpha \cdot \mathbf{p_i} + \beta mc^2 + V(\mathbf{r}_i)) \tag{3.3}$$

where α and β are the 4×4 Dirac matrices

$$\alpha_{(x,y,z)} = \begin{pmatrix} 0 & \sigma_{(x,y,z)} \\ \sigma_{(x,y,z)} & 0 \end{pmatrix}$$
$$\beta = \begin{pmatrix} \mathbf{1} & 0 \\ 0 & -\mathbf{1} \end{pmatrix}, \tag{3.4}$$

where $\sigma_(x,y,z)$ denotes the 2×2 Pauli matrices and $\mathbf{1}$ the 2×2 unit matrix; in addition, $\mathbf{p}_i$ is the momentum of the i-th electron. We now consider that the processes we are interested in (scattering and energy exchanges of x-ray photons with energies at most in the $\sim 10\,\mathrm{keV}$ range), always involve energies much smaller than the electron rest energy, $mc^2 \simeq 511\,\mathrm{keV}$, an energy scale that is indeed bigger than any binding energies of core levels that we want to investigate. This authorizes us to adopt the weakly relativistic limit of (3.3), which is considered and derived in great detail in Section 15 of [9]. To see the basic idea, we separate the four-component Dirac spinor into an upper and a lower two-component spinors Ψ_a and Ψ_b, so that the Dirac equation in the stationary case

$$H_{el}\Psi = \mathrm{i}\hbar\frac{\partial}{\partial t}\Psi = E\Psi \tag{3.5}$$

can be written as

$$c(\boldsymbol{\sigma}\cdot\mathbf{p})\Psi_b = (E - mc^2 - V(\mathbf{r}))\Psi_a = (E^{nr} - V(\mathbf{r}))\Psi_a\,, \tag{3.6}$$
$$c(\boldsymbol{\sigma}\cdot\mathbf{p})\Psi_a = (E + mc^2 - V(\mathbf{r}))\Psi_b = (2mc^2 + E^{nr} - V(\mathbf{r}))\Psi_b \tag{3.7}$$

where we defined the non-relativistic energy $E^{nr} = E - mc^2 \ll mc^2$. From this inequality and the structure of the two equations, one can already guess that Ψ_a is much larger than Ψ_b. Upon substituting Ψ_b from the second equation into the first

$$(\boldsymbol{\sigma}\cdot\mathbf{p})\frac{c^2}{2mc^2 + E^{nr} - V(\mathbf{r})}(\boldsymbol{\sigma}\cdot\mathbf{p})\Psi_a = [E^{nr} - V(\mathbf{r})]\Psi_a \tag{3.8}$$

we can expand

$$\frac{c^2}{2mc^2 + E^{nr} - V(\mathbf{r})} \simeq \frac{1}{2m}(1 - \frac{E^{nr} - V(\mathbf{r})}{2mc^2} + \ldots) \tag{3.9}$$

If we retain only the first term in the expansion, we recover the non-relativistic kinetic energy expression; including also the second gives the leading relativistic correction, of order v^2/c^2. In order to obtain the equation for the two-component spinor Ψ_a, we must carefully handle the commutation of the

p operators with the functions of **r**, and obtain, after dropping the a index (for details, see [9, 10])

$$\left[\frac{p^2}{2m} - \frac{p^4}{8m^3c^2} - \frac{e\hbar \mathbf{s}\cdot(\mathbf{E}\times\mathbf{p})}{2m^2c^2} - \frac{e\hbar^2}{8m^2c^2}\nabla\cdot\mathbf{E}\right]\Psi = E^{nr}\Psi\,, \tag{3.10}$$

where the vector $\nabla = (\frac{\partial}{\partial x}, \frac{\partial}{\partial y}, \frac{\partial}{\partial z})$, and the spin operator **s** appearing in the third term (representing the spin-orbit interaction) is defined as $\mathbf{s} = (1/2)\boldsymbol{\sigma}$, and the electric field **E** is the gradient of the potential energy V, divided by the (negative) electron charge.The second term in this equation represents the relativistic mass correction, and the last one is the so-called Darwin term, that is different from zero where the electric field has a non-vanishing divergence. Let us now come to the radiation field, that, on the other hand, is described by the electric and magnetic fields $\mathbf{E}, \mathbf{B}$, which obey Maxwell's equations [11], and which can also be described by introducing a scalar and a vector potential, $\Phi(\mathbf{r})$ and $\mathbf{A}(\mathbf{r},t)$

$$\begin{aligned}\mathbf{B} &= \nabla\times\mathbf{A}\\ \mathbf{E} &= -\nabla\Phi - (1/c)\frac{\partial\mathbf{A}}{\partial t}\,.\end{aligned} \tag{3.11}$$

For given $\mathbf{E}(\mathbf{r})$ and $\mathbf{B}(\mathbf{r})$, the definition of the vector and scalar potentials is not unique; when describing the fields of electromagnetic waves in vacuum, we can use this freedom to chose the *gauge* in such a way that the scalar potential vanishes, and the vector potential **A** is divergence free ($\nabla\cdot\mathbf{A} = 0$) [12]. This will turn out to be a convenient choice later. An arbitrary space- and time-dependent vector potential can be expanded in terms of plane waves, which are characterized by a wavevector **k** and by one of the two polarization modes labeled by λ. Let us write this expansion in the following form

$$\begin{aligned}\mathbf{A}(\mathbf{r},t) = \textstyle\sum_{\mathbf{k},\lambda}\left(\frac{hc^2}{\Omega\omega_{\mathbf{k}}}\right)^{1/2}\Big[&\mathbf{e}_\lambda(\mathbf{k})a(\mathbf{k},\lambda)\mathrm{e}^{\mathrm{i}(\mathbf{k}\cdot\mathbf{r}-\omega_{\mathbf{k}}t)}\\ &+\mathbf{e}^*_\lambda(\mathbf{k})a^\dagger(\mathbf{k},\lambda)\mathrm{e}^{-\mathrm{i}(\mathbf{k}\cdot\mathbf{r}-\omega_{\mathbf{k}}t)}\Big]\,.\end{aligned} \tag{3.12}$$

In this equation, Ω is the volume of the quantization box, and does not appear in any physically meaningful quantity in the following, $\omega_{\mathbf{k}}$ is just $c|\mathbf{k}|$, $\mathbf{e}_\lambda$ is the polarization vector associated to the mode λ, i.e. one of two orthogonal unit vectors in the plane normal to **k**. Furthermore, in a classical description of the field, $a(\mathbf{k},\lambda)$ and $a^\dagger(\mathbf{k},\lambda)$ are the amplitude of the corresponding mode

of the field and its complex conjugate. However, in the language of the second quantization formalism a and $a^\dagger$ are *operators*, respectively the annihilation and creation operators of a photon with quantum numbers $(\mathbf{k},\lambda)$. In this formalism the Hamiltonian of the field takes a very simple and appealing form

$$H_{rad} = \sum_{\mathbf{k},\lambda} \hbar\omega_{\mathbf{k}} \left(a^\dagger(\mathbf{k},\lambda) a(\mathbf{k},\lambda) + 1/2 \right) . \tag{3.13}$$

Turning now to the modifications of H_{el} in presence of the electromagnetic field, we follow the usual prescription to write the Hamiltonian for the motion of a charged particle in external electric and magnetic fields, that reproduces the equations of motion in the electric force and in the Lorentz force: we insert the $\mathbf{A}(\mathbf{r}_i)$ in the Dirac Hamiltonian as an additional term to the momentum operator [8, 9]

$$H'_{el} = \sum_{i=1}^{N} \left(c\alpha \cdot [\mathbf{p}_i - (e/c)\mathbf{A}(\mathbf{r}_i)] + \beta mc^2 + V(\mathbf{r}_i) \right) , \tag{3.14}$$

and follow the previous line of reasoning to obtain the non-relativistic limit of (3.14), which is considered and derived in great detail in Section 15 of [9]. The resulting Hamiltonian, to order $(v/c)^2$ is

$$\begin{aligned} H'_{el} = \sum_{i=1}^{N} \Big[& \; [\mathbf{p}_i - (e/c)\mathbf{A}(\mathbf{r}_i)]^2/(2m) \\ & - \mathbf{p}_i{}^4/8m^3c^2 \\ & + V(\mathbf{r}_i) - (e\hbar/mc)\mathbf{s}_i \cdot \mathbf{B} \\ & - (e\hbar/2m^2c^2)\mathbf{s}_i \cdot (\mathbf{E} \times [\mathbf{p}_i - (e/c)\mathbf{A}(\mathbf{r}_i)]) \\ & + (e\hbar^2/8m^2c^2)\nabla \cdot \mathbf{E} \Big] . \end{aligned} \tag{3.15}$$

In this equation, the first term on the r.h.s. is the usual modification of the kinetic energy in presence of a field, the second (the relativistic mass correction) does not involve the field and is therefore not relevant to our discussion; the fourth term is the interaction of the electron spin $\mathbf{s} = (1/2)\sigma$ with the magnetic field of the radiation, $\mathbf{B} = \nabla \times \mathbf{A}$, confirming that the Dirac equation implies that electrons have spin and a magnetic moment associated to it; the

fifth is the spin-orbit interaction term, with the usual modification of the momentum in presence of the field; and the last, the Darwin correction, is again independent of the radiation field, because the transversality of electromagnetic waves ($\mathbf{k}\cdot\mathbf{E}=0$) implies $\nabla\cdot\mathbf{E}=0$, so that there is no contribution to this term from the radiation electric field. After removing all the relativistic corrections to H'_{el} which are not affected by the radiation field, we are left with the following Hamiltonian $H=H'_{el}+H_{rad}$ for the system of electrons and the radiation field:

$$\begin{aligned} H=\sum_{i=1}^{N}\Bigg[&\frac{[\mathbf{p}_i-(e/c)\mathbf{A}(\mathbf{r}_i)]^2}{2m}+V(\mathbf{r}_i)-(e\hbar/mc)\mathbf{s}_i\cdot\mathbf{B}\\ &-(e\hbar/2m^2c^2)\mathbf{s}_i\cdot(\mathbf{E}\times[\mathbf{p}_i-(e/c)\mathbf{A}(\mathbf{r}_i)])\Bigg]\\ &+\sum_{\mathbf{k},\lambda}\hbar\omega_{\mathbf{k}}\left(a^{\dagger}(\mathbf{k},\lambda)a(\mathbf{k},\lambda)+1/2\right)\ . \end{aligned} \tag{3.16}$$

We are then in a position to separate all the terms mixing electron and photon variables, that constitute the *interaction Hamiltonian*, H_{int}

$$H = H_{el}+H_{rad}+H_{int}\ , \tag{3.17}$$

$$H_{el} = \sum_{i=1}^{N}\left[\frac{\mathbf{p}_i{}^2}{2m}+V(\mathbf{r}_i)+(e\hbar/2m^2c^2)\mathbf{s}_i\cdot(\nabla V(\mathbf{r}_i)\times\mathbf{p}_i)\right]\ , \tag{3.18}$$

$$H_{rad} = \sum_{\mathbf{k},\lambda}\hbar\omega_{\mathbf{k}}\left(a^{\dagger}(\mathbf{k},\lambda)a(\mathbf{k},\lambda)+1/2\right)\ , \tag{3.19}$$

$$\begin{aligned} H_{int} = \sum_{i=1}^{N}\Big[&(e^2/2mc^2)\mathbf{A}^2(\mathbf{r}_i)-(e/mc)\mathbf{A}(\mathbf{r}_i)\cdot\mathbf{p}_i\\ &-(e\hbar/mc)\mathbf{s}_i\cdot(\nabla\times\mathbf{A}(\mathbf{r}_i))\\ &+(e\hbar/2m^2c^3)\mathbf{s}_i\cdot[(\partial\mathbf{A}(\mathbf{r}_i)/\partial t)\times(\mathbf{p}_i-(e/c)\mathbf{A}(\mathbf{r}_i))]\Big]\\ \equiv\ & H'_1+H'_2+H'_3+H'_4\ . \end{aligned} \tag{3.20}$$

The total Hamiltonian, to the required order of relativistic corrections, is thus split into the Hamiltonian for electronic matter, (3.18), for the radiation field, (3.19) and the Hamiltonian describing the interaction between matter and radiation, (3.20). In the next section, scattering processes will be described as transitions between the eigenstates of H_{el} and H_{rad} induced by the perturbation H_{int}. This can be done by regarding the $\mathbf{A}$ field as a classical quantity, or alternatively and more elegantly, by considering it as an operator,

according to the expansion (3.12) in terms of annihilation and creation operators. Before proceeding to the implementation of this program, one should briefly explore the range of validity of the perturbation expansion. One way to approach this question is to ask under which conditions the interaction with the radiation fields leaves the structure of electronic energy levels and wavefunctions essentially unchanged. To this aim, we can compare the size of the electric field experienced by an electron inside an atom with the size of the radiation electric field. The magnitude of the atomic field has the order of magnitude of the hydrogen atom field, that is, in atomic units, simply $\sim e/a_B$ where a_B is the Bohr radius. This gives $E_{atom} \sim 5 \cdot 10^9$ V/cm . To compare this with the field of radiation, let us remember that if denote by I the intensity of radiation, i.e. the energy deposited on the unit surface in the unit time, the energy density (energy per unit volume) is I/c and it equals $(1/4\pi)E_{rms}^2$ [11]. So for a typical situation at a modern synchrotron beamline, where, say $10^{11} \times 1$ keV photons per second are delivered in a $1\,\mu\text{m}^2$ spot, even if we consider the peak intensity during one of $\sim 10^7$ pulses per second, each with a duration of ~ 10 ps, the peak electric field is of order of $\sim 10^5$ V/cm at most. We are therefore several order of magnitudes below the atomic field, the structure of the electronic energy levels is hardly affected and we are in a position to describe the effect of radiation as the occurrence of transitions of the electronic system from one unperturbed eigenstate to another, that we can compute by perturbation methods. However, as it has been the case for the IR and visible region, lasers can deliver a much higher intensity than other sources. Similarly, X-ray Free-Electron Lasers [13, 14, 15] are capable of delivering 10^{11} photons in one 10 fs pulse, with the same $1\,\mu\text{m}^2$ focus. The corresponding increase by ten orders of magnitude of the energy density leads to peak fields of order 10^{10} V/cm, quite comparable or exceeding atomic fields!

In this case, which we shall however not consider any further, perturbation theory is in trouble, and strong non-linear effects can be anticipated (for evidence of such behavior in absorption experiments, see [16, 17] for the theoretical investigation of possible effects in scattering experiments).

3.3 Cross Section for Non-Resonant Elastic Scattering

In developing the expressions for the scattering cross section, we closely follow the lucid discussion by Blume [18], warning the reader that this important paper unfortunately contains many misprints.

In this Section, our discussion is restricted to *elastic* scattering, i.e. to processes in which the sample (the system of electrons) is in the same state (for simplicity, let us say the ground state) before and after the scattering event. If we consider the scattering of an incoming photon with polarization $\mathbf{e}$ and wavevector $\mathbf{k}$ into an outgoing photon with polarization $\mathbf{e}'$ and wavevector $\mathbf{k}'$ (conservation of energy implies $|\mathbf{k}| = |\mathbf{k}'|$), we can describe the initial and final state of the system (sample plus radiation field) as

$$\begin{aligned} |i\rangle &= |0;\ldots,(\mathbf{e},\mathbf{k}),\ldots\rangle \\ |f\rangle &= |0;\ldots,(\mathbf{e}',\mathbf{k}'),\ldots\rangle\,, \end{aligned} \tag{3.21}$$

with an obvious notation labelling the ground state of the electronic system with $|0\rangle$, and the radiation field state with the quantum numbers of the photons present in that state.

It is then clear that the transition consists in the *annihilation* of one photon $(\mathbf{e},\mathbf{k})$, and in the *creation* of one photon $(\mathbf{e}',\mathbf{k}')$. This means that the operator $\mathbf{A}$, which is linear in the creation and annihilation operators, must operate twice. Therefore the lowest order contributing processes will come from applying second order perturbation theory to H_2' and H_3', which contain one $\mathbf{A}$ operator, and by first order perturbation theory applied to H_1' and H_4', which contain two $\mathbf{A}$ operators. As a matter of fact, H_4' contains two terms, respectively proportional to $\partial\mathbf{A}/\partial t \cdot \mathbf{p}$ and to $\partial\mathbf{A}/\partial t \cdot (e/c)\mathbf{A}$. However, we shall later see that the first one produces a negligible effect, so we will drop it and retain the second term only.

According to Fermi's Golden Rule of time-dependent perturbation theory, the number of transitions per unit time is proportional to

$$\begin{aligned} w = \left(\frac{2\pi}{\hbar}\right) \Bigg| &\langle f|H_1' + H_4'|i\rangle \\ &+ \sum_n \frac{\langle f|H_2' + H_3'|n\rangle\langle n|H_2' + H_3'|i\rangle}{E_0 - E_n + \hbar\omega_{\mathbf{k}}} \Bigg|^2 \delta(\hbar(\omega_{\mathbf{k}} - \omega_{\mathbf{k}'}))\,. \end{aligned} \tag{3.22}$$

In the second term, the sum over the complete set of eigenstates $|n\rangle$ of the unperturbed Hamiltonian, $H_{el} + H_{rad}$ appears, referred to as the sum over the intermediate states. The calculation of the matrix elements involve both electron and photon operators and is tedious, but straightforward. For example

$$\langle f|H_1'|i\rangle = \left(\frac{hc^2}{\Omega\,\omega_{\mathbf{k}}}\right)\left(\frac{e^2}{mc^2}\right) \sum_i \langle 0;(\mathbf{e}',\mathbf{k}')|(\mathbf{e}'^{*}\cdot\mathbf{e})a^{\dagger}(\mathbf{k}',\mathbf{e}')a(\mathbf{k},\mathbf{e})\mathrm{e}^{\mathrm{i}(\mathbf{k}-\mathbf{k}')\cdot\mathbf{r}_i}|0;(\mathbf{e},\mathbf{k})\rangle$$
$$= \left(\frac{hc^2}{\Omega\,\omega_{\mathbf{k}}}\right)\left(\frac{e^2}{mc^2}\right)(\mathbf{e}'^{*}\cdot\mathbf{e})\sum_i \langle 0|\mathrm{e}^{\mathrm{i}(\mathbf{k}-\mathbf{k}')\cdot\mathbf{r}_i}|0\rangle\ , \qquad (3.23)$$

after taking the photon annihilation and destruction operator matrix elements according to the usual rules. In this matrix element we recognize the *Thomson scattering* amplitude, with the dot product polarization dependence and the structure factor, expressed by the ground state expectation value of $\sum_i \mathrm{e}^{\mathrm{i}(\mathbf{k}-\mathbf{k}')\cdot\mathbf{r}_i}$. Notice also that the matrix element magnitude per electron is controlled by the quantity $r_0 \equiv e^2/mc^2$ which has the dimensions of length and is the *Thomson radius*, $r_0 = 2.818\cdot 10^{-13}$ cm.

We are now in a position to confirm that the scattering from the nuclei is negligible. In fact, to obtain the corresponding matrix element for nuclear scattering, we should simply replace the electronic positions with the atomic ones, and also replace e^2/mc^2, with Z^2e^2/Mc^2 , where Z and M are the nuclear charge and mass. However, M is roughly equal to $2Zm_n$, where m_n is the nucleon mass, and the mass ratio m_n/m is about 1850. Therefore, the scattering matrix element for a nucleus is $\sim Z/(2\times 1850)$ times smaller than that for an electron, and can be neglected because Z never exceeds 92. In addition, one should also note that there are Z times more electrons than nuclei!).

3.3.1 Thomson Scattering and Crystallography

Before proceeding to the evaluation of the matrix elements deriving from the other pieces of the interaction Hamiltonian, we briefly consider the implications of the H_1' matrix elements. As a matter of fact, we shall later show that, as long as the photon energy $\hbar\omega_{\mathbf{k}}$ is not close to any of the absorption edges of the atoms in the system, this is the dominant matrix element for the photon scattering process. Consider for example the radiation from a Mo x-ray tube, which allows to exploit the K_α line, with an energy of 17.4 keV. This is well above all edges of light atoms such as Al, Si, Ca or Ti, which are below 5 keV, and contributions other than H_1' are negligible. In this approximation,(3.22) simplifies to

$$w = \left(\frac{2\pi}{\hbar}\right) \left|\langle f|H_1'|i\rangle\right|^2 \delta\left(\hbar\left(\omega_{\mathbf{k}} - \omega_{\mathbf{k}'}\right)\right) \ . \tag{3.24}$$

We are now ready to replace (3.23) into (3.24). However, this gives a number of transitions per unit time which depends on the normalization volume. We would rather have a physically meaningful quantity, i. e. a *cross section*, defined as: the number of transitions per unit time, into photon states with energy $\hbar\omega_{\mathbf{k}'} < E < \hbar\omega_{\mathbf{k}'} + \mathrm{d}E$, with wavevector $\mathbf{k}'$ in the solid angle $\mathrm{d}O'$, divided by the number of incident photons per unit time and area. That is, in differential form

$$\left(\frac{\mathrm{d}^2\sigma}{\mathrm{d}E\mathrm{d}O'}\right) = \frac{w\rho(E)}{c/\Omega} \tag{3.25}$$

where ρ is the density of photon states (with specified polarization), i.e. the number of wavevectors within dO' satisfying periodic boundary conditions in a box of volume Ω and $\hbar\omega_{\mathbf{k}} \leq \hbar\omega_{\mathbf{k}'} \leq \hbar\omega_{\mathbf{k}} + \mathrm{d}E$, i.e.

$$\rho(E)\mathrm{d}E\mathrm{d}O' = \left(\frac{\Omega}{(2\pi)^3}\right)\left(\frac{E^2}{\hbar^3 c^3}\right)\mathrm{d}E\mathrm{d}O' \tag{3.26}$$

Finally, by putting Eqs. (3.22), (3.23), and (3.25) together, and upon multiplying (3.25) by $\mathrm{d}E$ and integrating (remember the Dirac δ in (3.22)) we obtain the important result

$$\left(\frac{\mathrm{d}\sigma}{\mathrm{d}O'}\right) = r_0^2 \left|\sum_j \langle 0|\mathrm{e}^{\mathrm{i}\mathbf{q}\cdot\mathbf{r}_j}|0\rangle\right|^2 (\mathbf{e}'^* \cdot \mathbf{e})^2 \tag{3.27}$$

after defining $(\mathbf{k} - \mathbf{k}') \equiv \mathbf{q}$, the *scattering vector*.

With reference to Fig. 3.1, define the *scattering plane* as that identified by $\mathbf{k}, \mathbf{k}'$, and introduce a specific basis for the polarization vectors, $\mathbf{e}_\pi$ *parallel* to the scattering plane, and $\mathbf{e}_\sigma$ *perpendicular* to the scattering plane. Define further the *scattering angle* 2θ (the factor 2 is a mere convention !) as the angle between $\mathbf{k}, \mathbf{k}'$. It is easy to see that the polarization factor $(\mathbf{e}'^* \cdot \mathbf{e})^2$ forbids σ to π transitions and viceversa, and in other cases is worth

$$\begin{aligned} (\mathbf{e}'^* \cdot \mathbf{e})^2 &= \quad 1 \qquad (\sigma \to \sigma) \\ (\mathbf{e}'^* \cdot \mathbf{e})^2 &= \cos^2(2\theta) \ \ (\pi \to \pi') \ . \end{aligned} \tag{3.28}$$

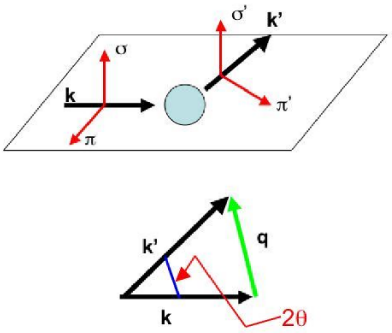

Fig. 3.1 Scattering and polarization geometry

For example, if the photon source is unpolarized, we have to average over the incoming polarizations, and we obtain

$$\left(\frac{\mathrm{d}\sigma}{\mathrm{d}O'}\right) = \frac{1}{2} r_0^2 \left(1+\cos^2(2\theta)\right) |F(\mathbf{q})|^2 \ , \tag{3.29}$$

where we defined

$$F(\mathbf{q}) = \sum_j \langle 0|\mathrm{e}^{\mathrm{i}\mathbf{q}\cdot\mathbf{r}_j}|0\rangle \ . \tag{3.30}$$

In full generality, let the scattering object be a system with N electrons, with its ground state $|0\rangle$ described by an antisymmetric wavefunction $\Psi(\mathbf{r}_1, \mathbf{r}_2, ..., \mathbf{r}_N)$, from which an electron density is derived as:

$$\rho(\mathbf{r}) = N \int \mathrm{d}\mathbf{r}_2 \mathrm{d}\mathbf{r}_3 \ldots \mathrm{d}\mathbf{r}_N \, |\Psi(\mathbf{r}, \mathbf{r}_2, ..., \mathbf{r}_N)|^2 \ . \tag{3.31}$$

It is then easy to see that

$$F(\mathbf{q}) = \int \mathrm{d}\mathbf{r} \mathrm{e}^{\mathrm{i}\mathbf{q}\cdot\mathbf{r}} \rho(\mathbf{r}) \ , \tag{3.32}$$

so that the scattering cross section with scattering vector $\mathbf{q}$, (3.27), is proportional to the absolute square of the Fourier transform of the electron density

at momentum $\mathbf{q}$. A knowledge of the Fourier transform at all wavevectors is of course equivalent to the knowledge of the electron density. However, much to the crystallographers' sorrow, we see that x-ray scattering only delivers the *absolute value* of the Fourier transform. To reconstruct the electron density one should also know the *phase* of each reflection, which, however, is a much more elusive quantity.

3.3.2 Non-resonant Magnetic Scattering

We now resume the systematic exploration of (3.22), and, after dealing with the matrix elements of H_1', we consider the remaining terms, which contribute exclusively to *magnetic* scattering.

The next task is the evaluation of $\langle f|H_4'|i\rangle$. Remember that H_4' contains two terms, respectively proportional to $\partial\mathbf{A}/\partial t\cdot\mathbf{p}$ and to $\partial\mathbf{A}/\partial t\cdot(e/c)\mathbf{A}$. However, we shall soon verify that the second order perturbation on the first term produces a contribution to the cross section which is a factor $(\hbar\omega/mc^2)^2$ smaller than the first order contribution of the second, so we will drop it and retain the second term only. We must first of all determine an expression for the operator $\partial\mathbf{A}/\partial t$ from (3.12). For one mode only, i.e. omitting for simplicity the sum over all $\mathbf{k},\lambda$,

$$\partial\mathbf{A}/\partial t = \left(\frac{hc^2}{\Omega\,\omega_{\mathbf{k}}}\right)^{1/2}\Big[-\mathrm{i}\;\;\omega_{\mathbf{k}}\mathbf{e}_\lambda(\mathbf{k})a(\mathbf{k},\lambda)\mathrm{e}^{\mathrm{i}(\mathbf{k}\cdot\mathbf{r}-\omega_{\mathbf{k}}t)} + \mathrm{i}\;\;\omega_{\mathbf{k}}\mathbf{e}^*_\lambda(\mathbf{k})a^\dagger(\mathbf{k},\lambda)\mathrm{e}^{-\mathrm{i}(\mathbf{k}\cdot\mathbf{r}-\omega_{\mathbf{k}}t)}\Big]\ . \quad (3.33)$$

Inserting this expression, the H_4' matrix element is readily evaluated:

$$\langle f|H_4'|i\rangle = -\mathrm{i}\left(\frac{e^2}{mc^2}\right)\;\left(\frac{\hbar\omega_{\mathbf{k}}}{mc^2}\right)\left(\frac{hc^2}{\Omega\,\omega_{\mathbf{k}}}\right) \sum_j\langle 0|\mathrm{e}^{\mathrm{i}(\mathbf{k}-\mathbf{k}')\cdot\mathbf{r}_j}\mathbf{s}_j\cdot(\mathbf{e}'^*(\mathbf{k}')\times\mathbf{e}(\mathbf{k}))|0\rangle\ . \quad (3.34)$$

One therefore sees immediately that a term containing the spin operators, i.e. a genuine *magnetic* scattering term appears, and that its magnitude compared

to the Thompson term is reduced by the factor $(\hbar\omega_{\mathbf{k}}/mc^2)$. This is a small number, because typically in the x-ray region $\hbar\omega_{\mathbf{k}} \sim 10\,\mathrm{keV}$, while $mc^2 = 511\,\mathrm{keV}$. Additional magnetic information is hidden in the second term in (3.22), which we now proceed to evaluate. The accessible intermediate states have either no photons, or two photons, and their energy is

$$|n\rangle = |\Psi_n\,;0,0\rangle; E_n = E(\Psi_n) \tag{3.35}$$

$$|n\rangle = |\Psi_n\,;(\mathbf{e},\mathbf{k}),(\mathbf{e}',\mathbf{k}')\rangle; E_n = E(\Psi_n) + 2\hbar\omega_{\mathbf{k}}\,. \tag{3.36}$$

The first set of terms (let us call them terms (a)) is reached by the action of the annihilation part of the $\mathbf{A}$ operator on the initial state; the second (terms (b)) by the action of the creation operator part. There is also an additional, important difference between the two kinds of terms: in case (a) the energy denominator can vanish, and give rise to a resonance, when $E_0 - E_n + \hbar\omega_{\mathbf{k}} = 0$; in case (b) it cannot, because $E_0 - E(\Psi n) - \hbar\omega_{\mathbf{k}} < 0$ always. To prevent an unphysical divergence of the scattering cross section, we must take into account that the intermediate states $|n\rangle$ are not really stationary, but have a finite lifetime, which is represented by adding a small imaginary part to the eigenvalue, which becomes important only near the resonance condition; i.e. $E(\Psi_n)$ is replaced by $E(\Psi_n) - \mathrm{i}\Gamma_n/2$. We want to examine the non-resonant case first, i.e. the case in which $\hbar\omega_{\mathbf{k}} \gg E(\Psi_n) - E_0$ for all states, or, more precisely, for all states $|n\rangle$ which give an appreciable contribution to the sum in (3.22). Using the following simple identities for the energy denominators:

$$\begin{aligned}
\frac{1}{E_0 - E(\Psi_n) + \hbar\omega_{\mathbf{k}} + \mathrm{i}\Gamma_n/2} &= \frac{1}{\hbar\omega_{\mathbf{k}}} \\
&\quad + \frac{E(\Psi_n) - E_0 - \mathrm{i}\Gamma_n/2}{\hbar\omega_{\mathbf{k}}} \frac{1}{E_0 - E(\Psi_n) + \hbar\omega_{\mathbf{k}} + \mathrm{i}\Gamma_n/2} \\
\frac{1}{E_0 - E(\Psi_n) - \hbar\omega_{\mathbf{k}}} &= -\frac{1}{\hbar\omega_{\mathbf{k}}} + \frac{E_0 - E(\Psi_n)}{\hbar\omega_{\mathbf{k}}} \frac{1}{E_0 - E(\Psi_n) - \hbar\omega_{\mathbf{k}}}\,,
\end{aligned} \tag{3.37}$$

it is easy to see that in this case the denominators are well approximated by $\pm\hbar\omega_{\mathbf{k}}$. As a matter of fact, as discussed in a recent work [19], the same conclusions hold even in the case in which $\hbar\omega_{\mathbf{k}}$ is much bigger than $E(\Psi_n) - E_0$ for some n, and much smaller for others, i.e. as long as it is far away from possible resonances. Substituting (3.12) into $H_2' + H_3'$, and paying due attention

to the action of photon creation and annihilation operators on the two kinds of intermediate states, we find for type (a) intermediate states

$$\langle f|H_2'+H_3'|n\rangle\ \langle n|H_2'+H_3'|i\rangle = \left(\frac{hc^2}{\Omega\,\omega_{\mathbf{k}}}\right)\left(\frac{e}{mc}\right)^2 \langle 0|\sum_{j=1}^{N}\left[\mathbf{e}'^{*}\cdot\mathbf{p}_j - \mathrm{i}\hbar(\mathbf{k}'\times\mathbf{e}'^{*})\cdot\mathbf{s}_j\right]\mathrm{e}^{-\mathrm{i}\mathbf{k}'\cdot\mathbf{r}_j}|n\rangle$$
$$\langle n|\sum_{j'=1}^{N}\left[\mathbf{e}\cdot\mathbf{p}_{j'} + \mathrm{i}\hbar(\mathbf{k}\times\mathbf{e})\cdot\mathbf{s}_{j'}\right]\mathrm{e}^{\mathrm{i}\mathbf{k}\cdot\mathbf{r}_{j'}}|0\rangle \tag{3.38}$$

while for type (b) intermediate states we obtain an expression differing only in that the operators acting between $\langle 0|$ and $|n\rangle$ and between $\langle n|$ and $|0\rangle$ are interchanged. This, together with the fact that the energy denominators, in the non-resonant approximation defined above, are independent of $|n\rangle$ and change sign for the two types of intermediate states, and with the *closure* relationship

$$\sum_n |n\rangle\langle n| = \mathbf{1} \tag{3.39}$$

where $\mathbf{1}$ denotes the unit operator, allows to write the second term in (3.22) as the expectation value of a commutator

$$\sum_n \frac{\langle f|H_2'+H_3'|n\rangle\langle n|H_2'+H_3'|i\rangle}{E_0-E_n+\hbar\omega_{\mathbf{k}}} \simeq \left(\frac{hc^2}{\Omega\,\omega_{\mathbf{k}}}\right)\left(\frac{e}{mc}\right)^2 \langle 0|\left[C',C\right]|0\rangle\ , \tag{3.40}$$

where

$$C' = \left[\mathbf{e}'^{*}_{\lambda'}\cdot\mathbf{p}_j - \mathrm{i}\hbar(\mathbf{k}'\times\mathbf{e}'^{*}_{\lambda'})\cdot\mathbf{s}_j\right]\mathrm{e}^{-\mathrm{i}\mathbf{k}'\cdot\mathbf{r}_j} \tag{3.41}$$
$$C = \left[\mathbf{e}_\lambda\cdot\mathbf{p}_j + \mathrm{i}\hbar(\mathbf{k}\times\mathbf{e}_\lambda)\cdot\mathbf{s}_j\right]\mathrm{e}^{\mathrm{i}\mathbf{k}\cdot\mathbf{r}_j}\ . \tag{3.42}$$

To calculate the commutator is a tedious operation, but is easily performed remembering the basic commutation rules for components of positions, momenta, spin and arbitrary functions of them, referred to the same electron

$$\begin{aligned}\left[r_\alpha, p_\beta\right] &= i\hbar\delta_{\alpha\beta}\\ \left[p_\alpha, f(\mathbf{r})\right] &= -i\hbar\partial f/\partial r_\alpha\\ \left[s_\alpha, s_\beta\right] &= i\hbar\varepsilon_{\alpha\beta\gamma}s_\gamma\ .\end{aligned} \tag{3.43}$$

Here the antisymmetric tensor $\varepsilon_{\alpha\beta\gamma}$ was introduced, and it is worthwhile to remember the expression of the cross product of two vectors in terms of it (summation over repeated indices is implied)

$$(\mathbf{v}_1 \times \mathbf{v}_2)_\alpha = \varepsilon_{\alpha\beta\gamma} \mathrm{v}_{1\beta} \mathrm{v}_{2\gamma} \,. \tag{3.44}$$

By a careful use of these rules, of the transversality conditions, $\mathbf{e} \cdot \mathbf{k} = 0$ and of a simple vector identity

$$(\mathbf{A} \times \mathbf{B}) \cdot (\mathbf{C} \times \mathbf{D}) \equiv (\mathbf{A} \cdot \mathbf{C})(\mathbf{B} \cdot \mathbf{D}) - (\mathbf{A} \cdot \mathbf{D})(\mathbf{B} \cdot \mathbf{C}) \tag{3.45}$$

which is applied to the four vectors: $(\mathbf{k} - \mathbf{k}') \equiv \mathbf{q}$, $\mathbf{p}_j$, $\mathbf{e}'^*$, $\mathbf{e}$, the patient reader should obtain

$$\begin{aligned} \sum_n \frac{\langle f|H_2' + H_3'|n\rangle\langle n|H_2' + H_3'|i\rangle}{E_0 - E_n + \hbar\omega_{\mathbf{k}}} &= -\mathrm{i}\left(\frac{hc^2}{\Omega\,\omega_{\mathbf{k}}}\right)\left(\frac{e^2}{mc^2}\right)\frac{\hbar\omega_{\mathbf{k}}}{mc^2} \\ &\left[\langle 0|\sum_j \mathrm{e}^{\mathrm{i}\mathbf{q}\cdot\mathbf{r}_j}\frac{\mathrm{i}\mathbf{q}\times\mathbf{p}_j}{\hbar k^2}|0\rangle(\mathbf{e}'^*\times\mathbf{e}) + \langle 0|\sum_j \frac{\mathrm{e}^{\mathrm{i}\mathbf{q}\cdot\mathbf{r}_j}\mathbf{s}_j}{k^2}|0\rangle\right. \\ &\left.\left[(\mathbf{k}'\times\mathbf{e}'^*)(\mathbf{k}'\cdot\mathbf{e}) - (\mathbf{k}\times\mathbf{e})(\mathbf{k}\cdot\mathbf{e}'^*) - (\mathbf{k}'\times\mathbf{e}'^*)\times(\mathbf{k}\times\mathbf{e})\right]\right] . \end{aligned} \tag{3.46}$$

Now that we have the second order contribution of the $\mathbf{A}\cdot\mathbf{p}$ term in H_2', we can substantiate our claim that the contribution of the $\partial\mathbf{A}/\partial t \times \mathbf{p}$ term of H_4' is negligible. In fact, the magnitude of the latter contribution would be similar to that of the former, which we just evaluated, except for some different prefactors. On the one hand, the time derivative introduces a factor $\omega_{\mathbf{k}}$, on the other, the constant in front of H_4' introduces, with respect to H_2', another factor of $\hbar/2mc^2$, so that all in all an extra factor $\hbar\omega_{\mathbf{k}}/2mc^2$ is obtained. This shows that the matrix element of the first part of H_4' is reduced by $(\hbar\omega_{\mathbf{k}}/2mc^2)^2$ with respect to the Thomson term, and therefore is negligible with respect to the other magnetic scattering terms, which are reduced by $\hbar\omega_{\mathbf{k}}/2mc^2$.

Finally, by putting Eqs. (3.22), (3.23), (3.34), (3.46), and (3.25) together, we can complete the cross section expression of (3.27) to obtain

$$\frac{\mathrm{d}\sigma}{\mathrm{d}O'} = r_0^2 \left| \sum_j \langle 0|\mathrm{e}^{\mathrm{i}\mathbf{q}\cdot\mathbf{r}_j}|0\rangle (\mathbf{e}'^{*}\cdot\mathbf{e}) \right.$$
$$\left. -\mathrm{i}\frac{\hbar\omega_{\mathbf{k}}}{mc^2}\left[\langle 0|\sum_j \mathrm{e}^{\mathrm{i}\mathbf{q}\cdot\mathbf{r}_j}\frac{\mathrm{i}\mathbf{q}\times\mathbf{p}_j}{\hbar k^2}|0\rangle\cdot\mathbf{P}_L + \langle 0|\sum_j \mathrm{e}^{\mathrm{i}\mathbf{q}\cdot\mathbf{r}_j}\mathbf{s}_j|0\rangle\cdot\mathbf{P}_S\right]\right|^2 , \tag{3.47}$$

where we introduced the polarization factors

$$\mathbf{P}_L = (\mathbf{e}'^{*}\times\mathbf{e}) \tag{3.48}$$
$$\mathbf{P}_S = (\mathbf{e}'^{*}\times\mathbf{e}) + [(\hat{\mathbf{k}}'\times\mathbf{e}'^{*})(\hat{\mathbf{k}}'\cdot\mathbf{e}) - (\hat{\mathbf{k}}\times\mathbf{e})(\hat{\mathbf{k}}\cdot\mathbf{e}'^{*}) - (\hat{\mathbf{k}}'\times\mathbf{e}'^{*})\times(\hat{\mathbf{k}}\times\mathbf{e})] . \tag{3.49}$$

In this equation, $\hat{\mathbf{k}}$ denotes the unit vector parallel to $\mathbf{k}$, and the indices L and S where adopted for the two factors because the second one is attached to the term related to the spin moment, while the first pertains to a term which, as we shall show, is related to the *orbital* moment. In fact, after noting that $|\mathbf{q}| = 2|\mathbf{k}|\sin\theta$, where 2θ is the scattering angle, the relevant quantity can be transformed as follows

$$\begin{aligned}
\sum_j \mathrm{e}^{\mathrm{i}\mathbf{q}\cdot\mathbf{r}_j}\frac{\mathrm{i}\mathbf{q}\times\mathbf{p}_j}{\hbar k^2} &= \frac{\mathrm{i}}{\hbar q}(4\sin^2\theta)\sum_j \mathrm{e}^{\mathrm{i}\mathbf{q}\cdot\mathbf{r}_j}\hat{\mathbf{q}}\times\mathbf{p}_j \\
&= \frac{\mathrm{i}}{\hbar q}(4\sin^2\theta)\hat{\mathbf{q}}\times\int \mathrm{d}\mathbf{r}\mathrm{e}^{\mathrm{i}\mathbf{q}\cdot\mathbf{r}}\frac{1}{2}\sum_j[\mathbf{p}_j\delta(\mathbf{r}-\mathbf{r}_j)+\delta(\mathbf{r}-\mathbf{r}_j)\mathbf{p}_j] \\
&= \frac{-\mathrm{i}m}{e\hbar q}(4\sin^2\theta)\hat{\mathbf{q}}\times\int \mathrm{d}\mathbf{r}\mathrm{e}^{\mathrm{i}\mathbf{q}\cdot\mathbf{r}}\mathbf{j}(\mathbf{r}) \\
&= \frac{-\mathrm{i}m}{e\hbar q}(4\sin^2\theta)\hat{\mathbf{q}}\times\mathbf{j}(\mathbf{q})
\end{aligned} \tag{3.50}$$

where the electrical current density operator $\mathbf{j}(\mathbf{r}) = (-e/2m)\sum_j[\mathbf{p}_j\delta(\mathbf{r}-\mathbf{r}_j)+\delta(\mathbf{r}-\mathbf{r}_j)\mathbf{p}_j]$ has been expressed in terms of the momentum and the density of electrons multiplied in symmetrized form, because they do not commute.

This current density describes the *microscopic* currents associated to the motion of the electrons, not the *macroscopic* ones, which we can assume to vanish in our system in the absence of external perturbations (remember that all matrix elements in a perturbation calculation refer to the unperturbed system eigenstates). The vanishing of macroscopic currents means that the flux

across any surface S internal to the sample vanishes, i.e.

$$\int_S \mathbf{j}(\mathbf{r}) \cdot \mathbf{n}_S \mathrm{d}S = 0 \,, \tag{3.51}$$

which implies that the microscopic current is divergence-free, i.e. $\nabla \cdot \mathbf{j}(\mathbf{r}) = 0$, and can therefore be expressed as the curl of a vector field. We write this field so that

$$\mathbf{j}(\mathbf{r}) = c[\nabla \times \mathbf{M}_L(\mathbf{r})]. \tag{3.52}$$

For the purposes of our discussion, we identify $\mathbf{M}_L(\mathbf{r})$ with the density of orbital magnetization. Although a formal identification between operators is analytically involved [20, 21], one can satisfy himself of the plausibility of (3.52) by the classical description of magnetic fields in matter; Maxwell's equations for the fields $\mathbf{H}$ and $\mathbf{B} = \mathbf{H} + 4\pi\mathbf{M}$ (no spin magnetization exists in the classical description, so here $\mathbf{M}$ means $\mathbf{M}_L$) prescribe that the microscopic currents are related to the curl of $\mathbf{M}$ by (3.52) (see for example [22]).

Equation (3.52) implies that $\mathbf{j}(\mathbf{q}) = -\mathrm{i}c\mathbf{q} \times \mathbf{M}_L(\mathbf{q})$. Therefore

$$\sum_j \mathrm{e}^{\mathrm{i}\mathbf{q}\cdot\mathbf{r}_j} \frac{\mathrm{i}\mathbf{q} \times \mathbf{p}_j}{\hbar k^2} = \frac{mc}{e\hbar q^2} \mathbf{q} \times [\mathbf{M}_L(\mathbf{q}) \times \mathbf{q}] \,. \tag{3.53}$$

We are now ready to collect all the bits and pieces in a formula for the differential cross section

$$\frac{\mathrm{d}\sigma}{\mathrm{d}O'} = r_0^2 \left| \sum_j \langle 0|\mathrm{e}^{\mathrm{i}\mathbf{q}\cdot\mathbf{r}_j}|0\rangle (\mathbf{e}'^* \cdot \mathbf{e}) \right.$$
$$\left. -\mathrm{i}\frac{\hbar\omega_\mathbf{k}}{mc^2} \left[\frac{mc}{e\hbar} \langle 0|\hat{\mathbf{q}} \times [\mathbf{M}_L(\mathbf{q}) \times \hat{\mathbf{q}}]|0\rangle \cdot \mathbf{P}_L + \frac{mc}{e\hbar} \langle 0|\mathbf{M}_S(\mathbf{q})|0\rangle \cdot \mathbf{P}_S \right] \right|^2 . \tag{3.54}$$

where the polarization factor $\mathbf{P}_L$ was redefined to include the angular factor

$$\mathbf{P}_L = (\mathbf{e}'^* \times \mathbf{e}) 4 \sin^2 \theta \,, \tag{3.55}$$

and the Fourier transform of the *spin* magnetization density was introduced

$$\mathbf{M}_S(\mathbf{q}) = \frac{e\hbar}{mc} \sum_j \mathrm{e}^{\mathrm{i}\mathbf{q}\cdot\mathbf{r}_j} \mathbf{s}_j \,. \tag{3.56}$$

We are now ready to obtain from (3.54) the basic properties of nonresonant magnetic scattering. In a system with an ordered magnetic structure, e.g. an antiferromagnet, the densities of (orbital and spin) magnetization are periodic functions, with Fourier transforms which are non vanishing only for selected $\mathbf{q}$ values corresponding to this periodicity. Some of these vectors may possibly concide with reciprocal lattice vectors of the crystallographic structure, others will correspond to new reflections (*magnetic* reflections) with nonvanishing intensity below the Néel temperature, below which the antiferromagnetic order sets in.

As already noticed, the prefactor $\hbar\omega_{\mathbf{k}}/mc^2$ reduces the intensity of the magnetic terms considerably with respect to the Thompson one. To reinforce this, while all core and valence electrons contribute to Thomson scattering, only electrons in partially filled shells can contribute to magnetic scattering as the orbital and spin moments of filled shells add up to zero. Therefore, apart from the first pioneering experiments [4], the high intensity of synchrotron light sources is necessary for these experiments.

It is important to notice that $\mathbf{P}_L$ contains the factor $4\sin^2\theta$, and since $|\mathbf{q}| = 2|\mathbf{k}|\sin\theta$, for a given reflection, i.e. for a given $\mathbf{q}$, $\sin\theta$ is proportional to $1/\hbar\omega_{\mathbf{k}}$. Thus, the weight of the orbital part decreases at high photon energies, where spin scattering dominates the magnetic cross section; more generally, the $\omega_{\mathbf{k}}$ dependence of the orbital term is not only in the prefactor.

The different polarization factors $\mathbf{P}_L$, $\mathbf{P}_S$ and the well known polarization properties of synchrotron radiation allow to separate the spin and the orbital contributions to the magnetic moments by changing the experimental geometry. This is a much more direct approach to the separation of the two contributions than it is possible with neutron scattering. This method was applied to rare earth systems such as Ho [7], to actinide systems such as UAs [23, 24] and more recently to 3d antiferromagnets such as NiO [25]. Together with the higher momentum resolution allowed by well collimated synchrotron beams, this orbit and spin separation justifies the interest of x-ray scattering for some cases, in spite of the more widespread use of neutron scattering to determine magnetic structures.

A further important point to mention about the magnetic terms in (3.54) is the imaginary prefactor $-\mathrm{i}\hbar\omega_{\mathbf{k}}/mc^2$. This means that, upon taking the square modulus, no interference of Thomson and magnetic scattering terms occurs, unless the structure factors

$$\sum_j \langle 0|e^{\mathrm{i}\mathbf{q}\cdot\mathbf{r}_j}|0\rangle \tag{3.57}$$

are complex (which means that the crystallographic structure is non-centrosymmetric), or that the polarization vectors are complex (corresponding to non-linear, i.e. elliptic or circular polarization). In such cases one has interference terms, and these can be useful, for example, in detecting magnetic scattering in ferromagnets [26, 27]. Very recently a further application to the multiferroic system $TbMnO_3$ [19] used charge-magnetic interference scattering to detect small ionic displacements that contribute to the electrical polarization.

3.4 Resonant Scattering

We now abandon the assumption of the non-resonant limit and consider the case in which $E(\Psi_n) - E_0 \simeq \hbar\omega_{\mathbf{k}}$, at least for one excited state Ψ_n (normally, in a solid there will be a continuum of states satisfying this condition). Returning to the expressions of the matrix elements of $H_2' + H_3'$ as written in (3.38), we want first of all to prove that the contribution of H_2' is always much larger than that of H_3'. To establish this, we begin by remarking that the most important excited states which are resonant with x-ray photons are those in which a core electron in one of the atoms is promoted to an empty one-electron state above the highest occupied orbital. Arguing within an approximate scheme in which the states $|0\rangle$, $|n\rangle$ are reasonably well described by an antisymmetric product of one-electron states, then the matrix elements of the operators H_2' or H_3', which are sums of one-electron operators, can be written [28] in terms of an overlap integral over $N-1$ of the coordinates, multiplied by a one-electron matrix element, i.e

$$\begin{aligned}\langle n|H_2' + H_3'|i\rangle &= \left(\frac{hc^2}{\Omega\,\omega_{\mathbf{k}}}\right)^{1/2}\left(\frac{e}{mc}\right)\sum_{j=1}^{N}\langle n|\,[\mathbf{e}\cdot\mathbf{p}_j + \mathrm{i}\hbar(\mathbf{k}\times\mathbf{e})\cdot\mathbf{s}_j]\,\mathrm{e}^{\mathrm{i}\mathbf{k}\cdot\mathbf{r}_j}|0\rangle \\ &= \left(\frac{hc^2}{\Omega\,\omega_{\mathbf{k}}}\right)^{1/2}\left(\frac{e}{mc}\right)\prod_{j=1}^{N-1}\int \mathrm{d}\mathbf{r}_j\,\psi_{vj}^{(n)*}(\mathbf{r}_j)\,\psi_{vj}^{(0)}(\mathbf{r}_j) \\ &\times \int \mathrm{d}\mathbf{r}_N\,\psi_{vN}^{(n)*}(\mathbf{r}_N)\,[\mathbf{e}\cdot\mathbf{p}_N + \mathrm{i}\hbar(\mathbf{k}\times\mathbf{e})\cdot\mathbf{s}_N]\,\mathrm{e}^{\mathrm{i}\mathbf{k}\cdot\mathbf{r}_N}\,\psi_c^{(0)}(\mathbf{r}_N)\,,\end{aligned} \tag{3.58}$$

where ψ_v is a one-electron valence wavefunction, either for the ground or the n-th excited states and ψ_c a core wavefunction which is exponentially decreasing, outside an appropriate core radius r_c. We can then argue that the main contribution to the integral comes from this inner region; and one can see that inside this region $\mathbf{k}\cdot\mathbf{r}_j \ll 1$, for the values of $k = |\mathbf{k}|$ of interest here. This is because at the resonance condition

$$k = \omega/c = E/\hbar c \,, \tag{3.59}$$

where E is the difference of the core and valence energy, i.e. the core ionization energy. This energy is related to the radius of the core orbital by the approximate hydrogen-like relationship

$$E \simeq \hbar^2/2mr_c^2 \tag{3.60}$$

whence one finds $r_c \simeq \hbar/\sqrt{2mE}$ and therefore

$$kr_c \simeq \sqrt{E/2mc^2}\,. \tag{3.61}$$

The right hand side is always small for all core levels, because $2mc^2$ is about 1 MeV, while the deepest core level (1s in Uranium) has a binding energy of about 116 keV. So, in this most extreme case, $kr_c \simeq 0.34$, and is less for all other core levels. It is therefore legitimate, for $r \leq r_c$, to expand

$$\mathrm{e}^{\mathrm{i}\mathbf{k}\cdot\mathbf{r}_j} \sim 1 + \mathrm{i}\mathbf{k}\cdot\mathbf{r}_j - (\mathbf{k}\cdot\mathbf{r}_j)^2/2 + \ldots \tag{3.62}$$

and to observe that the terms of the series are rapidly decreasing with increasing order (which is referred to as the multipole order). We can then reach the proof of the statement that H_2' matrix elements dominate over those of H_3', i.e. that the first term in the last integral of (3.58) dominates over the second. The point is that for given $\psi_{vN}^{(n)}, \psi_c^{(0)}$, the lowest nonvanishing order in the series (3.62) for the integral of $\mathbf{p}_N$ is lower by one than the lowest nonvanishing order for the second term (which contains the spin, but no $\mathbf{r}_N$ operator). Remember indeed that the selection rules for atomic transitions are the same for $\mathbf{p}$ or for $\mathbf{r}$ matrix elements (a manifestation of the Wigner-Eckart theorem [29]), and since the H_3'-related operator contains the spin but neither $\mathbf{p}$ nor $\mathbf{r}$'s, it is necessary to have one more $\mathbf{r}$ (with respect to the first term) in order to have a nonvanishing integral, i.e. to go to the next order in $\mathbf{k}\cdot\mathbf{r}_N$.Therefore, near the resonance condition, the resonant terms dominate the cross section, and,

among these, only the H_2' matrix elements need to be retained. Equation (3.22) becomes

$$
\begin{aligned}
w &= \frac{2\pi}{\hbar}\left|\sum_n \frac{\langle f|H_2'|n\rangle\langle n|H_2'|i\rangle}{E_0 - E_n + \hbar\omega_{\mathbf{k}} + \mathrm{i}\Gamma_n/2}\right|^2 \delta(\hbar(\omega_{\mathbf{k}} - \omega_{\mathbf{k}'})) \\
&= \frac{2\pi}{\hbar}\left|\left(\frac{hc^2}{\Omega\omega_{\mathbf{k}}}\right)\left(\frac{e}{mc}\right)^2 \sum_n \frac{\langle 0|\sum_{j=1}^N \mathbf{e}'^* \cdot \mathbf{p}_j \mathrm{e}^{-\mathrm{i}\mathbf{k}'\cdot\mathbf{r}_j}|n\rangle\langle n|\sum_{j'=1}^N \mathbf{e}\cdot\mathbf{p}_{j'}\mathrm{e}^{\mathrm{i}\mathbf{k}\cdot\mathbf{r}_{j'}}|0\rangle}{E_0 - E(\Psi_n) + \hbar\omega_{\mathbf{k}} + \mathrm{i}\Gamma_n/2}\right|^2 \\
&\quad \times \delta(\hbar(\omega_{\mathbf{k}} - \omega_{\mathbf{k}'}))\,.
\end{aligned}
\tag{3.63}
$$

As a matter of fact, the above equation contains a contribution that was already taken into account in the non-resonant part; remember (3.37), where the first piece on the r.h.s. was included in the previous Section. Therefore, only the second addendum needs to be considered here and that means that in (3.63) we must replace

$$
\frac{1}{E_0 - E(\Psi_n) + \hbar\omega_{\mathbf{k}} + \mathrm{i}\Gamma_n/2} \tag{3.64}
$$

with:

$$
\frac{E(\Psi_n) - E_0 - \mathrm{i}\Gamma_n/2}{\hbar\omega_{\mathbf{k}}} \frac{1}{E_0 - E(\Psi_n) + \hbar\omega_{\mathbf{k}} + \mathrm{i}\Gamma_n/2}\,. \tag{3.65}
$$

3.4.1 Electric Dipole Approximation

Let us then look in detail into the relevant matrix elements. Consider

$$
\langle n|\mathbf{e}\cdot\mathbf{p}_j \mathrm{e}^{\mathrm{i}\mathbf{k}\cdot\mathbf{r}_j}|0\rangle \simeq \langle n|\mathbf{e}\cdot\mathbf{p}_j(1 + \mathrm{i}\mathbf{k}\cdot\mathbf{r}_j + \ldots)|0\rangle \tag{3.66}
$$

and, for a given $|n\rangle$, consider only the lowest order term for which the matrix element does not vanish. We established already that all higher order terms are negligible in comparison to it. The largest contributions come from those $|n\rangle$'s for which the first term provides a nonvanishing contribution, so that the exponential is simply replaced by 1. These states are said to be accessible by *electric dipole* transitions. In a full quantum electrodynamical formulation, one can see that electric dipole transitions are induced by photons with a total

angular momentum of 1. The name "electric dipole" comes from the fact that in a non-relativistic theory, neglecting the spin-orbit interaction altogether, so that $H_{el} = \sum_j (\mathbf{p}_j^2/2m + V(\mathbf{r}_j))$, one can write

$$\begin{aligned} \langle n|\mathbf{e}\cdot\mathbf{p}_j|0\rangle &= m\langle n|\mathbf{e}\cdot\dot{\mathbf{r}}_j|0\rangle \\ &= \frac{-\mathrm{i}m}{\hbar}\langle n|\mathbf{e}\cdot[\mathbf{r}_j, H_{el}]|0\rangle \\ &= \frac{\mathrm{i}m}{\hbar}[E(\Psi_n) - E(0)]\langle n|\mathbf{e}\cdot\mathbf{r}_j|0\rangle \ . \end{aligned} \tag{3.67}$$

In view of this, and neglecting $\mathrm{i}\Gamma_n/2$ in the numerator of (3.65), the sum over intermediate states in (3.63) becomes

$$\frac{m^2}{\hbar^2}\sum_n \frac{(E(\Psi_n) - E(0))^3}{\hbar\omega_{\mathbf{k}}} \frac{\langle 0|\mathbf{e}'^*\cdot\mathbf{R}|n\rangle\langle n|\mathbf{e}\cdot\mathbf{R}|0\rangle}{E(\Psi_n) - E(0) + \hbar\omega_{\mathbf{k}} + \mathrm{i}\Gamma_n/2} \ , \tag{3.68}$$

where we defined

$$\mathbf{R} = \sum_j \mathbf{r}_j \ . \tag{3.69}$$

In order to make progress and to make contact with the literature [30], we express all vectors in terms of their *spherical* components, i.e. we define

$$R_0 = \mathrm{i}R_z, R_{\pm 1} = (\mp\mathrm{i}/\sqrt{2})(R_x \pm \mathrm{i}R_y) \ . \tag{3.70}$$

The definitions of the $0, \pm 1$ components apply to any vector, e.g. to the polarization $\mathbf{e}$ as well, and they are clearly inspired from the definition of the spherical harmonics for $l = 1$,

$$Y_{1,0} = \mathrm{i}\sqrt{\frac{3}{4\pi}}(z/r), Y_{1,\pm 1} = \mp\mathrm{i}\sqrt{\frac{3}{8\pi}}\left(\frac{x \pm \mathrm{i}y}{r}\right) , \tag{3.71}$$

where we adopted the convention for the phases given in [41]. It is easily verified that the scalar product becomes

$$\mathbf{e}\cdot\mathbf{R} = \sum_{m=-1}^{1} (-1)^{m-1} e_m R_{-m} \ . \tag{3.72}$$

It is then easy to see that

$$\langle 0|\mathbf{e}'^{*}\cdot\mathbf{R}|n\rangle\langle n|\mathbf{e}\cdot\mathbf{R}|0\rangle = \sum_{m,m'}(-1)^{m+m'}e'^{*}_{m}e_{m'}\langle 0|R_{-m}|n\rangle\langle n|R_{-m'}|0\rangle\ . \quad (3.73)$$

To simplify this expresssion further, one must take advantage of the symmetry of the physical system. The simplest case corresponds of course to the highest symmetry, i.e. the spherical symmetry of isolated atoms. Then, the eigenstates $|0\rangle$ and $|n\rangle$ are eigenstates of the angular momentum and of its z-component, and this implies that the sum is restricted to $m=-m'$, because the angular momentum selection rules say that, for the matrix elements

$$\begin{aligned}\langle 0|R_{-m}|n\rangle \neq 0 &\Rightarrow -m_0 - m + m_n = 0\ ,\\ \langle n|R_{-m'}|0\rangle \neq 0 &\Rightarrow -m_n - m' + m_0 = 0\ ,\\ &\Rightarrow m = -m'\end{aligned} \quad (3.74)$$

The sum in (3.73) is then simplified and it is worth noticing that

$$\begin{aligned}\langle 0|R_0|n\rangle\langle n|R_0|0\rangle &= -|\langle n|R_0|0\rangle|^2\\ \langle 0|R_{-1}|n\rangle\langle n|R_1|0\rangle &= |\langle n|R_1|0\rangle|^2\\ \langle 0|R_1|n\rangle\langle n|R_{-1}|0\rangle &= |\langle n|R_{-1}|0\rangle|^2\ .\end{aligned} \quad (3.75)$$

The first relationship may look surprising, but remember that, because of the factor i in the definition, coming from the chosen convention on the phases of the spherical harmonics, R_0 is an antihermitian operator. Another consequence of that is the fact that if

$$e_0 = \mathrm{i}e_z \quad (3.76)$$

it is also

$$e^{*}_0 = \mathrm{i}e^{*}_z\ , \quad (3.77)$$

i.e. the spherical component 0 of the complex conjugate need not be the complex conjugate of the 0 component. With the help of all of the above we can write

$$\begin{aligned}\langle 0|\mathbf{e}'^{*}\cdot\mathbf{R}|n\rangle\langle n|\mathbf{e}\cdot\mathbf{R}|0\rangle = -e'^{*}_0 e_0|\langle n|R_0|0\rangle|^2 + e'^{*}_1 e_{-1}|\langle n|R_1|0\rangle|^2\\ + e'^{*}_{-1}e_1|\langle n|R_{-1}|0\rangle|^2\ .\end{aligned} \quad (3.78)$$

Going back to cartesian coordinates for the polarization vectors, it is possible, with a bit of algebra to recast this expression in the following form

$$e_z'^* e_z |\langle n|R_0|0\rangle|^2 + \frac{1}{2}[e_x'^* e_x + e_y'^* e_y](|\langle n|R_1|0\rangle|^2 + |\langle n|R_{-1}|0\rangle|^2) - \frac{\mathrm{i}}{2}[e_x'^* e_y - e_x'^* e_y](|\langle n|R_1|0\rangle|^2 - |\langle n|R_{-1}|0\rangle|^2)\,. \quad (3.79)$$

We define

$$F^e_{1,m} = m_e \sum_n \frac{[E(\Psi_n) - E(0)]^3}{\hbar^3 \omega_{\mathbf{k}}} \frac{|\langle n|R_m|0\rangle|^2}{E(0) - E(\Psi_n) + \hbar\omega_{\mathbf{k}} + \mathrm{i}\Gamma_n/2}\,, \quad (3.80)$$

where the label e and 1 on F remind us that this refers to electric (e) dipole (l=1) contributions, and where we introduced the symbol m_e for the electron mass, to avoid any confusion with the index m, which runs over $0, \pm 1$; reinserting the prefactors present in (3.63) and those allowing to relate w to $\mathrm{d}\sigma/\mathrm{d}O'$, see (3.25), we finally obtain

$$\frac{\mathrm{d}\sigma}{\mathrm{d}O'} = |f_{res}|^2\,, \quad (3.81)$$

where f_{res} is the resonant scattering *amplitude*, given by

$$f_{res} = -r_0 \left[\frac{1}{2}\mathbf{e}'^* \cdot \mathbf{e}(F^e_{1,1} + F^e_{1,-1}) - \frac{\mathrm{i}}{2}(\mathbf{e}'^* \times \mathbf{e}) \cdot \hat{\mathbf{z}}(F^e_{1,1} - F^e_{1,-1}) + (\mathbf{e}'^* \cdot \hat{\mathbf{z}})(\mathbf{e}_\lambda \cdot \hat{\mathbf{z}})(F^e_{1,0} - \frac{1}{2}F^e_{1,1} - \frac{1}{2}F^e_{1,-1})\right]\,, \quad (3.82)$$

where the unit vector in the z direction (i.e. in the axis of quantization of the angular momenta), $\hat{\mathbf{z}}$, was introduced. Equation (3.82) was derived in [30] using the relativistic formalism of vector spherical harmonics, soon after the discovery of resonant magnetic scattering by Gibbs et al. [7]. Let us pause briefly to analyze some of the consequences of the results derived so far. The three terms in (3.82) describe resonant or anomalous scattering in general, and are rather different in nature. The first is proportional to $(F^e_{1,1} + F^e_{1,-1})$ and is therefore always present. The second is a genuinely magnetic term, because it originates from the difference between the 1 and the -1 components, which arise only in the presence of a magnetic *preference* for one sense of rotation around the quantization axis. Finally, the last term is nonvanishing for any anisotropic system, a system with a preferential axis, identified either by a crystal anisotropy or by a magnetic moment, which translates into a different occupation for one-electron orbitals with different orientation. The difference

in occupation translates into a difference in the value of individual $F^e_{1,m}$, which is strongly influenced (see (3.80)) by the availability of states with the appropriate symmetry, at or near the resonance energy, suitable to play the role of intermediate states.As an example, consider first an isotropic or cubic environment for an atom. In this case, $F^e_{1,m}$ is the same for all m 's and can be called simply F^e_1. Then

$$f_{res} = -r_0 \frac{1}{2} (\mathbf{e}'^* \cdot \mathbf{e})(2F^e_1) \; . \tag{3.83}$$

We can represent the polarization dependence by evaluating the above equation for the various cases arising when $\mathbf{e}', \mathbf{e}$ take all possible σ and π orientations and writing the result in terms of a *tensor* scattering amplitude [5, 6]

$$f_{res} = \mathbf{e}'^* \hat{f}_{res} \mathbf{e}. \tag{3.84}$$

The $\hat{f}_{res}$ tensor is represented in matrix form as

$$\hat{f}_{res} = -r_0 F^e_1 \begin{pmatrix} 1 & 0 \\ 0 & \cos(2\theta) \end{pmatrix} \tag{3.85}$$

where the rows correspond to $\mathbf{e}' = \sigma$ or π' respectively, and the columns to $\mathbf{e} = \sigma$ or π. Consider next the case in which the atom is in a orthorombically distorted environment, in which z is inequivalent to the x, y directions, so that $2F^e_{1,0} - (F^e_{1,1} + F^e_{1,-1}) \equiv F^e_{an} \neq 0$. For a geometry in which the scattering plane is the x, y plane, and the x axis is chosen parallel to the scattering vector $\mathbf{q}$ (see Fig. 3.2a), corresponding to the experimental situation sketched in Fig 3.2b, where the crystal surface and the directions of the incoming and scattered beams are visible, we find that

$$\begin{aligned} \hat{f}_{res} = -\frac{r_0}{2} \; & \left[(F^e_{1,1} + F^e_{1,-1}) \begin{pmatrix} 1 & 0 \\ 0 & \cos(2\theta) \end{pmatrix} \right. \\ & \left. + [2F^e_{1,0} - (F^e_{1,1} + F^e_{1,-1})] \begin{pmatrix} 1 & 0 \\ 0 & 0 \end{pmatrix} \right] \; . \end{aligned} \tag{3.86}$$

If the crystal in Fig. 3.2b is rotated by an angle ϕ about the x axis, that is around the scattering vector $\mathbf{q}$ (*azimuthal scan*), while leaving the scattering geometry, i.e. the directions of $\mathbf{k}$ and $\mathbf{k}'$ unchanged (it is not easy to rotate a synchrotron !), the molecular preferred axis is rotated by an angle ϕ as shown by the dashed line in Fig. 3.2a. The scattering amplitude becomes

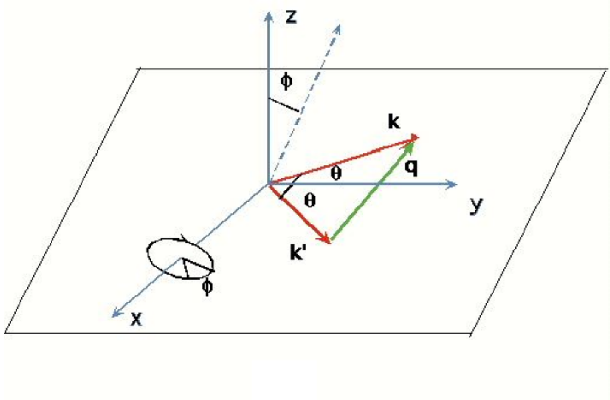

(a)

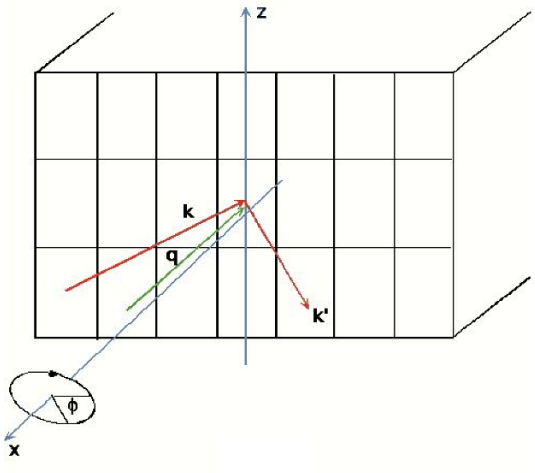

(b)

Fig. 3.2 **a** Sketch of the scattering plane with the scattering angle 2θ, and the azimuthal angle ϕ, describing rotations about the scattering vector **q**; **b** A sketch of the actual experimental geometry corresponding to **a**.

$$\hat{f}_{res} = -\ \frac{r_0}{2}\left[(F^e_{1,1}+F^e_{1,-1})\begin{pmatrix}1 & 0\\ 0 & \cos(2\theta)\end{pmatrix}\right.$$
$$\left.+\left[2F^e_{1,0}-(F^e_{1,1}+F^e_{1,-1})\right]\begin{pmatrix}\cos^2\phi & -\frac{1}{2}\sin\theta\sin(2\phi)\\ \frac{1}{2}\sin\theta\sin(2\phi) & \sin^2\theta\sin^2\phi\end{pmatrix}\right]. \tag{3.87}$$

This simple example is sufficient to demonstrate how, in the resonant regime, the charge-related scattering may display features such as non-diagonal tensor properties with respect to the polarization of the incoming and scattered beams, and the azimuthal angle dependence, which are absent for the non-resonant Thompson scattering. The tensor nature of the resonant scattering amplitude, which was traditionally written as a single complex number with the notation $f' + \mathrm{i}f''$ has become increasingly important in recent years. As we mentioned in passing, (3.82) also contains magnetic scattering components, as first observed in [7]. The reader may wonder where, in the formulation in terms of electric multipole transitions between the ground and the intermediate states, the sensitivity to magnetic moments may come from. This is a subtle but very important point. In fact, no spin operators appear in the resulting expressions. The sensitivity to magnetic moments comes from the combined action of two ingredients: the Pauli principle and the spin-orbit interaction. The Pauli principle enters because of the already mentioned strong dependence of the scattering amplitude on the availability of states, at or near the resonance energy, suitable to play the role of intermediate states. In a one-electron language, if states with a given spin are predominantly occupied, it is mostly states with the opposite spin which are available to be virtually filled by the promotion of a core electron in the first part of the resonant scattering process. Since the spin is conserved in the optical transition, it is mostly electrons with the same spin as the predominantly available intermediate states which are virtually excited. In the case of all core levels with $l \neq 0$, the spin-orbit interaction is nonvanishing and much larger than in the valence states (for example, the L_2 and L_3 core levels of the rare earths are separated by many hundreds of eV). In a given spin-orbit partner, states with spin up or down have a different orbital character (think for example of $L_{2,3}$ levels, where typically $(p_x + \mathrm{i}p_y)|s_z = -1/2\rangle$ states are, because of the spin-orbit interaction, linearly superposed to $p_z|s_z = +1/2\rangle$ states). Because of the selection rules to the available intermediate states, this orbital polarization translates into a difference between the transition rates for different m's, therefore in an imbalance among the corresponding $F^e_{1,m}$, which is in turn responsible for a nonvanishing magnetic scattering amplitude.The above qualitative description of resonant magnetic scattering must be modified for s core levels, which have a vanishing spin-orbit interaction. In this case, resonant magnetic scattering is also observable [**?**], but it must be ascribed to the much weaker spin-orbit interaction of the valence states, which acts to polarize the final states of given spin and to reproduce the same mechanism. We have so far considered the scattering amplitude for a single atom or ion. In order to consider a lattice of

atoms, we must perform a coherent superposition of the scattering amplitudes from all atoms, in which the amplitude from the atom sitting at $\mathbf{R}_{l,m,n}$ acquires a phase factor $e^{i\mathbf{q}\cdot\mathbf{R}_{l,m,n}}$. If the system displays crystallographic or magnetic order, such that the direction of the preferred axis $\mathbf{z}$ changes from atom to atom, this must also be taken into account, as it will affect the value of the scattering amplitude for given polarization, as visible from (3.82). In order to illustrate the consequences of these facts, let us consider the case of a basal-plane antiferromagnet, e.g. the rare earths Ho, Tb, and Dy, sketched in Fig. 3.3. All spins are ferromagnetically aligned in the planes, but their direction rotates by a fixed angle from one plane to the next. It was indeed in Ho, which displays a spiral antiferromagnetic phase in the $20\text{K} \leq T \leq 131\text{K}$ temperature range that the first observations of resonant magnetic scattering took place [7].

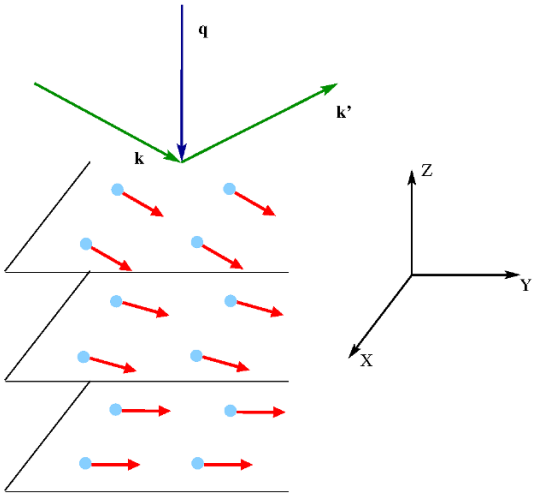

Fig. 3.3 Schematic view of a basal-plane antiferromagnet and of the scattering geometry.

With reference to Fig. 3.3, let us label the atomic positions by a single index $\mathbf{R}_n$, for simplicity, and let us identify the spin direction of the ion n with $\hat{\mathbf{z}}_n$. It is apparent that, with respect to the chosen x, y, z coordinate frame, this vector is given by

$$\hat{\mathbf{z}}_n = (\sin(\tau \cdot \mathbf{R}_n), \cos(\tau \cdot \mathbf{R}_n), 0) \ , \tag{3.88}$$

where τ is the wavevector associated to the spiral pitch, and if we define for short $(F^e_{1,1}+F^e_{1,-1}) \equiv F_0$, $(F^e_{1,1}-F^e_{1,-1}) \equiv F_1$ and $[2F^e_{1,0}-(F^e_{1,1}+F^e_{1,-1})] \equiv F_2$, we are ready to write the scattering amplitude

$$f = \sum_n \mathrm{e}^{\mathrm{i}\mathbf{q}\cdot\mathbf{R}_n} f_{res}(\mathbf{R}_n, \hat{\mathbf{z}}_n) \; . \tag{3.89}$$

For the case $\sigma \rightarrow \sigma'$, the F_1 component does not contribute, and we are left with

$$f = -\frac{r_0}{2} \sum_n \mathrm{e}^{\mathrm{i}\mathbf{q}\cdot\mathbf{R}_n} [F_0 + F_2 \sin^2(\tau \cdot \mathbf{R}_n)] \; . \tag{3.90}$$

Expressing the $\sin^2$ in terms of exponentials, a bit of algebra gives

$$f = -\frac{r_0}{2} \sum_{h,k,l} [(F_0 + \frac{1}{2}F_2)\delta(\mathbf{q} - \mathbf{G}_{hkl}) - \frac{1}{4}F_2\delta(\mathbf{q} - \mathbf{G}_{hkl} \pm 2\tau)] \; . \tag{3.91}$$

We thus see that the resonant scattering occurs at the crystallographic reciprocal lattice vectors $\mathbf{q} = \mathbf{G}_{hkl}$, with a charge and a magnetic component (F_0 and F_2 respectively) and also at the *second harmonic* magnetic satellite vectors, displaced by $\pm 2\tau$ from each crystallographic reflection. A complete analysis for different polarizations and different satellite is possible using the formula by Hannon and Trammel [7, 30].

The remarkable success of the formalism we just discussed deserves a moment of reflection. In fact, the derivation of the Hannon-Trammel formula rested on the assumption of spherical symmetry of the atoms (see 3.74, where this assumption was explicitly used). Later, we introduced the possibility for the atom to be e.g. in a tetragonal environment, or to have a preferential magnetic orientation, without affecting, however, the basic selection rules deriving from spherical symmetry. In other terms, the rotational character of the wavefunctions was assumed to be intact, external influences being limited to (gently) removing the degeneracies and thus affecting the occupation of the different atomic states. This is a typical situation for *weakly perturbed* atomic states. The reason why the Hannon-Trammel formula is so successful for core resonances of magnetic systems, is that core levels are of course very atomic-like, and that the intermediate states of highest interest in magnetic investigations are those of $d-$ or $f-$ electrons, that are to a larger or lesser extent localized, and preserve a pronounced atomic character.

The example presented so far corresponds to relatively "hard" x-rays, with wavelengths in the range of order ~ 0.1 nm. This wavelength corresponds to

the typical order of interatomic distances and is therefore extremely suitable to investigate crystallographic or, possibly, magnetic structures, with periods of the same order. There is however nothing, in our derivations, which would not equally well apply to softer x-rays, and allow the investigation of structures with longer periods. Modern technology for the growth of nanostructures, and in particular of multilayers, has led to the fabrication of structures with characteristic periods in the order of 1 nm or more, which are therefore accessible to investigation by soft x-rays. But also nature provides for systems with order parameters with periods compatible with soft x-ray wavelengths. As pointed out in [32], orbital order in $La_{0.5}Sr_{1.5}MnO_4$ as well as in other manganites, is within reach of the Mn L-edge resonances, with the advantage that L_2 and L_3 resonances access the $3d$ orbitals in the intermediate states, and should therefore be very sensitive to their orbital and magnetic order. This was confirmed by experiments [33, 34, 35, 36, 37] exploring the orbital and magnetic order reflections; comparing their dependence on the incoming photon energy with theoretical calculations within an atomic multiplet scheme in a crystal field [38, 39], it turns out that scattering at the L_2 resonance is very sensitive to orbital order, while the intensity at the L_3 resonance is mostly induced by the Jahn-Teller distortion. This developed in a very intensive field of investigation of strongly correlated systems, and in-vacuum diffractometers for soft x-ray scattering are nowadays quite common around synchrotron sources.

3.4.2 Electric Quadrupole Transitions

Our goal is now to derive expressions for electric quadrupole transitions, i.e. for the case in which the resonant transitions are allowed only when the second term in the expansion of $e^{i\mathbf{k}\cdot\mathbf{r}} \simeq 1 + i\mathbf{k}\cdot\mathbf{r} + \ldots$ is retained. The important matrix elements in (3.63) reduces to

$$\langle n|\mathbf{e}_\lambda \cdot \mathbf{p}_j e^{i\mathbf{k}\cdot\mathbf{r}_j}|0\rangle \simeq \langle n|(\mathbf{e}_\lambda \cdot \mathbf{p}_j)(i\mathbf{k}\cdot\mathbf{r}_j) + \ldots|0\rangle \; . \tag{3.92}$$

Using the same approximate trick as in (3.67), the operator $\mathbf{p}_j$ can be expressed in terms of the commutator of $\mathbf{r}_j$ and H, and allowing H to act on $\langle n|$ and on $|0\rangle$ by moving it next to them using the commutation rules one finds

$$\langle n|(\mathbf{e}_\lambda \cdot \mathbf{p}_j)(\mathbf{k}\cdot\mathbf{r}_j)|0\rangle = -\mathrm{i}\frac{m}{\hbar}(E(0)-E(\Psi_n)) \;\; \langle n|(\mathbf{e}_\lambda \cdot \mathbf{r}_j)(\mathbf{k}\cdot\mathbf{r}_j)|0\rangle - \langle n|(\mathbf{e}_\lambda \cdot \mathbf{r}_j)(\mathbf{k}\cdot\mathbf{p}_j)|0\rangle \; . \tag{3.93}$$

Adding to both sides of this equation the same quantity, namely the left hand side, it becomes

$$2\langle n|(\mathbf{e}_\lambda \cdot \mathbf{p}_j)(\mathbf{k}\cdot\mathbf{r}_j)|0\rangle = -\mathrm{i}\frac{m}{\hbar}(E(0)-E(\Psi_n))\langle n|(\mathbf{e}_\lambda \cdot \mathbf{r}_j)(\mathbf{k}\cdot\mathbf{r}_j)|0\rangle + \langle n|(\mathbf{e}_\lambda \cdot \mathbf{p}_j)(\mathbf{k}\cdot\mathbf{r}_j)|0\rangle - \langle n|(\mathbf{e}_\lambda \cdot \mathbf{r}_j)(\mathbf{k}\cdot\mathbf{p}_j)|0\rangle \; . \tag{3.94}$$

Application to the last two terms of this equation of the vector identity (3.45) finally yields

$$\langle n|(\mathbf{e}_\lambda \cdot \mathbf{p}_j)(\mathbf{k}\cdot\mathbf{r}_j)|0\rangle = -\mathrm{i}\frac{m}{2\hbar}(E(0)-E(\Psi_n))\langle n|(\mathbf{e}_\lambda \cdot \mathbf{r}_j)(\mathbf{k}\cdot\mathbf{r}_j)|0\rangle + \frac{1}{2}(\mathbf{k}\times\mathbf{e}_\lambda)\langle n|\mathbf{r}_j\times\mathbf{p}_j|0\rangle \; . \tag{3.95}$$

Now it is easy to recognize in the last term the matrix element between the ground and intermediate states of the orbital angular momentum operator (or, in the language of multipole expansions, the matrix element corresponding to *magnetic dipole* transitions). For the transitions resonant with x-ray photons, which involve promotion of a core electron above the Fermi level, the magnetic dipole matrix elements vanish, because of the orthogonality of the *radial* part of core and valence states, as the angular momentum operators only affect the *angular* part of the wavefunctions. Summarizing, one can conclude that the second term in the expansion of the plane-wave exponential produces terms with the matrix elements of products of two components of the position operator $\mathbf{r}_j$ (*electric quadrupole* terms) plus magnetic dipole terms, which are irrelevant in the x-ray range. In analogy to the discussion following (3.68), define the rank 2 quadrupole moment tensor, with cartesian components ($\alpha,\beta = x,y,z$)

$$Q^{(2)}_{\alpha\beta} = R_\alpha R_\beta - \frac{1}{3}R^2\delta_{\alpha\beta} \; . \tag{3.96}$$

Its spherical components are

$$Q_m^{(2)} = \sqrt{\frac{4\pi}{5}} R^2 Y_m^2(\theta,\phi) \tag{3.97}$$

with $m = -2,-1,...,2$. All matrix elements of importance for quadrupole resonant scattering can be written in terms of the quantities

$$F_{2,m}^e = \frac{m_e}{\hbar^3 c^2} \sum_n [E(\Psi_n) - E(0)]^3 \omega_{\mathbf{k}} \frac{|\langle n|Q_m^{(2)}|0\rangle|^2}{E(0) - E(\Psi_n) + \hbar\omega_{\mathbf{k}} + i\Gamma_n/2} \,. \tag{3.98}$$

The scattering amplitude at the quadrupole level comprises 13 different terms (see e.g. [40]) one of which contains no dependence on $\hat{\mathbf{z}}_n$ and is written as

$$-\frac{r_0}{3}(\mathbf{e}'^*_{\lambda'} \cdot \mathbf{e}_\lambda)(\mathbf{k}' \cdot \mathbf{k})[F_{2,2}^e + F_{2,-2}^e] \,. \tag{3.99}$$

There are then 2 terms in which there is a linear dependence on $\hat{\mathbf{z}}_n$

$$-\frac{r_0}{3}[(\mathbf{k}' \cdot \mathbf{k})(\mathbf{e}'^*_{\lambda'} \times \mathbf{e}_\lambda) \cdot \hat{\mathbf{z}}_n + (\mathbf{e}'^*_{\lambda'} \cdot \mathbf{e}_\lambda)(\mathbf{k}' \times \mathbf{k}) \cdot \hat{\mathbf{z}}_n][F_{2,2}^e - F_{2,-2}^e] \,. \tag{3.100}$$

The other terms have 2, or 3 or 4 factors of $\hat{\mathbf{z}}$ and they give rise to reflections up to the fourth harmonic magnetic satellites, in agreement with the observations of [7] in Ho.

3.5 Absorption Spectroscopies

It is actually possible to discuss the absorption spectroscopies very efficiently, by using the variety of results obtained so far, if we remember the general connection between the photon scattering amplitude and the optical absorption spectrum of the system by the *Optical Theorem* [41] of general scattering theory. This theorem states that

$$\frac{k}{4\pi}\sigma_t = \mathrm{Im}\, f(0) \,, \tag{3.101}$$

where σ_t is the total cross section, comprising all elastic and inelastic processes, and f(0) is the *forward* scattering amplitude, i.e. the amplitude of scattering for $\mathbf{k}' = \mathbf{k}$ and $\mathbf{e}' = \mathbf{e}$, which can be easily obtained as a special case of the general expressions derived in the preceding Sections. In the case of photons in the energy range of interest here, the total cross section σ_t for the

interaction with electronic matter is dominated by photoelectric absorption processes, all other processes having cross sections that are smaller by a few orders of magnitude (see [42] for typical examples). Therefore, the left-hand side of (3.101) reproduces, with good approximation, the absorption spectrum.

In the traditional crystallographic notation in which the atomic scattering amplitude is a simple scalar quantity, written as the sum of the non-resonant amplitude f_0 and the real and imaginary resonant parts $f' + \mathrm{i}f''$, the optical theorem identifies f'' as proportional to the optical absorption spectrum, because, in the case of forward scattering, $\mathbf{k} - \mathbf{k}' = 0$, f_0 is purely real. In our formulation, we can write $f = f_{0c} + f_{0m} + f_{res}$ and, for the pure real character of the charge (or Thomson) part f_{0c}, see (3.23); and the magnetic part, f_{0m}, (3.47) , it vanishes altogether as the orbital term is zero for $\mathbf{q} = 0$ and $\mathbf{P}_S$ is also zero under forward conditions (this requires a bit of vector algebra). So, in conclusion, the only contribution comes from the resonant amplitude. This result has general validity. However, in the spirit of concentrating on the conditions that are met in the investigation of magnetic systems, we shall make use of the expressions derived in the previous section under the assumptions underlying the results of Hannon and Trammel, that, as discussed there, are well suited for this case.

Considering the application of the theorem to the expression derived at the dipole level, (3.82), which provides the most intense resonances, gives the following expression [43] for the absorption cross section

$$\begin{aligned}\sigma_t = -\lambda r_0[\mathrm{Im}(F^e_{1,1} + F^e_{1,-1}) - \mathrm{i}(\mathbf{e}^* \times \mathbf{e}) \cdot \hat{\mathbf{z}}\,\mathrm{Im}(F^e_{1,1} - F^e_{1,-1}) \\ + |\mathbf{e} \cdot \hat{\mathbf{z}}|^2\,\mathrm{Im}(2F^e_{1,0} - F^e_{1,1} - F^e_{1,-1})] \end{aligned} \tag{3.102}$$

where $\lambda = 2\pi/k$ is the photon wavelength.Notice that the expression $(\mathbf{e}^* \times \mathbf{e})$ vanishes for a real polarization vector (i.e. for linear polarization) and is purely imaginary in other cases.Therefore the imaginary part of the expressions (3.80) is determined by

$$\begin{aligned}\mathrm{Im}\,F^e_{1,m} &= m_e \sum_n \frac{[E(\Psi_n) - E(0)]^3}{\hbar^3 \omega_{\mathbf{k}}} \frac{-\Gamma_n/2}{(E(0) - E(\Psi_n) + \hbar\omega_{\mathbf{k}})^2 + (\Gamma_n/2)^2} \\ \mathrm{Im}\,F^e_{1,m} &\equiv -w^e_{1,m} \end{aligned} \tag{3.103}$$

so that the absorption spectrum is described as a sum of Lorentzians, $w^e_{1,m}$, each with the broadening parameter determined by the inverse lifetime of the corresponding excited state.

In terms of this quantity the absorption cross section is written

$$\sigma_t = \lambda r_0[(w^e_{1,1} + w^e_{1,-1}) - \mathrm{i}(\mathbf{e}^* \times \mathbf{e}) \cdot \hat{\mathbf{z}}(w^e_{1,1} - w^e_{1,-1}) + |\mathbf{e} \cdot \hat{\mathbf{z}}|^2(2w^e_{1,0} - w^e_{1,1} - w^e_{1,-1})] \,. \quad (3.104)$$

and this expression is very convenient because it explicitly shows the dependence on photon polarization and is therefore immediately applicable to describing various forms of dichroism. As a first example, consider linear polarization; in the case $\mathbf{e} \parallel \hat{\mathbf{z}}$ or $\mathbf{e} \perp \hat{\mathbf{z}}$ one finds respectively

$$\sigma_{\parallel} = 2\lambda r_0 w^e_{1,0} \quad (3.105)$$

$$\sigma_{\perp} = \lambda r_0 \left(w^e_{1,1} - w^e_{1,-1}\right) \quad (3.106)$$

so that linear dichroism is expressed as

$$\sigma_{\parallel} - \sigma_{\perp} = \lambda r_0 \left(2w^e_{1,0} - w^e_{1,1} - w^e_{1,-1}\right) \,. \quad (3.107)$$

In the same way we can derive general expressions for the circular dichroism, a technique of very wide use in the study of magnetic systems since the discovery of sum rules [44, 45]. Consider first the Faraday geometry, in which $\mathbf{k} = \hat{\mathbf{z}}$. The two circular polarization states are: $\mathbf{e}_+ = -\mathrm{i}\frac{x+iy}{\sqrt{2}}$, $\mathbf{e}_- = \mathrm{i}\frac{x-iy}{\sqrt{2}}$, and with the help of the expressions

$$\mathbf{e}^*_+ \times \mathbf{e}_+ = -\mathbf{e}^*_- \times \mathbf{e}_- = \mathrm{i}\hat{\mathbf{z}} \quad (3.108)$$

we easily derive the circular dichroism formula

$$\sigma_+ - \sigma_- = 2\lambda r_0 \left(w^e_{1,1} - w^e_{1,-1}\right) \,. \quad (3.109)$$

In the more general case of a propagation direction forming an angle θ with the direction of magnetization $\hat{\mathbf{z}}$, that coincides with a symmetry axis of a cubic or hexagonal ferromagnet, some trigonometry delivers the following results for the absorption of photons circularly polarized in the plane normal to the propagation direction

$$\sigma_+ = \lambda r_0 \left[\left(w^e_{1,1} + w^e_{1,-1}\right) + \cos\theta \left(w^e_{1,1} - w^e_{1,-1}\right) + \frac{1}{2}\sin\theta^2 \left(2w^e_{1,0} - w^e_{1,1} - w^e_{1,-1}\right)\right] \quad (3.110)$$

$$\sigma_- = \lambda r_0 \left[\left(w^e_{1,1} + w^e_{1,-1} \right) \; - \cos\theta \left(w^e_{1,1} - w^e_{1,-1} \right) \right. \\ \left. + \frac{1}{2} \sin\theta^2 \left(2w^e_{1,0} - w^e_{1,1} - w^e_{1,-1} \right) \right] \quad (3.111)$$

so that the circular dichroism is, in this more general case

$$\sigma_+ - \sigma_- = 2\lambda r_0 \cos\theta \left(w^e_{1,1} - w^e_{1,-1} \right) \; . \quad (3.112)$$

3.6 Resonant Inelastic X-ray Scattering

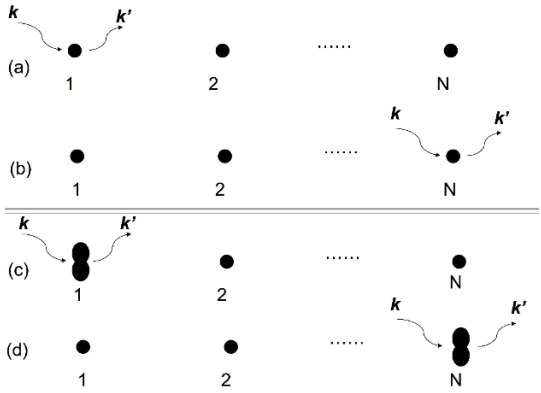

Fig. 3.4 Photon scattering from an atom chain. Upper panel: elastic scattering, the final state is the same, irrespective of which of the atoms is scattering the photon (the first one in **a**, the N-th in **b**). The amplitudes for the N different ways to reach the same final state must be first summed and than squared. Bottom panel: inelastic scattering: the final state is different, depending on which atom scatters the photon and is promoted to an excited state (the first in **c** or the N-th in **d**), therefore the amplitudes are first squared and then added.

In this Section inelastic processes are considered, in which the state of the material system after the scattering event (the final state) has a different energy than the initial state (for simplicity assumed to be the ground state). In recent

years, inelastic scattering with synchrotron radiation has acquired a growing importance.

Inelastic processes can take place in the non-resonant as well as in the resonant regime. The two regimes provide different information on the properties of the system, and both of them are in general extremely valuable. Here we shall mostly discuss the resonant regime, defined as usual by the condition that the incoming photon energy is close to one of the absorption edges of the system: this is because resonant inelastic scattering is much more relevant for the investigation of magnetic properties.

One thing that is important to underline at the outset is that inelastic scattering is a *photon-starved* technique. There is indeed a very large intensity difference between elastic and inelastic scattering: a simple argument to see that [46], at least in the limit of wavelength larger than the inter-atomic distance, is that the intensity of elastic scattering is proportional to N^2, the square of the number of scattering atoms; the intensity of inelastic scattering to N. A schematic illustration of the reason is offered in Fig. 3.4, for a chain of identical non-interacting atoms. The difference is that in elastic scattering, scattering processes through different atoms represent different paths through which the same final state is reached: the laws of quantum mechanics say that one must add the amplitudes for different paths, and then square; on the other hand, in the inelastic case, the atom contributing to an inelastic scattering process is left with some energy, i.e. in an excited state: scattering on different atoms lead therefore to different final states and now intensities must be added, after squaring the amplitudes. The argument can be carried over to the more realistic cases in which atoms are interacting, electrons are tunneling from one to the other and the energy eigenstates are Bloch states, and even electron-hole interactions can be included.

In the non-resonant case, we can proceed by generalizing the treatment of Section 3 (equation (3.27)) to include scattering from the initial electronic state $|i_e\rangle$, with energy E_i, to a different electronic state $|f_e\rangle$ with energy E_f (see (3.21)). One can show that the Thomson scattering analog becomes

$$\left(\frac{\mathrm{d}^2\sigma}{\mathrm{d}O'\mathrm{d}\omega_{\mathbf{k}'}}\right) = r_0^2\,\frac{\omega_{\mathbf{k}'}}{\omega_{\mathbf{k}}}\,\left(\mathbf{e}'^{*}\cdot\mathbf{e}\right)^2 S(\mathbf{q},\omega) \tag{3.113}$$

where the *dynamic structure factor* $S(\mathbf{q},\omega)$, with $\omega = \omega_{\mathbf{k}} - \omega_{\mathbf{k}'}$, is defined as

$$(\mathbf{q},\omega)=\sum_f\left|\langle f|\sum_j \mathrm{e}^{\mathrm{i}\mathbf{q}\cdot\mathbf{r}_j}|i\rangle\right|^2\delta\left(\frac{E_f-E_i}{\hbar}-\omega_{\mathbf{k}}+\omega_{\mathbf{k}'}\right)\,. \tag{3.114}$$

In a famous paper, Van Hove [47] showed how $S(\mathbf{q},\omega)$ is related to a density-density correlation function, in space and in time, of the system

$$S(\mathbf{q},\omega)=\int \mathrm{d}\mathbf{r}\mathrm{d}t\mathrm{e}^{\mathrm{i}(\mathbf{q}\cdot\mathbf{r}-i\omega t)}\int \mathrm{d}\mathbf{r}'\langle i|\rho(\mathbf{r}',0)\rho(\mathbf{r}+\mathbf{r}',t)|i\rangle\,. \tag{3.115}$$

This shows, not surprisingly, that the inelastic analog of the non-resonant charge scattering (Thomson scattering) allows to explore the spectrum of charge density fluctuations; this allows to investigate phonons, electronic excitations, plasmons [48]. One can expect that magnetic information is delivered by the inelastic analog of the non-resonant magnetic scattering terms: this is in principle the case, but if you remember that magnetic scattering amplitudes are reduced by the factor $\hbar\omega/mc^2$ with respect to charge scattering amplitudes, and that already magnetic elastic scattering is an experiment suffering from low-count rate, you can anticipate that non-resonant inelastic magnetic scattering shall be extremely difficult to measure; in fact, except for early magnetic scattering experiments in the Compton limit (when the transferred energy is much larger than the ionization energy) [48], there are hardly any further attempts in the literature.

We shall therefore turn to the resonant inelastic x-ray scattering (RIXS) case, defined as usual by the condition that the incoming photon energy is close to one of the absorption edges of the system. In this case one can consider the dominant resonant terms only, and obtain, in full analogy to (3.63)

$$w=\frac{2\pi}{\hbar}\sum_f\left|\sum_n\frac{\langle f|H_2'|n\rangle\langle n|H_2'|i\rangle}{E_0-E_n+\hbar\omega_{\mathbf{k}}+\mathrm{i}\Gamma_n/2}\right|^2\delta(\hbar(\omega_{\mathbf{k}}-\omega_{\mathbf{k}'})-(E_f-E_i))\,. \tag{3.116}$$

Figure 3.5 shows schematically how an inelastic scattering process can leave the system in a final state with an electron-hole pair in the valence levels or with a pair where the hole is in a core shell. In the latter case the term "resonant x-ray Raman scattering" is used. There an obvious similarity between resonant inelastic x-ray scattering (RIXS) and other techniques such as x-ray fluorescence spectroscopy and absorption spectroscopy in the fluorescence detection mode. The presence of an electron-hole pair in the final state also suggests an analogy with absorption spectroscopy, either in the visible-

UV region, for valence holes, or in the soft x-rays for the Raman case. There are however significant differences, because the inelastic scattering process has different selection rules, and the sampling depth of a technique using hard x-rays is always larger than that of soft x-ray spectroscopies. A good illustration of the relationship between inelastic scattering and absorption spectroscopy is provided by the results by Hämäläinen et al. [49] on the Dy L_3 edge in dysprosium nitrate. After quadrupolar excitation from the $2p_{3/2}$ to the $4f$ manifold by the incoming photon, a high resolution analyzer accepts only a narrow band of the outgoing photons corresponding to $3d_{5/2}$ electrons filling the $2p_{3/2}$ holes.

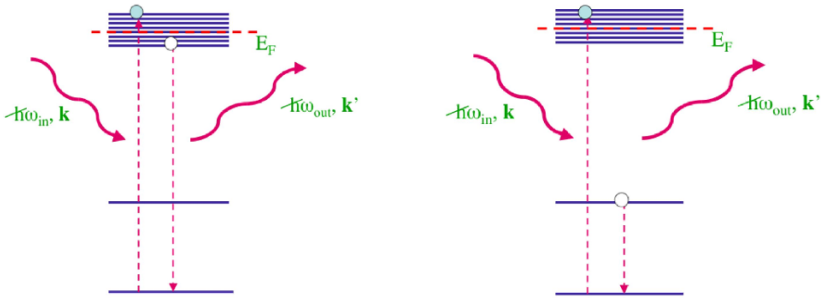

Fig. 3.5 Schematic description of resonant inelastic scattering processes

The outgoing photons can be analyzed both in energy and in momentum: this gives the possibility to map the momentum dispersion of elementary excitations. In order to be really interesting for the study of many-body systems, however, this must be done with an appropriate resolution; and although the enhancement due to the resonance is brought to bear, a RIXS experiment is always a compromise between resolution and count rate. They are therefore performed at modern high brilliance synchrotron sources; in addition, in recent years, a tremendous progress in the design of spectrometers has taken place and nowadays the best instruments are able to deliver spectra with resolving power $\Delta E/E$ exceeding 10,000. A figure of 33,000 around 1 keV is quoted for the instrument ADRESS at the Swiss Light Source, and the transmission of the beamline is delivering some $\simeq 10^{11} - 10^{12}$ photons per second on the sample [50].

To exemplify the remarkable progress of RIXS spectroscopy (for reviews, see [51, 52]), we shall briefly mention recent investigations of high-temperature cuprate superconductors and related compounds with strongly correlated electrons. Here the $L_{2,3}$ edges of Cu, in an energy region around 940 eV are conveniently investigated, as they are dipole-coupled to the Cu d-electrons, that are universally considered to play a key role in the superconductivity. In addition, the complex perovskite crystal structures of the cuprates have rather large unit cells, therefore rather small Brillouin zones; so that the momentum transfer region accessible to the soft x-ray photons near these edges covers about 80% of the way from the zone centre to the edge [53]. The study of momentum dispersion for a variety of excitations becomes therefore possible and can be of high value. Interestingly, besides charge and inter-orbital ($d-d$ electron) excitations, also magnetic excitations (spin waves) and their dispersion are accessible to this technique [54]. In the case of elastic scattering, we already explained the sensitivity to magnetic order of a resonant elastic scattering process based on electric dipole transitions (see the discussion in subsection 3.4.1) in terms of the strong spin-orbit interaction for electrons in the $L_{2,3}$ core levels. A similar argument [55] explains the possibility to explore magnetic excitations (i.e. spin-flip excitations) by RIXS. With reference to Fig. 3.6 , and to our previous discussion, we can understand how the mixed spin-up / spin-down character of the core wavefunctions allows to populate a spin-down level near the Fermi edge with the incoming photon, and to fill the hole by removing a spin-up electron near the Fermi level with the outgoing one, leaving a spin-flip excitation in the system. Remarkably, the dispersion of spin-waves measured by RIXS [54] agrees with that obtained by neutron scattering, and offers the possibility of a complementary technique in those cases (e.g. samples too small, low momentum region) where neutron techniques are difficult.

The complexity and variety of information contained in RIXS spectra makes theoretical calculations a major challenge. The approaches which have so far been applied most frequently are based either on atomic multiplet models, or on their extension to include the neighbouring ligands via Anderson impurity models or small cluster calculations [51, 52]. On the other hand, from the experimental point of view, this technique, in spite of all the difficulties connected to the low cross-section and the limitations in resolution, can provide rather unique information of importance for many-body physics. In conclusion, one can say that RIXS is a technique with great promise, as advances in instrumentation should lead to continued improvement in energy resolution.

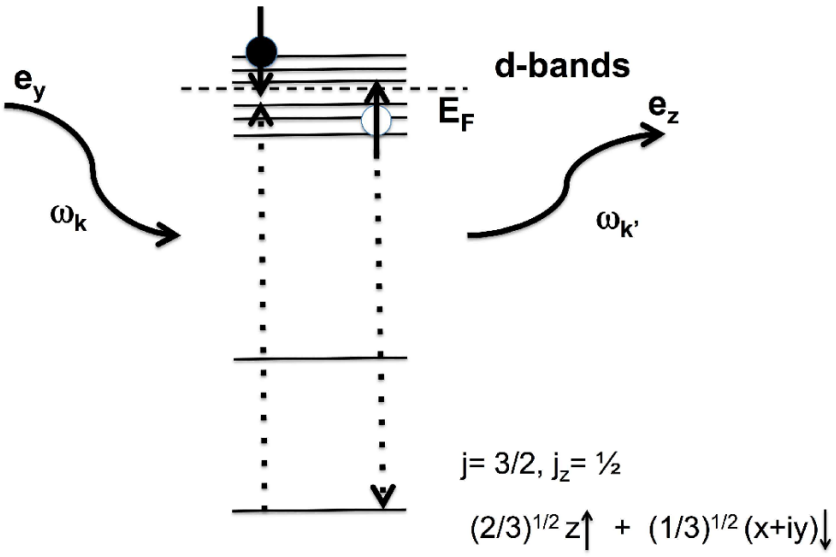

Fig. 3.6 Schematic description of spin-flip resonant inelastic scattering processes at the L_3 edge

References

1. F.E. Low, Phys. Rev. **96**, 1428(1954)
2. M. Gell-Mann and M.L. Goldberger, Phys. Rev. **96**, 1433(1954)
3. P. Platzman and N. Tzoar, Phys Rev. **B2**, 3556(1970)
4. F. de Bergevin and M. Brunel, Acta Cryst. **A37**, 314(1981)
5. D.H. Templeton and L.K. Templeton, Acta Cryst. A**36**, 237 (1980); *ibid.* A**38**, 62 (1982)
6. V.E. Dmitrienko. Acta Cryst. A**39**, 29 (1983)
7. D. Gibbs, D.R. Harshman, E.D. Isaacs, D.B. McWhan, D. Mills and C. Vettier, Phys. Rev. Lett. **61**, 1241(1988)
8. V.B. Berestetskii, E.M. Lifshitz and L.P. Pitaevskii, *Quantum Electrodynamics*, 2nd edition (Reed, Oxford, 1982), section 21.
9. A.I. Akhiezer and V.B. Berestetskii, *Quantum Electrodynamics*, (Wiley, New York, 1965), Sections 12 and 15.
10. J.J. Sakurai, *Advanced Quantum Mechanics*, (Addison, Reading, 1967), Section 3.3
11. J.D. Jackson, *Classical Electrodynamics*, 2nd edition (Wiley, New York, 1975), section 6.3.
12. L.D. Landau and E.M. Lifshitz, *The Classical Theory of Fields*, $4^t h$ edition (Reed, Oxford, 1975), section 46.

13. P. Emma, R. Akre, J. Arthur, R. Bionta, C. Bostedt, J. Bozek, A. Brachmann, P. Bucksbaum, R. Coffee, F. J. Decker et al., Nat. Photon. 4, 641 (2010).
14. T. Ishikawa, H. Aoyagi, T. Asaka, Y. Asano, N. Azumi, T. Bizen, H. Ego, K. Fukami, T. Fukui, Y. Furukawa et al., Nat. Photon. 6, 540 (2012).
15. M. Altarelli, R. Brinkmann, M. Chergui, W. Decking, B. Dobson, S. Duesterer, G. Gruebel, W. Graeff, H. Graafsma, J. Hajdu et al. (eds.), The European X-Ray Free-Electron Laser Technical Design Report, DESY 2006-097, 2006, http://xfel.desy.de/technical_information/tdr/tdr/
16. B. Nagler et al., Nature Phys. **5**,693 (2009)
17. A. Fratalocchi and G. Ruocco, Phys. Rev. Lett. **106**, 105504 (2011)
18. M. Blume, J. Appl. Phys. **57**, 3615 (1985)
19. H.C. Walker et al., Science **333**, 1273 (2011)
20. G. Trammel, Phys. Rev. **92**, 1387 (1953)
21. G. Steinsvoll et al., Phys. Rev. **161**, 499 (1963)
22. L.D. Landau and E.M. Lifshitz,*Electrodynamics of Continuous Media*, 2nd edition (Reed, Oxford, 1984), section 29, pp. 105-107
23. D.B. McWhan et al., Phys. Rev B**42**, 6007 (1990)
24. S. Langridge et al., Phys. Rev. B**55**, 6392 (1997)
25. V. Fenandez, C. Vettier, F de Bergevin, C. Giles and W. Neubeck, Phys. Rev. B**57**, 7870 (1998)
26. M. Brunel, G. Patrat, F. de Bergevin, F. Rousseaux and M. Lemonnier, Acta Cryst. **A39**, 84 (1983)
27. D. Laundy, S.P. Collins and A.J. Rollason, J. Phys. : Condens. Matter **3**, 369 (1991)
28. see e.g. S. Raimes *Many-Electron Theory*, (North Holland, Amsterdam, 1972)
29. see e.g. A.R. Edmonds, *Angular Momentum in Quantum Mechanics*, (Princeton University Press, Princeton, 1957)
30. J.P. Hannon, G.T. Trammel, M. Blume and D. Gibbs, Phys. Rev. Lett. **61**, 1245 (1988); *ibid.* (E) **62**, 2644 (1989).
31. see for example W. Neubeck, C. Vettier, K.B. Lee and F. de Bergevin, Phys. Rev. B**60**, R9912 (1992); A. Stunault, F. de Bergevin, D. Wermeille, C. Vettier, Th. Brückel, N. Bernhoeft, G.J. McIntyre and J.Y. Henry, Phys. Rev. B**60**, 10170 (1999)
32. C.W.M. Castleton and M. Altarelli, Phys. Rev B**62**, 1033 (2000)
33. S.B. Wilkins et al., Phys. Rev. Lett. **90**, 187201 (2003)
34. S.B. Wilkins et al., Phys. Rev. Lett. **91**, 167205 (2003)
35. K.J. Thomas et al., Phys. Rev. Lett. **92**, 237204 (2004)
36. S.S. Dhesi et al., Phys. Rev. Lett. **92**, 056403 (2004)
37. U. Staub et al., Phys. Rev B**71**, 214421 (2005)
38. S.B. Wilkins et al., Phys. Rev. B**71**, 245102 (2005)
39. N. Stojic et al., Phys. Rev. B**72**, 104108 (2005)
40. J.P. Hill and D.F. McMorrow, Acta Crystallog. **A52**, 10336 (1996).
41. L.D. Landau and E.M. Lifshitz, *Quantum Mechanics*, 3 rd edition (Reed, Oxford, 1977),Chapter 17
42. *X-ray Data Booklet*, edited by the Lawrence Berkeley National Laboratory, Update October 2009, Section 3.1 (available on the web at the site http://xdb.lbl.gov/)
43. P. Carra and M. Altarelli, Phys. Rev. Lett. **64**, 1286 (1990)
44. B.T. Thole, P. Carra, F. Sette, and G. van der Laan, Phys. Rev. Lett. **68**, 1943 (1992)
45. P. Carra, B.T. Thole, M. Altarelli, and X. Wang, Phys. Rev. Lett. **70**, 694 (1993)

46. V.B. Berestetskii, E.M. Lifshitz and L.P. Pitaevskii, *Quantum Electrodynamics*, 2nd edition (Reed, Oxford, 1982), section 60
47. L. Van Hove, Phys. Rev. **95**, 249 (1954)
48. W. Schülke, *Electron Dynamics by Inelastic X-ray Scattering*, (Oxford university Press, Oxford, 2007)
49. K. Hämäläinen, D.P. Siddons, J.B. Hastings and L.E. Berman, Phys. Rev. Lett. **67**, 2850 (1991).
50. V.N. Strocov et al., J. Synch. Rad. **17**, 631 (2010)
51. A. Kotani and S. Shin, Rev. Mod. Phys. **73**, 203 (2001)
52. L.J.P. Ament et al., Rev. Mod. Phys. **83**, 705 (2011)
53. G. Ghiringhelli et al., Science **337**, 821 (2011)
54. L. Braicovich et al., Phys. Rev. Lett. **104**, 077002 (2010)
55. M.W. Haverkort Phys. Rev. Lett. **105**, 167404 (2010)

Chapter 4
Free Electron Lasers

Andreas Fognini and Yves Acremann

Abstract Data storage applications of magnetism utilize dynamic processes on sub-nanosecond time scales and on length scales of less than 100 nanometers. Magnetization dynamics on the sub-picosecond time scale has been observed and may lead the way to novel devices. In order to investigate these processes it is essential to have a method-combining sub-micrometer spatial with sub-picosecond temporal resolution. Ultrafast x-ray pulses now offer this possibility. The radiation of free electron lasers (FELs) consists of sub-picosecond x-rays with unprecedented peak brightness. This chapter explains the basic principles of FELs. The peak intensity offers the possibility of imaging a fluctuating system (for example a ferromagnetic domain structure) within a single pulse. These imaging techniques as well as spectroscopic methods are explained. In order to perform time resolved experiments using large scale facilities it is essential to understand the techniques used to determine the timing between the pump laser and the x-ray probe pulses, a topic laid out.

Andreas Fogini
Laboratory for Solid State Physics, ETH Zurich, 8093 Zurich, Switzerland, e-mail: afognini@phys.ethz.ch

Yves Acreman
Laboratory for Solid State Physics, ETH Zurich, 8093 Zurich, Switzerland, e-mail: acremann@solid.phys.ethz.ch

E. Beaurepaire et al. (eds.), *Magnetism and Synchrotron Radiation: Towards the Fourth Generation Light Sources*, Springer Proceedings in Physics 151,
DOI: 10.1007/978-3-319-03032-6_4,

4.1 Introduction

Today, we are living in the information age. There is a huge demand to process, transmit, and store more and more data. This creates the need for faster processors, faster links, and smaller memory cells. This can only be achieved by making these devices smaller. State of the art transistors and magnetic bits in hard drives have a length scale of a few 10 nm. Saturation electron velocities in semiconductors are on the order of $v_d = 10^7$ cm/s. The time it takes for such an electron to pass through a transistor with $l = 10$ nm gate length is $l/v_d \approx 100$ fs. For the study of novel devices and materials a microscope is needed which can resolve these length- and timescales and beyond. Hence, light sources are necessary which provide photon pulses in the femtosecond regime with enough photon energy and brightness. The Heisenberg uncertainty $\Delta x \Delta E/c \approx \hbar$ tells us that we need a photon energy of about 10 eV to resolve a 10 nm structure. To look even deeper at the dynamics of the building blocks of matter, the atoms, hard x-rays > 1 keV are need.
Pump-probe techniques can see the dynamics of repeatable processes like magnetic switching in well defined structures and precessional dynamics. However, all fluctuating system like the critical fluctuations near a phase transition can not be viewed through the classical pump-probe approach. A single shot imaging method would be of great interest for all fluctuating systems. A light source which can provide photon pulses with the above required energy- and time-scale is a **free electron laser**.

4.1.1 Timescales in solids

Technology and ultrafast processes in solids are strongly connected. In Figure 4.1 we can see the time scales of processes in nature and in technological applications. The fastest technology today is based on femtosecond laser sources, which are the backbone for time resolved experiments. The fastest lasers pulses are a few cycles of the carrier long. Light pulses below a few femtoseconds can only be achieved by going to shorter wave lengths using high harmonic generation from femtosecond IR lasers. Electronic circuits in large-scale logic circuits operate at clock frequencies in the GHz range. The clock frequency is thereby not limited by the intrinsic switching time of the transistors, but by the heating power of the devices. Small and highly spe-

cialized circuits for high speed telecommunication applications and scientific instruments can operate on time scales of 10 ps.
Magnetic recording on computer hard disks is based on magnetization reversal by damping and is currently limited to a few 100 ps. Later we will discuss the dynamics of the magnetization.

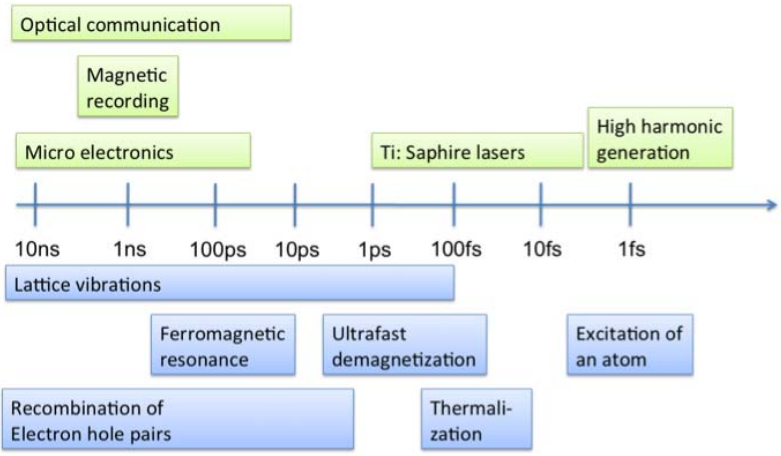

Fig. 4.1 Ultrafast processes and time scales in nature and technology.

In solids, three reservoirs can be used to describe the dynamics (Figure 4.2). If we excite a solid by an optical laser pulse, the energy is mainly transferred to the electron system. The photoexcitation of an electron is ultrafast on the time scale of a few femtoseconds. The electron-hole pair will thermalize within approximately 100 fs. This leads to thermally distributed electron hole pairs. If the solid is insulating, or semiconducting, the electrons and holes are separated by the band gap and the recombination can take many nanoseconds. If the electron system is excited, energy will be transferred to the lattice and the spins. The lattice vibration period can range from approx. 0.1 ps to seconds, depending on the phonon wavelength.The spin system is very complex. The complexity arises because of the interplay between angular momentum associated with the spins and the long-range interaction by the dipolar coupling of magnetic moments. Unlike the other reservoirs angular momentum conservation dominates the dynamics of the spin system. The transfer of an-

gular momentum from the spin system to the lattice often limits the technologically achievable switching speed.

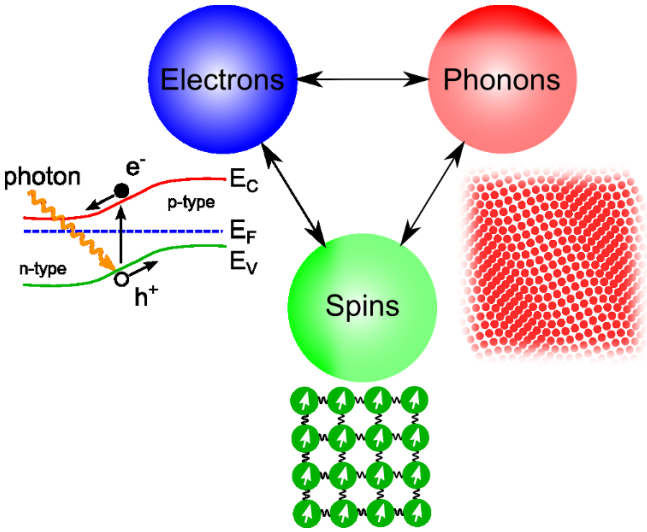

Fig. 4.2 A solid contains of three reservoirs which can be excited and have their independent temperatures: The electron bath, the lattice, and the spin system. Each of these reservoirs can show nanoscale dynamics.

4.1.2 Length- and timescales in magnetism

Magnetism arises because of the interplay between Coulomb energy and the Pauli principle. The balance of both causes very rich physics with largely varying length- and timescales. The length scales in magnetism can reach from macroscopically magnetized samples down to the lattice constant in antiferromagnets. The time scales span also over several order of magnitudes. Magnetite can be used to analyze the orientation of the ancient earth magnetic field million of years ago, whereas we don't even know yet what is the fastest time to manipulate the magnetization. The following tables (Tab. 4.1 and 4.2) give a brief overview of the time- and length-scales associated in

magnetism: k_F is the Fermi wave vector, J is the exchange energy, K the magneto-crystalline anisotropy constant.

RKKY wavelength of spin density oscillation near a magnetic ion	$\approx \pi k_F^{-1} \approx 0.2\,\text{nm}$
Minimum size of a magnetic particle before superparamagnetic breakdown	$\approx 10\,\text{nm}$
Domain wall width	$\approx \sqrt{J/K} \approx 20\,\text{nm}$

Table 4.1 Length scales in magnetism

Ferromagnetic damping	$\approx 1\,\text{ns}$
Magnetic precession	$\approx 100\,\mu\text{eV} \rightleftarrows \approx 50\,\text{ps}$
Data retention hard drive	$\approx 10\,\text{years}$
Magnetic polarization in magnetite	$> 10^6\,\text{years}$

Table 4.2 Energy- and time-scales in magnetism

4.2 Pulsed x-ray light sources

4.2.1 The slicing source

A slicing source offers pulses of 100 fs in the soft- and hard x-ray spectrum. The source is based on the idea of selecting a short part (or slice) of the picosecond x-ray pulse of a synchrotron and blocking the rest of the pulse. This way a short x-ray pulse can be obtained which can be used with any kind of detector. Figure 4.2.1 illustrates the principle of the source. The electric field of light in free space is purely transversal. Co-propagating a laser beam with an electron beam will not result in any transfer of energy between the two

beams. The situation is different in an undulator. There the electrons follow a sinusoidal motion. In some places the electron trajectory has a component parallel to the electric field of the laser. In an undulator we have the desired coupling between the electron- and the laser beam. An additional condition needs to be satisfied: The electric field of the laser must interact with the electron bunch in such a way that the part of the bunch to be influenced is affected by the same phase of the optical laser at every magnet of the undulator. This so called phase matching condition can be achieved by the fact that the electron bunch follows a longer trajectory than the light pulse which corresponds to the resonance condition of the undulator.

A slicing source consists of three parts:

- A modulator which allows for modulating the electron energy by a laser pulse
- A bending magnet which separates electrons of different energies
- The radiator (in form of a bending magnet or an undulator) which generates the x-ray radiation
- Apertures in the beamline to select the sliced part of the beam.

To perform experiments at a slicing source is challenging: The intensity of the sliced beam is weak compared to the intensity of the unsliced beam. The two beams are very close together and need to be separated very carefully. This requires also beamline optics which create very little stray light from the unsliced beam.

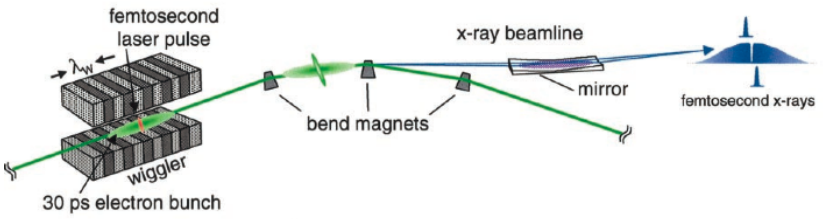

Fig. 4.3 Principle of a slicing source. From[1]. Reprinted with permission from AAAS.

4.2.2 The free electron laser

A free electron laser (FEL) can be viewed as a slicing source which uses the radiation generated by the undulator to slice the beam. If an ultrashort electron bunch is sent through an undulator it will spontaneously start to emit synchrotron radiation. The synchrotron radiation is emitted at the resonance of the undulator and will start to interact with the electron bunch itself. It turns out that the modification of the electron bunch is such that more synchrotron radiation will be emitted by the modified part of the bunch. If the charge of the bunch is large enough and the bunch length is sufficiently short (below a picosecond) the bunch can start to lase in the x-ray range. This process is called SASE (self-amplification of spontaneous emission). This way ultrashort pulses (<100 fs) of x-ray radiation can be generated. In contrast to a slicing source large pulse energies in the range of several mJ can be obtained. Currently several x-ray FELs are operational, for example FLASH (Hamburg) and LCLS (Stanford). Several sources are planned or under construction. The properties of FEL radiation are completely different compared to synchrotron radiation:

- FEL radiation is coherent
- The peak intensity dwarfs any other man-made x-ray source
- The beam tends to be unstable as the lasing process starts from noise
- The large size of the machine requires special timing stabilization measures
- Beamtime is very difficult to obtain

The necessary gain of a SASE free electron laser can only be achieved if electron bunches of a length below a picosecond of nanocoulomb charge are sent through the undulator. Due to space charge this cannot be achieved at synchrotron sources as Coulomb repulsion of the charge within one bunch would lead to instabilities of the electron bunch. In a synchrotron the electron bunch must be stable for hours. In contrast with a linear accelerator the electron bunch only needs to be stable for one pass through the accelerator. Time dilatation further increases the possible charge per electron bunch. Today's x-ray FELs are based on linear accelerators. The size of these machines imposes challenges in terms of stability and timing synchronization between the FEL and pump lasers.

4.2.3 The timing

Free electron lasers are large machines. For example the FEL in Hamburg (FLASH) measures from the injector down to the experimental hall roughly 300 m. This makes the synchronization of the FEL pulses to the pump laser next to the experiment very challenging. One degree of temperature change would already expand the length of FLASH by ≈ 5 mm and impose a time drift of ≈ 20 ps! But the experiment needs to have a time resolution < 100 fs. An elegant solution is to measure the arrival time of the relativistic electron bunch directly before the undulator with the voltage pulse which is induced by the relativistic electron bunch in small metal plates placed closely to the beam. This is accomplished by sampling this pulse (bandwidth 10 GHz) with the reference laser clock (sub-100 fs) in a Mach-Zehnder type electro-optic modulator (EOM) [2]. There is no time delay if the reference laser falls together with the zero crossing of the electrical pulse. The reference laser is transmitted over a length compensated fiber to exclude drifts from the reference side. The amplitude of the laser at the output of the EOM is hence a precise measure of the electron bunch arrival time. Interestingly, with an electrical bandwidth of "only" 10 GHz it is possible to achieve a RMS time resolution of 9 fs over 1.5 h [2].

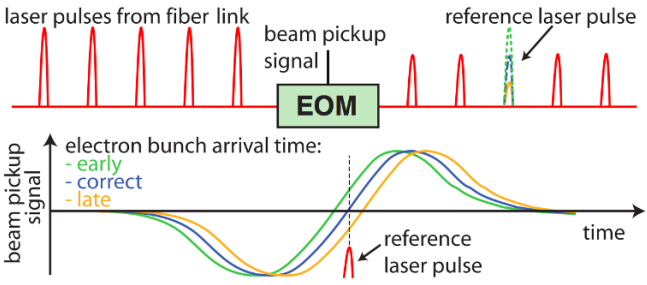

Fig. 4.4 Working principle of the beam arrival monitor at FLASH. The electric signal is compared to the reference laser in a EOM. If the electron bunch is late compared to the reference laser the signal is smaller and if it is early the signal is larger compared to no time delay. Reprinted with permission from [2]. Copyright 2010 by the American Physical Society .

4.3 Applications

4.3.1 Lensless imaging

At a free electron laser the pulse energy from a single FEL pulse can be too large for x-ray zone plates. The pulse fluence would destroy the zone plate. In addition, the coherent nature of the FEL radiation causes speckles on the sample, and is therefore not suitable for operating a transmission x-ray microscope. If single shot imaging is required, any scanning technique is ruled out as well. For single shot experiments at a free electron laser it would be desirable to avoid any optical element not needed.

The scattered wave of a sample illuminated by a plane wave is just the Fourier transform of the sample transmission. Unfortunately, x-ray detectors can only detect the square amplitude of the wave, but not the phase. The phase problem can be solved by several approaches which will be discussed briefly.

Phase retrieval

The classical phase retrieval algorithm has been developed by J. Fienup [3]. It is an iterative algorithm using known facts from the real space image and the diffraction pattern. In this algorithm, we assume we know the amplitudes of the scattering pattern, but we also have some knowledge of the real space image. In most cases, we know the size of our real space image as we may know that the sample is located inside an opaque frame. Initially, we start with the amplitudes from the scattering pattern and assign random phases to start. Here is the algorithm in pseudocode :

```
while (not converged){
    // assign the correct amplitudes in the
    // scattering pattern, keep the amplitudes.
    G = sqrt(I)*exp(i * phi);
    // now go to real space
    g = backFourierTransform(G);
    // multiply with 0 where there is no sample
    g = g * realSpaceSupport;
    // go back into reciprocal space
    G = fourierTransform(g);
}
```

There are many variations and improvements of this algorithm which help conversion, and add additional information which may be available as support. There has been a lot of progress in this field. Still, the reconstruction of the real space image from a diffraction pattern is difficult, especially if some information is missing (for example if the center of the scattering pattern needs to be blocked in order to protect the detector from the intense unscattered beam).

X-ray holography

In x-ray holography we add a small reference scatterer to the sample. This method has been developed for x-ray imaging by S. Eisebitt et al. [4], see figure 4.3.1. As a reference scatterer a small hole was drilled through the silicon nitride membrane next to the sample. The sample consisted of a magnetic worm domain pattern which was imaged by circular dichroism. The sample wave interferes on the detector with the reference wave generated by the reference hole. In this case the intensity on the detector reads

$$I = |\hat{R} + \hat{S}|^2 = |\hat{R}|^2 + |\hat{S}|^2 + \hat{R}\hat{\bar{S}} + \hat{S}\hat{\bar{R}}i\,, \tag{4.1}$$

where S is the sample's transmission function and R the transmission function of the reference.$\hat{}$ demotes the Fourier transform. There are the non-interfering scattering patterns between the sample wave and the reference wave, but there are also two interference terms! If we now take the back-Fourier-transform into real space and use the convolution theorem, we get back the real space image of the sample!

$$\check{I} = \cdots + R * \bar{S} + S * \bar{R} \tag{4.2}$$

$*$ denotes the convolution. Figure 4.3.1 shows the Fourier back transform of the scattering pattern. In the center we can see the auto-correlations $R * R$ plus $S * S$. But next to the autocorrelation, we can see the real space image of the sample being the convolution of the sample with the reference. So, the smaller we make the reference scatterer, the better resolution can be achieved. However, in this case the reference wave gets weaker so there is a trade-off between resolution and efficiency.

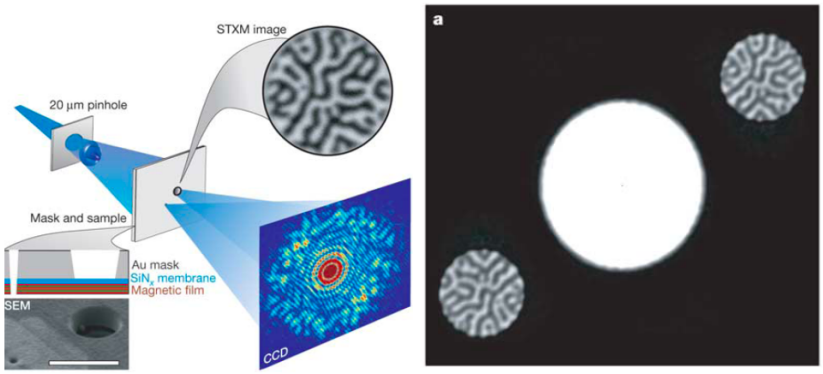

Fig. 4.5 Left: X-ray holography method developed by S. Eisebitt et al.. **Right:** Fourier back-transform of the holographic scattering pattern: next to the autocorrelation of the reference and sample structure we can see the convolution of the reference with the sample as a real space image of the sample. Reprinted with permission from Macmillan Publishers Ltd: Nature [4].

4.3.2 The Fresnel zone plate as a hologram

The use of Fresnel zone plates offers the highest spatial resolution and is discussed in detail in this section. The easiest way to understand the focusing properties of a zone plate is by viewing it as just being a hologram of a point source with a plane wave as the reference wave. If we illuminate this hologram by a plane wave, it will re-create the spherical wave which originates from the point source. Therefore, the zone plate focuses a plane wave onto a point.

Let us construct the zone plate as a hologram (in fact this has been the way of manufacturing zone plates before high resolution electron beam lithography techniques were available). To make a hologram, we interfere a plane wave reference beam with a spherical wave. As the detector is perpendicular to the **k**-vector of the plane wave, it's phase is constant. We define the wave function to be 1 on the plane. The spherical wave on the plane reads

$$\psi_R = 1; \qquad \psi_P = \frac{1}{r} e^{ikr} = \frac{1}{\sqrt{x^2+f^2}} e^{ik\sqrt{x^2+f^2}}, \tag{4.3}$$

where x is a coordinate on the plane and f is the distance of the plane to the point source; this is just the focal length! The interference pattern on the plane reads

$$|\psi_R + \psi_P|^2 = \cdots = 1 + \frac{1}{r^2} + \frac{2}{r}\cos(kr)\,. \tag{4.4}$$

For the zone plate only the oscillatory part is interesting

$$\frac{2}{\sqrt{x^2+f^2}}\cos(k\sqrt{x^2+f^2})\,. \tag{4.5}$$

For technical reasons we build binary zone plates, meaning that only transparent and opaque parts exist. To find the boundaries of the zones we need to find the zero-crossings

$$\frac{2\pi}{\lambda}\sqrt{x^2+f^2} = \frac{\pi}{2} + n\pi\,. \tag{4.6}$$

Solving for x:

$$x = \sqrt{\frac{\lambda^2}{4}\left(\frac{1}{2}+n\right)^2 - f^2} \tag{4.7}$$

The minimum of n is $n_{min} = \frac{2f}{\lambda} - \frac{1}{2}$. Now we re-define $n = n - n_{min}$ and obtain

$$x(n) = \sqrt{\frac{\lambda^2}{4}n^2 + \lambda f n} \approx \sqrt{\lambda f n}\,. \tag{4.8}$$

The inner zones are large and as we go to the outer zones the zones get smaller. The width of the n^{th} zone is

$$w = \frac{\lambda f}{2x_n}\,. \tag{4.9}$$

For example, for a zone plate with a focal length of 5 mm, the wavelength of 2 nm and a radius of 100 μm we get an outer zone width of 50 nm! The manufacturing process of high resolution zone plates is very difficult and requires advanced electron beam lithography techniques. The outermost zone does not only need to be small, but also very precisely placed relative to the center of the zone plate!

4.3.3 Photoemission for ultrafast magnetodynamics

The ultrafast reduction of the magnetization in nickel upon exciting the system with a high intensity ($\approx 10\,\mathrm{mJ/cm^2}$) infrared laser beam has been demonstrated in 1996 by Beaurepaire et al. [5]. In this experiment, the magneto optical Kerr (MOKE) effect has been employed where the polarization change of a reflected laser beam is a measure for the magnetic polarization state of the sample. Since MOKE is depending on the band structure around the Fermi level, a debate has been lead weather or not MOKE is a proper technique to measure magneto dynamics on $< 100\,\mathrm{fs}$ timescale [6, 7]. Nowadays, a consensus has been reached that ultrafast demagnetization truly exists. Complementary measurement techniques like x-ray magnetic circular dichroism [8, 9, 10, 11], photoemission [12, 13, 14], two photon-photon emission [15, 16], and second harmonic generation [6] showed the same ultrafast magnetic effect. After more than a decade of research, the fundamental principle of the ultrafast quenching of the magnetization is still poorly understood. The unresolved question is: Through which pathway(s) can the majority electrons transfer their spin to the phonon system? In terms of temporal magnetic reaction to a IR pump beam, three classes of materials can be distinguished:

The transition metal ferromagnets: Iron, Nickel, Cobalt, and certain alloys thereof show all an ultrafast quenching of the magnetization upon excitement by an intense IR laser.

The rare earth ferromagnets: Gadolinium and Terbium. These ferromagnets show a much slower quenching of the magnetization with respect to the transition metals on the order of several 100-femtoseconds. It is believed that the energetic and spacial separation of the $4f$ states which carry the magnetic moments to the conduction electrons ($5d$) lead to such a slow down.

Half- and semi- half metals: In these materials predominantly majority electrons have empty states above the Fermi level. This class shows the slowest quenching of the magnetization, in the order of picoseconds. For this material class the effect can be understood as a state blocking effect. Fermi's golden rule

$$T_{i\to f} = \frac{2\pi}{\hbar} \left|\langle f| H' |i\rangle\right|^2 \rho_f \tag{4.10}$$

implies that the transition rate $T_{i\to f}$ from an initial state $|i\rangle$ to a final state $|f\rangle$ is proportional to the density of empty minority states ρ_f, in our case. Nevertheless, this argumentation does not provide insight into the interac-

tion Hamiltonian H', and hence does not answer our initial question. The velocity of the quenching of the magnetization in half-metals can even be used to classify the degree of half-metallicity [17] since it is a measure of the empty states of the minority electrons.

A tool to further elucidate the nature of the ultrafast magnetization change is time- and spin-resolved photoemission. During the photoemission process the spin state is not altered in the dipole approximation. Hence, it can be used to study the dynamics of magnetization at different energy levels in the Fermi sea. Experimentally, this task is demanding for two reasons: Typically photoabsorption cross sections are small, and spin detectors have a low yield. This can be compensated by using high brightness light sources such as a FEL. Unfortunately, the FEL pulse can be so intense that the number of photoelectrons is so large that they start to interact with each other (space charge effect). Typically, space charge results in shifted and smeared out spectra. Space charge is unavoidable at photoemission experiments at FEL's. Therefore, at the start of every photoemission experiment at a FEL, the FEL beam needs to be attenuated to a level where the space charge effect is still bearable. If it is possible in the experiment, the photon energy can be lowered which results in less cascaded electrons and less space charge.
In our experiment, we used the electron cascade generated by FEL pulses of 180 eV photon energy. The cascaded electrons provide an inherent gain in the amount of electrons released by one photon and in the amount of the spin polarization, which is more than two times larger. This is due to the spin filter effect which states that electrons with the same magnetic polarization as the sample live longer, and therefore their probability of escape is larger. By using these gain features of the cascade, it is possible to compensate for the low efficiency of spin detectors and the low photoemission cross section. Our findings show that, indeed, the magnetization state of an 8 ML Fe film on W(110) can be altered by an intense IR beam below 100 fs. In future, time resolved photoemission studies might shed more light on the microscopic origin of the ultrafast demagnetization since photoemission has the unique capability to distinguish between spacial (surface, bulk), energy, and the symmetry of the states involved.

References

1. R. W. Schoenlein, S. Chattopadhyay, H. H. W. Chong, T. E. Glover, P. A. Heimann, C. V. Shank, A. A. Zholents, and M. S. Zolotorev, Science **287**, 2237 (2000)
2. F. Löhl, V. Arsov, M. Felber, K. Hacker, W. Jalmuzna, B. Lorbeer, F. Ludwig, K.-H. Matthiesen, H. Schlarb, B. Schmidt, P. Schmüser, S. Schulz, J. Szewinski, A. Winter, and J. Zemella, Phys. Rev. Lett. **104**, 144801, (2010)
3. J. R. Fienup, Appl. Opt. **21**, 2758 (1982)
4. S. Eisebitt, J. Luning, W. F. Schlotter, M. Lorgen, O. Hellwig, W. Eberhardt, and J. Stöhr, Nature **432**, 885 (2004)
5. E. Beaurepaire, J.-C. Merle, A. Daunois, and J.-Y. Bigot, Phys. Rev. Lett. **76**, 4250 (1996)
6. H. Regensburger, R. Vollmer, and J. Kirschner, Phys. Rev. B **61**, 14716 (2000)
7. B Koopmans, M. van Kampen, J. T. Kohlhepp, and W. J. M. de Jonge, J. Appl. Phys. **87**, 5070 (2000)
8. C. Boeglin, E. Beaurepaire, V. Halte, V. Lopez-Flores, C. Stamm, N. Pontius, H. A. Dürr, and J.-Y. Bigot, Nature **465**, 458 (2010)
9. I. Radu, K. Vahaplar, C Stamm, T. Kachel, N. Pontius, H. A. Durr, T. A. Ostler, J. Barker, R. F. L. Evans, R. W. Chantrell, A. Tsukamoto, A. Itoh, A. Kirilyuk, Th. Rasing, and A. V. Kimel, Nature **472**, 205 (2011)
10. T. Stamm, C. Kachel, N. Pontius, R. Mitzner, T. Quast, K. Holldack, S. Khan, C. Lupulescu, E. F. Aziz, M. Wietstruk, Dürr H. D., and W. Eberhardt, Nature Mater. **6**, 4 (2007)
11. Marko Wietstruk, Alexey Melnikov, Christian Stamm, Torsten Kachel, Niko Pontius, Muhammad Sultan, Cornelius Gahl, Martin Weinelt, Hermann A. Dürr, and Uwe Bovensiepen, Phys. Rev. Lett. **106**, 127401, (2011)
12. M. Lisowski, P. A. Loukakos, A. Melnikov, I. Radu, L. Ungureanu, M. Wolf, and U. Bovensiepen, Phys. Rev. Lett. **95**, 137402 (2005)
13. H.-S. Rhie, H. A. Dürr, and W. Eberhardt, Phys. Rev. Lett. **90**, 247201 (2003)
14. A. Scholl, L. Baumgarten, R. Jacquemin, and W. Eberhardt, Phys. Rev. Lett. **79**, 5146 (1997)
15. M. Cinchetti, M. Sánchez Albaneda, D. Hoffmann, T. Roth, J.-P. Wüstenberg, M. Krauß, O. Andreyev, H. C. Schneider, M. Bauer, and M. Aeschlimann, Phys. Rev. Lett. **97**,177201 (2006)
16. A. Weber, F. Pressacco, S. Günther, E. Mancini, P. M. Oppeneer, and C. H. Back, Phys. Rev. B **84**, 132412 (2011)
17. Georg M. Muller, Jakob Walowski, Marija Djordjevic, Gou-Xing Miao, Arunava Gupta, Ana V. Ramos, Kai Gehrke, Vasily Moshnyaga, Konrad Samwer, Jan Schmalhorst, Andy Thomas, Andreas Hutten, Gunter Reiss, Jagadeesh S. Moodera, and Markus Munzenberg, Nature Mater. **8**, 56 (2009)

Chapter 5
Magnetic imaging with polarized soft x-rays

Peter Fischer

Abstract Magnetic imaging with polarized soft x-rays offers several advantages compared to other techniques, which are available to visualize magnetic structures and magnetic behavior on microscopic levels. The ultimate spatial resolution for soft x-ray techniques, i.e. the diffraction limit set by the wavelength, will be in the few nm regime. The temporal resolution, given by the length of a single x-ray pulse is at 3rd generation synchrotron sources in the sub 100 ps regime, but should reach out into the fs regime at next generation x-ray sources, where single shot imaging should become feasible due to a sufficiently large number of photons per single x-ray pulse. The interaction of polarized soft x-rays with magnetic (ferromagnetic and antiferromagnetic) materials exhibits for element specific photon energies, which correspond to inner core electron binding energies significant magnetic cross sections. These magnetic dichroism effects serve as magnetic contrast mechanism for imaging and give quantitative information about magnetic ground state properties, such as magnetic spin and orbital moments. A full 3 dimensional information, specifically access to magnetic structures at interfaces can be obtained by imaging under certain geometries, as well as from computational magnetic tomography of 2 dimensional projection images.

Peter Fischer
Center for x-ray Optics, Lawrence Berkeley National Laboratory, Berkeley, CA USA e-mail: PJFischer@lbl.gov

E. Beaurepaire et al. (eds.), *Magnetism and Synchrotron Radiation: Towards the Fourth Generation Light Sources*, Springer Proceedings in Physics 151,
DOI: 10.1007/978-3-319-03032-6_5,

5.1 Introduction

One of the major science drivers during the last decade was nano-science and nano-technology which was set out to observe, understand and control matter down to atomic levels, where quantum behavior dominates. Nanomagnetism is one particular example, since the basic building blocks in magnetism, the spin of the electron is inherently of quantum mechanical origin. New and fundamental insight into the origin of magnetism can therefore be expected from nanomagnetism studies and, indeed, great achievements have been made so far [1]. In addition to the scientific curiosity in magnetism and magnetic materials, there is also a wealth of technological relevance in nanomagnetism research, which is evidenced for example by the achievements in magnetic information and sensor technologies. The increase of several orders of magnitude in magnetic storage density obtained over just a decade, i.e. from gigabytes to terabytes and beyond, can be considered as a success story in technological performance which is hardly bypassed by any other technology in history.

There are three essential components which need to come together to enable such progress:

- state-of-the-art synthesis, i.e. fabrication,
- analysis, i.e characterization, and
- theoretical description, i.e. modeling and understanding.

In **synthesis**, milestones in nanomagnetism were set by the capability to fabricate nanoscale magnetic systems, such as thin magnetic films and multilayers of high quality, nanopatterning e.g. by e-beam lithography, and to design novel magnetic materials, e.g. via molecular beam epitaxy (MBE) exhibiting unprecedented properties. Theory advances in nanomagnetism benefit from both advanced **modelling** as well as from increasing computing power and parallelized computing algorithms. Finally, novel **characterization** approaches, i.e. instrumentation and analytical techniques with nanoscale magnetic sensitivity, both spatial as well as elemental and temporal, are indispensable to nanomagnetism research.

Polarized soft x-rays techniques have become a major tool for probing magnetic materials, and magnetic imaging is among the most intriguing ones. Although there is a plethora of other magnetic imaging techniques (see e.g. [2]), which can be categorized according to the probes they are using into electron, photon or scanning probe techniques, soft x-ray microscopies stand

out by offering a unique combination of key advantages, which no other probe can easily offer.

- The **spatial resolution** which, due to the wavelength of soft x-rays in the nanometer regime, has its diffraction limit accordingly in the nanometer regime.
- The interaction of soft x-rays with matter, which is primarily photoabsorption, exhibits pronounced resonances for photon energies matching inner-core electron binding energies, thus providing images with inherent **elemental specificity**.
- The interaction of polarized soft x-rays with magnetic materials gives rise to strong magnetic dichroism effects, which allow for both **quantitative information** on spin and orbital magnetic moments, and which can be used in imaging as a strong **magnetic contrast** mechanism.
- The pulsed structure of soft x-rays at synchrotron sources enables to image the spin dynamics with a **temporal resolution** limited by the length of the x-ray pulses, which range from the sub–100 ps regime at current synchrotrons down to fs time scales at upcoming free electron lasers or high harmonic generation laboratory sources.
- The **high intensity** of x-rays, particularly at next generation light sources, enables to study small magnetic cross-sections, e.g. highly diluted magnetic samples, and to take snapshot images of the dynamics.
- Soft x-ray spectromicroscopy allows to image both **surface and bulk** properties depending on whether the limited escape depth of electrons or the penetration of x-rays is utilized.
- Finally, **three dimensional information** can be obtained in various ways, which allows to study in particular buried interfaces and complex magnetic structures.

This chapter will give an overview of the current capabilities of magnetic imaging with polarized soft x-rays by selected examples from current research. We will start with detailing the magnetic contrast and its specific features. We will then explain briefly the various types of soft x-ray microscopes, followed by a brief overview on the achieved spatial resolution. Combining the high spatial resolution with temporal resolution allows to image spin dynamics, i.e. the functionality of magnetic structures. The future possibilities at upcoming x-ray sources, such as free electron lasers or lab based x-ray sources providing ultrashort and intense x-ray pulses will enable to address both fundamental length and time scales in magnetic systems. Finally, we will briefly address the current efforts towards full 3-dimensional (3D) magnetic imaging.

5.2 Magnetic contrast with polarized soft x-rays

The interaction of polarized light in the optical regime with magnetic materials is described by the magneto-optical effects, which are well known for almost two centuries. The most prominent magneto-optical effects are the Kerr effect [3] and the Faraday effect [4]. The latter was discovered in 1845 by Michael Faraday, who found that the plane of linearly polarized light was rotated by passing through a flint glass in the presence of a magnetic field. Somewhat later a corresponding effect was discovered by John Kerr, who found that the polarization of light was rotated upon being reflected from the surface of iron. Various geometries, characterized by the relative orientation between the applied magnetic field and the direction and plane of the incoming light have been established and are named as polar Kerr effect when the magnetization is perpendicular to the magnetic surface, and as longitudinal Kerr effect when the magnetization is parallel to the surface and along the plane of the incident light, and lastly, as the transversal Kerr effect when the magnetization is in-plane of the surface but orthogonal to the plane of the incoming light. A theoretical model for the Kerr and the Faraday effect was established by Lorentz already in 1884 [5], who proposed that left and right circularly polarized light couples differently to the classical electron oscillators in the solid. Although the Faraday and the Kerr effect *per se* are rather weak for most materials and therefore provide only a weak magnetic contrast mechanism for magnetic imaging, the introduction of video microscopy and digital image processing has made magneto-optical microscopy based on the Faraday and the Kerr effect a widespread magnetic imaging technique [6]. Particularly, the availability of ultrashort optical laser pulses allows for studies of ultrafast spin dynamics [7]. However, there are two major shortcomings with magneto-optical imaging, namely the diffraction limited spatial resolution, which prevents to address the true nanoscale, and the very limited elemental sensitivity.

More than 35 years ago, Erskine and Stern [8] predicted strong dichroism effects in the x-ray regime and with the availability of polarized x-rays at synchrotron sources, first experiments were performed in the mid to late 1980s. Particularly, the first demonstration of strong x-ray magnetic circular dichroism (XMCD) effect at the L-edges of Fe, Co and Ni [9] (Fig. 5.1) at photon energies between 700 and 900 eV launched a “gold rush” towards exploiting those phenomena for the studies of magnetic properties in nanoscale magnetic systems. This excitement was further amplified with the formulation of

the so-called magneto-optical sum rules, which allowed to deduce from spectroscopic data in a quantitative and element specific manner the spin [10] and orbital [11] moments separately.

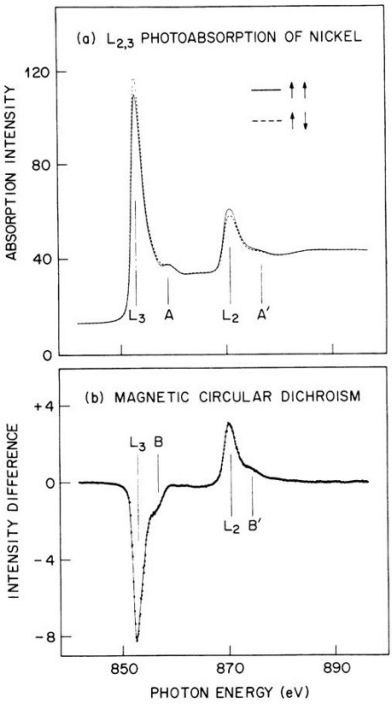

Fig. 5.1 First experimental demonstration of strong XMCD effect at the L edges in Ni. Reprinted figure with permission from [9]. Copyright (1990) by the American Physical Society

The x-ray magnetic circular dichroism effect describes the change in x-ray absorption, which is quantified by the very characteristic x-ray absorption coefficient μ. μ depends on the photon energy E and can be determined in an x-ray transmission experiment, where the incoming photon intensity $I_0(E)$ is reduced to $I(E)$ after the photons have penetrated a sample thickness d, following the well known exponential Beer-Lambert absorption law

$$I(E,d) = I_0(E)e^{-\mu(E)d}. \tag{5.1}$$

For circularly polarized x-rays the additional change in μ in magnetic materials, i.e. the XMCD effect, depends on the relative orientation between the helicity of the photons σ and the magnetization direction in the ferromagnetic sample $\mathbf{M}$. The XMCD signal scales with the scalar product between those two quantities

$$\text{XMCD} \sim \sigma \cdot \mathbf{M} \tag{5.2}$$

and therefore the largest change occurs between the parallel and antiparallel orientation of the magnetization and the polarization of the photons. It also scales with the amplitude of the magnetization and the degree of circular polarization. For a full (100%) polarization of the photons XMCD values can yield up to tens of percent.

Although the exchange interaction favors a parallel orientation of two individual spins, the energetic groundstate of an extended ferromagnetic system, i.e. the orientation of all the spins e.g. in a bulk magnet or a thin ferromagnetic film, is in general not the single domain state where all spins are parallel to each other, other competing interactions, most notably the magnetostatic, anisotropy and Zeeman interactions, yield a groundstate which is characterized by magnetic domains [2]. Each of those domain is uniformly magnetized and neighboring domains are separated by so-called domain walls to accommodate the transition from the spin orientation of one domain to the neighboring one. The size of these domains and domain walls depends on inherent materials parameter, such as anisotropy and exchange constants. For thin magnetic films and small confined structures, the relevant length scales are in the submicrometer regime and are therefore target for microscopic studies.

5.3 Types of magnetic soft x-ray microscopes

Rather soon after the discovery of the strong magnetic XCMD effects in the late 1980s, it was realized that XMCD can be used to image the magnetic domain structure and suitable x-ray microscopy techniques were employed for that purpose.

The first experimental demonstration in 1993 [12] used an x-ray photoemission electron microscope (X-PEEM) to image the magnetic domain structure in a ferromagnetic film for magnetic storage, where bit patterns were cre-

ated by switching the magnetization through locally applied magnetic fields (Fig. 5.2a). In an X-PEEM, the secondary electrons generated in the x-ray absorption process can escape the sample's surface and are transferred into an electron optical lens system to form an image on the CCD detector. The limited escape depth of those electrons to about 5–10 nm makes PEEM imaging an inherently surface sensitive technique. Further, the detection of electrons and the need to trace exactly their local position, imposes severe limitations for applying magnetic fields during the image recording process, which is of interest e.g. for the study of magnetization reversal on a microscopic length scale. X-PEEM samples should be conducting to avoid charging effects, but do not require particular sample fabrication, e.g. they can be deposited on various substrates as long as the sample's surface is smooth.

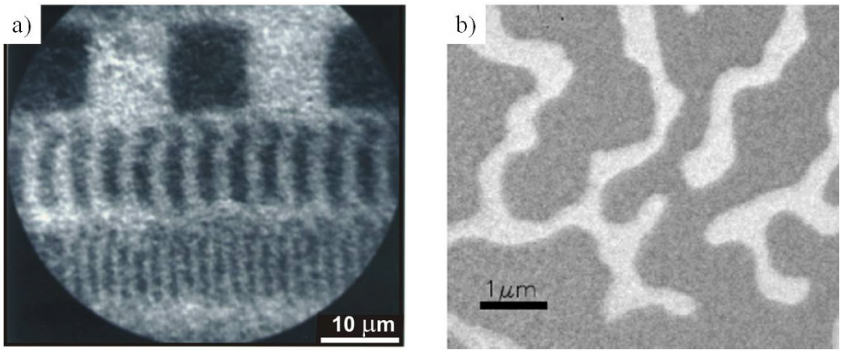

Fig. 5.2 **a** First magnetic soft x-ray microscopy image obtained with X-PEEM [12]. **b** First magnetic soft x-ray microscopy image obtained with a full-field zone plate based transmission microscope [13]

A complementary approach for magnetic soft x-ray microscopy utilizes x-ray microscopes, which directly use the photons for recording the images. This requires the availability of suited x-ray optics. W.C. Roentgen already pointed out in 1885 [14] that conventional lenses cannot be used to focus x-rays due to their refraction index for x-rays close to unity. It took nearly 85 years after Roentgen's discovery until x-ray optics were developed, which now allow for soft x-ray microscopy. With the advent of e-beam lithographic tools, first developed to generate small structures in semiconductor industry, and the availability of high intense x-ray sources at synchrotron facilities, made possible the development of Fresnel zone plate (FZP) optics, and thus

the first x-ray microscopes [15]. FZPs are diffractive elements [16]. They are essentially circular gratings where the line density increases with increasing radius (Fig.5.3). The performance of a FZP in terms of spatial resolution, numerical aperture ($N.A.$), focal length, depth of focus, etc. is in general determined by a few zone plate parameters only, so that state-of-the-art nanofabrication processes can tailor those optics to fit the experimental requirements. The width of the outermost zone ring Δr determines largely the spatial resolution, the focal length is set by the number of zones N, and the spectral bandwidth $\Delta\lambda/\lambda$ is inversely proportional to N. With the photon wavelength λ, the following relations hold

$$\text{spatial resolution} \sim \Delta r \sim \lambda/N.A. \tag{5.3}$$

$$\text{focal length} \sim 4N(\Delta r)^2/\lambda \tag{5.4}$$

$$\text{spectral bandwidth} \sim \Delta\lambda/\lambda \sim 1/N. \tag{5.5}$$

The first magnetic image taken with the full-field transmission soft x-ray microscope at BESSY I in Berlin in 1996 studied the magnetic domain structures in a perpendicularly magnetized thin film of a GdFe alloy [13] (Fig. 5.2b). Both PEEM and magnetic transmission soft x-ray microscopy (MTXM) have since then been used for a plethora of magnetic studies.

As with the X-PEEM technique, MTXM uses XMCD as magnetic contrast mechanism. Whereas the X-PEEM is surface sensitive, the MTXM technique, detecting the photons transmitted through the specimen, is complementary to X-PEEM by probing the bulk properties. The upper limit in thickness for MTXM is about 150–200 nm. The thinnest magnetic film, where magnetic domains could be observed so far in MTXM was a multilayered NiCo film with perpendicular magnetic anisotropy. Magnetic domains could be observed down to about 1 nm of Co thickness [17], which links nicely to the limited probing depth of X-PEEM, as mentioned in the previous paragraph. As a photon-only technique, MTXM can record the magnetic images in applied magnetic fields, which allows to study magnetization reversal processes in detail [18]. The sample fabrication for MTXM has to take into account the limited penetration depth of soft x-rays, which requires the specimens to be deposited onto x-ray transparent substrates. This problem is similar to transmission electron microscopy samples, and therefore MTXM can utilize largely techniques and substrates developped by this community. Commercially available Si_3N_4 membranes are generally substrates of choice for MTXM studies, but recently, great effort is made to develop x-ray transparent

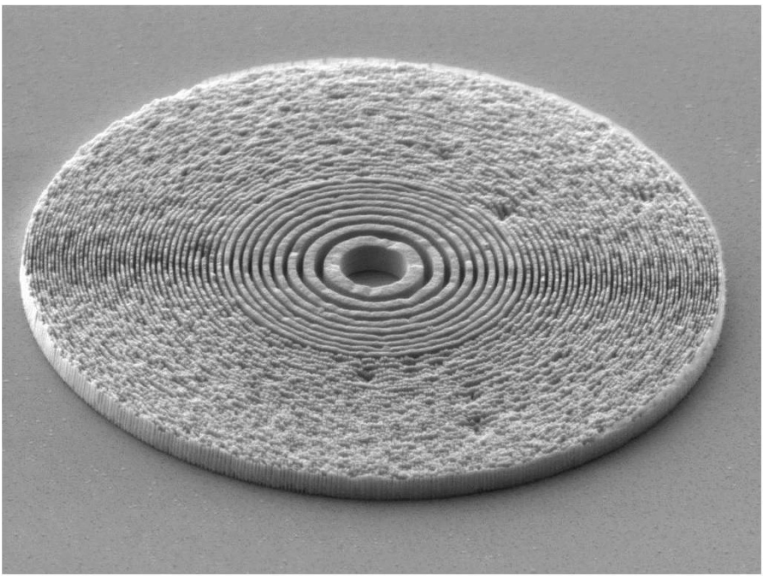

Fig. 5.3 Scanning electron microscopy image of a typical Fresnel zone plate, which is used for transmission soft x-ray microscopies. Typical values for the diameter are $D = 50\,\mu$m, number of zones $N = 500$, and $\Delta r \approx 20 - 25$ nm. Focal lengths at 700 eV photon energy are typically less than 1 mm

substrates, where epitaxial growth of films is also feasible. Ion beam assisted deposition (IBAD) onto MgO is one of the avenues at the moment [19, 20].

Similar to transmission electron microscopies, there are two different versions of TXM concepts using Fresnel zone plate optics. There are full-field Transmission soft x-ray Microscopes (TXM) (Fig. 5.4b) and Scanning Transmission x-ray Microscopes (STXM) (Fig. 5.4a).

The optical design of a full-field transmission soft x-ray microscope (TXM) is very similar to a conventional optical microscope. The main components are the source, the condenser, the sample, the objective lens and the detector. The full-field TXM XM-1 at the Advanced Light Source, will serve in the following as an example to explain the basic concepts (see Fig. 5.5).

XM-1 is using the radiation emitted at a bending magnet. At XM-1 both condenser and objective lenses are FZPs. The condenser zone plate (CZP) together with a small pinhole close to the sample provides a hollow cone illu-

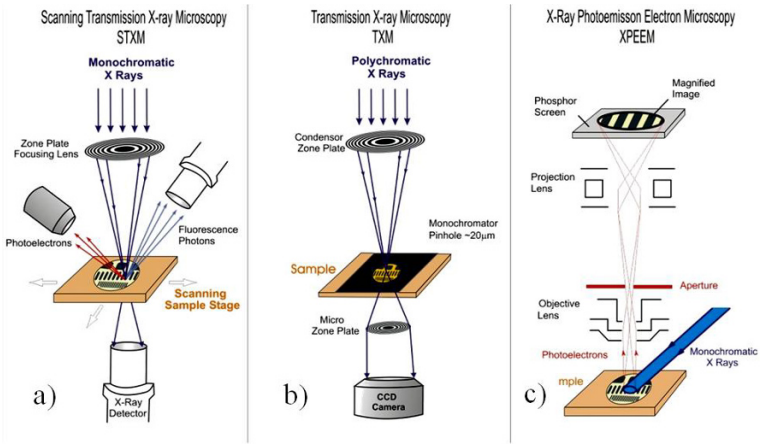

Fig. 5.4 There are 3 variants of soft x-ray microscopes, which are used for magnetic imaging in real space. **a** Scanning Transmission soft x-ray Microscopy (STXM), **b** Full-field Transmission soft x-ray Microscopy, and **c** x-ray PhotoEmission Electron Microscopy (X-PEEM). From [1]

mination of the sample and serves as monochromator, however, with a spectral resolution of only about 500, which translates into 1 eV at 500 eV. A second FZP downstream the sample, the so called micro zone plate (MZP), acts as the objective lens and generates a magnified image onto the CCD detector. The MZP provides largely the spatial resolution (see Sec.5.4). Time-resolved images with a temporal resolution down to about 70 ps can be obtained in a stroboscopic pump and probe scheme (see Sec.5.6). Circularly polarized light is obtained by masking the upper or lower half of the bending magnet radiation. However, linear polarization which is emitted in the plane of the electron orbits in the storage ring and which would allow to study e.g. antiferromagnetic systems cannot be used here. Since this instrument was originally not designed to do magnetic imaging, magnetic fields up to only several kOe field strengths can be achieved. And with the sample being in ambient conditions, experiments at variable temperatures, particularly at low temperatures, can neither be performed with this instrument.

The latest developments of full-field transmission soft x-ray microscopy has the potential to overcome the shortcomings of XM-1. The current full-field TXM at the synchrotron BESSY in Berlin, Germany uses an undulator source

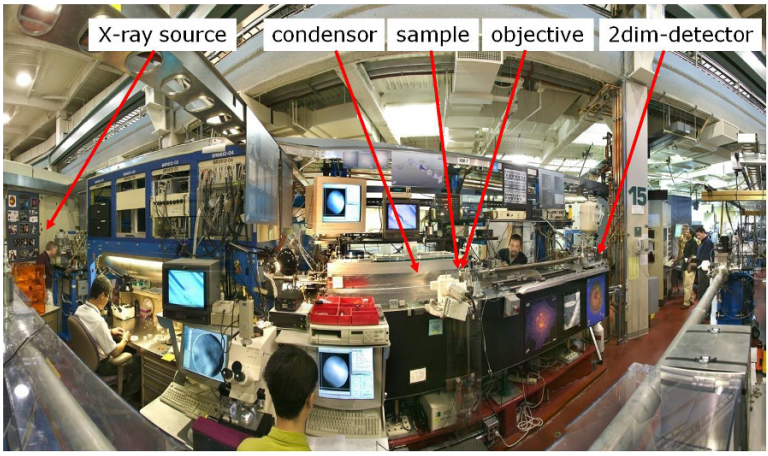

Fig. 5.5 Overview photograph of the full-field soft x-ray transmission microscope endstation XM-1 located at beamline 6.1.2 at the Advanced Light Source in Berkeley CA

which provides much higher intensity and better spectral purity. A plane grating monochromator allows high spectrally resolved imaging up to about 10^4 spectral resolution so that high resolution spectro-microscopy becomes feasible. The monochromatizing and the illuminating parts are separated and the illuminating concept of the sample utilizes a capillary condenser. Full-field images up to 15 μm field of view recorded in about 1 s with a spatial resolution down to 20 nm have been demonstrated [22]. A next generation TXM utilizing an elliptical polarized undulator (EPU) is currently being proposed for the Advanced Light Source (Fig. 5.6). This XM-3 instrument will be dedicated to spectro-microscopies studies in materials, environmental and energy related sciences, including magnetic materials. The undulator will allow to control the polarization and higher spectral purity, and the high intensity enables higher spatial resolution. Since the sample would be in a vacuum chamber, low temperatures and larger magnetic field will be feasible. Images will also be recorded in reflection geometry to gain access to buried interfaces, and hence to 3D information (see Sec. 5.7).

A scanning transmission x-ray microscope (STXM) uses the high resolution FZP used as objective lens in the TXM concept *downstream* of the

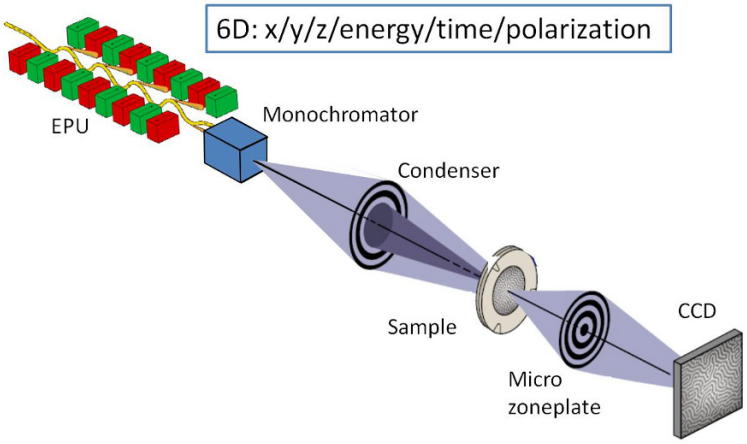

Fig. 5.6 Conceptual drawing of the next generation full-field transmission soft x-ray microscope XM-3 located at an elliptically polarized undulator source providing the capability to do up to 6-dimensional imaging

sample as a focussing device *upstream* the sample (see Fig. 5.4a and b)[1]. The transmitted intensity from that diffraction limited spot is detected by a point detector, such as an Avalanche Photo Diode (APD), and an image is obtained by either scanning the sample or the FZP optics, which makes this instrument for larger field of views rather slow compared to the speed of a full-field TXM [22]. However, STXMs have the advantage that they can easily utilize various detection channels, such as the fluorescence during the absorption process, or they can detect the sample current point-by-point in a non-transparent specimen. Further, new concepts combining various imaging techniques are being established. The nanoXAS project at the Swiss Light Source combines a Scanning Probe Microscope with a STXM to detect simultaneously the morphology of the sample and the x-ray absorption [23]. Another approach is the ptychographic method [24], which records a diffraction pattern for each scanning step in a STXM and holds the promise to push the spatial resolution to the wavelenght limited diffraction. However, enormous efforts in dealing

[1] A hybrid soft x-ray microscope combining a STXM and a TXM in one instrument is the TwinMic project, which is operational at Elettra,Trieste (Italy) [21].

with the amount of data for each image are still waiting to be resolved. Both of those latest developments have so far not been used for magnetic imaging.

As an alternative to using x-ray optics for imaging, the concept of lensless imaging has received a significant interest over the last decade and a large variety of techniques is currently under development. One of them is x-ray holographic imaging, where the sample is placed behind a lithographically manufactured mask with a micrometer-sized sample aperture and a nanometer-sized hole that defines a reference beam. Using the resonant x-ray magnetic circular dichroism effect, magnetic structures at a resolution of about 50 nm could be retrieved by a direct Fourier inversion of a holographically formed interference pattern [25, 26, 27]. Although the holographic method is well established since 1948, when D. Gabor invented holography [28], one of the major challenges for magnetic x-ray holography is the requirement to generate the reference wave, which requires a high precision reference hole on either the sample itself or on a mask which needs to be placed next to the sample. Another approach is coherent diffractive imaging (CDI), in which a series of scanned dichroic coherent diffraction patterns is recorded and numerically inverted to map its magnetic domain configuration [29]. However, most of the studies have been done so far on magnetic samples with strong contrast and domain sizes around 100 nm. Finally, hybrid approaches between real and reciprocal space have been attempted. In particular, the x-ray ptychographic method combines the STXM technique with CDI. Whereas this technique itself was developed in the 1970s for electron microscopy and consists of measuring multiple diffraction patterns by scanning a finite illumination on an extended specimen [30], ptychography has seen a significant revival recently utilizing x-rays. At each scanning point of a STXM instrument a full diffraction pattern is collected and then backtransformed into real space [24]. The promise is that a spatial resolution below 10 nm is easier to achieve than with CDI where the reconstruction procedures put very stringent requirements on data quality and sample preparation. Soft x-ray ptychography experiments on biological specimens in the water window have achieved about 50 nm spatial resolution [31]. In the hard x-ray regime, x-ray ptychography has been used for 3D imaging of bone structures with about 100 nm spatial resolution [32].

Since next generation x-ray free electron laser sources (X-FEL) are nearly fully coherent x-ray sources providing a huge peak intensity within a few fs short x-ray pulses, an enormous effort is currently underway to explore those imaging techniques, which require coherent light. However, there seems to be still a long way to go, particularly in terms of detector development and data

analysis of the enormous amount of data per single image, before any of these techniques will be accepted and utilized by a broad user community.

5.4 Pushing spatial resolution to fundamental magnetic length scales

With the fundamental magnetic length scales being in the sub-10 *nm* regime, state-of-the-art magnetic imaging techniques aim to push towards such a spatial resolution. Although there are magnetic imaging techniques, such as Spin-Polarized Scanning Tunneling Microscopies (SP-STM) [33], which have already achieved atomic resolution in magnetic imaging, they mostly lack of sufficient time resolution or elemental specificity, and are therefore limited to mostly static images of spin structures. As mentioned already on page 157 in this chapter, x-rays have the potential to combine those features in a unique way. To improve spatial resolution with Fresnel zone plate based x-ray microscopy the outermost width of the FZP has to decrease (see (5.3)). This requires advances in nanotechnology to fabricate high-quality devices.

Fig. 5.7 Instead of generating a high density, high aspect ratio FZP in one step, one utilizes the overlay technique, which breaks this process into multiple steps with less demanding properties. However, this can only be met, if a high precision alignment of the ZPs during the multiple steps can be achieved. From [34]

The challenge is that with decreasing Δr the distance to the neighboring ring also decreases, meaning that one has to fabricate high density concentric ring structures. Further, to maintain efficiency, a sufficient aspect ratio is also mandatory. One way to meet this challenge is the so-called overlay or double pattern technology [34] which allows to push the zone-width well below the one a single exposure pattern could achieve (Fig. 5.7). The challenge is,

however, that this technique relies on a very accurate overlay, to within just a few nm, of one pattern to another. This can be accomplished by specialized alignment algorithms and pattern generators. With this technique, progress in spatial resolution of FZP based soft x-ray microscope were able to demonstrate spatial resolution of test structures down to below 10 nm (Fig.5.8). Even more, this concept can be easily generalized to increase also the aspect ratio, which yields a higher diffraction efficiency of the zone plates. Hence, ultimately it can be used to do both, increasing spatial resolution and diffraction efficiency at the same time and thus breaking the currently required trade-off between these two competing lens properties. This will be requisite to enable magnetic imaging in a wide variety of applications. Recently, by optimization of various process steps such as lithography, electroplating, and resist coating, an aspect ratio of 19:1 has already been demonstrated [35].

Another concept to increase spatial resolution is to combine advanced thin film technology with e-beam lithography. By a conformal atomic layer deposition (ALD) of high refractive index material onto the side walls of a prepatterned template made from a low refractive index material, one can obtain a doubling of the effective line density of the coated material as compared with the template. This has been demonstrated recently to achieve a spatial resolution better than 10 nm [36].

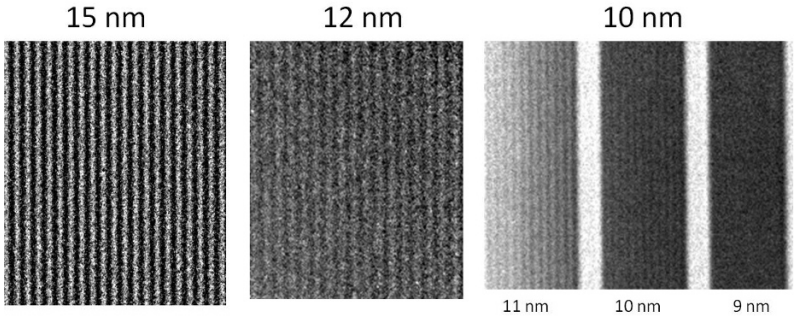

Fig. 5.8 Progress with FZP based soft x-ray microscopy since 2005. Whereas spatial resolution to below 10 nm has been already demonstrated, increase in efficiency is as important before it can be used for regular magnetic imaging

The quadratic decrease in focal length with increasing spatial resolution can be compensated e.g. by using the higher order diffraction of FZPs. Although progress has been achieved, the loss in diffraction intensity has to be compensated by stronger soft x-ray sources. Therefore higher order imaging can hardly be an option for bending magnet beamlines, but will require state-of-the-art undulator sources [37].

5.5 One example: Magnetic vortex structures

As one typical example of magnetic x-ray imaging with high spatial resolution, we want to introduce the topic of magnetic vortex structures (see Fig.5.9), which have attained significant interest in the recent past by the magnetism community [38, 39, 40, 41, 42, 43, 44, 45, 46, 47, 48, 49]. We will use this topic to show how soft x-ray magnetic microscopy can not only reveal details in the static spin configuration [50], but also how the fast dynamics of vortex structures can be studied (see Sec. 5.6).

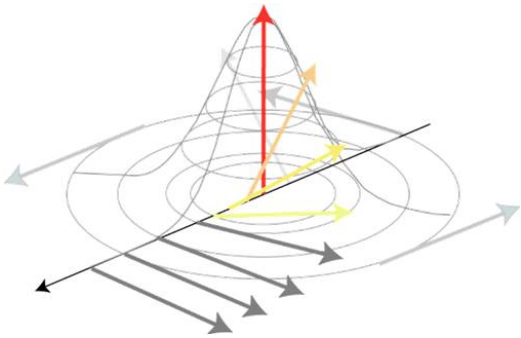

Fig. 5.9 Schematics of the spin configuration in a thin ferromagnetic disk.

To minimize its energy, the spin structure in a thin (less than a few hundred nm) ferromagnetic, e.g. permalloy ($Fe_{19}Ni_{81}$), disk of sub-micrometer diameter, exhibits a circulating component in the plane of the disk, which basically follows the shape of the sample. However, towards the center of the disk, the increase in exchange energy between neighboring spins, which tend to be an-

tiparallel, is overcome by pulling them out of the plane, so that at the center an out-of-plane structure appears, the so-called vortex core (VC). The circulating component, which can point into either clockwise or counterclockwise direction, is characterized by the chirality parameter C, which is either ± 1, and the corresponding VC orientation is characterized by the polarity parameter P, which is also either ± 1 depending on whether the VC points upward or downward the magnetic disk.

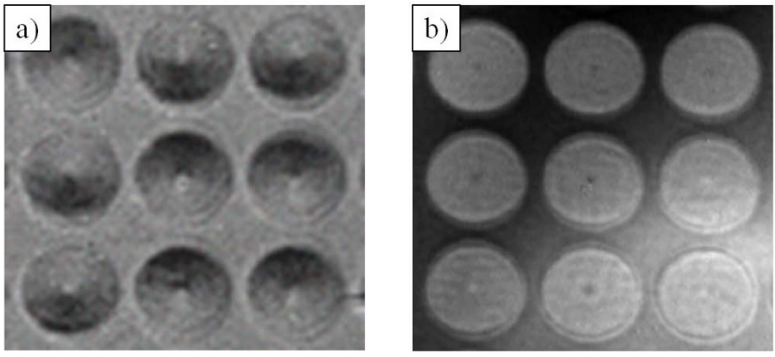

Fig. 5.10 Magnetic soft x-ray microscopy images of permalloy disk arrays, with height h=100 nm, and radii r=400 nm showing **a** the in-plane (chirality) and **b** the out-of-plane (polarity) spin configuration. From [51]

MTXM has the capability to image both the chirality and the polarity since the XMCD contrast scales with the projection of the magnetization onto the photon propagation direction. This can be simply achieved by tilting the sample's surface relative to the photon propagation direction [52]. Fig.5.10 shows two typical examples of an array of permalloy disk structures (height h=100 nm, and radii r=400 nm), where both the chirality (Fig. 5.10a) and the polarity (Fig. 5.10b) can be seen. In a recent study with MTXM it could be verified that the nucleation of magnetic vortex structures, which exhibit four different configurations for the two C and P values, does not occur with equal probability for each individual configuration. A symmetry-breaking interaction occurring at the surface of the disk could be identified to be one of the origins. For further details, we refer the reader to [53].

The high spatial resolution of the FZP optics used in MTXM allows to study further details of the vortex core profile. Micromagnetic simulations

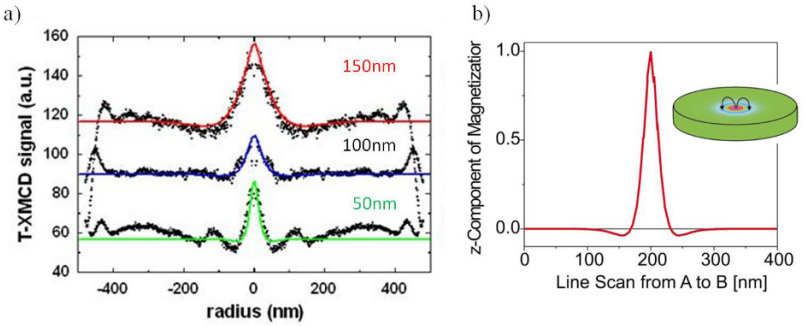

Fig. 5.11 **a** Intensity profiles of polarity images similar to the ones shown in Fig. 5.10b across the VC in the center for various disk thicknesses (Reprinted figure with permission from [50]. Copyright (2011) by the American Physical Society.) in comparison with **b** micromagnetic simulations (Reprinted figure with permission from [43]. Copyright (2003) by the American Physical Society)

have predicted that the dipolar field emerging from the VC closes back into the disk, thus creating a small dip in the intensity profile of the VC structure. In a recent MTXM study, where the VC profiles were studied as function of the disk thickness, such a dip could indeed be verified (Fig. 5.11) and was found in excellent agreement with full 3D micromagnetic simulations [50]. The latter included even a broadening of the VC profile inside the disk volume, a phenomenon which is described as the *barrel structure* in [2]. The decrease of the VC half-width-half-maximum (HWHM) at the surface, which is included in the *barrel model*, can also be seen with more surface sensitive imaging techniques such as Scanning Electron Microscopy with Polarization Analysis (SEMPA) [54]. Ultimately, the full structure of a VC would be an interesting research target for magnetic tomography, which will be addressed in Sec.5.7 further below.

The decrease of the VC size as function of disk thickness[2] was also addressed in this recent MTXM study, as seen in Fig. 5.11a [50]. The dependence of the HWHM values as function of disk thickness for a fixed radius of 500 nm is shown in Fig.5.12. The lines shown are results of micromagnetic simulations, where both the anisotropy (K) and a broadening value (σ) was

[2] The VC size also decreases with higher anisotropy, e.g. in Co disk of similar geometrical sizes the HWHM of the VC would be smaller.

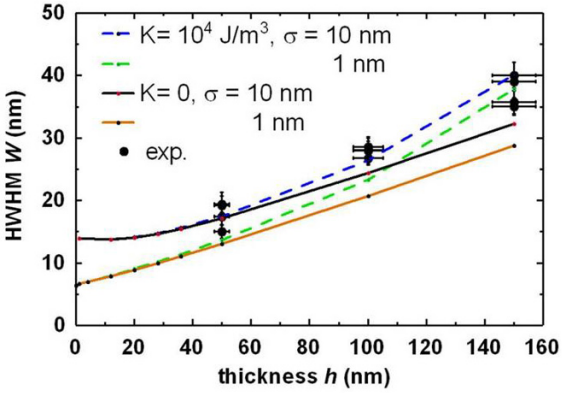

Fig. 5.12 The half-width-half-max (HWHM) values of the VC in permalloy disks decrease with decreasing film thickness. Values from TXM measurements are shown as data points, indicating the limit in spatial resolution. The various lines are from full 3D micromagnetic simulations with varying anisotropy values (K) and broadening (σ). Reprinted figure with permission from [50]. Copyright (2011) by the American Physical Society

used as parameter. The good agreement between the experimental and simulation data is evident. However, the current spatial resolution of FZP optics does not permit to extend such studies below about 50 nm disk thickness. To access those scientifically interesting and moreover technologically important regime, a further improvement of spatial resolution (and efficiency, since with a decreasing film thickness, the signal/noise ratio for the magnetic contrast drops significantly) is desperately needed.

5.6 Imaging spin dynamics down to fundamental magnetic time scales

In order to understand functionality, the dynamics of a system has to be taken into account. Time-resolved imaging of spin structures has thus received a great deal of attention. Analogous to the need to image magnetic structures down to their fundamental length scales, imaging their dynamical behavior down to fundamental time scales is as demanded. With the exchange interaction being the strongest interaction in magnetic systems, the corresponding

fundamental time scales of exchange interactions is typically in the tens of femtosecond regime [1]. However, the full range of magnetization dynamics of current scientific and technological interest covers the time scales from the nanosecond regime, where precessional and domain wall motion occur, as well as the picosecond time scale which originates from spin-orbit interactions (Fig. 5.13). In time resolved imaging, the temporal resolution obtained

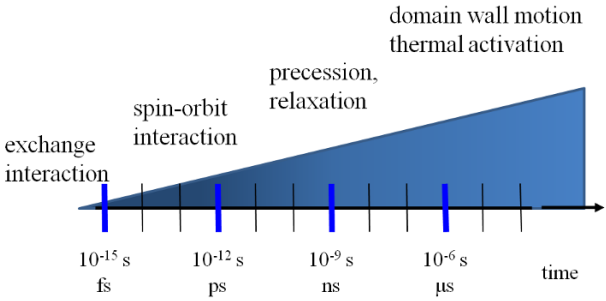

Fig. 5.13 Relevant magnetic timescales, which are of current interest to magnetic x-ray imaging

depends on the length of the probes. The fastest probes, which are being used for magnetic imaging are fast laser pulses, which reach into the low fs regime. However, as mentioned above (see p. 158) optical microscopies suffer from insufficient spatial resolution. The x-ray pulses from current third generation synchrotron sources, such as the ALS, have a typical duration of less than 100 ps and this is the timescale which can be easily accessed today. However, the number of photons per single electron bunch at those SR sources is very limited (about 10–20 photons/shot) and therefore a stroboscopic pump-probe experiment is needed to obtain time-resolved x-ray microscopy data since each image requires about 10^{9-10} photons. As the repetition rate of a SR machine is in the MHz regime, a sufficient number of photons for a single image can be achieved in tens of seconds and about 10^{8-9} pump-probe cycles have been applied to the sample. This poses a severe limitation to those studies, or vice versa, the obtained results need to be taken with great caution since

- only fully reproducible processes can be studied, such as vortex gyration and domain wall motion in confined structures, and

- only the fully reproducible part can be imaged, i.e. non-deterministic processes such as spin fluctuations cannot be addressed so far.

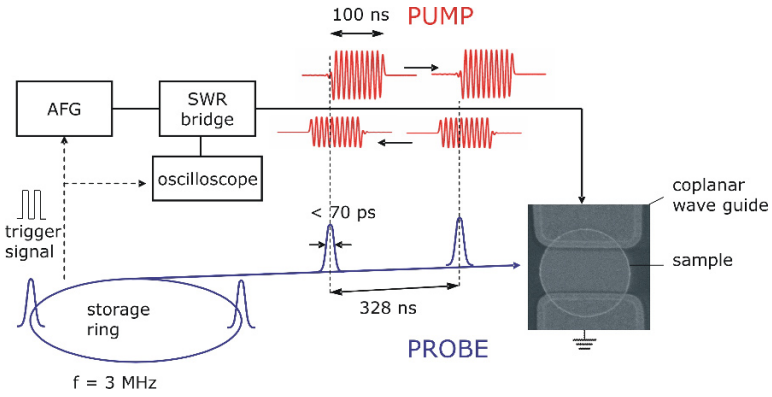

Fig. 5.14 Schematics of the stroboscopic pump-probe setup for time resolved MTM measurements. Reprinted figure with permission from [55]. Copyright (2008) by the American Physical Society

As a prototypical example to explain the capabilities of time resolved MTXM, we will use again magnetic vortices and in particular their gyrotropic motion. The energetically very stable configuration and the possibility to encode both C and P independently in a single unit has suggested magnetic vortex structures as an interesting concept for novel magnetic storage [56, 57, 58, 59] and logic units [60, 61]. However, this requires a detailed understanding of the dynamic behavior upon excitation of magnetic vortex structures and a plethora of studies have been focussing on those topics. The vortex ground state leads to a rich spin excitation spectrum, including translational, radial and azimuthal modes, which have been studied both theoretically and experimentally [46, 59, 62, 63, 64, 65]. A wealth of details have been studied and, for example, a good understanding is now available of how to switch the VC by magnetic field pulses and by spin polarized currents, or how the accompanying spin waves emerge [44, 49, 63, 65, 66, 67, 68, 69, 70, 71].

Two examples from time-resolved MTXM will now describe what information can be retrieved from studies of magnetic vortex structures. In the first experiment a single permalloy disk was placed between two contact pads, where a RF pulse sequence was launched to trigger a spin current in-

duced gyrational motion of the magnetic vortex structure in the permalloy disk (Fig. 5.14) [55]. The lengths of the x-ray pulses at the ALS are about 70 ps and the spatial resolution is around 25 nm. The gyrational motion of the VC was observed in this experiment up to a delay between the electronic pump and the x-ray probe pulse of several ns. From the observed clockwise gyration, a polarity value of P=-1 could be deduced. More importantly, the measurement of the gyration radius, which is possible due to the high spatial resolution as a function of excitation frequency, allowed to derive the polarization of the currents (Fig. 5.15) which yielded a value of 0.67 and which is a critical quantity to describe the strength of the spin torque acting on the vortex core [55].

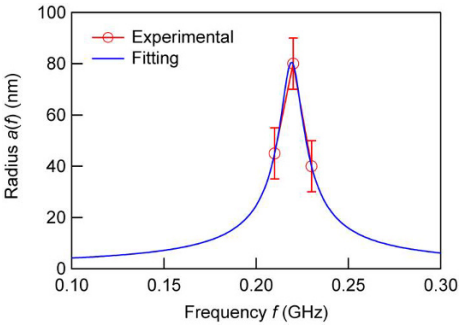

Fig. 5.15 Gyration radius of the vortex core in the permalloy disk as a function of the excitation frequency. Reprinted figure with permission from [55]. Copyright (2008) by the American Physical Society

The second example goes one step further towards the realization of a magnetic device, which is based on the dynamics of a magnetic vortex. There, the interaction of neighboring disks has to be studied in detail, first, to understand potential couplings, and second, to tailor such couplings e.g. in logic devices, where the coupling could be utilized to propagate a signal.

To address this problem, a sample was prepared where one ferromagnetic disk (Disk #1) was placed directly on top of a coplanar waveguide, whereas a second disk (Disk #2) of the same diameter and thickness was located a certain distance away from the first disk (Fig. 5.16). The gyrotropic motion of the vortex structure in Disk #1 was then triggered by a short electronic pulse running through the waveguide. With time-resolved full-field MTXM it was

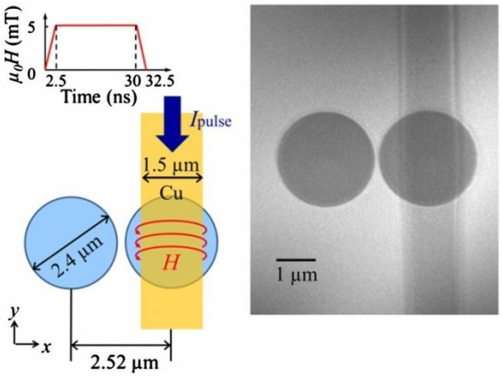

Fig. 5.16 Left: Schematics of the electronic pulse, which is launched into the waveguide. Right: Raw MTXM image showing the two ferromagnetic disks, with one placed on top of the waveguide [72]

then possible to observe the gyrational motion of both disks at the same time as a function of delay time between pump and probe pulse. From an analysis of the experimental data it could be demonstrated that the dipolar coupling between spatially separated magnetic disks can be utilized as a robust new mechanism for energy and information transfer with tunable energy transfer rates, low-power input signals and negligible energy loss in the case of negligible intrinsic damping (Fig. 5.17). This makes this concept an interesting alternative for implementation in applications for information-signal processing.

5.7 Towards three-dimensional magnetic x-ray imaging

Over the last decade research on magnetism was dominated by the desire to understand the properties of magnetic systems on the nanoscale. A reductionist, i.e. a top-down approach, was applied to dissect the complex magnetic behavior on a macroscopic scale to the building blocks on an atomic and molecular level. Undoubtedly, this scientific era has made great achievements and fundamental insight into nanomagnetism was obtained. Recently, it has been recognized, that the next step beyond the nanoscale will be governed by

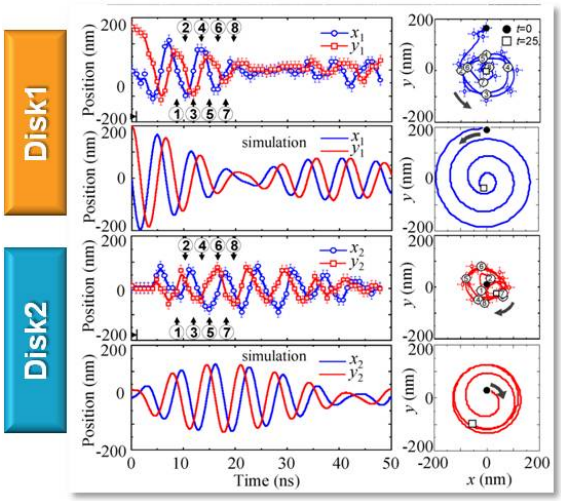

Fig. 5.17 Top: Position (x,y) of Disk #1 as derived from MTXM data in comparison with simulations. Bottom: Same for Disk #2. The oscillations are similar to the motion of coupled oscillators. From [72]

mesoscale phenomena [73], since those are expected to add complexity and functionality, which are essential parameters e.g. for the realization of next generation future devices.

Complexity in mesoscience will comprise both novel and emerging materials which can be tailored through synthesis, but also the investigation of buried interfaces and, related to that, the demand to image structures in all three dimensions, which will advance magnetic imaging to the next level beyond e.g. the 2D magnetism in thin films. Three-dimensional soft x-ray tomography using Fresnel zone plate based full-field and scanning transmission soft x-ray microscopies have been developed and are routinely used at various synchrotron sources, but almost exclusively for biological imaging [74]. However, a 3D imaging of magnetic structures is of large interest to understand e.g. interfaces in magnetic multilayers, the inner structure of magnetic nanocrystals, nanowires, nanotubes [75] or the functionality of artificial 3D magnetic nanostructures. Several x-ray 3D imaging approaches are currently investigated, such as utilizing standing waves in Bragg conditions [76], x-ray

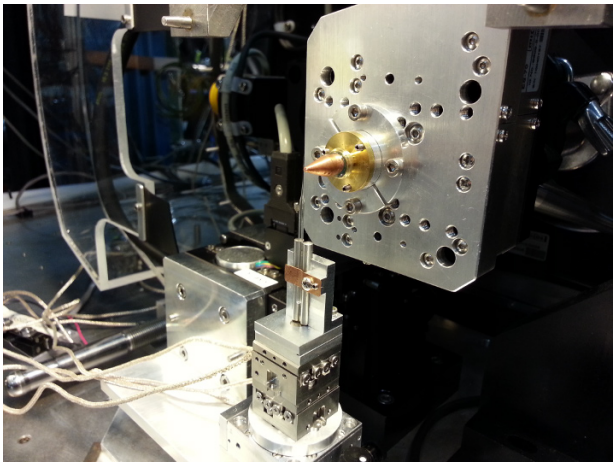

Fig. 5.18 Image of the tomography stage at the full-field TXM at the ALS. The sample is mounted on top of the glass tip

imaging in reflection geometry [77] or computational reconstruction of projection x-ray images.

One way to get tomographic information with full-field MTXM is to mount the sample, such as a nanotube onto a rotational symmetric substrate, e.g. a quartz tip which can be pulled down to less than 100 nm tip size and which is placed onto a high precision rotary stage to record an angular series (up to 360°) of high precision 2D projection images (Fig. 5.18). By applying state-of-the-art reconstruction algorithms [78] it is possible to retrieve the full 3D structure. Another approach is to utilize the short depth of focus (see (5.4)) to record images through focus and then reconstruct the tomographic information.

5.8 Conclusion

Magnetic imaging with polarized soft x-rays provides a unique combination of spatial and temporal resolution as well as inherent elemental and quantifiable sensitivity. There is a variety of techniques available, including both

real space and reciprocal space imaging. Full-field TXM will contribute significantly to future studies of mesoscale phenomena, including tomographic information. At future x-ray sources, such as x-ray free electron lasers single shot imaging capabilities with nanometer spatial and fs temporal resolution can be foreseen.

Acknowledgements The author would like to thank all his colleagues, who contributed to the work presented here, in particular M.-Y. Im, W. Chao, and E.H. Anderson (CXRO), L. Bocklage, and G. Meier (U Hamburg), K. Yamada, K. Kobayashi, T. Ono (U Kyoto), T. Sato, Y. Nakatani (U Chofu), H. Kohno (U Osaka), A. Thiaville (U Paris-Sud) S. Kasai (NIMS Tsukuba), S.-K. Kim, H. Jung, D.-E. Jeong, Y.-S. Choi, Y.-S. Yu, D.S. Han (SNU, Seoul), K.-S. Lee (UNIST), C.S. Fadley, A. Gray, J. Kortright, and F. Hellman (MSD LBNL) and the staff of the ALS and CXRO for excellent support. This work was supported by the Director, Office of Science, Office of Basic Energy Sciences, Materials Sciences and Engineering Division, of the U.S. Department of Energy under Contract No. DE-AC02-05-CH11231.

References

1. J. Stöhr and H.C. Siegmann, *Magnetism: from Fundamentals to Nanoscale Dynamics* (Springer Verlag, Berlin Heidelberg, 2006)
2. A. Hubert and R. Schäfer, *Magnetic Domains* (Springer, Berlin, 1998)
3. J. Kerr, Phil. Mag. **3**,321–343 (1877)
4. M. Faraday, Phil. Trans. Royal. Soc. (London) **136**, 1–20 (1846)
5. H.A. Lorentz, Théorie des phénoménes magneto-optiques récemment découverts, *Rapport présentés aux Congrès International de Physique, Paris* **3**, 1 (1900)
6. F. Schmidt, W. Rave, and A. Hubert, IEEE Trans. Mag. **21**, 1596 (1985)
7. W.K. Hiebert, A. Stankiewicz, and M.R. Freeman, Phys. Rev. B **79**, 1134 (1997)
8. J.L Erskine and E.A Stern, Phys. Rev. B **12**, 5016–5024 (1975)
9. C. T. Chen, F. Sette, Y. Ma, and S. Modesti, Phys. Rev. B **42**, 7262–7265 (1990)
10. P. Carra, B.T. Thole, M. Altarelli, and X. Wang, Phys. Rev. Lett. **70**, 694 (1993)
11. B.T. Thole, P. Carra, F. Sette, and G. van der Laan, Phys. Rev. Lett. **68**, 1943–1946 (1992)
12. J. Stoehr, Y. Wu, B.D. Hermsmeier, M.G. Samant, G. Harp, S. Koranda, D. Dunham, and B.P. Tonner, Science **259**, 658 (1993)
13. P. Fischer, G. Schütz, G. Schmahl P. Guttmann and D. Raasch, Z.f. Physik B **101**, 313–316 (1996)
14. W.C. Röntgen, über eine neue art von strahlen, *Sitzungsberichte der Physikalisch-Medizinischen Gesellschaft zu Würzburg*, p. 132 (1895)
15. B. Niemann, D. Rudolph, and G. Schmahl, Applied Optics **15**, 1883 (1976)
16. D.T. Attwood, *Soft x-rays and Extreme Ultraviolet Radiation* (Cambridge University Press, 1999)

17. F. Macia, P. Warnicke, D. Bedau, M.-Y. Im, P. Fischer, D. A. Arena, and A. D. Kent, J. Magn. Magn. Mat. **324**, 3629–3632 (2012)
18. M.-Y. Im, P. Fischer, T. Eimüller, G. Denbeaux, and S.-C. Shin, Appl. Phys. Lett. **83**, 4589–4591 (2003)
19. J.R. Groves, R.F. DePaula, L. Stan, R.H. Hammond, and B.M. Clemens, IEEE Transactions on Applied Superconductivity **19**, 3311 (2009)
20. C. Bordel, J. Juraszek, D. Cooke, C. Baldasseroni, S. Mankovsky, J. Minar, H. Ebert, S. Moyerman, E. Fullerton, and F. Hellman, Phys. Rev. Lett. **109**, 117201 (2012)
21. B. Kaulich, D. Bacescu, D. Cocco, J. Susini, C. David C, E. DiFabrizio, S. Cabrini, G. Morrison, J. Thieme J, and M. Kiskinova, J. Phys. IV **104**, 103–107 (2003)
22. P. Guttmann, C. Bittencourt, S. Rehbein, P. Umek, Xiaoxing Ke, G. Van Tendeloo, C.P. Ewels, and G.Schneider, Nature Photon. **6**,25–29 (2012)
23. I. Schmid, J. Raabe, C. Quitmann, S. Vranjkovic, H.J. Hug, and R.H. Fink, Journal of Physics: Conference Series 1 **86**, 012015 (2009)
24. P. Thibault, M. Dierolf, A. Menzel, O. Bunk, Ch. David, and F. Pfeiffer, Science **321**, 379 (2008)
25. S. Eisebitt, J. Lüning, W.F. Schlotter, M. Lörgen, O. Hellwig, W. Eberhardt, and J. Stöhr, Nature **432**, 885–888 (2004)
26. T. Hauet, C. M. Guenther, B. Pfau, M. E. Schabes, J. U. Thiele, R. L. Rick, P. Fischer, S. Eisebitt, and O. Hellwig, Phys. Rev. B **77**, 184421 (2008)
27. C. Tieg, R. Frömter, D. Stickler, S. Hankemeier, A. Kobs, S. Streit-Nierobisch, C. Gutt, G. Grübel, and H. P. Oepen, Optics Express **18**, 27251 (2010)
28. D. Gabor, Nature **161**, 777–785 (1948)
29. A. Tripathi, J. Mohanty, S. H. Dietze, O. G. Shpyrko, E. Shipton, E. E. Fullerton, S. S. Kimb, and I. McNulty, PNAS **108**, 13393 (2011)
30. W. Hoppe R. Hegerl, Ber. Bunsenges. Phys. Chem. **74**, 1148 (1970)
31. K. Giewekemeyer, M. Beckers, T. Gorniak, M. Grunze, T. Salditt, and A. Rosenhahn, Optics Express **19**, 1037 (2011)
32. Martin Dierolf, Andreas Menzel, Pierre Thibault, Philipp Schneider, Cameron M. Kewish, Roger Wepf, Oliver Bunk, and Franz Pfeiffer, Nature **467**, 436–439 (2010)
33. Roland Wiesendanger, Rev. Mod. Phys. **81**, 1495–1550 (2009)
34. W. Chao, B. H. Harteneck, J. A. Liddle, E. H. Anderson, and D. T. Attwood, Nature **435**, 1210 (2005)
35. E. Anderson and W. Chao, private communication.
36. J. Vila-Comamala, K. Jefimovs, J. Raabe, T. Pilvi, R. H. Fink, M. Senoner, A. Maaßdorf, M. Ritala, and C. David, Ultramicroscopy **109**, 1360-1364 (2009)
37. P. Guttmann, S. Werner, G. Schneider, S. Rehbein, S. Heim, Phys. Rev. Lett. **103**, 110801 (2009)
38. T. Shinjo, T. Okuno, R. Hassdorf, K. Shigeto, and T. Ono, Science **289**, 930 (2000)
39. A. Wachowiak, J. Wiebe, M. Bode, O. Pietzsch, M. Morgenstern, and R. Wiesendanger, Science **298**, 577 (2002)
40. J. Miltat and A. Thiaville, Science **298**, 555 (2002)
41. C. Phatak, M. Tanase, A.K. Petford-Long, and M. DeGraef, Ultramicroscopy **109**, 264 (2009)
42. J. Raabe, R. Pulwey, R. Sattler, T. Schweinbock, J. Zweck, and D. Weiss, J. Appl. Phys. **88**, 4437–4439 (2000)
43. J.K. Ha, R. Hertel, and J. Kirschner, Phys. Rev. B **67**, 224432 (2003)

44. S.B. Choe, Y. Acremann, A. Scholl, A. Bauer, A. Doran, J. Stöhr, and H. A. Padmore, Science **304**, 420 (2004)
45. J. Raabe, C. Quitmann, C. H. Back, F. Nolting, S. Johnson, and C. Buehler, Phys. Rev. Lett. **94**, 217204 (2005)
46. K. Buchanan, P.E. Roy, M. Grimsditch, F.Y. Fradin, K.Yu. Guslienko, S.D. Bader, and V. Novosad, Nature Phys. **1**, 172 (2005)
47. S. Kasai, Y. Nakatani, K.. Kobayashi, H. Kohno, and T. Ono, Phys. Rev. Lett. **97**, 107204 (2006)
48. B. Van Waeyenberge, A. Puzic, H. Stoll, K. W. Chou, T. Tyliszczak, R. Hertel, M. Fähnle, H. Brückl, K. Rott, G. Reiss, I. Neudecker, D. Weiss, C. H. Back, and G. Schütz, Nature **444**, 461 (2006)
49. K. Yamada, S. Kasai, Y. Nakatani, K. Kobayashi, H. Kohno, A. Thiaville, and T. Ono, Nature Mater. **6**, 270 (2007)
50. P. Fischer, M.-Y. Im, S. Kasai K. Yamada, T. Ono, A. Thiaville , Phys. Rev. B **83**, 212402 (2011)
51. P. Fischer, M.-Y. Im, C. Baldasseroni, C. Bordel, F. Hellman, J.-S. Lee, C.S. Fadley, J. Electron Spectrosc. Relat. Phenom. (2013), http://dx.doi.org/10.1016/j.elspec.2013.03.012
52. P. Fischer, T. Eimuller, G. Schutz, M. Kohler, G. Bayreuther, G. Denbeaux, and D. Attwood, J. Appl. Phys. **89**, 7159–7161 (2001)
53. M.-Y. Im, P. Fischer, Y. Keisuke, T. Sato, S. Kasai, Y. Nakatani, and T. Ono, Nature Comm. **3**,983 (2012)
54. S.-H. Chung, D.T. Pierce, and J. Unguris, Ultramicroscopy **110**, 177–181 (2010)
55. S. Kasai, P. Fischer, M-Y. Im, K. Yamada, Y. Nakatani, K. Kobayashi, H. Kohno, and T. Ono, Phys. Rev. Lett. **101**, 237203 (2008)
56. N. Ohshima K. Nakano and, D. Chiba and, S. Kasai, T. Sato, Y. Nakatani, K. Sekiguchi, K. Kobayashi, , and T. Ono, Appl. Phys. Lett. **99**, 262505 (2011)
57. B. Pigeau, G. de Loubens, O. Klein, A. Riegler, F. Lochner, G. Schmidt, L. W. Molenkamp, V. S. Tiberkevich, and A. N. Slavin, Appl. Phys. Lett. **96**, 132506 (2010)
58. A. Drews, B. Krüger, G. Meier, S. Bohlens, L. Bocklage, T. Matsuyama, and M. Bolte, Appl. Phys. Lett. **94**, 062504 (2009)
59. S.K. Kim, K.S. Lee, Y.S. Yu, and Y.S. Choi, Appl. Phys. Lett. **92**, 022509 (2008)
60. S. Barman, A. Barman, and Y. Otani, J. Phys. D: Appl. Physics **43**, 335001 (2010)
61. Y.S. Yu, H. Jung, K.S. Lee, P. Fischer, and S.K. Kim, Appl. Phys. Lett. **98**, 052507 (2011)
62. K. Yu. Guslienko, B.A. Ivanov, V. Novosad, Y. Otani, H. Shima, and K. Fukamichi, J. Appl. Phys. **91**, 8037 (2002)
63. Y.S. Choi, J.Y. Lee, M.W. Yoo, K.S. Lee, K.Y. Guslienko, and S.K. Kim, Phys. Rev. B **80**, 012402 (2009)
64. K.Yu. Guslienko and V. Novosad, J. Appl. Phys. **96**, 4451 (2004)
65. S.K. Kim, Y.S. Choi, K.S. Lee, K.Y. Guslienko, and D.E. Jeong, Appl. Phys. Lett. **91**, 082506 (2007)
66. S. Gliga, R. Hertel, and C. M. Schneider, J. Appl. Phys.**103**, 07B115 (2008)
67. M.W. Yoo, K.S. Lee, D.E. Jeong, and S.K. Kim, Phys. Rev. B **82**, 174437 (2010)
68. D.J. Keavney, X.M. Cheng, and K.S. Buchanan, Appl. Phys. Lett. **94**, 172506 (2009)

69. Ki-Suk Lee, SangKook Choi, and Sang-Koog Kim, Appl. Phys. Lett. **87**, 192502 (2005)
70. M. Fähnle R. Hertel, S. Gliga and C.M. Schneider, Phys. Rev. Lett. **98**, 117201 (2007)
71. B. Van Waeyenberge, A. Puzic, H. Stoll, K. W. Chou, T. Tyliszczak, R. Hertel, M. Fähnle, H. Brückl, K. Rott, G. Reiss, I. Neudecker, D. Weiss, C. H. Back, and G. Schütz, Nature **444**, 461 (2006)
72. H. Jung, K.-S. Lee, D.-E. Jeong, Y.-S. Choi, Y.-S. Yu, D.-S. Han, A. Vogel, L. Bocklage, G. Meier, M.-Y. Im, P. Fischer, and S.-K. Kim, NPG - Scientific Reports **1**, 59 (2011)
73. J. Hemminger : From quanta to the continuum : Opportinities For Mesoscale Science, A Report from the Basic Energy Sciences, University of California, Irvine, U.S. Department of Energy September 2012, Prepared by the BESAC Subcommittee on Mesoscale Science. http://science.energy.gov/ /media/bes/pdf/reports/files/OFMS_rpt.pdf (2012). Accessed 08 Apr 2013
74. C.A. Larabell and K.A. Nugent, Curr Opinion in Struct. Biology **20**, 623 (2010)
75. D. Rüffer, R. Huber, P. Berberich, S. Albert, E. Russo-Averchi, M. Heiss, J. Arbiol, A. Fontcuberta i Morral, and D. Grundler, Nanoscale **4**, 4989–4995 (2012)
76. A.X. Gray, F. Kronast, C. Papp, S.-H. Yang, S. Cramm, I. Krug, F. Salmassi, E. Gullikson, D. Hilken, E. Anderson, P. Fischer, C.M. Schneider, and C.S. Fadley, Appl. Phys. Lett. **97**, 062503 (2010)
77. G. Denbeaux, P. Fischer, F. Salmassi, K. Dunn, and J. Evertsen, In *Proc. 8th Int. Conf. x-ray Microscopy*, eds. S. Aoki, Y. Kagoshima and Y. Suzuki (IPAP Conf. Series 7, 2006) pp.375–386
78. Parkinson DY, Knoechel C, Yang C, Larabell CA, and Le Gros MA, J. Struct. Biol. **177**, 259–266 (2012)

Chapter 6
A Student's Introduction to Resonant Inelastic Soft X-ray Scattering

Sorin G. Chiuzbăian

Abstract Recent instrumental advances have opened an important window for studying magnetic excitations with resonant inelastic x-ray scattering (RIXS). This contribution outlines the main theoretical and experimental aspects underlying this spectroscopic technique. The aspects discussed cover self-absorption corrections, scattering geometry, resonant scattering cross sections and methods for identifying and exploiting spectral information. State of the art diffraction grating spectrometers are assessed in view of RIXS opportunities that lie ahead.

6.1 Introduction

The last decade has witnessed unprecedented advances in the use of resonant inelastic x-ray scattering (RIXS) for exploring neutral electronic, magnetic and vibrational excitations of matter. Amongst the factors that can be identified as being decisive for this development, we would stress the advances in the availability and production of highly brilliant x-ray beams, of course, but also progress in the fabrication of optical elements and very low noise two-dimensional detector arrays with high spatial resolution. They make it

Sorin G. Chiuzbăian
Laboratoire de Chimie Physique-Matière et Rayonnement, Université Pierre et Marie Curie and CNRS (UMR 7614), 11 rue Pierre et Marie Curie, 75005 Paris, France; e-mail: gheorghe.chiuzbaian@upmc.fr

E. Beaurepaire et al. (eds.), *Magnetism and Synchrotron Radiation: Towards the Fourth Generation Light Sources*, Springer Proceedings in Physics 151,
DOI: 10.1007/978-3-319-03032-6_6,

possible to progressively zoom-in on the energy scale that is relevant to the excitations. At present excitations with characteristic energies from several eV down to few tenths of an eV can be probed with element and momentum sensitivity. The focus of the technique has moved from charge excitations to studies on magnetic excitations and has opened exciting perspectives for investigating the magnetism of complex materials. The design of future soft x-ray instruments target energy resolutions of a few hundredths on an eV.

In the spirit of the Mittelwihr school, this contribution is meant to provide young scientists with a reliable starting point to develop their interest in the RIXS technique. Both theoretical and experimental aspects are considered more for a pedagogical approach than a detailed exploration of particular scientific cases. The few selected examples are intended to make the subject more accessible. For concision, they are restricted to RIXS with extreme ultraviolet photons (roughly 20 eV to 300 eV) and soft x-rays (300 eV to a few keV).

Some excellent review papers and books cover the subject in depth. The progress of RIXS in solids was reviewed by Kotani and Shin [1], Kotani [2] and more recently by Ament et al. [3]. Studies on strongly correlated electron systems with hard x-rays were recently reviewed by Rueff and Shukla [4]. The books by Schülke [5] and de Groot and Kotani [6] will provide the reader with comprehensive explanations. Results and theoretical perspectives for the use of RIXS in gases were presented by Gel'mukhanov and Ågren [7]. The contribution by M. Altarelli in this volume delivers a concise but complete introduction to photon scattering processes. Students are highly encouraged to consult the book by Stöhr and Siegmann [8] for an excellent introduction to x-ray spectroscopies and their application to magnetism.

6.2 Recording RIXS spectra

RIXS is a "photon-in photon-out" technique in which monochromatic x-rays with energy $\hbar\omega_{in}$ are scattered by a sample via two dipole-allowed transitions, the creation of a core hole and its decay. With hard x-rays higher order transitions, as for instance quadrupole contributions, can be involved. The sample can be solid, liquid or gaseous. The scattered x-rays are examined by means of a spectrometer which delivers the number of photons with the energy $\hbar\omega_{out}$ scattered within the acceptance angle of the instrument $\mathrm{d}\Omega$ and within an energy interval $\mathrm{d}(\hbar\omega_{out})$. Part of the x-rays are scattered elastically

($\hbar\omega_{out} = \hbar\omega_{in}$) and give rise to an elastic peak. The others are inelastically scattered thus leaving a part of their energy in the sample as neutral excitations: $\hbar\omega_{tr} = \hbar\omega_{in} - \hbar\omega_{out}$. Very small energy transfers might remain undetected when the energy resolution is not sufficient. In such cases the elastic peak averages over very small energy losses and is sometimes labeled "quasi elastic" ($\hbar\omega_{out} \approx \hbar\omega_{in}$). The scattering is equally accompanied by a momentum transfer $\hbar\mathbf{q}$ which depends on the energy of the photons and the scattering geometry (scattering angle 2θ, Fig. 6.1): $\hbar\mathbf{q} = \hbar\mathbf{k}_{in} - \hbar\mathbf{k}_{out}$. For photon energy losses of less than a few eV and average energies higher than a few hundreds of eV, one can approximate $k_{in} \approx k_{out}$ and therefore $q \approx 2k_{in}\sin\theta$.

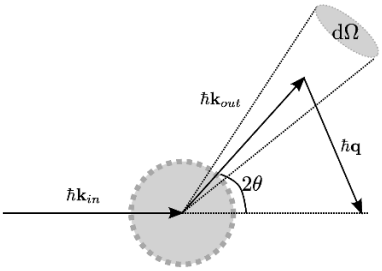

Fig. 6.1 Schematics of the scattering process

6.2.1 The absorption spectrum

For the scattering process to be resonant, the energy of the incoming photons $\hbar\omega_{in}$ is tuned to a specific absorption edge. Consequently the first step of a RIXS experiment is recording an x-ray absorption spectrum (XAS) to characterize the shape of the resonance and select the excitation energies across the absorption threshold. Soft x-ray photons cover, for instance, the $M_{2,3}$ ($3p-3d$) and $L_{2,3}$ ($2p-3d$) edges of $3d$ transition metals, the $N_{2,3}$ ($4p-5d$), $M_{4,5}$ ($3d-4f$) and $M_{2,3}$ ($3p-5d$) edges of lanthanides as well as the K ($1s-2p$) edges of light elements (C to F).

The XAS spectrum describes the number of core-hole excited states as a function of the energy of the incoming light. Ideally XAS is measured in the transmission mode. This means recording the x-rays transmitted through

a sample of given thickness x according to the Beer-Lambert law: $I(\hbar\omega,x) = I(\hbar\omega,0)\exp[-\mu(\hbar\omega)x]$, where $\mu(\hbar\omega)$ is the absorption coefficient at the photon energy $\hbar\omega$ and has the dimension of $[\text{length}^{-1}]$. The quantity $1/\mu(\hbar\omega)$ is called the attenuation length and represents the depth from the surface where the intensity drops by a factor of e. With soft x-rays the attenuation lengths are on the order of micrometers or less. Preparing solid samples with such thicknesses for XAS measurements in transmission mode is difficult in most cases and therefore some other modes are usually used to record absorption. When core-holes are created in the soft x-ray range, the Auger decay channel largely dominates the core-hole filling. Auger electrons travel to the surface and give rise to electron cascades resulting from inelastic collisions. The mean free path of the electrons is only on the order of few tens of angstroms, that is equivalent to a few lattice constants [9]. Electrons reaching the surface with sufficient energy will overcome the work function and escape from the sample. By measuring the sample drain current with a picoammeter it becomes possible to get a measure of the absorption in the *total electron yield* (TEY) mode. Similar to the x-ray attenuation length, it is convenient to define an *electron yield sampling depth* representing the depth from the surface which contributes to 63% of the TEY XAS signal [8]. Typical values for the electron yield sampling depth are on the order of nanometers with soft x-rays. Therefore, while TEY XAS measurements probe samples deeper than photoelectron emission measurements [9], the spectra originate from a region within a few nanometers from the surface and thus are subject to enhanced surface sensitivity.

An alternative for XAS measurements is recording the radiative decay channel with a photon detector (photodiode or multi-channel plate for instance). Such *fluorescence-yield* (FY) measurements conserve the probing depth of the x-rays. However FY XAS measurements should be carefully interpreted as the signal is not simply proportional to the absorption probability [10]. In fact the FY intensity contains the energy integrated RIXS cross section.

In the case of gas samples, the dimensions of the cell containing the gas can generally be adapted to allow for taking XAS data in the transmission mode.

6.2.2 Fluorescence and Raman-like losses

Figure 6.2 displays a model set of RIXS results. The XAS spectrum defines the incoming light energies for recording the RIXS spectra. To a certain extent, this means tuning the scattering via some particular core-hole state. In fact several core-hole states may be excited for a given fixed incoming photon energy.

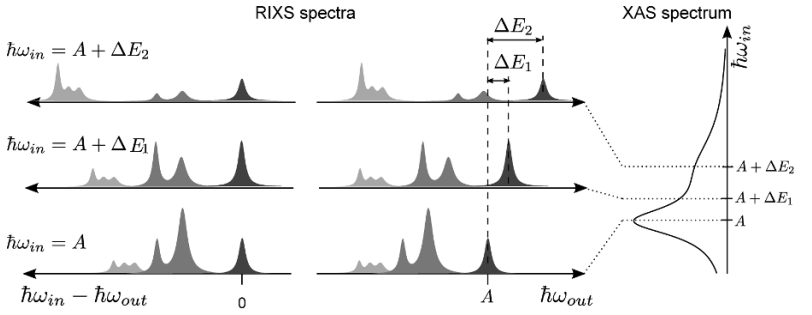

Fig. 6.2 Fluorescence and Raman-like spectral features in RIXS spectra. Spectra in left panel are displayed against transferred energy. The center panel shows same spectra displayed with the energy of scattered photons as abscissa. The panel on the right indicates the shape of the absorption threshold

The RIXS spectrum consists of three main regions:

i) The elastic peak region displaying the photons which are elastically or quasi-elastically scattered, within the resolving power of the experiment. Taking the transferred energy $\hbar\omega_{tr} = \hbar\omega_{in} - \hbar\omega_{out}$ as abscissa (Fig. 6.2, left), the elastic peak will stay at $\hbar\omega_{tr} = 0$. Obviously when the spectrum is represented against $\hbar\omega_{out}$ (see middle panel of Fig. 6.2), the elastic peak follows the variation of the incoming light energy.

ii) Certain energy losses can be found at constant transferred energy $\hbar\omega_{tr}$ with an intensity modulated by the position of $\hbar\omega_{in}$ on the XAS spectrum. These are similar to the Stokes peaks in classical Raman spectroscopy and are often quoted as resonant Raman peaks. The peaks correspond to well defined neutral excitations which are brought about during the scattering process. These will follow the displacement of the elastic peaks when taking $\hbar\omega_{out}$ as abscissa.

iii) Spectral weight which stays at constant emission energy $\hbar\omega_{out}$ is denoted as fluorescence. Indeed, exciting well above the resonance threshold, $\hbar\omega_{in} \gg A$, results in decoupled absorption and emission processes. In other words the emission does not feature a dependence on the incoming light energy. Even when the incoming photons are tuned to the resonance, some of the spectral weight still arises from fluorescence. Disentangling fluorescence spectral weight from Raman-like features may turn out to be complicated but remains essential for the interpretation of the RIXS spectra.

6.2.3 Self-absorption effects and sample orientation

The scattered photons are partially absorbed on their way to the surface of the sample, in the same manner the incoming light is gradually absorbed when propagating through the sample (see § 6.2.1). This results in a reduction of the measured RIXS signal and a modulation of the spectral intensities. This aspect is referred to as "self-absorption" and is briefly illustrated below.

We follow Eisebitt et al. [11] to consider the general case of x-rays impinging on the surface at a grazing angle α, the scattered photons being measured in a direction making the angle β with the surface (Fig. 6.3). The intensity of incoming photons with the energy $\hbar\omega_{in}$ along the direction x can be written as $I(\hbar\omega_{in},x) = I_0 \exp(-\mu_{in}x)$, where $\mu_{in} = \mu(\hbar\omega_{in})$ is the absorption coefficient for photons with the energy $\hbar\omega_{in}$. For the purpose of a simplified presentation we also neglect the non resonant absorption by other core levels or valence levels. Along dx at distance x from the surface, the number of absorbed photons is given by: $-\mathrm{d}I = I_0\mu_{in}\exp(-\mu_{in}x)\mathrm{d}x$. Part of these photons are scattered according to the probability $P_S(\hbar\omega_{in},\hbar\omega_{out})$ which corresponds to the theoretical RIXS spectrum. In other words, a number $P_S(\hbar\omega_{in},\hbar\omega_{out})I_0\mu_{in}\exp(-\mu_{in}x)\mathrm{d}x$ of photons with the energy $\hbar\omega_{out}$ will travel to the surface following a path y. Only $P_S(\hbar\omega_{in},\hbar\omega_{out})I_0\mu_{in}\exp(-\mu_{in}x)$ $\exp(-\mu_{out}y)\mathrm{d}x$ of these photons will reach the surface, the rest being absorbed on the way out. Here $\mu_{out} = \mu(\hbar\omega_{out})$ represents the absorption coefficient for photons with the energy $\hbar\omega_{out}$. Neglecting solid angles, the measured intensity is obtained by integrating between 0 and x_d where $x_d = d/\sin\alpha$ with d the thickness of the sample

$$I(\hbar\omega_{in},\hbar\omega_{out}) = P_S(\hbar\omega_{in},\hbar\omega_{out}) I_0 \mu_{in} \int_0^{x_d} \exp\left[-\left(\mu_{in} + \mu_{out}\frac{\sin\alpha}{\sin\beta}\right)x\right] \mathrm{d}x\,. \tag{6.1}$$

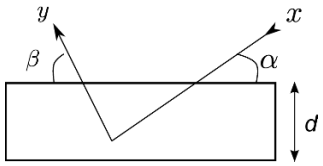

Fig. 6.3 Scheme for calculation of self-absorption effects

By calculating the integral and taking into account that the thickness of the sample d is far larger than the attenuation length, the measured intensity can be written as

$$I(\hbar\omega_{in},\hbar\omega_{out}) = P_S(\hbar\omega_{in},\hbar\omega_{out}) I_0 \frac{\mu_{in}}{\mu_{in} + \mu_{out}\dfrac{\sin\alpha}{\sin\beta}}\,. \tag{6.2}$$

The simplified relation (6.2) makes it easy to exemplify the self-absorption effects in an idealized case. We consider an XAS spectrum consisting of a single white line (see Fig. 6.4, upper left panel). For best visualization, the theoretical RIXS spectrum (upper right panel of Fig. 6.4) is considered to display an elastic peak and two Raman losses of equal intensity, for all incoming energies. The latter are marked with arrows on the XAS spectrum and denoted "1" (-1 eV from the XAS maximum) and "2" ($+1$ eV from the XAS maximum) and correspond to the points encompassing the full-width at half maximum of the absorption line. It is obvious that orienting the sample at almost normal incidence results in an inconvenient reduction of the measured intensity. However, even when the grazing incidence is chosen, the self-absorption can result in modulation of the measured intensities. For instance, if excitation "2" is considered, the elastic peak at $\hbar\omega_{out} = +1$ eV and the second loss at $\hbar\omega_{out} = -1$ eV are subject to similar self absorption effects. On the contrary, the first loss would come out with a photon energy corresponding to the absorption maximum and therefore it is measured with reduced intensity.

Corrections for self-absorption effects are always recommended when essential information is to be extracted from the intensity of the spectral weights in the RIXS spectra.

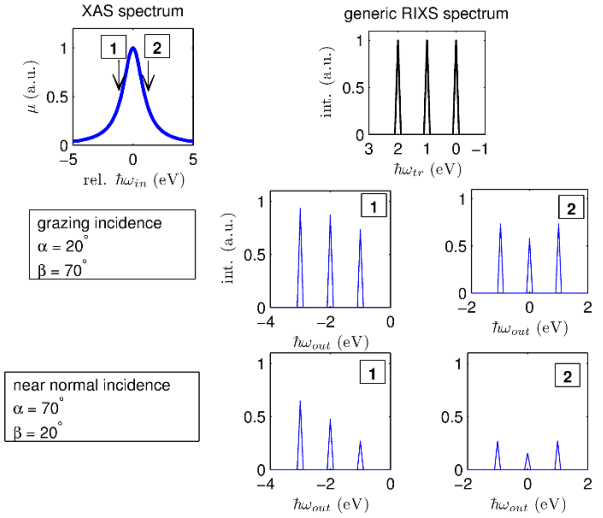

Fig. 6.4 Illustration of the self-absorption effects for two geometries at 90° scattering (see text and Fig. 6.3 for more details)

6.2.4 Scattering geometry

As indicated in § 6.2 the momentum transferred to the sample during the scattering process depends on the scattering angle 2θ and the photon energy: $q \approx 2k_{in} \sin\theta$. The momenta of interest are those that can be used to sample in sufficient detail and over a sufficient extension the Brillouin zone starting from the Γ point (center of the zone). Soft x-rays with energies from 500 to 1000 eV have wave vectors ranging from 2.53 Å^{-1} to 5.07 Å^{-1}. These values indicate that, in many cases, convenient scattering angles can be selected to map regions of interest in the first Brillouin zone. To illustrate this, Fig. 6.5

shows how photons with energies tuned to the Ni L_3 threshold would make it possible to map a large part of the first Brillouin zone of NiO. For simplicity we assume that all directions are possible for the incoming light wave vector with respect to the crystallographic axes. It should be noted, however, that when dealing with magnetic properties, as for instance the dispersion of magnetic excitations, it is necessary to take into account the magnetic Brillouin zone, which is smaller than the crystal Brillouin zone (see [12] for the case of NiO).

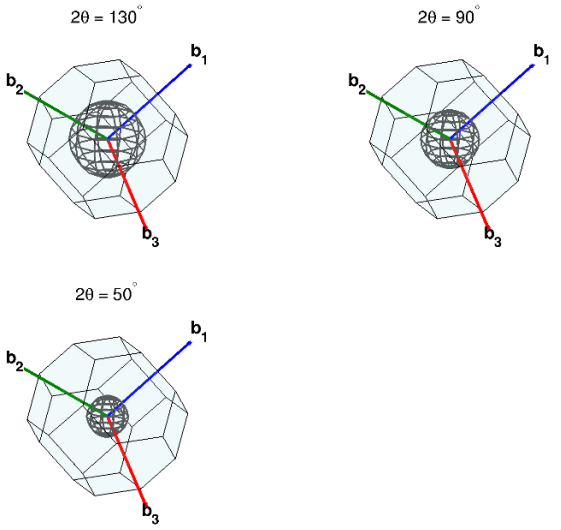

Fig. 6.5 Brillouin zone corresponding to the crystallographic primitive cell of NiO and the points (situated on the spheres) which can be accessed in RIXS experiments at the Ni L_3 edge ($\hbar\omega_{in} = 853\,\text{eV}$) with variable scattering angle and for all possible orientations of the sample. The transferred momenta are 0.80 Å^{-1}, 0.61 Å^{-1} and 0.43 Å^{-1}

Layered materials form a special case. For instance, cuprate superconductors have well defined sheets of CuO_2 planes. The crystallographic c parameter is substantially larger than the a and b lattice parameters. The magnetic excitations of interacting Cu^{2+} spins can propagate within the CuO_2 planes. It is therefore of interest to quantify the momentum transfer within the CuO_2

planes. Considering δ the angle between the transferred vector $\mathbf{q}$ and the vector $\mathbf{c}$ of the unit cell, the transferred momentum can be written $q_{\parallel} = q\sin\delta$. The expression of $q_{\parallel}$ indicates that momentum dependent measurements can be performed at fixed scattering angle ($q = \text{const.}$) by rotating the sample so as to modify the incidence angles at the CuO_2 planes.

6.3 RIXS cross section and Kramers-Heisenberg relation

Assuming constant detector efficiency and spectra corrected for self-absorption effects, the measured intensities of RIXS signal are directly proportional to the cross section of the inelastic scattering process. The scattering can be described in terms of the differential cross section $\mathrm{d}\sigma/\mathrm{d}\Omega$ which delivers the counting rate within a solid angle $\mathrm{d}\Omega$ in the $\mathbf{k}_{out}$ direction (see Fig. 6.1), normalized to the number of photons per unit time and unit surface incident on the system (see contribution by M. Altarelli in this volume and Ref. [13, 14])

$$\frac{\mathrm{d}\sigma}{\mathrm{d}\Omega} = \frac{\omega_{out}}{\omega_{in}}\frac{r_0^2}{m^2}\sum_f \left|\sum_n \frac{\langle\Phi_f|T^{(e)}|\Phi_n\rangle\langle\Phi_n|T^{(a)}|\Phi_i\rangle}{E_i+\hbar\omega_{in}-E_n-i\Gamma_n/2}\right|^2 \times\delta(E_i-E_f+\hbar\omega_{out}-\hbar\omega_{in})\,, \tag{6.3}$$

where $r_0 = e^2/(4\pi\varepsilon_0 mc^2) \approx 2.82\times10^{-15}$ m is the classical radius of the electron with m the mass of the electron, $T^{(a)} = \hat{e}_{in}\mathbf{p}e^{+i\mathbf{k}_{in}\mathbf{r}}$ and $T^{(e)} = \hat{e}^*_{out}\mathbf{p}e^{-i\mathbf{k}_{out}\mathbf{r}}$ are operators associated to the absorption and emission of a photon with $\mathbf{p}$ the electron momentum coupling to the electromagnetic vector potential $\mathbf{A}$ of the radiation, $\hat{e}_{in}$ ($\hat{e}_{out}$) the polarization vector of the incident (scattered) photon, $\hat{e}^*_{out}$ being the complex conjugate of $\hat{e}_{out}$. The expression (6.3) is known as the Kramers-Heisenberg relation. The differential cross section retains only the resonant part of the scattering process. The wave-functions $|\Phi_i\rangle$, $|\Phi_f\rangle$ and $|\Phi_n\rangle$ correspond to the initial state i, the final states f, as well as the intermediate states n (see Fig. 6.3.1). The final state can be the same as the initial state (elastic Rayleigh scattering) or some excited final state with the same number of electrons. Expression (6.3) contains some important aspects:

i) *Effective operators $T^{(a)}$ and $T^{(e)}$*
To calculate transition matrix elements $|\Phi_i\rangle \rightarrow |\Phi_n\rangle$ and $|\Phi_n\rangle \rightarrow |\Phi_f\rangle$, it is convenient to observe that $e^{+i\mathbf{kr}}$ can be evaluated in terms of series expansion $e^{+i\mathbf{kr}} = 1 + i\mathbf{kr} + (i\mathbf{kr})^2/2 + \cdots$. The series is rapidly converging

(see M. Altarelli) as $\mathbf{kr} \to 0$. A rough estimation of the $\mathbf{kr}$ values can be obtained from the energies of absorption threshold $\hbar\omega_{in}$ and the atomic number Z according to $\mathbf{kr} \approx \sqrt{\hbar\omega_{in}}/(80Z)$ [15]. For copper ($Z = 29$), the M (3p $\to$ 3d) and L ($2p \to 3d$) thresholds have approximate energies 75 eV and 930 eV, respectively, leading to $\mathbf{kr}$ on the order of 0.004 to 0.01. The exponential is practically reduced to 1 which defines what is known as the *electric dipole* approximation. Such transition can be visualized by charge movements along an axis. The remaining expression $\hat{e}\mathbf{p}$ contains both position coordinates and momentum but can be expressed in spatial form only as $\hat{e}\mathbf{r}$ using the relation $\mathbf{p} = (m/i\hbar)[\mathbf{r}, H]$. One obtains the known form of the electric dipole transition operators $T = \hat{e}\mathbf{r}$.

ii) *Selection rules*

An intuitive approach to selection rules can be obtained from symmetry considerations (see for example Ref. [16]). In systems with inversion symmetry, electric dipole transitions are only possible between orbitals with different parity, that is between even (*gerade* or *g*) and odd (*ungerade* or *u*) orbitals. The well known orbital selection rule forbids direct $-d$ or $f - f$ electric dipole transitions. The particularity of the x-ray scattering cross section $\mathrm{d}\sigma/\mathrm{d}\Omega$ is that it involves two dipole allowed transitions. Therefore it grants access to excited neutral final states with the same symmetry as the initial state through $u \to g \to u$ or $g \to u \to g$ sequences. This represents an important benefit compared to other techniques like electron energy loss spectroscopy [17] or optical spectroscopy. Though the latter can access $d - d$ or $f - f$ excitations through relaxation mechanisms, such as the breaking of the inversion symmetry due to lattice vibrations. Another

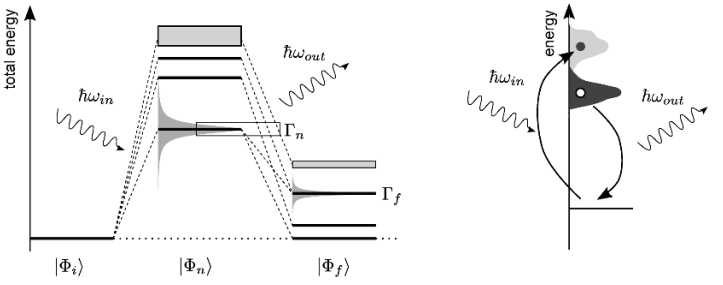

Fig. 6.6 (Left) Scattering paths in the total energy scheme. Due to finite width of the intermediate state, several scattering paths are open even if $\hbar\omega_{in}$ is perfectly defined. (Right) A *direct RIXS* process is sketched considering the electron energy as axis of ordinates

important aspect is the conservation of the spin through a dipole transition as the electric dipole operator does not act on the spin. However, in the intermediate state $|\Phi_n\rangle$, the presence of a core-hole involved in spin-orbit coupling results in the spin not being a "good" quantum number for describing the state of the system [18]. This has opened up the perspective of being able to study magnetic excitations with RIXS and sparked numerous studies in strongly correlated electron systems.

iii) *Resonance condition*

The validity of expression (6.3) is strictly restricted to incoming photon energies matching an absorption threshold $\hbar\omega_{in} \approx E_n - E_i$. Away from resonance, the expression must be completed with the non-resonant terms, as for instance the Thomson scattering. The division by zero is avoided by the complex part $i\Gamma_n/2$ which corresponds to the Lorentzian lifetime broadening Γ_n (FWHM) of the intermediate core-hole state $|\Phi_n\rangle$.

iv) *Core-hole lifetime*

Three processes compete for the spontaneous decay of the core-hole: the radiative channel (emission of a photon), the Auger channel and the Coster-Kronig decay (ejection of an electron). The time the core-hole "stays" in the system for interactions is defined by the decay process with the highest probability. In the case of 3d transition metals, the decay of $2p$ holes ($L_{2,3}$ edges) is dominated by Auger processes while $3p$ ($M_{2,3}$ edges) holes are mainly subject to Coster-Kronig decays [19]. Γ_n is on the order of one eV for core-holes created in the soft x-ray domain. Actually only about 0.1% of the core-holes created in the absorption lead to emission of a photon, which explains the very small scattering cross section. The link between energy broadening Γ_n and core-hole lifetime τ is established by the uncertainty relation $\Gamma_n\tau = \hbar$. In general Γ_n is taken to be constant across the absorption threshold for a given decay channel.

v) *Final state broadening*

The energy broadening of the core-hole does not propagate into the final states. Final states are broadened only by the intrinsic lifetime of final states Γ_f (Lorentz distribution). The latter is very small or negligible for core-hole free states having long lifetimes $\Gamma_f \ll \Gamma_n$. To point out this important aspect, the δ function in (6.3) can be replaced with:

$$\frac{\Gamma_f/(2\pi)}{(E_i - E_f + \hbar\omega_{in} - \hbar\omega_{out})^2 + (\Gamma_f/2)^2} \,. \tag{6.4}$$

This property is sometimes noted "subnatural" width or "Raman narrowing" of the measured final states.

vi) *Scattering paths and interference effects*

Among the various possible intermediate states $|\Phi_n^{(1)}\rangle$, $|\Phi_n^{(2)}\rangle$, $\cdots$, several can contribute to the global probability for reaching some given final state as long as selection rules are obeyed (see Fig. 6.3.1). The summation in (6.3) runs over products of amplitudes $\langle\Phi_f|T^{(e)}|\Phi_n\rangle\langle\Phi_n|T^{(a)}|\Phi_i\rangle$ which are weighted by the complex denominator. In general this would lead to a result like: $(\sum_t z_t)^2 = \sum_t z_t^2 + 2\sum_{t<s} z_t z_s$ with z_t complex values. If the cross terms $z_t z_s$ are sufficiently small compared to z_t^2, the square of the sum in $\mathrm{d}\sigma/\mathrm{d}\Omega$ can be simply written as the sum over the squares (see also [20]). Neglecting constants in (6.3), it becomes possible to write a simplified form of the scattering spectral shape [21]:

$$F(\hbar\omega_{in},\hbar\omega_{out}) = \sum_f \sum_n \frac{\langle\Phi_f|T^{(e)}|\Phi_n\rangle^2\langle\Phi_n|T^{(a)}|\Phi_i\rangle^2}{(E_i+\hbar\omega_{in}-E_n)^2+\Gamma_n^2/4} \times\delta(E_i-E_f+\hbar\omega_{out}-\hbar\omega_{in})\,. \tag{6.5}$$

The physical assumption made here to simplify the calculation is that the scattering probability can be written as a product of absorption and emission probabilities; each intermediate state can be excited with well-defined rate and this because there is no interference between "single" scattering paths $|\Phi_i\rangle \rightarrow |\Phi_n^{(a)}\rangle \rightarrow |\Phi_f^{(b)}\rangle$. However, this is generally not the case. Tuning the photon energy to a defined intermediate state also involves reaching the others with a reduced but finite amplitude. This aspect is usually termed an "interference effect". It is no longer possible to speak in terms of the probability of scattering via a well-defined intermediate core-hole state during the scattering process.

vii) *Energy conservation and virtual intermediate states*

As mentioned above, the conservation of the energy should be considered between initial $|\Phi_i\rangle$ and final states $|\Phi_f\rangle$ as indicated by the δ function. Due to finite broadening of the intermediate state, for the absorption step to the intermediate states $|\Phi_n\rangle$ and emission step from these states, the energy conservation is relaxed. Therefore $|\Phi_n\rangle$ are often termed "virtual".

viii) *Momentum conservation*

Analogous to the energy conservation, it is possible to apply momentum conservation only between initial and final states and precisely determine the momentum of excitations created during the scattering process.

ix) *Duration of the scattering process*
By considering the evolution in time for the wave packet of the intermediate state, Gel'mukhanov and Ågren [7] introduced the concept of "scattering duration time" $\tau_{sc} = 1/\sqrt{\Sigma^2 + (\Gamma_n/2)^2}$, where Σ represents the detuning with respect to the absorption edge $\Sigma = \hbar\omega_{in} - E_n + E_i$. The expression of τ_{sc} indicates that detuning from the absorption threshold grants some control over the dynamical processes which determine the RIXS spectral weight.

6.3.1 Elementary excitations

RIXS probes a broad range of excitations, going from inter-site electron transfers (charge transfer excitations) on the order of several eV, down to vibrational excitations (phonons in solids) at a few hundredths of an eV from the elastic peak (see Fig. 6.3.1). In this section the nature of different excitations is briefly discussed and accompanied by some examples. The reader may refer to the reviews indicated in § 6.1 for more extensive explanations.

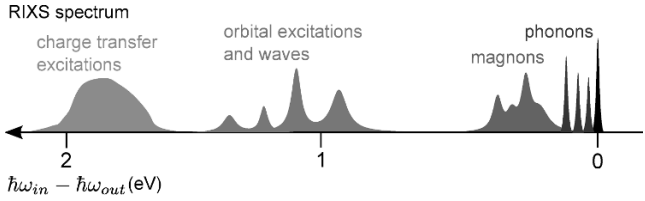

Fig. 6.7 Energy scale for different types of elementary excitations observed with RIXS in strongly correlated electron systems (after [3])

6.3.2 Charge transfer (CT) excitations

For an electron to hop between two sites in the crystal, an energy higher than the electronic gap must be provided. Such excitations across the gap are of paramount importance for understanding gap formation, as for instance in

the case of metal to insulator transitions. The relevance of CT excitations is equally relevant for the superexchange mechanisms of magnetic interactions.

The scientific case of NiO, mentioned in § 6.2.4, turns out to be an appropriate example to illustrate the excitations discussed here (see [22] for an overview on the NiO electronic structure). NiO features a cubic crystal structure of NaCl type. Each Ni^{2+} ion (electronic configuration [Ar]$3d^8 4s^0$) is octahedrally (O_h) surrounded by six O^{2-} ions. The antiferomagnetic coupling between the Ni spin magnetic moments is ensured by the superexchange via the O $2p$ states.

In strongly correlated materials such as NiO, the gap is determined by combining two different energy scales. One is due to the charge-transfer energy Δ needed to transfer an electron from a ligand L, here the oxygen, to the metal site: $\Delta = E(\mathrm{d}^{n+1}\underline{L}) - E(\mathrm{d}^n L)$ with $n = 8$ for Ni^{2+}. The other is the Coulomb repulsion energy U spent for an electron removal from a metal site and electron addition on another one: $U = E(\mathrm{d}^{n+1}) + E(\mathrm{d}^{n-1}) - 2E(\mathrm{d}^n)$. The gap is ruled by the smallest of these energies (see the original paper by Zaanen, Sawatzky and Allen [23] or more recently [24]) and accounts for the width W of the ligand band (here the O $2p$; states). Within this framework, NiO is identified as being in the charge-transfer limit.

What is the mechanism that triggers inter-site electron hopping during photon scattering? A simplified picture is obtained if one takes into consideration the intermediate core-hole state: the Coulomb interaction between the valence electrons and the core-hole pulls down the valence states. Electrons from ligand sites can compensate the apparent local charge deficit and therefore final states with ligand to metal electron transfers can be observed. A more rigorous description can be obtained within the Anderson impurity model [25]. The Ni ground state in NiO is described as a mixture between $d^8 L$, $d^9\underline{L}$ and $d^1 0\underline{L}^2$ states; it results in bonding, non-bonding and anti-bonding states which have finite population probabilities in both final and initial states of the scattering.

The way CT excitations are revealed in RIXS spectra is obviously modulated by the choice of the absorption edge. In the case of RIXS measurements performed at Ni $M_{2,3}$ threshold in NiO, the intensity of the CT spectral weight was below the detection limit [26], an aspect confirmed later for by a Co $M_{2,3}$ RIXS study of CoO [27]. For measurements at Ni $L_{2,3}$ edge in NiO, CT excitations with large spectral weight were found when exciting about 4 eV above the L_3 maximum [28]. Due to ligand band width W of several eV, the CT excitations are spread over a relatively broad range of transferred energies. It is also interesting to mention the hard x-ray studies of NiO at the Ni K edge [29]; it was shown that the intensity of the CT excitations is almost entirely

suppressed when applying high pressure (100 GPa) on the crystal, while their typical energies are conserved. It was suggested that the pressure leaves parameters like U and Δ unchanged while W is increased leading to a reduction of the electronic gap.

More complex CT excitations in NiO were also measured with incoming photons tuned to the O K edge [30] which revealed Ni to Ni non-local charge transfers taking place via the O 1s core-hole state.

6.3.3 Orbital excitations

The electronic structure of an isolated 3d transition metal ion with the electronic configuration d^n consists of a single fivefold degenerate energy level. In the case of Ni^{2+}, the term symbol ^{2S+1}L of the ground state is ^3F, four other terms designate excited states: ^1D, ^3P, ^1G and ^1S. The separation between the energies of these terms arises due to electron-electron repulsion. In the presence of an octahedral crystal field O_h, the degeneracy of the single atomic level is partially lifted, the atomic orbital being branched to a doublet e_g and a triplet t_{2g}. The atomic term symbol ^3F is spit into $^3A_{2g}$, $^3T_{2g}$ and $^3T_{1g}$, the ground state remains $^3A_{2g}$. The latter corresponds to a filled t_{2g} level and two spin-up electrons on e_g. Further ligand field terms are $^1E_{1g}$ and $^1T_{2g}$ originating from the atomic term ^1D, and $^3T_{1g}$ from ^3P. The others are derived in a similar manner (see [15, 31] for further details). The excited states correspond to a reorganization of the e_g and t_{2g} occupancy while the number of electrons stays constant and equal to eight. The representation of the ligand field term energies as function of the $10Dq$ value separating e_g and t_{2g} is known as Tanabe-Sugano diagram. In the case of the d^8 configuration, the separation between the term of the ground state $^3A_{2g}$ and the first excited term $^3T_{2g}$ matches the crystal field splitting $10Dq$.

During the resonant scattering process, any of the crystal field states can be reached in the final state. This powerful property is based on convenient orbital and spin selection rules (see § 6.3). Figure 6.8 shows the case of Ni $M_{2,3}$ RIXS measurements of NiO [26]. The spectra show a pure Raman regime, all losses being identified as orbital $d-d$ excitations. It becomes possible to "read out" the value of the crystal field splitting $10Dq = 1.05$ eV on the RIXS spectra.

The arguments exposed above were restricted to a local picture of the orbital excitations. It can be naively assumed that an on-site $d-d$ excitation

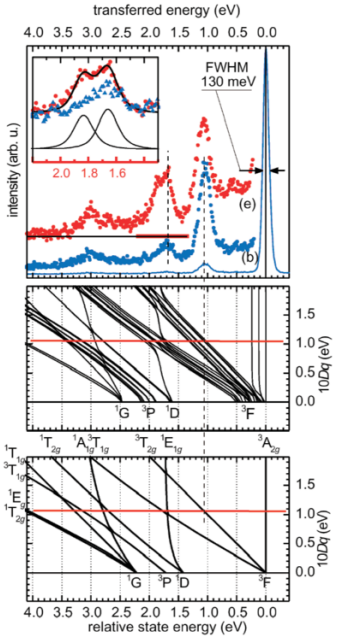

Fig. 6.8 $d-d$ excitations at the metal site in NiO studies with RIXS at the Ni $M_{2,3}$ threshold (from [26]). Lower panels shows the Tanabe-Sugano diagrams for d^8 in O_h field, the middle panel including the spin-orbit coupling and an exchange mean field. Upper panel displays the RIXS spectra taken at two energies across the absorption threshold

should have some impact on the orbital occupancy of the closest metal site through the mediation of ligand electronic states. Under favorable conditions, the orbital excitations would propagate through the crystal and give rise to an orbital wave or "orbiton", as originally proposed by Saitoh et al. [32]. Such propagating collective excitations are expected to feature dispersion. Clear evidence of orbital waves measured with RIXS was recently shown in the case of the spin-chain compound Sr_2CuO_3 by Schlappa et al. [33] (see Fig. 6.9).

6.3.4 Magnetic excitations

The possibility of exploring magnetic excitations with RIXS represents a major breakthrough for the technique. The mechanism that allows spin changes to be observed in resonant inelastic scattering processes is based on the large spin-orbit coupling present in the intermediate core-hole state. The angular

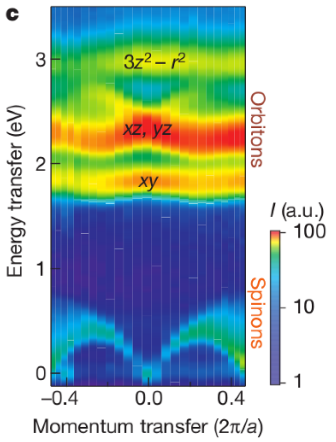

Fig. 6.9 Orbitons in Sr_2CuO_3 measured with RIXS at the Cu L_3 edge (from [33]). Cu^{2+} ions have a single hole in the d orbital; the position of the hole ($3z^2 - r^2$, xz, yz or xy) is indicated for all propagating orbital excitations

momentum of the photon is $L = 1$, so that $\Delta L_z = 0$, 1 or 2 can be exchanged through the coupling. Therefore magnetic excitations with $\Delta S_z = 0$, 1 or 2 can be created [3]. For simplicity it is instructive to deal with local "spin flips" in the case of NiO. In the absence of magnetic interactions, the ground state of Ni^{2+} in O_h symmetry is ${}^3A_{2g}$. NiO features an antiferromagnetic order with a Néel temperature of 523 K. The spin magnetic moments are aligned along the $\langle 11\bar{2} \rangle$ crystallographic direction. Each Ni^{2+} ion is subjected to six interatomic exchange interactions J with the surrounding Ni ions via the O $2p$; states. The result can be modeled as a mean magnetic field acting on the Ni^{2+} ions with an effective exchange strength $J_{\text{eff}} \approx 6J$. The mean field lifts the degeneracy of the ground state term ${}^3A_{2g}$ similar to a Zeeman splitting (see middle panel of Fig. 6.8 where $J_{\text{eff}} = 125$ meV is assumed). Three projections of the spin $S = 1$ are possible on the axis of quantization: the ground state with $S_z = -1$, as well as excited states with $S_z = 0$ and $+1$. According to these considerations, the RIXS spectrum features energy losses at J_{eff} (single spin-flip with $\Delta S_z = 1$) and $2J_{\text{eff}}$ (double amplitude spin-flip with $\Delta S_z = 2$) [34]. On the site where the resonant scattering takes place, Ni^{2+} spin momentum is left behind with a modified orientation, when compared to the antiferromagnetic magnetic ground state (see Fig. 6.10). Other flip possibilities also have finite probability, as for instance the flip on two Ni sites (double spin-flip) resulting in a global $\Delta S_z = 0$ and requiring an energy of $2J_{\text{eff}}$.

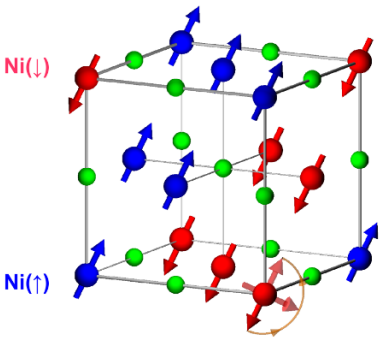

Fig. 6.10 Illustration of a local spin-flip in NiO

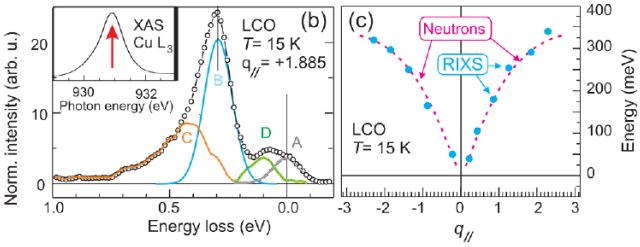

Fig. 6.11 Collective magnetic modes (magnons, denoted B and C) measured in the layered superconductor La_2CuO_4 (from [35]). The right panel shows a comparison for the dispersion of the single magnon B to inelastic neutron measurements

The magnetic excitations mentioned above are not localized but propagate in the crystal as well-defined spin-wave modes (magnons). These are collective excitations. As the scattering geometry defines the momentum transferred to the magnons, these photon energy losses provide a direct way for measuring spin wave modes, in a way comparable to inelastic neutron scattering. The first demonstration by Braicovich et al. [36] (see also Fig. 6.11) sparked a strong interest in studies on the magnetism of complex systems [3]. While the energy resolution attained in RIXS is still far from that reached with inelastic neutron scattering measurements, it provides an important alternate method. In particular RIXS can be performed on small samples, can probe an energy range of several eV and provides access to $\Delta S_z = 2$ modes, just to name a few relevant aspects.

6.4 Diffraction grating spectrometers for soft x-rays

The flourishing interest for RIXS is intimately associated to instrumental progresses. It is therefore timely to review the developments in the field.

Spectrometers for extreme ultraviolet photons (roughly 20 eV to 300 eV) and soft x-rays (300 eV to a few keV) are mostly based on diffraction gratings [37]. Alternatives exist but they are less competitive mainly because of practical aspects. There have been promising attempts to implement optical interferometric techniques [38, 39], but they are conditional on extreme mechanical precision: optical elements need to be positioned and moved with precisions comparable to the wavelength of the radiation, i.e. several to a few dozen nanometers. Moreover, for energies higher than 100 eV, multiple reflections result in a dramatic drop in efficiency. Crystals have been employed but in practice their usefulness is very limited compared to their performance in the hard x-ray region. Large defect-free crystals are needed with inter-atomic distances comparable to the photon wavelength (see [40] for a selection of available materials). Crystal spectrometers operating below 800 eV have limited energy windows (in accordance with Bragg's law) and have modest energy resolution.

The challenge for the optical design of modern instruments is to obtain increased energy resolution while maintaining a sufficiently large instrumental throughput. The latter is obviously needed to compensate for the extremely small scattering cross sections in the soft x-ray region. These objectives are antagonistic. Indeed, improving energy resolution can be achieved either with longer instruments and therefore smaller angular acceptance for a given size of the optical elements, or with higher line density gratings leading to lower diffraction efficiency. Both result in reduced photon throughput.

Several schemes for diffraction grating spectrometers are employed at synchrotron light sources around the world. The choice for a particular scheme is subject to a number of factors involving available space at the beamline, scientific objectives (energy range covered and energy resolution), strategy for the correction of optical aberrations or quality of available optical elements. Here the reader is provided with an overview of the salient features of each design as means of understanding their relevance to a particular research project.

The Rowland-circle mounting depicted in Fig. 6.12a is widely used as it is relatively straightforward to construct and set-up [41, 42]. It consists of a spherical or toroidal regularly line spaced (RLS) grating. The source (the sample itself or the input slit), the center of the grating and the detector are located

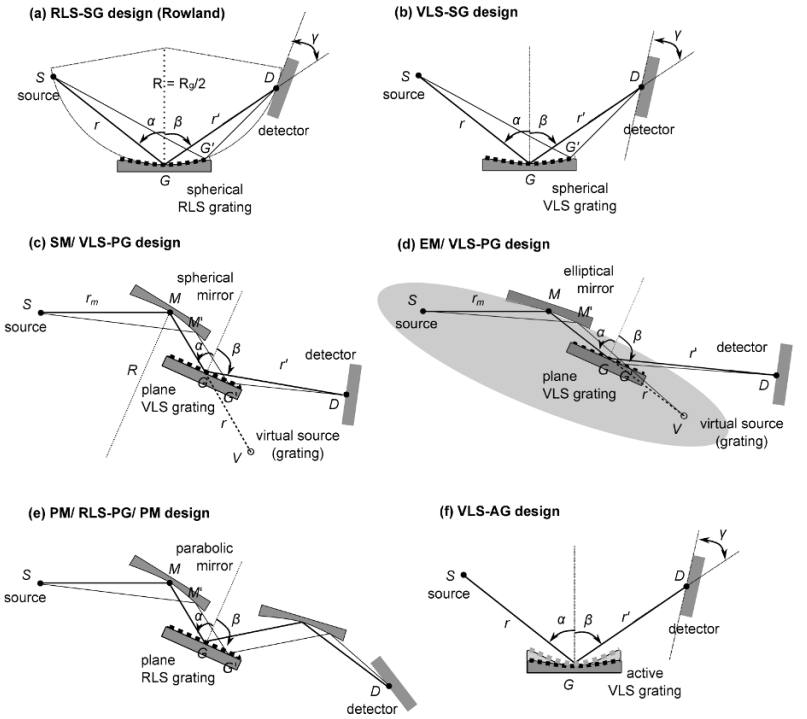

Fig. 6.12 Overview of optical schemes used for resolving the scattered photon spectra. **a** Regularly line spaced spherical grating (RLS-SG) or Rowland circle design. **b** Varied line spaced spherical grating (VLS-SG) scheme. **c** Spherical mirror with varied line spaced plane grating (SM/VLS-PG). **d** Elliptical mirror with varied line spaced plane grating (EM/VLS-PG). **e** Parabolic mirrors with regularly line spaced plane grating (PM/RLS-PG). **f** Varied line spaced active grating (VLS-AG) design.

on the Rowland circle with a diameter equal to the meridional radius of the grating. Spherical RLS diffraction gratings can be manufactured to very high standards. The key aspect of the Rowland mounting is given by the wavelength independent cancellation of optical aberrations up to the third order on condition that the optical magnification be constant and set to one (see [43] for a concise introduction to grating and mirror aberrations).

High reflectivity even in the soft x-ray region requires small incident grazing angles (0.7° to 3°) at the grating. The Rowland circle radius has to be large to attain high-resolution. This in turn means that light also impinges on

the detector at small grazing angles and microchannel plate (MCP) detectors, which maintain reasonable efficiency at glancing incidence have to be used. This is not the case for a back-illuminated charge coupled device (CCD). The energy range covered will depend, amongst other factors, on the distance that the detector can travel along the circle. Compact Rowland circle spectrometers are currently operational with moderate energy resolution on beamlines 7.0.1 and 8.0.1 of the Advanced Light Source. A high resolution instrument is under construction on the REIXS (10ID-2) beamline of the Canadian Light Source. The use of the Rowland mounting for very high resolution, means that it becomes necessary to take into account the weight of fourth order optical aberrations.

The use of varied line spacing (VLS) spherical diffraction gratings brings higher flexibility to the optical design (Fig. 6.12b). The ruling density has a polynomial dependence along the meridional coordinate which allows for improved correction of aberrations as well as for more convenient orientation of the focal curves. The groove spacing serves both to diffract the light and to correct for the optical aberrations of the concave surface. Recent high resolution implementations of the VLS-SG scheme can be found at the ID08 beamline of the European Synchrotron Radiation Facility [44], at the ADRESS (X03MA) beamline of the Swiss Light Source [45] and the BL07LSU beamline of the Japanese light source SPring8 [46]. The VLS-SG holds so far the highest resolving power value with $E/\Delta E \approx 10^4$ for the 5 m long SAXES spectrometer [45]. Recently we investigated the potential of this scheme for ultimate resolving power in a systematic study and established the optimization criteria needed to attain an almost straight focal curve [47]. Resolving powers well in excess of 3×10^4 were predicted at 930 eV for a 10 m long instrument.

The VLS-SG design is recommended when the emphasis is on energy resolution alone. On the other hand studying complex systems can make high throughput essential to cope with extremely low counting rates. One way to meet this demand is to use large x-ray mirrors in conjunction with diffraction gratings. Thus collecting photons and energy dispersion are handled independently. A first successful design of this kind was proposed by Hettrick and Underwood [48, 49]. It combines a spherical focusing mirror with a plane VLS grating [Fig. 6.12c]. The grating serves to diffract the light and to correct for the optical aberrations of the mirror by means of the VLS dependency. Long mirrors can be manufactured more cost effectively than long gratings and a long mirror can be used in conjunction with a short grating provided that the latter is employed in outside diffraction order, $m = -1$, meaning that

$\alpha < |\beta|$. This limits the line density that can be used since higher line density means larger $|\beta|$. Each of the two optical elements contributes some slope-errors which affect the overall resolving power. Thus the resolving power attained with an SM/VLS-PG is somewhat reduced compared to a VLS-SG. The SM/VLS-PG operates at constant included angle $2\theta = \alpha - \beta$ and the depth of focus at the detector is large so the detector can be kept at fixed distance from the grating (fixed exit arm). The energy window at the detector is changed by simply rotating the grating. A first implementation of this scheme for soft x-rays was a portable spectrometer presented by Hague et al. [50]. This instrument also featured a collecting pre-mirror. The MERIXS end-station on the 4.0.3 beamline of the Advanced Light Source accommodates a 2 m long SM/VLS-PG instrument designed for the $3p - 3d$ transitions in $3d$ transition metal compounds [51]. Another portable instrument designed for large photon throughput based on the same scheme was tested at the same light source [52]. The latter was designed to work at inside diffraction orders.

Replacing the spherical mirror of the SM/VLS-PG design with an elliptical mirror (EM/VLS-PG) represents a significant step forward. The features of the (SM/VLS-PG) are extended with the added possibility of using varied included angles 2θ to obtain high-resolution over a substantially broader energy range. This has become possible thanks to recent progress in the manufacturing techniques of aspherical mirrors. A 3 m long EM/VLS-PG instrument is installed on the Synchrotron SOLEIL SEXTANTS beamline. It covers 50 eV−1000 eV by means of two diffraction gratings only and offers resolving powers well in excess of 5000 [53].

The quest for higher photon throughput was also the main motivation for a PM/RLS-PG/PM design which combines a parabolic collimating mirror with a plane RLS diffraction grating and a second parabolic mirror which focuses onto the detector [39]. This scheme should be particularly effective at energies lower than 120 eV because it involves three reflections and quite large grazing angles. The original instrument [39] will come into operation on the SPECIES beamline of the MAX II storage ring in Sweden. Another PM/RLS-PG/PM is being commissioned at the BESSY II light source in Germany [54]. The latter design features sagittal focusing for the first parabolic mirror to reduce the impact of the slope errors.

An novel concept has been proposed at the NSRRC light-source drawing advantage from the development of "active" optical elements. Bending is used to provide optimized control of the optical aberrations. The VLS-AG design is basically the VLS-SG scheme, but it is expected to provide adapted con-

trol of optical aberrations when used in conjunction with an active grating monochromator on the beamline [55].

6.5 Conclusion

RIXS has joined the mainstream of x-ray spectroscopic techniques granting insight into the magnetism of correlated electron systems. The technique is nowadays rapidly evolving. Its powerful features motivate significant technical and financial efforts: nowadays very long instruments with a total length higher or equal to 10 m are designed or under construction at the European Synchrotron Radiation Facility (France), at the future MAX IV facility (Sweden), at The Diamond Light Source (UK) or the future The National Synchrotron Light Source II (USA).

In this chapter we addressed the main aspects dealing with RIXS performed with soft x-rays in an attempt to motivate the interest of young scientists for this technique by pointing out its strengths and specific aspects.

Acknowledgement

The writing of this chapter has benefited from stimulating discussions with Coryn Frank Hague, Jan Lüning and Jean-Michel Mariot at Laboratoire de Chimie Physique-Matière et Rayonnement. The author is grateful to C.F.H. and J.-M.M. for critical reading of the manuscript.

References

1. A. Kotani, S. Shin, Rev. Mod. Phys. **73**, 203 (2001)
2. A. Kotani, Eur. Phys. J. B **47**, 3 (2005)
3. L.J.P. Ament, M. van Veenendaal, T.P. Devereaux, J.P. Hill, J. van den Brink, Rev. Mod. Phys. **83**, 705 (2011)
4. J.P. Rueff, A. Shukla, Rev. Mod. Phys. **82**, 847 (2010)
5. W. Schülke, *Electron Dynamics by Inelastic X-Ray Scattering*, *Oxford Series on Synchrotron Radiation*, vol. 7 (Oxford University Press, Oxford, 2007)
6. F.M.F. de Groot, A. Kotani, *Core Level Spectroscopy of Solids* (CRC Press, Boca Raton, 2008)

7. F. Gel'mukhanov, H. Ågren, Phys. Rep. **312**, 87 (1999)
8. J. Stöhr, H.C. Siegmann, *Magnetism: From Fundamentals to Nanoscale Dynamics*. Springer Series in Solid-State Sciences (Springer, Berlin, 2006)
9. A. Zangwill, *Physics at Surfaces* (Cambridge University Press, Cambridge, 1988)
10. R. Kurian, K. Kunnus, P. Wernet, S.M. Butorin, P. Glatzel, F.M.F. de Groot, J. Phys.: Condens. Matter **24**, 452201 (2012)
11. S. Eisebitt, T. Böske, J.E. Rubensson, W. Eberhardt, Phys. Rev. B **47**, 14103 (1993)
12. M.T. Hutchings, E.J. Samuelsen, Phys. Rev. B **6**, 3447 (1972)
13. J.J. Sakurai, *Advanced Quantum Mechanics* (Addison-Wesley, Lebanon, 1967)
14. M. Blume, J. Appl. Phys. **57**, 3615 (1985)
15. F. de Groot, J. Vogel, *Neutron and X-ray Spectroscopy* (Springer, Berlin, 2006), chap. Fundamentals of x-ray absorption and dichroism: the multiplet approach, pp. 3–66
16. S.F.A. Kettle, *Symmetry and Structure: Readable Group Theory for Chemists* (John Wiley & Sons, New York, 2007)
17. B. Fromme, *d-d Excitations in Transition-Metal Oxides: A Spin-Polarized Electron Energy (SPEELS) Study*, *Springer Tracts in Modern Physics*, vol. 170 (Springer, Berlin, 2001)
18. F.M.F. de Groot, P. Kuiper, G.A. Sawatzky, Phys. Rev. B **57**, 14584 (1998)
19. O. Keski-Rahkonen, M.O. Krause, Atomic Data and Nuclear Data Tables **14**, 139 (1974)
20. J.E. Rubensson, J. Elec. Spec. Rel. Phenom. **110 - 111**, 135 (2000)
21. P. Glatzel, M. Sikora, M. Fernández-García, Eur. Phys. J. Special Topics **169**, 207 (2009)
22. S. Hüfner, Adv. Phys. **43**, 183 (1994)
23. J. Zaanen, G.A. Sawatzky, J.W. Allen, Phys. Rev. Lett. **55**, 418 (1985)
24. A.E. Bocquet, T. Mizokawa, K. Morikawa, A. Fujimori, S.R. Barman, K. Maiti, D.D. Sarma, Y. Tokura, M. Onoda, Phys. Rev. B **53**, 1161 (1996)
25. A.K. Masahiko Matsubara, Takayuki Uozumi, J.C. Parlebas, J. Phys. Soc. Jpn **74**, 2052 (2005)
26. S.G. Chiuzbăian, G. Ghiringhelli, C. Dallera, M. Grioni, P. Amann, X. Wang, L. Braicovich, L. Patthey, Phys. Rev. Lett. **95**, 197402 (2005)
27. S.G. Chiuzbăian, T. Schmitt, M. Matsubara, A. Kotani, G. Ghiringhelli, C. Dallera, A. Tagliaferri, L. Braicovich, V. Scagnoli, N.B. Brookes, U. Staub, L. Patthey, Phys. Rev. B **78**, 245102 (2008)
28. M. Magnuson, S.M. Butorin, A. Agui, J. Nordgren, J. Phys.: Condens. Matter **14**, 3669 (2002)
29. A. Shukla, J.P. Rueff, J. Badro, G. Vanko, A. Mattila, F.M.F. de Groot, F. Sette, Phys. Rev. B **67**, 081101 (2003)
30. L.C. Duda, T. Schmitt, M. Magnuson, J. Forsberg, A. Olsson, J. Nordgren, K. Okada, A. Kotani, Phys. Rev. Lett. **96**, 067402 (2006)
31. G. van der Laan, in *Magnetism: A Synchrotron Radiation Approach*, ed. by E. Beaurepaire, H. Bulou, F. Scheurer, J.-P. Kappler, (Springer, Berlin, 2006), p.143
32. E. Saitoh, S. Okamoto, K. Takahashi, K. Tobe, K. Yamamoto, T. Kimura, S. Ishihara, S. Maekawa, Y. Tokura, Nature **410**, 180 (2001)
33. J. Schlappa, K. Wohlfeld, K. Zhou, M. Mourigal, M. Haverkort, V. Strocov, L. Hozoi, C. Monney, S. Nishimoto, S. Singh, A. Revcolevschi, J.S. Caux, L. Patthey, H. Rønnow, J. van den Brink, T. Schmitt, Nature **485**, 82 (2012)

34. G. Ghiringhelli, A. Piazzalunga, C. Dallera, T. Schmitt, V.N. Strocov, J. Schlappa, L. Patthey, X. Wang, H. Berger, M. Grioni, Phys. Rev. Lett. **102**, 027401 (2009)
35. L. Braicovich, J. van den Brink, V. Bisogni, M.M. Sala, L.J.P. Ament, N.B. Brookes, G.M. De Luca, M. Salluzzo, T. Schmitt, V.N. Strocov, G. Ghiringhelli, Phys. Rev. Lett. **104**, 077002 (2010)
36. L. Braicovich, L.J.P. Ament, V. Bisogni, F. Forte, C. Aruta, G. Balestrino, N.B. Brookes, G.M. De Luca, P.G. Medaglia, F.M. Granozio, M. Radovic, M. Salluzzo, J. van den Brink, G. Ghiringhelli, Phys. Rev. Lett. **102**, 167401 (2009)
37. W.B. Peatman, *Gratings, Mirrors and Slits* (Taylor & Francis, London, 1997)
38. S.C. Locklin, E.J. Moler, J. Spring, Z. Hussain, M.R. Howells, Progress in soft-x-ray Fourier transform spectrometry. Tech. rep., Advanced Light Source, LBNL, Berkeley, CA (1998)
39. M. Agåker, J. Andersson, C.J. Englund, A. Olsson, M. Strom, J. Nordgren, Nucl. Instrum. Meth. A **601**, 213 (12009)
40. J.H. Underwood, in *X-ray Data Booklet* (Lawrence Berkeley National Laboratory, Berkeley, 2009), pp. 4.6–4.12
41. J. Nordgren, R. Nyholm, Nucl. Instrum. Meth. A **246**, 242 (1986)
42. T.A. Callcott, K.L. Tsang, C.H. Zhang, D.L. Ederer, E.T. Arakawa, Rev. Sci. Instrum. **57**, 2680 (1986)
43. M.R. Howells, in *X-ray Data Booklet* (Lawrence Berkeley National Laboratory, Berkeley, 2009), pp. 4.16–4.26
44. C. Dallera, E. Puppin, G. Trezzi, N. Incorvaia, A. Fasana, L. Braicovich, N. Brookes, J. Goedkoop, J. Synch. Rad. **3**, 231 (1998)
45. G. Ghiringhelli, A. Piazzalunga, C. Dallera, G. Trezzi, L. Braicovich, T. Schmitt, V.N. Strocov, R. Betemps, L. Patthey, X. Wang, M. Grioni, Rev. Sci. Instrum. **77**, 113108 (2006)
46. Y. Harada, M. Kobayashi, H. Niwa, Y. Senba, H. Ohashi, T. Tokushima, Y. Horikawa, S. Shin, M. Oshima, Rev. Sci. Instrum. **83**, 013116 (2012)
47. S.G. Chiuzbăian, C.F. Hague, J. Lüning, Appl. Optics **51**, 4684 (2012)
48. M.C. Hettrick, J.H. Underwood. US patent no 4,776,696: Optical system for high resolution spectrometer/monochromator (1988)
49. J.H. Underwood, J.A. Koch, Appl. Optics **36**, 4913 (1997)
50. C.F. Hague, J.H. Underwood, A. Avila, R. Delaunay, H. Ringuenet, M. Marsi, M. Sacchi, Rev. Sci. Instrum. **76**, 023110 (2005)
51. Y.D. Chuang, J. Pepper, W. McKinney, Z. Hussain, E. Gullikson, P. Batson, D. Qian, M.Z. Hasan, J. Phys. Chem. Solids **66**, 2173 (2005)
52. O. Fuchs, L. Weinhardt, M. Blum, M. Weigand, E. Umbach, M. Bar, C. Heske, J. Denlinger, Y.D. Chuang, W. McKinney, Z. Hussain, E. Gullikson, M. Jones, P. Batson, B. Nelles, R. Follath, Rev. Sci. Instrum. **80**, 063103 (2009)
53. S.G. Chiuzbăian, et al. (to be published)
54. R. Könnecke, R. Follath, N. Pontius, J. Schlappa, F. Eggenstein, T. Zeschke, P. Bischoff, J.S. Schmidt, T. Noll, C. Trabant, S. Schreck, P. Wernet, S. Eisebitt, F. Senf, C. Schüßler-Langeheine, A. Erko, A. Föhlisch, J. Electron Spectrosc. (2012) In press
55. H.S. Fung, C.T. Chen, L.J. Huang, C.H. Chang, S.C. Chung, D.J. Wang, T.C. Tseng, K.L. Tsang, AIP Conf. Proc. **705**, 655 (2004)

Chapter 7
Synchrotron-radiation studies of topological insulators

Philip Hofmann

Abstract Topological insulators are a recently discovered class of materials with entirely novel properties. While their bulk electronic structure is that of an insulator, topological considerations force the surfaces to support metallic states that bridge the bulk band gap. This Chapter gives an accessible introduction to these materials, with special emphasis on synchrotron radiation-based experimental techniques that have been used for their experimental discovery.

7.1 Introduction

Topological insulators (TIs) are a recently discovered [1, 2, 3, 4, 5, 6, 7, 8, 9, 10, 11, 12] class of quantum materials that are currently attracting a lot of attention. The most interesting aspect of the TIs is, in fact, not that they are bulk insulators but that their surfaces support localized metallic states with some special properties, among others a characteristic spin texture. Most importantly, the existence of these metallic states is not a surface property, it is required by the topology of the bulk band structure. While the details of the surface (structure, reconstructions) still matter for the dispersion and Fermi contour of the surface states, their very existence is, in a sense, a bulk property.

Philip Hofmann
Department of Physics and Astronomy, Aarhus University, Ny Munkegade 120, DK-8000 Aarhus C, e-mail: philip@phys.au.dk

E. Beaurepaire et al. (eds.), *Magnetism and Synchrotron Radiation: Towards the Fourth Generation Light Sources*, Springer Proceedings in Physics 151,
DOI: 10.1007/978-3-319-03032-6_7,

Synchrotron-radiation based angle-resolved photoemission spectroscopy (ARPES) has been one of the most important tools to prove the existence of the topological surface states and spin-resolved ARPES has been able to confirm the predicted non-degeneracy of the states with respect to spin and the spin texture [10, 11, 13, 14, 15, 16]. The power of ARPES derives from the possibility of a direct spectroscopic view of the state's dispersion and of many-body effects such as the lifetime of the states. ARPES also stands out as an important technique because it has so far not been easy to probe the transport properties of the surface states directly [17, 18, 19, 20, 21, 22, 23, 24, 25, 26, 27, 28]. Superficially, this may appear surprising because a metallic surface on an insulating bulk crystal should be easy to detect. Unfortunately, this is not the case and many transport measurements have been dominated by the bulk states. The reason for this is the high bulk conductivity of the materials, which have a small band gap, many charged impurities and typically a high dielectric constant leading to poor screening between the impurities. The surface conductance, on the other hand, is not well known and lifetime ARPES studies could help to elucidate the processes that limit the lifetime of excited surface state carriers in transport.

This Chapter is not meant as a comprehensive review of topological insulators or of their study with ARPES but merely as an accessible introduction to the field for the non-specialist. We do not attempt to describe the historical development of the important discoveries in detail, nor do we show the original figures from such work. Instead, the emphasis is on a didactic presentation. We also discuss only one single material as an example for the important concepts, the widely-studied TI Bi_2Se_3 [13, 12, 29]. There are a number of excellent reviews on TIs already published [30, 31, 32, 33, 34] and the reader is referred to these for a comprehensive description of the field.

In the following sections, we will first discuss the basic physical ideas that lead to the existence of topologically protected surface states on an insulator. Different explanations will be given, ranging from a simple hand-waving explanation to a practical description of how to determine if a material is a topological insulator. Following this, we will discuss how different TI states (bulk and surface) can be detected by ARPES and what their spectroscopic signature is. The chapter concludes with a discussion of how the electron-phonon coupling affects the lifetime of the surface states on Bi_2Te_3.

7.2 Basic principles behind topological insulators

One of the most interesting questions in TI physics is how it is possible that the bulk electronic structure implies the existence of metallic surface states on a insulating material. In the following, we will encounter different pictures explaining this. Note that the term "topological insulator" might be slightly misleading because the materials are, in fact, not insulators with a large gap energy E_g (in the sense that $E_g \gg k_B T$ at room temperature) but small gap semiconductors with $E_g \approx$300 meV.

Metallic surface states on semiconductors are not an unusual phenomenon and simple electron counting arguments often dictate the surface of a truncated bulk semiconductor to be metallic [35]. On the other hand, the surfaces often undergo geometric reconstructions that change the periodicity parallel to the surface, leading to larger unit cells and non-metallic states. A simple model for such rearrangements is a Peierls distortion in a one-dimensional metallic chain that leads to an energy gain via a metal-insulator transition. On real surfaces, the picture is much more complex but the essence is that metallic semiconductor surfaces are usually just a coincidence [36]. They are not stable against, e.g. a structural rearrangement of the atoms.

The existence of topological surface states, on the other hand, cannot depend on the structural details of the surface. A simple explanation for the stable existence of metallic states between two different semiconducting materials is given in Fig. 7.1. Consider a "normal" semiconductor with a well-separated valence band (VB) and conduction band (CB) and the chemical potential (or Fermi energy E_F) in between. The VB and CB shall each have a characteristic colour, which for a "normal" material shall be blue and red, respectively. We will later discuss the meaning of the colour in more detail and we will see that it is related to the parity of the bands (we limit the discussion to materials with inversion symmetry). Now suppose that we have another type of semiconductor, a TI, also with a well-defined band gap but an inverted order of the colours, i.e. a red VB and blue CB. If we join these two materials under the condition that we can only join states of identical character, the blue and red states have to cross the Fermi energy at the interface, giving rise to two metallic states located there. This is the essence of a topologically protected metallic interface or surface state.

The crucial point is that the existence of the crossing is not a surface property but a bulk property. An excellent analogy is the situation that arises when two countries are to be joined by a road bridge, with the difficulty that the

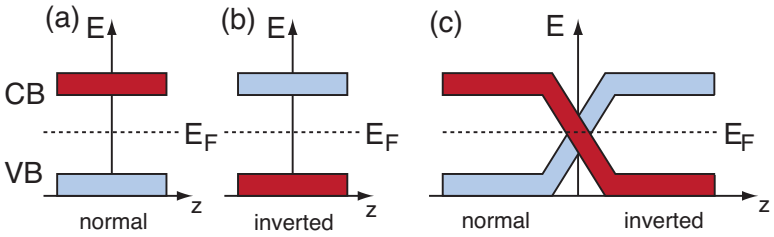

Fig. 7.1 Strongly simplified band diagram for semiconductors, showing the valence band (VB) and conduction band (CB) energies as a function of position (i.e. the edges signify the macroscopic ends of the sample). **a** Colour (parity) ordering of VB and CB in a normal semiconductor. **b** Semiconductor with an inverted band gap. (c) Joining a semiconductor with a normal band gap and one with an inverted band gap while maintaining the symmetry of the states gives rise to metallic interface states

driving rules in one country enforce right-hand traffic and in the other left-hand traffic. A possible solution to this problem is the traffic flipper bridge shown in Fig. 7.2, a proposal for a boundary crossing between Hong Kong with mainland China. In this case, the colour of the bands in Fig. 7.1 is representing the traffic side (left-hand vs. right-hand) and this is a bulk property of the two countries, requiring a node in the bridge. The solution is not unique: the node could be included in a more complex structure road layout, or there could be a higher number of crossings, as long as the total number of crossings is odd. But the bulk topology of the countries dictates the existence of at least one node somewhere near the border and the flipper bridge is the simplest topological solution to the problem.

In a material, the colour of the bands in Fig. 7.1 represents the parity of the bulk bands. In a TI, the bulk band structure has an inverted parity ordering due to the strong spin-orbit interaction. A very simple illustration of this is given in Fig. 7.3. Consider the most important orbital angular momentum contribution to the electronic states of a semiconductor near the valence band maximum (VBM) and conduction band minimum (CBM), assuming a direct band at the Brillouin zone centre. In a "normal" material the VBM has mostly p character (negative parity) whereas the CBM has mostly s character (positive parity). If we now consider materials with a strong spin-orbit interaction, this lifts the degeneracy of the p level, leading to the creation of $j = 1/2$ and a $j = 3/2$ states. If the splitting is sufficiently strong, the $j = 3/2$ state can move above the s state, giving rise to the desired band parity inversion and the creation of a TI material.

Fig. 7.2 Proposed "flipper bridge" between Hong Kong (left-hand traffic) and mainland China (right-hand traffic). Design by nl architects (www.nlarchitects.nl). Picture used with permission

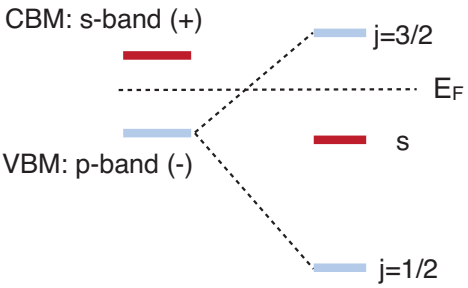

Fig. 7.3 Strongly simplified illustration of the effect of spin-orbit coupling on the symmetry of the valence band maximum (VBM) and conduction band minimum (CBM). For weak coupling, the CBM has *s*-orbital character and positive parity, the VBM has *p* character and negative parity. Strong coupling can move the $j = 3/2$ level above the *s* level, leading to a parity-inverted band gap

These simple pictures give an intuitive explanation for the topological stability of interface states, but they have a number of severe shortcomings, as far as the details are concerned, and leave several questions open. Fig. 7.3, for

instance, explains the origin of the parity inversion but it is merely a picture derived from atomic states, not bands. This leads to some apparent contradictions, for example that the number of filled states is not conserved. Also, the pictures above may explain the existence of topologically protected interface states between two materials, but not the existence of such states at a surface, between a TI and vacuum. We come back to these points further down in the text.

For now, we approach the idea of topologically protected surface states from another angle, by starting out with "normal" surface states in the presence of strong spin-orbit coupling. Consider a free electron-like surface state with a parabolic dispersion around the centre of the surface Brillouin zone (SBZ) $\bar{\Gamma}$, as shown in Fig. 7.4a. Such surface states are commonly found on the (111) surfaces of the noble metals Cu, Ag and Au [37]. On metals, such surface-localized solutions of the Schrödinger equation, can only exist in projected gaps of the bulk band structure. For the noble metal (111) surfaces such gaps are present around the Fermi energy at the $\bar{\Gamma}$ point because of the characteristic shape of the bulk Fermi surfaces which are almost spherical but have "necks" into the neighbouring Brillouin zone around the L symmetry point [38]. The projected bulk states and the gap are not shown in Fig. 7.4a.

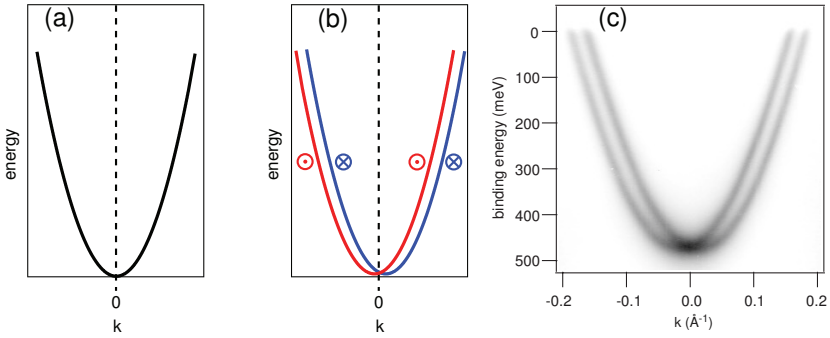

Fig. 7.4 **a** One dimensional cut through the two-dimensional dispersion of a free electron-like surface state, as found on the (111) surfaces of the noble metals. **b** The same state under the influence of strong spin-orbit coupling (Rashba effect). The spin-degeneracy is lifted and the spin directions of the individual branches are indicated by the arrow heads. **c** ARPES measurement of the spin-orbit split surface state on the Au(111) surface. High photoemission intensity is dark. After Ref. [39]

A strong spin-orbit interaction changes the dispersion of such a surface state by lifting the spin degeneracy, as shown in Fig. 7.4b. Formally, this can be described by the so-called Rashba model [40, 41]. This model was originally developed to describe the interaction of a two-dimensional electron gas (2DEG) with an electric field perpendicular to the 2DEG's plane. A fast-moving electron in the plane will experience the Lorentz-transformed electric field as a magnetic field in the plane but perpendicular to its direction of motion. The electron's energy depends then on the orientation of the spin magnetic moment with respect to this magnetic field, parallel or anti-parallel, lifting the spin degeneracy in the dispersion. The model can be solved analytically, starting from from the free electron Schrödinger equation in two dimensions with the added energy for the spin-orbit interaction

$$H_{so} = -\frac{\hbar}{4m_e c^2}(\mathbf{p}\times\mathbf{E})\sigma = -\frac{\hbar}{4m_e c^2}(\nabla V\times\mathbf{p})\sigma\,, \tag{7.1}$$

where $\mathbf{p}$ is the momentum operator, $\mathbf{E}$ the electric field perpendicular to the surface with the generating potential V and σ the Pauli spin operator. The constants and the electric field strength can be represented by a parameter α and the interaction is added to the Hamiltonian of the free electron, leading to

$$-\frac{\hbar^2\nabla^2}{2m_e}\psi(\mathbf{r}) + \alpha(\mathbf{n}\times\mathbf{p})\sigma\psi(\mathbf{r}) = E\psi(\mathbf{r})\,, \tag{7.2}$$

with $\mathbf{n}$ being a unit vector normal to the surface. This problem can be solved analytically and the resulting energies are

$$E = \frac{\hbar^2 k^2}{2m_e} \pm \alpha\hbar k\,, \tag{7.3}$$

where the $\pm$ sign corresponds to the different spin directions. This dispersion shown in Fig. 7.4b.

The analytically predicted dispersion for the Rashba effect has been confirmed by high-resolution ARPES measurements of the surface state on Au(111), the heaviest noble metal with the strongest spin-orbit interaction [42, 43]. If we, for now, just regard the ARPES intensity as a "picture of the band structure", the result of such a measurement as shown in Fig. 7.4c [39] fits excellently with the prediction of the model.

From equation 7.3 it can be seen that the state is always degenerate at the SBZ centre. This is not a coincidence or a special feature of the Rashba model

but a result of time-reversal symmetry which assures the so-called Kramers degeneracy. Consider a solution of the Schrödinger equation with wave vector and spin given by $(\mathbf{k}, \leftarrow)$. Time-reversal symmetry guarantees a degenerate solution with $(-\mathbf{k}, \rightarrow)$. For $\mathbf{k} = (0,0)$ the states must thus be degenerate. Time-reversal symmetry is assumed to hold at the surface but it could possibly be broken by a magnetic field.

Degeneracies in otherwise spin-split surface states can also be enforced at other points in $\mathbf{k}$-space, due to the combination of time-reversal symmetry and crystal symmetry. Consider for example a hexagonal SBZ in Fig. 7.5a and a surface state with $(\mathbf{k} = \bar{M}, \leftarrow)$ at the $\bar{M}$ point. Time-reversal symmetry dictates a degenerate state with $(-\mathbf{k}, \rightarrow)$ but due to the symmetry of the lattice, $-\mathbf{k}$ is also an $\bar{M}$ point, equivalent to the staring point. Thus, there must be two degenerate states at this point (and every equivalent $\bar{M}$ point) with both spins, $\rightarrow$ and $\leftarrow$.

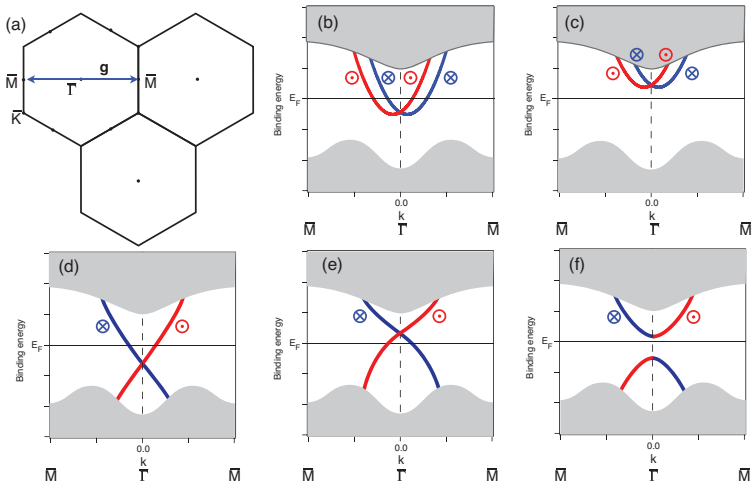

Fig. 7.5 **a** Hexagonal surface Brillouin zone with high-symmetry points. The $\bar{M}$ point can be identified as a time-reversal invariant momentum. **b** and **c** Rashba-split free electron-like surface state in a projected bulk band gap. The state in **b** is metallic but it can be emptied by lifting the entire dispersion above the Fermi level as in **c**. **d** and **e** Topologically protected spin-split surface state. While the dispersion of the state depends on the details of the potential, time reversal symmetry protects it against a band gap opening, such that the situation in **f** cannot be realized

Points such as $\bar{M}$ in the hexagonal lattice are called surface time-reversal invariant momenta Λ_a (TRIM). They are characterized by the property that $\Lambda_a = -\Lambda_a + \mathbf{g}$ where $\mathbf{g}$ is a surface reciprocal lattice vector. There are always four possible TRIMS for the two-dimensional reciprocal lattice spanned by the vectors $\mathbf{b}_1$ and $\mathbf{b}_2$. The reciprocal lattice vectors are given by $\mathbf{g} = n\mathbf{b}_1 + m\mathbf{b}_2$. One TRIM corresponds to $(m,n) = (0,0)$ and the other three are placed half-way to the points for which $(m,n) = (1,0),(0,1),(1,1)$, i.e. the remaining three independent combinations of the indices.

We now discuss the topological stability from the perspective of the surface states in the presence of strong spin orbit splitting. Consider an insulator with a hexagonal Brillouin zone and the projection of the bulk bands along one direction, for example $\bar{\Gamma} - \bar{M}$. This projection is shown as grey areas in Fig. 7.5. The absolute band gap in a semiconductor is of course also reflected in a projected band gap around the Fermi energy E_F. In Fig. 7.5b we imagine that the surface hosts a free electron-like surface state, split by the Rashba effect. The surface state is only partially filled, crosses E_F, and the surface is therefore metallic. There is, however, no special topological protection of this metallic surface state. We could imagine to hole-dope the surface such that the entire dispersion is lifted above E_F, rendering the surface semiconducting as in Fig. 7.5c.

The situation is different for the surface state dispersion shown in Fig. 7.5d. In this case, a change in the dispersion could still be achieved by changing the potential near the surface. It would, for example, be possible to move the crossing point of the two spin-polarized branches above the Fermi energy as in Fig. 7.5e, but it would not be possible to open a gap in the dispersion as in Fig. 7.5f. This would violate time reversal symmetry that guarantees a spin-degenerate state at $\bar{\Gamma}$. The state in Fig. 7.5d and Fig. 7.5e is thus a time-reversal symmetry protected state. Such states are found on the surfaces of the TIs and the dispersion of the states is very similar to the one shown here.

What is now special about the surface state in Fig. 7.5d compared to the state in Fig. 7.5b? It is not the dispersion as such. In fact, the dispersion of the state in Fig. 7.5d could be a magnified version of the usual Rashba dispersion in the immediate vicinity of the crossing point, with the states disappearing in the projected bulk state continuum before the k^2 term in the dispersion of (7.3) becomes significant. The important difference is rather the number of Fermi level crossings between the SBZ centre and the SBZ boundary or, more precisely, between the surface TRIM at $\bar{\Gamma}$ and the surface TRIM $\bar{M}$ at the SBZ boundary. If the state shows an even number of Fermi level crossings between

two surface TRIMS, it can be removed, but if it shows an odd number of crossings, it is topologically protected.

The important point is now that the number (even or odd) of Fermi level crossings between two surface TRIMs can be predicted solely by the bulk band structure of the material. A mere knowledge of the bulk bands thus permits statements about the existence of topologically protected surface states, not merely interface states as in the simple examples given in the beginning of this section. A second material is not required for stable states or, in a sense, vacuum can be viewed as a material with "normal" band ordering. Note that the topological considerations do not give a detailed prediction of the surface band structure, they merely predict if an odd or even number of surface state Fermi level crossings is present (actually, the predictions are somewhat stronger than this [44], but this is of no concern here). Again the analogy with the bridge in Fig. 7.2 is useful. If we were told that a bridge had been installed that takes care of the traffic-flip problem, we could predict that there must be an odd number of crossings built into such a bridge but not how many (given common sense and budget restrictions, the answer would likely to be one).

We now illustrate how the number of surface state crossings between two surface TRIMs can be derived from the bulk band structure. This has been described in detail using the example of the TI $Bi_{1-x}Sb_x$ by Teo, Fu and Kane [44]. We follow their treatment here but we use the TI Bi_2Se_3 as an example. The bulk structure, bulk band structure as well as the bulk and surface BZ for the (111) surface of this material are given in Fig. 7.6.

We first define the bulk TRIMs Γ_i in analogy to the surface TRIMS by $-\Gamma_i = \Gamma_i + \mathbf{G}$ where $\mathbf{G}$ is a bulk reciprocal lattice vector. There are eight bulk TRIMS. In Bi_2Se_3 these are Γ, Z, three F points and three L points (see Fig. 7.6b; note that the BZ actually contains two Z points and six F and L points, but they are shared between two neighbouring zones). For each TRIM, the so-called parity invariants δ_i for the occupied bands are calculated by

$$\delta(\Gamma_i) = \prod_n \xi_{2n}(\Gamma_i) \tag{7.4}$$

where the $\xi_{2n}(\Gamma_i) = \pm 1$ are the parity eigenvalues of the $2n$th occupied band at Γ_i, obtained from a bulk band structure calculation. Note that the bulk inversion symmetry of Bi_2Se_3 causes the bulk bands to be spin-degenerate because a state at $(\mathbf{k}, \leftarrow)$ has a degenerate partner with $(-\mathbf{k}, \leftarrow)$ due to inversion but also one with $(-\mathbf{k}, \rightarrow)$ due to time-reversal. The index n in equation 7.4 counts all the states, i.e. each spin-degenerate band is counted twice. The product is

therefore only over every other (spin-resolved) band, such that every parity eigenvalue only appears once.

The topological character character of the bulk insulator is given by the so-called $\mathbf{Z}_2$ invariant ν_0. For $\nu_0 = 1(-1)$ the material is a topological (trivial) insulator. ν_0 can be calculated from the parity invariants at the eight TRIMs by

$$(-1)^{\nu_0} = \prod_{n=1}^{8} \delta(\Gamma_i). \tag{7.5}$$

For Bi_2Se_3 , we have 28 valence electrons per unit cell (2×5 from Bi and 3×6 from Se), giving rise to 14 filled bands. The bulk parity invariants for the Z, L and F TRIMs are all calculated to be 1 but for the bulk Γ point δ_i is found to be -1 [12, 45]. The product of (7.5) is thus found to be -1, hence $\nu_0 = 1$ and Bi_2Se_3 is established to be a topological insulator.

The bulk parity invariants can also be used to describe fundamental properties of the surface electronic structure. To do this, the so-called surface fermion parity π_i can be determined for each surface TRIM. Essentially, π_i is obtained by projecting out the bulk parity invariants onto the corresponding surface TRIMs, using the relation $\pi(\lambda_a) = \delta(\Gamma_i)\delta(\Gamma_j)$. [1] We apply this to the (111) surface of Bi_2Se_3 with the SBZ shown in Fig. 7.6b. In this case, $\pi(\bar{\Gamma})$ has to be calculated from the parity invariants of the bulk Γ and Z points, which are -1 and 1, respectively, and hence $\pi(\bar{\Gamma}) = -1$. For $\bar{M}$, on the other hand, $\pi(\bar{M}) = \delta(L)\delta(F) = 1$. Consequently, the surface fermion parity changes from -1 to 1 along the path from $\bar{\Gamma}$ to $\bar{M}$. Such a change can be shown to imply an odd number of surface state Fermi level crossings along the line connecting the two TRIMS, and a closed Fermi contour around the surface TRIM with $\pi = -1$i . These requirements are fulfilled by the electronic structure shown in Fig. 7.5d and this electronic structure is, indeed, also observed for Bi_2Se_3.

[1] Note that this treatment is somewhat simplified as the number of occupied bulk bands and the position of the surface cleavage plane can give rise to sign changes in the π values. This affects the predictions about the detailed surface electronic structure but not the existence of the topologically protected states.

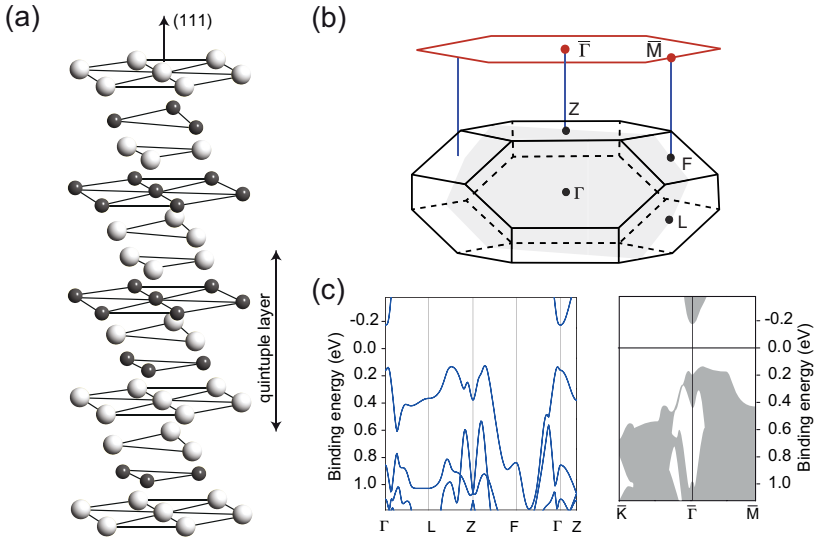

Fig. 7.6 **a** Crystal structure of Bi_2Se_3 with the quintuple layer building blocks. **b** Bulk and surface Brillouin zones with bulk time-reversal invariant momenta (TRIMs) and their projection to surface TRIMs. **c** Bulk band structure along selected high symmetry points and projection on the (111) surface after Ref. [46]

7.3 Angle-resolved photoemission spectroscopy (ARPES)

ARPES has without question been a key-technique in identifying the topological surface states on TI and we will illustrate the power of the technique in the next section. Here we briefly discuss the principle of ARPES as far as required for the rest of this Chapter. For more detailed information about this well-established technique, the reader is referred to a number of excellent reviews and books [47, 48, 49, 50, 51, 52]).

The working principle of ARPES is illustrated in Fig. 7.7. Incoming UV photons cause the emission of photoelectrons from the solid and these electrons are detected by a spectrometer. The emission is only studied in a small range of solid angle, defined by the emission angles θ and ϕ. The photoe-

mission intensity of the emitted electrons is measured as a function of kinetic energy and intensity maxima in this distribution are assigned to emission from particular states in the sample. Thus, one measures the kinetic energy and the **k**-vector for such states outside the surface and the objective of the analysis is to work back to the binding energy and **k**-vector inside the solid, i.e. to the band structure. It is also possible to measure the spin of the photoelectrons and to use this in order to draw conclusions about the spin of the states in the sample. This technique of spin-polarized ARPES suffers from very inefficient detectors and therefore poor resolution and statistics. For identifying the spin texture of the topological surface states, however, it is indispensable.

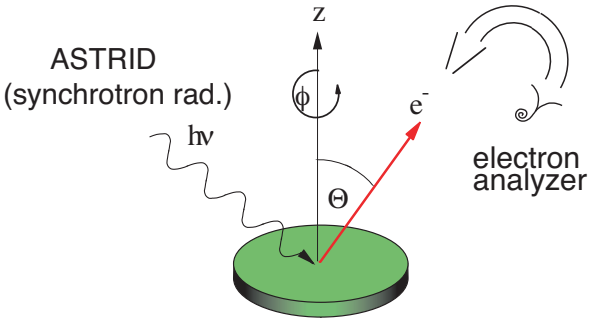

Fig. 7.7 Working principle of angle-resolved photoemission spectroscopy (ARPES). The technique is based on the photoelectric effect where the absorption of UV-photons leads to electron emission. The electron emission current is measured as a function of direction with respect to the sample surface normal and as a function of kinetic energy. This is achieved by a hemispherical electron analyser with an entrance lens and an electron counter. It is also possible to measure the spin of the photoelectrons by replacing the electron counter with a spin-sensitive detector

It is useful to first establish the purely kinematic conditions for the observation of a state in ARPES. Energy conservation demands that emission from a state with binding energy E_b (with respect to the Fermi level) leads to a photoelectron with kinetic energy $E_{kin} = h\nu - E_b - \Phi$, where $h\nu$ is the photon energy and Φ the sample's work function. Momentum conservation, on the other hand, is more involved because the introduction of the surface breaks the translational periodicity of the crystal in the z direction. The wave vector in that direction k_z is thus no longer well-defined. The components of the wave vector parallel to the surface ($\mathbf{k}_{\|}$), on the other hand, are still well defined and

must be conserved in the photoemission process. $\mathbf{k}_\parallel$ of the electron outside the surface (and thus also from the state inside the surface) is obtained from

$$\mathbf{k}_\parallel = (\sin(\phi)\hat{\mathbf{x}} + \cos(\phi)\hat{\mathbf{y}})\sin(\theta) \cdot \sqrt{\frac{2m_e E_{kin}}{\hbar^2}} \,. \tag{7.6}$$

For surface-localized states, such as the topological state, the dispersion of the band only depends on $\mathbf{k}_\parallel$; k_z is not a relevant quantum number and the kinematic conditions are sufficient to extract the surface state dispersion from the measured photoemission intensity.

The fact that the surface state binding energy is independent of k_z also implies that the state will be observed to be at the same binding energy, regardless of the photon energy used in the experiment. To see this, consider Fig. 7.8a that shows the dispersion of a bulk initial state, a surface state, and a final state as a function of k_z. The surface state energy does not depend on k_z but the energy of the two other states does. In the photoemission process, occupied initial states are excited into unoccupied final states and the photon energy thus determines the permitted k_z for the transition from initial state to final state. For the surface state, the kinetic energy of the photoemitted electron depends on the photon energy but the measured binding energy (with respect to the Fermi energy) does not. The absence of dispersion upon a change in photon energy is thus a necessary condition for identifying a state as a surface state.

As pointed out above, the wave vector in the z direction is not a good quantum number near the surface because the translational symmetry in this direction is broken. Even if we ignore this fundamental problem for the time being, it would not be possible to recover k_z inside the sample from the value measured outside because in order to do this the dispersion of the final states would have to be known [51]. This is evident from Fig. 7.8b that shows illustrates photoemission from a bulk band at two different photon energies. The k_z value of the emitted electron depends on the dispersion of initial state and final state, as these define the k_z value for which the photon energy corresponds to the energy difference between these bands.

Despite these difficulties, it is often still possible to recover k_z of the initial state from photoemission spectra taken as a function of $h\nu$, at least for high symmetry points in the BZ where the dispersion reaches an extremum. Once the photon energy for these extrema is known, a frequently used approach to recover k_z for the remaining dispersion is the assumption of free electron final states. k_z plus or minus a reciprocal lattice vector can then be calculated by

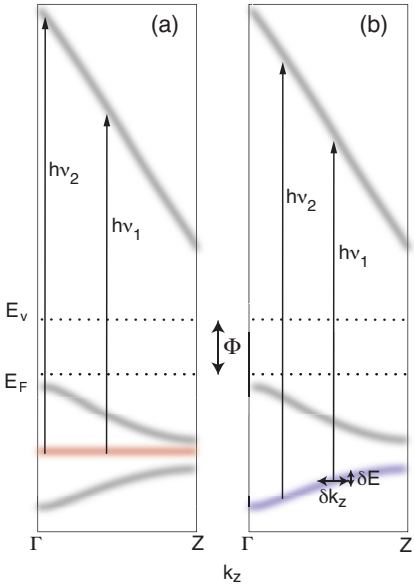

Fig. 7.8 Schematic picture of the photoemission process from different types of electronic states. E_F and E_V are the Fermi and vacuum level, respectively. Φ is the work function. Shown is the dispersion of different states as a function of wave vector perpendicular to the surface k_z. **a** The dispersion of a surface state does not depend on k_z and therefore the observed binding energy for this state (distance from E_F) does not depend on the photon energy $h\nu$. **b** Bulk states measured with different photon energies appear at different binding energies in the spectrum, i.e. they show dispersion. The fact that k_z is not well-defined leads to a broadening δk_z that is then reflected in an energy broadening δE of the observed peaks

$$k_z = \sqrt{2m_e/\hbar^2(V_0 + E_{kin})}\,, \tag{7.7}$$

where V_0 is the so-called inner potential. V_0 can be determined iteratively by requiring the resulting k_z to be consistent with the binding energy extrema at high symmetry points.

The problem that k_z is not well-defined anymore cannot be neglected either. In particular, the finite escape depth of the photoelectron leads to a k_z broadening δk_z. As the bulk state disperses in the k_z direction, this also leads to an energy broadening δE, as illustrated in Fig. 7.8b.

For surface states, and two-dimensional states in general, there is no additional broadening and this permits a much more far-reaching interpretation of the photoemission intensity. Indeed, the photoemission intensity can be can be interpreted in terms of the state's hole spectral function $\mathscr{A}$ weighted by the Fermi-Dirac distribution f and a matrix element $|M_{fi}|$

$$I(E_{kin},\mathbf{k}) \propto |M_{fi}|^2 f(h\nu - E_{kin} - \Phi, T)\mathscr{A}(h\nu - E_{kin} - \Phi, \mathbf{k}) \,, \tag{7.8}$$

at least when infinitely good energy and angular resolution are assumed. The spectral function can be written as

$$\mathscr{A}(\omega,\mathbf{k},T) = \frac{\pi^{-1}|\Sigma''(\omega,\mathbf{k},T)|}{[\hbar\omega - \varepsilon(\mathbf{k}) - \Sigma'(\omega,\mathbf{k},T)]^2 + \Sigma''(\omega,\mathbf{k},T)^2} \,, \tag{7.9}$$

where $\varepsilon(\mathbf{k})$ is the single-particle dispersion. Σ' and Σ'' are the real and imaginary part of the so-called self-energy that contains the information about many-body effects. As evident from (7.9), Σ' leads to a deviation of the state's dispersion from the single-particle case and Σ'' gives rise to a broadening that corresponds to a finite hole lifetime $\tau = \hbar/2\Sigma''$. The possibility to access the self-energy by ARPES thus gives direct information on the state lifetime and this is determined by many-body effects, such as electron-defect scattering or electron-phonon scattering.

7.4 Measured electronic structure of topological insulators

In this final section we show how the surface electronic structure of the prototypical TI Bi_2Se_3 can be determined by ARPES. We will illustrate how the topological states are identified, how their spin texture is confirmed by spin-resolved ARPES and how information about many-body effects can be obtained, using the example of the electron-phonon coupling.

7.4.1 Observation of the topological surface states

We address the situation for the (111) surface of Bi_2Se_3 which is the only surface of this material that could be prepared so far. The reason why investigations are restricted to the (111) surface derives from the bulk structure of Bi_2Se_3 that is a stack of covalently bonded quintuple layers, separated by gaps with largely van der Waals bonding (see Fig. 7.6a. The (111) surface of the material can very easily be prepared by cleaving the sample parallel to the quintuple layers. However, cleaves in other directions have not been achieved yet.

Turning back to the topological considerations, we have found that Bi_2Se_3 (111) shows a change of surface fermion parity values between $\bar{\Gamma}$ with $\pi = -1$ and $\bar{M}$ with $\pi = 1$. As stated above, this implies an odd number of Fermi level crossings between these surface TRIMS. Actually, the topological predictions are even stronger than this, requiring that the surface TRIM with the negative surface fermion parity must be enclosed by an odd number of Fermi contours.

Fig. 7.9 shows cuts through a three-dimensional ARPES data set taken in the vicinity of the $\bar{\Gamma}$ point of Bi_2Se_3(111). Two types of cuts are show. On the left hand side the photoemission intensity is shown as a function of $\mathbf{k}_{\parallel} = (k_x, k_y)$ at fixed binding energies and on the right hand side it is shown as a function of binding energy and a specific high-symmetry direction in the $\mathbf{k}_{\parallel}$ plane. Clearly a cone-shaped state is identified that is very similar to the schematic state shown in Fig. 7.5d. The state crosses the Fermi energy where the photoemission intensity drops to zero. At a binding energy of ≈ 0.3 eV, the dispersion meets in the degeneracy point at $\bar{\Gamma}$. This particular dispersion and this point are often referred to as the Dirac cone and Dirac point, respectively. From such a data set alone, is very tempting to identify the Dirac cone as the topological surface state because of its metallic nature and its dispersion that is consistent with the topological predictions.

Apart from the Dirac cone, broader features are observed at higher binding energies. These will be shown to derive from the uppermost valence band in Bi_2Se_3. Finally, a diffuse intensity at the Fermi energy is observed in the centre of the SBZ. This is caused by conduction band states, implying that this band is at least partly occupied. Indeed, the sample in question is degenerately *n*-doped, something that is frequently observed in pristine Bi_2Se_3 samples. This degenerate *n*-doping does not affect the possibility to observe the topological surface states by ARPES but it renders it very difficult to measure their contribution in transport experiments where the strongly doped bulk dominates.

Before we discuss the further experimental evidence that the cone-shaped state is in fact the topological surface state, consider a sketch of this state in Fig. 7.10a. The state has a cone-line shape, it is not spin degenerate except for the $\bar{\Gamma}$ point and it is centred around this point. The general topology of this state is consistent with the the predictions based on the surface fermion parity. There is an odd number (one) of Fermi level crossings between $\bar{\Gamma}$ and $\bar{M}$ and the $\bar{\Gamma}$ point is encircled by an odd number of Fermi contours (also one). No other surface states have been observed in the rest of the surface Brillouin zone of Bi_2Se_3 .

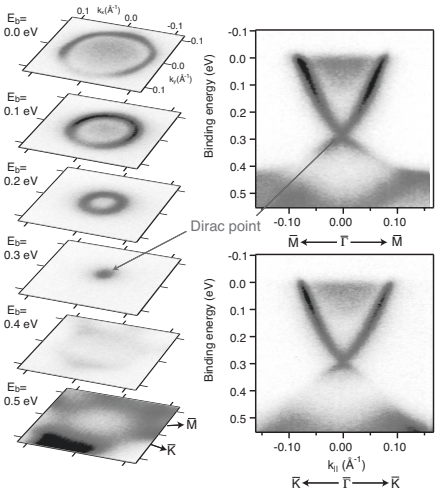

Fig. 7.9 Photoemission intensity from Bi_2Se_3 in the vicinity of the surface Brillouin zone centre. Different cuts through a three dimensional data set of the photoemission intensity $I(k_x, k_y, E_b)$ are shown. The left hand side shows cuts in $\mathbf{k}_\parallel$ at different binding energies. The right hand side shows the the dispersion of the states along two high-symmetry directions. The Dirac-cone shaped topological surface state can be easily identified, as well as states from the valence band and the conduction band (adapted from [53]

An important characteristic of the state is the non-degeneracy with respect to spin and the spin texture. The spin is expected to rotate on the constant energy surfaces of the cone while being perpendicular to the $\mathbf{k}_\parallel$ of the state. The sense of rotation is the same as for the inner branch of a Rashba-split state (see Fig. 7.5), as the state can be viewed as derived from a Rashba state. Time-reversal symmetry for a non-degenerate state dictates that the spin of a state with $\mathbf{k}_\parallel$ is anti-parallel to that of the state with $-\mathbf{k}_\parallel$. Consequently, these two states are orthogonal and one expects a lack of backscattering in the system. In other words, a hole on one side of a constant energy surface cannot be filled by an electron on the opposite side (see Fig. 7.10). This is a celebrated result for topological insulators and can be made visible by experiments with scanning tunnelling spectroscopy [54, 55]. Not surprisingly, the same behaviour had also been found earlier for surface states on materials with very strong Rashba splitting in the surface states, which leads to an electronic structure that is very similar to that in the topological insulators [56]. For the later discussion, it is important to note that, strictly spoken, only direct backscattering is spin-forbidden. Near-backscattering is merely unlikely (because the spin projection is still small) and near-forward scattering is hardly affected by the spin texture. Formally, this is described by a factor of $0.5(1+\cos\alpha)$, where α is the angle between the two $\mathbf{k}_\parallel$ vectors involved in the scattering process [39].

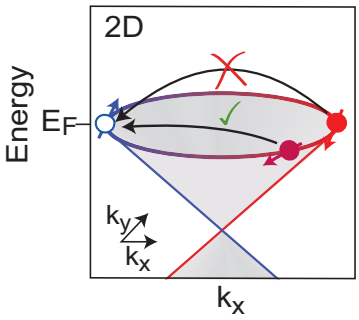

Fig. 7.10 Schematic representation of the surface state dispersion, the spin texture and possible scattering events for Bi_2Se_3. A hole at a constant energy surface on the left cannot be filled by elastic scattering of an electron at the opposite side of the Fermi contour because this process is spin forbidden. But it can be filled by scattering from any other state on the Fermi contour

The surface character of the observed state can be confirmed by performing experiments at different photon energies. According to the previous section, the surface state binding energy should not be affected by the choice of photon energy, in contrast to the energy of the bulk states. The result of such an energy scan is shown in Fig. 7.11. The upper panel of Fig. 7.11a-b shows the the photoemission intensity as a function of binding energy and $\mathbf{k}_{\parallel}$ for two photon energies (19.2 and 26.6 eV, respectively). Clearly, the topological surface state is observed at the same position, confirming the assignment as a two-dimensional state. The bulk VB and CB, on the other hand, change their appearance somewhat. This is more clearly seen in the data shown in Fig. 7.11c that shows the photoemission intensity in normal emission only (i.e. the centre of the images in (a),(b)) as a function of binding energy and k_z. k_z has been determined using free electron final states (7.7) with an inner potential of $V_0 = 11.8$ eV. In this representation of the data, the dispersion of the CB and VB is clearly visible and high symmetry points can be identified (Γ and Z). Such scans permit the determination of parameters such as the size of the band gap and width of the bands.

While the surface assignment of the topological state has thus been confirmed, we are lacking the confirmation of the expected spin texture and in particular of the non-degenerate character of the state. This is crucial for being able to assign the observed dispersion to a topological surface state rather than to an ordinary surface state. Fig. 7.12 shows the result from a spin-resolved ARPES experiment [57, 58]. The data points show the spin polarization in a scan along the $\bar{\Gamma} - \bar{M}$ direction that includes the two Fermi level crossings of the topological state, as indicated in the inset of the figure. The degree of spin

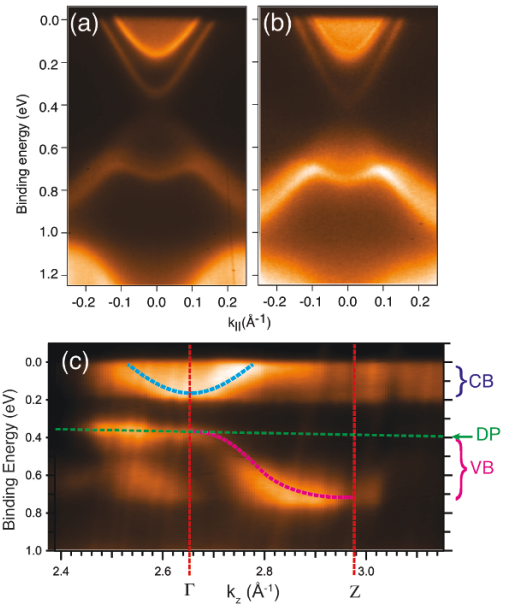

Fig. 7.11 **a** and **b** Photoemission intensity from the surface and bulk states in Bi_2Se_3 at two different photon energies (19.2 and 26.6 eV, respectively). **c** Photoemission intensity in normal emission, showing the dispersion of the bulk CB and VB (emphasized by dashed lines). Note that the entire electronic structure gradually shifts to higher binding energies over time, an effect that is caused by contamination-induced band bending [14, 53]. The shift results in the small shift of the Dirac point (DP) (and the entire surface state dispersion) over the width of the scan

polarization is measured in the direction parallel to the surface but perpendicular to the scan direction. The states crossing the Fermi level are found to be strongly spin-polarized but in opposite directions, consistent with the expected polarization in a Rashba model. This does not only confirm the expected spin texture but also the assumption that the state is not spin-degenerate, apart from at the $\bar{\Gamma}$ point.

With this, it is firmly established that the observed state is in fact the predicted topological surface state. The combination of high-resolution spin-integrated ARPES and spin-resolved ARPES has been used to identify topological states on many different TI materials [11, 14, 16, 59].

Recently, a number of studies have reported the observation of a strong circular dichroism in the ARPES intensity from topological surface states [60, 61, 62, 63, 64] and it has been discussed if and how this can be related to the spin texture of the state. An example of the observed circular dichroism is given in Fig. 7.13 that shows polarization-dependent measurements of the photoemission intensity as a function of $\mathbf{k}_{||}$ at an energy 150 meV above the Dirac point in Bi_2Se_3 ((a) and (b)), as well as circular dichroism obtained from these two data sets in an equivalent image (c) and quantitatively along the

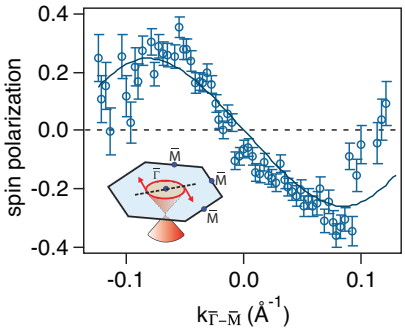

Fig. 7.12 Spin polarization of the topological surface state on Bi_2Se_3 measured by spin-resolved ARPES. The data show the determined polarization in the direction parallel to the surface and perpendicular to $\bar{\Gamma} - \bar{M}$ at a binding energy ≈ 100 meV above the Dirac point. The direction of the scan and the resulting spin polarization are indicated in the inset [58]

circumference of the circular contour (d) [64]. The strong effect of the light's polarisation is evident . The observed circular dichroism has been linked to the spin texture of the surface state and the technique has been proposed as an effective method to determine this spin texture. The detailed mechanism for this is still disputed but it appears likely that the circular dichroism is actually a consequence of the orbital texture rather than the spin texture. However, since spin and orbital degrees of freedom are very strongly coupled in a TI surface state, it may be possible to exploit the circular dichroism as a viable and efficient way to gain information about the state's spin texture.

7.4.2 Dynamics of the surface states: Electron-phonon coupling

With the existence of the topological surface states firmly established, ARPES can be used to study the dynamics of these states. Of particular interest in this context is the sensitivity of the surface state electrons to defect scattering or electron-phonon scattering. After all, these processes limit the lifetime of excited carriers and thereby the surface channel conductivity. This is especially important because the bulk TI materials are found to be rather conductive, as explained above, and the desired transport situation is to have the surface state conductance dominate over the bulk conductance.

Possible scattering process for the surface state electrons were summarized in Fig. 7.10. These processes are related to elastic scattering, i.e. defect scattering. The situation for electron-phonon scattering is not very different.

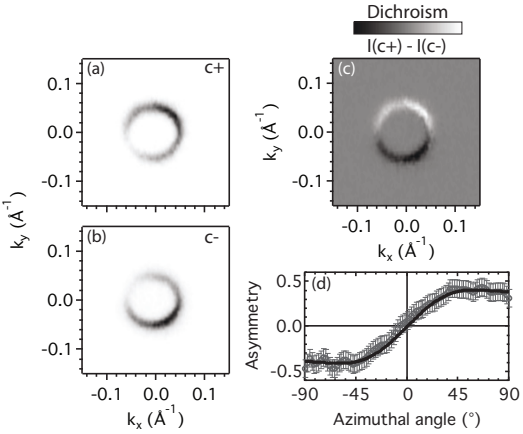

Fig. 7.13 Circular dichroism in ARPES from the topological surface state on Bi_2Se_3, approximately 150 meV above the Dirac point. **a** and **b** Photoemission intensity for light with right and left circular polarization, respectively. **c** Normalized difference between the two. **d** Quantitative dichroism along the circular contour. Data from [64]

Instead of taking the required momentum from an impurity scattering event, it is provided by the emission or absorption of a phonon. The process is not strictly elastic because the phonon energy has to be taken into account. However, since this energy is usually very small, it is often sufficient to consider the so-called quasi-elastic approximation where it is entirely neglected [65]. In this case, the situation is very similar to Fig. 7.10. In particular, the phase space restriction due to the spin texture is identical.

In contrast to defect scattering, however, it is easy to probe the strength of the electron-phonon coupling by changing the number of available phonons for scattering processes via the sample temperature. Fig. 7.14a-c show the dispersion of the surface state on Bi_2Se_3 measured at three different temperatures (after Ref. [66]). The temperature effect over this range is not very big and the state appears sharp over the tested temperature range.

A more systematic analysis of the temperature-dependent width is given in Fig. 7.14d that shows the temperature-dependent width of the state measured for many different sample preparations (via cleaving bulk crystals) but for only two temperatures per sample cleave. The reason why not more temperatures were measured is the rapid change of the surface electronic structure

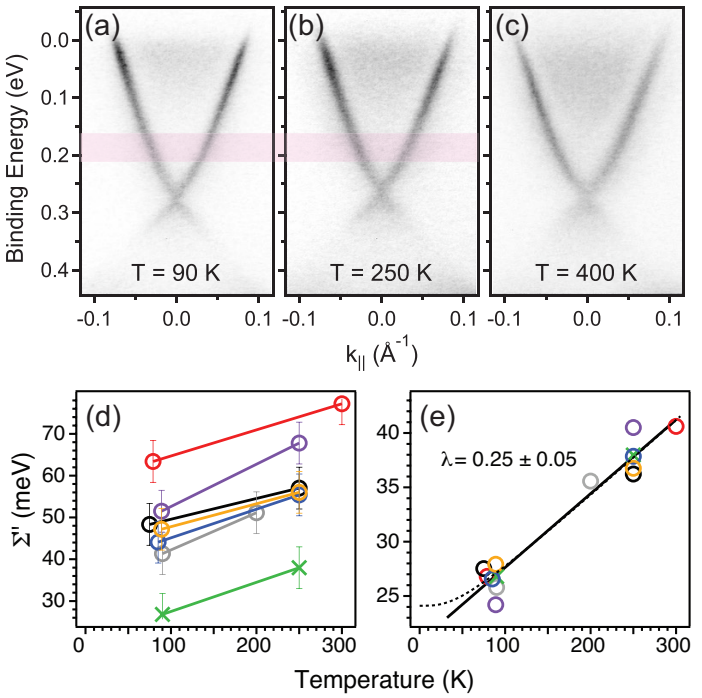

Fig. 7.14 Electron-phonon scattering on Bi_2Se_3 studied by ARPES. **a** to **c** Dispersion of the topological surface state at three temperatures. The shaded area indicates the energy range used for a quantitative determination of the linewidth. **d** Temperature-dependent width (expressed by the imaginary part of the self-energy) for different sample preparations. **e** The same data but with individual data sets rigidly shifted in order to account for different amounts of defect scattering. The dashed line shows a Debye model fit to the width and the solid line the high temperature (linear) limit. Data from Ref. [66]

after cleaving. Two temperatures could be measured in a time interval short enough for this not to be an issue.

The width of the state is expressed in terms of the imaginary part of the self-energy Σ''. This quantity is related to the inverse lifetime of the photohole via $\Sigma'' = \hbar/2\tau$ and it is thus found that the lifetime increases at low temperatures, as expected. The data points have been collected in the energy range where the surface state is far away from the bulk bands, such that bulk-surface scattering cannot play a role. We see that the absolute Σ'' values for the different data

sets are quite different but the difference between the two temperatures is similar. This is, in fact, to be expected because different sample cleaves lead to surfaces with a different amount of static defects. These give rise to an offset between the measurements but they do not affect the temperature dependence.

Fig. 7.14e shows the same data but the different data sets have been shifted rigidly in energy in order to account for the different defect concentrations, and such that the data can be fitted by a theoretical model with a constant defect concentration. The theoretically expected Σ'' in the Debye model is shown as a dashed line and its high temperature limit as a solid line [52]. Qualitatively, the shape of the dashed line is easy to understand: Far below the Debye temperature of the sample, the phonons are frozen out and the electron-phonon contribution to the (inverse) lifetime of the state is constant. At very high temperatures, on the other hand, the temperature dependence is linear, independent of the model used for the phonon dispersion. The slope is given by $2\pi k_B \lambda$, where λ is the so-called electron-phonon mass enhancement parameter. The transition between these two regions is more complicated and depends on the model used.

The result of this type of analysis is a value for λ, quantifying the electron-phonon coupling strength. In the analysis shown here, $\lambda = 0.25 \pm 0.05$ was found. To put this into context, λ values for strong coupling BCS-type superconductors are found to be around 1, whereas they are around 0.1 for a weak-coupling good conductor, such as copper. It is thus evident that the coupling strength for the surface state of Bi_2Se_3 is not especially small. We can also compare the λ value to the fictitious situation of an isolated surface state, i.e. a surface state without the bulk present, such that only intra-state scattering is possible. This has been calculated for the well-studied noble metal surface states and for the Ag(111) state it has been found to be much weaker that the for Bi_2Se_3 ($\lambda = 0.02$) [67].

7.5 Conclusion

We have illustrated that synchrotron radiation-based ARPES is an essential experimental technique to study the surface electronic structure of TIs. It can be used to observe the topological surface state band dispersion and to distinguish these states from bulk states. Spin-resolved ARPES and possibly also circular dichroism ARPES can give essential information about the spin texture of the states. Further research on these materials will almost cer-

tainly involve other synchrotron radiation-based techniques that have not been discussed here. An interesting research field is the adsorption of potentially magnetic impurities on the surface, something that could locally break time-reversal symmetry. Here x-ray magnetic circular dichroism is an essential technique to determine the magnetic properties of the adsorbate [68]. Another example is the structural determination of TI surfaces. The standard technique for this is low-energy electron diffraction but due to the complex structure and the distance of the interesting van der Waals gaps below the surface, it can be foreseen that synchrotron radiation-based surface x-ray diffraction may play an important role.

7.6 Acknowledgement

I gratefully acknowledge discussions with many students and colleagues who helped me to understand the physics of the topological surface states. I thank Justin Wells for making me aware of the "flipper bridge" in Fig. 7.2 and Kamiel Klaasse from NL Architects for letting me use this picture. I also like to thank Gabriel Landoldt and Hugo Dil for providing me with unpublished data for Fig. 7.11, Phil King for Fig. 7.13 and Edward Perkins for a careful proofreading of the manuscript.

References

1. C. L. Kane and E. J. Mele, Phys. Rev. Lett. **95**, 146802, (2005)
2. C. L. Kane and E. J. Mele, Phys. Rev. Lett. **95**, 226801, (2005)
3. Shuichi Murakami, Phys. Rev. Lett. **97**, 236805, (2006)
4. B. Andrei Bernevig and Shou-Cheng Zhang, Phys. Rev. Lett. **96**, 106802, (2006)
5. B. Andrei Bernevig, Taylor L. Hughes, and Shou-Cheng Zhang, Science **314**, 1757 (2006)
6. Liang Fu and C. L. Kane, Phys. Rev. B **76**, 045302 (2007)
7. Liang Fu, C. L. Kane, and E. J. Mele, Phys. Rev. Lett. **98**, 106803, (2007)
8. J. E. Moore and L. Balents, Phys. Rev. B **75**, 121306 (2007)
9. Markus Konig, Steffen Wiedmann, Christoph Brune, Andreas Roth, Hartmut Buhmann, Laurens W. Molenkamp, Xiao-Liang Qi, and Shou-Cheng Zhang, Science **318**, 766 (2007)
10. D. Hsieh, D. Qian, L. Wray, Y. Xia, Y. S. Hor, R. J. Cava, and M. Z. Hasan, Nature **452**, 970 (2008)

11. D. Hsieh, Y. Xia, L. Wray, D. Qian, A. Pal, J. H. Dil, J. Osterwalder, F. Meier, G. Bihlmayer, C. L. Kane, Y. S. Hor, R. J. Cava, and M. Z. Hasan, Science **323**, 919 (2009)
12. Haijun Zhang, Chao-Xing Liu, Xiao-Liang Qi, Xi Dai, Zhong Fang, and Shou-Cheng Zhang, Nature Physics, **5**, 438 (2009)
13. Y. Xia, D. Qian, D. Hsieh, L. Wray, A. Pal, H. Lin, A. Bansil, D. Grauer, Y. S. Hor, R. J. Cava, and M. Z. Hasan, Nature Physics **5**, 398 (2009)
14. D. Hsieh, Y. Xia, D. Qian, L. Wray, J. H. Dil, F. Meier, J. Osterwalder, L. Patthey, J. G. Checkelsky, N. P. Ong, A. V. Fedorov, H. Lin, A. Bansil, D. Grauer, Y. S. Hor, R. J. Cava, and M. Z. Hasan, Nature **460**, 1101 (2009)
15. Y. L. Chen, J. G. Analytis, J. H. Chu, Z. K. Liu, S. K. Mo, X. L. Qi, H. J. Zhang, D. H. Lu, X. Dai, Z. Fang, S. C. Zhang, I. R. Fisher, Z. Hussain, and Z. X. Shen, Science **325**, 178 (2009)
16. D. Hsieh, Y. Xia, D. Qian, L. Wray, F. Meier, J. H. Dil, J. Osterwalder, L. Patthey, A. V. Fedorov, H. Lin, A. Bansil, D. Grauer, Y. S. Hor, R. J. Cava, and M. Z. Hasan, Phys. Rev. Lett. **103**, 146401 (2009)
17. J. G. Checkelsky, Y. S. Hor, M.-H. Liu, D.-X. Qu, R. J. Cava, and N. P. Ong, Phys. Rev. Lett. **103**, 246601 (2009)
18. Dong-Xia Qu, Y. S. Hor, Jun Xiong, R. J. Cava, and N. P. Ong, Science **329**, 821 (2010)
19. James G. Analytis, Jiun-Haw Chu, Yulin Chen, Felipe Corredor, Ross D. McDonald, Z. X. Shen, and Ian R. Fisher, Phys. Rev. B **81**, 205407 (2010)
20. James G. Analytis, Ross D. McDonald, Scott C. Riggs, Jiun-Haw Chu, G. S. Boebinger, and Ian R. Fisher, Nature Physics **6**, 960 (2010)
21. H. Steinberg, D.R. Gardner, Y.S. Lee, and P. Jarillo-Herrero, Nano Lett. **10** 5032 (2010)
22. J. G. Checkelsky, Y. S. Hor, R. J. Cava, and N. P. Ong, Phys. Rev. Lett. **106**, 196801 (2011)
23. J. Chen, X. Y. He, K. H. Wu, Z. Q. Ji, L. Lu, J. R. Shi, J. H. Smet, and Y. Q. Li, Phys. Rev. B **83**, 241304 (2011)
24. Sungjae Cho, Nicholas P. Butch, Johnpierre Paglione, and Michael S. Fuhrer, Nano Lett. **11**, 1925 (2011)
25. Faxian Xiu, Liang He, Yong Wang, Lina Cheng, Li-Te Chang, Murong Lang, Guan Huang, Xufeng Kou, Yi Zhou, Xiaowei Jiang, Zhigang Chen, Jin Zou, Alexandros Shailos, and Kang L. Wang, Nat. Nano. **6**, 216 (2011)
26. N. P. Butch, K. Kirshenbaum, P. Syers, A. B. Sushkov, G. S. Jenkins, H. D. Drew, and J. Paglione, Phys. Rev. B **81**, 241301 (2010)
27. Yong Seung Kim, Matthew Brahlek, Namrata Bansal, Eliav Edrey, Gary A. Kapilevich, Keiko Iida, Makoto Tanimura, Yoichi Horibe, Sang-Wook Cheong, and Seongshik Oh, Phys. Rev. B **84**, 073109 (2011)
28. A. A. Taskin, Satoshi Sasaki, Kouji Segawa, and Yoichi Ando, Phys. Rev. Lett. **109**, 066803 (2012)
29. Peng Cheng, Canli Song, Tong Zhang, Yanyi Zhang, Yilin Wang, Jin-Feng Jia, Jing Wang, Yayu Wang, Bang-Fen Zhu, Xi Chen, Xucun Ma, Ke He, Lili Wang, Xi Dai, Zhong Fang, Xincheng Xie, Xiao-Liang Qi, Chao-Xing Liu, Shou-Cheng Zhang, and Qi-Kun Xue, Phys. Rev. Lett. **105**, 076801 (2010)
30. S. C. Zhang, Physics **1**, 6 (2008)
31. Joel E. Moore, Nature **464**, 194 (2010)
32. M. Z. Hasan and C. L. Kane, Rev. Mod. Phys. **82**, 3045 (2010)

33. Desheng Kong and Yi Cui, Nat. Chem. **3**, 845 (2011)
34. Xiao-Liang Qi and Shou-Cheng Zhang, Rev. Mod. Phys. **83**, 1057 (2011)
35. H. Lüth, *Surfaces and interfaces of solid materials*, 3rd edn.(Springer Verlag 1992)
36. E. Tosatti, in *Electronic surface and interface states on metallic systems*. ed. by E. Bertel and M. Donath (World Scientific, Singapore, 1995) p.67
37. F. Reinert, G. Nicolay, S. Schmidt, D. Ehm, and S. Hüfner, Phys. Rev. B **63**, 115415 (2001)
38. N. E. Ashcroft and N. D. Mermin, *Solid state physics*, (Saunders College, Philadelphia, international edition, 1976)
39. I. A. Nechaev, M. F. Jensen, E. D. L. Rienks, V. M. Silkin, P. M. Echenique, E. V. Chulkov, and Ph. Hofmann, Phys. Rev. B **80**, 113402 (2009)
40. É. I. Rashba, Soviet Phys. - Sol. State, **2**, 1109 (1960)
41. Y. A. Bychkov and É. I. Rashba, J. Phys.C: Cond. Mat., **17**, 6039 (1984)
42. S. LaShell, B. A. McDougall, and E. Jensen, Phys. Rev. Lett. **77**, 3419 (1996)
43. F. Reinert, J. Phys.:Cond. Mat. **15**, S693 (2003)
44. Jeffrey C. Y. Teo, Liang Fu, and C. L. Kane, Phys. Rev. B **78**, 045426 (2008)
45. Wei Zhang, Rui Yu, Hai-Jun Zhang, Xi Dai, and Zhong Fang, New J. Phys. **12**, 065013 (2010)
46. S. Eremeev, Yu. Koroteev, and E. Chulkov, JETP Lett. **91**, 387 (2010)
47. F. J. Himpsel and N. V. Smith, Physics Today, **38**, 60 (1985)
48. E. W. Plummer and W. Eberhardt, Adv. Chem. Phys. **49**, 533 (1982)
49. S. D. Kevan (ed.), *Angle-resolved photoemission*, volume 74 of *Studies in Surface Chemistry and Catalysis*, (Elsevier, Amsterdam, 1992)
50. R. Matzdorf, Surf. Sci. Rep. **30**, 153 (1998)
51. S. Hüfner, *Photoelectron spectroscopy*, 3rd edn .(Springer, Berlin, 2003)
52. Ph. Hofmann, I. Yu Sklyadneva, E.D.L Rienks, and E.V. Chulkov, New J. Phys. **11**, 125005 (2009)
53. M. Bianchi, D. Guan, S. Bao, J. Mi, Bo B. Iversen, P. D. C. King, and Ph. Hofmann. Nature Comm. **1**, 128 (2010)
54. Pedram Roushan, Jungpil Seo, Colin V. Parker, Y. S. Hor, D. Hsieh, Dong Qian, Anthony Richardella, M. Z. Hasan, R. J. Cava, and Ali Yazdani, Nature **460**, 1106 (2009)
55. Tong Zhang, Peng Cheng, Xi Chen, Jin-Feng Jia, Xucun Ma, Ke He, Lili Wang, Haijun Zhang, Xi Dai, Zhong Fang, Xincheng Xie, and Qi-Kun Xue, Phys. Rev. Lett. **103**, 266803 (2009)
56. J. I. Pascual, G. Bihlmayer, Y. M. Koroteev, H. P. Rust, G. Ceballos, M. Hansmann, K. Horn, E. V. Chulkov, S. Blügel, P. M. Echenique, and Ph. Hofmann, Phys. Rev. Lett. **93**, 196802 (2004)
57. M. Hoesch, T. Greber, V. Petrov, A. Muntwiler, M. Hengsberger, W. Auwarter, and J. Osterwalder, J. Electron. Spectr. Rel. Phen. **124**, 263 (2002)
58. Gabriel Landolt and Jan Hugo Dil, unpublished results
59. Su-Yang Xu, Y. Xia, L. A. Wray, S. Jia, F. Meier, J. H. Dil, J. Osterwalder, B. Slomski, A. Bansil, H. Lin, R. J. Cava, and M. Z. Hasan, Science **332**, 560 (2011)
60. Seung Ryong Park, Jinhee Han, Chul Kim, Yoon Young Koh, Changyoung Kim, Hyungjun Lee, Hyoung Joon Choi, Jung Hoon Han, Kyung Dong Lee, Nam Jung Hur, Masashi Arita, Kenya Shimada, Hirofumi Namatame, and Masaki Taniguchi, Phys. Rev. Lett. **108**, 046805 (2012)

61. Jin-Hong Park, Choong H. Kim, Jun-Won Rhim, and Jung Hoon Han, Phys. Rev. B **85**, 195401 (2012)
62. Y. H. Wang, D. Hsieh, D. Pilon, L. Fu, D. R. Gardner, Y. S. Lee, and N. Gedik, Phys. Rev. Lett. **107**, 207602 (2011)
63. Y. Ishida, H. Kanto, A. Kikkawa, Y. Taguchi, Y. Ito, Y. Ota, K. Okazaki, W. Malaeb, M. Mulazzi, M. Okawa, S. Watanabe, C.-T. Chen, M. Kim, C. Bell, Y. Kozuka, H. Y. Hwang, Y. Tokura, and S. Shin, Phys. Rev. Lett. **107**, 077601 (2011)
64. M.S Bahramy, P. D. C. King, A. de la Torre, J. Chang, M. Shi, L. Patthey, G. Balakrishnan, Ph. Hofmann, R. Arita, N. Nagoasa, and F. Baumberger, Nature Comm.**3**, 1159 (2012)
65. B. Hellsing, A. Eiguren, and E. V. Chulkov, J. Phys.: Cond. Mat., **14**, 5959 (2002)
66. Richard C. Hatch, Marco Bianchi, Dandan Guan, Shining Bao, Jianli Mi, Bo Brummerstedt Iversen, Louis Nilsson, Liv Hornekær, and Philip Hofmann, Phys. Rev. B **83**, 241303 (2011)
67. A. Eiguren, B. Hellsing, E. V. Chulkov, and P. M. Echenique, Phys. Rev. B **67**, 235423 (2003)
68. J. Honolka, A. A. Khajetoorians, V. Sessi, T. O. Wehling, S. Stepanow, J.-L. Mi, B. B. Iversen, T. Schlenk, J. Wiebe, N. B. Brookes, A. I. Lichtenstein, Ph. Hofmann, K. Kern, and R. Wiesendanger, Phys. Rev. Lett. **108**, 256811 (2012)

Chapter 8
Anisotropic x-ray magnetic linear dichroism

Gerrit van der Laan

Abstract In this Chapter, the reader will be able to gain a deeper understanding in the angular dependence of x-ray absorption (XA) and x-ray magnetic linear dichroism (XMLD). The scattering tensor provides a general framework for the XA intensity, which is a function of the relative orientation of the magnetization **M**, the x-ray polarization **E** and the crystalline axes. In cubic crystal field, the XMLD is a linear combination of two independent spectra, which means that the maximum of the XMLD will be photon energy dependent and no longer at $\mathbf{E} \parallel \mathbf{M}$. The angular dependence of the XMLD can be separated into an isotropic part, which rotates with **M**, and an anisotropic part, which depends on the orientation of the crystal axes. At the Ni^{2+} L_2 edge, where the isotropic part vanishes, the angular dependence is fully determined by the anisotropic part, which obtains maximal intensity when **E** and **M** have equal but opposite angles with respect to the [100] direction. In the past this complication has not been appreciated, leading in confusion and misinterpretation in the literature.

Gerrit van der Laan
Diamond Light Source, Harwell Science and Innovation Campus, Didcot, Oxfordshire OX11 0DE, United Kingdom, e-mail: gerrit.vanderlaan@diamond.ac.uk

E. Beaurepaire et al. (eds.), *Magnetism and Synchrotron Radiation: Towards the Fourth Generation Light Sources*, Springer Proceedings in Physics 151,
DOI: 10.1007/978-3-319-03032-6_8,

8.1 Introduction

Why would we revisit x-ray magnetic linear dichroism (XMLD)? Well, there are good reasons for this. Compared to its circular sibling, XMLD has long been regarded as an ugly duckling, but one day it flies out as a beautiful wild swan. XMLD is the only substitute of x-ray magnetic circular dichroism (XMCD) for studying antiferromagnets. It is important for magnetic domain imaging with photoemission electron microscopy (PEEM), and forms the basis for x-ray resonant processes, such as x-ray resonant scattering, resonant Raman, resonant photoemission, etc. However, XMLD is more complicated than previously thought. Until recently, the complexity of its angular dependence has not been fully realized—not even in the text book by Stöhr and Siegmann [1].

XMLD has since long been established as a probe to study antiferro- as well as ferro- and ferri-magnetic materials [2, 3, 4, 5, 6]. The $L_{2,3}$ spectra of localized $3d$ transition metal ions for different crystal field strengths have been successfully calculated using multiplet theory [7]. For itinerant $3d$ metallic systems the line shapes of the $L_{2,3}$ XMLD spectra can be explained using the effective exchange field splitting of the core hole [8]. Sum rules for XMLD relate the integrated intensity over the L_3 and L_2 edges to the expectation values of the charge quadrupole moment and the anisotropic spin-orbit interaction [9]. Although the integrals in the case of XMLD are smaller than for XMCD, their study has provided important insights in the microscopic origin of the magnetocrystalline anisotropy [10, 11] . Kuneš and Oppeneer [12] calculated a huge magnetocrystalline anisotropy of the XMLD spectra at the $L_{2,3}$ edges of cubic Fe, Co, and Ni metal, which displayed an opposite sign along the different high-symmetry quantization axes. The anisotropy in the XMLD line shape of itinerant metals was explained using the model for the effective exchange field splitting of the core hole [8]. The sign reversal of the XMLD signal was observed in $LaFeO_3$ [13] by Czekay et al. The large anisotropy in the XMLD was confirmed by multiplet structure calculations by taking properly into account the core-valence Coulomb and exchange interactions [14, 15]. Freeman et al. [14] found experimentally a large anisotropy in the XMLD line shape at the Mn^{2+} $L_{2,3}$ edge in (Ga,Mn)As, in good agreement with atomic multiplet calculations. Since the half filled $3d$ shell of Mn carries no orbital moment, the angular dependence can not be ascribed to the magnetocrystalline anisotropy and indeed the integrated intensities of the $L_{2,3}$ XMLD vanish. The calculations showed that the $3d$ spin-orbit interaction has

little or no effect on the XMLD line shape and that the angular dependence disappears when the crystal-field interaction is switched off.

Using vector magnet magnetometry the full angular dependence of the XMLD has been investigated and compared to multiplet calculations for the transition metal $L_{2,3}$ edges of $Ga_{1-x}Mn_xAs$ [14], Fe_3O_4 [15], $NiFe_2O_4$, NiO [16, 17, 18], $CoFe_2O_4$ [19], Co-based Heusler alloys [20], $La_{0.7}Sr_{0.3}FeO_3$ [21], and Ga_xFe_{1-x} [11], as well as the rare earth $M_{4,5}$ edges of EuO [22]. It was found that in cubic symmetry the angular dependent XMLD could be described by a linear combination of two independent spectra, which are called fundamental spectra [14, 15].

For antiferromagnetic systems, the spin orientation has been studied using the linear polarization dependence of the intensity ratio of the two peaks of the L_2 XA edge. Alders et al. [23, 24] have measured a NiO sample with a statistical distribution of $\langle \pm 1 \pm 1 \pm 2 \rangle$ possible spin directions. In their analysis, which is correct for axial symmetry, the spin orientation with respect to the crystallographic axes was not explicitly taken into account. However, the same approach was later used to analyze the antiferromagnetic domain structures of $LaFeO_3$ [25, 26, 27] and NiO [28, 29, 30, 31, 32, 33], not realizing that the XMLD strongly depends on the crystal field orientation. It was first demonstrated by Arenholz et al. [16] that for a correct interpretation of the XA and XMLD spectra the relative orientation of light polarization and magnetization with respect to the crystal frame have to be taken into account. This has subsequently been applied in several recent studies of various NiO surfaces and interfaces [17, 18, 34, 35, 36].

8.2 Wonderful symmetry

A change in magnetization direction results in a different distribution over the magnetic sublevels m of the atom in a crystal field. A change in polarization direction gives different selection rules ($\Delta m = 0, \pm 1$) for the electric-dipole transitions from ground to the final state. Changing both the magnetization and polarization direction can under symmetry conditions result in the same spectrum.

The ground state in octahedral crystal field splits into E and T_2 orbitals with charge densities along different directions. The E orbitals are aligned towards the neighboring atoms whereas the T_2 orbitals point in between. The energy splitting allows us to spectroscopically distinguish between both types

of orbitals. Generally, when the energy degeneracy is broken, each level set obtains a different angular dependence. Therefore, energy splitting and angular distribution are two different sides of the same coin.

Insight in (dis)symmetry can be gained from the Neumann's principle (1885), which states that "*the symmetry elements of any physical property of a crystal must include the symmetry elements of the point group of the crystal*", or from a general principle formulated by Pierre Curie in 1893: "*When definite dissymmetry is found in some phenomena, the same dissymmetry should be found in the causes that produced them*" [37, 38]. Applying this wisdom to XA, this means that in spherical symmetry (SO_3) there will be two different XA spectra (i.e. for light polarization parallel and perpendicular to the magnetization) and the difference of these XA spectra lead to single XMLD spectrum. If the magnetization (with symmetry C_∞) is along a high symmetry axis of a cubic crystal there will be only one XMLD spectrum. However, when the magnetization is along arbitrary direction there should be more than one XMLD spectrum. The number of distinct XA spectra is determined by the number of different irreducible representations (irreps) in the point group of the crystal. The number of independent XMLD spectra is one less than the number of XA spectra.

We first need to remind ourselves of some elementary point group theory. Starting from the states $|\ell m\rangle$ in SO_3 symmetry we can branch down to the irreps $|\ell\Gamma\rangle = \sum_m |\ell m\rangle\langle \ell m|\ell\Gamma\rangle$ in point group G and then further down to the irreps $|\ell\Gamma\gamma\rangle = \sum_\Gamma |\ell\Gamma\rangle\langle\ell\Gamma|\ell\Gamma\gamma\rangle$ in point group g of lower symmetry. The different partners in the relevant point groups are shown in Fig. 8.1, and we will rely heavily on these new friends in the next section.

Taking the magnetization $\hat{\mathbf{M}}$ and electric-dipole polarization $\hat{\mathbf{E}}$ and $\hat{\mathbf{E}}'$ for incident and scattered x-rays along arbitrary directions, the spectral intensity is separated in an angular and a physical part

$$I(\hat{\mathbf{E}},\hat{\mathbf{E}}',\hat{\mathbf{M}},\omega) = \sum_{k\Gamma\Gamma'\Gamma''\gamma\gamma'\gamma''} \left[C^{(1)}_{\Gamma'\gamma'}(\hat{\mathbf{E}}')\, , C^{(1)}_{\Gamma''\gamma''}(\hat{\mathbf{E}})\, , C^{(k)}_{\Gamma\gamma}(\hat{\mathbf{M}}) \right]^{(0)}_0 F^{(k)}_{\Gamma\gamma}(\omega)\, , \tag{8.1}$$

where the sum runs over all irreps γ of the point group of the crystal. The angular part is formed by the invariant triple tensor product containing polynomial functions $C^{(\ell)}_{\Gamma\gamma}(\theta,\phi)$ of rank ℓ and irrep $\Gamma\gamma$. The physical part is formed by $F^{(k)}_{\Gamma\gamma}(\omega)$, which gives the frequency dependent intensity as a scalar property [39, 40, 41]. It is independent of $\hat{\mathbf{M}}$, but is different for each irrep.

We define the k-th rank tensors

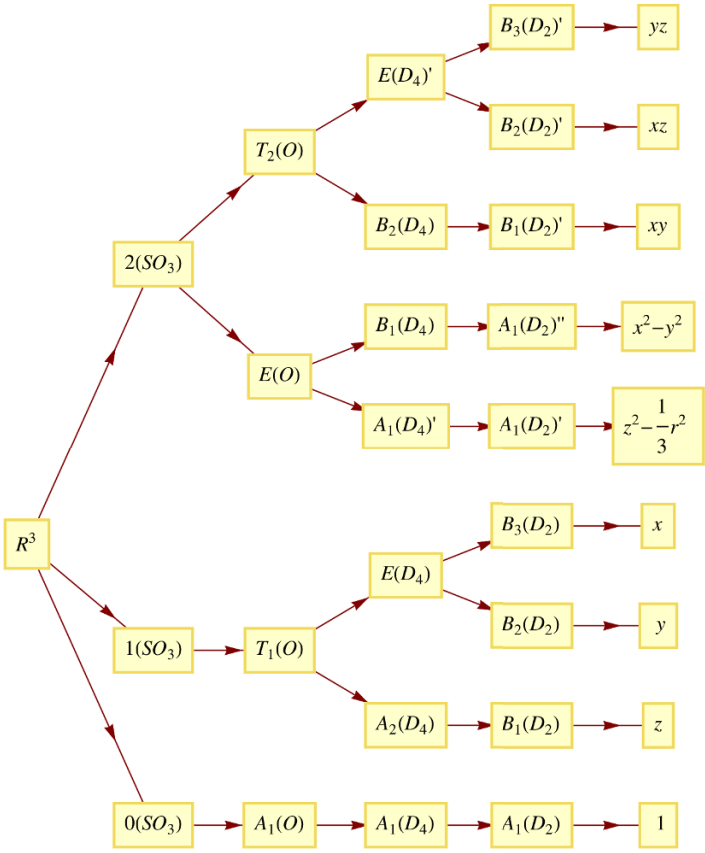

Fig. 8.1 Tree plot of the partners for the point group chain $R^3 \supset SO_3 \supset O \supset D_4 \supset D_2$ in Mulliken notation up to rank two. The last column gives the Cartesian functions of corresponding symmetry. The number of independent XA spectra for each point group symmetry is determined by the number of different partners

$$\mathscr{F}^{(k)}(\hat{\mathbf{M}},\omega) \equiv \sum_{k'\Gamma\gamma} C^{(k')}_{\Gamma'\gamma}(\hat{\mathbf{M}}) F^{(k')}_{\Gamma\gamma}(\omega)\,, \tag{8.2}$$

where $k' = k, k+2, \cdots$. Thus k' and k need to have the same parity, i.e., either even (gerade) or odd (ungerade). The crystal field is able to mix in the higher

k terms, however their magnitude is often small. Furthermore, from now on, we will no longer explicitly carry along the ω in the variable specification.

For electric dipole radiation the scattering tensor $\mathscr{F}$ is composed of a scalar $\mathscr{F}^{(0)}$, a pseudovector (antisymmetric) tensor $\mathscr{F}^{(1)}(\hat{\mathbf{M}})$ and a symmetric tensor $\mathscr{F}^{(2)}(\hat{\mathbf{M}})$, and the scattering intensity is generally given as

$$I(\hat{\mathbf{E}},\hat{\mathbf{E}}',\hat{\mathbf{M}}) = (\hat{\mathbf{E}}^{\star}\cdot\hat{\mathbf{E}}')\mathscr{F}^{(0)} - \mathrm{i}(\hat{\mathbf{E}}^{\star}\times\hat{\mathbf{E}}')\cdot\mathscr{F}^{(1)}(\hat{\mathbf{M}}) + \hat{\mathbf{E}}^{\star}\cdot\mathscr{F}^{(2)}(\hat{\mathbf{M}})\cdot\hat{\mathbf{E}}' \,, \tag{8.3}$$

with magnetization unit vector $\hat{\mathbf{M}} = (\hat{x},\hat{y},\hat{z})$ and polarization unit vector $\hat{\mathbf{E}} = (\hat{\varepsilon}_x,\hat{\varepsilon}_y,\hat{\varepsilon}_z)$. For x-ray absorption we take $\hat{\mathbf{E}}' = \hat{\mathbf{E}}$.

8.3 Scattering intensity for different symmetries

We aim to write out (8.3) explicitly as a function of $\hat{\mathbf{M}}$ and $F^{(k)}$. Armed with the gained knowledge about the symmetry groups we are able to write out the scattering intensity in Cartesian tensor form, which is most useful from viewpoint of experimental geometry.

8.3.1 Spherical symmetry

In spherical symmetry (SO_3) it is straightforward to write out (8.3 as a vector product in $\hat{\mathbf{M}}$, since all $F^{(k)}$ have only a single irrep. Fig. 8.1 shows that $F^{(0)}$ has irrep $\mathbf{0} = \{1\}$, $F^{(1)}$ has irrep $\mathbf{1} = \{x, y, z\}$ and $F^{(2)}$ has irrep $\mathbf{2} = \{z^2 - \frac{1}{3}r^2, x^2 - y^2, xy, yz, xz\}$. In order that $\mathscr{F}^{(2)}(\hat{\mathbf{M}})$ has zero trace, we take $\mathscr{F}^{(0)} = F^{(0)} - \frac{1}{3}F^{(2)}$. The scattering intensity of (8.3) becomes

$$\begin{aligned} I(\hat{\mathbf{E}},\hat{\mathbf{E}}',\hat{\mathbf{M}}) = \hat{\mathbf{E}}^{\star}\cdot\hat{\mathbf{E}}'\left[F^{(0)} - \frac{1}{3}F^{(2)}\right] - \mathrm{i}(\hat{\mathbf{E}}^{\star}\times\hat{\mathbf{E}}')\cdot\hat{\mathbf{M}}\,F^{(1)} \\ + (\hat{\mathbf{E}}^{\star}\cdot\hat{\mathbf{M}})(\hat{\mathbf{E}}'\cdot\hat{\mathbf{M}})\,F^{(2)} \,. \end{aligned} \tag{8.4}$$

For $\hat{\mathbf{E}}' = \hat{\mathbf{E}}$ this gives the x-ray absorption, which depends only on the included angle ($\hat{\mathbf{E}}$,$\hat{\mathbf{M}}$), as expected for spherical symmetry.

With magnetization unit vector

$$\hat{\mathbf{M}} = (\hat{x},\hat{y},\hat{z}) = (\sin\theta\cos\phi, \sin\theta\sin\phi, \cos\theta) \,, \tag{8.5}$$

i.e., $\hat{x}^2+\hat{y}^2+\hat{z}^2=1$, the scattering tensor can be cast in the Cartesian form

$$\mathscr{F}_{SO_3\|[xyz]}=\begin{pmatrix} F^{(0)}+(\hat{x}^2-\frac{1}{3})F^{(2)} & -\hat{z}F^{(1)}+\hat{x}\hat{y}F^{(2)} & \hat{y}F^{(1)}+\hat{x}\hat{z}F^{(2)} \\ \hat{z}F^{(1)}+\hat{x}\hat{y}F^{(2)} & F^{(0)}+(\hat{y}^2-\frac{1}{3})F^{(2)} & -\hat{x}F^{(1)}+\hat{y}\hat{z}F^{(2)} \\ -\hat{y}F^{(1)}+\hat{x}\hat{z}F^{(2)} & \hat{x}F^{(1)}+\hat{y}\hat{z}F^{(2)} & F^{(0)}+(\hat{z}^2-\frac{1}{3})F^{(2)} \end{pmatrix}. \tag{8.6}$$

Taking $\hat{\mathbf{M}}=\hat{z}$ = (0,0,1), (8.6) simplifies to the familiar result [42, 43, 44, 45]

$$\mathscr{F}_{SO_3\|[001]}=\begin{pmatrix} F^{(0)}-\frac{1}{3}F^{(2)} & -F^{(1)} & 0 \\ F^{(1)} & F^{(0)}-\frac{1}{3}F^{(2)} & 0 \\ 0 & 0 & F^{(0)}+\frac{2}{3}F^{(2)} \end{pmatrix}, \tag{8.7}$$

which is clearly invariant under ϕ rotation about the z axis.

8.3.2 Cubic symmetry

For octahedral crystal field symmetry it is seen from Fig. 8.1 that $F^{(0)}$ has irrep $A_1=\{1\}$, $F^{(1)}$ has irrep $T_1=\{x,y,z\}$ and $F^{(2)}$ has irreps $E=\{z^2-\frac{1}{3}r^2, x^2-y^2\}$ and $T_2=\{xy, yz, zx\}$. Thus $F^{(2)}$ splits into diagonal elements of irrep E and non-diagonal elements of irrep T_2, which means that the intensity depends on the crystal field orientation. The scattering intensity of (8.3) can be written as

$$\begin{aligned} I(\hat{\mathbf{E}},\hat{\mathbf{E}}',\hat{\mathbf{M}}) = {} & \hat{\mathbf{E}}^\star\cdot\hat{\mathbf{E}}'\left[F^{(0)}_{A_1}-\frac{1}{3}F^{(2)}_{A_1}\right]-\mathrm{i}(\hat{\mathbf{E}}^\star\times\hat{\mathbf{E}}')\cdot\hat{\mathbf{M}}F^{(1)}_{T_1} \\ & +(\hat{\mathbf{E}}^\star\cdot\hat{\mathbf{M}})(\hat{\mathbf{E}}'\cdot\hat{\mathbf{M}})F^{(2)}_{T_2}-\sum_i E^\star_i M_i E'_i M_i\left[F^{(2)}_E-F^{(2)}_{T_2}\right]. \end{aligned} \tag{8.8}$$

Note that the linear XA is symmetric upon exchange of $\hat{\mathbf{M}}$ and $\hat{\mathbf{E}}$. It should further be pointed out that, as allowed by (8.3), $\mathscr{F}^{(1)}(\hat{\mathbf{M}})$ contains also a higher order term $\hat{\mathbf{M}}(\hat{\mathbf{M}}^2-\frac{3}{5})F^{(3)}_{T_1}$. Although this term is much smaller than $\hat{\mathbf{M}}F^{(1)}_{T_1}$, it has never the less been observed experimentally [46]. Likewise, $\mathscr{F}^{(2)}(\hat{\mathbf{M}})$ can contain higher order terms with $F^{(4)}_E$ and $F^{(4)}_{T_2}$, although so far these have not been observed.

Using the symmetry considerations the Cartesian tensor along $C_4 \parallel \langle 001 \rangle$ with $\hat{\mathbf{M}} = (\hat{x}, \hat{y}, \hat{z})$ is

$$\mathscr{F}_O = \begin{pmatrix} F_{A_1}^{(0)} + (\hat{x}^2 - \frac{1}{3})F_E^{(2)} & -\hat{z}F_{T_1}^{(1)} + \hat{x}\hat{y}F_{T_2}^{(2)} & \hat{y}F_{T_1}^{(1)} + \hat{x}\hat{z}F_{T_2}^{(2)} \\ \hat{z}F_{T_1}^{(1)} + \hat{x}\hat{y}F_{T_2}^{(2)} & F_{A_1}^{(0)} + (\hat{y}^2 - \frac{1}{3})F_E^{(2)} & -\hat{x}F_{T_1}^{(1)} + \hat{y}\hat{z}F_{T_2}^{(2)} \\ -\hat{y}F_{T_1}^{(1)} + \hat{x}\hat{z}F_{T_2}^{(2)} & \hat{x}F_{T_1}^{(1)} + \hat{y}\hat{z}F_{T_2}^{(2)} & F_{A_1}^{(0)} + (\hat{z}^2 - \frac{1}{3})F_E^{(2)} \end{pmatrix} . \tag{8.9}$$

8.3.3 Orthorhombic symmetry

For orthorhombic crystal field symmetry the scattering intensity obeys the general form in (8.3), where both $\mathscr{F}^{(1)}(\hat{\mathbf{M}})$ and $\mathscr{F}^{(2)}(\hat{\mathbf{M}})$ depend on the direction of $\hat{\mathbf{M}}$ with respect to the crystal frame.

Fig. 8.1 shows that for orthorhombic (D_{2h}) symmetry $F^{(0)}$ has irrep $A_1 = \{1\}$, $F^{(1)}$ has irreps $B_1 = \{z\}$, $B_2 = \{y\}$ and $B_3 = \{x\}$, and $F^{(2)}$ has irreps $A_1 = \{z^2 - \frac{1}{3}r^2, x^2 - y^2\}$, $B_1 = \{xy\}$, $B_2 = \{zx\}$ and $B_3 = \{yz\}$. The Cartesian tensor along $C_2 \parallel \langle 001 \rangle$ with $\hat{\mathbf{M}} = (\hat{x}, \hat{y}, \hat{z})$ is

$$\mathscr{F}_{D_2}^{(0)} = \begin{pmatrix} F_{A_1}^{(0)} - \frac{1}{3}F_{A_1}^{(2)} & 0 & 0 \\ 0 & F_{A_1}^{(0)} - \frac{1}{3}F_{A_1}^{(2)} & 0 \\ 0 & 0 & F_{A_1}^{(0)} - \frac{1}{3}F_{A_1}^{(2)} \end{pmatrix} \Rightarrow \left[F_{A_1}^{(0)} - \frac{1}{3}F_{A_1}^{(2)} \right] ,$$

$$\mathscr{F}_{D_2}^{(1)} = \begin{pmatrix} 0 & -\hat{z}F_{B_1}^{(1)} & \hat{y}F_{B_2}^{(1)} \\ \hat{z}F_{B_1}^{(1)} & 0 & -\hat{x}F_{B_3}^{(1)} \\ -\hat{y}F_{B_2}^{(1)} & \hat{x}F_{B_3}^{(1)} & 0 \end{pmatrix} \Rightarrow \begin{pmatrix} \hat{x}F_{B_3}^{(1)} \\ \hat{y}F_{B_2}^{(1)} \\ \hat{z}F_{B_1}^{(1)} \end{pmatrix} ,$$

$$\mathscr{F}_{D_2}^{(2)} = \begin{pmatrix} \hat{x}^2F_{A_1}^{(2)} + (\hat{y}^2 - \hat{z}^2)F_{A_1}^{(2)} & \hat{x}\hat{y}F_{B_1}^{(2)} & \hat{x}\hat{z}F_{B_2}^{(2)} \\ \hat{x}\hat{y}F_{B_1}^{(2)} & \hat{y}^2F_{A_1}^{(2)} + (\hat{z}^2 - \hat{x}^2)F_{A_1}^{(2)} & \hat{y}\hat{z}F_{B_3}^{(2)} \\ \hat{x}\hat{z}F_{B_2}^{(2)} & \hat{y}\hat{z}F_{B_3}^{(2)} & \hat{z}^2F_{A_1}^{(2)} + (\hat{x}^2 - \hat{y}^2)F_{A_1}^{(2)} \end{pmatrix} , \tag{8.10}$$

which for clarity is written out in tensors of different rank. $\mathscr{F}^{(2)}$ contains three different irreps A_1 which form linear combinations. Note that the linear XA is in this low symmetry is no longer symmetric upon exchange of $\hat{\mathbf{M}}$ and $\hat{\mathbf{E}}$ [19].

Table 8.1 Linear x-ray absorption I_{XA} in cubic crystal field for $\hat{\mathbf{M}}$ and $\hat{\mathbf{E}}$ along different high symmetry directions. The last column gives $\hat{\mathbf{E}}\cdot\mathscr{F}^{(2)}(\hat{\mathbf{M}})\cdot\hat{\mathbf{E}}$ in spectroscopic notation. Note that $\hat{\mathbf{E}}\cdot\mathscr{F}^{(0)}\cdot\hat{\mathbf{E}} = F^{(0)}_{A_1} - \frac{1}{3}F^{(2)}_{E} = I^{\mathrm{iso}}_{\mathrm{XA}} - \frac{1}{3}I_0$

M	**E**	I_{XA} (O symmetry)	I_{XA} (spectr. notation)
[100]	[100]	$F^{(0)}_{A_1} + \frac{2}{3}F^{(2)}_{E}$	I_0
[100]	[010], [001]	$F^{(0)}_{A_1} - \frac{1}{3}F^{(2)}_{E}$	0
[110]	[110]	$F^{(0)}_{A_1} + \frac{1}{6}F^{(2)}_{E} + \frac{1}{2}F^{(2)}_{T_2}$	$\frac{1}{2}(I_0 + I_{45})$
[110]	$[1\bar{1}0]$	$F^{(0)}_{A_1} + \frac{1}{6}F^{(2)}_{E} - \frac{1}{2}F^{(2)}_{T_2}$	$\frac{1}{2}(I_0 - I_{45})$
[110]	[001]	$F^{(0)}_{A_1} - \frac{1}{3}F^{(2)}_{E}$	0
[111]	[111]	$F^{(0)}_{A_1} + \frac{2}{3}F^{(2)}_{T_2}$	$\frac{1}{3}(I_0 + 2I_{45})$
[111]	$[11\bar{2}]$, $[\bar{1}10]$	$F^{(0)}_{A_1} - \frac{1}{3}F^{(2)}_{T_2}$	$\frac{1}{3}(I_0 - I_{45})$

8.4 Various ways to obtain the XMLD

So far we only looked at the scattering and XA, but we will now consider the XMLD in more detail. Assume three orthogonal linear polarization directions E_1, E_2 and E_3 and with magnetization direction $M_1 \parallel E_1$. The isotropic XA is

$$I^{\mathrm{iso}}_{\mathrm{XA}} \equiv \frac{1}{3}\left[I_{\mathrm{XA}}(E_1,M_1) + I_{\mathrm{XA}}(E_2,M_1) + I_{\mathrm{XA}}(E_3,M_1)\right] , \tag{8.11}$$

which is invariant, i.e., orientation independent. Ideally, one would like to define the XMLD as

$$I_{\mathrm{XMLD}}(E_1,M_1) \equiv I_{\mathrm{XA}}(E_1,M_1) - \frac{1}{2}I_{\mathrm{XA}}(E_2,M_1) - \frac{1}{2}I_{\mathrm{XA}}(E_3,M_1) . \tag{8.12}$$

Such a geometry with three orthogonal vectors is not practical to measure, so that one normally settles for

$$I_{\rm XMLD}(E_1,M_1)_2 = I_{\rm XA}(E_1,M_1) - I_{\rm XA}(E_2,M_1)\ ,$$
$$I_{\rm XMLD}(E_1,M_1)_3 = I_{\rm XA}(E_1,M_1) - I_{\rm XA}(E_3,M_1)\ . \qquad (8.13)$$

Substitution gives

$$I_{\rm XMLD}(E_1,M_1) = \frac{1}{2} I_{\rm XMLD}(E_1,M_1)_2 + \frac{1}{2} I_{\rm XMLD}(E_1,M_1)_3\ . \qquad (8.14)$$

Note that $I_{\rm XMLD}(E_1,M_1)$ is only unambiguously defined for $M_1 \parallel C_3$, C_4, C_6 and C_∞ axes, otherwise the E_2 and E_3 directions give different results.

The XA and XMLD spectra can be readily obtained using multiplet calculations [7]. In this Chapter we are primarily interested in the angular dependence of the XMLD, which is governed by symmetry arguments, without having to make assumptions about the energy dependence of the spectra, so that we can make use of generic spectra along the high symmetry axes.

Table 8.1 gives the XA intensity in cubic symmetry along high symmetry axes obtained from (8.9). It can be verified that for $\hat{\mathbf{M}} \parallel [100]$ and $\hat{\mathbf{M}} \parallel [111]$ the $I_{\rm XA}$ in the perpendicular plane is constant, which is due to the C_4 and C_3 symmetry axis, respectively. This is not true for other directions, as e.g. is seen for $\hat{\mathbf{M}} \parallel [110]$.

We will now change from the group symmetry notation to a spectroscopic notation. Using the XMLD in the cubic symmetry, we define

$$I_0 \equiv I(E_{[100]},M_{[100]}) - I(E_{[010]},M_{[100]}) = F^{(2)}_{E}\ ,$$
$$I_{45} \equiv I(E_{[110]},M_{[110]}) - I(E_{[1\bar{1}0]},M_{[110]}) = F^{(2)}_{T_2}\ ,$$
$$I_{[111]} \equiv I(E_{[111]},M_{[111]}) - I(E_{[11\bar{2}]},M_{[111]}) = F^{(2)}_{T_2}\ ,$$
$$I^{\rm iso}_{\rm XA} \equiv \frac{1}{3}\left[I(E_{100]},M_{[100]}) + I(E_{[010]},M_{[100]}) + I(E_{[001]},M_{[100]})\right] = F^{(0)}_{A_1}\ ,$$

where the results at the right-hand site are obtained from the XA given in Table 8.1. The I_0 and I_{45} are two independent spectra with different ω dependence, i.e., different spectral shape, which are sometimes called 'fundamental spectra'. Since $I_{[111]}$ is equal to I_{45}, it does not give an extra fundamental spectrum.

8.5 XMLD in the (001) plane

We will now illustrate the consequences of the theory for the (001) plane in cubic symmetry. This geometry gives simple expressions for the XMLD angular dependence, yet it clearly reveals the dependence on the crystallographic axes and shows the details to be taken into account. Moreover, this plane is often studied experimentally.

Using (8.9), the XA in the (001) plane is

$$\mathscr{F}_O^{(001)} = \left[I_{\rm iso} - \frac{1}{3}I_0\right] + \begin{pmatrix} \hat{x}^2 I_0 & \hat{x}\hat{y} I_{45} \\ \hat{x}\hat{y} I_{45} & \hat{y}^2 I_0 \end{pmatrix} . \tag{8.15}$$

Using

$$I_{\rm XMLD}(\varepsilon,\mu) \equiv I_{\rm XA}(\varepsilon,\mu) - I_{\rm XA}(\varepsilon+90^\circ,\mu) , \tag{8.16}$$

where ε and μ are the angles of $\hat{\mathbf{E}}$ and $\hat{\mathbf{M}}$ with respect to the [100] axis, i.e., $\hat{\mathbf{E}} = (\hat{\varepsilon}_x, \hat{\varepsilon}_y) = (\cos\varepsilon, \sin\varepsilon)$ and $\hat{\mathbf{M}} = (\hat{x}, \hat{y}) = (\cos\mu, \sin\mu)$, gives an angular dependence

$$\begin{aligned} I_{\rm XMLD}(\varepsilon,\mu) &= I_0 \cos 2\varepsilon \cos 2\mu + I_{45} \sin 2\varepsilon \sin 2\mu \\ &= \frac{1}{2}(I_0 + I_{45})\cos(2\varepsilon - 2\mu) + \frac{1}{2}(I_0 - I_{45})\cos(2\varepsilon + 2\mu) . \end{aligned} \tag{8.17}$$

where I_0 is the $I_{\rm XMLD}(\varepsilon,\mu)$ for $\varepsilon = \mu = 0^\circ$ and I_{45} is that for $\varepsilon = \mu = 45^\circ$.

Equation (8.17) is a sum over terms containing an angular and an energy dependent factor. As an illustration, the ε dependence of the XA spectra and corresponding XMLD for fixed μ is shown in Fig. 8.2a and its decomposition into the terms with I_0 and I_{45} is displayed in Fig. 8.2b. Obviously, the I_0 and I_{45} terms have maximum intensities at $\varepsilon = 0^\circ$ and 45°, respectively. In the (001) plane, with only two instead of three spectra, the average XA is $I_{\rm XA}^{\rm av} = I_{\rm XA}^{\rm iso} + \frac{1}{6}I_0$.

It can be immediately verified that along high symmetry axes there is only one XMLD spectrum. Substitution of either $\mu = 0^\circ$ or 45° into (8.17) leads to

$$\begin{aligned} I_{\rm XMLD}(\varepsilon, \mu = 0^\circ) &= I_0 \cos 2\varepsilon , \\ I_{\rm XMLD}(\varepsilon, \mu = 45^\circ) &= I_{45} \sin 2\varepsilon , \end{aligned} \tag{8.18}$$

for arbitrary ε. Only in the special cases with $\hat{\mathbf{M}}$ along a high-symmetry axis ($\langle 100\rangle$ or $\langle 110\rangle$) one measures a single spectrum (I_0 or I_{45}, respectively) where

the direction of $\hat{\mathbf{E}}$ affects the magnitude of the XMLD but not its spectral shape. At $\mu \neq 0^\circ$ and 45°, the I_{XMLD} is a linear combination of I_0 and I_{45}. Thus in the frequently encountered geometry with $\hat{\mathbf{M}}$ along a high-symmetry axis the full angular dependence of the XMLD remains hidden, which might explain the ignorance in much of the literature. In order to study the angular dependence, $\hat{\mathbf{M}}$ has to be forced along a non-symmetry direction using an applied magnetic field or bias field.

8.6 Separation into the isotropic and anisotropic part

The angular dependence of the XMLD in (8.17) can be written as a sum over a rotational invariant term, which is independent of the crystal axes, and a term which depends on the orientation with respect to the crystalline axes,

$$I_{\mathrm{XMLD}}(\varepsilon,\mu) = I^{\mathrm{iso}}_{\mathrm{XMLD}}(\varepsilon,\mu) + I^{\mathrm{ani}}_{\mathrm{XMLD}}(\varepsilon,\mu)\ . \tag{8.19}$$

The decomposition of the angular dependent XMLD into isotropic and anisotropic parts is illustrated in Fig. 8.2c.

The *isotropic part*, i.e., the rotational invariant contribution,

$$I^{\mathrm{iso}}_{\mathrm{XMLD}}(\varepsilon,\mu) = \frac{1}{2}(I_0 + I_{45})\cos(2\varepsilon - 2\mu)\ , \tag{8.20}$$

depends only on the difference $|\varepsilon - \mu|$ between the angles of $\hat{\mathbf{E}}$ and $\hat{\mathbf{M}}$. Hence, the angular distribution is rigidly fixed to the direction $\hat{\mathbf{M}}$ and does not depend on the crystal frame orientation. This can be verified in Fig. 8.2c, which shows that for $I^{\mathrm{iso}}_{\mathrm{XMLD}}$ [red (dark) line] the maximum is along $\hat{\mathbf{M}}$, i.e., at $\varepsilon = \mu$. Thus the isotropic part of the XMLD behaves as what could be considered "normal" for a situation where the crystal field can be neglected. The isotropic part can be measured directly at $\varepsilon = \mu = 22.5^\circ$, where the anisotropic part vanishes.

The *anisotropic part*, i.e., the rotational dependent contribution,

$$I^{\mathrm{ani}}_{\mathrm{XMLD}}(\varepsilon,\mu) = \frac{1}{2}(I_0 - I_{45})\cos(2\varepsilon + 2\mu)\ , \tag{8.21}$$

depends on the directions of $\hat{\mathbf{E}}$ and $\hat{\mathbf{M}}$ with respect to the crystal axes. It can be verified from Fig. 8.2c that for $I^{\mathrm{ani}}_{\mathrm{XMLD}}$ [green (gray) line] the maximum is at $\varepsilon = -\mu$. The anisotropic part is responsible for the "bad" behavior of the

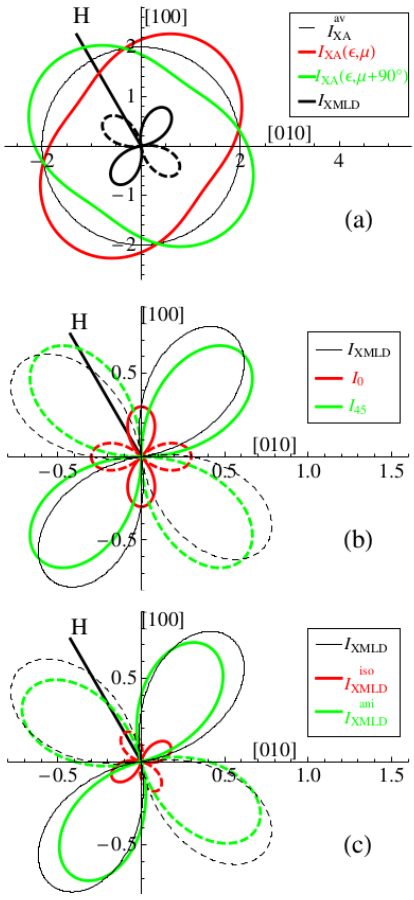

Fig. 8.2 (Color online) Polar plots of the XA and XMLD intensities in the (001) plane as a function of the angle ε for the linear polarization $\hat{\mathbf{E}}$ with fixed angle μ for the magnetization axis $\hat{\mathbf{M}}$ (indicated by the thick line) obtained using (8.17) for the chosen parameter values $I_{XA}^{av} = 2$, $I_0 = 0.6$, $I_{45} = -1$, and $\mu = -30°$ with respect to the [100] crystal axis. This is representative for a situation where I_0 and I_{45} have opposite sign but not completely cancel each other. Drawn (dashed) lines correspond to positive (negative) intensities. **a** I_{XA}^{av} (thin black line), $I_{XA}(\varepsilon,\mu)$ [red (dark) line], $I_{XA}(\varepsilon,\mu+90°)$ [green (gray) line], and their intensity difference, $I_{XMLD}(\varepsilon,\mu)$ (thick black line). **b** Decomposition of I_{XMLD} (thin black line) into contributions from I_0 [red (dark) line] and I_{45} [green (gray) line]. **c** Decomposition of I_{XMLD} (thin black line) into its isotropic and anisotropic part, I_{XMLD}^{iso} [red (dark) line] and I_{XMLD}^{ani} [green (gray) line]. As seen the maximum of I_{XMLD}^{iso} is along $\hat{\mathbf{M}}$, i.e., at $\varepsilon = \mu = -30°$, whereas the maximum of I_{XMLD}^{ani} is at $\varepsilon = -\mu = 30°$ (Ref. [36])

XMLD, resulting in a situation where the maxima of the XMLD and XA do no longer coincide with the direction of $\hat{\mathbf{M}}$ (c.f. Fig. 8.2). Hence, the separation of the XMLD into its isotropic and anisotropic parts offers a powerful way to find the influence of the crystal-field interaction.

8.6.1 Weak crystal field

In the absence of crystal field symmetry, $I_{45} = I_0$, so that the anisotropic part vanishes and the XMLD is proportional to $I_0 \cos(2\varepsilon - 2\mu)$, which depends only on the difference between the two angles. The XMLD is maximum for $\varepsilon = \mu$, i.e., $\hat{\mathbf{M}} \| \hat{\mathbf{E}}$.

An interesting case arises in rare earths and actinides, where the crystal field is weak compared to the spherical symmetric potential due to spin-orbit and electrostatic interactions. This makes the separation of the XMLD into anisotropic and anisotropic parts particularly beneficial. For weak crystal field, the anisotropic part in the XMLD is small, i.e., $|I_0 - I_{45}| \ll |I_0 + I_{45}|$. For the Eu $M_{4,5}$ XMLD of ferromagnetic EuO, a small $I_0 - I_{45}$ spectrum could be extracted with a magnitude proportional to the effective crystalline electric field. [22]

In the next section we will show that precisely the opposite situation occurs for the Ni^{2+} L_2 edge, where the XMLD contains only an anisotropic part.

8.7 The peculiar case of the Ni^{2+} L_2 edge

Theoretical spectra can be obtained using atomic multiplet calculations [7, 47, 48] for the electric-dipole transition Ni^{2+} $3d^8 \rightarrow 2p^5 3d^9$ in octahedral crystal field of $10Dq = 1.4$ eV, which has a ground state $(t_2^6 e^2, {}^3A_2)T_2$. In the calculation the directions of the magnetization and x-ray polarization can be chosen along arbitrary directions. Multiplet calculations performed with $\hat{\mathbf{E}}$ and $\hat{\mathbf{M}}$ separately incremented in steps of 5° over the full angular range confirmed the analytical relation in (8.17) to high accuracy, which suggests that possible higher-order terms must be very small [36].

The calculated I_0 and I_{45} spectra are shown in Fig. 8.3b together with the experimental results for different Ni^{2+} compounds. For the entire L_2 edge,

$I_{45} \approx -I_0$, however, the L_3 edge shows a strongly different I_{45} and I_0 as a function of photon energy.

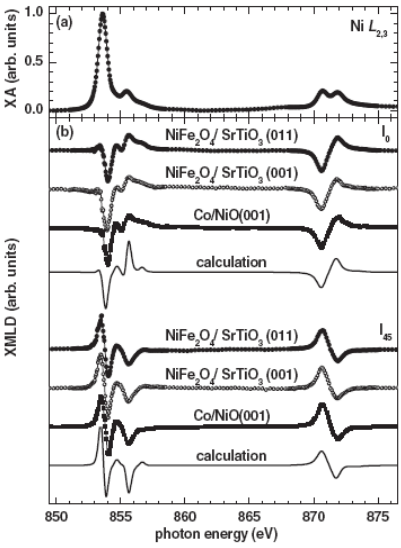

Fig. 8.3 Comparison of the experimentally obtained fundamental XMLD spectra together with results from atomic multiplet calculations. **a** Measured Ni $L_{2,3}$ XA for $NiFe_2O_4/SrTiO_3$. **b** Calculated XMLD spectra I_0 and I_{45}. Experimental data for $NiFe_2O_4/SrTiO_3$ (011) and (001) and Co/NiO (001). The multiplet calculations are shown by solid lines. For the L_2 edge, it is clearly seen that $I_{45} \approx -I_0$, so that the isotropic XMLD vanishes and only the anisotropic XMLD remains (Ref. [16])

The expressions for the angular dependence given in Sec. 8.3 are valid for the entire $L_{2,3}$ spectrum. If we now restrict us to the Ni^{2+} L_2 edge a more specific rule can be derived [16].This rule uses the fact that at this edge, $I_{45} \approx -I_0$, as evidenced by the calculated and experimental spectra shown in Fig. 8.3b. It should be noted that this relation is a peculiarity of the Ni^{2+} L_2 edge and is not true for the L_3 edge, [14, 15] but it holds to some extent for other L_2 edges, such as for Co^{2+} (Ref. [19]), Fe^{3+}, and Mn^{2+} (Ref. [14]). The reason that the two fundamental spectra for the L_2 XMLD have approximately the same shape is related to the reduced number of allowed transitions for the $j = \frac{1}{2}$ core-hole state. The electric-dipole selection rules restrict the set of final states that can be reached.

Substitution of $I_{45} = -I_0$ reduces (8.17) to

$$I_{\mathrm{XMLD}}^{L_2}(\varepsilon, \mu) = I_0 \cos(2\varepsilon + 2\mu), \tag{8.22}$$

which removes the isotropic part and retains only the anisotropic part. Therefore, the XMLD at the L_2 edge is strongly dependent on the orientation of $\hat{\mathbf{M}}$

and $\hat{\mathbf{E}}$ with respect to the crystal axes. The maximal intensity is obtained when $\hat{\mathbf{M}}$ and $\hat{\mathbf{E}}$ have equal angles of opposite sign with respect to the [100] axis.

In the past, the orientation of the Ni spins has been determined under the assumption that the second peak in the L_2 absorption edge is maximal when $\hat{\mathbf{M}} \parallel \hat{\mathbf{E}}$. However, this is only correct if the crystal field symmetry would play no role. As was recently found [16], a proper description of the angular dependent XMLD in cubic symmetry requires a linear combination of two fundamental spectra, I_0 and I_{45}. Taking into account the angular dependence, two extreme cases occur in the (001) plane: For $\hat{\mathbf{M}} \parallel \langle 100 \rangle$ the XMLD is pure I_0 and for $\hat{\mathbf{M}} \parallel \langle 110 \rangle$ the XMLD is pure I_{45}. The L_2 absorption edge consists of a well resolved double peak structure which is well suited to study the spin orientation. The relation $I_{45} \approx -I_0$ means that the second peak is maximal not only for $\hat{\mathbf{E}} \parallel \hat{\mathbf{M}} \parallel \langle 100 \rangle$ but also for $\hat{\mathbf{E}} \perp \hat{\mathbf{M}} \parallel \langle 110 \rangle$. While in the latter case the spins are perpendicular instead of parallel to $\hat{\mathbf{E}}$, both orientations give the same Ni^{2+} L_2 XA spectrum. It is therefore vital in the analysis of PEEM images to take into account the angular dependence of the XMLD with respect to the crystal frame in order to retrieve the spin axes of the antiferromagnetic NiO domains.

References

1. J. Stöhr, H.C. Siegmann, *Magnetism. From Fundamentals to Nanoscale Dynamics* (Springer Verlag, Heidelberg, 2006)
2. B.T. Thole, G. van der Laan, G.A. Sawatzky, Phys. Rev. Lett. **55**, 2086 (1985)
3. G. van der Laan, B.T. Thole, G.A. Sawatzky, J.B. Goedkoop, J.C. Fuggle, J.M. Esteva, R. Karnatak, J.P. Remeika, H.A. Dabkowska, Phys. Rev. B **34**, 6529 (1986)
4. P. Kuiper, B.G. Searle, P. Rudolf, L.H. Tjeng, C.T. Chen, Phys. Rev. Lett. **70**, 1549 (1993)
5. M.M. Schwickert, G.Y. Guo, M.A. Tomaz, W.L. O'Brien, G.R. Harp, Phys. Rev. B **58**, R4289 (1998)
6. J.B. Kortright, S.K. Kim, Phys. Rev. B **62**, 12216 (2000)
7. G. van der Laan, B.T. Thole, Phys. Rev. B **43**, 13401 (1991)
8. G. van der Laan, Phys. Rev. B **55**, 8086 (1997)
9. G. van der Laan, Phys. Rev. Lett. **82**, 640 (1999)
10. G. van der Laan, J. Phys.:Condens. Matter **10**, 3239 (1998)
11. E. Arenholz, G. van der Laan, A. McClure, Y. Idzerda, Phys. Rev. B **82**, 180405(R) (2010)
12. J. Kuneš, P.M. Oppeneer, Phys. Rev. B **67**, 024431 (2003)
13. S. Czekaj, F. Nolting, L.J. Heyderman, P.R. Willmott, G. van der Laan, Phys. Rev. B **73**, 020401 (2006)

14. A.A. Freeman, K.W. Edmonds, G. van der Laan, N.R.S. Farley, T.K. Johal, E. Arenholz, R.P. Campion, C.T. Foxon, B.L. Gallagher, Phys. Rev. B **73**, 233303 (2006)
15. E. Arenholz, G. van der Laan, R.V. Chopdekar, Y. Suzuki, Phys. Rev. B **74**, 094407 (2006)
16. E. Arenholz, G. van der Laan, R.V. Chopdekar, Y. Suzuki, Phys. Rev. Lett. **98**, 197201 (2007)
17. E. Arenholz, G. van der Laan, F. Nolting, Appl. Phys. Lett. **93**, 162506 (2008)
18. H. Ohldag, G. van der Laan, E. Arenholz, Phys. Rev. B **79**, 052403 (2009)
19. G. van der Laan, E. Arenholz, R.V. Chopdekar, Y. Suzuki, Phys. Rev. B **77**, 064407 (2008)
20. N.D. Telling, P.S. Keatley, G. van der Laan, R.J. Hicken, E. Arenholz, Y. Sakuraba, M. Oogane, Y. Ando, K. Takanashi, A. Sakuma, T. Miyazaki, Phys. Rev. B **78**, 184438 (2008)
21. E. Arenholz, G. van der Laan, F. Yang, N. Kemik, M.D. Biegalski, H.M. Christen, Y. Takamura, Appl. Phys. Lett. **94**, 072503 (2009)
22. G. van der Laan, E. Arenholz, A. Schmehl, D.G. Schlom, Phys. Rev. Lett. **100**, 067403 (2008)
23. D. Alders, J. Vogel, C. Levelut, S.D. Peacor, T. Hibma, M. Sacchi, L.H. Tjeng, C.T. Chen, G. van der Laan, B.T. Thole, G.A. Sawatzky, Europhys. Lett. **32**, 259 (1995)
24. D. Alders, L.H. Tjeng, F.C. Voogt, T. Hibma, G.A. Sawatzky, C.T. Chen, J. Vogel, M. Sacchi, S. Iacobucci, Phys. Rev. B **57**, 11623 (1998)
25. A. Scholl, J. Stöhr, J. Lüning, J.W. Seo, J. Fompeyrine, H. Siegwart, J.P. Locquet, F. Nolting, S. Anders, E.E. Fullerton, M.R. Scheinfein, H.A. Padmore, Science **287**, 1014 (2000)
26. A. Scholl, F. Nolting, J. Stöhr, T. Regan, J. Lüning, J.W. Seo, J.P. Locquet, J. Fompeyrine, S. Anders, H. Ohldag, H.A. Padmore, J. Appl. Phys. **11**, 7266 (2001)
27. J. Lüning, F. Nolting, A. Scholl, H. Ohldag, J.W. Seo, J. Fompeyrine, J.P. Locquet, J. Stöhr, Phys. Rev. B **67**, 214433 (2003)
28. J. Stöhr, A. Scholl, T.J. Regan, S. Anders, J. Lüning, M.R. Scheinfein, H.A. Padmore, R.L. White, Phys. Rev. Lett. **83**, 1862 (1999)
29. F.U. Hillebrecht, H. Ohldag, N.B. Weber, C. Bethke, U. Mick, M. Weiss, J. Bahrdt, Phys. Rev. Lett. **86**, 3419 (2001)
30. H. Ohldag, T.J. Regan, J. Stöhr, A. Scholl, F. Nolting, J. Lüning, C. Stamm, S. Anders, R.L. White, Phys. Rev. Lett. **87**, 247201 (2001)
31. H. Ohldag, A. Scholl, F. Nolting, S. Anders, F.U. Hillebrecht, J. Stöhr, Phys. Rev. Lett. **86**, 2878 (2001)
32. A. Scholl, M. Liberati, E. Arenholz, H. Ohldag, J. Stöhr, Phys. Rev. Lett. **92**, 247201 (2004)
33. M. Finazzi, A. Brambilla, P. Biagioni, J. Graf, G.H. Gweon, A. Scholl, A. Lanzara, L. Duo, Phys. Rev. Lett. **97**, 097202 (2006)
34. I.P. Krug, F.U. Hillebrecht, M.W. Haverkort, A. Tanaka, L.H. Tjeng, H. Gomonay, A. Fraile-Rodriguez, F. Nolting, S. Cramm, C.M. Schneider, Phys. Rev. B **78**, 064427 (2008)
35. G. van der Laan, E. Arenholz, Eur. Phys. J. Special Topics **169**, 187 (2009)
36. G. van der Laan, N.D. Telling, A. Potenza, S.S. Dhesi, E. Arenholz, Phys. Rev. B **83**, 064409 (2011)
37. J.F. Nye, *Physical Properties of Crystals* (Clarendon Press, Oxford, 1957)

38. Y.I. Sirotin, M.P. Shaskolskaya, *Fundamentals of Crystal Physics* (Mir Publishers, Moscow, 1982)
39. G. van der Laan, J. Phys. Soc. Jpn **63**, 2393 (1994)
40. P. Carra, B.T. Thole, Rev. Mod. Phys. **66**, 1509 (1994)
41. M.W. Haverkort, N. Hollmann, I.P. Krug, A. Tanaka, Phys. Rev. B **82**, 094403 (2010)
42. J.P. Hannon, G.T. Trammell, M. Blume, D. Gibbs, Phys. Rev. Lett. **61**, 1245 (1988)
43. M. Blume, D. Gibbs, Phys. Rev. B **37**, 1779 (1988)
44. M. Blume, in *Resonant anomalous x-ray scattering*, ed. by G. Materlik, C.J. Sparks, K. Fischer (Elsevier Science, Amsterdam, 1994), p. 495
45. G. van der Laan, C. R. Physique **9**, 570 (2008)
46. K.W. Edmonds, G. van der Laan, A. Freeman, N.R.S. Farley, T.K. Johal, R.P. Campion, C.T. Foxon, B.L. Gallagher, E. Arenholz, Phys. Rev. Lett. **96**, 117207 (2006)
47. G. van der Laan, I.W. Kirkman, J. Phys.:Condens. Matter **4**, 4189 (1992)
48. G. van der Laan, Lect. Notes Phys. **697**, 143 (2006)

Chapter 9
25 years of magnetic x-ray dichroism

Gerrit van der Laan

Abstract A historical overview of magnetic x-ray dichroism is presented. I describe the first theoretical and experimental results that have led to the development of this powerful technique for element-specific magnetometry. The theoretical progress of the sum rules is also described, starting with the spin-orbit sum rule for the isotropic spectrum which led on to the spin and orbital moment sum rules for x-ray magnetic circular dichroism. The latter has been particularly useful to understand the magnetic anisotropy in thin films and multilayers. Further developments of circular dichroism in (resonant) photoemission and Auger, as well as x-ray detected optical activity, also are summarized. Currently, magnetic x-ray dichroism finds a wide application in x-ray spectroscopy and imaging for the study of magnetic materials and it is considered to be one of the most important discoveries in the field of magnetism in the last few decennia. It is hard to imagine modern research into magnetism without the aid of polarized x-rays.

Gerrit van der Laan
Diamond Light Source, Harwell Science and Innovation Campus, Didcot, Oxfordshire OX11 0DE, United Kingdom, e-mail: gerrit.vanderlaan@diamond.ac.uk

E. Beaurepaire et al. (eds.), *Magnetism and Synchrotron Radiation: Towards the Fourth Generation Light Sources*, Springer Proceedings in Physics 151,
DOI: 10.1007/978-3-319-03032-6_9,

9.1 Introduction

A variety of techniques exists to measure the magnetic properties of materials. Most of them provide a macroscopic measurement. They are sensitive to the total magnetization of the measured system and can not discern between the contributions of different atoms in an alloy or multilayer, or between different origins, such as orbital and spin contributions. Furthermore, the tiny quantities of materials present in many technologically interesting samples, such as magnetic nanostructures, or difficult to obtain samples, such as nanocrystals or biomaterials, necessitates a very sensitive measuring method. Such measurements have become possible using the element-specific technique of x-ray absorption spectroscopy (XAS), in which magnetic sensitivity is obtained by using circularly or linearly polarized x-rays. In XAS, the atom absorbs a photon, giving rise to the transition of an electron from a core shell to an empty state above the Fermi level. Due to the (electric-dipole) selection rules, which depend on the polarization of the light, the allowed final states become sensitive to the symmetry of the initial state. Magnetic x-ray dichroism (MXD) is the difference in the absorption by a magnetic material of x-rays with different polarization state.

Only a quarter of a century ago, it was first observed that the x-ray absorption edge structure of a magnetically ordered material can be polarization dependent. The resulting x-ray circular or linear magnetic dichroism (XMCD or XMLD) is linear or quadratic proportional, respectively, to the magnetic moment. The analysis of the measurements has been considerably simplified by the discovery of the sum rules, which offer an element- and shell-specific method to determine the ground-state properties of the local electronic structure of metal compounds and alloys. For the isotropic x-ray absorption spectrum the branching ratio of core-valence transitions is linearly related to the expectation value of the angular part of spin-orbit operator in the valence states. For the XMCD, the sum rule analysis relates the integrated intensities to the orbital and spin magnetic moments. The orbital moment provides an insight into the microscopic origin of anisotropic magnetic properties, such as the magnetocrystalline anisotropy and easy-magnetization direction, which are of great technological importance.

The origin of dichroism in x-ray photoemission differs from that of x-ray absorption. Dichroic photoemission requires either core-valence interaction or an effective spin field on the core state. Sum rules were derived for photoemission from an incompletely filled localized shell, such as the $4f$ in rare

earths, relating the integrated intensities to various ground state spin-orbital coupled moments. The angular dependence of the polarized photoemission can be separated from the physical properties and provides a way to measure higher magnetic moments.

9.2 A sensational discovery of invisible rays

On 8 November 1895, Wilhelm Conrad Röntgen accidentally produced and detected electromagnetic radiation in a wavelength range known today as x-rays or "Röntgenstrahlung" [1], an achievement that earned him the first Nobel Prize in Physics in 1901. His discovery became quickly known to the world, not through the scientific channels but through the press who eagerly picked up on "a sensational discovery of invisible rays" which made it possible to see through clothing and human flesh. It resulted in a worldwide frenzy among scientists, free to produce x-rays using cathode-ray tubes [2]. Röntgen had deliberately not patented his discovery, convinced it belonged to the world at large. The physical properties of x-rays and their interaction with matter were soon studied at every major laboratory in the world [3, 4]. Already by the end of 1896, well over a thousand books and papers had been published on x-rays and their applications.

It was soon realized that the optical properties of x-rays greatly differ from those of visible light. The short wavelength makes a description of light-matter interactions as a continuous dielectric tensor, as used in the visible, less appropriate, and a better description is given by atomic scattering factors [5]. Away from the atomic absorption edges, the refractive index deviates only a small amount from unity [6].

Hard x-rays have high penetration power and their wavelength is comparable to the size of atomic spacings, leading to diffraction effects, which became an important tool in crystallography to study the periodicity of materials. To date, 28 Nobel Prizes have been awarded to scientists working with x-ray crystallography, an indication of its crucial importance. A century ago, Max von Laue (Nobel Prize 1914) undertook seminal experiments and William Bragg and his son Lawrence (Nobel Prize 1915) discovered 'Bragg's law' for x-ray diffraction. This transformed our perception of crystals and their atomic arrangements, and led to some of the most significant scientific findings of the last century–such as revealing the structure of DNA by James Watson and Francis Crick (Nobel Prize in Medicine 1962) and hemoglobin and myoglobin

by John Kendrew and Max Perutz (Nobel Prize in Chemistry 1962). Charles Barkla (Nobel Prize 1917) obtained polychromatic scattered x-rays with a polarization rate close to 100% [7, 8], while he also demonstrated that the atomic number Z can be obtained with x-rays. Further on the honors list are Karl Siegbahn (Nobel Prize 1924 for x-ray spectroscopy) and Arthur Compton (Nobel Prize 1927 for 'Compton scattering').

Moving on to the development of magneto-optics in the visible, in 1845, Michael Faraday discovered the "Faraday effect". This causes a rotation of the plane of polarization of the light, which is linearly proportional to the component of the magnetic field in the direction of propagation. In 1886, Pieter Zeeman discovered the "Zeeman effect" of splitting a spectral line into several components in the presence of a static magnetic field, which gave rise to magnetic dichroism [9]. Such magneto-optical effects in the visible were also anticipated for x-rays but it would take until 1986 before these effects were actually demonstrated for x-rays. This discovery had to await the advent of the synchrotron, capable of producing intense, monochromatized and low divergent x-ray beams.

9.3 An early attempt to observe the x-ray magneto-optical effect

In 1975, Erskine and Stern [10] predicted that by using circularly polarized light the x-ray absorption at core valence transitions can provide magnetic information about the ground state of the material. This was based on the expressions for the Faraday effect in terms of the conductivity tensor in a magnetic field similar to the visible range [11]. In the visible and near-uv range the magneto-optical absorption is typically of the order of 10^{-3} of the ordinary optical absorption, however, for core levels the anticipated effect would be much larger due to the strong spin-orbit interaction.

The theoretical approach was cast into a single-particle model of optical transitions from a core state of prescribed symmetry described by atomic wave functions into component conduction-band states with symmetry corresponding to the allowed optical transitions. In the transition matrix elements the small energy variation of the radial part was neglected.

The calculations for the magneto-optical Kerr effect (MOKE) at the $M_{2,3}$ ($3p \rightarrow 3d$) edge of Ni ($\sim$64 eV) predicted a change of $\sim$10% in reflection of p-polarized light due to magnetic dichroism. The $M_{2,3}$ magneto-optical effect

results predominantly from spin-orbit splitting of the $3p$ core state in conjunction with the final $3d$-state spin polarization. The calculated spectrum exhibits features that are directly related to electronic structure parameters, including the $3p$ core spin-orbit splitting and the unfilled $3d$-band spin polarization.

In pursuit of confirming the predicted x-ray magneto-optical effect, Keller and Stern performed a search for circular dichroism at the Gd L_3 edge ($2p \rightarrow 5d$, 7.24 keV) of a foil of $Gd_{18}Fe_{82}$ amorphous alloy in transmission geometry. The alloy was ferrimagnetically ordered at room temperature employing a small electromagnet. Circularly polarized x-rays were obtained at the Cornell High Energy Synchrotron Source (CHESS) using radiation from a bending magnet above and below the orbital plane (the so called inclined angle view) and at the Stanford Synchrotron Radiation Lab (SSRL) using a 43 μm thin silicon phase plate. Lock-in techniques were used to enhance the sensitivity, however, no dichroism could be measured above the noise level. It was stated that the magnetic x-ray absorption coefficient was at least 0.0005 smaller than the linear absorption coefficient at the Gd white-line energy.

9.4 Emerging opportunities with soft x-rays

After the discovery of synchrotron radiation in 1947, parasitic use of synchrotron radiation for experiments began in the early sixties. The first dedicated second-generation synchrotron radiation source to produce x-rays opened in 1981, which was the Synchrotron Radiation Source (SRS) at Daresbury Laboratory in Cheshire, England, soon followed by other facilities around the globe. Such sources offered a broad spectrum (from microwaves to hard x-rays), high flux, high brilliance, high stability (submicron source stability) as well as properties that were only fully appreciated later, such as polarization, spatial coherence and pulsed time structure.

In the eighties, grating monochromators were available for the UV and VUV region, but their performance in the soft x-ray region was limited and insufficient to resolve the details of the near-edge structure. Also multilayers as monochromator elements offered insufficient energy resolution [12]. The only possibility therefore was to push down the lower energy limit of double-crystal monochromator by using crystals of larger d spacing, which had to be resistant to the heat load of the beam. Acid phthalate crystals, such as KAP(100), can be used above 550 eV, but suffer severely from radiation damage, unless protected by a multilayer as first optical element [13]. The natural

mineral beryl (morganite) gave access to the soft x-ray energy range 800-1550 eV, which includes the Ni $L_{2,3}$ [14] and Cu $L_{2,3}$ edges [15], but leaves the lighter $3d$ transition metal edges out of reach. Beryl$(10\bar{1}0)$ also covers all the $M_{4,5}$ edges of the rare earths with an energy resolution gradually increasing from a Gaussian standard deviation $\sigma = 0.25$ eV for 800-900 eV to $\sigma =$ 0.4 eV for 1200-1500 eV, which is comparable to the core-hole lifetime width [16]. Although measurements in the soft x-ray region had to be done under high vacuum, this technology was readily available as it was part and parcel of the operation of the storage ring.

Thole et al. [16] measured the $M_{4,5}$ absorption spectra of all the rare-earth metals and showed that there was an excellent agreement with multiplet calculations performed for the transitions $3d^{10}4f^n \rightarrow 3d^9 4f^{n+1}$. The high energy resolution of the beryl crystal monochromator allowed the observation of the details of the multiplet structure. The electron localization increases along the f series [17], which means that most rare earth solids have localized $4f$ electrons, except for the lighter elements, such as cerium. For given localized $4f^n$ configuration the line shape of the XAS spectrum is the same, since the crystal field interaction and hybridization are considered to be very weak.

9.5 Prediction and first observation of x-ray magnetic dichroism

In 1985, Thole et al. [18] predicted that the line shape of the $M_{4,5}$ absorption edges of a rare earth ion, whose ground state is split by a magnetic field, depends on the relative orientation between the magnetization direction and the polarization vector of the x-rays. Since the electric-dipole transitions from the ground state can reach only a limited subset of final states, they provide a fingerprint for the specific ground state, which gives a high sensitivity to crystal field, spin-orbit interaction, site symmetry and spin configuration. The light polarization dependence makes the absorption sensitive to the magnetic ground state, which leads to a difference in intensity. It is worth noting that the strong magnetic dichroism arises from electric-dipole transitions and not from magnetic-dipole transitions.

These calculations by Thole et al. [18] demonstrated that x-ray absorption can be used to determine the local magnetic moment of rare-earth atoms in a magnetically ordered material, the orientation of the local moment relative to the total magnetization direction, as well as the temperature and field de-

pendence thereof. The relative magnitude of the dichroism with respect to the XAS is a measure for the magnetic moment. The XMCD is proportional to $\langle J_z \rangle = \langle M \rangle$. The XMLD is proportional to $\langle J_z^2 \rangle = \langle M^2 \rangle$, which means this latter technique is useful for antiferromagnets where $\langle M \rangle = 0$.

In 1986—one year after the theoretical prediction—the experimental proof of XMLD was given by van der Laan et al. [19]. The measurements were performed at the 540 MeV storage ring l'Anneau de Collision d'Orsay (ACO) at the Laboratoire pour l'Utilisation du Rayonnement Electromagnétique (LURE) in Orsay near Paris. The setup of the original experiment is shown in Fig. 9.1a [19]. A single crystal of the terbium iron garnet, $Tb_3Fe_5O_{12}$ (TbIG) was mounted on a rotatable helium-flow cryostat in an ultrahigh vacuum of 10^{-10} Torr. The temperature obtained at the surface of the sample was 55 K. A Co_5Sm permanent magnet provided a field of 2 kG along the [111] surface normal, which is the easy direction of magnetization of TbIG. Synchrotron radiation from ACO with 100 mA ring current was monochromatized using a constant-deviation double-crystal monochromator equipped with beryl crystals. The emitted radiation in the equatorial plane of the storage ring is linearly polarized. In the actual setup it was *s* polarized with respect to the beryl crystals and *p* polarized with respect to the sample. The x-ray absorption at the Tb M_5 ($3d_{5/2} \rightarrow 4f$) edge was measured using the total-electron yield method, and obtained for different angles, α, between the polarization vector of the incident radiation and the [111] magnetization direction.

The measured spectra give a good agreement with the Boltzmann-averaged sum of the absorption intensities for transitions with linearly polarized x-rays. The experimental Tb M_5 spectra for various values of α are shown in Fig. 9.1b, where the solid lines are theoretical fits. As seen, the intensities of the two major peaks have a strongly different polarization dependence. As confirmed by the calculation in Fig. 9.1c, parallel polarization with respect to the net magnetization enhances the low-energy peak, whereas perpendicular polarization increases the high-energy peak.

9.6 X-ray magnetic circular dichroism in absorption

In 1987, Schütz and co-workers [20] measured the magnetic circular dichroism with hard x-rays.[1] The measured transmission of synchrotron radia-

[1] Note that in the older literature, XMCD is usually denoted as CMXD.

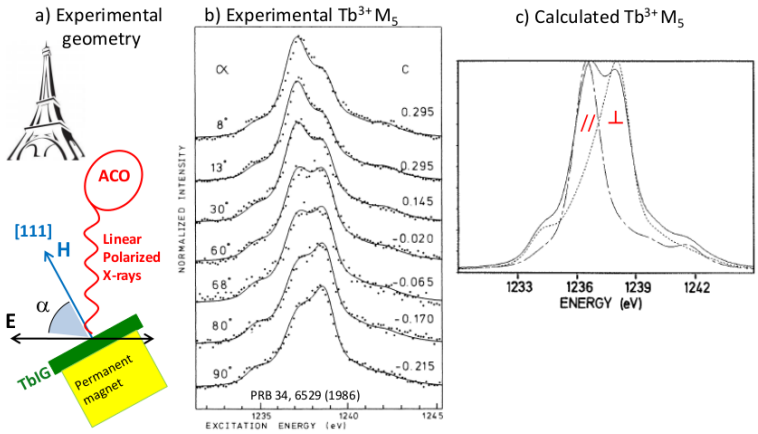

Fig. 9.1 Experimental proof of x-ray magnetic dichroism. **a** Experimental set-up. **b** Experimental M_5 absorption spectra of TbIG at various values of α, which is the angle between the polarization vector of the x-rays and the magnetization direction. The solid lines are fits giving the value of C, which contains the measurement angle α, the umbrella angle of the garnet structure, and the temperature dependent magnetization ($C = 0$ at the magic angle $\alpha = 54.7°$) [19]. (c) Calculated Tb M_5 ($3d_{5/2} \rightarrow 4f$) spectra for unpolarized x-rays (solid) and polarized x-rays with $\mathbf{H} \parallel \mathbf{E}$ (dashed) and $\mathbf{H} \perp \mathbf{E}$ (dotted).

tion through a magnetized iron foil at energies above the K-absorption edge showed relative differences for right and left circular polarization of several times 10^{-4}. The observed spin dependence of the near-edge photoabsorption is proportional to the difference of the spin densities of the unoccupied bands. The unoccupied spin-bands are otherwise only accessible with great difficultly, such as by spin-polarized inverse photoelectron spectroscopy.

In the XMCD experiment, x-rays from the storage ring DORIS at the Deutsches Elektron Synchrotron (DESY) in Hamburg were monochromatized using a Si(311) double-crystal monochromator. The incident x-rays passed a vertically adjustable double slit, which is fixed to a double-ionization chamber so that two beams symmetrically to the electron orbit passed with opposite sense of elliptical polarization. The targets were placed inside a water-cooled solenoid, producing a magnetic field of up to 0.2 T with its direction (anti)parallel to the photon propagation direction. The direction of the magnetic field was flipped every second. The foil had to be placed into the beam

by an angle relative to field direction which causes a reduced effective polarization. The measurements were performed at room temperature.

The data could be explained using a simple two-step picture in a single particle model. In the first step circularly polarized x-rays excite a spin-polarized electron from the unpolarized core hole. In the second step this electron drops into the exchange split unoccupied density-of-states. The dipole-transition-matrix elements from the $1s$ state to a continuum $p_{1/2}$ and $p_{3/2}$ doublet are slightly different because of their spin-orbit splitting which gives a photoelectron polarization of $\sim 10^{-2}$. Therefore, the K absorption contains a small spin-dependent part if the unoccupied valence p states are spin polarized as in magnetic materials. Comparison of the calculated differences of the spin densities of the empty states as a function of energy gave a good agreement with calculations obtained by the Korringa-Kohn-Rostoker (KKR) band-structure method. Soon after, Ebert et al. [21, 22] gave a description of the absorption of circularly polarized x-rays based on a spin-polarized version of relativistic multiple-scattering theory. The effect results in analogy to the Fano effect [23] in the visible from the conservation of the angular momentum in the absorption process together with the spin-orbit coupling acting on the initial and/or final states.

The measurement of the spin-dependent variation in the absorption near the K edge in ferromagnetic iron was repeated by Collins et al. [24] using circularly polarized x-rays from the Synchrotron Radiation Source (SRS) at Daresbury Laboratory by monitoring the fluorescence signal with a solid state Ge detector at 90° to the incident beam. They found that the magnetic modulation of the absorption coefficient was in agreement with a first-principles spin-polarized band calculation, but that the dichroism was about twice as small as reported by Schütz et al., who overestimated the degree of circular polarization.

Since the XMCD is caused by the spin-orbit coupling in the p final states, the dichroism at the K edge is rather small. Larger effects can be found at the L edges, where the angular part of the dipole matrix elements leads to a bigger electron polarization. Schütz and co-workers [25] measured the magnetic dichroism spectra of a wide range of other ferromagnetic materials, such as the $L_{2,3}$ edges of Gd and Tb and $5d$-impurities in iron.

Schütz and co-workers [20] also observed a small spin-dependent absorption in the extended x-ray absorption fine structure (EXAFS) region up to 200 eV above the Fe K edge. The absorption fine structure results from interference between outgoing electron waves and those backscattered by neighboring atoms. If the outgoing electron wave is polarized after absorption of cir-

cularly polarized x-rays, the backscattering amplitude will be sensitive to the spin polarization of the neighbors resulting from exchange interaction. This effect gives information on the magnetic neighborhood of the absorbing atom.

9.7 XMCD at the $3d$ transition metal $L_{2,3}$ edges

From a spintronic perspective, the $3d$ transition metal $L_{2,3}$ absorption edges are probably the most important edges, however their dichroism was only first measured in 1990. As mentioned in Sec. 9.4, this was mainly due to the poor accessibility of the soft x-ray range below 800 eV. Fortunately, improvements in the performance of grating monochromators, especially the design of the double-headed Dragon, opened up this new territory [26].

Kao et al. [27] measured the specular reflectivity of p-polarized light near the Fe $L_{2,3}$ absorption edges from a single-crystal iron film with an external magnetic field perpendicular to the scattering plane. Large changes in reflectivity were observed upon reversal of the direction of the magnetic field. This resonant magnetization-sensitive effect can be attributed to the interference between magnetic and nonmagnetic contribution to the resonant scattering. Similar effects can be expected in other ferromagnetic and ferrimagnetic systems. The reflectivity and scattering spectra at resonance contain both the real imaginary part of the scattering cross section, which makes the analysis more complicated compared to absorption spectra [28, 29].

Chen et al. measured the XMCD at the $L_{2,3}$ edges ($2p \rightarrow 3d$ transitions) of Ni [30]; followed by that of Co and Fe ferrites and garnets [31]. The measurements were performed using the Dragon monochromator at the National Synchrotron Light Source in Brookhaven. The transitions from the $2p$ core level take place directly to the empty $3d$ states, which are magnetically polarized, hence giving a strong dichroism. In the Ni L_3 edge, the XAS shows a satellite at 6.3 eV, whereas the XMCD shows a satellite at 3.7 eV. This could be explained with multielectron calculations including configuration interaction on the basis of the Anderson impurity model, which shows that the spectrum contains a main peak p^5d^{10} and a satellite peak p^5d^9 [32, 33].

Koide et al. [34] measured the XMCD in the $3d$-metal $M_{2,3}$ edges ($2p \rightarrow 3d$ transitions) which shows a strong Fano line shape. The experimental XMCD of Ni metal is quite different that predicted by the exchange-split-valence-band model of Erskine and Stern [10], but it could be explained by multielectron calculations [33].

9.8 Other noteworthy developments

In 1990, Carra and Altarelli [35] presented a theoretical formulation of linear and circular dichroism in the absorption of x-rays in terms of the electric multipole-expansion. These authors demonstrated that the usually neglected electric quadrupole transitions can be as important as the dipole terms for the interpretation of magnetic dichroism experiments in transition metals and rare earths. The quadrupolar effect in XMCD was unambiguously evidenced in 1995 by measuring the temperature and angular dependences at the L edges of rare earths compounds [36, 37].

The magnetization profile of magnetically ordered patterns in ultrathin films was determined by circular dichroism in x-ray resonant magnetic scattering [38] When this technique was applied to single crystalline FePd alloy layers, magnetic flux closure domains were found whose thickness can constitute a large fraction ($\sim$25 %) of the total film. It was demonstrated that soft x-ray resonant scattering can be used to obtain the magnetization profile of magnetic patterns in thin films by using the circular dichroism to recover the phase relation [38].

9.9 Multiplet calculations

In the development of XMCD, experimental and theoretical results followed each other very closely and often they went hand-in-hand. As already mentioned in Secs. 9.4 and 9.7, a one-electron model is not suitable to calculate localized $3d$ and $4f$ metal compounds due of the presence of electron-correlation effects in these materials. An atomic multi-electronic approach which puts electrostatic (Coulomb and exchange) interactions on an equal footing and also includes crystal- or ligand-field interactions, has shown to give an excellent agreement with experimental x-ray absorption spectra, as demonstrated by multiplet calculations for the $2p^6 3d^n \rightarrow 2p^5 3d^{n+1}$ transitions in $3d$ compounds [39, 40, 41].

Such atomic multiplet calculations were also able to give accurate MXD spectra, which are likewise determined by angular momentum coupling. This was already demonstrated for rare-earth materials, where the magnetic interaction can be treated as a perturbation of the spherical symmetry [18]. In the case of the $3d$ metals, the ground and excited states are calculated in the pres-

ence of crystal field symmetry, which gives an energy splitting of magnetic sublevels with different $|m|$ values [42]. Multiplet calculations in crystal field symmetry are performed using the chain of groups approach, exposed by Butler [43]. This approach starts with the calculation of the reduced-matrix elements of the necessary operators in the spherical group using Cowan's atomic multiplet program [44]. The Wigner-Eckart theorem is then applied to obtain the reduced matrix elements in the desired point group, where the required isoscalar factors are obtained from Butler's point-group program [45].

9.10 The rise of magneto-optical sum rules

The postulation of the orbital sum rule in 1992 [46] transformed XMCD into the very powerful technique that it is today. Here we will describe the development of the x-ray magneto-optical sum rules from its beginning.

In 1972, Starace [47] showed that the integrated intensity of the isotropic XAS is proportional to the number of holes, n_h, in the valence $3d$ or $4f$ shell. While absolute measurements of the intensity are difficult, this first rule turned out to be most useful to normalize the intensity of the dichroism spectra on a *per hole* basis. Never the less, the number of holes will have to be estimated using, e.g., band structure calculations.

In 1988, Thole and van der Laan derived a sum rule for the branching ratio of the isotropic x-ray absorption, which was shown to be linearly proportional to the expectation value of the angular part of the ground-state spin-orbit operator per hole [48, 49, 50]. It was already known that the branching ratio of the $L_{2,3}$ XAS depends on the relative population of the $j_d = \frac{3}{2}$ and $\frac{5}{2}$ levels in the ground state of a d metal. This is because for dipole selection rules the $p \rightarrow d$ transitions at the L_3 edge are allowed from $j_p = \frac{3}{2}$ to $j_d = \frac{3}{2}$ and $\frac{5}{2}$, whereas at the L_2 edge the transitions from $j_p = \frac{1}{2}$ are only allowed to $j_d = \frac{3}{2}$. For $p \rightarrow d$ transitions, the spin-orbit sum rule can be stated as

$$B \equiv \frac{I(L_3)}{I(L_3)+I(L_2)} = \frac{2}{3} + \frac{1}{3}\frac{\langle \underline{w} \rangle}{n_h} , \tag{9.1}$$

where

$$\langle \underline{w} \rangle \equiv \langle g | \sum_{i=1}^{h} \ell_i \cdot s_i | g \rangle = -\frac{3}{2} n^h_{3/2} + n^h_{5/2} , \tag{9.2}$$

is the expectation value of the angular part of the spin-orbit interaction for the d hole ground state, and $n^h_{3/2} + n^h_{5/2} = n_h$. Note that $\langle \underline{w} \rangle$ is different from the spin-orbit interaction term in the Hamiltonian, $\mathscr{H}_{\rm SO} = \zeta_{3d} \mathbf{L} \cdot \mathbf{S}$.

For $j = \ell + s = \frac{5}{2}$ holes, $\langle \underline{w} \rangle / n_h = 1$, which results in the maximum value $B = 1$. For $j = \ell - s = \frac{3}{2}$ holes, $\langle \underline{w} \rangle / n_h = -\frac{3}{2}$, which gives the minimum value $B = \frac{1}{6}$. In absence of d spin-orbit interaction, $B = \frac{2}{3}$. As the $j = \frac{5}{2}$ holes are energetically more favorable (at least in absence of other interactions), $\langle \underline{w} \rangle \geq 0$ and $B \geq \frac{2}{3}$.

A rigorous proof of the spin-orbit sum rule was given using angular momentum coupling [48]. It is interesting to note that the various steps of the derivation can be found back in all magneto-optical sum rules.

This result shows that the branching ratio of the XAS is determined by the spin-orbital character of the ground state, which at first was seen as surprising because the prevailing opinion was that the XAS spectra were dominated by final state effects. It is of course much more interesting to measure the properties of the ground state than those of the final state. The model is generally applicable and explains the strong deviations of the $L_{2,3}$ branching ratio from the statistical value for in $3d$ transition metals, alloys, and compounds [49]. Since the spin-orbit interaction is obtained per hole, its influence on the branching ratio is stronger at the end of the transition series, although in rare earths it is still easily observable in Ce compounds [51].

When the core level j is not a good quantum number, the sum rule is no longer exact. The presence of a strong core-hole interaction gives a large mixing of the two core j levels (called jj mixing), which leads to an addition contribution in the branching ratio [49]. Only under favorable conditions such as for the $N_{4,5}$ and $M_{4,5}$ edges of the actinides, the jj mixing is small [17, 52].

Application of the spin-orbit sum rule to actinides showed that for curium metal the $5f$ angular momentum coupling plays a decisive role in the formation of the magnetic moment [53]. The Cm $5f^7$ state in intermediate coupling is strongly shifted towards the LS coupling limit due to exchange interaction, unlike Pu $5f^5$ and Am $5f^6$, where the effective spin-orbit interaction prevails. Essentially, the lowest energy spin-orbit level $j = \frac{5}{2}$ cannot contain more than six f electrons, hence the additional f electron in Cm has to go into the energetically unfavorable $j = \frac{7}{2}$ level, which leads a lower exchange energy.

Recently, the spin-orbit sum rule has been generalized for electric-multipole transitions in non-resonant inelastic x-ray scattering [54]. It gives the counter-intuitive result that the different ranks of the multipole transitions from a deep core hole have a strongly different sensitivity to the valence spin-orbit inter-

action of the material. In actinides, the proportionality factor between the $5f$ spin-orbit interaction and the core-level branching ratio is opposite in sign for octupole and triakontadipole transitions [55].

9.11 The XMCD sum rules

In 1992, Thole et al. [46] derived the famous sum rule that relates the integrated signal of the XMCD to the ground-state orbital magnetic moment $\langle L_z \rangle$. A simple intuitive demonstration of this sum rule for one-electron wave functions (Slater determinants), which are eigenstates of L_z, was published by Altarelli [56] using the properties of the squared $3j$ symbols, while a pictorial demonstration was provided in Ref. [57]. Carra et al. [58] derived a second sum rule for XMCD, which gives the relation between the branching ratio of the XMCD and the spin magnetic moment $\langle S_z \rangle$ and magnetic dipole term $\langle T_z \rangle$ in the ground state. Carra et al. first reported the quadrupole moment sum rule for XMLD and also extended the results to electric-quadrupole transitions [59].

9.11.1 The machinery spitting out the sum rules

First, the expression for the transition probability is separated into a dynamic and a geometric part. The former gives the radial part, while the latter gives the angular dependent part. The radial part is assumed to be constant over the region of the spectrum and hence can be factored out. The transition probabilities of the polarized spectra are then obtained using Fermi's golden rule. The integrated intensities ρ_q for q polarized light are obtained by summing the $c \rightarrow \ell$ transition probability over the final states f and the components γ and m of c and ℓ, respectively, where for simplicity we assume diagonal basis states $m' = m$, $\sigma' = \sigma$ and $\gamma' = \gamma$, as in SO_2 symmetry,

$$\rho_q = \sum_{f\gamma m\sigma} \langle g|\ell_{m\sigma} c^\dagger_{\gamma\sigma}|f\rangle\langle f|\ell^\dagger_{m\sigma} c_{\gamma\sigma}|g\rangle \begin{pmatrix} \ell & 1 & c \\ -m & q & \gamma \end{pmatrix}^2 . \tag{9.3}$$

The values $q = -1, 0, +1$ correspond to right-circularly, z, and left circularly polarized radiation, respectively. The relative intensities $lm \rightarrow c\gamma$ are given

by the squared $3j$-symbol (denoted by the parentheses), which is nonzero for $m = q + \gamma$, and $\ell^{\dagger}_{m,\sigma}$ ($c^{\dagger}_{\gamma,\sigma}$) and $\ell_{m,\sigma}$ ($c_{\gamma,\sigma}$) denote the creation and annihilation operators of the valence (core) electron.

Final states $|f\rangle$ that cannot be reached in the dipole transition do not contribute to the intensity. By extending the set of final states to the whole Hilbert space and using the completeness relation, one can remove the core-hole operators and so obtain integrated signals which depend only on ground state operators, and since $|c^{\dagger}\rangle = \langle c| = 0$ we can write

$$\sum_{f\gamma m\sigma} \langle g|\ell_{m\sigma}c^{\dagger}_{\gamma\sigma}|f\rangle\langle f|\ell^{\dagger}_{m\sigma}c_{\gamma\sigma}|g\rangle = \sum_{m}\langle g|\ell_{m\sigma}\ell^{\dagger}_{m\sigma}|g\rangle = \sum_{m\sigma} n_{m\sigma} \,, \tag{9.4}$$

where $n_{m\sigma}$ is the number of holes with indices m and σ.

Substitution of (9.4) into (9.3) and recoupling the angular momenta by rewriting the squared $3j$-symbol using theorem 4 of Yutsis, Levinson, and Vanagas (YLV4) [60] gives

$$\rho_q = \sum_{m\sigma x} n_{m,\sigma}(2x+1) \begin{Bmatrix} \ell & x & \ell \\ 1 & c & 1 \end{Bmatrix} \begin{pmatrix} 1 & x & 1 \\ -q & 0 & q \end{pmatrix} \begin{pmatrix} \ell & x & \ell \\ -m & 0 & m \end{pmatrix} . \tag{9.5}$$

We now define the integrated intensities ρ^x of the fundamental spectra as linear combinations of the integrated intensities ρ_q of the primitive spectra,

$$\rho^x \equiv \sum_q (-1)^{1-q} \begin{pmatrix} 1 & x & 1 \\ -1 & 0 & 1 \end{pmatrix}^{-1} \begin{pmatrix} 1 & x & 1 \\ -q & 0 & q \end{pmatrix} \rho_q \,. \tag{9.6}$$

This simply gives $\rho^0 \equiv \rho_1 + \rho_0 + \rho_{-1}$, $\rho^1 \equiv \rho_1 - \rho_{-1}$, and $\rho^2 \equiv \rho_1 - 2\rho_0 + \rho_{-1}$, where $x = 0$, 1, and 2 denote the isotropic spectrum and the circular and linear dichroism, respectively.

For the $\ell = c + 1$ case (e.g., $p \to d$ or $d \to f$) substitution of (9.5) into (9.6) gives

$$\rho^0 = \frac{1}{2\ell+1}\sum_{m\sigma} n_{m\sigma} = \frac{1}{2\ell+1} n_h \,, \tag{9.7}$$

$$\rho^1 = \frac{1}{\ell}\sum_{m\sigma} n_{m\sigma} m = \frac{1}{\ell}\langle L_z\rangle \,, \tag{9.8}$$

$$\rho^2 = \frac{3}{\ell(2\ell-1)}\sum_{m\sigma} n_{m\sigma}\left[m^2 - \frac{1}{3}\ell(\ell+1)\right] = \frac{3}{\ell(2\ell-1)}\langle Q_{zz}\rangle \,, \tag{9.9}$$

which gives the number of holes n_h in the ℓ shell, its orbital moment and charge quadrupole moment, respectively. In intermediate coupling and in the presence of hybridization the occupation numbers have of course non-integer values.

The use of the sum rules can be demonstrated by the example of the transition $p^6d^n \rightarrow p^5d^{n+1}$ in a transition metal. The transition probabilities of the primitive spectra with different polarization are calculated using the square of the $3j$ symbol in (9.3), and the results are displayed in Fig. 9.2a. Left-circularly polarized light (L) with selection rule $q = -\Delta m = +1$ gives transition probabilities of $\frac{1}{30}$, $\frac{1}{10}$ and $\frac{1}{5}$ for excitation into the m = 0, 1 and 2 sublevel, respectively of the ground state d state to the $\gamma = -1, 0, +1$ level of the c core hole. Using time-reversal symmetry, $\{L, \pm m\} \leftrightarrow \{R, \mp m\}$, gives the transition probabilities for right-circularly polarized light (R). Z-polarized light (perpendicular to the plane of L and R) gives transition probabilities of $\frac{2}{15}$, $\frac{1}{10}$ and 0 for excitation into the $|m|$ = 0, 1, and 2 sublevels, respectively.

The fundamental spectra, shown in Fig. 9.2b, are linear combinations of the primitive spectra using (9.6). In the isotropic spectrum, the transition probability is constant, i.e., independent of m. In the XMCD, the transition probability is linear in m. In the linear dichroism, the transition probability has the shape of a parabola, and is thus quadratic in m. For an arbitrary initial state, the integrated intensity is the sum over m and spin σ of the occupation number n_m times the transition probability. For the isotropic spectrum, XMCD and XMLD this gives $\langle n \rangle$, $\langle L_z \rangle$, and $\langle Q_{zz} \rangle$, respectively. Applying the Wigner-Eckart theorem to obtain the reduced matrix elements in the desired point group [44], the sum rules can be extended to crystal field symmetry [57].

Sum rules that involve the spin need a separate integration over the intensity of spin-orbit split core levels. This demands that the angular momentum j of the core hole is a good quantum number, which is fulfilled when the core spin-orbit interaction is much larger than the core-valence interactions. Taking the weighted difference over the spin-orbit split core levels the sum rule gives

$$\delta^1 \equiv \left(\sum_{j=c+\frac{1}{2}} - \frac{c+1}{c} \sum_{j=c-\frac{1}{2}} \right) \rho^1 = \frac{2}{3} \langle S_z \rangle + \frac{2}{3} \frac{2\ell+3}{\ell} \langle T_z \rangle \, . \tag{9.10}$$

In the limit of small $3d$ spin-orbit interaction, the magnetic dipole term, $\langle T_z \rangle = [\sum_i s_i - 3\hat{r}_i(\hat{r}_i \cdot s_i)]_z$, describes the difference between the charge quadrupole moment for spin down and spin up electrons, $\mathbf{T} = \frac{1}{2}(Q^{\downarrow} - Q^{\uparrow})\hat{\mathbf{S}}$. Since

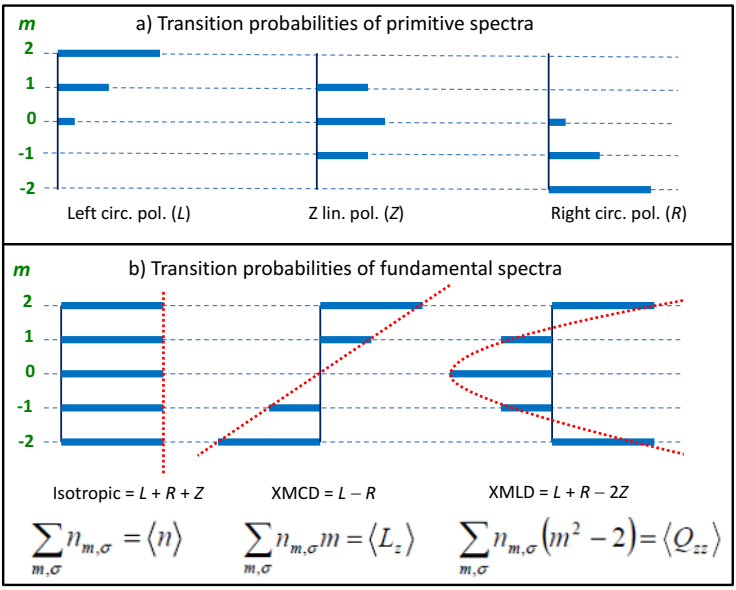

Fig. 9.2 Pictorial demonstration of the sum rules. **a** The transition probabilities of each magnetic d shell sublevel m for the $p \rightarrow d$ absorption excited with left-circular (L), linear (Z) and right-circular (R) polarized x-rays. **b** The transition probabilities for the resulting isotropic spectrum, XMCD and XMLD, which multiplied by the occupation numbers, $n_{m,\sigma}$, and summed over m and σ give the expectation values of the number of holes, n, the orbital moment, L_z, and the quadrupole moment, Q_{zz}, respectively.

the quadrupole moment is a second rank tensor with vanishing trace, the contributions of **T** over three orthogonal directions should be zero [61]. Alternatively, one can determine $\langle S_z \rangle$ at the magic angle (54.7°), where $\langle T_z \rangle$ has to vanish [62].

While $\langle T_z \rangle$ is often small in cubic $3d$ transition metals, this is not the case in $4f$ and $5f$ metals [63]. Collins et al. [64] measured the XMCD in a ferromagnetic uranium monosulphide crystal by monitoring the fluorescence signal over the uranium $M_{4,5}$ edges. The contribution of $\langle T_z \rangle$ to the dichroism signal in US is larger than that of $\langle S_z \rangle$.

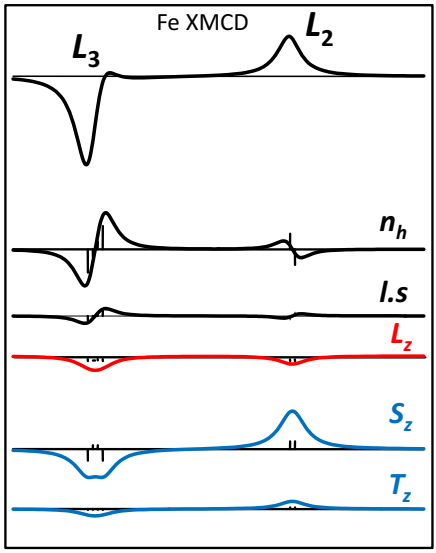

Fig. 9.3 Relative contributions to the energy dependence of the Fe $2p$ XMCD spectrum arising from the various ground state moments for iron metal. n_h = number of holes, $\ell \cdot s$ = scalar part of spin-orbit interaction, L_z = orbital moment, S_z = spin moment and T_z = magnetic dipole term. The red and blue spectra relate to the sum rules for the orbital and spin magnetic moments, respectively. The upper spectrum shows the sum of all contributions, which resembles the experimental Fe $L_{2,3}$ XMCD spectrum. For further details see Ref. [65].

9.11.2 Energy dependence of the ground state moments

It is also illustrative to demonstrate the sum rules from the perspective of the ground-state moments [66]. In Fig. 9.3, the Fe $L_{2,3}$ XMCD spectrum is decomposed into its contributions from the separate ground-state moments [65]. It is seen that the shape and magnitude of the XMCD are mainly determined by n_h and S_z. However, only for L_z, the XMCD has a non-zero intensity integrated over both edges. For S_z and T_z the XMCD does not vanish over each separate edge but integrated over both edges the intensity is zero. For n_h and the spin-orbit interaction, $\ell \cdot s$, the integrated intensity of of XMCD vanishes for each edge, but these still contribute to the energy dependence across each

edge. This is also the case for the higher moments, such as Q_{zz}, as shown in Ref. [65]. Hence, this not only illustrates that the integrated intensities over the L_3 and L_2 edges are related to the orbital and spin moments, but also that they do not depend on the other ground-state moments. It also means that a correct differential formulation of the sum rules needs to include all ground state moments!

9.11.3 Possible causes of concerns

It should be mentioned that at first not everyone was equally convinced by the sum rules. One of the "objections" commonly heard was that the 3*d* metals are spin-only magnets which have no orbital magnetic moment, as was reinforced by some standard solid-state text books. However, this can be readily dismissed. While in 3*d* metals the orbital part to the magnetic moment is small, it is manifestly present in, e.g., the magnetic anisotropy [67].

Another objection was that in intermediate coupling there might be cross terms, leading to interference terms. However, the sum rules can also be derived for jj-coupled operators. By including cross terms between the $j = \ell \pm \frac{1}{2}$ levels, it could be shown that the sum rules are generally applicable in intermediate coupling [63, 68].

A further commonly heard argument was that the sum rules are valid for the atomic case but not for the band structure case, or vice versa, valid for the band structure case but not for the atomic case. However, several theorists successfully rederived the sum rules for the band structure case, such as Ankudinov and Rehr [69] using the independent electron approximation, Ebert [70] using first-principles spin-polarized relativistic multiple-scattering calculations, and Wu et al. [71] using local density band structure calculations. Furthermore, in an atomic model the sum rules are exact as long as jj mixing can be neglected. Large deviations due to jj mixing arise when the L_3 and L_2 start to overlap, such as in the Mn $L_{2,3}$ spectrum, which can be taken into account by a correction factor [72].

Another argument was that hybridization effects could spoil the sum rule. However, Benoist et al. [73] derived corrections to the atomic orbital sum rule for XMCD in solids using orthonormal linear muffin-tin orbitals (LMTOs) as a single-particle basis for electron band states.

Nowadays doubts about the sum rules have evaporated, but only to be replaced by repetitive discussions about their accuracy. Under the proper as-

sumptions (such as the absence of jj mixing) the derivation of the sum rules is exact. The practical limitations of the sum rules are well known (see, e.g., Refs. [74, 75]) and an error bar of 5-10% is nowadays commonly accepted.

9.11.4 Sum rules for other x-ray spectroscopies

Sum rules for integrated dichroism were also derived for other x-ray spectroscopies, using a similar methodology as for XAS and XMCD sum rules, by using angular momentum coupling to describe the angular part of the transition matrix elements, and by treating the radial part of the matrix element as a constant factor. Luo et al. [76] gave sum rules for resonant x-ray magnetic scattering, using the fast collision approximation. Thole and van der Laan [77, 78] derived sum rules for spin resolved and dichroic photoemission, particularly the $4f$ photoemission from rare earths. Carra and Thole [79] gave rules for anisotropic x-ray anomalous diffraction in the presence of crystal field symmetry.

Sum rules were furthermore derived for spectroscopies that required to take into account the angular dependence of the emitting photon or electron, such as resonant photoemission [80] and resonant inelastic x-ray scattering (resonant Raman scattering) [81, 82, 83].

9.12 Determining the magnetic anisotropy

In $3d$ transition metals, the spin-orbit constant is between 40 and 80 meV [41], which is small compared to the bandwidth of a few eV, so that a perturbative treatment is justified. Bruno [84] showed using perturbation theory that the dependence on the electronic structure can be separated from the angular dependence, which allows us to calculate the different anisotropy constants directly from the unperturbed band structure. While perturbation theory enables to calculate directly the anisotropy constants without having to calculate explicitly the total energy of the system as a function of the magnetization direction, it would not take into account any changes of the Fermi surface. Bruno [84] showed that if the majority spin band is completely filled, the magnetocrystalline anisotropy energy (MAE) is proportional to the anisotropy in the orbital magnetic moment. Wang et al. [85] and van der Laan [67] showed that

the MAE contains additional contributions due to the spin-flip term and the magnetic dipole term.

Since the sum rule relates the integrated XMCD signal to the orbital moment projected along the beam direction, the anisotropy in the orbital moment can be obtained from the angular dependence of the integrated XMCD. This was experimentally confirmed for a Au/Co/Au staircase structure by Weller et al. [86, 87], although a proportionality factor is required to scale the anisotropic part.

Instead of obtaining the MAE from XMCD measurements along two different beam directions, the magnetic anisotropy can actually also be obtained from a single XMCD measurement in *transverse geometry* ($\mathbf{M} \perp \mathbf{P}$) [62, 88]. By forcing the electron spins out of the easy direction using an external magnetic field and measuring the perpendicular component of the orbital moment with the photon helicity vector perpendicular to the magnetization direction it is possible to determine directly the element-specific easy-direction of magnetization. The relation between the angular dependence of XMCD with arbitrary directions of $\mathbf{M}$ and $\mathbf{P}$ and its anisotropic ground-state moments is found in Ref. [89]. The angular dependent XMCD is strongly sensitive to the strain-induced electronic structure changes in magnetic transition metal oxides. It can be described as a sum over an isotropic and anisotropic contribution, the latter linearly proportional to the axial distortion due to strain [90].

An even a more direct way to obtain the MAE is to measure the anisotropy in the spin-orbit interaction, which is proportional to the branching ratio of the XMLD [91]. Although XMLD has a much smaller sensitivity than XMCD, it could be measured on GaFe alloy thin films, which show large magnetostrictive properties [92].

9.13 Circular dichroism in x-ray photoemission

In 1990, Baumgarten et al. [93] reported magnetic circular dichroism in the Fe $2p$ core-level photoemission from ferromagnetic iron, which they ascribed to the exchange splitting of the core-hole levels.

An explanation of circular dichroism in photoemission was given in terms of core-valence interaction using a multi-electron model [94, 95], which can be applied to localized transition-metal, rare-earth and actinide compounds. In contrast to x-ray absorption, the angular-dependent part of the electrostatic interaction between the core hole and localized valence holes is essential for

circular dichroism in core-level photoemission. In absorption the dichroism is a consequence of the Pauli principle. The polarized light creates polarized electrons which cannot go freely into the magnetic $3d$ shell. In contrast, in x-ray photoemission spectroscopy the core electron is ejected into a continuum shell which has no interaction, and the dichroism arises from the electrostatic interaction between the core hole and the polarized $3d$ electrons. The p-d Coulomb and exchange interactions couple the d^n spin to the spin of the core hole and then the $2p$ spin-orbit interaction couples this spin to the core electron orbital, which interacts with the light. An itinerant-electron model cannot describe the multiplet effects arising from the many-electron Coulomb and exchange interactions, so that in this case the assumption is that the splitting occurs by an effective spin field in combination with spin-orbit interaction [96].

In a series of three papers, Thole and van der Laan present a general theory for spin polarization and magnetic circular and linear dichroism in photoemission from core and valence states in localized magnetic systems using a multi-electron approach [97, 78, 98].

The first paper [97] explain the origin of the spin polarization and magnetic dichroism . The six different ways to orient the polarizations of the magnetization, the electric vector of the light, and the spin of the photoelectron allow measurements of different kinds of correlations between the corresponding atomic properties: the valence spin, the core hole orbital momentum and the core hole spin, respectively. The fundamental spectra can be defined as those linear combinations of the polarized spectra that are directly connected to physical properties. This allows us to analyze exchange and hybridization effects, as was illustrated by the $2p$ and $3p$ photoemission of ferromagnetic Ni metal. A large enhancement of the surface orbital magnetic moment at the surface of Ni(100) was evidenced by magnetic circular dichroism in photoemission [99], as predicted by band structure calculations.

The second paper [78] showed that for the emission from an incompletely filled localized shell, such as the $4f$ shell in the rare earths, the integrated intensities of the magnetic circular dichroism and spin spectrum are proportional to the ground-state orbital and spin magnetic moment, respectively. In fact, each fundamental spectrum can be related to a particular ground state property.

The third paper [98] gives a detailed analysis of the angular dependence of the photoemission. The geometry can be separated from the physical properties and the angular dependence provides a way to measure higher magnetic moments. The interference term between the $\ell - 1$ and $\ell + 1$ emission chan-

nels allows us to measure the odd magnetic moments using linearly polarized light. In angle-integrated photoemission these magnetic moments can only be measured using circularly polarized light. This chiral geometry is the origin of the effect observed by Roth et al. [100], who in 1993 reported a new type of magnetic linear dichroism in angle dependent photoemission. For p-polarized light under oblique incidence the Fe $3p$ core level peak position and line shape change when the sample magnetization is reversed.

9.14 Circular dichroism in resonant x-ray processes and Auger

Magnetic dichroism plays furthermore an important role in second-order coherent processes, such as resonant diffraction, resonant inelastic x-ray scattering (RIXS), and resonant photoemission (RESPES). Thole et al. [101] demonstrated that the possibilities of XAS are greatly extended by detecting the polarization of the core hole using the angle dependence of the resonant photoemission, where the polarization of the hole is transferred to the localized final state and the emitted photoelectron. In the transverse geometry, where the dichroism in the $2p$ absorption is forbidden, a circular dichroism of 9% was observed in the autoionization decay into a $3p^4$ state.

Consider the resonant photoemission as a two-step process, starting with an excitation from a core level to the valence shell, after which the core hole decays into two shallower core holes under emission of an electron. The two core holes form well defined states, which can be selected by the energy of the emitted electron. The non-spherical core hole and the selected final state cause a specific angle and spin distribution of the emitted electron. The experiment is characterized by the magnetic and nonmagnetic moments being measured, the polarization and direction of the light and the spin and angular distribution of the emitted electron. The intensity is a sum over ground state expectation values of tensor operators multiplied by the probability of creating a polarized core hole using polarized light multiplied by the decay probability of such a core hole into the final state [80]. Spin polarization is due to odd moments of the core hole. This core polarization analysis generalizes the use of sum rules in XAS where the integrated peak intensities give ground state expectation values of operators such as the spin and orbital moments. The photoemission decay makes it possible to measure new linear combinations of operators. The general formulation for second-order processes shows that in the presence of

core-valence interactions the two-step model may break down due to interference terms between intermediate states separated by more than their lifetime width.

Dürr et al. [102] observed a strong magnetic circular dichroism in the $L_3M_{2,3}M_{2,3}$ Auger-electron emission spectra measured on Fe and Co metal in the off-resonance energy region with the light helicity vector perpendicular to the magnetization direction, despite the fact that this emission is expected to be symmetry forbidden in this geometry. The effect was ascribed to spin-dependent screening of the intermediate core-hole state. The experimental results could be explained quantitatively by taking into account the exchange interaction of the spin-orbit split core states with the spin-polarized valence band [103]. This behavior is completely different from the measurements at resonance, i.e., at the L_3 absorption edge, where the strong MCD signal for Fe, Co, and Ni is due to the large spin polarization of the $2p$ core hole which is caused by unoccupied $3d$ states with predominantly minority spin in the vicinity of the Fermi level.

9.15 X-ray detected optical activity

In the absence of magnetism, linear dichroism arises from the charge anisotropy, as theoretically analyzed in detail by Brouder [104] for crystal fields lower than cubic symmetry, which was later generalized using group theory [57]. The linear dichroism in anisotropic crystals can be very large, as was, e.g., observed at the Fe $L_{2,3}$ edge of gillespite $BaFeSi_4O_{10}$, where the Fe d^6 ion has as square planar coordination [105].

The optical activity discussed in the previous sections is induced by pure transitions and has even parity. Optical transitions can be expanded in multipole terms, such as electric dipole ($E1$ = parity odd, time even), electric quadrupole ($E2$ = parity even, time even), magnetic dipole ($M1$ = parity even, time odd) and higher-order terms that can normally be neglected [106]. Optical activity induced by pure transitions must have even parity; only interference terms can give odd parity. In the visible the $E1M1$ interference allows the detection of natural circular dichroism or optical rotation in powdered samples or in solution and single crystals. However, in the case of x-ray absorption, which involves core to valence shell excitations, the $M1$ transitions are practically forbidden due to the restriction imposed by the monopole selection rule for the radial part. While in the visible region the $E2$ transitions are neg-

ligibly small, their magnitude increases with photon energy, so that for harder x-rays the $E1E2$ interference can become significant. In this way, Goulon et al. [107] were able to observe x-ray natural circular dichroism (XNCD) at the I $2s$ and $2p$ edges of lithium iodate, a compound lacking inversion symmetry. These measurements were made possible thanks to the intense circularly polarized x-ray beams produced by the insertion device on beamline ID12A at the ESRF. Natoli et al. [108] showed that the measured dichroism was in agreement with theoretical model calculations. While XMCD requires parity even and time odd symmetry, XNCD requires parity odd and time even symmetry. Non-reciprocal linear dichroism, which is parity odd and time odd, which in 2000 was observed by Goulon et al. [109] in the low-temperature antiferromagnetic insulating phase of a Cr-doped V_2O_3 crystal in which one single antiferromagnetic domain was grown by magnetoelectric annealing. This field has continued to flourish and more recent developments have been described in Ref. [110]. Sum rules for x-ray detected optical activity have been reviewed in Refs. [45, 110, 111].

9.16 Epilogue

After its discovery a quarter century ago, x-ray magnetic dichroism quickly attracted the attention of the wider magnetism community working with synchrotron radiation. At the first Mittelwihr School on Synchrotron Radiation and Magnetism [112] in 1989, x-ray magnetic dichroism figured already as high as spin-resolved photoemission, which nowadays it has overtaken as the preferred standard method to obtain spin dependent information from magnetic materials.

The derivation of the sum rules enormously simplified the analysis of XMCD, leading to an explosion in the use of this technique for wider applications. The sum rules are independent of the theory, because they apply to both atomic and band structure models. The development of XMCD has greatly benefitted from the strong theoretical involvement of pioneers, such as Theo Thole and Paolo Carra, who both unfortunately deceased at a too young age. An obituary of Theo Thole can be found in Ref. [113] and a special issue of *Journal of Electron Spectroscopy* is dedicated to his work [114].

The usefulness of XMCD was not equally recognized in all corners of the scientific community. A press release from the *The Royal Swedish Academy of Sciences* issued on 12 October 1994 [115], which announced the Nobel Prize

in Physics to Bertram Brockhouse and Clifford Shull for the development of the neutron diffraction technique, contained the following rather surprising paragraph:

> "Magnetic structures: Neutrons are small magnets, as are the atoms of a magnetic material. When a neutron beam strikes such material, the neutrons can therefore change direction through magnetic interaction with the atoms of the material. This gives rise to a new type of neutron diffraction (the type described earlier is based on neutron interaction with atomic nuclei) which can be used to study the relative orientations of the small atomic magnets. *Here, too, the x-ray method has been powerless and in this field of application neutron diffraction has since assumed an entirely dominant position.* It is hard to imagine modern research into magnetism without this aid."

On the contrary, it would be fair to say that—certainly since 1994—x-rays have taken over the dominant position from neutrons, and that nowadays it is hard to image modern research into magnetism without the aid of polarized x-rays. This was recognized by the 2000 Agilent Technologies Europhysics Prize for Outstanding Achievement in Condensed Matter Physics for "*Pioneering work in establishing the field of magnetic x-ray dichroism*", which was awarded to Paolo Carra, Gisela Schütz-Gmeineder and Gerrit van der Laan [116].

Today, the applications of XMCD are vast and provide almost endless possibilities to study magnetic materials [117]. XMCD can be used for magnetic imaging on the nanoscale using x-ray transmission microscopy and for x-ray holography, using the coherent properties of synchrotron radiation [118, 119, 120]. Another recent development is ferromagnetic resonance (FMR) detected by time resolved XMCD, which makes FMR element- and site-specific [121, 122]. By exploiting the pulsed time structure of the storage ring synchrotron radiation the relative phase of precession in individual magnetic layers of of a spin valve structure can be studied [123].

XMCD can be used also to study the origin of magnetism and anisotropy in ferromagnetic semiconductors, such as in $(Ga_{1-x}Mn_x)As$ [124]. While most applications have been in solid-state physics and technology, more recently the field of research has broadened considerably. New applications have emerged in areas such as chemistry, biology and earth sciences. For instance, in environmental sciences and microbiotechnology, XMCD has become a unique and powerful technique to determine the relative site occupations in (bio)spinels and other ternary oxides [125, 126].

Rapidly increasing information density of modern magnetic data storage devices requires an answer to the question of the fundamental limits in bit

size and writing speed. Time-resolved XMCD with femtosecond laser excitation is used to study magnetic switching, giving information of the driving force behind femtosecond spin-lattice relaxation [127]. In soft x-ray resonant emission the core-hole clock effect can be used to study the spin dependent screening in ferromagnetic metals on a femtosecond timescale [128].

References

1. W.C. Röntgen, Sitz. Ber. Phys. Med. Ges. Würzburg **9**, 132 (1895). Translated by A. Stanton, Nature, **53**, 274 (1896).
2. The cathode ray tube site (www.crtsite.com)
3. R.F. Mould, Phys. Med. Biol. **40**, 1741 (1995)
4. A. Rogalev, F. Wilhelm, N. Jaouen, J. Goulon, J.P. Kappler, Lect. Notes Phys. **697**, 71 (2006)
5. B.L. Henke, E.M. Gullikson, J.C. Davis, Atomic Data and Nuclear Data Tables **54**, 181 (1993)
6. D. Attwood, *Soft x-rays and extreme ultraviolet radiation. Principles and applications* (Cambridge University Press, Cambridge, 1999)
7. C.G. Barkla, Phil. Trans. A **204**, 467 (1905)
8. C.G. Barkla, Proc. Roy. Soc. London A **77**, 247 (1906)
9. P. Zeeman, *Research in magneto-optics* (MacMillan and Co., London, 1913)
10. J.L. Erskine, E.A. Stern, Phys. Rev. B **12**, 5016 (1975)
11. H.S. Bennett, E.A. Stern, Phys. Rev. **137**, A448 (1965)
12. M.P. Bruijn, J. Verhoeven, M.J. van der Wiel, G. van der Laan, J.B. Goedkoop, J.C. Fuggle, A.A. MacDowell, Nucl. Instrum. Meth. Phys. Res. A **253**, 135 (1986)
13. G. van der Laan, J.B. Goedkoop, J.C. Fuggle, M.P. Bruijn, J. Verhoeven, M.J. van der Wiel, A.A. MacDowell, J.B. West, I.H. Munro, Nucl. Instrum. Meth. Phys. Res. A **255**, 592 (1987)
14. G. van der Laan, J. Zaanen, G.A. Sawatzky, R.C. Karnatak, J.M. Esteva, Phys. Rev. B **33**, 4253 (1986)
15. G. van der Laan, R.A.D. Pattrick, C.M.B. Henderson, D.J. Vaughan, J. Phys. Chem. Solids **53**, 1185 (1992)
16. B.T. Thole, G. van der Laan, J.C. Fuggle, G.A. Sawatzky, R.C. Karnatak, J.M. Esteva, Phys. Rev. B **32**, 5107 (1985)
17. K.T. Moore, G. van der Laan, Rev. Mod. Phys. **81**, 235 (2009)
18. B.T. Thole, G. van der Laan, G.A. Sawatzky, Phys. Rev. Lett. **55**, 2086 (1985)
19. G. van der Laan, B.T. Thole, G.A. Sawatzky, J.B. Goedkoop, J.C. Fuggle, J.M. Esteva, R. Karnatak, J.P. Remeika, H.A. Dabkowska, Phys. Rev. B **34**, 6529 (1986)
20. G. Schütz, W. Wagner, W. Wilhelm, P. Kienle, R. Zeller, R. Frahm, G. Materlik, Phys. Rev. Lett. **58**, 737 (1987)
21. H. Ebert, P. Strange, B.L. Gyorffy, J. Appl. Phys. **63**, 3055 (1988)
22. H. Ebert, B. Drittler, R. Zeller, G. Schütz, Solid State Commun. **69**, 485 (1989)
23. U. Fano, Phys. Rev. **178**, 131 (1969)

24. S.P. Collins, M.J. Cooper, A. Brahmia, D. Laundy, T. Pitkanen, J. Phys.: Condens. Matter **1**, 323 (1989)
25. G. Schütz, R. Wienke, W. Wilhelm, W. Wagner, P. Kienle, R. Zeller, R. Frahm, Z. Phys. B **75**, 495 (1989)
26. C.T. Chen, F. Sette, N.V. Smith, Appl. Optics **29**, 4535 (1990)
27. C. Kao, J.B. Hastings, E.D. Johnson, D.P. Siddons, G.C. Smith, G.A. Prinz, Phys. Rev. Lett. **65**, 373 (1990)
28. J.M. Tonnerre, L. Séve, D. Raoux, G. Soullié, B. Rodmacq, P. Wolfers, Phys. Rev. Lett. **75**, 740 (1995)
29. G. van der Laan, C. R. Physique **9**, 570 (2008)
30. C. T. Chen, F. Sette, Y. Ma, S. Modesti, Phys. Rev. B **42**, 7262 (1990)
31. F. Sette, C.T. Chen, Y. Ma, S. Modesti, N.V. Smith, in *X-ray absorption fine structure*, ed. by S.S. Hasnain (Ellis Horwood, Chichester, UK, 1991), p. 96
32. T. Jo, G.A. Sawatzky, Phys. Rev. B **43**, 8771 (1991)
33. G. van der Laan, B.T. Thole, J. Phys.: Condens. Matter **4**, 4181 (1992)
34. T. Koide, T. Shidara, H. Fukutani, K. Yamaguchi, A. Fujimori, S. Kimura, Phys. Rev. B **44**, 4697 (1991)
35. P. Carra, M. Altarelli, Phys. Rev. Lett. **64**, 1286 (1990)
36. C. Giorgetti, E. Dartyge, C. Brouder, F. Baudelet, C. Meyer, S. Pizzini, A. Fontaine, R.M. Galéra, Phys. Rev. Lett. **75**, 3186 (1995)
37. J.C. Lang, G. Starjer, C. Detlefs, A.I. Goldman, H. König, X.D. Wang, B.N. Harmon, R.W.M. Callum, Phys. Rev. Lett. **74**, 4935 (1995)
38. H.A. Dürr, E. Dudzik, S.S. Dhesi, J.B. Goedkoop, G. van der Laan, M. Belakhovsky, C. Mocuta, A. Marty, Y. Samson, Science **284**, 2166 (1999)
39. G. van der Laan, B.T. Thole, G.A. Sawatzky, M. Verdaguer, Phys. Rev. B **37**, 6587 (1988)
40. B.T. Thole, G. van der Laan, P.H. Butler, Chem. Phys. Lett. **149**, 295 (1988)
41. G. van der Laan, I.W. Kirkman, J. Phys.: Condens. Matter **4**, 4189 (1992)
42. G. van der Laan, B.T. Thole, Phys. Rev. B **43**, 13401 (1991)
43. P.H. Butler, *Point group symmetry applications, Methods and tables* (Plenum, New York, 1981)
44. R.D. Cowan, *The theory of atomic structure and spectra* (University of California Press, Berkeley, 1981)
45. G. van der Laan, Lect. Notes Phys. **697**, 143 (2006)
46. B.T. Thole, P. Carra, F. Sette, G. van der Laan, Phys. Rev. Lett. **68**, 1943 (1992)
47. A.F. Starace, Phys. Rev. B **5**, 1773 (1972)
48. B.T. Thole, G. van der Laan, Phys. Rev. A **38**, 1943 (1988)
49. B.T. Thole, G. van der Laan, Phys. Rev. B **38**, 3158 (1988)
50. G. van der Laan, B.T. Thole, Phys. Rev. Lett. **60**, 1977 (1988)
51. G. van der Laan, B.T. Thole, G.A. Sawatzky, J.C. Fuggle, R.C. Karnatak, J.M. Esteva, B. Lengeler, J. Phys. C: Solid State Phys. **19**, 817 (1986)
52. G. van der Laan, K. Moore, J.G. Tobin, B.W. Chung, M.A. Wall, A.J. Schwartz, Phys. Rev. Lett. **93**, 097401 (2004)
53. K.T. Moore, G. van der Laan, R.G. Haire, M.A. Wall, A.J. Schwartz, P. Söderlind, Phys. Rev. Lett. **98**, 236402 (2007)
54. G. van der Laan, Phys. Rev. Lett. **108**, 077401 (2012)
55. G. van der Laan, Phys. Rev. B **86**, 035138 (2012)

56. M. Altarelli, Phys. Rev. B **47**, 597 (1993)
57. G. van der Laan, J. Phys. Soc. Jpn **63**, 2393 (1994)
58. P. Carra, B.T. Thole, M. Altarelli, X. Wang, Phys. Rev. Lett. **70**, 694 (1993)
59. P. Carra, H. König, B.T. Thole, M. Altarelli, Physica B **192**, 182 (1993)
60. D.A. Varshalovich, A.N. Moskalev, V.K. Khersonskii, *Quantum Theory of Angular Momentum* (World Scientific, Singapore, 1988)
61. J. Stöhr, H. König, Phys. Rev. Lett. **75**, 3748 (1995)
62. H.A. Dürr, G. van der Laan, Phys. Rev. B **54**, R760 (1996)
63. G. van der Laan, B.T. Thole, Phys. Rev. B **53**, 14458 (1996)
64. S.P. Collins, D. Laundy, C.C. Tang, G. van der Laan, J. Phys.: Condens. Matter **7**, 9325 (1995)
65. G. van der Laan, Phys. Rev. B **55**, 8086 (1997)
66. B.T. Thole, G. van der Laan, M. Fabrizio, Phys. Rev. B **50**, 11466 (1994)
67. G. van der Laan, J. Phys.: Condens. Matter **10**, 3239 (1998)
68. G. van der Laan, Phys. Rev. B **57**, 112 (1998)
69. A. Ankudinov, J.J. Rehr, Phys. Rev. B **51**, 1282 (1995)
70. H. Ebert, Rep. Prog. Phys. **59**, 1665 (1996)
71. R. Wu, D. Wang, A.J. Freeman, Phys. Rev. Lett. **71**, 3581 (1993)
72. K.W. Edmonds, N.R.S. Farley, T.K. Johal, G. van der Laan, R. P. Campion, B.L. Gallagher, C.T. Foxon, Phys. Rev. B **71**, 064418 (2005)
73. R. Benoist, P. Carra, O.K. Andersen, Eur. Phys. J. B **18**, 193 (2000)
74. M. Altarelli, P. Sainctavit, in *Magnetism and synchrotron radiation*, ed. by E. Beaurepaire, B. Carrière, J.P. Kappler (Les Editions de Physique, Les Ulis, 1996), p. 65
75. G. van der Laan, J. Synch. Rad. **6**, 694 (1999)
76. J. Luo, G.T. Trammell, J.P. Hannon, Phys. Rev. Lett. **71**, 287 (1993)
77. B.T. Thole, G. van der Laan, Phys. Rev. Lett. **70**, 2499 (1993)
78. G. van der Laan, B.T. Thole, Phys. Rev. B **48**, 210 (1993)
79. P. Carra, B.T. Thole, Rev. Mod. Phys. **66**, 1509 (1994)
80. G. van der Laan, B.T. Thole, J. Phys.: Condens. Matter **7**, 9947 (1995)
81. M. van Veenendaal, P. Carra, B.T. Thole, Phys. Rev. B **54**, 16010 (1996)
82. L. Braicovich, A. Tagliaferri, G. van der Laan, G. Ghiringhelli, N.B. Brookes, Phys. Rev. Lett. **90**, 117401 (2003)
83. F. Borgatti, G. Ghiringhelli, P. Ferriani, G. Ferrari, G. van der Laan, C.M. Bertoni, Phys. Rev. B **69**, 134420 (2004)
84. P. Bruno, Phys. Rev. B **39**, 865 (1989)
85. D.S. Wang, R. Wu, A.J. Freeman, Phys. Rev. B **47**, 14932 (1993)
86. D. Weller, J. Stöhr, R. Nakajima, A. Carl, M.G. Samant, C. Chappert, R. Mégy, P. Beauvillain, P. Veillet, G.A. Held, Phys. Rev. Lett. **75**, 3752 (1995)
87. H.A. Dürr, G. van der Laan, B.T. Thole, Phys. Rev. Lett. **76**, 3464 (1996)
88. H.A. Dürr, G. Guo, G. van der Laan, J. Lee, G. Lauhoff, J.A.C. Bland, Science **277**, 213 (1997)
89. G. van der Laan, Phys. Rev. B **57**, 5250 (1998)
90. G. van der Laan, R.V. Chopdekar, Y. Suzuki, E. Arenholz, Phys. Rev. Lett. **105**, 067405 (2010)
91. G. van der Laan, Phys. Rev. Lett. **82**, 640 (1999)
92. E. Arenholz, G. van der Laan, A. McClure, Y. Idzerda, Phys. Rev. B **82**, 180405 (2010)

93. L. Baumgarten, C.M. Schneider, H. Petersen, F. Schafers, J. Kirschner, Phys. Rev. Lett. **65**, 492 (1990)
94. G. van der Laan, Phys. Rev. Lett. **66**, 2527 (1991)
95. B.T. Thole, G. van der Laan, Phys. Rev. Lett. **67**, 3306 (1991)
96. G. van der Laan, Phys. Rev. B **51**, 240 (1995)
97. B.T. Thole, G. van der Laan, Phys. Rev. B **44**, 12424 (1991)
98. B.T. Thole, G. van der Laan, Phys. Rev. B **49**, 9613 (1994)
99. G. van der Laan, M.A. Hoyland, M. Surman, C.F.J. Flipse, B.T. Thole, Phys. Rev. Lett. **69**, 3827 (1992)
100. C. Roth, F.U. Hillebrecht, H.B. Rose, E. Kisker, Phys. Rev. Lett. **70**, 3479 (1993)
101. B.T. Thole, H. Dürr, G. van der Laan, Phys. Rev. Lett. **74**, 2371 (1995)
102. H.A. Dürr, G. van der Laan, D. Spanke, F.U. Hillebrecht, N.B. Brookes, J. Electron Spectrosc. Relat. Phenom. **93**, 233 (1998)
103. A. Chassé, H.A. Dürr, G. van der Laan, Y. Kucherenko, A.N. Yaresko, Phys. Rev. B **68**, 214402 (2003)
104. C. Brouder, J. Phys.: Condens. Matter **2**, 701 (1990)
105. G. van der Laan, P.F. Schofield, G. Cressey, C.M.B. Henderson, Chem. Phys. Lett. **252**, 272 (1996)
106. G. van der Laan, J. Synch. Rad. **8**, 1059 (2001)
107. J. Goulon, C. Goulon-Ginet, A. Rogalev, V. Gotte, C. Malgrange, C. Brouder, C.R. Natoli, J. Chem. Phys. **108**, 6394 (1998)
108. C.R. Natoli, C. Brouder, P. Sainctavit, J. Goulon, C. Goulon-Ginet, A. Rogalev, Eur. Phys. J. B **4**, 1 (1998)
109. J. Goulon, A. Rogalev, C. Goulon-Ginet, G. Benayoun, L. Paolasini, C. Brouder, C. Malgrange, P.A. Metcalf, Phys. Rev. Lett. **85**, 4385 (2000)
110. A. Rogalev, J. Goulon, F. Wilhelm, A. Bosak, in *Magnetism and synchrotron radiation, new trends*, ed. by E. Beaurepaire, H. Bulou, F. Scheurer, J.P. Kappler (Springer, Berlin, 2010), Springer Proceedings in Physics 133, p. 169
111. J. Goulon, A. Rogalev, F. Wilhelm, C. Goulon-Ginet, P. Carra, I. Marri, C. Brouder, J. Exp. Theor. Phys. **97**, 402 (2003)
112. E. Beaurepaire, B. Carrière, J.P. Kappler (eds.), *Rayonnement Synchrotron Polarisé, Electrons Polarisés et Magnétisme, Mittelwihr* (IPCMS, Strasbourg, 1989)
113. G. van der Laan, J. Synch. Rad. **3**, 248 (1996)
114. Special issue dedicated to the late Theo Thole, J. Electron Spectrosc. Relat. Phenom. **86**, 1 (1997)
115. http://www.nobelPrize.org/nobel_Prizes/physics/laureates/1994/press.html
116. http://www.psi-k.org/awards_vanderlaan.shtml
117. G. van der Laan, J. Phys.: Conf. Ser. **430**, 012127 (2013)
118. S. Eisebitt, J. Lüning, W.F. Schlotter, M. Lürgen, O. Hellwig, W. Eberhardt, J. Stöhr, Nature **432**, 885 (2004)
119. T. Duckworth, F. Ogrin, S.S. Dhesi, S. Langridge, A. Whiteside, T. Moore, G. Beutier, G. van der Laan, Opt. Express **19**, 16223 (2011)
120. T.A. Duckworth, F.Y. Ogrin, G. Beutier, M. Dupraz, S.S. Dhesi, S. Langridge, A. Whiteside, T. Moore, F. Yakhou, G. van der Laan, New J. Phys., in print (2013)
121. J. Goulon, A. Rogalev, F. Wilhelm, N. Jaouen, C. Goulon-Ginet, G. Goujon, J.B. Youssef, M.V. Indendom, JETP Lett. **82**, 696 (2005)

122. M.K. Marcham, P.S. Keatley, A. Neudert, R.J. Hicken, S.A. Cavill, L.R. Shelford, G. van der Laan, N.D. Telling, J.R. Childress, J.A. Katine, P. Shafer, E. Arenholz, J. Appl. Phys. **109**, 07D353 (2011)
123. M.K. Marcham, L.R. Shelford, S.A. Cavill, P.S. Keatley, W. Yu, P. Shafer, A. Neudert, J.R. Childress, J.A. Katine, E. Arenholz, N.D. Telling, G. van der Laan, R.J. Hicken, Phys. Rev. B **87**, 180403 (2013)
124. K.W. Edmonds, G. van der Laan, A. Freeman, N.R.S. Farley, T.K. Johal, R.P. Campion, C.T. Foxon, B.L. Gallagher, E. Arenholz, Phys. Rev. Lett. **96**, 117207 (2006)
125. R.A.D. Pattrick, G. van der Laan, C.M.B. Henderson, P. Kuiper, E. Dudzik, D.J. Vaughan, Eur. J. Mineral. **14**, 1095 (2002)
126. V.S. Coker, A.G. Gault, C.I. Pearce, G. van der Laan, N.D. Telling, J.M. Charnock, D.A. Polya, J.R. Lloyd, Environ. Sci. Technol. **40**, 7745 (2006)
127. C. Stamm, T. Kachel, N. Pontius, R. Mitzer, T. Quast, K. Holldack, S. Khan, C. Lupulesco, E.F. Aziz, N. Wietstruk, H.A. Dürr, W. Eberhardt, Nature Mater. **6**, 740 (2007)
128. L. Braicovich, G. Ghiringhelli, A. Tagliaferri, G. van der Laan, E. Annese, N.B. Brookes, Phys. Rev. Lett. **95**, 267402 (2005)

Chapter 10
Advanced Instrumentation for x-ray Magnetic Circular Dichroism

Andrei Rogalev, Fabrice Wilhelm, José Goulon and Gérard Goujon

Abstract This chapter accounts for selected instrumentation developments carried out over the past 15-20 years at the ESRF beamline ID12 which is dedicated to polarization dependent x-ray spectroscopy in the energy range $2.0 \leq \hbar\omega \leq 15$ keV. Emphasis is laid on problems associated with either the control or the conversion of the polarization state of the x-ray beam as well as advanced x-ray detection systems. We highlight two recent science-driven instrumentation developments initiated at the ID12 beamline: the first one deals with measurements of x-ray Magnetic Circular Dichroism (XMCD) under high static magnetic field up to 17 teslas; the second example concerns x-ray Detection of Magnetic Resonance (XDMR).

Andrei Rogalev
European Synchrotron Radiation Facility, B.P. 220, F-38043, Grenoble, France, e-mail: rogalev@esrf.fr

Fabrice Wilhelm
European Synchrotron Radiation Facility, B.P. 220, F-38043, Grenoble, France, e-mail: wilhelm@esrf.fr

Jose Goulon
European Synchrotron Radiation Facility, B.P. 220, F-38043, Grenoble, France, e-mail: goulon@esrf.fr

Gerard Goujon
European Synchrotron Radiation Facility, B.P. 220, F-38043, Grenoble, France, e-mail: goujon@esrf.fr

E. Beaurepaire et al. (eds.), *Magnetism and Synchrotron Radiation: Towards the Fourth Generation Light Sources*, Springer Proceedings in Physics 151,
DOI: 10.1007/978-3-319-03032-6_10,

10.1 Introduction

Discovery of x-ray Magnetic Linear Dichroism (XMLD) in 1986 [1] and x-ray Magnetic Circualr Dichroism (XMCD) in 1987 [2] ushered in a new era of magnetism research with objectives that previously would have been unattainable. Because of their inherent element and orbital specificity and ability to probe extremely small sample volumes, these spectroscopies have become an essential tool in understanding the magnetism of complex materials. Derivation of magneto-optical sum rules [3, 4] has greatly strengthened the XMCD, making this technique capable to disentangle orbital and spin contributions to the total magnetic moment carried by the absorbing atom.

It is also in the beginning of 1990s, that the advent of the third generation synchrotron radiation facilities offered the scientific community the x-ray spectroscopy beamlines with greatly improved flux and full polarization control. As a result, polarization dependent x-ray spectroscopy in the last 25 years has become a standard tool in modern magnetism research, leading to a deeper understanding of the microscopic origin of magnetic state of matter, as well as to major technological advances. To remain at the forefront in new emerging areas of magnetism research, however, requires continued improvements to both the instrumentation and optics in order to provide greater flux, improved polarization control, higher detection sensitivity and enhanced sample environments.

In the present paper, we describe the ESRF beamline ID12 which has been precisely optimized for spectroscopic applications requiring a full control of the polarization of x-ray photons in the energy range $2.0 \leq \hbar\omega \leq 15\,\mathrm{keV}$ [5, 6]. The beamline has been in the user operation since the beginning of 1995. From the very beginning, there was the implicit commitment to try to push the frontiers of x-ray Absorption Spectroscopy. Moreover ID12 beamline has been used during the construction phase of the ESRF as a test-bench for advanced instrumentation in x-ray absorption spectroscopy (XAS). This is because measurements of tiny dichroic signals free of any experimental artefacts are extremely demanding from the quality of the whole beamline. Much time and efforts have been invested, day after day, to improve the quality and the reliability of the instrumentation including optical components, in particular, x-ray monochromator but also various types of x-ray detectors [7]. We would like to stress that all technical developments have always been driven by the need to optimize a critical instrumentation in order to tackle a new scientific problem.

Over the years, ID12 beamline has contributed to spectacular progress observed in polarization dependent x-ray Absorption Spectroscopy with the emergence of a rich variety of dichroisms exploiting either:

- Magneto-Optical effects: e.g. x-ray Magnetic Linear Dichroism; x-ray Magnetic Circular Dichroism; x-ray Resonant Magnetic Scattering (XRMS),
- Optical Activity[1] [8]: *i.e.* x-ray Natural Circular Dichroism (XNCD), Circular Dichroism in Diffracted Anomalous Near Edge Structure (CD-DANES), x-ray Magnetochiral Dichroism (XMχD), Non-Reciprocal x-ray Magnetic Linear Dichroism (NR-XMLD).

10.2 Description of the beamline

10.2.1 Sources of polarized x-rays

What makes beamline ID12 fairly specific is that the users can have a full control of the polarization state of the x-ray beam over a wide energy range from 2 to 15 keV. Either circularly or linearly polarized x-ray photons can be generated by helical undulators installed at the ID12 straight section of the storage ring, i.e. HELIOS-II and APPLE-II.

The HELIOS-II undulator [10] consists of two planar arrays of permanent magnets: the upper one produces a vertical sinusoidal magnetic field while the lower produces a horizontal field, both field distributions featuring the same spatial periodicity ($\lambda_u = 52$ mm). The undulator has three degrees of freedom: two vertical translations (i.e. one for each individual girder resulting in a change of the horizontal and the vertical half-gaps respectively) and one axial translation of the upper girder resulting in a variation of the phase (Φ) between the horizontal B_x and vertical B_z magnetic fields. Whenever Φ is set to $\lambda_u/2$ or to zero, then the emitted radiation is linearly polarized in a plane making an angle $\alpha = arctan(B_x/B_z)$ with respect to the orbit plane. Moreover, x-ray photons with pure vertical or pure horizontal linear polarizations can be

[1] X-ray Optical Activity is very valuable tool to study systems with broken inversion symmetry. Such systems play a fascinating role not only in physics but also in chemistry and in life sciences, where molecular recognition processes are controlled by chirality. Moreover, x-ray optical activity appears as a new element specific spectroscopy to study orbital magnetism in parity non-conserving solids, and offers unique experimental access to orbital anapole moments and to a whole family of related operators [9].

generated by opening completely either the vertical or the horizontal half-gap so that $B_z = 0$ or $B_x = 0$. Circularly polarized x-rays are emitted when B_x is equal to B_z and the phase is set either to $\pi/2$ or to $-\pi/2$. The change of the helicity of the x-rays can, therefore, be done easily by translating the upper girder by 26 mm (from $+\lambda_u/4$ to $-\lambda_u/4$). The time required for this motion is typically less than 3 seconds. After the installation of a narrow-gap vacuum chamber within the ID12 straight section, the smallest half-gaps of HELIOS-II undulator could be closed down to 6.2 mm. Thus, the energy range that can be covered with the first harmonic of HELIOS-II operated in the pure helical mode was considerably extended toward the soft x-ray range. At present, dichroism experiments can be performed with this undulator over an energy range which extends from 2.05 keV (limited by Si $< 111 >$ monochromator) up to 6.2 keV.

For the experiments at higher photon energies ($\hbar\omega \geq 5$ keV) it is preferable to use radiation emitted by an APPLE-II type helical undulator which is also installed on the straight section ID12. Its fundamental harmonic in pure helical mode spans from 5.1 to 8.5 keV. An APPLE-II undulator consists of four identical arrays of permanent magnets arranged in four quadrants around the axis. Two arrays (upper right and lower left) are movable while two others are fixed. In the APPLE-II undulator, the variation of the phase is accomplished by translating movable magnetic rows longitudinally in the same direction. The position of these rows corresponding to pure helical mode is approximately equal to $\pm\lambda_u/3$. The helicity of the emitted x-rays can be changed in about 2 seconds. Note that not only the helicity but also the spectrum of APPLE-II undulator depends strongly on the value of phase. Unfortunately, the phase reversal of APPLE-II is a process which results in a huge change of the emitted power and in a dramatic redistribution of the relative intensities of high-order harmonics. This places additional constraints on the stability of the various optical components of the beamline.

It is important to underline that any changes of the undulator gaps and/or phases do not affect the position and the angles of the x-ray beam emitted by undulators. Equally important is the fact that the closed orbit and the dynamics of the electron beam in the storage ring are also unperturbed by the gaps or phase changes and the use of the undulators is fully transparent for any other beamline around the storage ring.

10.2.2 Beamline optics

The critical choice has been made from the beginning to operate beamline ID12 systematically windowless: this is desirable not only to preserve a high flux at low energy (i.e. below 4 keV), but also because it is mandatory to keep all optical components clean over long periods of operation. This choice had indeed strong implications regarding the design of UHV components and their cost. The first component of the beamline is a non-standard but very accurate primary slits which are used to extract the on-axis radiation from the undulators. A UHV-compatible mechanical chopper consisting of a rotating slotted Al disc is installed immediately after the slits. The chopper causes a square-wave modulation of x-ray beam at a typical frequency of *ca.* 67 Hz and also contributes in reducing (by a factor of 2) the heat load on the beamline optics.

The monochromator is the most critical component of any beamline designed for spectroscopy applications. This is because the quality of the spectra can be dramatically spoiled by a poor energy resolution, by the transmission of unwanted harmonics or by instabilities of the exit beam during energy scans, etc. Beamline ID12 is equipped with a UHV compatible, fixed-exit, double-crystal monochromator manufactured by KoHzu Seiki Co. following specifications imposed by the ESRF. The exceptional quality of the mechanics, in particular the high precision of the translation stages, allows one to obtain a fixed exit beam (within $\pm$ 5 μm) over the whole range of Bragg angles that are accessible (6° - 80°). The monochromator is most often equipped with a pair of Si $<111>$ crystals. Note that the temperature of each individual crystal is kept at $-140°C$ ($\pm 0.2°$) using a cryogenic cooling system developed in-house and which proved to be totally free of undesirable vibrations. Given the modest power density delivered on-axis by helical undulators in pure helical mode (compared to a standard planar undulator or a wiggler), it is not surprising that the heat-load effects are now practically undetectable (the measured stability of the rocking curve is better than 0.1 arcsec over periods of several hours). For two consecutive energy scans we obtained an excellent reproducibility of typically 1 meV or even better.

A major concern in circular dichroism experiments is the determination of the circular polarization rate of the monochromatic beam, which depends not only on the polarization of the undulator radiation but also on the polarization transfer by all optical components including the monochromator [11]. In fact, the monochromator does not preserve the initial degree of polarization of the undulator beam, except for pure σ or π linearly polarized beams. In

the case of Si $< 111 >$ monochromator, high circular polarisation rate of the x-ray undulator beam ($\geq 97\%$) drops down to very low values at photon energies around *ca.* 2.8 keV: this implies that x-ray circular dichroism measurements should be most difficult in the corresponding energy range. Moreover, when the helicity of the incident x-ray beam is reverted, indeed the circular polarization rate of the monochromatic x-ray beam is altered, but there is also a quite significant change affecting the Stokes-Poincaré component P'_2, i.e. the linear polarization rates at 45° and 135° respectively, whereas Stokes-Poincaré component P'_1 remains totally unaffected. This can have dramatic consequences for all types of circular dichroism measurements (i.e. XMCD as well as XNCD) on *biaxial* crystals because the weak XNCD signal can often be masked by a much stronger linear dichroism signal. Similar difficulty is also to be expected for circular dichroism measurements on uniaxial crystals, i.e. whenever the optical axis of the sample is not strictly parallel to the direction of propagation of the x-rays.

It is therefore highly desirable to perform x-ray polarimetry measurements which is usually done by combining a quarter-wave plate with a linear polarization analysis. X-ray phase plates exploit the birefringence of perfect crystals under the conditions of Bragg diffraction: it means that the refraction indices are different for the σ and π polarization components [12]. The most convenient experimental configuration consists in using the forward-diffracted beam outside the range of total reflection since the transmitted beam is not deviated [13]. Due to the difference in the refraction indices, the diffraction by a perfect crystal induces a phase shift ϕ between the σ and π components of the wave transmitted by the crystal

$$\phi \propto -(\pi/2)\frac{A \cdot z}{\Delta\Theta} \tag{10.1}$$

where z is the beam path inside the crystal, Θ is the angle between the incident-beam wavevector and the normal to the crystal surface, $\Delta\Theta$ is the angular offset (defined as the difference between the true angle of incidence Θ and the Bragg angle Θ_0 at the middle of the reflection profile) and A is a factor that depends on photon energy and on the nature of the crystal.

Whenever the angular offset is adjusted so that the phase shift ϕ is equal to $\pm\pi/2$, then the crystal acts as a quarter wave plate (QWP) and an incoming circularly polarized x-ray beam is converted into a linear polarized beam. For a given crystal, the best efficiency is obtained for strong reflections. Since one uses the forward diffracted beam rather far from the Bragg condition, the absorption by the crystal is very little affected by the Bormann

effect and the transmitted intensity can be approximated by $1 - exp(-\mu_0 \cdot z)$. However, the σ and π components may not be attenuated in the same proportions so that the polarization vector is rotated (with respect to the plane of diffraction of the phase plate) by the angle $\alpha \neq 45^\circ$ satisfying the condition: $\alpha = arctan(\sqrt{I_\sigma / I_\pi})$ [14]. Owing to the necessity to minimize the absorption losses, diamond crystals are usually preferred for experiments above 3 keV even though ultra-thin silicon crystals have been successfully used at photon energies of 3.1 keV [15] or even of 2.8 keV [14].

To fully characterize the polarization state of the monochromatic beam, we found most convenient to insert downstream with respect to the monochromator a UHV compatible QWP chamber equipped with a diamond single crystal. A 0.9 mm thick $< 111 >$ diamond phase plate exploiting the asymmetric $(11\bar{1})$ reflection is typically used in the energy range 5 - 10 keV with the incident beam nearly perpendicular to the crystal surface. The QWP can be easily inserted into the monochromatic x-ray beam or be removed from the beam. It is combined with a linear polarimeter which consists of either a kapton foil scattering at 90° or a single crystal diffracting at 90°.

We have reproduced in Fig.10.1a typical profile of the $(11\bar{1})$ diamond QWP at 6.45893 keV recorded by monitoring the intensity of the vertically polarized component. Polarization analyzer was a Si $< 400 >$ crystal diffracting at 90.0083°. The typical offset value resulting in the desired $\pm\pi/2$ phase shift was of the order of ± 135 arcsec whereas the Darwin width of $(11\bar{1})$ reflection was only ≈ 9 arcsec. For these measurements we have used the fundamental harmonic of the APPLE-II undulator with the gap of 19.1 mm and undulator phase set to +12.69 mm corresponding to the right circular polarization. The measured circular polarization rate of monochromatic x-rays was of the order of 91%.

A pair of *vertically* focusing mirrors (VF-2M device) was also installed downstream of the monochromator. The choice of this configuration was dictated by two considerations: (i) the VF-2M device should not affect the energy resolution of the monochromator; (ii) large demagnification factors could be obtained for samples located close enough to the mirrors assuming that the curvature of the mirrors can be increased without damaging their figure slope error. The transmission of the VF-2M was measured to be ca. 70% at 8 mrad incidence angle using an x-ray beam of about 3 keV. Vertical focus sizes of the order of 20 μm (FWHM) is typically obtained at the sample location using a full undulator beam. For delicate experiments at low photon energy, the VF-2M device indeed can be exploited as a highly efficient harmonic filter.

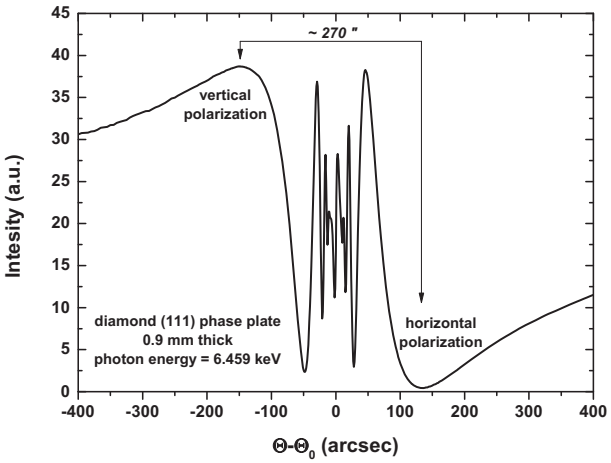

Fig. 10.1 Intensity profile measured by the Si $< 400 >$ linear analyzer on varying the offset of the diamond QWP. The fundamental harmonic (peaking at $\approx$6.45 keV) of the APPLE-II undulator in a pure circular mode with the phase set to $+\pi/2$

Since their development almost 15 years ago [16], the use of x-ray refractive lenses has rapidly expanded and they are now a standard optical element on many beamlines. Compared to other focusing elements, refractive lenses present several attractive features, being simple to align and relatively insensitive to misorientations. Since refractive lenses are in-line optics, they are more stable with respect to angular variations in comparison with deflecting optics. Surprisingly, it is a general belief that they can be used only with high energy photons, typically above 6 keV. In fact, as we have shown, Be refractive lenses can be perfectly used at lower photon energies down to, at least, 2 keV. This became possible with improved lens fabrication technology making available Be lenses with small radius of parabola apex and very thin sidewalls. The focal spot of $\leq 1.5\,\mu$m (FWHM) with the flux gain of about 300 was achieved at 2.5 keV using only two parabolic lenses with parabola apex radius of 200 μm. The measured focal distance of the set-up was 95 cm. Such a long focal distance is another great advantage of refractive lenses, in particular for spectroscopic applications. This leaves enough space not only to mount an I_0 monitor but also to use a rather complex sample environment,

e.g. superconducting magnet. Translation of the lenses along the x-ray beam allows one to correct easily for chromatic aberrations and to perform x-ray absorption spectroscopy, including dichroism, experiments with a spatial resolution of the order of 1 μm and even better.

10.2.3 x-ray Detectors

All standard fluorescence detectors, all beam intensity monitors or beam position monitors at the beamline are (single- or multi-anode) ion implanted Si P^+NN^+ photodiodes developed in close collaboration with Canberra-Eurisys. The very high efficiency, the fast response time and the excellent linearity make photodiodes the best detectors for x-ray spectroscopy. Photodiodes also benefit from the great advantage to be fully UHV compatible: this is not a marginal advantage given the wide energy range covered by beamline ID12. Another valuable advantage regarding XMCD experiments is that the photodiodes are not sensitive to magnetic fields, at least up to 20 T. Unfortunately, photodiodes exhibit a rather large dark current which is temperature dependent and may drift with time. A very efficient way to get rid of all these shortcomings is to exploit a synchronous detection technique based on a square wave modulation of the incident x-ray beam using a chopper.

A lot of efforts has been invested into the design and the commissioning of highly sensitive intensity monitors (I_0 monitors) featuring low insertion losses. Recent attempts to use CVD diamond diodes on ID12 failed because such detectors do not meet (yet) the highly demanding linearity criteria of x-ray Absorption Spectroscopy or x-ray dichroism [17]. According to our experience, the most reliable option is still to detect the x-ray fluorescence of a thin foil in the backward direction. Using a photodiode with a central hole (circular or oblong) we could make the design of the I_0 chamber very compact. Since the foil is mounted normal to the incident beam, the absorption losses are minimized whereas the distance to the diode can be optimized to maximize the solid angle in which the fluorescence photons are collected and thus maximize the detection sensitivity. Due to its high symmetry this detector is not sensitive to small changes of the beam energy profile. Much attention had to be paid to the thickness uniformity of the foil: the most frequently used foils are either a 4 μm Ti foil (for photon energies above 6 keV) or a 0.5 μm thick Si_3N_4 membrane (for energy range above 2keV). Such I_0 monitors can easily be transformed into *semi-transparent beam position monitors* by using

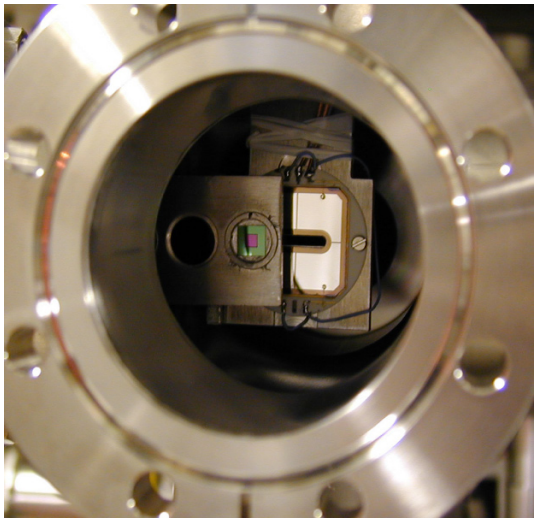

Fig. 10.2 Picture of a beam intensity (position) monitor; a scattering Si_3N_4 membrane is well apparent whereas the translator is slightly moved away allowing two quadrants of the diode with its (oblong) hole to be visible (reproduced from Ref. [7])

a 4-quadrant photodiode with a central hole. We checked that such a beam position monitor could really offer a vertical or lateral resolution which was of the order of 1-2 μm. A picture of one of our beam intensity/position monitors is shown on Fig. 10.2.

The square modulated diode photocurrent is first pre-amplified using an ultra low-noise electrometer manufactured by NOVELEC S.A. The noise level of a standard fluorescence detector was measured at highest gain setting and was found to be $\leq$ 5 fA RMS in a 3 Hz bandwidth. Under normal operation conditions, the readout electronics provides the user with a dynamic range reserve truly in excess of 10^6: this is essential to record high quality x-ray dichroism spectra. The output of each electrometer includes a fast voltage-to-frequency converter operated from 1 to 10 MHz with a residual non-linearty $\leq$ 70 ppm. Optical fibers link the electrometer to a gated digital lock-in exploiting the low-frequency modulation of the x-ray beam: the so-called Frequency Integrated Digital Lockin (FIDL) boards which were developed in-house. The FIDL boards combine 12 lock-in channels, all perfectly synchronized. The FIDL boards also offer following advantages: (i) the raw data are stored in "on-board" SDRAMs with local pre-processing capabilities; (ii) each channel

can accommodate a "double modulation" which is a very attractive option for dichroism experiments exploiting ac modulation techniques; (iii) modulation frequencies can be as high as 50 kHz.

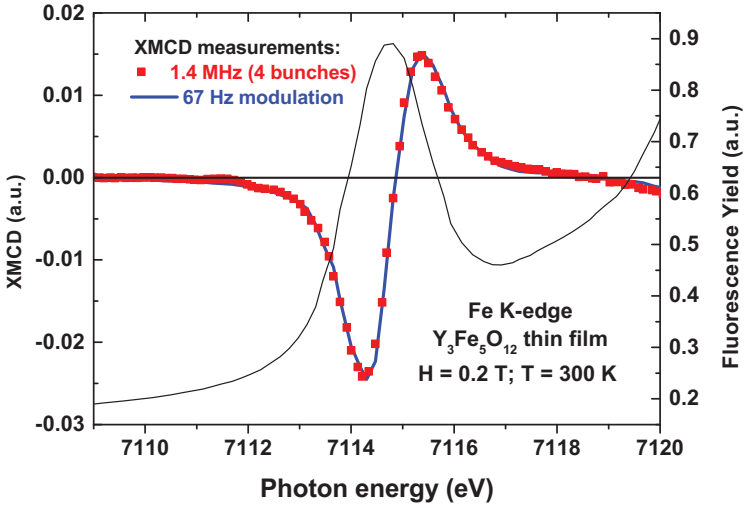

Fig. 10.3 Fe K-edge XANES (thin black line) and XMCD spectra (thick blue line and red squares) of $Y_3Fe_5O_{12}$ thin film measured by detecting the high frequency time structure of the x-ray beam at 1.4 MHz in the 4 bunch filling mode. The XMCD spectra recorded under the same conditions but in multibunch mode using a standard detection system is also shown for comparison

Over the years, much efforts have been invested by the beamline staff in order to develop new solid state detectors optimized for our specific applications. A recent example concerns the development of fast detectors which have the capability to fully exploit the time structure of the x-ray beam of the ESRF arising from both the bunch structure of the beam and the storage ring filling pattern. With exception of the uniform filling mode, all other modes exhibit fundamental beam modulation frequencies in a few MHz range (from 355 kHz up to 5.6 MHz). These values are easily compatible with the implementation of digital techniques to process the signal with front end ADCs. To reach their ultimate detection speed, photodiodes should be properly reverse

biased in order to maximize the thickness of the depleted layer and minimize the diode capacitance. On the other hand, when the photodiode is reverse biased, its finite shunt resistance will cause an undesirable, temperature dependent (noisy) DC dark current. The in-house development of wide band preamplifiers allowed us to implement a gated synchronous time-average data acquisition technique [18] exploiting the natural modulation of the x-ray beam up to, at least, 1.4 MHz. This particular implementation of a digital lockin comes with decisive advantages over traditional analog lockin amplifiers: the system is naturally locked, independently of the signal level and it is not sensitive to the modulation and signal shapes. Moreover, the digital system returns the true signal shape and all its harmonics (as far as the sampling frequency allows).

The performances of the new detection system are illustrated in figure 10.3 in which we have reproduced the Fe K-edge XMCD spectrum of a YIG thin film: the corresponding spectrum was recorded with a readout electronics exploiting directly the modulation of the x-ray beam at 1.4 MHz in the standard 4-bunch operation mode, *i.e.* with a beam current of only ≈ 20 mA. For the sake of comparison, we added on the same plot the XMCD spectrum recorded on the same sample in the standard multibunch operation mode, *i.e.* with a beam current of ≈ 200 mA). The latter spectrum was recorded with a standard detection system exploiting the modulation of the x-ray beam at 67 Hz using a mechanical beam chopper. Indeed, the signal-to-noise ratio achieved with both detection systems is excellent eventhough the experiment carried out in the 4-bunch mode at low current was much more demanding.

For the experiments requiring energy resolution, a 35 element silicon drift diode (SDD) detector array has also been developed in collaboration with Eurisys-Mesures (now Canberra Eurisys). This detector consists of an array of 7×5 cylindrical Si drift-diodes with an active area of 10 mm^2 for each diode. The detector is cooled down to the optimum temperature ($T \simeq 143$ K). The FWHM energy resolution of the individual diodes measured with a ^{55}Fe source was as good as 129 eV using a standard pulse processing time of 12 μs whereas a peak-to-background (PTB) ratio in excess of 1000 was obtained. Under normal operating conditions at beamline ID12, the peaking time can be reduced down to 0.5 μs in order to maximize the counting rate ($\geq 10^5$ counts per second) but at the expense of some deterioration of the energy resolution. The detector is systematically operated windowless: this allowed us to extend the operation of the detector down to the soft x-ray range where scattering is a major problem.

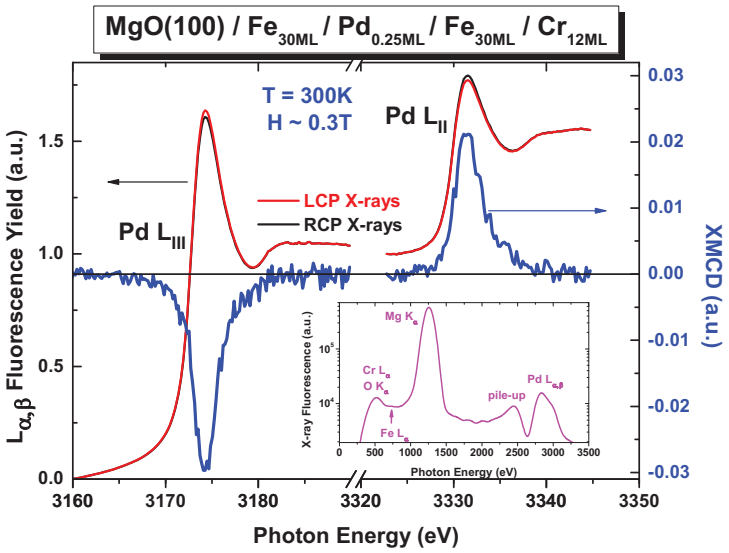

Fig. 10.4 XANES and XMCD spectra of $Fe_{30ML}/Pd_{0.25ML}/Fe_{30ML}$ trilayer at the Pd $L_{II,III}$ edges. Measurements were performed at room temperature and under applied magnetic field of 0.3T. Insert: x-ray emission spectrum of the sample with excitation at the Pd L_{II}-edge

To illustrate the excellent performances of the 35-element Si drift diode detector, we have reproduced in Fig. 10.4 the XMCD spectra recorded at the Pd $L_{II,III}$ absorption edges from only of a quarter of a monolayer of Pd sandwiched between 30 atomic layers of Fe deposited on MgO support and capped with 12 atomic layers of Cr. As one can see on the insert of the Fig. 10.4, the emission spectrum is strongly dominated by the Mg K_α emission line, while not resolved Cr L_α, Fe L_α and O K_α lines are of about the same intensity as Pd $L_{\alpha,\beta}$ lines. This shows that the working energy range of SDD is extended down to at least 500 eV. Remember that the circular polarization rates of the monochromatic beam at the Pd $L_{II,III}$-edges are only 12% and 19%, respectively: this clearly indicates that the corresponding XMCD spectra were recorded under particularly unfavorable experimental conditions. The counting rates (counts per second, cps) in the Pd L_α line was *ca.* 2×10^4 cps per single SDD with a peaking time of 0.5 μs. Although the x-ray beam was impinging on the sample with an angle of incidence of *ca.* 15°, the beam foot-

print was quite small: $300\times30\,\mu m^2$. This is because we had to close down the slits in order to avoid the saturation of the detector by the intense soft x-ray fluorescence signal from the substrates. Note that this is the first time that high quality XMCD spectra could be measured on buried submonolayers in the hard x-ray range.

10.3 Experimental methods and related instrumentation

10.3.1 High Field x-ray Magnetic Circular Dichroism

So far, XMCD has been extensively used to investigate mainly ferro- or ferrimagnetic materials, and only very few studies have been performed on paramagnetic compounds. This is partly because a sufficiently high magnetic field for magnetizing paramagnetic or antiferromagnetic materials was not available at synchrotron facilities. Fields of 1-2 T are generally used for conventional XMCD experiments. However, a high magnetic field could be the essential parameter to explore new phenomena in materials with important magnetic degrees of freedom. In order to achieve this goal, the external magnetic field has to be comparable with the magnitude of the basic magnetic interaction energies. This typically requires magnetic fields of the order of several 10 T.

Anticipating the growing interest in research under high magnetic fields, a new experimental station dedicated to high field XMCD has been opened to users in 2010. It is based on a high-vacuum ($< 10^{-7}$ mbar) 52 mm cold bore solenoid superconducting magnet producing an horizontal magnetic field of 17 teslas. The magnet is equipped with 2 access ports (CF 100) along the horizontal axis (parallel to the field), one for the incoming x-ray beam and detector insert and another one for the sample cryostat. The superconducting solenoid coil built by Cryogenic Ltd is wound in three main section, the outer being of copper stabilized filamentary NbTi, and the inner of filamentary Nb_3Sn conductor. This assembly design offers the advantage to reduce the nominal inductance of the magnet. This has a direct consequence to reduce the helium consumption, to minimize the remnant field and, most important, to minimize the total stored energy. The coil is energized by a a 15 V, 150 A high-resolution (20-bit) four-quadrant power supply with an integrated low-current option. This power supply is specifically designed to ensure a fast

sweep ramping of 2 teslas/minute. The integrated low-current facility allows obtaining very low field in the region of ± 0.05 T with a resolution of 10^{-6} G and avoiding a significant remnant field in the magnet. The field homogeneity is better than 0.1% in a 10 mm diameter spherical volume. The temporal drift of the field is about 2×10^{-5} per hour while the long term stability of the magnetic field is better than 0.01% over a period of 12 hours. It is very important for XMCD measurements that for opposite directions of the field the relative difference in amplitudes does not exceed 5×10^{-5}.

The helium continuous flow cryostat was built by the ESRF Sample Environment Support Group. Its main feature is that it is *"amagnetic"*. All pieces of the cryostat were machined using ceramic based tools in order to avoid any metallic contamination. The absolute value of magnetic susceptibility of parts exposed to the magnetic field, in the zone where it is above 1 T, is of the order of 10^{-5} or less. The temperature on the sample can be set in the range 2.05 K to 325 K with a stability $\Delta T/T < 10^{-3}$. All spectra are measured using total fluorescence yield detection mode. A Si photodiode with an oblong hole mounted on a liquid nitrogen shield of the magnet and is collecting the fluorescence photon in a "backscattering" geometry over a wide solid angle.

This new high-field experimental station becomes a unique experimental platform for basic research on magnetism and appears to be the workhorse of our XMCD measurements. For example, it has been of great help to unravel the origin of paramagnetic response in pure metallic Au nanoparticles [19]. Pure metallic Au nanoparticles with diameters of a few nm have been grown onto the naturally thiol-containing proteinatious surface layer (S layer) of *Sulfolobus acidocaldarius* without any chemical functionalization by thiol groups. Macroscopic magnetization measurements using SQUID ($1.8\,\mathrm{K} < \mathrm{T} < 300\,\mathrm{K}$ and $0 < \mathrm{H} < 7\,\mathrm{T}$) reveal that these nanoparticles are superparamagnetic at low temperatures. XMCD measurements performed at the $L_{2,3}$-edges of Au unambiguously confirmed that magnetic signal is intrinsic and originates from 5d states of gold. Analysis of XMCD data, shown on Fig. 10.5a, using sum rules yields $m_L = 0.0113(3)\,\mu_B$ and $m_S = 0.0397(5)\,\mu_B$ giving a net average magnetic moment per Au atom $m_{Au} = 0.051(1)\,\mu_B$ at T = 2.2 K and H = 17 T. The observed magnetic moment is about 100 times larger than those previously found by XMCD in Au-thiol capped nanoparticles. Note, that the Pauli paramagnetic contribution amounts to only 7% of the total XMCD signal [20].

Isothermal field-dependent XMCD data were recorded by flipping the helicity of the x-ray beam, at the photon energy corresponding to the maximum of XMCD signal at the L_3 edge, while varying the field $-17 < H < +17$ T, at

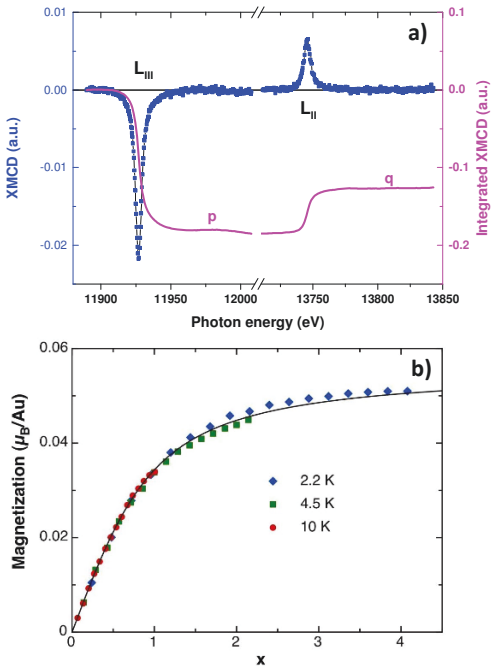

Fig. 10.5 **a** XMCD spectra at the $L_{2,3}$ edges of Au nanoparticles measured under applied field of 17 T and at 2.2 K ; **b** XMCD(x) curves measured at T = 2.2, 4.5 and 10 K up to H = 17 T where $x = \frac{M_{part}H}{k_BT}$, with M_{part} = 2.4(1) μ_B. They are fitted by a Langevin function (solid line)

T = 2.2, 4.5 and 10 K, as shown in Fig. 10.5b. The field dependence of the magnetization is well described by the classical Langevin function

$$M(H) = m_{at}\left[coth\left(\frac{M_{part}H}{k_BT}\right) - \frac{k_BT}{M_{part}H}\right] \tag{10.2}$$

where m_{at} is the average magnetic moment per Au atom, and M_{part} the mean magnetic moment per Au particle. The shape of the Langevin curve gives, therefore, information on the magnetic moment of each individual particle. The data are plotted in Fig. 10.5b as a function of $x = \frac{M_{part}H}{k_BT}$, with M_{part} = 2.4(1) μ_B . Making a very rough assumption that all Au atoms are equally magnetically polarized, then we deduce that average size of nanoparticles is about 45 atoms. Besides, the EXAFS recorded at the Au L_3-edge shows that the internal structure of Au nanoparticles is fcc, and Au-S bonds are located at the particle surface. The latter were also unambiguously confirmed by S K-edge x-ray absorption measurements. This is precisely the charge transfer between S-layer and Au 5d states, leading to an increase of the hole charge carrier density in the Au 5d band, that explains the magnetism of pure metallic Au nanoparticles.

10.3.2 Natural and Magnetic Linear Dichroism with a QWP

The use of a Quarter Wave Plate on ID12 is by no means restricted to polarimetry measurements. It was particularly attractive to use it for x-ray linear dichroism experiments at ID12 because a circularly polarized x-ray beam emitted by a helical undulator can be easily converted with a QWP into linearly polarized beams with a full control of the orientation of the polarization vector: we simply need to rotate the QWP around the beam direction. This is a fairly substantial advantage for polarization dependent XAFS studies on anisotropic systems since we no longer need to rotate the crystal in Natural Linear Dichroism experiments or to change the direction of the magnetic field in Magnetic Linear Dichroism. Moreover, direct measurements of the differential absorption spectra for two orthogonal polarizations are highly desirable in linear dichroism experiments: instead of rotating the QWP (or the sample) by 90°, it is much faster to invert the angular offset (ca. $\pm$100 arcsec for a 0.9 mm thick diamond $< 11\bar{1} >$ crystal) because this can be done very quickly using a digital piezoactuator. In this way, it becomes feasible to rotate the polarization vector by 90° several times for each data point of XANES or EXAFS scans. Obviously, such an experiment becomes inherently much less sensitive to low-frequency instabilities of the source and small linear dichroism signals can be measured more accurately.

To illustrate the potentiality of this technique we have reproduced in Fig. 10.6 the Fe K-edge x-ray linear dichroism spectra recorded on a $Y_3Fe_5O_{12}$

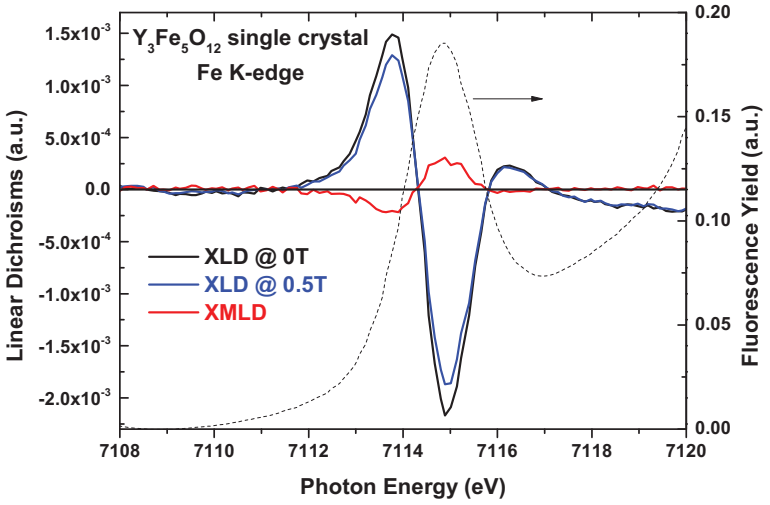

Fig. 10.6 X-ray absorption and linear dichroism spectra in the vicinity of the Fe *K*-edge in a $Y_3Fe_5O_{12}$ single crystal

single crystal. Since the crystal symmetry is cubic, the observed x-ray linear dichroism (XLD) signal can be assigned only to pure quadrupolar transitions $1s \rightarrow 3d$ located as expected at the pre-edge peak of the XANES spectrum. The x-ray magnetic linear dichroism spectrum was obtained from a direct difference between XLD spectra recorded with a magnetic field of 0.5 T applied perpendicular to the beam direction and with zero field. The XMLD spectrum is still dominated by $1s \rightarrow 3d$ transitions and has nearly the same spectral shape but its amplitude hardly exceeds 2×10^{-4} with respect to the edge jump. For comparison the XMCD signal at the Fe *K*-edge in Yttrium Iron Garnet [21] is nearly 30 times larger than the XMLD signal and the corresponding spectral distributions are fairly different although electric quadrupole transitions are certainly contributing in both cases. This comparison clearly shows that the two experiments yield complementary information especially in the energy range where the electric quadrupole transitions to the localized $3d$ states are expected to contribute. Even though the XMLD signal is much weaker than the XMCD signal, the signal-to-noise ratio achieved with only

a few averaged scans was already excellent. We would like to mention that high quality measurements of x-ray Linear Dichroism appear to be crucial to identify the origin of magnetism in diluted magnetic semiconductors with wurtzite structure, e.g. GaN:Mn [22] or ZnO:Co [23].

10.3.3 X-ray Detected Magnetic Resonance

Another illustrative example of the science-driven instrumentation development initiated at the ID12 beamline is X-ray Detection of Magnetic Resonance (XDMR) [24], in which XMCD is used to probe the resonant precession of the magnetization pumped by microwave radiation. This pump-probe technique is the only spectroscopy that allows one to study dynamical aspects of orbital and spin magnetism separately, and therefore, could be seen as the dynamic extension of XMCD. In favorable cases, XDMR can be even site-selective probe [24]. Particularly interesting, XDMR experiments carried out at K-edges can be a unique source of information regarding dynamical aspects of orbital magnetism, a subject that could not be investigated experimentally before. Over the past decade, XDMR has emerged as a powerful experimental tool to study magnetization dynamics [25, 26, 27, 28] and is expected to become a state-of-the-art technique at XFEL facilities.

However, there is a serious difficulty with XDMR which is that, within the existing technology, there is no x-ray detector fast enough to record directly a signal oscillating at microwave or even radio frequencies (RF). This consideration led us to concentrate first on measurements carried out in longitudinal detection geometry, i.e. with the x-ray wavevector parallel to the external bias field H_0: in this configuration, one measures a dc signal proportional to the pumping power which can be modulated at low frequency. The price to be paid is in the very weak intensity of the measured signal which is inherently a non-linear second order effect. To enhance sensitivity, it is desirable to increase the microwave power at the expense of running into the non-linear foldover regime of ferromagetic resonance (FMR) [29].

Further efforts were invested next in a frequency down conversion or (super-) heterodyne detection of the XDMR signal oscillating at the microwave frequency. This is the case of transverse detection geometry since the x-ray wavevector is perpendicular to the external bias field H_0: in this configuration one measures an ac signal proportional to magnetization oscillating at microwave frequency. Indeed, the time structure of the x-ray beam

in the storage ring was most propitious for a super-heterodyne detection of the XDMR spectra. This can be easily understood by observing that, in the frequency domain, the Fourier transform spectrum of the x-ray bunches consists of a series of discrete harmonics of the RF frequency (352.2 MHz) with a Gaussian envelope. Assuming that the ESRF bunch length is typically of the order of 50 ps, the FWHM of the Gaussian distribution in the frequency domain is expected to be 8.79 GHz which corresponds to the 25$^{\text{th}}$ harmonics of the RF frequency of the machine. In other terms, it would be a lot easier to detect a weak XDMR signal at an intermediary IF frequency (e.g. 455 kHz) corresponding to the beating frequency of the microwave pump field and the high frequency modulation of the incident x-ray typically associated with the relevant n$^{\text{th}}$ harmonic of the RF frequency in the storage ring. This strategy has, however, four major implications:

- The resonance frequency of the cavity has to be carefully adjusted according to the following equation: $F_{cav} = n \times \text{RF} \pm \text{IF}$.
- There is still the need to develop x-ray detectors having the capability of detecting a very weak signal (≈ 10 pA) at the selected IF frequency
- The frequency stability of the microwave spectrometer has to be comparable with the stability of the RF frequency of the machine because one wants to achieve the highest spectral purity of the IF signal
- The x-ray source should exhibit a negligible noise level at the IF frequency. Moreover the time structure of each individual bunch should be perfectly reproducible and very stable in order to avoid large, noisy fluctuations of the intensity of the IF beating signal.

Conceptually, one would expect the proposed heterodyne detection mode to benefit of shorter bunch lengths in the time domain. At present, given the specification of the ESRF storage ring, the sensitivity of the method will drop down above 20 GHz.

A spectrometer has been built at the ESRF which should allow us to record XDMR spectra at high microwave pumping power over the whole microwave frequency range 1-18 GHz. All experiments reported below were performed on inserting the sample into home-made TE_{102} rectangular X-band cavities. In this cavity, the electrical continuity of the walls was preserved using a polished Be window ($\oslash$ 31 mm; thickness: 25 μm) which made it also possible to collect the x-ray fluorescence photons over a large solid angle using a Si photodiode located very close to the sample. The photodiodes designed for this experiment have a large active area (300 mm^2) and a 4 mm $\oslash$ hole at their center to let the incident x-ray beam pass through the Si wafer and en-

ter the microwave cavity. For a transverse XDMR experiment, the resonance frequency of the microwave cavity should obviously match as closely as possible the frequency of selected RF harmonics. Special resonators were thus carefully optimized for these experiments which also require a very high frequency stability and a very low phase noise. In this paper, we present only an experiment carried out in the transverse geometry using the 24^{th} harmonics of the RF frequency. The resonance frequency of the empty cavity was $F_{cav} \approx 8.4517$ GHz with Q_L still in excess of 4000.

Considerable improvement in the detection sensitivity was achieved recently with a super-heterodyne detection in which we exploit a 180° bi-phase modulation technique (BPSK). In this experiment, we found it essential to drive the microwave generator (Anritsu MG-3692A) with the same (ultra-stable) external 10 MHz reference clock as the one used to drive the RF master clock generator of the storage ring. Moreover, the microwaves were phase-modulated at a very low modulation frequency: $\mathrm{F_{bpsk}} = \mathrm{RF}/(992 \times 132) = 2.68948$ kHz. Defining next the XDMR resonance frequency as $F_{MW} = 24 \times \mathrm{RF} + \mathrm{IF}$, we are interested in measuring in the photodiode output not only the beating signal at the intermediate frequency IF, but also the modulation satellites at frequencies $\mathrm{IF} \pm \mathrm{F}_{bpsk}$. It is the aim of some additional electronics to carry out a translation in the frequency domain of the detector output signal by a frequency shift strictly equal to IF. This was achieved by properly combining a comb generator delivering a reference signal for LO = 24×RF = 8.45266 GHz, a microwave mixer with outputs in phase quadrature and two RF mixers. Two distinct channels of the Agilent Vector Signal Analyser (VSA) are then used to carry out a vector decomposition of the XDMR signal providing us with the whole phase information of the resonance. It is a major advantage of the proposed detection electronics to be now insensitive to any undesirable changes of the RF frequency of the machine required to stabilize the electron beam in the storage ring.

In order to illustrate the performance of the ESRF XDMR spectrometer in the transverse geometry, we present spectra recorded at the Fe *K*-edge in yttrium iron garnet. A high quality 8.9 μm thick film of yttrium iron garnet (YIG) grown by liquid phase epitaxy on a gadolinium gallium garnet (GGG) crystal substrate cut parallel to its (111) planes. Samples ($2 \times 2\,\mathrm{mm}^2$) were glued on low loss sapphire rods (⊘ 4 mm) having a flat surface parallel to the rod axis. For the experiments reported here, the YIG film was rotated around the rod axis at the magic angle: $\beta'' = 54.73°$. The XDMR spectra displayed in Fig. 10.7a were recorded in the *field-scan* mode at the Fe *K*-edge, the x-ray

monochromator being preset at energy E=7114.3 eV, i.e. the energy of the first extremum in the Fe *K*-edge XMCD spectrum (see Fig. 10.3).

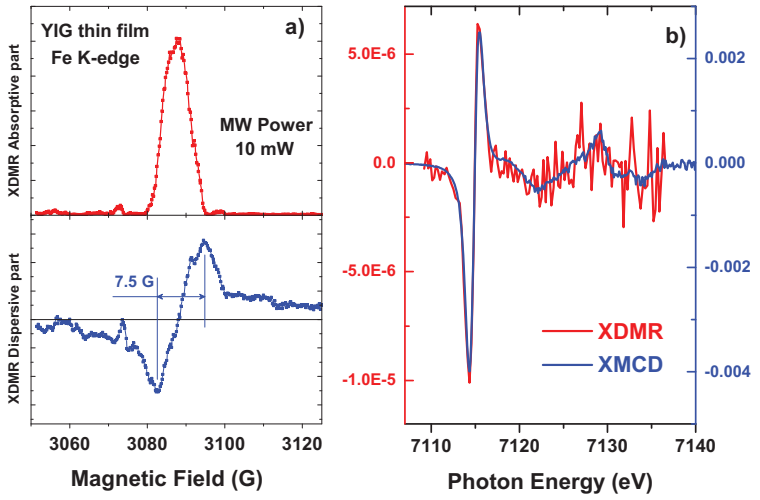

Fig. 10.7 **a** Absorptive and dispersive parts of the Transverse-XDMR spectra of a YIG film rotated at the magic angle; the spectra were recorded in the *field-scan* mode at the Fe K-edge; **b** Comparison of the static Fe K-edge XMCD spectrum with Transverse-XDMR spectrum recorded in *energy-scan* mode

The absorptive and dispersive components of the XDMR detected resonance were obtained in exploiting the two VSA channels. Both spectra exhibit a rather impressive signal-to-noise ratio although the pumping power was only 10 mW, i.e. two orders of magnitude smaller than in the experiments typically carried out in the longitudinal geometry and shown in Fig. 10.7a. With such a low pumping power, there is no significant foldover distortion and the linewidth was narrowed down to 7.5 G. We also reproduced in figure 10.7b transverse-XDMR spectra recorded in the *energy-scan* mode, i.e. as a function of the x-ray photon energy across the Fe K-edge. Note the outstanding signal-to-noise ratio in the spectrum: even the first magnetic EXAFS wiggles can be seen. Of course, we have checked that the sign of the XDMR spectra recorded with right- and left- circularly polarized x-rays is nicely in-

verted while the amplitude of the signal remains constant. This is a critical test which establishes the full reliability of our measurements.

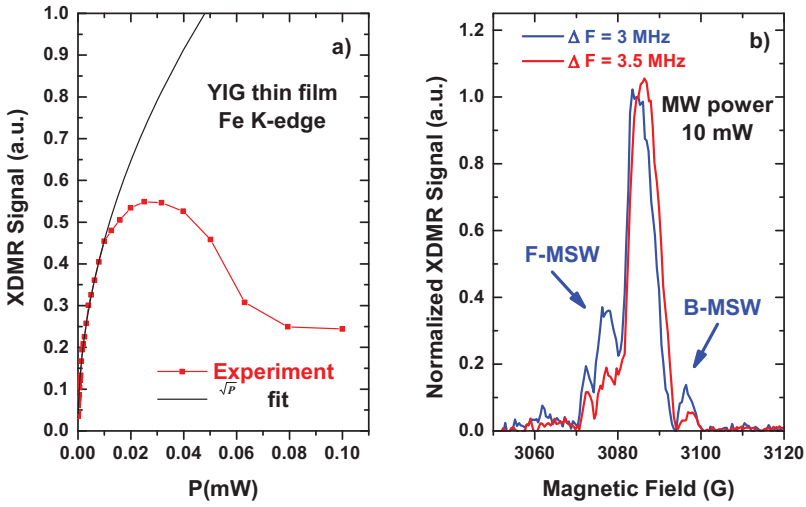

Fig. 10.8 **a** Saturation as a function of the incident microwave power of the Transverse-XDMR signal measured at the Fe *K*-edge in a YIG thin film rotated at the magic angle; **b** Growth of low-order magnetostatic wave satellites when the effective field is artificially increased by detuning the cavity

For the sake of comparison, we also added in Fig 10.7b the *static* Fe K-edge XMCD spectrum normalized to the edge jump: interestingly, there is no significant difference between the reference XMCD spectrum and the Transverse-XDMR spectrum. One important implication of this result is that the opening angle of precession (θ_0) should remain constant over the whole band of final states probed by the excited photoelectrons even in the domain of magnetic EXAFS. In other terms, θ_0 should be the same at energies corresponding to two extrema of the XMCD spectrum: this might cast doubt about the small variations of θ_0 which we found in exploiting the measurements carried out in longitudinal geometry [29]. It would be premature to draw such a conclusion because: (i) the incident power was much lower; (ii) there are strong arguments to suspect that the longitudinal and transverse magnetization

components should not be affected in the same way by 2-magnon annihilation processes. At this stage, let us point out that it is not a trivial exercise to extract the opening angle θ_0 from a transverse-XDMR signal measured with the described super-heterodyne detection even though this signal is proportional to $\sin\theta_0$: the difficulty arises from the fact that the proportionality factor depends on the amplitude of the 24^{th} harmonics of the RF, the amplitude of which -in turn- depends on the *true* shape of the electron bunches in the machine which we *assumed* (for simplicity) to be Gaussian with a constant bunch length.

Remarkable sensitivity of the super-heterodyne detection makes it nevertheless very attractive: high quality Fe K-edge XDMR spectra of YIG thin films could be recorded with microwave power as low as 100 μW. As illustrated by Fig. 10.8a, transverse-XDMR signal is linear with the microwave field $h \propto \sqrt{(P)}$, where P is the incident power, up to 10 mW incident power, whereas the saturation being clearly observed above *ca.* 40 mW. There are other options to enter into the non-linear regime: (i) one can tune the microwave frequency closer to the resonance of the cavity; (ii) with overcoupled cavities, one can approach closer to the so-called critical coupling. In figure 10.8b, we have reproduced two XDMR spectra recorded in the saturation regime while keeping an incident power of 10 mW: we simply detuned the cavity by 3.5 MHz and by 3.0 MHz. Both Forward- and Backward- low order magnetostatic waves satellites start now growing and become rapidly rather broad. These spectra clearly indicate that orbital magnetization components precessing at the iron sites can couple to magnetostatic waves most probably through dipole-dipole interactions.

Acknowledgements The performances of beamline ID12 and the service provided to our users greatly benefitted from the skillful and highly professional assistance of our technicians: L. Leclerc, S. Feite and P. Voisin. Special thanks are also due to J. Chavanne and Ch. Penel who were in charge of the design, construction and installation of our various helical undulators. Invaluable technical assistance by M.-C. Dominguez is warmly acknowledged here. Many thanks to Irina Snigireva and Anatoly Snigirev for fruitful collaboration on use of Be refractive lenses. The authors are indebted to J. Ben Youssef for providing us with epitaxial YIG thin films. We are grateful also to J. Arabski for the fabrication of Fe/Pd/Fe trilayer. Very warm acknowledgments are finally due to J. Bartolome, F. Bartolome and L.M. Garcia for a long standing collaboration in the field of hard x-ray magnetic circular dichroism of metallic nanoparticles.

References

1. G. van der Laan, B.T. Thole, G.A. Sawatzky, J.B. Goekoop, J.C. Fuggle, J.-M. Esteva, R. Karnatak, J.P. Remeika, and H.A. Dabkowska, Phys. Rev. B **34**, 6529 (1986)
2. G. Schütz, W. Wagner, W. Wilhelm, P. Kienle, R. Zeller, R. Frahm and G. Materlik, Phys. Rev. Let. **58**, 737-740 (1987)
3. B.T. Thole, P.Carra, F.Sette, and G. van der Laan, Phys. Rev. Lett. **68**, 1943 (1992)
4. P.Carra, B.T. Thole, M.Altarelli, and X. Wang, Phys. Rev. Lett. **70**, 694 (1993)
5. J. Goulon, A. Rogalev, Ch. Gauthier, Ch. Goulon-Ginet, S. Pasté, R. Signorato, C. Neuman, L. Varga, C. Malgrange, J. Synch. Rad. **5**, 232 (1998)
6. A.Rogalev, J. Goulon, Ch. Goulon-Ginet, C. Malgrange in, *Magnetism and Synchrotron Radiation*, Lectures Notes in Physics, vol.565, ed by E. Beaurepaire, F. Scheurer, G. Krill and J.-P. Kappler, (Springer,Berlin, Heidelberg New York 2001) pp. 60-86.
7. J. Goulon, A. Rogalev, G. Goujon, Ch. Gauthier, E. Moguiline, A. Solé, S. Feite, F. Wilhelm, N. Jaouen, Ch. Goulon-Ginet, P. Dressler, P. Rohr, M.-O. Lampert, R. Henck, J. Synch. Rad. **12**, 57 (2005)
8. A. Rogalev, J. Goulon, F. Wilhelm, Comptes Rendus Physique **9**, 642 (2008)
9. J. Goulon, A. Rogalev, F. Wilhelm, C. Goulon-Ginet, P. Carra, I. Marri and C. Brouder, J. Exp. Theor. Phys. **97**, 402-431 (2003)
10. P. Elleaume, J. Synch. Rad. **1**, 19 (1994)
11. C. Malgrange, C. Carvalho, L. Braicovich, J. Goulon, Nucl. Instrum. Methods A **308**, 390 (1991)
12. V.E. Dmitrienko and V.A. Belyakov, Sov. Phys. Uspekhi. **32**, 697 (1989)
13. V.E. Dmitrienko and V.A. Belyakov, Sov. Tech. Phys. Lett. **6**, 621 (1980)
14. J. Goulon, C. Malgrange, C. Giles, C. Neumann, A. Rogalev, E. Moguiline, F. De Bergevin, C. Vettier, J. Synch. Rad. **3**, 272 (1996)
15. L. Bouchenoire, R.J.H. Morris and Th.P.A. Hase, Appl. Phys. Lett. **101**, 064107 (2012)
16. A. Snigirev, V. Kohn, I. Snigireva, B. Lengeler, Nature **384**, 49 (1996)
17. P. Bergonzo, A. Brambilla, D. Tromson, R.D. Marshall, C. Jany, F. Foulon, C. Gauthier, V.A. Sole, A. Rogalev, J. Goulon, J. Synch. Rad. **6**, 1 (1999)
18. G. Goujon, A. Rogalev, J. Goulon, S. Feite and F. Wilhelm, J. Phys.: Conf. Ser. **425** 082002 (2013)
19. J. Bartolome, F. Bartolome, L.M. Garcia et al., Phys. Rev. Lett. **109**, 247203 (2012)
20. M. Suzuki, N. Kawamura, H. Miyagawa, J. S. Garitaonandia, Y. Yamamoto, and H. Hori, Phys. Rev. Lett. **108**, 047201 (2012)
21. A. Rogalev, J. Goulon, F. Wilhelm, C. Brouder, A. Yaresko, J. Ben Youssef, M.V. Indenbom, J. Magn. Magn. Mat. **321**, 3945 (2009)
22. E. Sarigiannidou, F. Wilhelm, E. Monroy, R. M. Galera, E. Bellet-Amalric, A. Rogalev, J. Goulon, J. Cibert, and H. Mariette, Phys. Rev. B **74** 041306(R) (2006)
23. A. Ney, K. Ollefs, S. Ye, T. Kammermeier, V. Ney, T. C. Kaspar, S. A. Chambers, F. Wilhelm, A. Rogalev, Phys. Rev. Lett. **100** 157201 (2008)
24. J. Goulon, A. Rogalev, F. Wilhelm, Ch. Goulon-Ginet, G. Goujon, J. Synch. Rad. **14**, 257 (2007)
25. D.A. Arena, Y. Ding, E. Vescovo, S. Zohar, Y. Guan, W.E. Bailey, Rev. Sci. Instrum. **80**, 083903 (2009)

26. G. Boero, S. Rusponi, J. Kavich, A. Lodi Rizzini, C. Piamonteze, F. Nolting, C. Tieg, J.-U. Thiele, P. Gambardella, Rev. Sci. Instrum. *80*, 123902 (2009)
27. M.K. Marcham, P.S. Keatley, A. Neudert, R.J. Hicken, S.A. Cavill, L.R. Shelford, G. van der Laan, N.D. Telling, J.R. Childress, J.A. Katine, P. Shafer, E. Arenholz, J. Appl. Phys. **109**, 07D353 (2011)
28. J. Goulon, A. Rogalev, F. Wilhelm, G. Goujon, A. Yaresko, Ch. Brouder and J. Ben Youssef, New J. Phys. **14**, 063001 (2012)
29. J. Goulon, A. Rogalev, F. Wilhelm, N. Jaouen, Ch. Goulon-Ginet, Ch. Brouder, Eur. Phys. J. B **53**, 169 (2006)

Chapter 11
Ultrafast magnetization dynamics investigated with femtosecond time-resolved x-ray magnetic circular dichroism

Uwe Bovensiepen and Nicolas Bergeard

Abstract X-ray magnetic circular dichroism is well known to provide quantitative and element-specific information on the magnetic moment in magnetically ordered materials. In recent years magnetic order in optically excited states and the respective ultrafast relaxation dynamics became a topic of considerable interest. On pico- and femtosecond timescales such dynamics is analyzed by pump-probe experiments which are nowadays carried out employing table-top femtosecond laser setups and large scale facilities like synchrotron light sources or free electron lasers. Here, we motivate the problem of ultrafast, laser-induced magnetization dynamics and review results of near-infrared laser pump and x-ray magnetic circular dichroism probe experiments.

11.1 Introduction

In the last two decades magnetization dynamics driven by the shortest available laser pulses in the range of pico- to femtoseconds have been widely inves-

Uwe Bovensiepen
Faculty of Physics, University Duisburg-Essen Lotharstrasse 1, 47057 Duisburg, Germany, e-mail: uwe.bovensiepen@uni-due.de

Nicolas Bergeard
IPCMS, Université de Strasbourg, 23 rue du Loess BP43, 67034 Strasbourg Cedex 2, France, e-mail: nicolas.bergeard@ipcms.unistra.fr

E. Beaurepaire et al. (eds.), *Magnetism and Synchrotron Radiation: Towards the Fourth Generation Light Sources*, Springer Proceedings in Physics 151,
DOI: 10.1007/978-3-319-03032-6_11,

tigated in magnetically ordered materials [1]. On the one hand, these efforts were motivated by the expectation that an analysis of magnetization dynamics directly in the time domain will lead to novel information which is complementary to the more established frequency domain methods. On the other hand, the laser-excited non-equilibrium state of a magnetic material could feature properties different from the thermodynamic ground state. Such phenomena have the potential for applications in, e.g., extremely fast memory or logic devices [2].

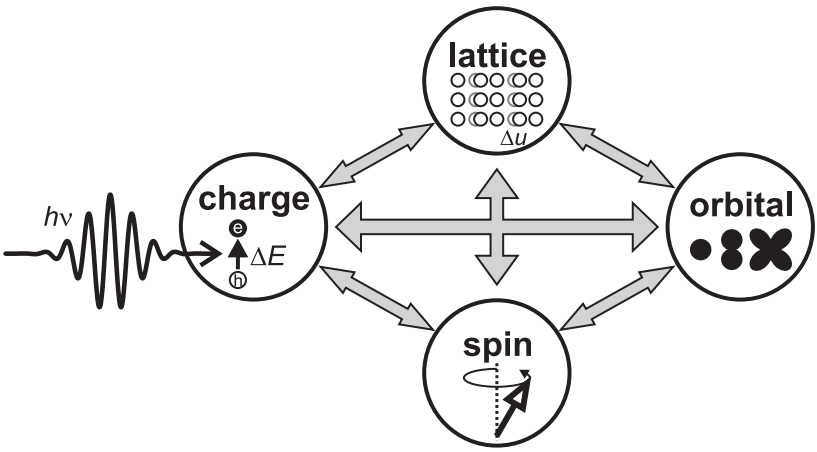

Fig. 11.1 Illustration of the degrees of freedom and their mutual interactions in a solid. The discussion provided here is based on a primary excitation of electrons by the femtosecond laser pulse of photon energy $h\nu = \Delta E$. Phonons represent excitations of the lattice by a displacement Δu of the ion core. Spin precession around an external magnetic field or spin wave excitations represent the dynamics of the spin systems. The orbital and angular moments are important in understanding spin-lattice interaction, as discussed below

However, the understanding of even the most basic phenomena in ultrafast magnetization dynamics like the photo-induced reduction of a magnetization after optical excitation by a femtosecond laser pulse [3, 4, 5], is still controversial [6, 7] and not understood. For the analysis of femtosecond laser-induced dynamics it is helpful to consider the charge, lattice, spin, and orbital degrees of freedom of a solid, which are illustrated by Fig. 11.1 together with their mutual interactions. The pump laser pulse deposits energy in the solid through absorption of photons and excitations of hot electrons and holes. This

excess energy is dissipated subsequently, according to the respective interaction strength, as excitations of the further degrees of freedom. The use of femtosecond laser pulses in combination with time-resolved detection specific to these degrees of freedom offers opportunities to analyze the energy redistribution directly in the time domain and to determine the respective interaction strength. To reach this goal several time-resolved methods have to be combined and employed on similar or comparable materials and samples. In this chapter we will focus on time-resolved photoelectron spectroscopy and x-ray magnetic circular dichroism as examples of methods which probe the electron and spin subsystems. Based on modelling we will conclude on the role of the lattice degree of freedom. The relevance of the orbital degree of freedom will be studied by comparison with appropriate materials.

The chapter is structured as follows. In the remaining introductory part of this section, equilibrium spin-wave dynamics and photo-excited non-equilibrium conditions in metallic ferromagnets will be addressed. In Section 11.2, the generation of femtosecond x-ray pulses in the so-called slicing operation and the experimental realization at BESSY II synchrotron light source at the Helmholtz Zentrum Berlin, Germany, will be described. Section 11.3 provides a review of recent experimental results which have been obtained using time-resolved x-ray magnetic circular dichroism on the femtoslicing facility at BESSY II. We do not intend to provide a complete review of the field but aim at a reader with a background in x-ray absorption who is interested in a basic understanding of ultrafast magnetization dynamics with an emphasis on time-resolved soft x-ray spectroscopy. Therefore, we restrict ourselves to discuss selected examples of this rather new approach to ultrafast magnetization and spin dynamics by femtosecond time-resolved x-ray magnetic circular dichroism.

11.1.1 Spin dynamics in metallic ferromagnets

The excitations of a ferromagnetically ordered system with a magnetization $\mathbf{M}$ are described by the dispersion relation of magnons or spin waves $\Omega(q)$. The involved frequencies range from GHz for modes in the center of the Brillouin zone [1], which are investigated with ferromagnetic resonance or Brillouin light scattering [8], to high frequency magnons towards the Brillouin zone

[1] A frequency of 10 THz corresponds to an energy of the mode of $\hbar\Omega = 41.4$ meV.

boundary at 10 – 100 THz. These are typically probed by inelastic neutron scattering [9] in the bulk of ferromagnetic materials. At surfaces, the energy loss of reflected spin-polarized electrons is analyzed in spin-polarized energy loss spectroscopy [10]. Both methods provide information on the frequency and the lifetime of magnons by means of the energy change and the line width in the spectrum, respectively. In ferromagnetic metals, the line width of magnon signatures strongly depends on the magnon frequency. For zone center modes analyzed by ferromagnetic resonance the line width is usually about $0.1 - 5\,\mu$eV [11, 12] which provides an estimate of the respective relaxation times $\tau = \hbar/\Gamma$ ranging from 7 ns to 140 ps. The line width of high frequency magnons is typically $10 - 100$ meV and therefore considerably broader. The relaxation time becomes as short as several 10 fs [10]. Such short relaxation times are explained by very efficient relaxation channels for these excitations. For metallic ferromagnets the high frequency spin waves interact in particular with electronic excitations [13, 14]. Low frequency spin waves have obviously a smaller phase space available for their relaxation and couple to phonons and other magnons. It is important to note that in such a line width discussion, inelastic and elastic relaxation, which result respectively in population decay and phase decoherence, add up to the total line width following Matthiesen's rule. Therefore, it is more appropriate to refer to a relaxation time rather than to a life time.

We consider spin waves as the quantized excitations of a ferromagnet in a *single* particle limit where the magnetization **M** remains essentially unchanged taking the sensitivity of experimental methods into account. In the following we will discuss on what time scale **M** can be modified by an optical excitation. To generate a sizeable photo-induced change like several percent of **M**, *many* particles have to be excited. Since generation of magnons might be a reasonable starting point to reduce the magnetization we can expect that the magnetization can be modified on a time scale at which magnons are generated and / or relax, which is in the femtosecond time regime (see above). Such ultrafast time scales can be investigated by pump-probe experiments which are based on a separation of an excitation (pump) and a time-delayed detection (probe) by employing correlation techniques [15].

A first experiment was carried out by Vaterlaus et al. on a Gd film by time- and spin-resolved photoelectron detection [16]. In this study a 10 ns laser pulse at 2.15 eV photon energy served as a pump pulse. It was synchronized to a 60 ps probe pulse at 3.2 eV which generated the photoelectrons analyzed regarding their spin polarization. Albeit the time-resolution of this experiment was limited, a response of the detected spin polarization, which was delayed

with respect to the optical excitation, was observed. The determined delay of (100 ± 80) ps was assigned to the spin-lattice relaxation time of Gd. Few years later Beaurepaire et al. performed a femtosecond time-resolved experiment by detecting the magneto-optical Kerr effect in a Ni film. A drop in the magneto-optical signal close to 50% was found to occur within a delay of 1 ps after optical excitation and represents the first observation of femtosecond magnetization dynamics [3]. An independent experiment by Hohlfeld et al. confirmed this observation [4] soon after and was followed by many reports since then [1]. At the time, this was an unexpected result because the change in **M** of the sample as a whole requires a transfer of the respective angular momentum to another degree of freedom like the crystal lattice as suggested by the Einstein-de Haas effect. However, the problem was, and we have to say, still is that the magnetization change occurs on a time scale at which spins cannot *a priori* be assumed to interact with the lattice efficiently [6, 7]. Up to now, no agreement on the process underlying femtosecond demagnetization has emerged, although several scenarios are under discussion. Here, we do not aim at a complete review of this discussion since it is ongoing. We will restrict ourselves to a brief description of the mechanisms under consideration which is useful for our focus on time-resolved x-ray magnetic dichroism. These mechanisms are (i) phonon- or defect-mediated spin-flip scattering which transfer with each scattering event magnetic moment from the spin system to the lattice [17]; (ii) magnon emission at so-called hot-spots of the exchange-split electronic band structure originating from spin-orbit coupling [18]; (iii) superdiffusive spin-dependent transport phenomena, which are proposed to transfer spin-polarization out of the sample part probed experimentally [19]. While the first two scenarios imply a reduction of **M**, the latter one proposes a constant **M** combined with a spatial rearrangement of the local spin density within the sample.

Note that laser-induced magnetization dynamics was also observed in dielectric and semiconducting materials. However, so far no femtosecond x-ray experiments were performed. For a review and further literature covering dynamics in these materials see Ref. [1].

11.1.2 The photo-excited state and its relaxation in metallic ferromagnets

Interaction of femtosecond laser pulses with metals consists primarily of a transient polarization of the quasi-free electron density which is driven by the optical field. In case of reflection, this transient light polarization decays by emission of photons. In case of photon absorption, the transient polarization transforms into electron-hole pairs whose difference in binding energies equals the energy of the absorbed photon. Under the employed experimental conditions *hot* electron densities of $10^{18} - 10^{22}\,\mathrm{cm}^{-3}$ are excited. Therefore, the excited charge carriers scatter with each other, which leads within several 100 fs to a thermalized electron distribution function which is characterized by electron temperature T_e on the order of 1000 K [20, 21, 22].

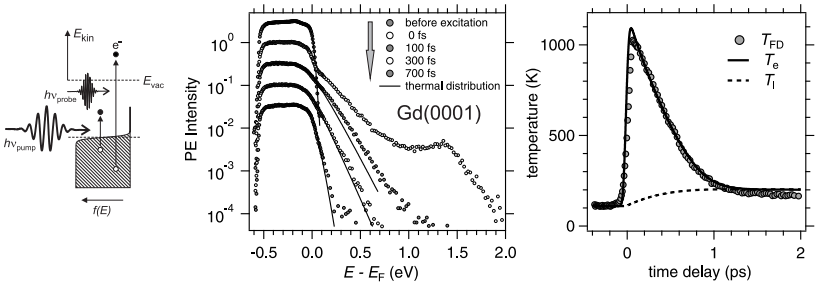

Fig. 11.2 The optically excited state of a 20 nm epitaxial film Gd(0001)/W(110) is analyzed by femtosecond time-resolved photoelectron spectroscopy. Left panel: Scheme of the experiment. Center panel: Symbols represent the photoelectron intensity in normal emission direction on a logarithmic scale at selected time delays; solid lines indicate thermalized electron distribution functions. Right panel: Electron temperatures extracted from the thermalized distribution functions are shown by circles and the result of a calculation following the two-temperature model for the time-dependent electron and lattice temperatures T_e and T_l are depicted by solid and dashed lines, respectively. Data were recorded at 10 K equilibrium temperature, at $0.25\,\mathrm{mJ.cm}^{-2}$ absorbed pump laser fluence, and are taken from [22] with permission of IOP publishing, copyright 2007

Such excited electron distributions are analyzed experimentally e.g. by time-resolved optical [20] and photoelectron spectroscopy [22]. In the latter, an infrared (IR) pump pulse is followed by an ultraviolet (UV) probe pulse which generates photoelectrons as illustrated by Fig. 11.2, left. These are analyzed regarding energy and momentum by an electron spectrometer [23, 24].

Such experiments were carried out for noble metals [23] as well as for the model ferromagnets Ni [21] and Gd [22]. The center panel shows exemplary data for Gd(0001). Thanks to the large dynamical range of the spectra the time-dependent evolution of the electron distribution can be analyzed directly. During the optical excitation, i.e. at a time delay of 0 fs, the distribution function is clearly non-thermal, which is recognized from the spectrum shown on a logarithmic intensity axis in Fig. 11.2, center panel. It presents a kink at the Fermi energy E_F and a cutoff near the sum of the pump photon energy $h\nu_{pump} = 1.5\,eV$ and E_F. With increasing time delay the deviation between a thermalized and the measured distribution function recedes and becomes negligible after 300 fs. Therefore, the so-called two-temperature model [25], which assumes that the energy absorbed from the pump laser pulse is converted directly into an increase of T_e, is in fact a simplification of the real situation. However, its estimations can still be a good guidance for a quantitative discussion in many metals. The reason is that beside the non-equilibrium state in the electronic system it provides quantitative information on heat transfer to the lattice by e-ph coupling and cooling of T_e. [2] Returning to Fig. 11.2 we consider in the next step the thermalized part of the electron distribution function for all delays and plot the respective, experimentally determined T_e in the right panel as a function of time delay. A calculation by the two-temperature model employing known material constants and experimental parameters provides a very reasonable quantitative description, see Ref. [22] for details. Within 100 fs a T_e near 1000 K is reached. This high value only takes the thermalized electrons into account and relaxes within 1.5 ps due to e-ph coupling to a temperature of 200 K, which is 100 K above the equilibrium temperature at which the experiment was carried out. This value of 200 K also represents the equilibrated state of the charge and the lattice degrees of freedom with $T_l = T_e$ at this delay. Note that time-resolved electron diffraction experiments provide the complementary experimental information on lattice excitations by analyzing the transient Debye-Waller Factor [28]. In Fig. 11.2 small deviations between the experimental data and the modelling of $T_e(t)$ occur within the time regime of electron thermalization up to about 200 fs since non-thermal electrons are neglected. Later for delays > 1.5 ps T_e drops faster than suggested by the model, which is attributed to transport effects across the W-Gd interface not taken into account here. For a more extensive discussion of this model we refer to the literature [20, 29, 26]. For the purpose of the present overview, we

[2] Note that in some metals pronounced deviations from the two-temperature model were reported due to transport effects [26, 27]

conclude that the two-temperature model provides a reasonable quantitative estimate of the (i) time-dependent electronic temperatures and the respective excess energy densities reached by a fs laser excitation and (ii) energy dissipation by e-ph coupling to the lattice. Fig. 11.2, right, shows directly that under excitation conditions typically applied in experimental studies of ultrafast magnetization dynamics electronic temperatures of 1000 K or above are reached within few 100 fs. Furthermore it highlights that the excess energy in the electronic subsystem is dissipated to and equilibrates with lattice excitations in about 1 ps. [3]

11.2 Experimental aspects

Various forms of x-ray dichroic spectroscopy are well known for their unique way to investigate magnetic properties on short length scales with element specificity and orbital/spin momentum sensitivity [32]. In particular, XMCD [33] and X-ray Magnetic Linear Dichroism (XMLD) [34] in the soft x-ray energy range can be considered as milestones here. For XMCD, the so-called sum rules are established as a powerful tool to distinguish the orbital and spin contribution of the magnetic moment in the case of transition metals [35, 36, 37, 38]. To add femtosecond time-resolution here, a serious technological challenge had to be solved, i.e. the generation of sub-picosecond light pulses in the soft x-ray regime, preferably with circularly polarization. Nowadays, sub-picosecond x-ray pulses are available from table-top laser setups [39, 40, 41] and at free electron laser such as FERMI@elettra (Trieste), FLASH (Hamburg), or LCLS (Stanford), as well as in the third-generation synchrotron light sources, the ALS (Berkeley), BESSY II (Berlin), and the SLS (Villigen). It is worth to emphasize in the present context that BESSY provides circularly polarized x-ray pulses from an insertion device, in the soft x-ray energy range with a duration around 100 fs [42, 43, 44]. [4] In this section we therefore discuss the generation of sub-picosecond x-ray pulses and the setup used to perform pump-probe experiments on the fs-slicing endstation at BESSY II.

[3] For higher laser pump fluence this time scale increase but remains near 1 ps [30, 31].

[4] Ultrashort circularly polarized pulses are also available at the LCLS. The polarization is obtained by transmission through a thin ferromagnetic film [45].

11.2.1 Generation of sub-picosecond x-ray pulses employing bunch slicing

In synchrotron radiation (SR) facilities, x-rays are emitted as pulses, whose duration is determined by the length of electron bunches in the storage ring. In normal mode operation the time duration of x-ray pulses is between 30 and 100 ps. It can be reduced to few picoseconds if the electron optics in the storage ring is operated in the so-called low-α mode [46]. This mode was initially developed to produce intense and coherent THz emission [47], but it also offers the possibility to perform time-resolved spectroscopy with picosecond resolution [48]. The duration of x-ray pulses in the low-α mode is limited to picoseconds due to stability requirements of the electron orbit in the storage ring.

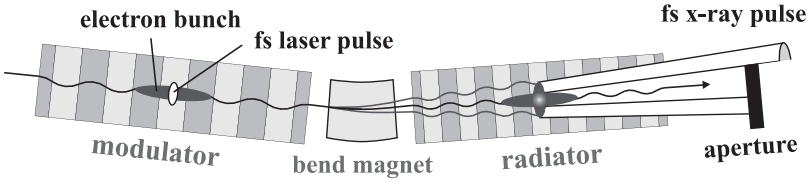

Fig. 11.3 Scheme of the part of the storage ring BESSY II essential for generation of fs x-ray pulses with polarization control. In the first undulator (modulator) the electron energy is modified by interaction with the laser pulse within an ultrashort slice of the bunch. In the bending magnet the different fractions of the bunch are dispersed spatially according to their respective energy. In the second undulator (radiator) the femtosecond x-ray pulses are generated. The figure is extracted from Ref. [44]. Copyrighted 2006 by the American Physical Society

A further reduction of the x-ray pulse duration to the sub-picosecond regime is possible in the so-called femtosecond slicing [42]. This mode, which was first realized at the ALS in Berkeley [43], employs energy modulation of an ultrashort "slice" of the full electron bunch inside an insertion device. This slice is generated by interaction of a fraction of the electrons in a bunch with a femtosecond laser pulse and is used subsequently for generation of the x-ray pulse. We will outline below the underlying concept and the experimental realization. For a more detailed and complete description we refer the reader to the original literature [42, 44].

Fig. 11.3 depicts the setup at the slicing facility at BESSY II. It employs two insertion devices which are separated by a bending magnet. The first insertion device acts as a modulator in which by interaction with the laser pulse the electron energy is modulated within the slice, whose length corresponds approximately to the duration of the driving laser pulse. The principle of the energy modulation is well-known from accelerator physics [49]. In brief, an undulator is required in order to enable energy transfer between an electron bunch with a copropagating laser beam by introducing a transversal velocity component to the electron bunch. Energy transfer between the electrons in the bunch and the laser field is determined by the phase of the laser field experienced by an electron at the entrance of the undulator. Energy is transferred to or from that electron which results in a sinusoidal energy modulation with the period of one laser wave length. In femtosecond slicing energy is transferred from the laser pulse to the sliced electrons in the bunch. This laser-modified bunch is send through a bending magnet in which electrons are dispersed according to their energy and propagate further into the second insertion device which is termed radiator. As shown in Fig. 11.3, the femtosecond part of the bunch emits the x-rays generated in the radiator in a different direction than the ps part of the bunch. The latter part of x-rays can be blocked by an aperture while the fs fraction enters the beamline and becomes available for pump-probe experiments.

The photon flux provided by the sliced electrons is four orders of magnitude lower than for the full bunch. In the configuration used at BESSY II, 10^3 to 10^4 photons per pulse and per 0.1%bw are emitted by the undulator from the sliced bunch [44]. The radiator allows to set a particular polarization and energy required for a certain experiment. The actual duration of x-ray pulses is mostly determined by the duration of the sliced electron bunch. Although the latter is elongated due to energy-dependent path length differences between the modulator and the radiator, a duration of 100 fs is achieved for x-ray pulses. Since the radiation is generated by an undulator, the photon energy is tunable between 400 and 1400 eV. In addition, the radiator design allows polarization control, from linear to circular. Thereby, the requirements to perform time-resolved x-ray spectroscopy including XMCD are met in combination with sub-picosecond time resolution. What remains is to provide spatial and temporal overlap of the x-ray pulses with the pump pulses at the sample of interest.

11.2.2 Experimental setup for time-resolved XMCD

Considering typical foci of 100 μm and a propagation length on the experimental floor of several 10 m, the challenge in ensuring spatial and temporal overlap becomes quite obvious. Employing beam pointing stabilization and solid optical mounts a successfully operating beamline was established as a user facility in recent years. The setup used for the experiments discussed in Sec. 11.3 is sketched in Fig. 11.4. Very recently, the setup was upgraded regarding the laser system and the beamline, which is to be discussed in a forthcoming publication.

The Ti:Sapphire femtosecond laser system provides laser pulses of 780 nm wave length with 2 mJ energy per pulse at a repetition rate of 1 kHz. Its output is split by a beam splitter to generate pump and probe pulses. One part of the pulse is sent into the insertion device for generation of the femtosecond x-ray pulses. The remaining part is sent on the sample following a variable optical delay in order to scan the time delay between pump and probe. X-rays are detected in transmission through thin film samples supported by a thin foil.

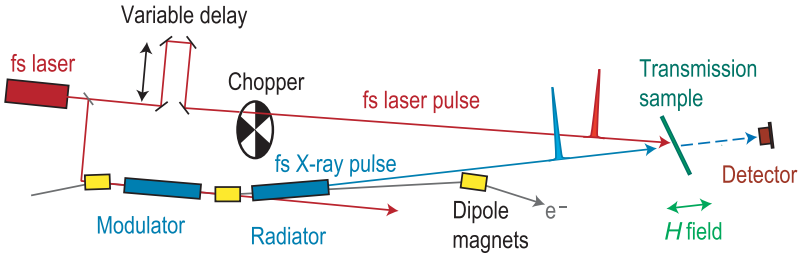

Fig. 11.4 Scheme of the pump-probe experiment at the fs slicing beamline at BESSY II. The chopper allows separation of spectral features for the pumped with respect to the unpumped state. The variable delay facilitates the analysis as a function of pump-probe delay. X-rays transmitted though the sample are detected by an avalanche photodiode detector for different applied magnetic fields. Reprinted by permission from Macmillan Publishers Ltd: [Nature] [5], copyright 2007

We turn to a first example of laser-induced changes in x-ray transmission for Ni which were investigated by employing the full 50 ps bunch as a starting point [50]. The XAS spectrum is measured by recording the transmission through a thin film sample as a function of the photon energy of x-ray pulses with linear polarization. Measuring the XMCD spectrum required the

transmission spectrum of the sample with circular polarization for two opposite orientations of the sample's magnetization. The XAS and XMCD spectra measured at the L_3 edge of a 35 nm thick Ni layer deposited on a 500 nm thick Al foil without and with laser excitation are displayed in Fig. 11.5. The time delay was fixed in this case to 100 ps. While the absorption spectrum does not show pronounced changes, comparison of the dichroic spectra demonstrate a pronounced laser-induced loss of magnetization of more than half compared to the state before laser excitation. This example shows clearly that the method is sensitive to laser-induced changes of the magnetization on picosecond timescales. Considering the discussion of the transient electron and lattice temperatures in Sec. 11.1, electron and lattice subsystems can be considered to be equilibrated at this 100 ps delay. Therefore a temperature increase as a consequence of laser excitation can explain the observed reduction of magnetization well.

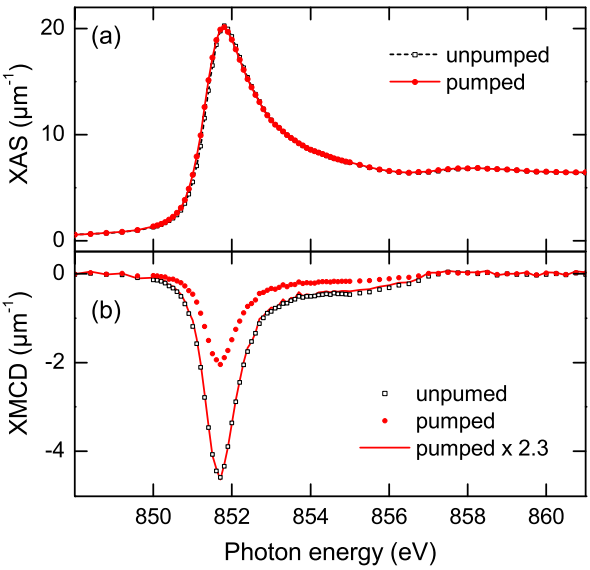

Fig. 11.5 **a** XAS spectra recorded in the normal operation mode of BESSY II in the vicinity of the L_3 edge of a 30 nm Ni layer before (unpumped) and 100 ps after optical excitation (pumped). **b** Respective XMCD spectra. The solid line indicates that the pumped spectrum is identical to the unpumped one if it is multiplied by a factor of 2.3. Figures adapted with permission from [50]. Copyrighted 2009 by the American Physical Society

Such an experiment in the normal operation mode with several 10 ps x-ray pulse duration is very useful for preparation purposes of the femtosecond analysis, which is discussed in the subsequent section.

11.3 Experimental results of fs time-resolved XMCD for $3d$ and $4f$ ferromagnets

The advantages of XMCD spectroscopy are its element specificity including the sensitivity to the $4f$ magnetic moments in rare-earth compounds and the separation of the spin and the orbital magnetic moments in transition metals [35, 36]. In this section, we review selected experiments performed at the femtoslicing beamline at BESSY II, which employed femtosecond time-resolved XMCD.

11.3.1 Itinerant systems

We start with itinerant systems and discuss two experiments analyzing the ultrafast dynamics in Ni [5, 51] and in a $Co_{50}Pd_{50}$ alloy [52].

11.3.1.1 Ultrafast magnetization dynamics in Ni

The first experiment using femtosecond time-resolved XMCD (tr-XMCD) was carried out with Ni [5]. The energy of x-ray pulses was kept fixed and set to the maximum XMCD at the L_3 edge before optical pumping. The decrease of the transient XMCD, which is displayed on Fig. 11.6, demonstrates that the ferromagnetic order in Ni is reduced by more than 50% with a characteristic time scale of (120 ± 70) fs, which is in agreement with previous optical experiments [3].

11.3.1.2 Validity of sum rules on the sub-picosecond range

In order to apply the sum rules, both the XMCD and the isotropic XAS spectra are needed [38, 32]. It is essential to cross check the validity of sum

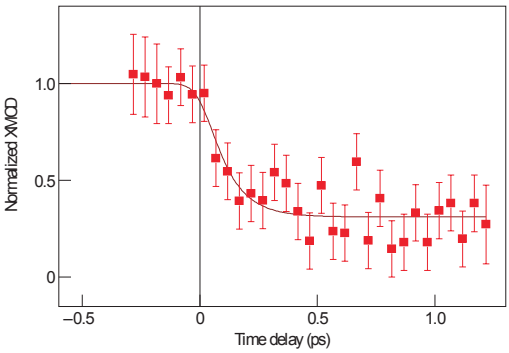

Fig. 11.6 Time-dependent XMCD at the L_3 edge of Ni (symbols) within 1 ps and fit by a single exponential decay (solid line). Reprinted by permission from Macmillan Publishers Ltd: [Nature] [5], copyright 2007

rules in the optically excited, non-equilibrium state. With this goal XAS and XMCD spectra were computed at the $L_{2,3}$ edges of a transition metal in the optically excited state by Oppeneer and coworkers [53]. *Ab initio* calculations taking into account the laser-induced repopulation of electronic states and an enhanced transient electron temperature (see Sec. 11.1.2) were carried out [5]. The repopulation of electrons causes a shift of the XAS line at the L_3 edge towards lower energy as well as a broadening of the edge, as depicted on Fig. 11.7a (top panel). This can be understood by the following argument: On the one hand, some states accessible in the x-ray absorption process ($h\nu = 851$ eV) at equilibrium become occupied due to the absorption of pump photons ($h\nu = 1.5$ eV), which reduces the x-ray absorption yield at higher energy, just above the absorption edge. On the other hand, states which are occupied under equilibrium conditions become available for x-ray absorption just below the edge, explaining the increased absorption yield at lower x-ray photon energy. The difference of XAS spectra before and after pumping are displayed Fig. 11.7a (bottom panel) and compare well with the experimental data obtained by Stamm et al. in Fig. 11.7b [5]. The computed spectra reproduce the features observed experimentally at the $L_{2,3}$ edges of Ni.

The calculated XMCD spectra at the Ni $L_{2,3}$ edges before and after pumping [53] are shown in Fig. 11.7c. Repopulation and a thermalized hot distribu-

[5] The employed computational method has already been used to compute XAS and XMLD spectra under static conditions before [54, 55].

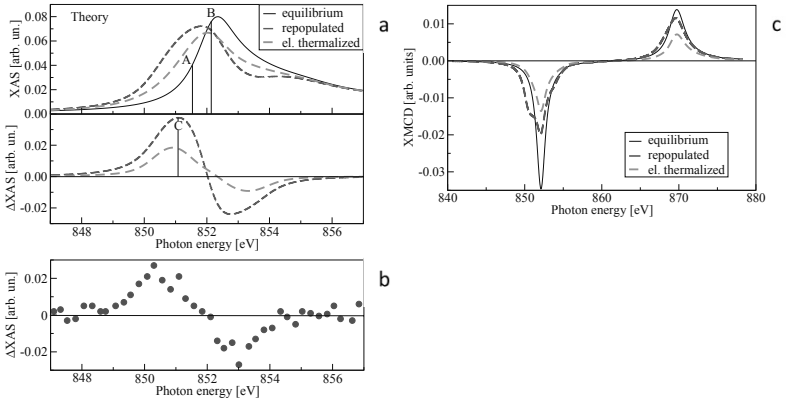

Fig. 11.7 **a** top: Computed XAS spectra at the L_3 edge of Ni before (solid line) and after (dashed lines) the pump excitation; bottom: Difference between XAS spectra before and after the pump excitation. **b** Difference between experimental XAS spectra at the L_3 edge of Ni before and at a delay of 200 fs (data taken from [5]). **c** Calculated XMCD spectra at the $L_{2,3}$ edges of Ni before and after the pump laser excitation. Figures extracted from [53] and figure 11.7b reprinted with permission from Macmillan Publishers Ltd: [Nature] [5], copyright 2007

tion of electrons, cause a decrease of XMCD at both edges. Electronic repopulation induces in addition a modification of the XMCD spectrum. As a consequence, the reduction of XMCD is not linearly distributed over the absorption edge. Therefore, changes over the whole absorption edge have to be taken into account. This is achieved experimentally by averaging over an energy range determined by the resolution of the femtoslicing beamline monochromator, which is on the order of the broadening of a typical L_3 edge [56].

In a next step, the sum rules were applied to determine the orbital and spin magnetic moment of Ni on a fs time scale theoretically. In the case of repopulation of electrons, the total spin should be conserved, since spin flips due to photon absorption are forbidden in the dipole approximation. The effective orbital momentum measured in XMCD can be modified in response to the optical excitation among 4*sp* and 3*d* states. In the case of thermalized electrons at higher temperature, both the spin and the orbital magnetic moments are expected to decrease, which is observed in the calculations. Based on this result, it was concluded that the sum rules remain valid on the sub-picosecond time scale.

11.3.1.3 Experimental determination of the transient spin and orbital magnetic moment

The first experimental observation of ultrafast dynamics in the orbital and spin magnetic moment was reported for Ni [5, 50, 51]. In order to apply the sum rules, XMCD and XAS spectra at the L_3 and L_2 edges of Ni have been recorded. The relations between the XMCD amplitude at the L_3 and L_2 edges and the spin and the orbital magnetic moment with quantum numbers S and L, respectively, are given by Eqs. 11.1 and 11.2 [51]. D_3 and D_2 denote the XMCD while A_3 and A_2 denote the integrated signal of the XAS spectra at L_3 and L_2 edges respectively [6], $\hbar$ is the Planck constant divided by 2π, and n_h is the number of holes in the valence band [7].

$$S\hbar = -\frac{1}{2}\frac{D_3 - 2D_2}{A_3 + A_2}\hbar n_h \tag{11.1}$$

$$L\hbar = -\frac{2}{3}\frac{D_3 + D_2}{A_3 + A_2}\hbar n_h \tag{11.2}$$

XAS spectra of the Ni L_3 and L_2 edges were measured before and 200 fs after the pump excitation. The XAS integrated over the whole $L_{2,3}$ edges is constant within error bar of the experiment. As a consequence, the authors of Ref. [51] considered $A_3 + A_2$ to be constant as a function of time delay. The resulting time-dependent XMCD at the Ni L_3 and L_2 edges are shown in Fig. 11.8a. The time-dependent spin and orbital magnetic moment obtained by Eqs. 11.1, 11.2 are depicted in Fig. 11.8b.

The orbital contribution to the static magnetization in Ni is about 10% [2]. The larger spin part explains the different amplitudes observed in Fig. 11.8b. The quenching of the spin magnetic moment occurs within (130 ± 40) fs, which is in agreement with previous experiments on the full magnetization [3, 5]. Due to the limited experimental accuracy for the orbital part it was difficult to extract a separate characteristic time here. However, the exponential function used to fit the data for S also fits the variation of L. On this basis Stamm et al. concluded that within the experimental accuracy, orbital and spin magnetic moments are reduced in Ni simultaneously [51]. According to this observation, electron orbits do not act as an angular momentum sink

[6] The absorption of photon in the continuum, which is superimposed with the resonant 2p to 3d absorption, is removed by a double step function (see [51]).

[7] The dipolar term, which leads to errors in the order of 0.1, is neglected [32].

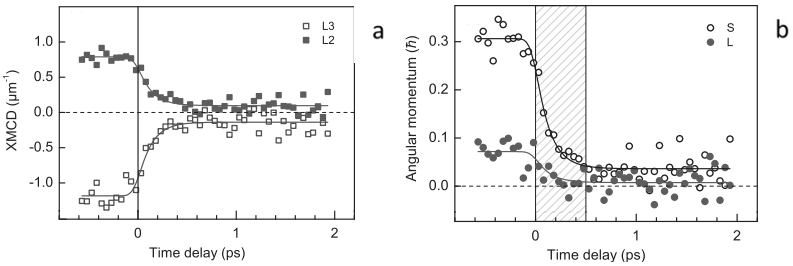

Fig. 11.8 **a** Transient XMCD at the L_3 (open squares) and at the L_2 (filled squares) edges of a 17 nm Ni layer as a function of time delay. The data are fitted with an exponential decay and the time constant is 130 fs for both data sets (solid lines). **b** Spin (S) and orbital (L) momentum as a function of time delay. S and L have been calculated using XMCD at the L_3 and L_2 edges and Eqs. 11.1 and 11.2. Note that L, S refer in Ref. [51] to magnetic moments, rather than to quantum numbers as in Eqs. 11.1 and 11.2. The data are fitted with exponential decay function with a 130 fs time constant (solid lines). Figures adapted with permission from [51]. Copyrighted 2010 by the American Physical Society

and another spin-lattice relaxation channel has to be active, as for instance phonon-mediated spin-flips [6], to explain the loss of magnetic order.

11.3.1.4 Spin and orbital magnetic moment dynamics in $Co_{50}Pd_{50}$

A similar experiment was conducted for a $Co_{50}Pd_{50}$ alloy, which displays perpendicular magnetization anisotropy (PMA). The dynamics of spin and orbital magnetic moments, extracted also following Eqs. 11.1 and 11.2, are displayed in Fig. 11.9a while the ratio between L_z and S_z is displayed on Fig. 11.9b. A variation of 29% of this ratio was reported in connection with different characteristic times for the reduction spin and orbital magnetic moments, which are $\tau_S = (280 \pm 20)$ fs and $\tau_L = (220 \pm 20)$ fs, respectively.

This work on CoPd reports a dynamics of orbital and spin magnetism with two different time constants. The fact that the reported difference is barely outside the error bar shows that both contributions to the magnetic moment exhibit very similar dynamics also in this material. The study suggests an influence of the magnetic anisotropy on the ultrafast magnetization dynamics on the femtosecond time scale. Another report, which is reviewed in the next section, concludes, however, that the magnetic anisotropy acts on the picosecond time scale. Therefore, a quantitative description of the influence of mag-

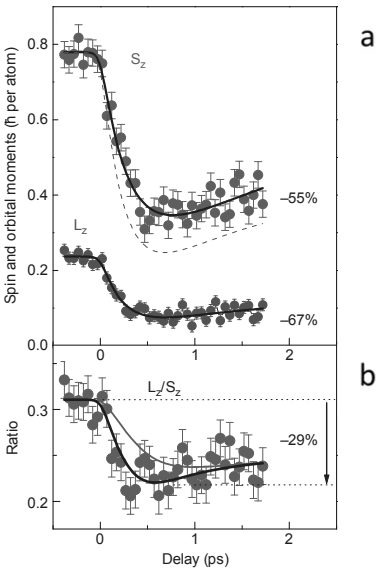

Fig. 11.9 **a** S_z (top) and L_z (bottom) representing the spin and orbital magnetic moment along the sample surface normal direction of a 15 nm $Co_{50}Pd_{50}$ layer as a function of time delay. **b** Ratio between L_z and S_z as a function of time delay. The data are fitted with exponential decay function (solid lines). Figures adapted by permission from Macmillan Publishers Ltd: [Nature] [52], copyright 2010

netic anisotropy on ultrafast magnetization dynamics would be very helpful to achieve understanding of this aspect.

11.3.1.5 Discussion

At the end of the section on magnetization dynamics of itinerant systems we would like point out that at present the mechanism facilitating transfer of angular momentum on the femtosecond time scale is controversial. The simultaneous reduction of spin and orbital magnetic moments in Ni has been interpreted by Stamm et al. [5, 51] as an indication that the transfer of S to the lattice is realized without transient increasing of L in agreement with phonon- or defect-mediated spin-flips [17, 6]. However, the phonon-mediated spin-flip scenario was recently questioned due to quantitative arguments regarding the spin-flip efficiency [7]. On another hand, superdiffusive spin currents excited by the pump laser provide a realistic description of the Ni experiment [19]. Future studies can be expected to clarify this point.

11.3.2 Lanthanide based systems

In lanthanide elements, the magnetic moment is carried mainly by the $4f$ electrons. These electrons are localized around the nucleus and the long range magnetic order is mediated by indirect exchange coupling through $5d6s$ electrons [57]. In rare-earth/transition metals (RE/TM) alloys, the macroscopic ordering of $4f$ magnetic moments has the same origin, but it is affected by the $3d_{\mathrm{TM}}$ electrons [58].

In pump-probe experiments, the IR laser pump pulse excites delocalized electrons [59]. In the introduction of this chapter, we pointed out that previous experiments in Gd observed laser-induced demagnetization on a time scale of 100 ps [16], which was recently confirmed by time-resolved linear magnetic dichroism in photoemission from the $4f$ electronic states [30]. However, in the latter experiment the time resolution suffered from the pulse duration of 50 ps of the probe pulse, since the full bunch of a synchrotron pulse was employed. Recently, the dynamics of the $4f$ magnetic moments has been observed in lanthanides on a time scale faster than the equilibrium spin-lattice coupling time [16, 30] by employing tr-XMCD at the M_5 edge of Tb and Gd with femtosecond resolution [48]. Later, tr-XMCD with femtosecond resolution has been used to investigate the dynamics of Gd and Fe in an $Gd_{25}Fe_{65.6}Co_{9.4}$ amorphous alloy [60]. Those two experiments will be discussed now.

11.3.2.1 Two-step ultrafast demagnetization in ferromagnetic lanthanides

Gd and Tb differ in the electron population of the $4f$ level by one electron. This results in a clear difference of $L = 0$ and 3, respectively, leading to an about 100 times larger, single ion magnetic anisotropy of Tb, and a slightly smaller lattice constant for Tb [61]. The valence electron properties are, however, barely affected. The laser-induced demagnetization of $4f$ magnetic moments in Gd and Tb was measured by XMCD at first in the low α mode with a x-ray pulse duration of 10 ps (see Sec. 11.2.1). The obtained data are shown in Fig. 11.10a. The transient XMCD signal for both elements are quite different. For Gd, half of the demagnetization occurred in the first 10 ps and the magnetization reaches a minimum only after 200 ps. For Tb, the minimum of demagnetization is reached already after 20 ps and the recovery of the magnetization before excitation is progressing from this delay time on,

which is clearly earlier than in Gd. In the case of Gd this remagnetization proceeds within 500 ps. This delay regime was not investigated in the x-ray measurement, but the recovery behavior of $M(t)$ is known from magneto-optical pump-probe experiments [62, 31].

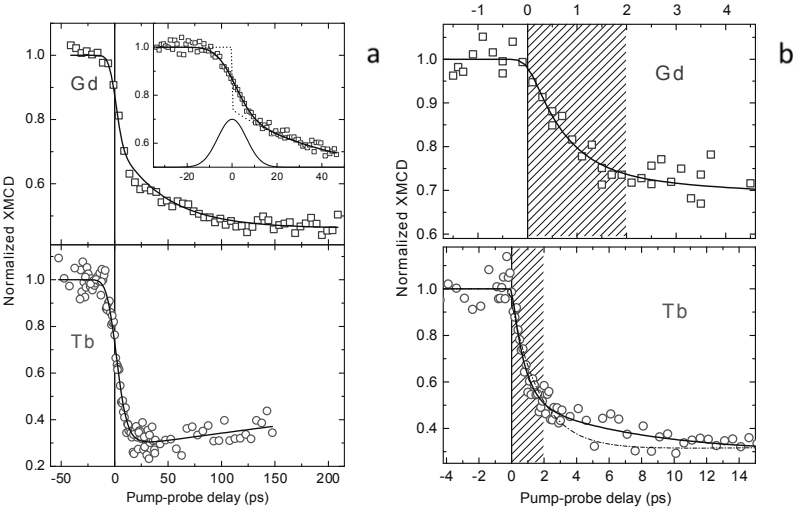

Fig. 11.10 **a** Transient XMCD at the M_5 edge of Gd (top) and Tb (bottom) as a function of time delay recorded with 10 ps x-ray pulse duration. The inset (top) displays a smaller time window for Gd dynamics to emphasize the two steps demagnetization. **b** Transient XMCD at the M_5 edge of Gd (top) and Tb (bottom) as a function of time delay recorded by employing 100 fs x-ray pulses. Data are fitted with double exponential decay functions (solid lines). Figures adapted with permission from [48]. Copyrighted 2011 by the American Physical Society

To resolve the magnetization dynamics of Gd during the first 10 ps, the experiment was done with femtosecond resolution employing fs slicing. The transient XMCD at the M_5 edges of Gd and Tb is depicted in Fig. 11.10b as a function of time delay. A demagnetization of 30% for Gd and 50% for Tb is observed within 2 ps after excitation. For subsequent delays, a slower demagnetization is observed for both elements. These experimental results establish a two step demagnetization of $4f$ magnetic moments in Gd and Tb, which is characterized by a faster and a slower time scale, referred to as τ_1 and τ_2, respectively. A quantitative analysis employing double exponential

decay functions provided $\tau_1^{\mathrm{Gd}} = (0.76 \pm 0.25)$ ps, $\tau_2^{\mathrm{Gd}} = (40 \pm 10)$ ps and $\tau_1^{\mathrm{Tb}} = (0.74 \pm 0.25)$ ps, $\tau_2^{\mathrm{Tb}} = (8 \pm 3)$ ps as the characteristic times. It is concluded that the slower time scales differ and the faster ones are identical for Gd and Tb within the experimental uncertainty.

As discussed in Sec. 11.1.2 of this chapter, equilibration of the photoexcited electrons with the lattice requires about 1 ps in Gd [22]. Thus, the faster demagnetization step occurs during the presence of hot electrons, i.e. in a non-equilibrium regime, and the slower demagnetization proceeds in a time regime after electron-lattice thermalization, i.e. in a quasi-equilibrium regime.

The difference in the slower time constants ($\tau_2^{\mathrm{Gd}} = 40$ ps and $\tau_2^{\mathrm{Tb}} = 8$ ps) is attributed to the difference in direct spin-lattice coupling of $4f$ magnetic moments in the two elements. The $4f$ electrons of Tb have a large orbital momentum ($L = 3$) and exhibit a strong spin-lattice coupling, which provides a more efficient channel to transfer angular momentum in Tb directly. The $L = 0$ of $4f$ electrons in Gd requires $5d$ electrons to explain spin-lattice coupling, which is weak under equilibrium conditions [61] and considered as indirect [48]. The experimental finding $\tau_2^{\mathrm{Gd}} > \tau_2^{\mathrm{Tb}}$ implies that the indirect coupling is also weaker dynamically and therefore affects the magnetization on a longer time scale.

The characteristic times obtained for the fast demagnetization are within the accuracy identical for Gd and Tb. Based on the very similar $5d$ electronic structure of Tb and Gd, hot electron driven enhancement of spin-lattice coupling has been suggested [48]. In this picture, spin-flip scattering (see Sec. 11.1.1) occurs among hot $5d$ electrons [6], which interact with the $4f$ electrons and their magnetic moments. After relaxation of hot $5d$ electrons, i.e. after 1 ps, this channel is therefore no longer available. Recently, time-resolved photoemission experiments provided further insight into the dynamics of majority and minority $5d$ electrons [63].

11.3.2.2 Transient ferromagnetic order in ferrimagnetic rare-earth/transition metals alloys

Having discussed the spin dynamics in $5d6s$ electronic bands and their interaction with $4f$ electrons according to the intraatomic $4f$-$5d$ interaction in elemental Gd and Tb, we turn now to systems combining lanthanides and transition metals. For GdFe alloys, the ordering of Gd magnetic moments is also explained by indirect exchange coupling, however, $5d_{\mathrm{Gd}}$ and $3d_{\mathrm{Fe}}$ electrons are contributing as itinerant electrons. Antiferromagnetic inter-

atomic coupling between $3d_{\mathrm{Fe}}$ and $5d_{\mathrm{Gd}}$ electrons competes with ferromagnetic intraatomic exchange coupling between $4f_{\mathrm{Gd}}$ and $5d_{\mathrm{Gd}}$ electrons [58]. This competition leads to ferrimagnetic order since two antiferromagnetically coupled sublattices with different sublattice magnetization are formed, as illustrated in Fig. 11.11a. Employing the element-selectivity of time-resolved XMCD, an analysis of the separate dynamics of the two sublattices becomes feasable. Such results can be expected to provide insight into the role of exchange coupling on ultrafast magnetization dynamics.

Radu et al. studied the magnetization dynamics of Gd and Fe in a $Gd_{25}Fe_{65.6}Co_{9.4}$ ferrimagnetic alloy by time-resolved XMCD [60]. The composition of the alloy has been chosen in order to obtain a temperature of magnetic compensation $T_{\mathrm{comp}} = 250\,\mathrm{K}$ [8]. The initial temperature of the sample was set to $T = 80\,\mathrm{K}$ and the fluence of the pump laser was set in order to heat the lattice above T_{comp} in the presence of a magnetic field to trigger a magnetization reversal [64]. The dynamics of both sublattices was recorded with femtosecond time resolution. The observed transient XMCD recorded at the Gd M_5 and the Fe L_3 edge is shown in Fig. 11.11b.

At negative delays, the XMCD signals of Gd and Fe exhibit an opposite sign, which is consistent with an antiferromagnetic coupling [65]. At delays $t > 2$ ps, XMCD of Gd and Fe shows again an opposite sign, but the sign of the total magnetization is reversed with respect to the state before optical excitation, i.e. the magnetization direction was switched. Considering the temporal evolution of both sublattice magnetizations one recognizes that they exhibit different characteristic times $\tau_1^{\mathrm{Fe}} = (100 \pm 25)$ fs and $\tau_1^{\mathrm{Gd}} = (430 \pm 100)$ fs. The reversal of Fe sublattice magnetization occurs 300 fs after laser excitation, while it is found at 1.5 ps for Gd. Therefore, the magnetization dynamics of the ferrimagnet results in a transient ferromagnetic state which is observed between 300 fs and 1.5 ps. In this time window the two sublattice magnetizations point in the same direction [60] and a novel non-equilibrium state of magnetic order has been identified by the help of time-resolved XMCD. This transient ferromagnetic state has recently been used to explain ultrafast magnetization switching in similar films in absence of magnetic fields [66].

[8] The temperature of magnetic compensation is the temperature at which the magnetization of the Fe sublattice compensates the magnetization of the Gd sublattice as a consequence of the different temperature dependence of the two sublayer magnetizations. The magnetization of Gd is larger compared to the Fe magnetization for $T < T_{\mathrm{comp}}$. For $T > T_{\mathrm{comp}}$, the magnetization of Fe becomes larger. For all temperatures, the larger magnetization points along the external magnetic field.

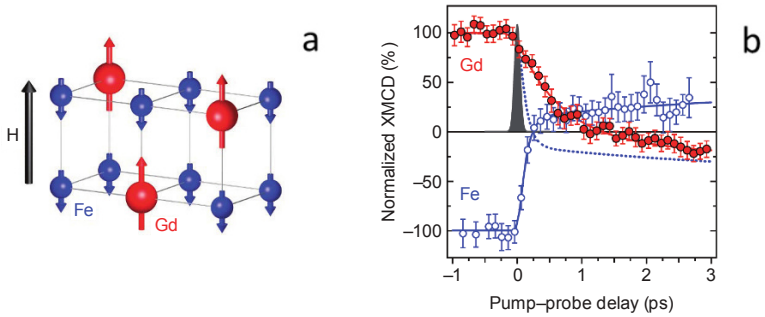

Fig. 11.11 **a** Sketch of the antiferromagnetic coupling between the Gd (longer arrows) and Fe (smaller arrows) sublattices. **b** XMCD signal as a function of time delay at the Gd M_5 edge (filled circles) and at the Fe L_3 edge (open circles). The experimental time resolution of 100 fs is depicted by the filled area of a Gaussian curve at 0 fs. The data are fitted with a double exponential decay (solid lines). Figures adapted by permission from Macmillan Publishers Ltd: [Nature] [60], copyright 2011

11.4 Summary

In this overview, we highlighted time-resolved x-ray magnetic circular dichroism as an unique tool to investigate ultrafast magnetization dynamics. We started by a general introduction to magnetization dynamics, focusing on ultrafast laser-induced dynamics. We proceeded by discussing the generation of femtosecond x-ray pulses in the femtosecond slicing mode at BESSY II of the Helmholtz-Zentrum Berlin, Germany. We finally presented selected experiments which have exploited the opportunities of femtosecond time-resolved XMCD. We discussed the laser-induced quenching of the 3*d* magnetic moment in Ni as well as the spin and orbital dynamics in Ni and $Co_{50}Pd_{50}$. In lanthanides a two-step demagnetization dynamics was observed at the 4*f* magnetic moments in Gd and Tb. Finally, the element specificity of tr-XMCD was used to investigate the separate sublattice magnetization dynamics of Gd and Fe in a ferrimagnetic alloy. It revealed an novel transient ferromagnetic state. In all the results presented here, the transient transmission of a thin magnetic layer deposited on thin membranes was measured. This approach results in considerable limitations due to heat accumulation within the sample. The development of time resolved resonant soft x-ray reflectivity and scattering [67] will widely increase the range of materials and the respective transient

phenomena which can be tackled by time-resolved soft x-ray spectroscopies in near future.

Acknowledgements The authors would like to acknowledge H. A. Dürr, A. Eschenlohr, K. Holldack, T. Kachel, A. Melnikov, N. Pontius, C. Stamm, M. Weinelt, M. Wietstruk for fruitful collaboration and S. Khan for proof reading the manuscript. We are grateful for support from the Helmholtz Zentrum Berlin through access to beamlines of BESSY II and from the German Federal Ministry of Education and Research through the FEMTOSPEX project 05K10PG2.

References

1. Andrei Kirilyuk, Alexey V. Kimel, and Theo Rasing, Rev. Mod. Phys. **82**, 2731 (2010)
2. J. Stöhr and H.-C. Siegmann in *Magnetism: From fundamentals to nanoscale dynamics*, volume 152 of *Springer Series in Solid State Science* (Springer, Berlin, Heidelberg, New York, 2006)
3. E. Beaurepaire, J.-C. Merle, A. Daunois, and J.-Y. Bigot, Phys. Rev. Lett. **76**, 4250 (1996)
4. J. Hohlfeld, E. Matthias, R. Knorren, and K. H. Bennemann, Phys. Rev. Lett. **78**, 4861 (1997)
5. C. Stamm, T. Kachel, N. Pontius, R. Mitzner, T. Quast, K. Holldack, S. Khan, C. Lupulescu, E. F. Aziz, M. Wietstruk, H. A. Dürr, and W. Eberhardt, Nature Mater. **6**, 740 (2007)
6. B. Koopmans, G. Malinowski, F. Dalla Longa, D. Steiauf, M. Fähnle, T. Roth, M. Cinchetti, and M. Aeschlimann, Nature Mater. **9**, 259 (2010)
7. K. Carva, M. Battiato, and P. M. Oppeneer, Phys. Rev. Lett. **107**, 207201, (2011)
8. B. Hillebrands and K. Ounadjela, in *Spin Dynamics in Confined Magnetic Structures I, Topics in Applied Physics*, (Springer, 2002)
9. G. Shirane, V. J. Minkiewicz, and R. Nathans, J. Appl. Phys. **39**, 383 (1968)
10. R. Vollmer, M. Etzkorn, P. S. Anil Kumar, H. Ibach, and J. Kirschner, Phys. Rev. Lett. **91**, 147201 (2003)
11. S.S. Kalarickal, P. Krivosik, M. Wu, C.E. Patton, M.L. Schneider, P. Kabos, T.J. Silva, and J.P. Nibarger, J. Appl. Phys. **99**, 093909 (2006)
12. W. Platow, A.N. Anisimov, G.L. Dunifer, M. Farle, and K. Baberschke, Phys. Rev. B, **58**, 5611 (1998)
13. H. Ibach and H. Lüth, in *Solid-State Physics*, (Springer, 4th edition, 2009)
14. J. Hong and D. L. Mills, Phys. Rev. B, **59**, 13840 (1999)
15. W. Demtröder, in *Laser Spectroscopy, Vol. 2: Experimental Techniques*, (Springer, 4th edition, 2008)
16. A. Vaterlaus, T. Beutler, and F. Meier, Phys. Rev. Lett. **67**, 3314 (1991)
17. B. Koopmans, J. J. M. Ruigrok, F. Dalla Longa, and W. Jonge, Phys. Rev. Lett. **95**, 267207 (2005)

18. M. Pickel, A. B. Schmidt, F. Giesen, J. Braun, J. Minár, H. Ebert, M. Donath, and M. Weinelt, Phys. Rev. Lett. **101**, 066402 (2008)
19. M. Battiato, K. Carva, and P. M. Oppeneer, Phys. Rev. Lett. **105**, 027203 (2010)
20. J. Hohlfeld, S.-S. Wellershoff, J. Güdde, U. Conrad, V. Jähnke, and E. Matthias, Chem. Phys. **251**, 237 (2000)
21. H.-S. Rhie, H. A. Dürr, and W. Eberhardt, Phys. Rev. Lett. **90** 247201 (2003)
22. U. Bovensiepen, J. Phys.: Condens. Matter **19**, 083201 (2007)
23. W. S. Fann, R. Storz, H. W. K. Tom, and J. Bokor, Phys. Rev. B **46**, 13592 (1992)
24. U. Bovensiepen and P. S. Kirchmann, Las. Photon. Rev. **6**, 589 (2012)
25. S.I. Anisimov, B.L. Kapeliovich, and T.L. Perelman, Sov. Phys. JETP **39**, 375 (1974)
26. M. Lisowski, P.A. Loukakos, U. Bovensiepen, J. Stähler, C. Gahl, and M. Wolf, Appl. Phys. A: Mat. Sci. Proc. **78**, 165 (2004)
27. X. Liu, R. Stock, and W. Rudolph, Phys. Rev. B **72**, 195431 (2005)
28. M. Ligges, I. Rajkovic, P. Zhou, O. Posth, C. Hassel, G. Dumpich, and D. von der Linde, Appl. Phys. Lett. **94**, 101910 (2009)
29. M. Bonn, D. N. Denzler, S. Funk, M. Wolf, S.-S. Wellershoff, and J. Hohlfeld, Phys. Rev. B **61**, 1101 (2000)
30. A. Melnikov, H. Prima-Garcia, M. Lisowski, T. Gießel, R. Weber, R. Schmidt, C. Gahl, N. M. Bulgakova, U. Bovensiepen, and M. Weinelt, Phys. Rev. Lett. **108**, 107202 (2008)
31. M. Sultan, A. Melnikov, and U. Bovensiepen, Phys. Stat. Sol. B **248**, 2323 (2011)
32. J. Stöhr, J. Magn. and Magn. Mater. **200**, 470 (1999)
33. C. T. Chen, F. Sette, Y. Ma, and S. Modesti, Phys. Rev. B **42**, 7262 (1990)
34. G. van der Laan, B.T. Thole, G.A. Sawatzky, J.B. Goedkoop, J.C. Fuggle, J.-M. Esteva, R. Karnatak, J.P. Remeika, and H.A. Dabkowska, Phys. Rev. B **34**, 6529 (1986)
35. B.T. Thole, P. Carra, F. Sette, and G. van der Laan, Phys. Rev. Lett. **68**, 1943 (1992)
36. Paolo Carra, B. T. Thole, Massimo Altarelli, and Xindong Wang, Phys. Rev. Lett. **70**, 694 (1993)
37. J. Stöhr and H. König, Phys. Rev. Lett. **75**, 3748 (1995)
38. C.T. Chen, Y.U. Idzerda, H.J. Lin, N.V. Smith, G. Meigs, E. Chaban, G.H. Ho, E. Pellegrin, and F. Sette, Phys. Rev. Lett. **75**, 152 (1995)
39. T. Popmintchev, M.C. Chen, D. Popmintchev, P. Arpin, S. Brown, S. Ališauskas, G. Andriukaitis, T. Balčiunas, Oliver D. Mücke, A. Pugzlys, A. Baltuška, B. Shim, S. E. Schrauth, A. Gaeta, C. Hernández-García, L. Plaja, A. Becker, A. Jaron-Becker, M.M. Murnane, and H.C. Kapteyn, Science **336**, 1287 (2012)
40. T. Pfeifer, C. Spielmann, and G. Gerber, Rep. Prog. Phys. **69**, 443 (2006)
41. S. Corde, K. Ta Phuoc, G. Lambert, R. Fitour, V. Malka, A. Rousse, A. Beck, and E. Lefebvre, Rev. Mod. Phys. **85**, 1 (2013)
42. A. A. Zholents and M. S. Zolotorev, Phys. Rev. Lett. **76**, 912 (1996)
43. R.W. Schoenlein, S. Chattopadhyay, H. Chong, T.E. Glover, P.A. Heimann, C.V. Shank, A.A. Zholents, and M.S. Zolotorev, Science, **287**, 2237 (2000)
44. S. Khan, K. Holldack, T. Kachel, R. Mitzner, and T. Quast, Phys. Rev. Lett. **97**, 074801 (2006)
45. T. Wang, D. Zhu, B. Wu, C. Graves, S. Schaffert, T. Rander, L. Müller, B. Vodungbo, C. Baumier, D.P. Bernstein, B. Bräuer, V. Cros, S. De Jong, R. Delaunay, A. Fognini, R. Kukreja, S. Lee, V. Lopez-Flores, J. Mohanty, B. Pfau, H. Popescu, M. Sacchi, A.B. Sardinha, F. Sirotti, P. Zeitoun, M. Messerschmidt, J.J. Turner, W.F. Schlotter,

O. Hellwig, R. Mattana, N. Jaouen, F. Fortuna, Y. Acremann, C. Gutt, H. A. Dürr, E. Beaurepaire, C. Boeglin, S. Eisebitt, G. Grübel, J. Lüning, J. Stöhr, and A.O. Scherz, Phys. Rev. Lett. **108**, 267403 (2012)
46. H. Wiedemann, Particle Accelerator Physics, (Springer, 2007)
47. M. Abo-Bakr, J. Feikes, K. Holldack, P. Kuske, W. B. Peatman, U. Schade, G. Wüstefeld, and H.-W. Hübers, Phys. Rev. Lett. **90**, 094801 (2003)
48. M. Wietstruk, A. Melnikov, C. Stamm, T. Kachel, N. Pontius, M. Sultan, C. Gahl, M. Weinelt, H. A. Dürr, and U. Bovensiepen, Phys. Rev. Lett. **106**, 127401 (2011)
49. K. Wille, *The physics of particle accelerators: An introduction*, (Oxford University Press, Oxford, 2000)
50. T. Kachel, N. Pontius, C. Stamm, M. Wietstruk, E. F. Aziz, H. A. Dürr, W. Eberhardt, and F. M. F. de Groot, Phys. Rev. B **80**, 092404 (2009)
51. C. Stamm, N. Pontius, T. Kachel, M. Wietstruk, and H. A. Dürr, Phys. Rev. B **81**, 104425 (2010)
52. C. Boeglin, E. Beaurepaire, V. Halté, V. López-Flores, C. Stamm, N. Pontius, H. A. Dürr, and J.Y. Bigot, Nature **465**, 458 (2010)
53. K. Carva, D. Legut, and P.M. Oppeneer, EuroPhys. Lett. **86**, 57002 (2009)
54. J. Kuneš, P. M. Oppeneer, H.Ch. Mertins, F. Schäfers, A. Gaupp, W. Gudat, and P. Novák, Phys. Rev. B **64**, 174417 (2001)
55. J. Kuneš and P.M. Oppeneer, Phys. Rev. B **67**, 024431 (2003)
56. A. Erko, A. Firsov, and K. Holldack, AIP Conf Proc **1234**, 177 (2010)
57. I.A. Campbell, J. Phys. F: Met. Phys. **2**, L47 (1972)
58. M.S.S Brooks, L. Nordstrom, and B. Johansson, J. Phys.: Condens. Matter. **3**, 2357 (1991)
59. J.L. Erskine and E.A. Stern, Phys. Rev. B **8**, 1239 (1973)
60. I. Radu, K. Vahaplar, C. Stamm, T. Kachel, N. Pontius, H.A. Drr, T.A. Ostler, J. Barker, R.F.L. Evans, R.W. Chantrell, A. Tsukamoto, A. Itoh, A. Kirilyuk, T. Rasing, and A.V. Kimel, Nature **472**, 205 (2011)
61. B. Coqblin, *The electronic structure of rare-earth metals and alloys*, (Academic Press, London and New York, 1977)
62. M. Lisowski, P.A. Loukakos, A. Melnikov, I. Radu, L. Ungureanu, M. Wolf, and U. Bovensiepen, Phys. Rev. Lett. **95**, 137402 (2005)
63. Robert Carley, Kristian Döbrich, Björn Frietsch, Cornelius Gahl, Martin Teichmann, Olaf Schwarzkopf, Philippe Wernet, and Martin Weinelt, Phys. Rev. Lett. **109**, 057401 (2012)
64. C. D. Stanciu, A. Tsukamoto, A. V. Kimel, F. Hansteen, A. Kirilyuk, A. Itoh, and Th. Rasing, Phys. Rev. Lett. **99**, 217204 (2007)
65. E. Goering, S. Gold, and G. Schütz, J. Synch. Rad. **8**, 422 (2001)
66. T.A. Ostler, J. Barker, R.F.L. Evans, R.W. Chantrell, U. Atxitia, O. Chubykalo-Fesenko, S. El Moussaoui, L. Le Guyader, E. Mengotti, L.J. Heyderman, F. Nolting, A. Tsukamoto, A. Itoh, D. Afanasiev, B.A. Ivanov, A.M. Kalashnikova, K. Vahaplar, J. Mentink, A. Kirilyuk, Th. Rasing, and A.V. Kimel, Nature Comm. **3**, 666 (2012)
67. K. Holldack, N. Pontius, E. Schierle, T. Kachel, V. Soltwisch, R. Mitzner, T. Quast, G. Springholz, and E. Weschke, Appl. Phys. Lett. **97**, 062502 (2010)

Index

E. Beaurepaire et al. (eds.), *Magnetism and Synchrotron Radiation: Towards the Fourth Generation Light Sources*, Springer Proceedings in Physics 151,
DOI: 10.1007/978-3-319-03032-6,